IntechOpen

Carbon Nanotubes

Recent Progress

Edited by Mohammed Muzibur Rahman and Abdullah Mohamed Asiri

CARBON NANOTUBES - RECENT PROGRESS

Edited by **Mohammed Muzibur Rahman** and **Abdullah Mohamed Asiri**

Carbon Nanotubes - Recent Progress
http://dx.doi.org/10.5772/intechopen.68691
Edited by Mohammed Muzibur Rahman and Abdullah Mohamed Asiri

Contributors

Parvathalu Kalakonda, Mohammed Muzibur Rahman, Norihiro Shimoi, Shashank Pant, Devashree Atre, Seyyed Alireza Hashemi, Seyyed Mojtaba Mousavi, Ali Mohammad Amani, Yasuhiko Hayashi, Karthik Paneer Selvam, Maik Scholz, Mahfoudh Raissi, Xianqi Wei, Xiaogang Sun, Jie Wang, Manyuan Cai, Long Chen, Zhiwen Qiu, Xu Li, Wei Chen, Keiichi Shirasu, Go Yamamoto, Toshiyuki Hashida, Daniel Nelias, Jin-Seok Park, Bu-Jong Kim, Kazi Hanium Maria, Tetsu Mieno, Antonio Paolo Carlucci, Luciano Strafella, Antonio Ficarella, Domenico Laforgia, Bruce Chehroudi, Krzysztof Winkler, Emilia Gradzka, Arezoo Tahmourespour, Geoffrey Mitchell, Meruyert Nazhipkyzy, Saeed Mohan, Fred Davis, Silambarasan Duraisamy, Surya Velappa Jayaraman, Vasu Veerapandy, Iyakutti Kombiah

Notice

First published in London, United Kingdom, 2018 by IntechOpen
eBook (PDF) Published by IntechOpen, 2019
IntechOpen is the global imprint of INTECHOPEN LIMITED, registered in England and Wales, registration number: 11086078, The Shard, 25th floor, 32 London Bridge Street
London, SE19SG – United Kingdom
Printed in Croatia

British Library Cataloguing-in-Publication Data
A catalogue record for this book is available from the British Library

Additional hard and PDF copies can be obtained from orders@intechopen.com

Carbon Nanotubes - Recent Progress
Edited by Mohammed Muzibur Rahman and Abdullah Mohamed Asiri

p. cm.

Print ISBN 978-1-78923-052-9

Online ISBN 978-1-78923-053-6

eBook (PDF) ISBN 978-1-83881-343-7

Meet the editors

Mohammed Muzibur Rahman received his BSc and MSc degrees from Shahjalal University of Science and Technology, Sylhet, Bangladesh, in 1999 and 2001, respectively. He received his PhD degree from the Chonbuk National University, South Korea, in 2007. After receiving his PhD degree, he worked as a postdoctoral fellow and assistant professor in pioneer research centers and universities located in South Korea, Japan, and Saudi Arabia (2007 to 2011). Presently, he is working as an associate professor in Center of Excellence for Advanced Materials Research (CEAMR) and Chemistry Department at King Abdulaziz University, Saudi Arabia, since 2011. He published more than 214 research articles and several proceedings in well-known high-impact ISI journals, attended more than 60 international and domestic conferences, and published several book chapters and 7 books as an editor. His research work has been largely in the area of carbon nanotubes, nanotechnology, sensors, surface chemistry, electrochemistry, instrumental science, nanomaterials, self-assembled monolayers, photochemistry, -chips and devices, etc.

Abdullah Mohamed Asiri received his PhD degree from the University of Wales, College of Cardiff, UK, in 1995. He is the head of the Chemistry Department at King Abdulaziz University since October 2009, and he is the founder and the director of the Center of Excellence for Advanced Materials Research (CEAMR). He is a professor of Organic Photochemistry. His research interest covers color chemistry, synthesis of novel photochromic and thermochromic systems, synthesis of novel coloring matters and dyeing of textiles, materials chemistry, nanochemistry, nanotechnology, polymers, and plastics. He is the editor in chief of King Abdulaziz University Journal of Science. He is also a member of the Editorial Board of Pigments and Resin Technology (UK), Organic Chemistry in Sight (New Zealand), and Recent Patents on Materials Science (USA). He is the vice-president of Saudi Chemical Society (Western Province Branch).

Contents

Preface XI

Section 1 Introduction 1

Chapter 1 **Introductory Chapter: Carbon Nanotubes and Their Applications 3**
Mohammed Muzibur Rahman and Abdullah Mohamed Asiri

Section 2 State-of-the-Art Physical 9

Chapter 2 **Rapid Growth of Dense and Long Carbon Nanotube Arrays and Its Application in Spinning Thread 11**
Yasuhiko Hayashi, Karthik Paneer Selvam and Maik Scholz

Chapter 3 **Stability and Reliability of an Electrical Device Employing Highly Crystalline Single-Walled Carbon Nanotubes as a Field Emitter 29**
Norihiro Shimoi

Chapter 4 **Carbon Nanotubes as a Pulsed Electron Sources 51**
Xianqi Wei

Chapter 5 **Electric Field Induced Alignment of Carbon Nanotubes: Methodology and Outcomes 71**
Ali Mohammad Amani, Seyyed Alireza Hashemi, Seyyed Mojtaba Mousavi, Seyyed Milad Abrishamifar and Arash Vojood

Chapter 6 **Mechanical and Fracture Properties of Carbon Nanotubes 89**
Keiichi Shirasu, Go Yamamoto, Daniel Nelias and Toshiyuki Hashida

Chapter 7 **Charged Carbon Nanotubes 109**
Devashree Atre and Shashank Pant

Section 3 State-of-the-Art Nanocomposites 125

Chapter 8 **Highly Anisotropic Polymer Composites Based on Carbon Nanotubes 127**
Geoffrey R. Mitchell, Fred J. Davis, Saeed Mohan and Meruyert Nazhipkyzy

Chapter 9 **Recent Progress on Electrochemical Capacitors Based on Carbon Nanotubes 147**
Emilia Grądzka and Krzysztof Winkler

Chapter 10 **Studies of Nanocomposites of Carbon Nanotubes and a Negative Dielectric Anisotropy Liquid Crystal 189**
Parvathalu Kalakonda and Germano S Iannacchione

Section 4 State-of-the-Art Electrochemical 207

Chapter 11 **Applications of Carbon Nanotubes to Flexible Transparent Conductive Electrodes 209**
Bu-Jong Kim and Jin-Seok Park

Chapter 12 **Production of Water Dispersible Carbon Nanotubes and Nanotube/Cellulose Composite 235**
Kazi Hanium Maria and Tetsu Mieno

Section 5 State-of-the-Art Energy 261

Chapter 13 **The Porous Carbon Nanotube-Cellulose Papers as Current Collector and Electrode for Lithium Ion Battery and Supercapacitor Applications 263**
Xiaogang Sun, Manyuan Cai, Long Chen, Zhiwen Qiu, Jie Wang, Xu Li and Wei Chen

Chapter 14 **Potential Application of Photo-thermal Volumetric Ignition of Carbon Nanotubes in Internal Combustion Engines 307**
Antonio Paolo Carlucci, Bruce Chehroudi, Antonio Ficarella, Domenico Laforgia and Luciano Strafella

Chapter 15 **Reversible and Reproducible Hydrogen Storage in Single-Walled Carbon Nanotubes Functionalized with Borane 331**
Duraisamy Silambarasan, Velappa Jayaraman Surya, Veerapandy Vasu and Kombiah Iyakutti

Preface

It gives us immense pleasure in introducing a book titled *Carbon Nanotubes - Recent Progress* based on state of the art of physical, state of the art of nanocomposites, state of the art of electrochemical, as well as state of the art of energy with their outstanding and potential applications. These deal with advanced nanotechnological aspects of the synthesis, growth, development, and potential applications of carbon or hybrid materials such as CNTs. The discussion of these aspects develops through the fundamentals and applied experimental routes in conventional methods via the interaction of carbon nanotubes to finally comprise the interfacing of the science and technological worlds. Today, CNT has undoubtedly accomplished its conventional essence and has taken new directions from preparation to applications in research and development (R&D) areas of science. The new paths and emerging frontiers are branching out from time to time around this advanced nanotechnology stage on nanotubes. Advances in carbon materials with instrumentation for evaluating the structural model materials now enable us to understand quite broadly almost all the events that take place for CNTs at least at nano-level.

Authors Y. Hayashi et al. introduce the rapid growth of dense and long carbon nanotube arrays that have succeeded in surpassing their challenges by synthesizing dense and long CNT arrays. In this contribution, they conclude in their chapter the aids in unveiling the current achievements in the growth of dense and long CNT arrays and their application in spinning threads or CNT yarns with numerous other possible applications.

Shimoi's efforts to construct a field emission cathode with SWCNTs have so far only helped average out a nonhomogeneous electron emitter plane with large FE current fluctuations and a short emission lifetime. The utilization of CNTs to obtain an effective cathode, one with a stable emission and low FE current fluctuation, relies on the ability to disperse CNTs uniformly in liquid media. Highly crystalline SWCNT-based FE lighting elements that exhibit stable electron emission, a long emission lifetime, and low-power consumption for electron emitters are successfully manufactured. This FE device employing highly crystalline SWCNTs has the potential for conserving energy through low-power consumption in our habitats. Additionally, the attempt to apply highly crystalline SWCNTs as electron emission source was successfully achieved to obtain a planar light-emission device with low-power consumption. Highly crystalline SWCNTs are an electrical element that can make a significant improvement in FE characteristics. A thin cathodic electrode film assembled via a wet process employing a highly crystalline SWCNT is expected to provide energy conservation as an FE electron emission source. By combining such elemental technologies, both of the control the on-and-off switching of electron emissions in an arbitrary manner and the amplification of the luminance output with the persistence characteristics of a fluorescent screen, a flat-panel light-emission device with high brightness efficiency with an energy conserve driving method, was assembled for

the first time in the world. Finally, the application of FE electron sources employing highly crystalline SWCNTs was determined to be effective for conserving energy based on such results and is expected to establish other devices that are driven with low-power consumption in the future.

Authors P. Kalakonda et al. interpret that these results arising from the LC-CNT surface interaction lead to pinning orientational order uniformly along the CNT, without pinning the position of the 9OO4 molecule. These effects of incorporating CNTs with LC are likely due to elastic coupling between CNT and LC. This changes the elastic properties of composites and thermal anisotropic properties of CNT. Here, the complex-specific heat is reported over a wide temperature range for a negative dielectric anisotropy alkoxyphenylbenzoate liquid crystal (9OO4) and CNT composites as a function of carbon nanotube concentration. It has been observed that the combination of CNT and LC provides a very useful way to align CNTs and also dramatically increases the order in the liquid crystal performance, which is useful in LCD. They have presented a detailed calorimetric study on the effect of carbon nanotubes on phase transitions of the 9OO4/CNT nanocomposites as a function of CNT concentration. The complex-specific heat was measured over a wide range of temperature for negative dielectric anisotropy alkoxyphenylbenzoate-9OO4)/CNT composites as a function of CNT concentration.

In this contribution, S.A. Hashemi et al. introduce aligned CNT network within the matrix via various kinds of electric fields (AC and DC) that were evaluated. In this case, alignment mechanism of CNTs within the matrix and two useful techniques for justification of CNT alignment throughout the matrix were examined and presented, respectively. Afterward, effective factors in the matter of CNT alignment and applicable procedures for fabrication of nanocomposites containing aligned CNTs were studied and presented, respectively. At the end, significant effects of CNT alignment on overall properties of nanocomposites that include electrical and mechanical properties were evaluated. Achieved results revealed that alignment of CNTs within the matrix can lead to significant improvement in the electrical and mechanical properties of nanocomposites at same filler loading compared with random distribution of CNTs within the matrix, while production steps and conditions can also highly affect the outcome data. In fact, CNTs act as path for transferring current from negative to positive electrode. This phenomenon can boost both electrical and mechanical properties of developed nanocomposites at same filler content. On the other hand, achieved results revealed that the overall properties of nanocomposites that include mechanical and electrical properties are higher for parallel direction than perpendicular direction and random distribution of CNTs within the matrix, which is due to the desire of CNTs in the formation of longitudinal connections than transverse connections. Finally, by aligning CNTs within the matrix, significant improvement in overall properties of nanocomposites at same filler loadings compared with random distribution can be achieved, which is very essential for aerospace and aviation industries that encounter with serious limits in the matter of structures' weight.

Author X. Wei focuses on the field emission of CNT cold cathodes as an electron source, including how to synthesize it by CVD method and how to realize its electron emission. In addition, they report pulsed electron emission of CNT cathodes. The combination of the laser pulse and the cold cathode will offer the possibility of pulsed field emission. Our approach demonstrates the growth mechanism and the emission mechanism of CNTs, which are beneficial for controlling performance of its fascinating application on emerging fields. Generally, the thermal effect will lead to a response time, but the field emission is instantaneous. For the pulsed field emission, the response time and pulse broadening are the weaknesses caused by thermal

effect. Especially, in the short emission electronic pulses, pulse broadening limits the possibility of the high frequency and short pulse because of the thermal effect.

Shirasu et al. review the general and recent studies, in which they investigate the nominal tensile strength and strength distribution of MWCNTs synthesized by the CVD method, followed by a series of high-temperature annealing steps that culminate with annealing at 2900 °C. The structural-mechanical relationships of such MWCNTs are investigated through tensile-loading experiments with individual MWCNTs, Weibull-Poisson statistics TEM observation, and Raman spectroscopy analysis. They also reviewed the nominal tensile strength and Weibull scale and shape parameters of the nominal tensile strength distribution of MWCNTs based on our recent studies. The comparatively low value of the shape parameter for MWCNTs resulted from the irregular nanotube structure, which reflects a larger tube defect density relative to conventional fiber materials. Nonetheless, the MWCNTs with an intermediate level of crystallinity produced complete fracture of nanotube walls and exhibited higher nominal tensile strength, suggesting that there is an optimal nanotube defect density for increasing the nominal tensile strength, not too low but also not too high, so as to permit an adequate load transfer between the nanotube walls. To improve the properties of macroscopic CNT composite performance, the structure and properties of MWCNT yarns and sheets must be optimized at all hierarchical levels: from individual MWCNTs to MWCNT bundles, MWCNT networks, and MWCNT yarns and sheets. Future research efforts aimed at each of the following levels should be pursued to improve mechanical properties, particularly the nominal tensile strength of CVD-grown MWCNTs: (1) improved synthesis methods should be developed to reduce structural defects such as *discontinuous flaws* and *kinks and bends*, and (2) the degree of interwall crosslinking and load transfer between adjacent nanotube walls should be optimized by posttreatments, such as thermal annealing and electron irradiation. We believe that the above improvements might enable the realization of higher nominal tensile strength. More well-defined CNT architectures should contribute to enhanced mechanical properties as well as improved electrical and thermal properties of MWCNT yarns and composites.

Bu-Jong Kim et al. focus on the properties of CNTs, and their applications especially for flexible TCEs are presented, including the preparation details of CNTs based on solution processes, the surface modification of flexible substrates, and the various types of hybrid TCEs based on CNTs. Here, transparent conductive electrodes (TCEs) have attracted great interest because of their wide applications in solar cells, liquid crystal displays (LCDs), organic light-emitting diodes (OLEDs), and touch screen panels (TSPs). Indium-tin-oxide (ITO) thin films as TCEs possess exceptional optoelectronic properties, but they have several disadvantages, such as a brittle nature due to their low fracture strain and lack of flexibility, a high processing temperature—which damages the flexible substrates—low adhesion to polymeric materials, and relative rarity on Earth, which makes their price unstable. This has motivated several research studies lately for developing alternative materials to replace ITO, such as metal meshes, metal nanowires, conductive polymers, graphene, and carbon nanotubes (CNTs). Out of the above candidates, CNTs have advantages in chemical stability, thermal conductivity, mechanical strength, and flexibility. CNTs have excellent chemical stability, thermal and electrical conductivity (high intrinsic conductivity), mechanical strength, flexibility, solution processability, and potential for production at a low cost. Based on these advantages, the CNT-based TCEs are presented. Here, it was illustrated that the adhesion of the CNTs was remarkably improved after the surface modification via corona pretreatment of the PET substrates. Then, in this contribution, the hybrid-type TCEs, which can be commercialized in various applications, were

fabricated, and their characteristics were demonstrated. In particular, the studies about improving the electrical conductivity and transmittance of CNTs-TCEs may warrant increased interest. Finally, in authors' chapter, the metal-based TCEs coated with CNTs were considered as an effective structure to resolve the high reflectance generated by the intrinsic properties of metals. Until now, the TCEs fabricated using only CNTs had insufficient properties for applications to electronic devices. Various hybrid types of CNT-based TCEs, however, could have potential in the application to next-generation flexible and stretchable electronics to overcome various issues.

Authors K.H. Maria et al. describe the polymer wrapping methods, which used to disperse CNT by using gelatin, an environmentally friendly and easily decomposable biopolymer. The amino acid chain of gelatin becomes immobilized by the physical adsorption in the side wall of the CNTs through hydrophobic-hydrophobic interaction and results in the untangling of the CNT bundles. The dispersed solution remains stable for more than a month. Furthermore, this technique does not affect the physical properties of CNTs while enabling their dispersion in aqueous solutions. In addition, gelatin can be easily removed from the nanotubes after the dispersion of nanotubes by heating in water and filtration. Gelatin-dispersed CNTs are homogeneously mixed with the cellulose suspension and dried at room temperature to produce CNT/cellulose composite paper sheet. Adding MWNTs in composite improves the mechanical, thermal, and electrical properties of cellulose. SEM investigation confirms the homogeneous distribution of MWNTs in the cellulose, which can be attributed to the improvement of its characteristics. Both sides of the CNT/cellulose sheet show the uniform electrical conductivity, which is enhanced by increasing the MWNT content. IR image of the sheet clearly shows the temperature homogeneity of the surface. Thermal stability and the flame retardancy of the sheet are also found to be improved. The sheet has also strong absorbing of electromagnetic waves, which makes them important for microwave technology applications. The potential applications of CNTs as composites offer new opportunities to produce cost-effective electronics. CNT-based sheet has been prepared by using a papermaking process. MWNTs improve the mechanical, thermal, and electrical properties of cellulose. SEM investigation confirms the homogeneous distribution of MWNTs in the cellulose, which can be attributed to the improvement of its characteristics. These electrically conductive and electromagnetic-wave-absorption properties can be useful in radar wave absorbing, electrothermal heating elements, 2D electric circuit applications, electromagnetic shields, etc.

Authors A.P. Carlucci et al. describe that to improve performance and lower pollutant levels, researchers have proposed alternatives to conventional ignition or combustion processes, such as HCCI combustion, whose critical requirement for proper operation is the precise control of the autoignition timing within the engine operating cycle. Here, an innovative volumetrically distributed ignition approach is proposed to control the onset of the autoignition process, taking advantage of the optical ignition properties of carbon nanotubes when exposed to low-consumption light source. It is shown that this ignition method enhanced the combustion of methane, hydrogen, LPG, and gasoline (injected in liquid phase). Results for this new ignition method show that pressure gradient and combustion efficiency are increased, while combustion duration and ignition delay decreased. A direct observation of the combustion process indicates that these benefits are due to the spatially distributed ignition followed by a faster consumption of the air/fuel mixture. The use of this ignition system is therefore proposed as a promising technology for the combustion management in internal combustion engines, specifically for HCCI engines. In this contribution, the promising results in enhancing the combus-

tion of methane, hydrogen, LPG, and gasoline applying this novel approach to initiate combustion are shown. In particular, the abovementioned fuels have been mixed with air in a constant-volume vessel and ignited with nano-powder or a conventional spark ignition system. In fact, the new light-activated distributed ignition demonstrates superior performance, which includes a shorter combustion duration, a shorter ignition delay period, and an increased pressure peak and improved combustion efficiency. A direct observation of the combustion process has established that benefits shown here are due to the fact that photothermal ignition system establishes a spatially distributed ignition, which consequently leads to a faster consumption of the air/fuel mixture in the test vessel. Higher pressure peaks and shorter rapid rising period are achieved by the fact that the new ignition system leads to more ignition nuclei that burn near-simultaneously, hence contributing to a volumetrically distributed combustion process in the combustion chamber, drastically different from the flame front propagation observed with the spark ignition. Moreover, it was demonstrated for the first time that the proposed ignition system is able to ignite air/gasoline mixtures when liquid gasoline fuel is injected into chamber, without isolating/encapsulating the nano-energetic material. High-speed camera images acquired during combustion process indicate that photothermal ignition resulted in volumetrically distributed quasi-homogeneous ignition followed by a better and faster consumption of the air/fuel mixture with no discernible flame front. This behavior is in contrast to what was observed with the spark ignition, namely, a single ignition point followed by a flame propagation across the combustion chamber. Finally, these results are considered to be of scientific and practical importance, because the combustion process, initiated in mixtures with extremely lean air/fuel ratios of interest in lean-burn HCCI engines, would allow substantial reductions of fuel consumption, nitrogen oxides, and soot emissions.

In E. Gradzka et al.'s reviews on the theoretical and practical aspects of electrochemical capacitors based on carbon nanotubes, in particular, recent improvements in the capacitance properties of the systems are discussed. In the first part, the charge storage mechanisms of the electrochemical capacitors are briefly described. The next part of the review is devoted to the capacitance properties of pristine single- and multiwalled carbon nanotubes. The major portion of the review is focused on the capacitance properties of modified carbon nanotubes. The electrochemical properties of nanotubes with boron, nitrogen, and other atoms incorporated into the carbon network structure as well as nanotubes modified with different functional groups are discussed. Special attention is paid to the composites of carbon nanotubes and conducting polymers, transition metal oxides, carbon nanostructures, and carbon gels. In all cases, the influences of different parameters such as porosity, structure of the electroactive layer, conductivity of the layer, nature of the heteroatoms, solvent, and supporting electrolyte on the capacitance performance of hybrid materials are discussed. Finally, the capacitance properties of different systems containing carbon nanotubes are compared and summarized. In the development of electrochemical capacitors, carbon nanotubes and their composites have been widely used as electrode materials. The specific capacitance of pristine carbon nanotubes is relatively low and depends on many factors such as the kind of carbon nanotubular material, i.e., single- or multiwalled; its orientation, i.e., open or closed tips; surface area; synthesis method; solvent; and supporting electrolyte. Compared with pristine carbon nanotubes, functionalized carbon nanotubes by heteroatoms or functional groups attached to nanotube walls are expected to display improved capacitance performance. The formation of composites based on carbon nanotubes provides especially high surface area due to the presence of CNTs, which is very important in the case of storage systems. Moreover, it enhances the properties of both the carbon nanotubes and the second component. Apart from the improvement in capaci-

tance performance, the addition of CNTs reduces cost compared to metal oxide; improves stability compared to conducting polymers, which exhibit rapid degradation in performance after repetitive cycles because of their swelling and shrinking; and improves the poor volumetric performance of supercapacitors based on other carbon nanomaterials. The capacitance properties strongly depend on the localization of the redox system. It was found that encapsulation of the redox phase inside a nanotubular material provides higher specific capacitance than a redox system situated outside of carbon nanotubes. Recently, a new generation of cheap storage systems based on mesoporous carbon aerogels was discovered. However, in this case, there is a problem with the nonhomogeneous spread of carbon nanotubes within the whole network of carbon aerogel. Hence, increasing attention is needed to solve this problem because this system could be the future for storage devices. A very promising system seems to be the attachment of redox-active nanoparticles to carbon nanotubes. Compared to bulk materials, they exhibit unique properties arising from their nanoscale sizes, such as high electrical conductivity, large surface area, short path lengths for the transport of ions, and high electrochemical activity. Ultrafast compact capacitors based on 3D hybrid structures that increase the accessible surface area and allow fast ion diffusion are introducing a new class of electrode materials for storage devices.

Authors G.R. Mitchell et al. describe in their chapter that CNTs have some exceptional properties for the design of multiscale nanocomposite materials. Due to the unique properties of nanotubes, they offer promise in composite materials with a large portion of current research on these materials dedicated to embedding them in a polymer matrix. They first consider recent developments in the synthesis of carbon nanotubes and their properties such as stiffness and trajectory. Next they detail the challenges of dispersion and alignment that are presented in the preparation of polymer/CNT composites. Finally, they review the existing literature to identify the progress made in preparing high-performance polymer/CNT composites and their properties and present one particular solution. Finally, there are great opportunities for the inclusion of CNTs in the emerging technology of additive or direct digital manufacturing. The future is especially promising in this area.

In the chapter by authors D. Silambarasan et al., they describe the hydrogenation and dehydrogenation studies of SWCNTs functionalized with BH_3. The SWCNTs are successfully functionalized with BH_3 using $LiBH_4$ as the precursor. The deposition process involves a simple drop casting method. The presence of BH_3 in the functionalized sample is confirmed using IR study. From XPS study, apart from C, the presence of Li, B, and O is also observed in the functionalized sample. Then, the functionalized samples are hydrogenated for different time duration. A maximum storage capacity is achieved at 50ºC, which is close to the US DOE target for a HSM to be used for on-board applications. Based on thermal annealing, a systematic investigation on desorption of hydrogen is carried out. The evidences for desorption are provided by Raman, CHNS-elemental, and TG/TDS measurements. The results show that thermal annealing treatment induces desorption of hydrogen from the hydrogenated functionalized SWCNTs. The deterioration level of the sample is also checked using Raman analysis. Overall, this investigation shows that the SWCNTs functionalized with BH_3 may be a suitable hydrogen storage system that is capable of storing and releasing hydrogen under optimum conditions suitable for hydrogen-based fuel cells used in vehicular applications.

Authors D. Atre et al. describe the degree of functionalization on CNTs greatly, which affects their properties; the structure and dynamics of water confined inside pristine and functionalized/charged carbon nanotubes (CNTs) are of prime importance. The presence of charges on the sur-

face of CNTs results in hydrophobic to hydrophilic transitions, which increase their occupancy of the water molecules, thereby breaking down 1D water wires, as seen in pristine CNTs. Finally, charged or functionalized carbon nanotubes behave quite differently compared to pristine CNTs. Functionalization not only affects properties like band gap, conductivity, and metallic nature of CNTs, but it also greatly affects the properties of confined fluids. The functionalization of CNTs changes the overall nature of the CNTs and increases the hydrophilicity, which varies almost linearly with the degree of functionalization. As the degree of functionalization provides us with a handle on the properties of confined water, it might be interesting to see if we can use carbon nanotubes as a prototype for studying complex biological system like aquaporins.

In this book, X. Sun et al. focused on a new type of carbon nanotube-cellulose composite materials as current collector of LIBs and as electrodes of SCs to improve and enhance their energy/power density and cyclic performance. CNTs have been widely used as conductive agent for both anodes and cathodes to replace super carbon black to satisfy the multifunctional requirements for LIBs. Generally, LIB and supercapacitors (EDLCs and LIC) are the most commonly used energy storage services for mobile application. Lithium ion batteries are currently the most popular type of battery for powering portable electronic devices and are growing in popularity for defense, automotive, and aerospace applications. Here, CNTs and CNTCP for primary/second batteries and supercapacitor applications were reported. It has a great potential application value for the porous carbon nanotube-cellulose papers as current collectors and electrodes in lithium ion battery and supercapacitors. However, there are still some problems to be solved. The pore size and porosity and carbonization process of CNTCPs need to be innovated to improve the strength and electrical conductivity. New high flexibility and strength of nanofibers need to be developed to adapt to electrolytes due to the cellulose papers, which are easily destroyed in liquid. Further investigations need to be done to overcome technological barriers for industrial applications of CNTCP in LIBs and SCs.

This work aims to bridge the gap between undergraduates, graduates, and scientists in applied carbon material as well as composite sciences, in order to initiate researchers into CNT study in a straightforward way as possible and to introduce the researchers to the opportunities offered by the applied science and technological fields. I worked unswervingly to complete this work on *Carbon Nanotubes - Recent Progress* under InTechOpen publisher. I hope that this contribution would further enhance the applied carbon materials in nano- and bioscience, especially in bringing new entrants into the applied and hybrid CNT science and technology fields, and help scientists to forward and develop their own field of specialization.

Mohammed Muzibur Rahman
Center of Excellence for Advanced Materials Research (CEAMR) and Chemistry department
Faculty of Science, King Abdulaziz University, Saudi Arabia

Abdullah Mohamed Asiri
Center of Excellence for Advanced Materials Research (CEAMR) and Chemistry department
Faculty of Science, King Abdulaziz University, Saudi Arabia

Introduction

Chapter 1

Introductory Chapter: Carbon Nanotubes and Their Applications

Mohammed Muzibur Rahman and
Abdullah Mohamed Asiri

Additional information is available at the end of the chapter

http://dx.doi.org/10.5772/intechopen.75738

1. Introduction

Carbon nanotubes (CNTs) is smart carbon materials which significantly utilized for the potential applications, large-scale synthesis, structural evaluation, and physical as well as chemical properties of carbon nanotubes and/or related conjugated carbon materials. Here, the various areas of carbon nanotubes (CNT) related topics including carbon materials for their various synthesis methodologies, total morphological, orientational, elemental, structural evaluations and characterizations as well as potential applications in different fields including bio-materials as well as nanomaterials for scaffolds as promising cell carrier for tissue engineering, designing antimicrobial polymeric bio-composite mats and natural medicinal plant polymer for cosmeceutical applications, carbon nanotubes/silicon composites to materials of Li secondary batteries, CNT composites with metal oxides as well as hierarchical crystalline nanotube on the cooperative Phenomena of Functional Molecular Group as the Target of Expression of New Physical and chemical Properties were discussed in this chapter.

2. Literature review

Substantial nanotube discovery which originated to existent in 1991 was CNTs. That buckyballs are spherical and round, nanotubes are tubic cylinders which are not folded round to generate to sphere [1]. CNTs are confined of C-atom connected in hexagonal shapes, with every C-atom covalently-bonded to three other C-atoms. CNTs have average dia. as lower as <1.0 nm and sizes up to several centimeters. A carbon nanotube is a long-tube-shaped carbon-material, made of only carbon, having a diameter measuring in nanometer scale. A nanometer

is one/billionth of a meter, or about 10,000 times smaller than a normal human hair. CNTs are exceptional and unique because the bonding between the carbon-atoms is very strong and the tubes can have extreme characteristic aspect ratios. Generally CNTs are allotropes of carbon with a cylindrical tubic nanostructure. These tubic-cylindrical carbon molecules have unusual properties, which are valuable for nanotechnology, nano-electronics, optics-electronics and other fields of nanomaterials science and technology. Due to the nanomaterial's extraordinary strength and stiffness, nanotubes have been created with L-to-D (Length-to-diameter) ratio [2] considerably bigger than for any other modified material. Additionally, due to CNTs exceptional characteristic property such as thermal conductivity, mechanical, and electrical, CNTs find potential applications as additives to different structural nanomaterials [3, 4]. For large number of potential applications with CNTs, the challenge lies in the alignment and ordering of CNTs to take advantages of their highly anisotropic thermal, electrical, physical characteristics. CNTs have emerged as a new category of nano-sized particles for incorporation into various liquid crystal systems, attracting favorable interest from both basic level science research and as well as industrial applications [1]. As a result of the exceptional properties of CNTs, the novel materials can be envisioned that exhibit property enhancements at lower concentration than in conventional composite technology [5]. CNTs also represent a promising material due to their unique physicochemical properties: their nanoscale needle shape, high chemical stability, thermal conductivity, and mechanical strength, which confer an advantage in the fabrication of field emitters. The utilization of CNTs relies on their electronic properties since they can be either metallic or semi-conductive, depending on the geometric configuration of a graphene sheet rolled up as a tube (i.e., diameter and chiral angle) [6–9]. Global attention on CNTs also attracted by many researchers have evaluated the extraordinary properties of CNTs toward development of nanocomposites and sheets holding highly oriented CNTs with enhanced electrical and mechanical properties. Exert of electrical field to a matrix containing CNTs can also lead to expansion of a highly oriented network from the negative electrode toward the positive electrode, which acting as a pathway for transferring current from the negative electrode toward the positive electrode [10–14]. The CNT arrays or vertically aligned CNTs itself is an extensive area of research apart from its originator CNT. As one can expect the complexity to grown long continuous CNTs [15, 16], scientist and researchers have derived out a brilliantly new idea of CNT yarn. The idea of aligning carbon nanotubes into arrays was perceived in 1994 by Ajayan et al. [17] by cutting thin slices of the nanotube-polymer composites. One of the most promising CNT applications of the field emission is an electron source. Lots of electronic devices are based on electron sources which are the most crucial component served as state-of-art vacuum nano-electronics and emerging novel devices in nowadays, such as field emission displays, emerging sensor, energy storage equipment, scanning ultrafast electron microscopes, X-ray generators, free electron lasers, Terra Hartz sources and so on [18–20]. Recently, such electron sources have intrigued a strong interest and encouraged the further studies of pulsed electron emission, opening the door to high-tech novel devices. For example, pulsed electron emission opens a way toward the time resolved electron microscopy, because electrical gating and source control enable time resolution down to picoseconds, while using optical control enables creation of electron pulses with duration down to tens of femtoseconds. Such dense and short electron bunches can become a popular platform for material and device imaging, inspection, and

failure analysis. They would enable exciting technological developments like four-dimensional time resolved electron microscopy, spectroscopy, holography, single-electron sources, and carrier envelope phase detection [21, 22]. Many other investigations in terms of electrode materials are focused on CNTs and their modified or hybrid materials. Compared with aluminum foil or copper foil, metal-free current collector is a research hotspot, CNT film or cellulose papers used as negative electrode or anode current collector was applied in flexible lithium ion battery in many researches [23, 24]. Different modern and advanced techniques have been developed for exploring the mechanical properties of individual carbon materials or CNTs. One method for measuring the Young's modulus of a CNT is to fabricate a nanotube beam that is clamped at each end to a ceramic membrane (or otherwise supported) and to measure its vertical deflection versus the force applied at a point midway along its length [25]. The atomic force microscope is a natural and convenient means for studying the Young's modulus of CNTs, because it allows measurement of the deflection of a sample as a function of applied force when used in contact mode [26].

Furthermore, CNTs, which have potential in chemical stability, thermal and electrical conductivity, mechanical strength, and flexibility, may be the best alternative materials for application in flexible transparent conductive electrodes. Actually, CNTs in some applications, which have low conductivity regardless of transmittance, are being commercialized. The rough surface of CNT films due to their tubular structures brings about a serious problem in the application of organic light-emitting diodes [27]. In CNTs, a relatively high contact resistance of the tube-tube junction may lead to insufficient sheet resistance [28]. Regarding this issue, the separation method of metallic and semiconducting components in CNTs by controlling the diameter and chirality of CNTs has been introduced in this book. CNTs have an affinity to also aggregate owing to the van der Waals attractive interaction between their sidewalls [29]. This tube-to-tube contacts results hydrophobic nature of CNTs which is responsible for their poor solubility in water, and also incompatible with a majority of solvents [30]. As a result, CNTs are precipitated in solvent, which the lack of solubility and the difficulty of manipulating them in solvents limit the development of CNT-based devices or composites of interest for new applications. In order to obtain fine dispersion in the selected solutions specially water, it is important to break the cohesion of aggregated CNTs. Development of efficient processes and chemical treatments that are able to control the quality of the CNT samples and to induce both their dispersion and partial or complete de-bundling remains highly challenging.

3. Conclusion

Finally, the growth of dense and long CNT arrays and their application in spinning threads or CNT yarns, non-homogeneous electron emitter plane with large FE current fluctuations and a short emission life-time, LC-CNT surface interaction lead to pinning orientational order uniformly along the CNT, aligned-CNT network within the matrix via electric fields, tensile strength and strength distribution of CNTs, hybrid-types of CNTs-based electronic devices, polymer wrapping methods by disperse CNT using gelatin for making decomposable biopolymer, electrochemical capacitors based on CNTs, hydrogenation and dehydrogenation

studies of CNTs functionalized with $BH_{3,}$ etc. are discussed. Here, we believe that it offers a broad field of existing developments in recent development of carbon nanotube technology research and an excellent introduction to preparation, synthesis, potential characteristic properties in field of materials and composites for their potential applications. This work aims to bridge the gap between undergraduate, graduate, and researches in carbon materials, nanomaterials, polymers, biomaterials, nanocomposites, catalysis as well as bio-medical sciences, in order to initiate scientist/researchers into different carbon nanotubes study in as straight-forward way as conceivable and also introduce the researcher to the opportunities offered by the science and technological fields. We hope, it will offer the evaluation of the state-of-the-art methods and advances of carbon researches and bio-science and nanotechnologies. Distinguished scientist were significantly contributed to present their novel ideas and recent advanced development in the field of carbon materials, carbon nanotubes, or carbon nanotube conjugated related materials in various research and practical fields. The prime goal is to introduce audience about CNTs for the students, researchers, technologists, physicists, chemists, biologists, engineers and professionals who are interested in carbon nanotubes and associated carbon related materials.

Author details

Mohammed Muzibur Rahman* and Abdullah Mohamed Asiri

*Address all correspondence to: mmrahmanh@gmail.com

Center of Excellence for Advanced Materials Research (CEAMR) and Chemistry Department, Faculty of Science, King Abdulaziz University, Jeddah, Saudi Arabia

References

[1] Iijima S. Helical microtubules of graphitic carbon. Nature. 1991;**354**:56-58

[2] Wang X, Li Q, Xie J, Jin Z, Wang J, Li Y, Jiang K, Fan S. Fabrication of ultralong and electrically uniform single-walled carbon nanotubes on clean substrates. Nano Letters. 2009;**9**:3137-3141

[3] Gullapalli S, Wong MS. Nanotechnology: A guide to nano-objects. Chemical Engineering Progress. 2011;**107**:28-32

[4] Dekker C. Carbon nanotubes as molecular quantum wires. Physics Today. 1999;**52**:22-28

[5] Thostenson ET, Ren ZF, Chou TW. Advances in the Science and technology of carbon nanotubes and their composites: A review. Composites Science and Technology. 2001;**61**:1899

[6] Hamada N, Sawada S, Oshiyama A. New one-dimensional conductors: Graphitic microtubules. Physical Review Letters. 1992;**68**:1579-1581

[7] Saito R, Fujita M, Dresselhaus G, Dresselhaus MS. Electronic structure of chiral graphene tubules. Applied Physics Letters. 1992;**60**:2204-2206

[8] Tanaka K, Okahara K, Okada M, Yamabe T. Electronic properties of bucky-tube model. Chemical Physics Letters. 1992;**191**:469-472

[9] Kim JY, Kim M, Kim HM, Joo J, Choi JH. Electrical and optical studies of organic light emitting devices using SWCNTs-polymer nanocomposites. Optical Materials. 2002; **21**:147-151

[10] Gupta P, Rajput M, Singla N, Kumar V, Lahiri D. Electric field and current assisted alignment of CNT inside polymer matrix and its effects on electrical and mechanical properties. Polymer. 2016;**89**:119-127

[11] Khan SU, Pothnis JR, Kim JK. Effects of carbon nanotube alignment on electrical and mechanical properties of epoxy nanocomposites. Composites Part A: Applied Science and Manufacturing. 2013;**49**:26-34

[12] Ma C, Zhang W, Zhu Y, Ji L, Zhang R, Koratkar N, Liang J. Alignment and dispersion of functionalized carbon nanotubes in polymer composites induced by an electric field. Carbon. 2008;**46**:706-710

[13] Mecklenburg M, Mizushima D, Ohtake N, Bauhofer W, Fiedler B, Schulte K. On the manufacturing and electrical and mechanical properties of ultra-high wt.% fraction aligned MWCNT and randomly oriented CNT epoxy composites. Carbon. 2015;**91**:275-290

[14] Wang Q, Dai J, Li W, Wei Z, Jiang J. The effects of CNT alignment on electrical conductivity and mechanical properties of SWNT/epoxy nanocomposites. Composites Science and Technology. 2008;**68**:1644-1648

[15] Pan ZW, Xie SS, Chang BH, Wang CY, Lu L, Liu W, Zhou WY, Li WZ, Qian LX. Very long carbon nanotubes. Nature. 1998;**13**:631-632

[16] Zhu HW, Xu CL, Wu DH, Wei BQ, Vajtai R, Ajayan PM. Direct synthesis of long single-walled carbon nanotube strands. Science. 2002;**3**:884-886

[17] Ajayan PM, Stephan O, Colliex C, Trauth D. Aligned carbon nanotube arrays formed by cutting a polymer resin-nanotube composite. Science. AAAS-Weekly Paper Edition. 1994;**265**(5176):1212-1214

[18] Nojeh A. Hindawi: Carbon nanotube electron sources: From electron beams to energy conversion and optophononics. ISRN Nanomaterials. 2014;**2014**(1):879827-879851

[19] Tian S, Li H, Zhang Y, Liu S, Fu Y. Elsevier: Potential field emitters: HfC nanorods sheathed with a HfO_2 nanoshell. CrystEngComm. 2014;**16**(15):3186-3191

[20] Xu NS, Huq SE. Elsevier: Novel cold cathode materials and applications. Materials Science and Engineering R. 2005;**48**(2-5):47-189

[21] Zhang P, Lau YY. Nature: Ultrafast strong-field photoelectron emission from biased metal surfaces: Exact solution to time-dependent Schrödinger equation. Scientific Reports. 2016;**6**:19894-19906

[22] Lyashenko DA, Svirko YP, Petrov MI, Obraztsov AN. Springer: The laser assisted field electron emission from carbon nanostructure. Journal of the European Optical Society-Rapid Publications. 2017;**13**(1):4-10

[23] Zhang J, Yang N, Yang X, et al. Hollow sulfur@graphene oxide core–shell composite for high-performance Li–S batteries. Journal of Alloys and Compounds. 2015;**650**:604-609

[24] Stoeck U, Balach J, Klose M, et al. Reconfiguration of lithium sulphur batteries: "Enhancement of Li–S cell performance by employing a highly porous conductive separator coating". Journal of Power Sources. 2016;**309**:76

[25] Salvetat JP, Kulik AJ, Bonard JM, Briggs GAD, Stöckli T, Méténier K, Bonnamy S, Béguin F, Burnham NA, Forró L. Elastic modulus of ordered and disordered multiwalled carbon nanotubes. Advanced Materials. 1999;**11**:161-165

[26] Elumeeva KV, Kuznetsov VL, Ischenko AV, Smajda R, Spina M, Forró L, Magrez A. Reinforcement of CVD grown multi-walled carbon nanotubes by high temperature annealing. AIP Advances. 2013;**3**:112101

[27] Ok K-H, Kim J, Park S-R, Kim Y, Lee C-J, Hong S-J, Kwak M-G, Kim N, Han CJ, Kim J-W. Ultra-thin and smooth transparent electrode for flexible and leakage-free organic light-emitting diodes. Scientific Reports. 2015;**5**:9464

[28] Blackburn JL, Barnes TM, Beard MC, Kim Y-H, Tenent RC, McDonald TJ, Bobby T, Coutts TJ, Heben MJ. Transparent conductive single-walled carbon nanotube networks with precisely tunable ratios of semiconducting and metallic nanotubes. ACS Nano. 2008;**2**:1266-1274

[29] Fei B, Lu H, Hu Z, Xin JH. Solubilization, purification and functionalization of carbon nanotubes using polyoxometalate. Nanotechnology. Feb 21, 2006;**17**:1589-1593

[30] Krueger A. Carbon nanotubes. In: Carbon Materials and Nanotechnology. Weinheim: Wiley-VCH; 2010. pp. 123-281

Section 2

State-of-the-Art Physical

Chapter 2

Rapid Growth of Dense and Long Carbon Nanotube Arrays and Its Application in Spinning Thread

Yasuhiko Hayashi, Karthik Paneer Selvam and Maik Scholz

Additional information is available at the end of the chapter

http://dx.doi.org/10.5772/intechopen.70702

Abstract

Carbon nanotubes (CNTs), a dependable allotrope of carbon, are foreseen to lead technology further to its reach. Also, the most researched carbon allotrope in its form. Drawable CNTs have recently unraveled numerous possible applications utilizing vertically aligned CNTs also termed as "CNT forest." In recent years, the rapid growth of dense and long carbon nanotube arrays has succeeded in surpassing its challenges by synthesizing dense and long CNT arrays. Length, density, and drawability tuning in the synthesis of CNT arrays have always been a complex issue lately. However, numerous research techniques emerged focusing on length and density control. Hence, this book chapter aids in unveiling the current achievements in the growth of dense and long CNT arrays and their application in spinning threads or CNT yarns with numerous other possible applications.

Keywords: CNTs, rapid growth, CNT yarns, dry spinning, vertically aligned CNTs

1. Introduction

Carbon nanotubes (CNTs) have not yet been into its full-fledged practical applications. However, it is prophesied to acquire the industrial and commercial market soon confidently. CNT arrays aka vertically aligned CNTs (VACNTs) itself are broad areas of research apart from its originator CNT. As one can expect the complexity to grow long continuous CNTs [1, 2], scientists and researchers have derived out a brilliantly new idea of CNT yarn. The idea of aligning carbon nanotubes into arrays was perceived in 1994 by Ajayan et al. [3] by cutting thin slices of the nanotube-polymer composite, which followed by the idea of aligned phases in applications like aligned liquid crystals [4], carbon fiber-reinforced polymer [5], and so on. Soon in 1995, Heer et al. produced CNT films from aligned CNT [6]. Later, in 1996 large-scale synthesis of aligned

carbon nanotubes was reported by Li et al. [7] with chemical vapor deposition (CVD) growth of CNTs using iron nanoparticles catalyzed mesoporous silica, which extended the research on aligned carbon nanotubes. The urge to produce long CNTs gave rise to CNT yarns, and therefore CNT yarns were introduced as a substitute to long CNTs. On the other hand, CNT films from aligned CNT have also gained attention and encouraged research in those directions.

The understanding of the VACNTs and their growth parameters is a cumbersome issue, as too many factors are interlinked to each other making it a slightly challenging and complicated discussion. Nevertheless, for the easy understanding, we have mentioned subheadings in this chapter discussing each issue detailing all factors as deeply as possible to attain the VACNT growth and application in the spinning thread.

CNT forest aka aligned carbon nanotubes (ACNTs) or vertically aligned CNT (VACNT) arrays have been disabling its limitations as aggressive research is going on worldwide. Many practical applications have been demonstrated using CNT forest. CNT array research has grown widely in all directions. Not long ago, the research on CNT arrays has peaked, and relatively high number of research reports has published lately. Pushing the limit and experimenting with all possible applications.

The pathway to CNT yarns can be realized by the chart shown in **Figure 1**.

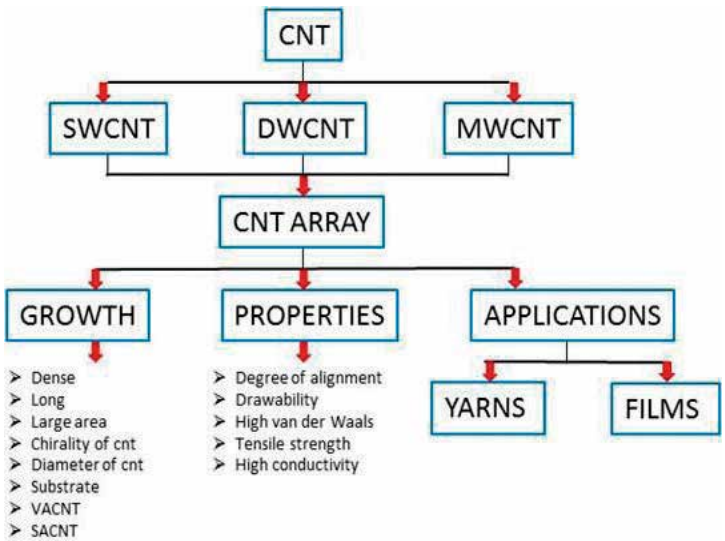

Figure 1. Showing all the parameters of CNT in application to CNT yarn and the factors for this growth.

2. Growth of CNT arrays/VACNTs

Before proceeding to the segment of dealing with the properties and modification of VACNTs, their various applications and research background and potential applications as CNT yarns

and sheets. The growth mechanism and types should be apparently introduced to give a bright idea about all the necessary factors employed in growing the VACNTs.

Many experiments performed by numerous research groups worldwide are taken into consideration in briefing all the possibilities of growth and application of CNT array and CNT yarns/films derived from them. After seeing the background of the research and how CNT array research has been disabling its limitations and improvising every year, the potential applications of CNT arrays can be estimated.

The methods that can grow CNTs or specifically VACNTs are discussed below.

2.1. Chemical vapor deposition (CVD)

Chemical vapor deposition is the most practiced and renowned method for growing CNT arrays. The initial steps include substrate preparation for the growth of CNT arrays, and the most common substrate used is silicon with several tens to few hundred nanometres thick layer of Al_2O_3 or SiO_2. To this substrate, a metal catalyst is deposited such as ferrocene which deposits Fe nanoparticles of few tens of nanometers. In a quartz tube, the Fe-coated substrate is placed. Then, this setup is put into a furnace, with one end of the quartz tube fed with reactive mixture gases (carbon precursor gas and carrier gas) and the other end to a vacuum pump. The quartz tube is then pressurized to certain total pressure say 200 Torr, and gases flow rates of 380 sccm for carbon precursor (C_2H_4) and carrier gas flow rate at 190 sccm. The temperature in the furnace increased to 650 °C which allows the catalyst to decompose the carbon and grow into CNT array. The reaction time and the flow rate decide the lengths of the CNT arrays [60]. CVD technique has further progressed into water-assisted CVD, where the reaction gas mixture and water vapor are combined. This method yielded in producing long and aligned CNT arrays [8, 9].

2.2. Floating catalyst chemical vapor deposition (FCCVD)

Floating catalyst chemical vapor deposition (FCCVD) method is also carried out in a quartz tube reactor and all other parameters being alike with CVD. The difference is avoiding metal catalyst deposition onto the substrate used for CNT growth. Instead, it the metal catalyst is passed into the quartz tube along with the reaction mixture gas. Hence, the name is derived as floating catalyst CVD, considering an example for the growth of CNT arrays. Ferrocene is injected into the reactor along with ethanol and thiophene at a rate of 0.15 ml min^{-1}, and the Ar-H_2 gas mixture is fed as a carrier gas at 4000 sccm with the temperature being 1300 °C [10]. FCCV methods avoid the deposition of the catalyst layer onto the substrate reducing one step of processing of CNT arrays. In another experiment, a comparatively low temperature of 800 °C was used to grow a 500 μm height of CNT array. Ferrocene was dissolved in xylene and fed to a horizontal furnace containing quartz tube with the substrate [11].

Thus, it leaves us with the idea about all the parameters involved in growing a CNT array by CVD technique as listed below:

1. Substrate
2. Oxide layer
3. Metal catalyst
4. Reaction gas mixture
5. Carbon precursor
6. Carrier gas
7. Pressure
8. Flow rate
9. Temperature
10. Reaction time

Now, a careful observation to make is that the parameters mentioned above are variable. Hence, it opens a broad range of experimental possibilities to grow CNT arrays.

3. Drawing of yarns and sheets

There are two methods employed commonly to spin or to draw the CNTs or CNT arrays into CNT yarn and CNT sheets/films.

3.1. Wet process

In a broad sense, wet process method to draw CNT yarns/fibers/threads does not have a direct comparison with dry-drawing method. It is naturally due to the dissimilarities between wet and dry processes. Though technically both process yield CNT yarns as the final product, the initial process is vastly different. The wet chemical process uses CNTs, whereas dry process uses VACNT. However, considering the end product's perspective, both methods can be compared.

In the wet process, CNTs are dispersed in a dispersant (acid), and then the CNTs are pumped out through a nozzle via coagulant, which aligns the CNTs into yarns/fibers. Chlorosulfonic acid is one such superacid allowing the CNTs to dissolve [12].

3.2. Dry process

Spinning CNT yarns or drawing CNT sheets from CNT arrays is among the two-step dry methods the most widely used. The synthesis mentioned above CNT forests is the first step. In the second phase of fabricating yarns or sheets, a cluster or bundle of CNT is pulled out of the assembly. The following nanotubes get attached through interconnected bundles at the top and bottom of the previous CNTs, thus forming a network of axially aligned CNTs. Kuznetsov et al. [13] show that the interconnection density is a key parameter for the ability

of an MWNT forest to be drily drawable into sheets and yarns. After drawing out the CNT network from the forest in most of the cases to forming yarns, the network is twisted [14–16]. It leads to a rapid densification and increases the mechanical strength considerably. Some research groups apply additional liquid agents instead of twisting [17]. These agents help to densify the yarns leading to a functionalized surface of the yarns [18]. With this additional treatment, mechanical strength is further increased. Additional investigations were done in the direction of heating the yarns while spinning and using multiple arrays at once to form yarns [19] as shown in **Figure 2**.

The comparison of wet process and dry process is mentioned in **Table 1**.

The understanding of aligned carbon nanotubes and its possible applications as yarns and films can be divided into the following segments.

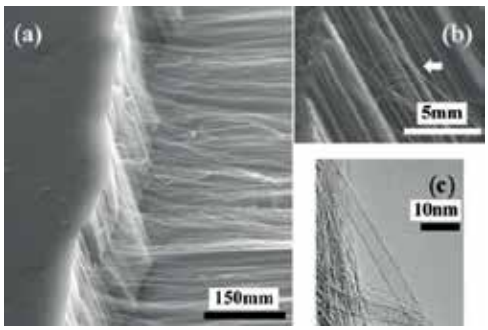

Figure 2. Showing a typical CNT forest observed under scanning electron microscopy produced by our group.

	Wet process	Dry process
Binder	Required	Not required
Residual catalyst particle	Can sometimes be found	No particle (bottom growth)
CNT dispersion	Required	Not required
NT length	Uses very short CNTs	Uses long and aligned CNTs
Simplicity in process	Complicated	Very simple

Table 1. The comparison between wet and dry processes of CNT yarn spinning.

4. Factors influencing drawing/spinning of CNT yarns and CNT films

4.1. Long and dense growth of Vertically Aligned/Super aligned CNTs (VACNT/SACNT)

4.2. Drawing of CNT Yarns/fibers using ACNTs

4.3. Drawing of CNT sheets/films using ACNTs

4.1. Long and dense growth of aligned/super-aligned CNTs

Some of the core challenges relating to CNT array's growth are:

4.1.1. Long heights of the CNT

4.1.2. Area of the substrate

4.1.3. Density of the CNTs per unit area

4.1.4. Degree of alignment of the CNTs

Other parameters concerning growth of VACNTs

4.1.5. Directing number of walls and diameter of the CNT array

4.1.6. Directing the chirality of the CNT in the array

4.1.7. Directing purity and catalyst

4.1.1. Long heights/lengths of CNT forest

Growing CNTs vertically in a long length is a critical challenge in the CNT array growth. Achieving long CNT forest can result in higher lengths of CNT yarns or films per unit area. In the application's point of view, obtaining drawable CNT forest is the real challenge. Many researchers have reported many possible lengths of drawable CNT forests. Hence, the following discussion is the current possible maximum drawable CNT forest heights which give an insight in the initial heights obtained for CNT forests. Few examples are briefed below for taming the inkling of the process for lengthy heights of CNT forest.

The record for the large height of VACNT array was reported in 2014 by Cho et al. [20], with a height of 21.7 mm, and not tested for drawability. Its water-assisted thermal CVD process produced such long VACNTs, and most of the CNTs were double walled. The growth rate was calculated to be 27.47 μm min^{-1}.

Another report stated that 4.7-mm-long CNT arrays were grown with high efficiency and long-life catalyst film using Al_2O_3 and Fe as buffer layer and catalyst. The VACNTs were spinnable [21]. Similarly, in another event, 4-mm high-quality CNT array was grown without water assistance and showed that the catalyst lifetime lasted for 3 h [22] as illustrated in **Figure 3**.

In a recent report, aligned spinnable CNTs of heights 400 μm were synthesized by Alvarez et al. [23]; Fe and Co are used as the catalyst sources with 1.2 nm thin film. About 5 nm Al_2O_3-layered Si wafer was used to accommodate the Fe and Co catalyst. The substrate was annealed at 400 °C under Ar gas flow; then, the temperature was increased to 700 °C, and ethylene was fed at 300 sccm with 1000 sccm of Ar for 20 min. In another report of drawable VAMWCNT, the height of was 2.0 mm (2000 μm) grown in 16 min that account for 0.1 mm min^{-1} by Inoue et al. [24]. It was synthesized by conventional CVD system with iron chloride ($FeCl_2$) as catalyst and acetylene as a carbon source. The same group has previously reported drawable VAMWCNT array measuring a height of 2.1 mm with same precursor material, but

http://dx.doi.org/10.5772/intechopen.70702

Figure 3. Depicting the lengths of VACNTs grown with growth time of 3 h, 2 h, 1 h 30 min 10 min (reprint from Ref. [22] with permission).

the process time was 20 min [25]. The method does not include pre-deposition of the catalyst layer. Instead, it uses iron chloride powder and acetylene gas because iron chloride has a high dehydrogenation activity on acetylene. They termed the process as chlorine-mediated chemical vapor deposition (CM-CVD).

In 1999, Shoushan et al. [26] have achieved 30–240 μm heights of MWCNT-VACNT grown by CVD reaction times of 5–60 min. The condition for growth is electrochemical etching of porous silicon of 2 in diameter, patterning with 5-nm-thick layer of Fe by electron beam evaporation with a shadow mask. The substrate was placed in the quartz tube reactor housed in a tube furnace. The operating temperature was 700 °C with Ar flow; ethylene was then flown at 1000 sccm for 15–60 min. The diameters of the MWCNT-VACNT were found to be 16 ± 2 nm. Ren et al. [27] have grown 0.1–50 μm heights of VACNTs using plasma-enhanced chemical vapor deposition (PECVD).

Lee et al. measured the possibility in factor determining the upper limit to the height of spinnable carbon nanotube forests [28]. By synthesizing CNT forests at different growth times such as 3, 6, 9, 12, 15, and 60 min. The heights were found to be 260 μm for 3 min growth time and 1.7 mm height for 60 mm growth time. An important observation was made, as the growth time increased the degree of alignment decreased. It was verified by Raman analysis as it showed G and D bands intensity ratios different at top and bottom.

Hence a clear observation can be made by all the reports is that the process time with a certain flow rate of the precursor yields in governing the lengths of VACNT. Also, these parameters have a grave effect on the degree of alignment of the VACNTs.

4.1.2. Large area growth of VACNT

It can be understood that the first challenge which lies in the geometry for VACNTs has a large area with long and densely aligned CNTs arrays. For large scale growth of CNT on a large area array, many researcher groups have been experimenting with it since a decade. CNT array growth area on large wafers has attained a growth area of 8-inch (18 cm) by Chen et al. [29]

in 2010, and the super-aligned CNT film (SACNT) was free-standing, ultra-thin, lightweight transparent and conductive. The height of the SACNT array was 250 μm, and transmittance was measured up to 83%. This high area SACNT can be employed in many advanced applications such as transparent conducting films by replacing conventional indium tin oxide (ITO).

Previously, Zhang et al. [30], have grown SACNT on a 4-inch diameter wafer, using low-pressure CVD (LP-CVD) system. To guarantee the uniformity LP-CVD system was suggested. Also, SWCNT arrays were grown using water-assisted CVD method on a 100 mm (3.9 inches) substrate [9].

4.1.3. Dense CNT forest (yarns/films)

Similar to the height of the CNTs in the CNT array, CNTs density is also a key factor classifying the application of the grown CNT array. The density depends on two factors mainly the thickness of the CNTs in the array and number of walls of the CNTs in the array and to some extent on the degree of the alignment of the CNTs in the array.

Many researcher groups have succeeded to obtain persistent densities in the past decade; one such report attained a density of 22 SWNTs in 1 × 0.75 μm [31]. Nevertheless, the drawability was not determined this VACNT. Furthermore, SWCNT array is grown by a water-assisted report a high density of 6.4×10^{11} cm^{-2}. High-density growth was possible due to the petite catalyst size of 0.5 nm [9].

In a recent report, density of CNT arrays in CNT films was improved by eliminating the pores and gaps in the thin film resulting in density improvement by 109% [32], which also, in turn, improved the mechanical strength of 765 ± 15 and 184 ± 58 MPa and electrical conductivity to $(1.65 \pm 0.15) \times 10^5$ and $(1.04 \pm 0.10) \times 10^5$ S m^{-1}. The pores and gaps were eliminated by synthesizing continuous CNT aerogel by FCCVD method. With precursor containing ethanol as the carbon source with ferrocene, thiophene, and deionized water carrier gas was a mixture of H_2 and Ar which was fed to the furnace at 1200–1300 °C. Sock-like aerogel was formed by millions of CNTs which was densified by spraying ethanol. After that the film was passed through smooth plates at 100 N pressure, which further densified the film, again the film was rolled by two oppositely rolling rollers to improve the packing density.

As noticed, two approaches can be established to obtain dense CNT arrays, that is, by growing dense CNT arrays in the initial process, or densifying the CNT yarns after drawing/spinning (post-treatment) of CNT arrays.

4.1.4. Alignment of carbon nanotubes

Ordinary CNT array and super-aligned CNT array are presently known classifications of CNT arrays concerning the degree of alignment of CNTs.

The degree of alignment is a deciding factor for the successful drawing of the CNT yarn or CNT films. The degree of alignment is a subject depending upon the van der Waals forces between two consecutive CNTs in the array. Hence van der Waals forces are responsible for holding the successive CNTs together. These, van der Waals forces are dependent on the

surface property of the CNTs. Therefore, the surface purity of the CNTs is crucial for the drawability of the CNT array.

High alignment: floating catalyst; chemical vapor deposition method, is a reliable method to synthesize highly aligned CNT sheets, as the fabrication process is easy and low cost [10].

Other growth governing parameters are:

Directing number of walls and diameter of the CNT array.

Directing the chirality of the CNT in the array.

Directing purity and catalyst.

As mentioned above the many factors govern the growth and alignment of VACNT in such regard it involves parameters like a catalyst, the thickness of the catalyst nanoparticles thin film, precursor, growth method, carrier gas, flow rate, time of the process, initialization and termination of VACNT growth process, and substrates of growth.

4.1.5. Directing number of walls and diameter of the CNT array

Principally, a number of walls and diameter control is a significant research alongside VACNTs, and numerous fruitful and reproducible synthesis parameters have been established.

Controlling the catalyst size by sulfur is a recent report which claimed that the controlling of particle size by influencing the catalyst size by sulfur. The injecting time and temperature of sulfur resulted in controlling the majority of the CNTs walls to SWCNT, DWCNT, and MWCNT [33]. In another event, water-assisted growth CNT arrays yielded in SWCNTs with a uniform diameter. The mechanism behind the uniformity was prophesied as water contributes to uniform catalyst distribution. Hence high-density uniform SWCNT arrays were obtained [9]. By using FCCVD method DWCNTs were achieved by coating a monolayer of the organic polymer during the process of CVD [34]. An example is shown in **Figure 4**.

Buffer layer influence on catalyst morphology and spinnability of VACNT.

The spinnability of VACNT depends on buffer layer thickness such as Al_2O_3 of a narrow window. Also, the buffer layer thickness regulates size and distribution of catalyst particles. In an ideal circumstance, uniformly distributed, dense and small-sized catalyst nanoparticles yield the excellent product. Al_2O_3 was thermally grown followed by Fe layer, and VACNT was grown, and spinnability was tested at different thicknesses keeping one constant at a time. It was found that at a low thickness of Fe like <0.8 nm VACNTs grown are short. However, for 1 nm Fe layer the VACNT averaged to 0.7 μm and the thickness of 1–1.2 nm resulted in highly spinnable VACNTs. Moreover, it was found that Al_2O_3 layer is beneficial for the spinnability of VACNTs [35].

4.1.6. Directing the chirality of the CNT in the array

As it is quite familiar that CNTs can be classified into three types of chirality, that is, armchair, chiral, and zigzag, depending on the specific discrete angle rolling of the graphene. Not

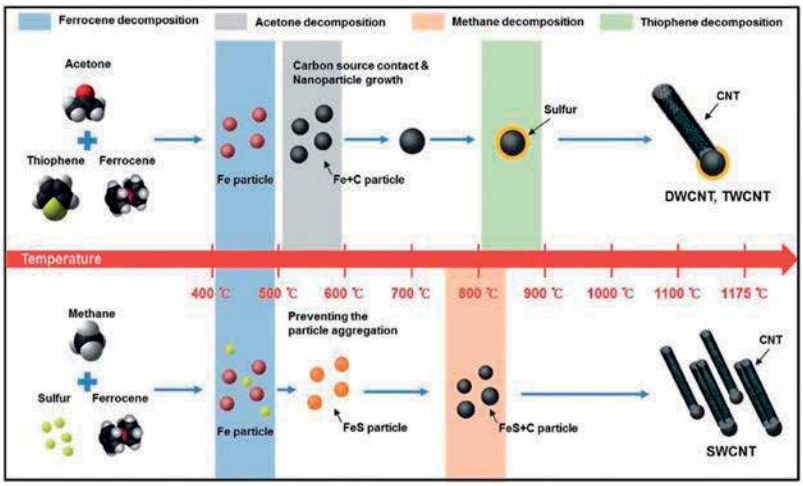

Figure 4. Showing the growth of CNTs at various temperatures (reprinted from Ref. [33] with permission).

considerable research has driven researchers in atomic level structural control for directing the chirality of the CNT in the array.

4.1.7. Directing the purity and catalyst

The most commonly used catalyst for synthesizing ACNTs is ferrocene; the catalyst plays a crucial role in guiding the number of walls, size, and layers of CNTs in the ACNTs. This catalyst can also be a cause for impurity as there is a possibility of the catalyst embeds into the CNTs while growing. Mostly the concentration of catalyst particle depends on the type of synthesis. If the synthesis is CVD method, the impurity is relatively less than that of FCCVD method.

4.2. Drawing of CNT yarns and fibers using VACNTs

It is challenging to grow long CNTs which lead to a spinning method to obtain long CNT spinning threads. A typical CNT yarn drawing is shown in **Figure 5**.

The model anticipated for drawing of VACNTs into yarns is realized by Zhang et al. [30]. It is recorded that pulling of yarns while observing under scanning electron microscope and optical microscope revealed that super-aligned CNTs (SACNTs) hold strong van der Waal forces which keep the CNTs aligned. Also, the SACNTs bundles are joined end to end resulting in a continuous yarn, which was not for the case of normally aligned CNTs. Hence SACNTs possess van der Waals forces which can be used to spinning CNT yarn. It was also stated that the difference between normally aligned CNTs and SACNTs was that the SACNTs had very clean surfaces.

An optimum condition for the growth and direct drawing of, number of walls controlled VACNTs was performed by design of experiment method. All factors responsible for the direct spinning process such as regulating the flow rates of carbon source, catalyst source, sulfur, water, hydrogen, and reaction temperature were evaluated [36].

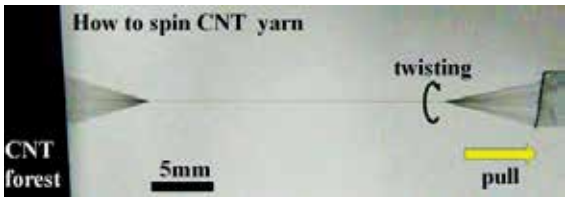

Figure 5. A simple dry drawing of CNT forest into yarns by twisting.

CNT yarn drawing speed and spinning rates.

Apart from the challenges mentioned above in growing VACNTs, regarding industrial application and mass production of CNTs, drawing speed and spinning rates play a prominent role.

Alvarez et al. developed a dry spinning process which has improved drawing rates at about 15.93 m s^{-1} [23]. Improved drawing rates were achieved by using spinnable CNT arrays which get entirely separated from the growth substrate and the growing nanoparticle. Due to the nature of separating from the growth substrate, the CNT threads have higher diameter uniformity. The substrates can be reused for CNT forest growth as the CNT is wholly detached from the substrate and the nanoparticle. It was also possible to produce long CNT fibers by joining CNT ribbons from different batches. A typical 8-inch diameter substrate can spin 316 m length of CNT yarn [37].

4.3. Drawing of CNT sheets/films using ACNTs

Like the drawing of CNT yarns, CNT sheets can be drawn using ACNTs produced by CVD process or rolled out from when produced by FCCVD process, or to deposit on to a surface while synthesizing CNTs. The CNT sheet drawing process is slightly different from CNT yarn. In a recent report CNTs synthesized by FCCVD method could deposit on an ethanol pre-wetted paper [38]. Xu et al. reported continuous production of CNT cylinder film. Moreover, the film had the strength of 9.6 GPa. FCCVD method was used to synthesize continuous production of CNT cylinder which was rolled onto a roller with densifying by ethanol [39].

5. Properties of CNT yarns and CNT films

5.1. Electrical properties

Electrical properties of CNT yarns can be stated as the most important property of CNT yarns, as the CNT yarns are highly suitable for electrical and electronic applications. Many researchers suggest numerous methods to improve the conductivity of the CNT yarns. Ideally, yarns drawn from metallic SWCNT would constitute for maximum electrical conductivity. However, the growth of metallic SWCNT is a great challenge. The electrical conductivity of CNT yarns is dependent on the intertube spacing, purity, and as mentioned before chirality of the CNT. Therefore, densification, eliminating impurities, and controlling chirality are a possible technique to improve the electrical conductivity.

For CNT yarns spun from DWCNT with diameters of 5–20 μm, the electrical conductivity and maximum current carrying, the capability was calculated to be 5.9×10^5 S m^{-1} and 1×10^5 A cm^{-1} [40] by high current-induced thermal burnout analysis in the air. Doping is also a possible approach to improve the electrical conductivity of CNT yarns, in such an event iodine doped CNT cables have resulted in specific conductivity greater than that of metals [41]. With an electrical resistivity of 10^{-7} ohm, for DWCNT drew cables.

Improving the electrical conductivity methods include mechanical condensation and acid treatment of CNT yarns, which increased the conductivity of the CNT yarns by nine times [42]. Which leads to a maximum current density of 66,000 A cm^{-2}. It was also observed that mechanical condensation reduced resistance only a few ohms but increased the electrical conductivity by four times. Further acid (HNO_3) treatment drastically reduced resistance by 50% and improving the conductivity. Acid treatment helps in eliminating amorphous carbon and catalyst particle on the surface of the CNTs hence improving the conductivity. Metal deposition on CNT yarn has also been produced by depositing Cu and Au, on CNT yarns by electroless deposition, the metal-doped CNT yarns had metal like conductivities but the strength reduced by 30–50% [43].

5.2. Mechanical properties

The mechanical strength of CNT yarn relies upon all the major components of CNT yarn synthesis. Mechanical strength also varies with the length of the CNT yarn. Hence comparing all the reports about mechanical strength with constant length is a difficult issue. Researchers mostly pick the most suitable lengths to determine the mechanical properties and many methods to improve the mechanical strength. Hence it takes the sharp eye in concluding the best-obtained result till date, however, it is very beneficial to know all the approaches taken in improving the mechanical strength.

Oxygen plasma-treated CNT yarn improved the tensile strength and Young's moduli to 2.2 GPa and 200 GPa, respectively [44]. Crosslinking technique is a new technology established in CNT yarns and found to improve the strength from 0.2 to 1.4 GPa [45]. Shrinking effect caused by passing freshly produced CNT yarn into volatile solvents (water, ethanol, and acetone) has found to increase the tensile strength to 1 GPa, in which acetone is resulting in the best tensile strength [46]. Small-molecule functionalized with electron beam irradiation improved the tensile strength by 25% upon functionalization, and a total increase of 88% tensile strength was observed when irradiated with the electron beam after functionalization [47]. In a report, recently it was found that mechanical strength of CNT yarns can improve by acid treatment followed by epoxy treatment [48]. Moreover, a maximum stiffness of 62.0 GPa was recorded. Also, CNT films have strengths up to 9.6 GPa produced by FCCVD method [39].

5.3. Other properties

Apart from the mechanical and electrical properties of VACNT, thermal properties of VACNTs has also been a locus point in determining the underlying properties of VACNTs. In a study, thermal transfer speed in highly aligned CNTs was investigated to determine

the thermal damping mechanism in SACNT Bucky papers. It is found that the heat transfer speed is different for different densities of SACNT Bucky papers. It was about 562.2 6 55.4 $mm^2\ s^{-1}$ for parallel SACNT Bucky papers [49]. Concerning with the electrochemical property of SACNTs a surface oxidized by H_2O_2 and HNO_3 to CNT film was observed to have a high cycle performance rate of 364 and 391 mA h g^{-1} [50]. FCCVD grown CNTA electrode in an organic electrolyte had a specific capacitance of 24.5 Fg^{-1} higher than that of aqueous electrolyte [11].

6. Applications

6.1. CNT fiber/yarn/thread

Replacing electrical wires with CNT yarns is the primary application of CNT yarns, in such an attempt insulation of CNT yarns, was made to replace existing copper wiring [51].

CNT fibre microelectrodes as dopamine sensor [52], as special oxygen-containing functional groups, were observed on the surface of carbon.

Weavable non-volatile memory devices by carbon fibers [53] using MWCNT fibers for an electrode with graphene oxide as the active material. In which MWCNT array is wound over a glass rod and densifying with ethanol and coating with graphene oxide of 10–20 nm. MWCNT and graphene oxide are joined non-covalently. With further processing, it works as a fiber based memory cell which exhibits write once and read many times type memory effect.

Pure 3D CNT aerogels were produced by the spontaneous expansion of SACNT films, the expansion of SACNT films was formed by soaking in a mixture of H_2SO_4 and H_2O_2. This soaking resulted in producing aerogels with a tremendously low apparent density of 0.12 mg cm^{-3} and a porosity of 99.95% [54], which leads to applications such as energy storage, catalysis as they show high adsorption abilities.

Water transport phenomena through VADWCNT array was reported by Matsumoto et al. [55]. By Parylene-C coating one side of the VADWCNT array and then peeling off the other end of VADWCNT array from the Si substrate. Finally, the Parylene-C was finely milled to expose the CNT array which was a flexible and durable membrane. Then it was used to be tested for water transport by dead-end filtration apparatus.

Wire-shaped micro-supercapacitors with aligned titania wire were wounded by CNT yarn [56]. Field emission applications [26, 57]. By functionalizing walls by H_2O_2 and HNO_3 treatment and increasing the cycle rate performance, CNT yarns can be used as electrodes for Li-ion batteries [50]. Neurotransmitter dynamic detection by CNT yarn electrodes [58].

6.2. Applications of CNT films/sheets

Platinum-coated CNT films were demonstrated to have used in fuel cells and solar cells [38]. CNT sheets are produced by SWCNTs as electrochemical actuators [59].

Acknowledgements

The authors thank SGU-MEXT for their kind support for providing funds for PhD degree students in Japan.

Author details

Yasuhiko Hayashi[1]*, Karthik Paneer Selvam[1] and Maik Scholz[2]

*Address all correspondence to: hayashi.yasuhiko@okayama-u.ac.jp

1 Graduate School of Natural Science and Technology, Okayama University, Okayama, Japan

2 Leibniz Institute for Solid State and Material Research Dresden, Dresden, Germany

References

[1] Pan ZW, Xie SS, Chang BH, Wang CY, Lu L, Liu W, Zhou WY, Li WZ, Qian LX. Very long carbon nanotubes. Nature. 1998;**13**:631-632

[2] Zhu HW, CL X, DH W, Wei BQ, Vajtai R, Ajayan PM. Direct synthesis of long single-walled carbon nanotube strands. Science. 2002;**3**:884-886

[3] Ajayan PM, Stephan O, Colliex C, Trauth D. Aligned carbon nanotube arrays formed by cutting a polymer resin-nanotube composite. Science-AAAS-Weekly Paper Edition. 1994;**265**(5176):1212-1214

[4] Gray GW, Winsor PA. Liquid Crystals and Plastic Crystals. Vol. 2. London: Ellis Horwood; 1974

[5] Dresselhaus MS, Dresselhaus G, Sugihara K, Spain IL, Goldberg HA. Synthesis of graphite fibres and filaments. In: Graphite fibers and filaments. Berlin, Heidelberg: Springer; 1988. pp. 12-34

[6] de Heer WA, Bacsa WS, Chatelain A, Gerfin T, Humphrey-Baker R. Aligned carbon nanotube films: Production and optical and electronic properties. Science. 1995;**12**(5212):845

[7] Li WZ, Xie SS, Qian L, Chang BH. Large-scale synthesis of aligned carbon nanotubes. Science. 1996, 1701;**274**(5293):6

[8] Yun Y, Shanov V, Tu Y, Subramaniam S, Schulz M. Growth mechanism of long aligned multiwall carbon nanotube arrays by water-assisted chemical vapor deposition. The Journal of Physical Chemistry. B. 2006;**110**:23920-23925

[9] Wyss R, Klare J, Park H, Noy A, Bakajin O, Lulevich V. Water-assisted growth of uniform 100 mm diameter SWCNT arrays. ACS Applied Materials & Interfaces. 2014;**6**: 21019-21025

[10] Liu Q, Li M, Gu Y, Zhang Y, Wang S, Li Q, Zhang Z. Highly aligned dense carbon nanotube sheets induced by multiple stretching and pressing. Nanoscale. 2014;**6**:4338-4344

[11] Zhang H, Cao G, Yang Y. Electrochemical properties of ultra-long, aligned, carbon nanotube array electrode in organic electrolyte. Journal of Power Sources. 2007;**172**:476-480

[12] Davis V, Parra-Vasquez A, Green M, Rai P, Behabtu N, Prieto V, Booker R, Schmidt J, Kesselman E, Zhou W, Fan H, Adams W, Hauge R, Fischer J, Cohen Y, Talmon Y, Smalley R, Pasquali M. True solutions of single-walled carbon nanotubes for assembly into macroscopic materials. Nature Nanotechnology. 2009;**4**:830-834

[13] Kuznetsov AA, Fonseca AF, Baughman RH, Zakhidov AA. Structural model for dry-drawing of sheets and yarns from carbon nanotube forests. ACS Nano. 2011;**5**:985-993

[14] Miao M. Electrical conductivity of pure carbon nanotube yarns. Carbon. 2011;**49**:3755-3761

[15] Miao M. The role of twist in dry spun carbon nanotube yarns. Carbon. 2016;**96**:819-826

[16] Zhao J, Zhang X, Di J, Xu G, Yang X, Liu X, Yong Z, Chen M, Li Q. Double-peak mechanical properties of carbon-nanotube fibers. Small. 2010;**6**:2612-2617

[17] Liu K, Sun Y, Lin X, Zhou R, Wang J, Fan S, Jiang K. Scratch-resistant, highly conductive, and high-strength carbon nanotube-based composite yarns. ACS Nano. 2010;**4**:5827-5834

[18] Cai J, Min J, McDonnell J, Church J, Easton C, Humphries W, Lucas S, Woodhead A. An improved method for functionalisation of carbon nanotube spun yarns with aryldiazonium compounds. Carbon. 2012;**50**:4655-4662

[19] Jayasinghe C, Amstutz T, Schulz M, Shanov V. Improved processing of carbon nanotube yarn. Journal of Nanomaterials. 2013:1-7

[20] Cho W, Schulz M, Shanov V. Growth and characterization of vertically aligned centimeter long CNT arrays. Carbon. 2014;**72**:264-273

[21] Li QW, Zhang XF, DePaula RF, Zheng LX, Zhao YH, Stan L, Holesinger TG, Arendt PN, Peterson DE, Zhu YT. Sustained growth of ultralong carbon nanotube arrays for fiber spinning. Advanced Materials. 2006;**18**:3160-3163

[22] Luo Y, Wang X, He M, Li X, Chen H. Synthesis of high-quality carbon nanotube arrays without the assistance of water. Journal of Nanomaterials. 2012:1-5

[23] Alvarez N, Miller P, Haase M, Kienzle N, Zhang L, Schulz M, Shanov V. Carbon nanotube assembly at near-industrial natural-fiber spinning rates. Carbon. 2015;**86**:350-357

[24] Inoue Y, Suzuki Y, Minami Y, Muramatsu J, Shimamura Y, Suzuki K, Ghemes A, Okada M, Sakakibara S, Mimura H, Naito K. Anisotropic carbon nanotube papers fabricated from multiwalled carbon nanotube webs. Carbon. 2011;**49**:2437-2443

[25] Inoue Y, Kakihata K, Hirono Y, Horie T, Ishida A, Mimura H. One-step grown aligned bulk carbon nanotubes by chloride mediated chemical vapor deposition. Applied Physics Letters. 2008;**92**:213113

[26] Fan S, Chapline MG, Franklin NR, Tombler TW, Cassell AM, Dai H. Self-oriented regular arrays of carbon nanotubes and their field emission properties. Science. 1999;**22**:512-514

[27] Ren ZF, Huang ZP, Xu JW, Wang JH, Bush P, Siegal MP, Provencio PN. Synthesis of large arrays of well-aligned carbon nanotubes on glass. Science. 1998;**6**:1105-1107

[28] J Lee EO, Kim H-J, Cho S, Kim T, Lee S, Park J, Kim H, Lee K-H. Journal of Materials Science. The reason for an upper limit to the height of spinnable carbon nanotube forests. 2013;**48**:6897-6904

[29] Feng C, Liu K, Wu J, Liu L, Cheng J, Zhang Y, Sun Y, Li Q, Fan S, Jiang K. Flexible, stretchable, transparent conducting films made from superaligned carbon nanotubes. Advanced Functional Materials. 2010;**20**:885-891

[30] Zhang X, Jiang K, Feng C, Liu P, Zhang L, Kong J, Zhang T, Li Q, Fan S. Spinning and processing continuous yarns from 4-inch wafer scale super-aligned carbon nanotube arrays. Advanced Materials. 2006;**19**:1505-1510

[31] Ding DY, Liu J. Growth of high-density parallel arrays of long single-walled carbon nanotubes on quartz substrates. Journal of the American Chemical Society. 2008;**130**:5428-5542

[32] Han B, Xue X, Xu Y, Zhao Z, Guo E, Liu C, Luo L, Hou H. Preparation of carbon nanotube film with high alignment and elevated density.Carbon 2017;**122**:496-503

[33] Lee S-H, Park J, Kim H-R, Lee J, Lee K-H. Synthesis of high-quality carbon nanotube fibers by controlling the effects of sulfur on the catalyst agglomeration during the direct spinning process. RSC Advances. 2015;**5**:41894-41900

[34] Naraghi M, Filleter T, Moravsky A, Locascio M, Loutfy R, Espinosa H. A multiscale study of high performance double-walled nanotube−polymer fibers. ACS Nano. 2010;**4**: 6463-6476

[35] Zhang Y, Sun G, Zhan Z, Zheng L. Influence of Al_2O_3 buffer layer on catalyst morphology and spinnability of carbon nanotube arrays. Journal of Materials Science. 2017;**52**: 6196-6204

[36] Lee S-H, Park J, Kim H-R, Lee T, Lee J, Im Y-O, Lee C-H, Cho H, Lee H, Jun C-H, Ahn Y-C, Lee I-B, Lee K-H. Synthesis of carbon nanotube fibers using the direct spinning process based on design of experiment DOE. Carbon. 2016;**100**:647-655

[37] Liu K, Zhu F, Liu L, Sun Y, Fan S, Jiang K. Fabrication and processing of high-strength densely packed carbon nanotube yarns without solution processes. Nanoscale. 2012; **4**(11):3389-3393

[38] Luo X, Huang X, Wang X, Zhong X, Meng X, Wang J. Continuous preparation of carbon nanotube film and its applications in fuel and solar cells. ACS Applied Materials & Interfaces. 2016;**8**:7818-7825

[39] Xu W, Chen Y, Zhan H, Wang J. High-strength carbon nanotube film from improving alignment and densification. Nano Letters. 2016;**16**:946-952

[40] Song L, Toth G, Wei J, Liu Z, Gao W, Ci L, Vajtai R, Endo M, Ajayan PM. Sharp burn-out failure observed in high current-carrying double-walled carbon nanotube fibers. Nanotechnology. 2011;**8**(1):015703

[41] Zhao Y, Wei J, Vajtai R, Ajayan PM, Barrera EV. Iodine doped carbon nanotube cables exceeding specific electrical conductivity of metals. Scientific Reports. 2011;**1**:83

[42] Liu P, Hu D, Tran T, Jewell D, Duong H. Electrical property enhancement of carbon nanotube fibers from post treatments. Colloids Surfaces Physicochem Engineering Aspects. 2016;**509**:384-389

[43] Randeniya L, Bendavid A, Martin P, Tran C. Composite yarns of multiwalled carbon nanotubes with metallic electrical conductivity. Small. 2010;**6**:1806-1811

[44] Wei H, Wei Y, Wu Y, Liu L, Fan S, Jiang K. High-strength composite yarns derived from oxygen plasma modified super-aligned carbon nanotube arrays. Nano Research. 2013;**6**:208-215

[45] Kim H, Lee J, Park B, Sa J-H, Jung A, Kim T, Park J, Hwang W, Lee K-H. Improving the tensile strength of carbon nanotube yarn via one-step double [2+1] cycloadditions. Korean Journal of Chemical Engineering. 2016;**33**:299-304

[46] Liu K, Sun Y, Zhou R, Zhu H, Wang J, Liu L, Fan S, Jiang K. Carbon nanotube yarns with high tensile strength made by a twisting and shrinking method. Proceedings of SPIE. 2010;**21**:045708

[47] Miller S, Williams T, Baker J, Solá F, Lebron-Colon M, McCorkle L, Wilmoth N, Gaier J, Chen M, Meador M. Increased tensile strength of carbon nanotube yarns and sheets through chemical modification and electron beam irradiation. ACS Applied Materials & Interfaces. 2014;**6**:6120-6126

[48] Tran T, Fan Z, Mikhalchan A, Liu P, Duong H. Post-treatments for multifunctional property enhancement of carbon nanotube fibers from the floating catalyst method. ACS Applied Materials & Interfaces. 2016;**8**:7948-7956

[49] Zhang G, Liu C, Fan S. Directly measuring of thermal pulse transfer in one-dimensional highly aligned carbon nanotubes. Scientific Reports. 2013;**3**:2549

[50] Li M, Wu Y, Zhao F, Wei Y, Wang J, Jiang K, Fan S. Cycle and rate performance of chemically modified super-aligned carbon nanotube electrodes for lithium ion batteries. Carbon. 2014;**69**:444-451

[51] Kurzepa L, Lekawa-Raus A, Patmore J, Koziol K. Replacing copper wires with carbon nanotube wires in electrical transformers. Advanced Functional Materials. 2014;**24**:619-624

[52] Roberts J, Moody B, McCarty G, Sombers L. Specific oxygen-containing functional groups on the carbon surface underlie an enhanced sensitivity to dopamine at electrochemically pretreated carbon fiber microelectrodes. Langmuir. 2010;**26**:9116-9122

[53] Sun G, Liu J, Zheng L, Huang W, Zhang H. Preparation of Weavable, All-Carbon Fibers for Non-Volatile Memory Devices. Angew Chem-ger Edit. 2013;**125**:13593-13597

[54] Luo Y, Luo S, Wu H, Li M, Wang K, Yan L, Jiang K, Li Q, Fan S, Wang J. Self-expansion construction of ultralight carbon nanotube aerogels with a 3D and hierarchical cellular structure. Small. 2017:1700966

[55] Matsumoto H, Tsuruoka S, Hayashi Y, Abe K, Hata K, Zhang S, Saito Y, Aiba M, Tokunaga T, Iijima T, Hayashi T, Inoue H, Amaratunga G. Water transport phenomena through membranes consisting of vertically-aligned double-walled carbon nanotube array. Carbon. 2017;**120**:358-365

[56] Chen T, Dai L. Flexible and wearable wire-shaped micro supercapacitors based on highly aligned titania and carbon nanotubes. Energy Storage Materials. 2016;**2**:21-26

[57] Wei Y, Jiang J, Liu L, Chen Z, Fan F. Vacuum-breakdown-induced needle-shaped ends of multiwalled carbon nanotube yarns and their field emission applications. Nano Letters. 2007;**7**:3792-3797

[58] Schmidt A, Wang X, Zhu Y, Sombers L. Carbon nanotube yarn electrodes for enhanced detection of neurotransmitter dynamics in live brain tissue. ACS Nano. 2013;**7**:7864-7873

[59] Mukai K, Asaka K, Sugino T, Kiyohara K, Takeuchi I, Terasawa N, Futaba D, Hata K, Fukushima T, Aida T. Highly conductive sheets from millimeter-long single-walled carbon nanotubes and ionic liquids: Application to fast-moving, low-voltage electromechanical actuators operable in air. Advanced Materials. 2009;**21**:1582-1585

[60] Bronikowski M. CVD growth of carbon nanotube bundle arrays. Carbon. 2006;**44**: 2822-2832

Chapter 3

Stability and Reliability of an Electrical Device Employing Highly Crystalline Single-Walled Carbon Nanotubes as a Field Emitter

Norihiro Shimoi

Additional information is available at the end of the chapter

http://dx.doi.org/10.5772/intechopen.72581

Abstract

Carbon nanomaterial is drawing keen interest from researchers as well as materials scientists. Carbon nanotubes (CNTs)—and their nanoscale needle shape—offering chemical stability, thermal conductivity, and mechanical strength exhibit unique properties as a quasi-one-dimensional material. Among the expected applications, field emission electron sources appear the most promising industrially and are approaching practical utilization. However, efforts to construct a field emission (FE) cathode with single-walled carbon nanotubes (SWCNTs) have so far only helped average out a non-homogeneous electron emitter plane with large FE current fluctuations and a short emission life-time because they failed to realize a stable emission current owing to crystal defects of the carbon network in CNTs. The utilization of CNTs to obtain an effective cathode, one with a stable emission and low FE current fluctuation, relies on the ability to disperse CNTs uniformly in liquid media. In particular, highly crystalline SWCNTs hold promise to obtain good stability and reliability. The author successfully manufactured highly crystalline SWCNTs-based FE lighting elements that exhibit stable electron emission, a long emission life-time, and low power consumption for electron emitters. This FE device employing highly crystalline SWCNTs has the potential for conserving energy through low power consumption in our habitats.

Keywords: single-walled carbon nanotube, high crystallization, field emission, wet coating process, thin film, scratch, planar light source, cathode luminescence

1. Introduction

The further development of electronic systems necessitates the production of efficient devices employing carbon nano-materials. Carbon nanotubes (CNTs) represent a promising material due to their unique physicochemical properties: their nanoscale needle shape, high chemical

stability, thermal conductivity, and mechanical strength. These properties confer an advantage in the fabrication of field emitters. The utilization of single-walled carbon nanotubes (SWCNTs) relies on their electronic properties since they can be either metallic or semiconductive, depending on the geometric configuration of a graphene sheet rolled up as a tube (i.e., diameter and chiral angle) [1–4].

CNTs express one-dimensional circumscription effects and have characteristics as quantum wires coherently [5–7], and CNTs have the highest Young's modulus of all known materials mechanically [8]. Owing to these outstanding properties, wide-ranging applications for nanotubes are currently under investigation, including their use as electron field emitters [9], probes in scanning-type microscopes [10], gas (e.g. hydrogen) storage materials [11], and as electrode materials for secondary batteries as well as in capacitors [12]. Among these proposed applications, field emission electron sources appear the most promising industrially and in fact are approaching practical utilization. When a highly electrical field in the order of 10^3 V/μm is applied onto a surface of an electron emitter, electrons emit from inside the emitter's solid to a vacuum atmosphere by the quantum-mechanical tunneling effect. This phenomenon is called the field emission. Such an extremely high field can be obtained on the sharp tip having a thin needle because electric fields concentrate at the top of the sharp tip. It is said that the carbon nanotubes possess the following physical or chemical properties for field emitters: 1) a high aspect ratio with a sharp tip, 2) high mechanical strength, and 3) high chemical stability. Field emission (FE) phenomenon from an isolated single multiwalled carbon nanotube (MWCNT) was first reported by Rinzler et al. [13] in 1995, and FE from a MWCNT film was reported by de Heer et al. that same year [14]. Subsequently, many experimental studies on FE from MWCNTs [15–18] and SWCNTs [19] have appeared. Field emission microscopy (FEM) has also been used to clarify the geometric structures of the nanotube tips [16, 19]. Moreover, many studies have attempted to employ CNTs as field emitters in a display cathode with a lower driving voltage and stable electron emission. These trials mostly involve the vertical alignment of the CNTs in their fabrication that are synthesized by plasma-enhanced chemical vapor deposition (PECVD) or laser abrasion fabrication; for example, screen printing with high-viscosity submicron to micron scale metal-particle paste to fabricate patterned field emitters has been proposed [20–22]. However, these approaches could not obtain the homogeneous electron emitter plane with small FE current fluctuations as they failed to construct a uniform thin film employing a homogeneous dispersion of CNTs.

The utilization of CNTs to obtain an effective cathode—with both a stable field emission and low FE current fluctuation—hinges on the ability to disperse them uniformly in liquid media. In particular, highly crystalline SWCNTs can be expected to emit electrons stably with a low turn-on and driving voltage, yet their homogeneous dispersion has yet to be reported. For this study, we selected a low-viscosity solvent with an In_2O_3-SnO_2 (tin-doped indium oxide; ITO) precursor solution as the conductive matrix material being dispersed highly crystalline SWCNTs. A dispersant was added to obtain the well-dispersed highly crystalline SWCNTs, and the mixture with the ITO solvent, highly crystalline SWCNTs, and the dispersant was agitated by an ultra-sonic homogenizer.

This chapter first briefly reviews the synthesis of highly crystalline SWCNTs by arc discharge and their structural characterization [23], followed by a discussion of the characteristic properties

of FE from the arc-produced nanotubes, concluding with a description of the application of the nanotube emitters in a flat-panel lighting device. Here, the author successfully manufactured SWCNT-based field emission lighting elements exhibiting stable electron emission, adequate luminance, and low power consumption for the electron emitters.

2. Experimental crystallization of annealed SWCNTs

Purified and highly crystalline SWCNTs synthesized by arcing and sintered at high temperature in a vacuum have been expected to serve as an electrical source material for a field emitter though the homogeneous dispersion of highly crystalline SWCNTs has yet to be reported. This is because highly crystalline SWCNTs have almost no defects in the carbon network on their surface, nor do they combine with another functional group of dispersants. It is difficult for SWCNTs aggregated as a secondary particle to separate uniformly into single nanotubes. Furthermore, despite the necessity of a thin film homogeneously dispersing highly crystalline SWCNTs for a field emission cathode plate, as yet no method for synthesizing a thin film with SWCNTs for a field emitter exhibiting a good homogeneity of plane-light emission has been developed.

In this chapter, commercial arc-SWCNTs (ASP-100F, Hanwha Chemicals Co. Ltd., Korea) were used. The SWCNTs were annealed at a high temperature (around 1000 K) in a high vacuum (pressure, $>10^{-5}$ Pa) to obtain highly crystalline SWCNTs. **Figure 1** shows transmission electron microscopy (TEM, HR-3000, Hitachi High-Technologies Corporation, Japan) images of the SWCNTs (a) after and (b) before annealing as a reference. As shown in **Figure 1(a)**, the crystallinity of the SWCNTs was significantly improved after annealing at a high temperature in a tight vacuum.

Here, analytical grade reagents were used in the experiments. The annealed arc-SWCNTs checked for high crystallization were measured by Raman-shift. The Raman spectrum measured by the blue laser beam (Blue) at a 473 nm wavelength is shown in **Figure 2**. Raman peaks from the G+ band mode (1590 cm^{-1}) and from the G_ band mode (1565 cm^{-1}) presumed to be nanotube structures. A Raman peak intensity of near 1350 cm^{-1} from the D band mode indicated lacks of carbon network on a nanotube. The intensity ratio between the G+ band and the D band was 0.0096; this value confirms that the SWCNT has a carbon network with high crystallization.

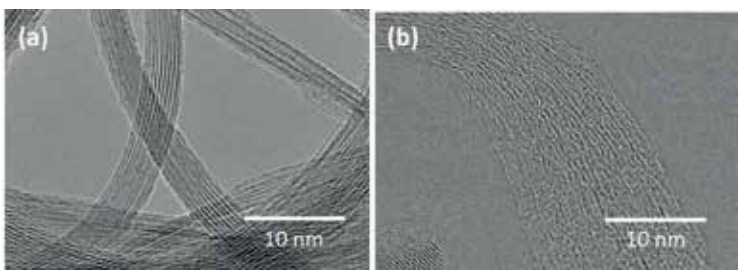

Figure 1. TEM images with annealed and unannealed SWCNTs [24]. (a) Highly crystalline SWCNTs with annealing treatment. (b) SWCNTs with crystal defects without annealing treatment.

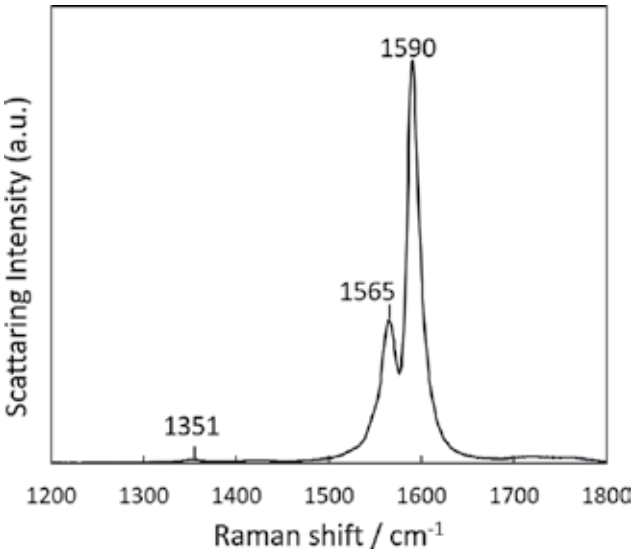

Figure 2. Raman spectrum with G and D band modes of annealed SWCNTs. [25].

3. Construction of a thin film including highly crystalline SWCNTs for field emission

A wet-coating process was adopted to fabricate a cathode with stable FE at a low driving voltage using SWCNTs. The homogeneous dispersion of SWCNTs in a liquid medium was the key. Highly crystalline SWCNTs are expected to lower the threshold field and emit electrons stably at a low driving voltage, but no homogeneous dispersion of SWCNTs in liquids has ever been reported. In general, a dispersant is used to facilitate the homogeneous dispersion of nano-carbon materials in liquids; however, highly crystalline SWCNTs cannot bind to the functional groups in a dispersant because there are very few defective binding sites in their carbon network that can be used to bind to these in the dispersant. We attempted to separate highly crystalline SWCNT aggregates physically into uniform single nanotubes in a low-viscosity solvent containing an In_2O_3-SnO_2 (tin-doped indium oxide; ITO) precursor solution. A nonionic dispersant was added to the solvent to facilitate the dispersion of SWCNTs, and the mixture was agitated with ceramic beads in a shaking machine.

The physical properties for producing a mixture including highly dispersant SWCNTs are as follows: Butyl acetate 99%, ethyl cellulose (EC) (abt. 49% ethoxy 100 cP), and sodium *linear*-alkyl-benzenesulfonate 95% (DBS) were obtained from Wako Co. Ltd. Japan. The initial mixture was prepared by mixing the SWCNTs powder with the ITO precursor from Kojundo-Kagaku Co. Ltd. Japan and the DBS and the EC in a proportion of about 1: 600: 1: 4. The last component, EC, was tried in different proportions. The mixture was later agitated with ZrO_2 beads of different diameters in various concentrations from 4 g to 8 g in a shaking machine at periods ranging from 6 h up to 12 h. In all cases, the resulting mixture solution shown in **Figure 3** had low viscosity. The TEMs of the annealed SWCNTs are shown in **Figure 3**; almost only carbon nanotubes can be seen in the micrographs, with no other carbon contamination present.

http://dx.doi.org/10.5772/intechopen.72581

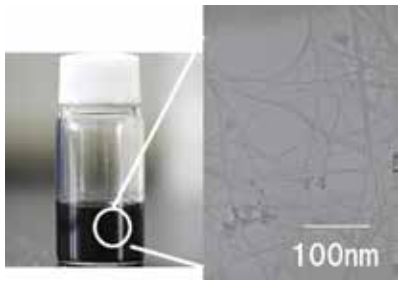

Figure 3. Dispersed SWCNTs mixture and TEM observation [25].

In order to confirm the crystallinity of SWCNTs, the TG first derivative (dTG) curves for both of the annealed SWCNTs and non-annealed samples presented in **Figure 4** indicate the weight fraction of tubes at each burning temperature. It is generally known that the burning temperature of SWCNTs is inversely proportional to the amount of crystal defects in the SWCNTs; hence, the SWCNT crystallinity can be inferred from the shape of the dTG curves. There are a few peaks in the non-annealed SWCNT dTG curve, indicating a range of different crystallinities; the burning temperature of the SWCNTs increased after annealing, signaling an increase in the degree of crystallinity of the SWCNTs. However, the non-annealed SWCNT dTG curve also indicated the presence of some lower crystallinity tubes that might affect the field-emission stability.

The relationship between dispersion concentration and crystallinity retention rate for highly crystalline SWCNT dispersions prepared by ultra-sonication and agitation with ceramic beads is shown in **Figure 4**. The dispersion concentration in **Figure 5** was calculated from the ratio of dispersion transparency before and after centrifugation of the solution, as determined by UV–vis measurements, and includes highly crystalline SWCNT aggregates. The crystallinity retention was calculated from the dot product of dTG measurement curves obtained before and after dispersion of the highly crystalline SWCNTs and is presented as cosθ. A reduction in cosθ correlates to a deterioration in the crystallinity of the dispersed highly crystalline SWCNTs. Thus, **Figure 5** indicates that the SWCNT crystallinity deteriorates with

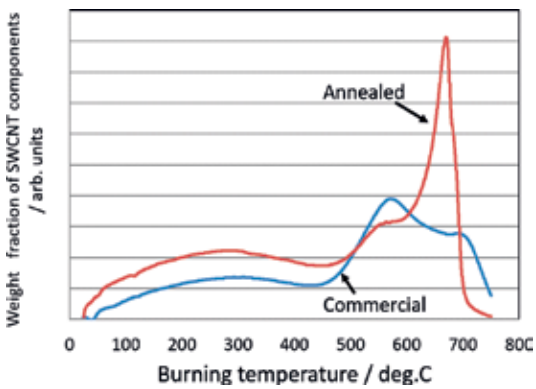

Figure 4. First derivative thermogravimetric curves of the commercial and annealed single-walled carbon nanotubes measured under an air atmosphere.

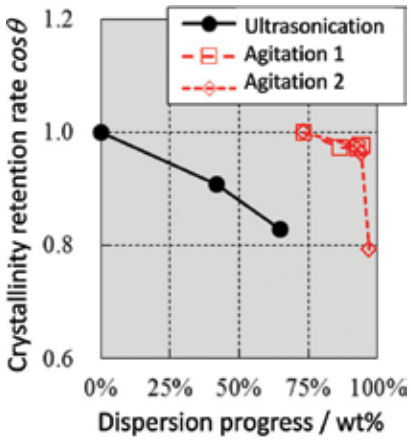

Figure 5. Dispersion concentration vs. crystallinity retention rate for highly crystalline single-walled carbon nanotubes dispersed by ultra-sonication and agitation. Ultra-sonication at 40 kHz was performed for 0, 5, and 10 hours. Agitation was carried out under different conditions and repeated several times.

increasing sonication time; we presume this to be an effect of the uncontrollable cavitation that occurs during ultra-sonication. The agitation method was the most successful method for highly crystalline SWCNT dispersion, with a concentration of more than 90 wt% and minimal crystallinity deterioration achieved. However, it should be noted that the crystallinity of the dispersed highly crystalline SWCNTs also deteriorates with repeated milling and at higher operation pressures. This is likely owing to a difference in atom binding energy and cohesion energy depending on the higher-order structure of SWCNTs [25, 26].

In this chapter attempts were made to disperse SWCNTs with a low-viscosity butyl acetate solvent including an organic In_2O_3-SnO_2 (ITO) precursor and non-ionic dispersant. The author successfully employed a dispersion method for highly crystalline SWCNTs to obtain a mixture of them dispersed as thin bundles, aggregating with a few nanotubes. The agitated mixture was sprayed onto a metal-coated glass substrate heated to around 400 K, and the coated film was sintered at 900 K in a vacuum to remove any organic components and then form bridges in order to produce a conductive ITO film. After a film coated with the mixture was sintered in a vacuum, it was activated by scratching it appropriately to obtain field emission properties with a low turn-on field. **Figure 6** shows SEM images of an ITO film with dispersed SWCNTs after vacuum sintering. The ITO film was scratched by a thin metal rod; this revealed SWCNTs or their bundles protruding from both sides of the edge of the ITO film. As shown in **Figure 6(a)**, highly crystalline SWCNT bundles were dispersed. As shown in **Figures 6(b)** and **6(c)**, the SWCNT bundles were exposed in the scratched grooves on the ITO film subjected to activation treatment. The white circles in the SEM image of **Figure 6(a)** indicate the exposed SWCNT bundles that were exposed by scratching the ITO film in which SWCNTs were dispersed. White circles show the distances between their points to be almost identically aligned. SWCNTs in the ITO film were dispersed homogeneously and lay in random directions. Thus, SWCNTs would appear in same direction in the ITO film with the same probability, and homogeneously dispersed SWCNTs protruding from the grooved face of the ITO film could be observed.

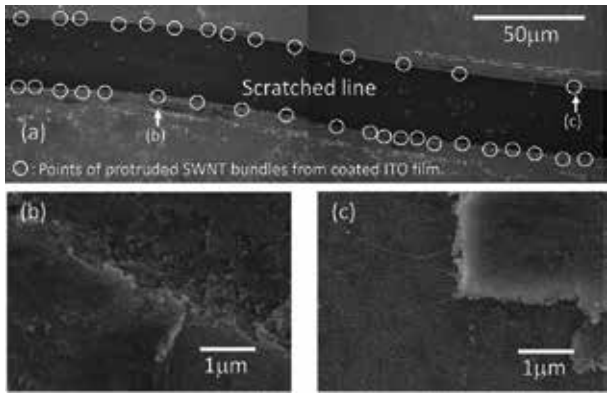

Figure 6. SEM images of ITO film with dispersant SWCNTs after sintering [25]. (a) Overview of a scratched ITO film. White circles indicate points of SWCNT bundles protruding from the ITO film as measured by SEM. (b) and (c) enlarged images arrowed in the image of (a). The white arrows indicates SWCNTs from the grooved face.

In this chapter, the SWCNTs coating weights per unit area were controlled by the numbers of spray cycles to verify both the field emission property and brightness efficiency of a flat-plane light emission panel. The sintered film was fabricated using an activation process without the standing or aligning treatment of the CNTs in order to emit electrons easily at low voltage.

Then the SWCNTs for the field emitter protruding from the grooved face were aligned in a direction parallel to the ITO film plane and substrate per the schematic drawing in **Figure 7**, which shows schematic drawings of the models with random directions for the SWCNTs. The dotted square boxes indicate scratched areas, and the tops of SWCNTs that possibly emit electrons are highlighted with red circles in the area. These depend on the density of the SWCNTs in a coated film. The direction of the SWCNTs exposed by scratching aligns in a direction parallel to the substrate, so electrical fields are yielded at the top of each SWCNT uniformly without the fluctuation of the protruding SWCNT length. We thus obtained high homogeneity for the electron plane-emission with the dispersion and density of SWCNTs in the coated film.

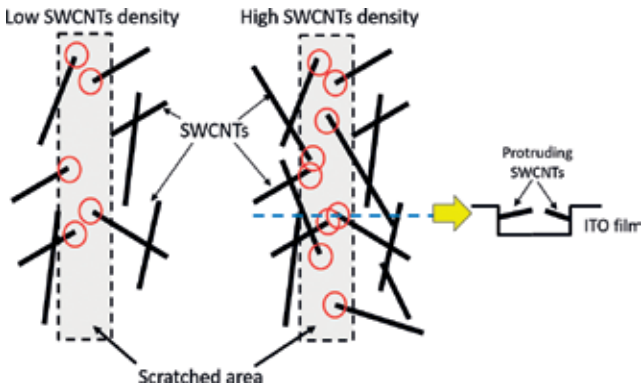

Figure 7. Images of frequency in the exposure of SWCNTs in a scratched area in cases of both low and high SWCNT density. Red circles indicate the exposed tops of SWCNTs. [25].

4. Field emission properties

This activated field emission (FE) cathode employing highly crystalline SWCNTs has the potential to yield a new flat-plane light emission device and so provide a novel approach to daily lighting needs while also contributing to energy-saving through its low power consumption. FE properties were measured with a phosphor anode plate on a sputtered ITO pattern film and 1.0 millimeter glass plate as a spacer as shown in **Figure 8**.

The sample shown in **Figure 8** was set into the electrical circuit in **Figure 9** to measure field emission and brightness properties. This measurement system was constructed with a power supply unit having an amplifier, a function generator, an oscilloscope as a field emission current monitor, and a PC for data storage. The voltage for the sample was designed for a periodic voltage at 60 Hz of the triangle wave for field emission measurements. The field emission current was converted to bias voltage data by a resistor at around 10 to 1 MΩ for the purpose of preventing signal noise from any leaking current appearing in measurement applications.

The author attempted to control field emission characteristics by the weight of the SWCNTs included in a coated ITO film with activation by a simple scratching. **Figure 10** shows the current density-electrical field characteristics of the cathode with a 20 x 20 mm diode depending on the content of the SWCNTs in the coating film. For example, the contents for measurements were chosen at 1.07, 0.69, 0.35, and 0.09 mg/cm^2. The turn-on field increased as the SWCNT density rose to around 0.8 to 1.7 V/μm. The high SWCNT density obtained a low driving supply because of the increase in the field emission site available to emit electrons from the tip of each SWCNT.

The F-N electron tunneling function has been proposed as follows [27]:

$$I = a * V^2 * \exp\left(-\frac{b}{V}\right) \tag{1}$$

where

$$a = \alpha * A * \beta^2 * \exp\left(\frac{B * 1.44E-7}{\phi^{0.5}}\right)/(1.1 * \phi) \tag{2}$$

$$b = \frac{0.95 * B * \phi^{3/2}}{\beta} \tag{3}$$

$$A = 1.54E-6, B = 6.87E+7 \tag{4}$$

From Eq. (1), V means a voltage added between two electrodes; this is converted to an electrical field by the gap of the measurement sample in **Figure 8**. I indicates a current flow passing through the phosphor plate in the anode area at 20 × 20 mm^2. α is equivalent to the electron emission site area for the field emission based on Fowler-Nordheim tunneling, β is the field enhancement factor of the electrical field localized at the top of a SWCNT against a macroscopic applied electric field, and ϕ of 4.7 eV is the work function in the bulk region of carbon materials. **Figure 11** shows the distributions of α and β converted from the current density-electrical field characteristics by Eqs. (1), (2), (3) and (4) against the SWCNT coating density.

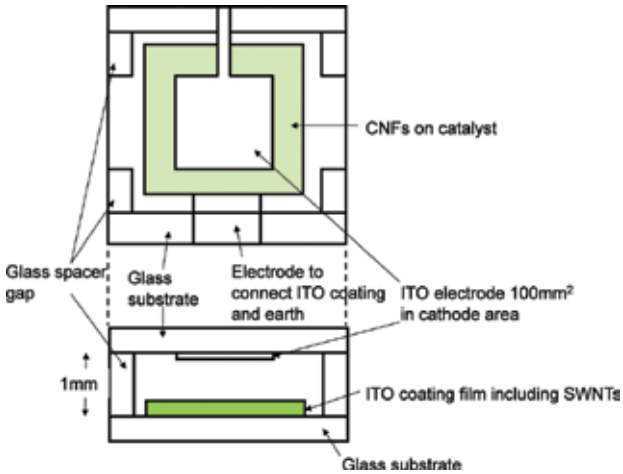

Figure 8. Schematic diagram of the system for FE measurement having a diode structure [25].

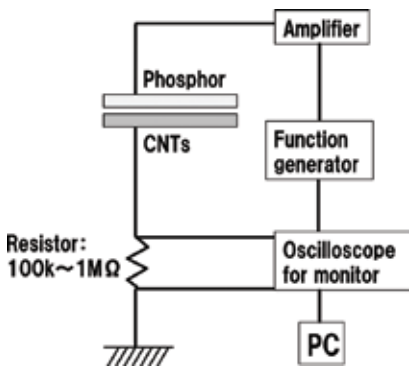

Figure 9. Schematic diagram of the electrical circuit system for FE measurement with a diode structure [25].

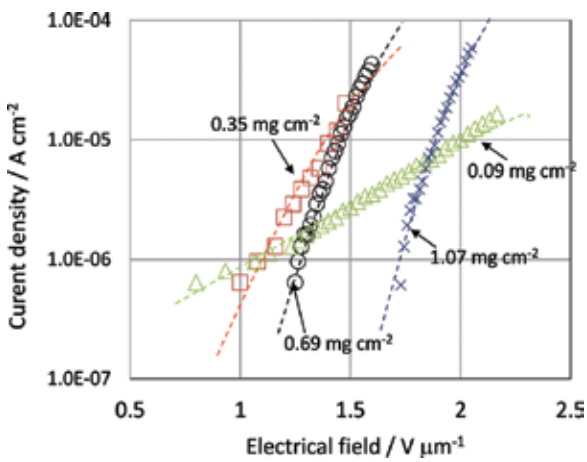

Figure 10. Current density-electrical field characteristics of certain conditions: 0.09, 0.35, 0.69, and 1.07 mg/cm² [25].

The flat emission-plane—especially for the content of SWCNTs at 0.69 mg/cm^2—from the diode generated a stable, homogeneous brightness of over 2000 cd/m^2 in the sampling area of 400 mm^2 without any brightness fluctuation. The brightness of the sample with the content of SWCNTs at 0.69 mg/cm^2 was measured at nine locations in the emission area, as captured by a charge coupled device (CCD) camera in **Figure 12**. Furthermore, the differences between each brightness result of the measurement points in the plane shown in **Figure 8** were within 5% of those shown in **Figure 13**; accordingly, stable brightness uniformity was achieved in the plane-emission area.

$$Brightness\ \ Efficiency(lm/W) = \frac{Brightness(cd/m^2) \times Lighting\ area(m^2) \times 3.14}{Voltage \times 0.5 \times FE\ \ Current \times \exp(-2.4)} \tag{5}$$

As calculated by the luminance measured by a luminance meter and the load power compensated as a direct current (DC) load power for the effective voltage of the triangle wave—indicated as *Voltage* × *0.5* in Eq. (5)—as a bias voltage and effective field emission current, which was indicated as *FE Current* × *exp.(−2.4)* in Eq. (5), the author was able to achieve a brightness efficiency calculated by Eq. (5) of more than 70 lm/W within an area of approximately 25 cd/m^2 of brightness standard deviation by controlling the contents of SWCNTs in the coated film. Phosphor plates for brightness efficiency measurements were chosen for their green lighting from Nichia-Kagaku Co. Japan. The green circular points in **Figure 14** indicate the brightness efficiency with a green phosphor emitting light. The square blue points represent the deviation of brightness employing the green light in the plane-emission area shown in **Figure 12**. The brightness properties from the developed cathode depended on the content of the SWCNTs and could be obtained with high brightness homogeneity and high driving efficiency by controlling the SWCNT density in the coated ITO film. However, the brightness efficiency in case of a SWCNT density of more than 0.69 mg/cm^2 decreased with an increase in the SWCNT density from **Figure 14**. This is probably owing to the electrical field strength for field emission focused on each top of the SWCNTs being weaker than 0.69 mg/cm^2; though SWCNTs as electron emission sites are sufficient for obtaining a high field emission current. This can be explained by the tendency of the field enhancement factor in **Figure 11**, which causes the distance between neighboring SWCNTs as field emitters to narrow with the increase in SWCNTs density. Moreover, the tendency of the brightness deviation is for a stability of more than around 0.69 mg/cm^2. Most likely, this is because enough SWCNTs for field emitters exist in the ITO film for a high SWCNT density. From **Figure 14**, it is apparent that a high brightness efficiency could be obtained by controlling the SWCNTs density in the ITO film. To our knowledge, this is the first time a field emitter plane device has achieved a high brightness efficiency of over 70 lm/W.

Figure 15 shows the field emission life time up to 100 hours at SWCNT contents of 0.09, 0.35, and 0.69 mg/cm^2. FE-current was measured as a peak of field emission current with a periodic voltage of the rectangular wave with a frequency of 60 Hz and duty ratio of 10%, and initial FE-current density was adjusted approximately to 45 mA/ cm^2. This result implies that the radioactive half-time will be over 5000 hours at 0.69 mg/cm^2, and other samples with a SWCNT density of more than 0.69 mg/cm^2 have the same emission-life tendency as at 0.69 mg/cm^2. Attenuation of the loading field emission current depends on the uniformity of the loading power, equal to the electrical field strength, given to each SWCNT for field emitters. A field emitter-plane employing SWCNTs will have the high stability with a high crystallization of

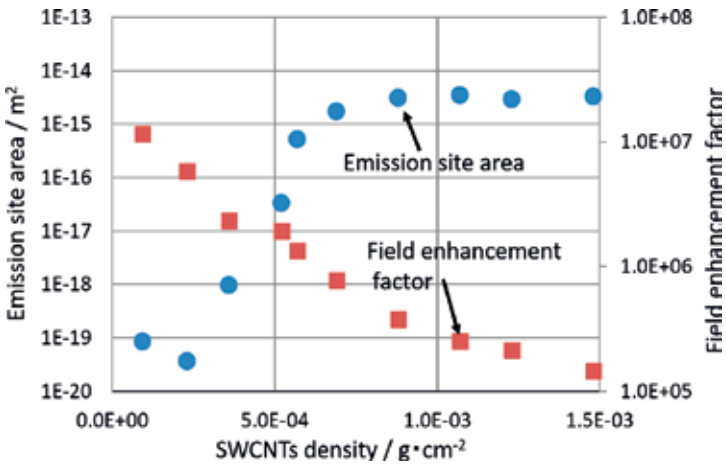

Figure 11. The dependence between the emission site area, field enhancement factor, and SWCNT density [25].

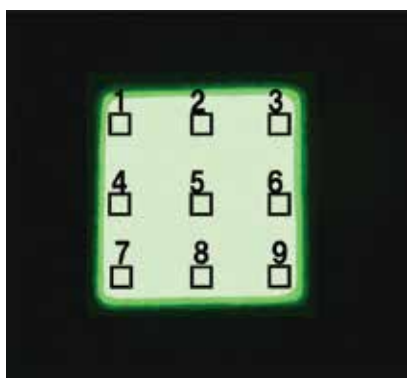

Figure 12. Light emission brightness image of the SWCNT content 0.69 mg/cm² among nine areas captured by CCD through a ND filter. The added voltage between the anode and cathode is 3.0 kV with a peak-to-peak range of periodic voltage in the triangle wave; the flow current is 250 μA as a peak currentw [25].

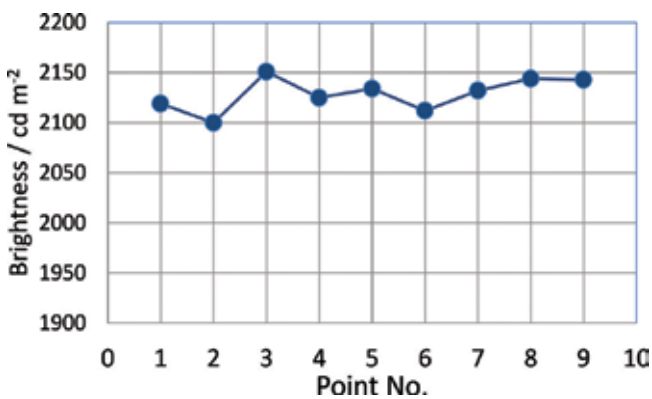

Figure 13. Brightness results at the points of flat light emission in **Figure 12** [25].

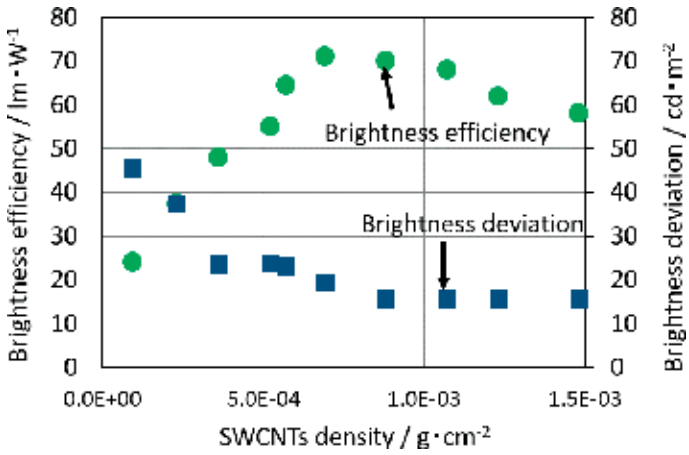

Figure 14. SWCNT content density with the dependence of brightness efficiency indicated on the left vertical axis and brightness homogeneity on the right vertical axis. The peak-to-peak voltage condition of the triangle wave is fixed at 5 kV [25].

the SWCNTs and high emission site homogeneity from **Figures 11** and **14**, and it will obtain a long emission life-time to withstand practical use as a plane-light emitting device. The coated, highly crystalline SWCNT cathode has potential for realizing a visible ray flat plane-emission device with low power consumption and a long product life cycle.

Figure 16 shows the distance distribution between neighboring SWCNTs depending on the SWCNT density. The results were measured from the total number of SWCNTs protruding from the groove face of an arbitrarily scratched ITO film by visual observation with an SEM image, as that in **Figure 7**. SWCNTs were exposed from the side wall of the grooved face into the ITO film. The distance between SWCNTs protruding from the grooved face depends on

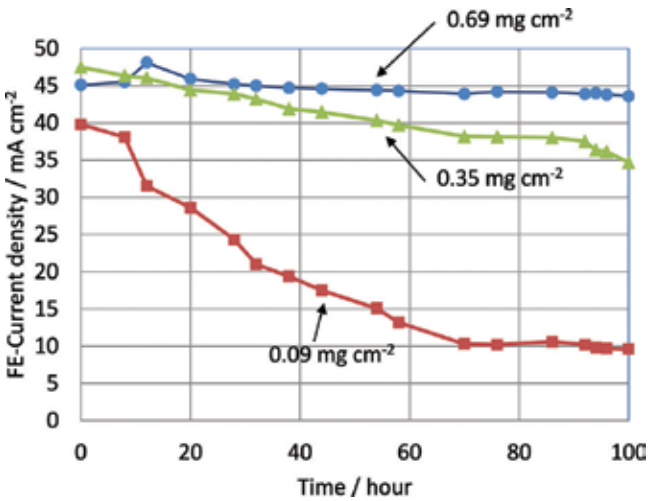

Figure 15. The lifetime of field emission current density up to 100 hours. The half time against the initial field emission current density of 0.69 mg/cm^2 will be over 5000 hours [25].

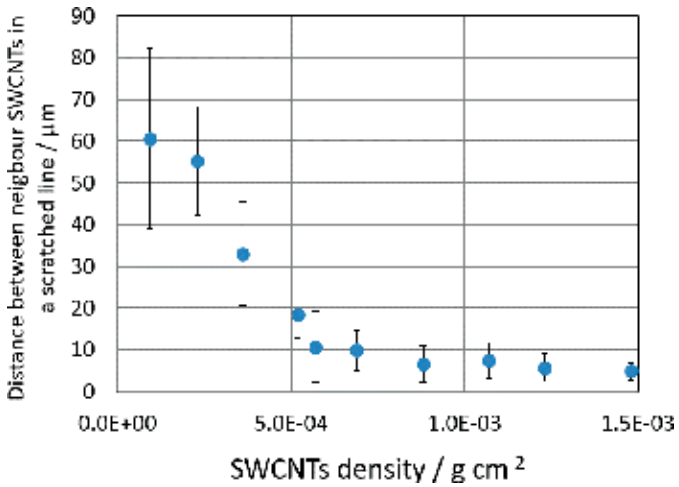

Figure 16. The dependence on the distance between neighboring SWCNTs protruding from the edges of ITO film and SWCNT density [25].

the SWCNTs density; it averages approximately 10 μm at 0.69 mg/cm^2. If SWCNTs are well dispersed in the ITO film and align randomly, their protrusions aligning along a direction in the groove made by a voluntary scratching process appear uniform. The protruding SWCNT length measured by SEM was generally 4–6 μm. The ratio of the average distance and length of SWCNTs via SEM images was nearly 2, and it is believed that the electrical field to obtain a high field emission current is added at the top of each protruding SWCNT of 0.69 mg/cm^2 [28]. Then the SWCNTs for the field emitter protruding from the grooved face were aligned in a direction parallel to the ITO film plane and substrate as shown in **Figure 6** and the schematic drawing in **Figure 7**, which shows such drawings of the models with random directions for the SWCNTs. The dotted square boxes indicate scratched areas, and the tops of SWCNTs that possibly emit electrons are highlighted with red circles in them. These depend on the density of the SWCNTs in a coated film. The direction of the SWCNTs exposed by scratching aligns in a direction parallel to the substrate, thereby uniformly yielding electrical fields at the top of each SWCNT without any fluctuation of the protruding SWCNT length. We thus obtained high homogeneity of the electron plane-emission with the dispersion and density of SWCNTs in the coated film.

The flat plane-emission from the simple diode panel generated a stable and homogeneous brightness of over 2000 cd/m^2 in the sampling area as shown in **Figure 12** without current fluctuation in the plane. The current fluctuation of emissions from the flat plane panel with an added voltage of 4 kV DC was stable over a period of 150 minutes as shown in **Figure 17**. This degree of electron emission stability is excellent for highly purified and crystallized SWCNTs in a diode panel. In particular, highly crystallized SWCNTs have no defects in their carbon network [23, 29], and such perfect crystallization prevents SWCNTs from breaking down with a large field emission current. Previously, it was necessary for a stable field emission current by CNTs with low power consumption to construct the triode structure, to synthesize carbon nanotubes designed with vertical alignment and standing height uniformly on an electrode by CVD with high temperature, and to obtain a high vacuum atmosphere around over 10^{-6} Pa in a panel [30]. In this study, we were able to obtain a stable large field emission current in a simple diode panel for the first time ever.

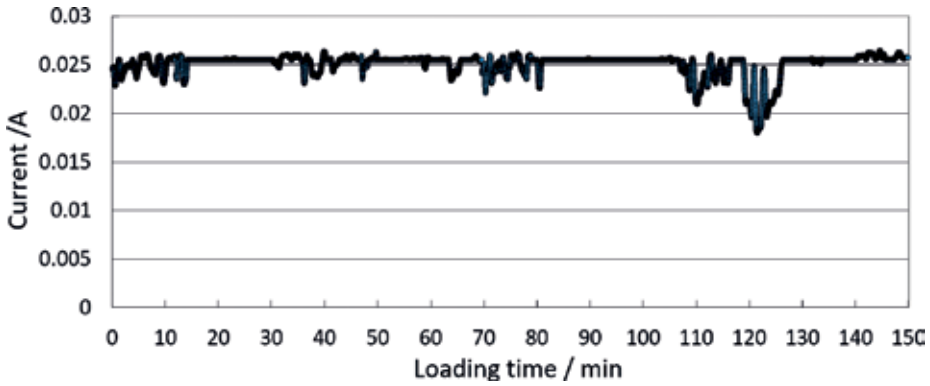

Figure 17. Current fluctuation with 4kVDC loading for 150 minutes [31].

5. Basic design of the triode structure

The following time, a triode structure employing highly crystalline SWCNTs was attempted to serve as a prototype device of a flat-panel illumination shown in **Figure 18**. This device had a cathodoluminescence structure and had three electrodes for the FE electron emissions as a cathode, the switching of FE electron emissions on and off as a gate, and the radiation of visible rays by electron impact as an anode electrode. The cathode and the gate electrode, which apply voltage sequentially (called as line sequential scanning method) for electron emissions from the cathodes respectively, were patterned along the same line referred to **Figure 18**. Furthermore, a mixture of the long afterglow phosphor (P-1 from Mitsubishi Chemical) material with fluorescent material (P-22 from Nichia) that conducts a high luminance output was used for the anode electrode.

A stripe patterned structure was adopted for the gate electrodes used for on/off switching of the FE electrons, as shown in **Figure 18**. An FE electron emission site existed at the edges of

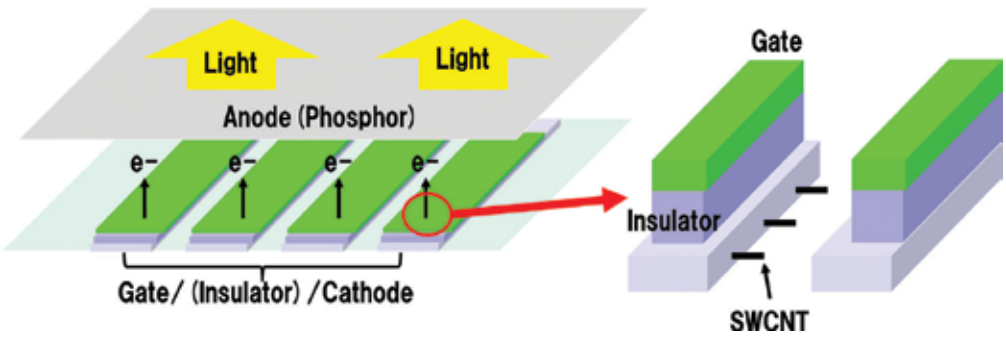

Figure 18. Basic structure of the triode flat-panel light-emission device [32]. Copyright (2017) The Japan Society of Applied Physics.

the tops of the SWCNTs, exposed on the both sides of the nicks scraped on the coating by a picking tool [25]. Thus, no exposed SWCNT was raised for field emission of electrons. The edges of the SWCNTs, as well as the width of the stripe patterned gate electrodes referred to **Figure 18**, were designed in an attempt to minimize the driving voltage for on/off switching of the FE electrons. In relation to the field intensity at the edges of the tops of the SWCNTs exposed on the both sides of the nick in **Figure 18**, the electrical potential distribution in the space, along with the electrode width dependence of electrical potential distribution at the edges of the SWCNTs, were simulated according to the surface charge method [33–36].

The cathode electrodes were grounded stationary while the anode electrode applied a direct-current (DC) voltage. The acceleration conditions for the electrons irradiated on the phosphor were taken into consideration to obtain a high brightness efficiency within a few kilo-volts. Conditions to apply electrical potential to emit FE electrons were controlled for the gate electrodes because the FE electrons were emitted at constant field intensity.

The length of the SWCNTs protruded from the wall, the width of the nicks made using a picking tool and the aperture of the stripe patterned electrodes of the gate electrodes were designed at 1 μm, 30 μm, and 40 μm, respectively. This was done to change the voltage applied to the gate electrodes to the negative direction in order to transit of electrical potential. A schematic diagram of the calculation model, as well as the calculation results, is shown in **Figure 19**.

The electrical potential along the z-axis in cases where the voltage applied to the gate electrodes set at 0, −1, −3, and −5 V was calculated. The z-axis was defined as the direction extended from the origin located above the edge of the SWCNT where electrons are emitted. The potential distribution depended on the voltage applied to the gate electrode. It was determined that the threshold voltage of the FE electron emissions was reached at a voltage of approximately −3 V applied to the gates of the corresponding model. We attempted to fabricate a prototype device of a triode planar light-emitting device based on the above calculation results.

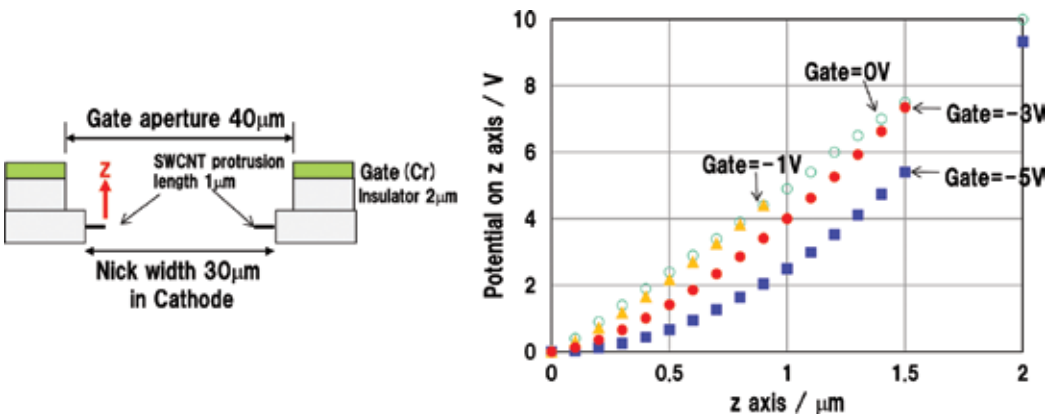

Figure 19. Schematic diagram of (left) calculation model and (right) calculation results [32]. Copyright (2017) The Japan Society of Applied Physics.

6. Correlation between driving power and light-emitting characteristics of a light-emission device

The prototype trial pattern for a triode-structure planar light-emission device is shown in **Figure 20**. Thin silicon oxidation film as an insulation layer was formed on a silicon wafer by using thermal oxidation treatment to assemble cathode, insulator and gate electrodes. The electrodes were laminated outward nearest the silicon oxide film by using the SWCNTs within an ITO film for the cathode electrode, a silicon oxide film of 1-μm thickness (formed using the TEOS-CVD method) as an insulation film, and a thin chrome film as a gate electrode. Gate electrodes, insulation films and cathodic electrodes installed SWCNTs were designed in a stripe pattern at the FE electron emission area as shown in **Figure 20**. The cathode electrodes between the gate electrodes were scratched in a line using a picking tool to expose and protrude the SWCNTs as FE emitters. The light-emitting area was designed to have an area of 15 × 15 mm^2.

Electron leakage at the gate electrodes was verified when electrons were emitted from the SWCNTs. The cathode and gate electrodes were installed on the ground. The spectra detected at the both electrodes being applied a pulse voltage is expressed in **Figure 21**. The voltage applied to the anode electrode by blue solid line and the current flowing through the cathode and gate electrodes are respectively represented by solid lines of red and gray. Almost no current was flowing through the gate electrode, while the FE current loading between the cathode and anode electrodes was confirmed.

A pulsed voltage was applied to the gate electrode, and a waveform was prepared to apply negative voltage by adding an offset voltage as a pulse signal. The system was driven by an operation mechanism to cut off the FE current, and it timed with the application of a few volts at the gate in the negative direction. A schematic diagram of the loading system for the prototype trial pattern for a triode-structure planar light-emission device is shown in **Figure 22**.

Conditions of the light emission, when switching on/off of the gate electrode, are shown in **Figure 23**. A stable FE current flowed between the cathode and anode electrodes when the voltage on the gate was 0 V. However, when a voltage of −3 V was applied to the gate electrode, we could find no current was flowing between the cathode and anode electrodes. These results of lighting emission indicated a successful control of the on-and-off switching of the current by switching gate electrodes.

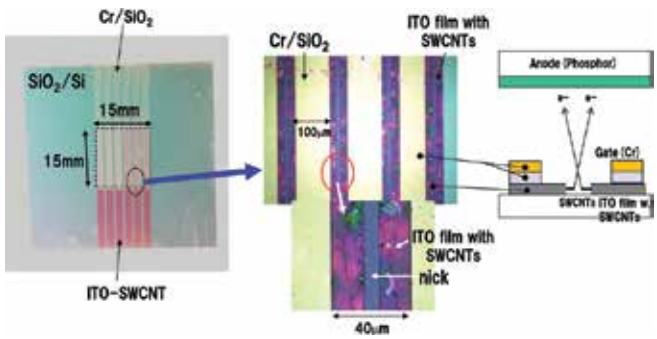

Figure 20. Prototype trial pattern of cathode gate electrode structure [32]. Copyright (2017) The Japan Society of Applied Physics.

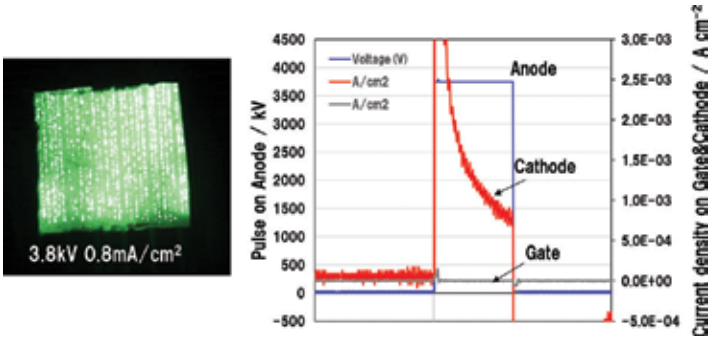

Figure 21. Cathode and gate-anode electrodes: Synchrony of a leaked current flowing through cathode and gate electrodes with signals of voltage applied to the anode, and depiction of a leaked current flowing through gate electrode [32]. Copyright (2017) The Japan Society of Applied Physics.

A mixed powder with the long-afterglow-type (P-1) and the high-luminance-output-type (P-22) phosphors was employed as a fluorescent material for the line scanning sequential test. The weight ratio of the mixture was designed to obtain the highest brightness efficiency. The frame scanning frequency was 60 Hz. A sequential timing chart to apply voltage to the gate electrodes on the six electrode lines of the prototype device was adopted for our development. We developed a scanning algorithm to amplify the light-emission luminance by overlapping the afterglow component of the long-afterglow-type phosphor with the high-luminance-output fluorescent material component of the subsequent frame scanning.

The FE current value flowing throughout the device and the luminance output from the anode were controlled by the voltage applied to the gate electrodes. The correlation between the energy power consumption and the luminance output by driving the device is shown in **Figure 24** from the results of light-emission evaluations. We could succeed to obtain a high luminance output of over 12,000 cd/m² and higher with a power consumption of approximately 0.1 W during driving the test panel. This outcome indicates that we were able to derive the higher performance in the world for a flat-panel light-emission device by achieving a brightness efficiency of 87 lm/W.

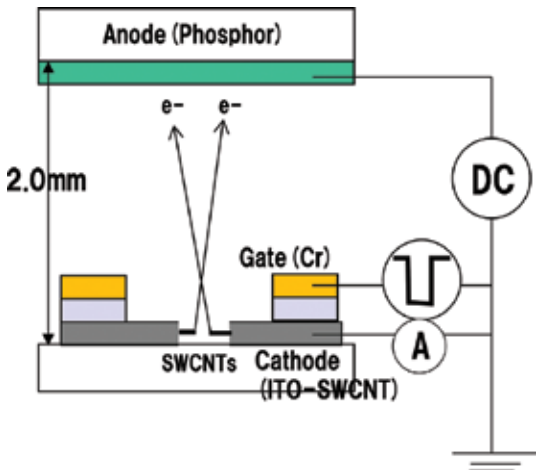

Figure 22. Schematic diagram of electrode wire connections and electrical circuit for drive [32]. Copyright (2017) The Japan Society of Applied Physics.

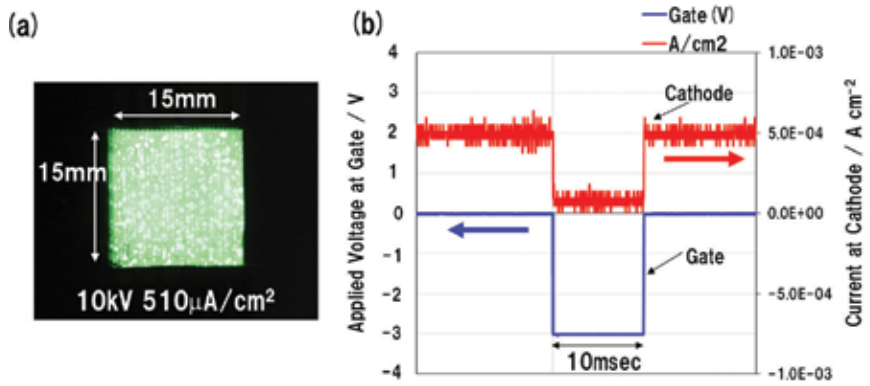

Figure 23. (a) Flat-panel light emission driven by line-sequential scanning (shaded by ND filter) [32]. (b) On-and-off chart for voltage applied to gate electrode and current flowing through cathode [32]. Copyright (2017) The Japan Society of Applied Physics.

We succeeded in assembling an FE planer electron-emission source pattern via a line-sequential-scanning method with an optimized design that the individual gate electrodes driven with an on/off FE current flowing. This was accomplished while conserving energy in cathode electrodes activated by making up scratching to emit electrons more effectively from the cathodic electrode employing a highly crystalline SWCNT. We also succeeded in amplifying the luminance-output by combining long-afterglow and high-luminance phosphors for an anode electrode to overlap the afterglow component of fluorescent materials to establish a basic design for assembling a triode flat-panel light-emission device with a line scanning sequential method. To the best of our knowledge, the creation of a flat-panel light-emission device that could achieve to obtain a high brightness efficiency of 87 lm/W was a remarkable outcome for the first time ever. Improvements to the driving performance for electron emissions at FE sources largely depend on the application of the highly crystalline SWCNTs. We believe this achievement assumes a leading role in electronic device creation through the effective use of a highly crystalline SWCNT, and we confidently need to promote its industrial design for practical use.

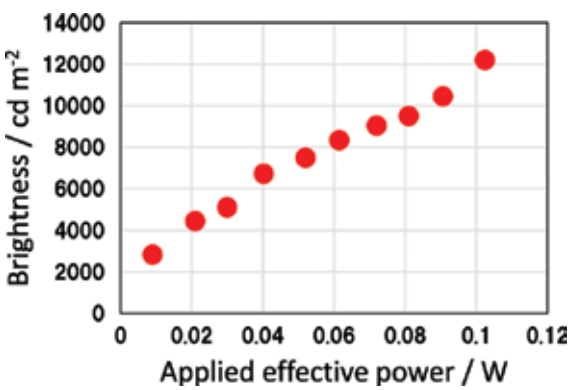

Figure 24. Relationship between power consumption and output luminance of triode flat-panel light-emission device [32]. Copyright (2017) The Japan Society of Applied Physics.

7. Conclusion

The attempt to apply highly crystalline SWCNTs as electron emission source was successfully achieved to obtain a planar light-emission device with low power consumption. Highly crystalline SWCNTs are an electrical element that can make a significant improvement in FE characteristics. A thin cathodic electrode film assembled via a wet process employing a highly crystalline SWCNT is expected to provide energy conservation as an FE electron emission source. By combining such elemental technologies both of the control the on-and-off switching of electron emissions in an arbitrary manner and the amplification of the luminance output with the persistence characteristics of a fluorescent screen, a flat-panel light-emission device with high brightness efficiency with an energy conserve driving method was assembled for the first time in the world.

The application of FE electron sources employing highly crystalline SWCNTs was determined to be effective for conserving energy based on such results, and is expected to establish other devices that are driven with low-power consumption in the future.

Acknowledgements

This work was partially supported by DOWA Holdings Co. Ltd. The author thanks the co-researchers from DOWA for their discussions and suggestions.

Author details

Norihiro Shimoi

Address all correspondence to: norihiro.shimoi.c8@tohoku.ac.jp

Graduate School of Environmental Studies, Tohoku University, Sendai, Japan

References

[1] Hamada N, Sawada S, Oshiyama A. New one-dimensional conductors: Graphitic microtubules. Physical Review Letters. 1992;**68**:1579-1581

[2] Saito R, Fujita M, Dresselhaus G, Dresselhaus MS. Electronic structure of chiral graphene tubules. Applied Physics Letters. 1992;**60**:2204-2206

[3] Tanaka K, Okahara K, Okada M, Yamabe T. Electronic properties of bucky-tube model. Chemical Physics Letters. 1992;**191**(5):469-472

[4] Kim J-Y, Kim M, Kim HM, Joo J, Choi J-H. Electrical and optical studies of organic light emitting devices using SWCNTs-polymer nanocomposites. Optical Materials. 2002; **21**:147-151

[5] Ebbesen TW, Lezec HJ, Hiura H, Bennett JW, Ghaemi HF, Thio T. Electrical conductivity of individual carbon nanotubes. Nature. 1997;**382**:54-56

[6] Wildoerm JWG, Venema LC, Rinzler AG, Smalley RE, Dekker C. Electronic structure of atomically resolved carbon nanotubes. Nature. 1998;**391**:59-62

[7] Odom TW, Huang JL, Kim P, Lieber CM. Atomic structure and electronic properties of single-walled carbon nanotubes. Nature. 1998;**391**:62-64

[8] Treacy MMJ, Ebbesen TW, Gibson JM. Exceptionally high Young's modulus observed for individual carbon nanotubes. Nature. 1996;**381**:678-680

[9] Saito Y, Uemura S, Hamaguchi K. Cathode ray tube lighting elements with carbon nanotube field emitters. Japanese Journal of Applied Physics. 1998;**37**:L346-L348

[10] Dai H, Hafner JH, Rinzler AG, Colbert DT, Smalley RE. Nanotubes as nanoprobes in scanning probe microscopy. Nature. 1996;**384**:147-150

[11] Dillon AC, Jones KM, Bekkedahl TA, Kiang CH, Bethune DS, Haben MJ. Storage of hydrogen in single-walled carbon nanotubes. Nature. 1997;**386**:377-379

[12] Niu C, Sichel EK, Hoch R, Moy D, Tennent H. High power electrochemical capacitors based on carbon nanotube electrodes. Applied Physics Letters. 1997;**70**:1480-1482

[13] Rinzler AG, Hafner JH, Nikolaev P, Lou L, Kim SG, Tomanek D, et al. Unraveling nanotubes: Field emission from an atomic nanowire. Science. 1995;**269**:1550-1553

[14] De Heer WA, Chatelain A, Ugarte D. A carbon nanotube field emission source. Science. 1995;**270**:1179-1180

[15] Collins PG, Zettl A. A simple and robust electron beam source from carbon nanotubes. Applied Physics Letters. 1996;**69**:1969-1971

[16] Saito Y, Hamaguchi K, Hata K, Uchida K, Tasaka Y, Ikazaki F, et al. Conical beams from open-ended nanotubes. Nature. 1997;**389**:554-555

[17] Bonard JM, Maier F, Stoeckli T, Chatelain A, De WA, Salvetat JP, et al. Field emission properties of multiwalled carbon nanotubes. Ultramicroscopy. 1998;**73**:7-15

[18] Fransen MJ, van Rooy TL, Kruit P. Field emission energy distributions from individual multiwalled carbon nanotubes. Applied Surface Science. 1999;**146**:312-327

[19] Saito Y, Hamaguchi K, Nishino T, Hata K, Tohji K, Kasuya A, et al. Field emission patterns from single-walled carbon nanotubes. Japanese Journal of Applied Physics. 1997;**36**:L1340-L1342

[20] Ren ZF, Huang ZP, Xu JW, Wang JH, Bush P, Siegal MP, et al. Synthesis of large arrays of well-aligned carbon nanotubes. Science. 1998;**282**:1105-1107

[21] Tsai SH, Chao CW, Lee CL, Shih HC. Bias-enhanced nucleation and growth of the aligned carbon nanotubes with open ends under microwave plasma synthesis. Applied Physics Letters. 1999;**74**:3462-3464

[22] Kim JM, Choi WB, Lee NS, Jung JE. Field emission from carbon nanotubes for displays. Diamond and Related Materials. 2000;**9**:1184-1189

[23] Iwata S, Sato Y, Nakai K, Ogura S, Okano T, Namura M, et al. Novel method to evaluate the carbon network of single-walled carbon nanotubes by hydrogen physisorption. Journal of Physical Chemistry Letters. 2007;**111**:14937-14941

[24] Shimoi N. Effect of increased crystallinity of single-walled carbon nanotubes used as field emitters on their electrical properties. Journal of Applied Physics. 2015;**118**:214304

[25] Shimoi N, Adriana LE, Tanaka Y, et al. Properties of a field emission lighting plane employing highly crystalline single-walled carbon nanotubes fabricated by simple processes. Carbon. 2013;**65**:228-235

[26] Popov VN. Carbon nanotubes: Properties and application. Materials Science & Engineering R: Reports. 2004;**43**(3):61-102

[27] Fransen MJ, van Rooy TL, Kruit P. Field emission energy distributions from individual multiwalled carbon nanotubes. Applied Surface Science. 1999;**146**:312-327

[28] Nilsson L, Groening O, Emmenegger C, Kuettel O, Schaller E, Schlapbach L. Scanning field emission from patterned carbon nanotube films. Applied Physics Letters. 2000; **76**:2071-2073

[29] Tohji K, Goto T, Takahashi H, et al. Purifying single-walled nanotubes. Nature. 1996; **383**(6602):679-679

[30] Anantram MP, Leonard F. Physics of carbon nanotube electronic devices. Reports on Progress in Physics. 2006;**69**(3):507-561

[31] Garrido SB, Shimoi N, Abe D, Hojo T, Tanaka Y, Tohji K. Plannar light source using a phosphor screen with single-walled carbon nanotubes as field emitters. Review of Scientific Instruments. 2014;**85**:104704

[32] Shimoi N, Abe D, Matsumoto K, Sato Y, Tohji K. Low-power-consumption flat-panel light-emitting device driven by field-emission electron source using high-crystallinity single-walled carbon nanotubes. Japanese Journal of Applied Physics. 2017;**56**:065101

[33] Murata H, Shimoyama H, Ohye T. Computer simulation of electric field analysis for vertically aligned carbon nanotubes: I. Simulation method and computing model. Proceedings of SPIE. 2001;**4510**:156-162

[34] Shimoyama H, Murata H, Ohye T. Computer simulation of electric field analysis for vertically aligned carbon nanotubes: II. Electric field on the nanotube apex. Proceedings of SPIE. 2001;**4510**:163-171

[35] Shimoi N, Tanaka S-I. Numerically optimized bundle size and distribution of carbon nanofibers for a field emitter. Carbon. 2010;**48**:905-911

[36] Thostenson ET, Ren ZF, Chou TW. Advances in the science and technology of carbon nanotubes and their composites: a review. Composites Science and Technology. 2001; **61**:1899-1912

Chapter 4

Carbon Nanotubes as a Pulsed Electron Sources

Xianqi Wei

Additional information is available at the end of the chapter

http://dx.doi.org/10.5772/intechopen.70528

Abstract

One of the most promising applications of carbon nanotubes (CNTs) is the emission electronics, in which CNTs are used as a field emission electron source. Lots of electronic devices are based on electron sources, which are the most important components served as state-of-art nanoelectronics devices in nowadays, such as field emission displays, miniature mass spectrometers, scanning ultrafast electron microscopes, X-ray generators, free electron lasers, THz sources, and so on. Field electron emission is based on the physical phenomenon of quantum tunneling, in which electrons are emitted from the surface of materials into vacuum on the condition of applied voltage. CNTs have many advantages as field emitters comparing with conventional metallic emitters like familiar examples of tungsten, gold, copper, and molybdenum. Electron emission from cold cathodes of CNTs has attracted attentions of numerous scientists, and substantial researches have been conducted on their properties and applications. In this chapter, we will focus on the field emission of CNT cold cathodes as an electron source, including of how to synthesize it by chemical vapor deposition (CVD) method and how to realize its electron emission. In addition, we will report pulsed electron emission of CNT cathodes. The combination of the laser pulse and the cold cathode will offer the possibility of pulsed field emission. Our approach demonstrates the growth mechanism and the emission mechanism of CNTs, which is beneficial for controlling the performance of its fascinating application on emerging fields.

Keywords: carbon nanotubes (CNTs), cathodes, field emission, laser, pulse

1. Introduction

Electron field emission (or field emission for short), is a tunnel effect of electron induced by high electric field at the surface of a solid material. A distinct advantage is that no extra energy is needed for the electron tunneling process. One of the most promising applications of the field emission is an electron source. Lots of electronic devices are based on electron

sources, which are the most crucial component served as state-of-art vacuum nanoelectronics and emerging novel devices in nowadays, such as field emission displays, emerging sensor, energy storage equipment, scanning ultrafast electron microscopes, X-ray generators, free electron lasers (FELs), THz sources, and so on [1–3].

With the advent of electron beam from nanometer-scale field emitters induced by femtosecond laser, electron sources are gradually replaced by ultrafast pulsed electron sources. These sources could potentially output extremely high emission current in a very short time, providing sufficient brightness, high-energy density, high frequency (up to optical frequency), and ultrashort coherent electron bunches [4–6]. Recently, such electron sources have intrigued a strong interest and encouraged the further studies of pulsed electron emission, opening the door to high-tech novel devices. For example, pulsed electron emission opens a way toward the time-resolved electron microscopy, because electrical gating and source control enable time resolution down to picoseconds, while using optical control enables creation of electron pulses with duration down to tens of femtoseconds. Such dense and short electron bunches can become a popular platform for material and device imaging, inspection, and failure analysis. They would enable exciting technological developments like four-dimensional (4D) time resolved electron microscopy, spectroscopy, holography, single-electron sources, and carrier envelope phase detection [7, 8]. Besides, pulsed electron sources are also becoming a hot topic in fields of medicine, physics, chemistry, industry, and communication, both in military and domestic industries.

In the past few decades, metallic nanotips have been considered an attractive and popular candidate as emitters of field emission cold cathodes, such as W, Mo, Au, Cu, Co, and so on. However, it is certainly worth considering that the complicated process of manufacture and thermal ablation of metallic nanotips result in poor thermal stability and mechanical properties for practical application. Besides, metallic tips suffer from serious thermal effect in pulsed field emission, because of illuminating metallic emitters for a long time by induced laser. Moreover, with the development of technology, the main trend of new generation electronic devices faces a great challenge on limitations of high power, high frequency, and compact small size. Conventional metallic emitters cannot satisfy the higher requirements of emerging devices, which have to provide high-energy density and pulsed emission electric current [9]. High-performance field emitters with adequate excellent emission properties are highly desired. To extend the studies on conventional metallic nanotips, this paper studies the pulsed electron emitters in a popular material of CNTs.

Since the discovery by Iijima in 1991, CNTs have received more and more research interests. One of the most popular studies is about the intriguing explorations of the high-performance field emitter as an emission electron source due to the CNTs' extraordinary instinct properties of high aspect ratio, good electrical conductivity, excellent thermal conductivity, robust chemical and mechanical properties. CNTs have been considered promising field emission candidates since they were first demonstrated as electron field emitters in 1995 [10–12]. These years, considerable researches have been conducted on their useful properties, as well as synthesis methods and various applications [13]. Here, we mainly introduce the property and application about the field emission of CNTs, which are synthesized by high temperature catalytic chemical vapor deposition (CVD) method.

http://dx.doi.org/10.5772/intechopen.70528

2. Growth of CNTs

2.1. Carbon nanotube arrays (CNT arrays)

The growth of CNT arrays follows a high temperature catalytic chemical vapor deposition (for short CVD) with iron phthalocyanine ($FeC_{32}N_8H_{16}$). In the growth process, the phthalocyanines act as not only a carbon source but also as a metallic catalyst. The growth temperature is 800–900°C for 15 min. The flow rate of hydrogen and argon are 25 and 60 sccm, respectively. The prepared CNT arrays are multi-walled nanotubes with the height of 6–10 μm and the diameter of 20–100 nm, as shown in **Figure 1**. The densely packed CNTs grow on the surface of the Si substrate. The roots stand vertically on the substrate surface and the tips entangles with each other. Detailed structures of CNT arrays are characterized by TEM as shown in **Figure 1(c)**. The synthesized CNT arrays are multi-walled nanotubes, and the interlayer spacing is about 0.34 nm, which is close to the (002) crystal plane of graphite. Besides, Raman Spectroscopy is employed to perform the Raman pattern of CNT arrays as shown in **Figure 1(d)**. Two of the sharp peaks are present at 1350 and 1350 cm^{-1}, respectively, corresponding to the disorder-induced D band and the tangential mode G band of the main Raman feature of multi-walled CNTs. Moreover, the ratio of intensities of the D and G bands, which is less than one indicates a high quantity of structure defects. And, the second-order 2D band, which is caused by the double resonant Raman scattering with two-phonon emissions, appears at 2700 cm^{-1} [4, 14].

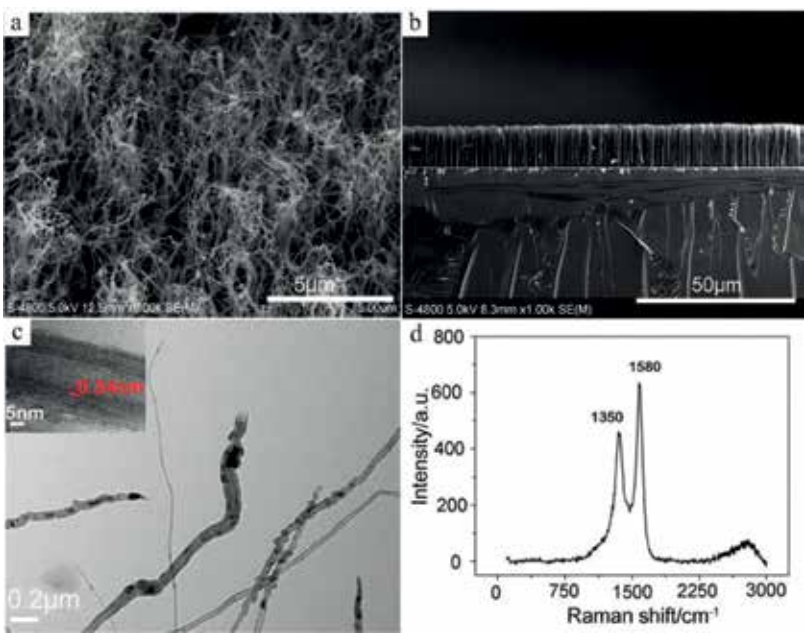

Figure 1. CNT arrays. (a) Top view, (b) sectional view, (c) TEM, (d) Raman spectrum.

2.2. Carbon nanotubes arrays-graphene composite (CNTs-G)

CNTs have been considered as a promising emitter because of their unique properties. For example, the electrical conductivity is about 10^5 S/cm and thermal conductivity is 3500 W/mK, which is better than that of many metallic emitters [15, 16]. Graphene, a desired electrical and thermal transport medium with two-dimensional sp^2 hybridized carbon atoms, is potential for field emission because of its remarkable electronic, mechanical, and thermal properties. However, the CNTs emitters are commonly attached onto the electrode surface to form the CNTs cathodes, resulting in a large contact resistance and unstable emission current. Graphene, a transparent cathode, have to design a special structure for field emission. The field emission still faces great challenges on stability and thermal effect, especially in pulsed field emission. In this part, we report the composite of CNTs-G to improve the electric and thermal transport as an emitter.

2.2.1. Bottom-up structure of the CNTs-G composite

CNTs-G composite grows by the same method as CNT arrays but the different parameters of gas flow rate. The reducing gas of hydrogen is 10 sccm and protective gas of argon is 60 sccm, respectively. The composite of CNTs-G consists of graphene sheets and CNT arrays. Graphene sheets is on the top surface and CNT arrays is on the bottom attached on the substrate surface, as shown in **Figure 2**. Graphene sheets and CNT arrays combine together tightly and form a three-dimensional (3D) cathode, which is completely different from the

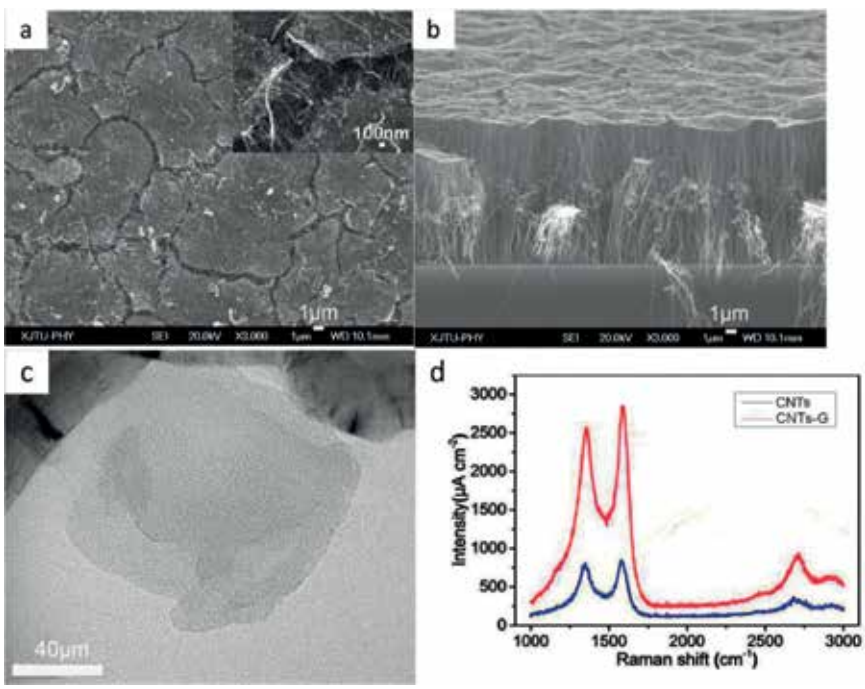

Figure 2. The composite of carbon nanotube arrays-graphene (CNTs-G). (a) Top view, (b) sectional view, (c) TEM, (d) Raman spectrum.

CNTs/graphene composite fabricated by transfer technology. The interaction between CNTs and graphene is mainly due to the Van der Waals force for the CNTs/graphene composite. Here, the 3D CNTs-G composite is directly synthesized, which is quite different from physical contact of the CNTs/graphene composite between the interface of CNTs and graphene. The 3D composite, having the vertically CNT arrays and the outstanding graphene, could provide a good electrical and thermal contact and exhibits a high performance as a thermal interface material.

The graphene sheets on the top surface of the CNTs-G composite are characterized by TEM, as shown in **Figure 2(c)**, and the composite shows a typical peak of 2D band at 2700 cm^{-1} in comparison with CNT arrays, as shown in **Figure 2(d)**. To obtain more detailed information on the chemical composition and surface electronic state of the CNTs-G composite, the X-ray photoelectron spectroscopy (XPS) examination is implemented, as shown in **Figure 3**. It can be clearly observed that Fe, O, N, and C elements exist in the spectrum. The elements of Fe and N arise from the carbon source of iron phthalocyanine ($FeC_{32}N_8H_{16}$). And, a sharp peak for C1s at 284.8 eV is observed to evaluate the binding behavior of the elements in the CNTs-G composite, which is ascribed to the graphitic carbon [17, 18].

2.2.2. Top-down structure of the CNTs-G composite

The principle of field emission is based on the application of a very high electric field to extract electrons from a metal or a highly doped semiconducting surface. However, if the field emission cathode surface has a high point or a protrusion, electrons may be extracted at

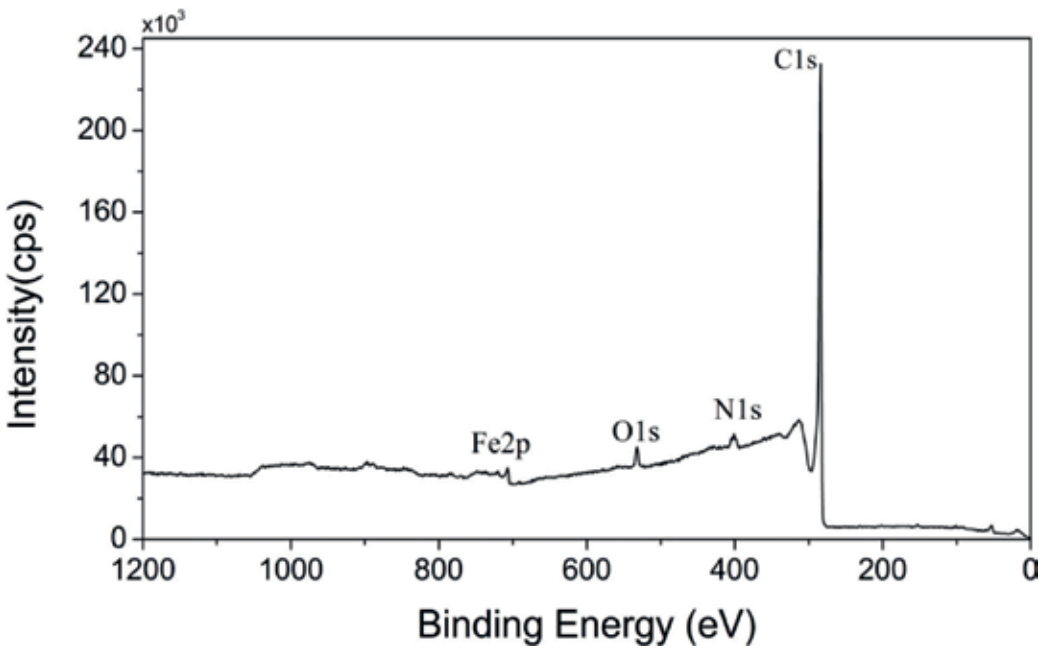

Figure 3. The full survey spectrum XPS spectra of the CNTs-G composite.

a considerably lower applied gap field. This is because the lines of force converge at the sharp point and the physical geometry of the tip provides a field enhancement [3]. So, it is desired a composite of CNTs-G, which is a top-down 3D structure. That is, CNT arrays are on the top surface of graphene, and it is tightly attached on the substrate surface as an electrode. This 3D CNTs-G composite is different from the above in the part (i). Graphene films are on the bottom grown on the substrate and CNT arrays are on the top surface, as shown in **Figure 4**. This composite was found by accident, when grew patterned CNT arrays.

From the EDX analysis shown in **Figure 4(d)**, it indicates that the composite mainly consists of C, Fe, and Si elements. The element of Fe results from the iron phthalocyanine ($FeC_{32}N_8H_{16}$), and the Si results from the substrate. Raman spectrum is carried out to further determine the structure information, as shown in **Figure 4(c)**. In comparison with CNT arrays, the Raman spectrum of films on the substrate have a typical peak at 2700 cm^{-1}, which is in accord with the 2D peak of graphene. The ratio of 2D peak height/G peak height indicates the films are

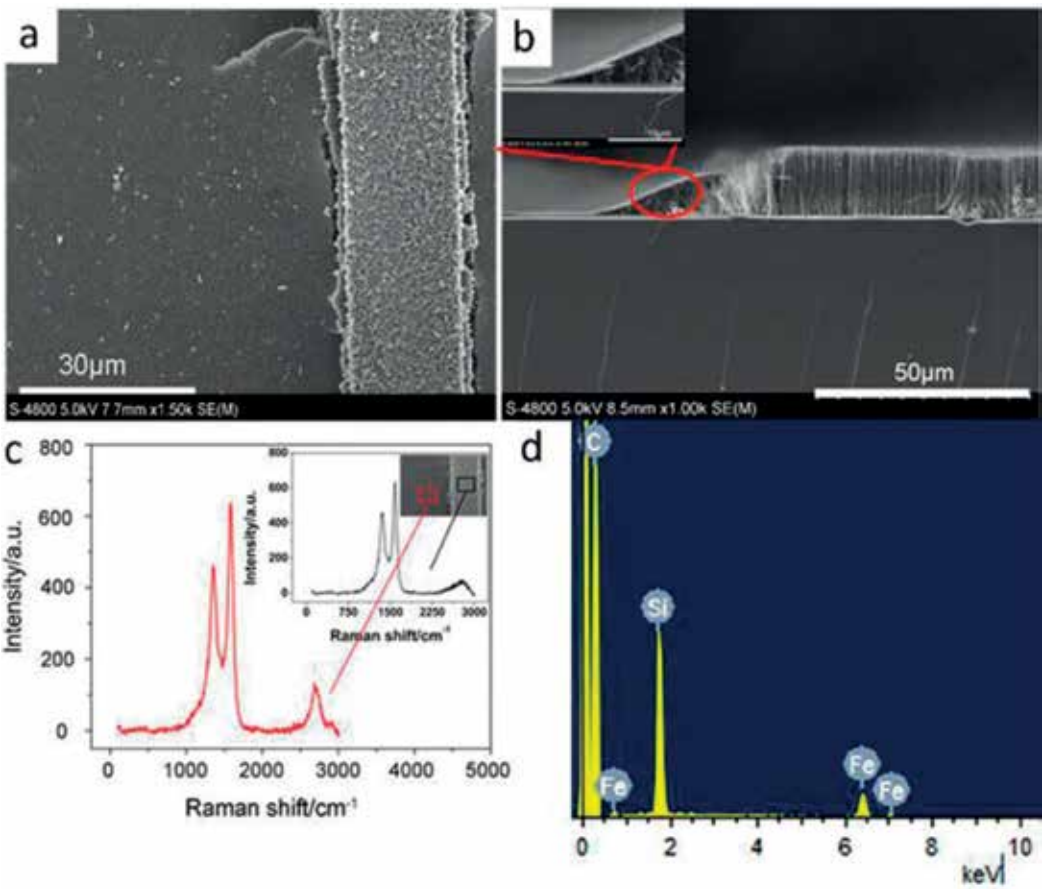

Figure 4. The top-down structure of CNTs-G composite. (a) Top view of a ribbon of CNT arrays; (b) cross sectional view; (c) Raman spectrum; (d) EDX analysis.

the multilayer graphene films. Due to the CNT arrays as field emitters and high electrical and thermal conductive of graphene films as electrode, the composite could provide a good electrical and thermal contact and exhibits a high-performance field emission.

3. Field emission

The phenomenon of the field emission is associated with a quantum mechanical tunneling process whereby electrons tunnel through a potential barrier under the influence of a high electric field. The field emission characteristic is usually described by F-N theory, given by:

$$\ln\left(\frac{J}{V^2}\right) = \ln A - \frac{B}{V} \tag{1}$$

where $A = 1.54 \times 10^{-6} S \frac{\beta^2}{\varphi}$ and $B = \frac{-6.83 \times 10^7 \varphi^{3/2} d}{\beta}$, S is the effective area of field emitters, β is the field enhancement factor, φ is the work function of field emitters, d is the distance of anode–cathode [3, 19]. Generally, it was used to improve the field emission properties by enhancing β. The sharp tips or small radius curvature of the emitter apex gives a high local electric field enhancement. In the past few years, to improve β of CNTs, novel composites of CNTs/graphene hybrids, three-dimensional CNTs and plasma treatment of CNTs have been reported to explore optimized CNTs emitters. In this part, we will introduce a cylindrical structure of CNT arrays cathodes. The morphology of CNT arrays on cylindrical substrate can be controlled by tuning the size of the substrate diameter. The work function φ of CNT arrays is supposed to 4.89 eV in this paper [20].

3.1. Planar structure

The area of CNT arrays grown on the flat substrate of Si is about 1.7 cm × 1.8 cm. The field emission measurement is carried out using diode parallel plate in vacuum 5×10^{-5} Pa. The anode–cathode spacing is 400 μm. The experimental set-up is shown in **Figure 5(a)**. **Figure 5(b)** gives the current density versus voltage (*J-V*) curves. The turn-on voltage is about 700 V (defined as the applied voltage required to generate an emission current density of 1 mA/cm^2). The insert of top left in **Figure 5(b)** is Fowler-Nordheim (F-N) plots corresponding to *J-V* curves, and the bottom right is the picture of current emission on 1500 V. The F-N curve follows the linear relationship, confirming that the detected current is in agreement with field emission mechanism.

3.2. Cylindrical structure

In the previous research, CNTs were synthesized on a flat substrate such as Si, SiO_2, and Au. Nevertheless, we present a method to synthesize CNT arrays on cylindrical waveguide of the optical fiber substrate. CNT arrays are synthesized on the fiber surface by CVD using a same method as reported the above. The substrate is commercial quartz optical fiber with a diameter of 220 μm. To prepare fiber substrate before CNTs growth, the polymer coating

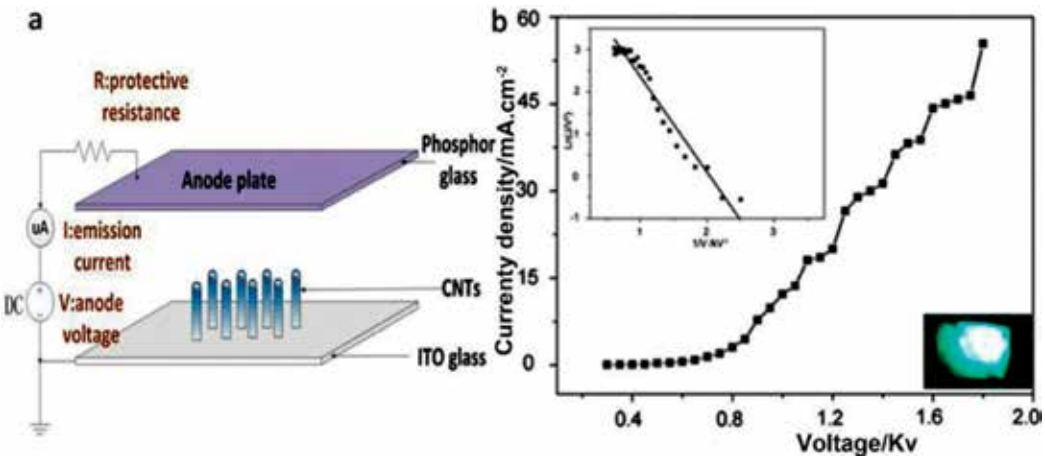

Figure 5. The field emission of the CNT arrays on Si substrate. (a) Structure diagram of experimental set-up, (b) measurement results of the field emission.

layer should be removed. Then, quartz optical fiber is corroded in dilute hydrofluoric acid (~13 wt.% HF) to the desired size by controlling the corrosion time. After treatment, the prepared fiber is used as substrate for the growth of CNT arrays.

The microstructures and morphologies of the products are characterized by SEM, TEM, and Raman spectroscopy. **Figure 6(a)** is an overall view, showing the densely packed CNT arrays covered on the fiber surface. Detailed structures of CNT arrays are characterized by TEM. **Figure 6(b)** and **(c)** are the low-magnification and high-resolution TEM image. The synthesized CNT arrays are multi-walled nanotubes with the diameters of 20–100 nm. As shown in **Figure 7(c)**, the interlayer spacing is about 0.34 nm, which is close to the (002) crystal plane of graphite. Besides, Raman pattern of CNT arrays is showed in **Figure 6(d)**. The D band appears at 1352 cm^{-1}, G band appears

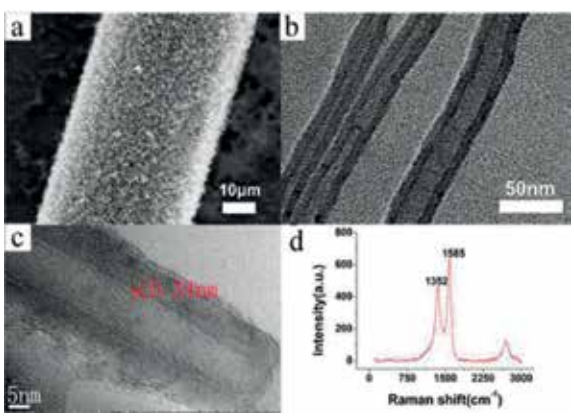

Figure 6. The scanning electron micrograph (SEM) image of CNT arrays covered on the surface of fiber substrate. (a) a overall view, (b) a low-magnification TEM image of CNTs, and (c) a high-resolution TEM image of a CNT. (d) the Raman spectrum of CNT arrays.

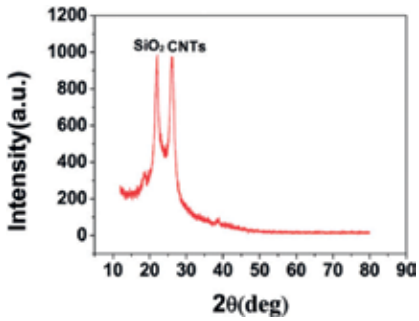

Figure 7. The X-ray diffraction pattern of CNT arrays covered on the quartz fiber surface.

at 1585 cm^{-1}, and 2D band appears at 2700 cm^{-1}, which is in agreement with the typical Raman feature of multi-walled CNTs [4, 14]. To further characterize the detailed information of the CNT arrays covered on the surface of fiber substrate, the X-ray diffractometer is employed to analyze. As shown in Figure 7, the XRD pattern of CNT arrays on fiber substrate exhibits a sharp (002) Bragg reflection at about $2\theta = 26.2°$, which is derived from the ordered arrangement of the concentric cylinders of graphitic carbon. And the peak centered on $2\theta = 21.9°$ shows the SiO_2 resulting from the quartz fiber substrate. **Figure 8(a)** is a cross-section SEM image of CNT arrays covered on the fiber substrate. CNT arrays vertically stand on the fiber surface with the uniform length and roots density. **Figure 8(c)** is a zoom in image of the CNTs roots marked in **Figure 8(a)**. The dense roots are highly aligned and vertically stand on fiber surface. The surface morphology of the CNTs

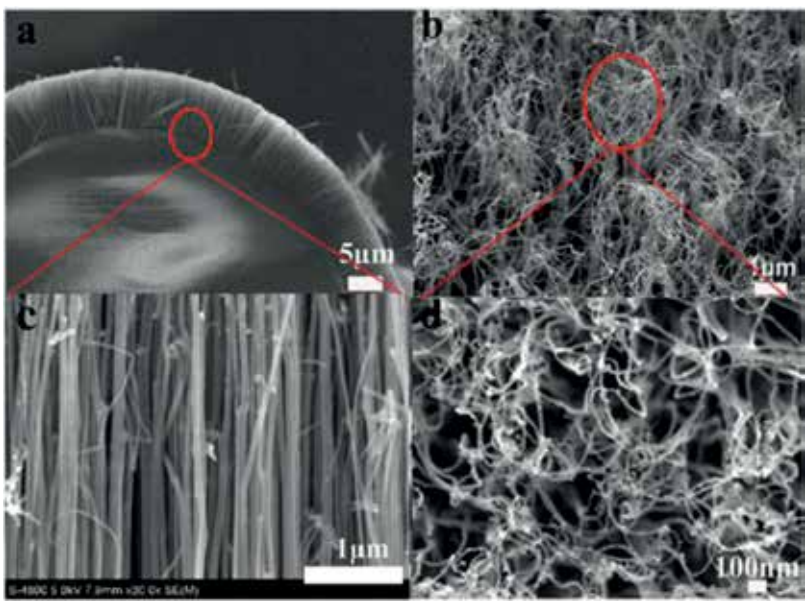

Figure 8. The SEM images of CNT arrays synthesized on the fiber substrate with the diameter of 200 μm, (a) the cross-section SEM image, (b) the top view SEM image of the surface morphology, (c) a zoomed in view of the roots, (d) a zoomed in top view of the tips.

tips are showed in **Figure 8(b)**, and a magnified top view image shows in **Figure 8(d)**. Though the dense roots of CNT arrays vertically attach on the fiber surface, the tips radiate outward dispersedly along the radial direction of fiber substrate [14]. With the fiber diameter decreased, the gaps between the CNT arrays tips are obviously distinct. And for that, the change of fiber diameter will greatly affect the tips morphology of CNT arrays, which cover on the cylindrical surface of optical fiber substrate. Decreasing the fiber diameter, the gaps between CNT tips will enlarge. The distance between the neighboring CNT arrays tips is greatly dependent on the fiber substrate, which could be changed by simply tuning the fiber diameter, as shown in **Figure 9**. **Figure 9(a)**, **(b)** is the overall view of CNT arrays covered on the surface of fibers with diameters of 200 and 20 μm. It is noticeable that remarkable cracks on fiber substrate with diameter of 20 μm, because the tips gap of nanotubes is large on a smaller diameter curve surface. **Figure 9(c)** is a cross-section image of CNT arrays covered on the cylindrical surface of 200 μm diameter fiber, and **Figure 9(d)** is CNT arrays on the surface of fiber with a smaller diameter of 20 μm [14]. **Figure 10** gives the field emission measurement results of CNT arrays covered on fiber substrates with diameters of 200, 100, 40, 30, and 20 μm. **Figure 10(a)** is the *J-V* curves. For the fiber substrate with the diameter of 20 μm, the CNTs cathode performs the minimum turn-on voltage V_{to} (the applied voltage requires to generate an emission current density of 1 mA/cm^2), yielding the maximum emission current at a low applied voltage than the others. When the diameter of fiber substrate decreases from 200 to 20 μm, the turn-on voltage V_{to} obviously decreases and the emission current density increased at the same applied voltage. β of the CNT arrays increases from 7823 to 11,631, and the turn-on voltage V_{to} decreases from 1290 to 109 V, corresponding to the data as shown in **Table 1**.

It is a well-known fact that β of nano cathodes has a significant effect on field emission properties. This is because the local electric field on the sharp emitters resulting in a field enhancement, which is expressed as β. However, there is a screening effect on the top tips of emitters, because of close spacing on dense individual tips. Screening effect weaken

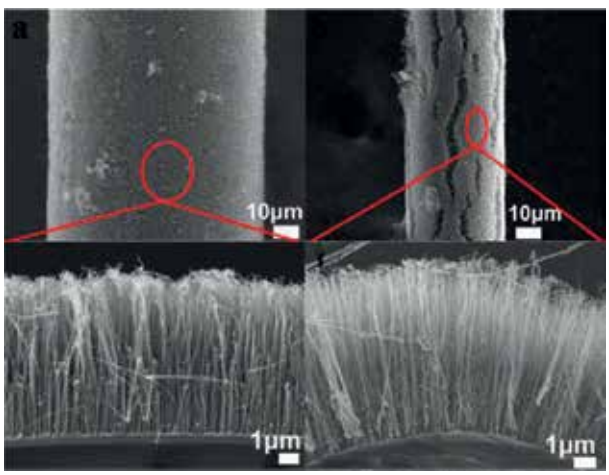

Figure 9. (a) The overall view of CNT arrays on fiber surfaces with diameters of 200 μm; (b) overall view of CNT arrays on fiber surface with diameter of 20 μm; (c) and (d) are cross-section images of CNT arrays on the surface of fiber substrate with the diameter of 200 and 20 μm, respectively.

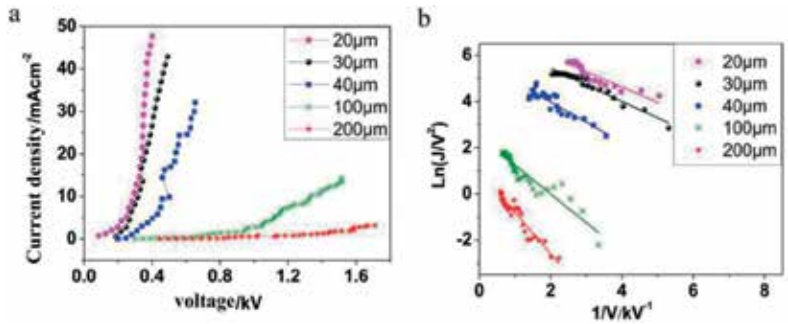

Figure 10. Field emission results of CNT arrays covered on fibers surfaces with diameters of 20, 30, 40, 100, and 200 μm. (a) *J-V* curve of emission current, (b) the F-N plots.

Diameter (μm)	20	30	40	100	200
V_{to}	109	190	270	730	1290
β	11.631	11.338	10.562	9247	7823

Table 1. The turn-on voltage (V_{to}) and the field enhancement factor (β) of CNTs cathodes covered on fibers surfaces with diameters of 20, 30, 40, 100, and 200 μm.

β of the emitter and result in a high V_{to} and small emission current, which is a defect for field emission. Thus, β is greatly dependent on the surface morphology of cathodes. The method of growing CNT arrays on fiber surface is efficient and feasible to tuning β by fiber diameter. With the fiber diameter decreasing, the gaps of tips enlarge and β increase subsequently because of weakening screening effect of CNT emitters. [14]. To illustrate the screening effect on the tips of CNT arrays, a simple electrostatic simulation is carried out by commercial software (Comsol 3.5a, emes mode of AC/DC Module). **Figure 11** shows the simulation results, performing equipotential lines of the electrostatic field near CNT

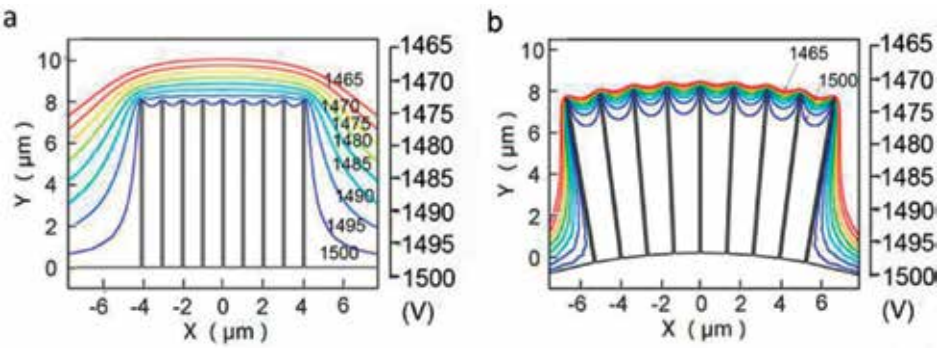

Figure 11. Simulation potential lines of the electric field near CNTs tips on a surface with diameter (Comsol 3.5a, emes mode of AC/DC module). (a) 200 μm, and (b) 20 μm, respectively. The unit in color bar is volt. The color bar ranges from −1500 to −1465 V.

tips on fiber substrates, a circular curving surface with curvature radius 200 and 20 μm, as shown in **Figure 11(a)** and **(b)**, respectively. With the curvature radius of substrate reduce, the spacing and the density of the equipotential lines on tips surface increase. This result demonstrates the decreased screening effect of the CNT arrays that lies on a smaller diameter fiber substrate.

4. Laser-induced field emission

Laser-induced field emission could offer opportunities for dramatic improvements in performance of electronic devices due to the possibility of manipulation and control of coherent electron motion in ultrafast spatiotemporal scales [8, 21]. As one of the most important cold cathode materials, CNTs have been widely studied. Synthesis of well-aligned CNTs on substrates of various geometries is also of special interest to the exploration of laser-induced field emission. Here, CNT arrays on fiber substrate serve as an emitter to explore the mechanism of laser-induced field emission.

From Eq.(1), we know that enhancing β or decreasing φ can improve field emission properties. As for a given material for cathode, φ is a constant. Generally, enhancing β by changing the tip morphology of the emitters is one of the main strategies. Herein, the improvement of field emission can be attributed to decreasing φ of CNT arrays because of the photon absorption. In this part, it will take advantage of laser leakage from an optical fiber to illuminate the cathode for realizing laser-induced field emission.

The cathode of laser-induced field emission is the CNT arrays emitters, which cover on the fiber substrate, as reported in **Figure 6**. **Figure 12** shows the schematic diagram of laser-induced field emission measurement set-up for the cathode of CNT arrays on an optical fiber.

The field emission properties of the cathode are measured in two cases: with laser-on and laser-off. **Figure 13(a)** shows the measurement results of the CNT arrays cathodes on optical fiber with the diameter of 30 μm. The turn-on voltage (a voltage requires an emission current density reaching to 1 mA·cm^{-2}) of laser-on state is 0.89 kV ($V_{\text{to-on}}$), and 1.01 kV ($V_{\text{to-off}}$) on laser-off state. $V_{\text{to-on}}$ is much lower than $V_{\text{to-off}}$. Besides, emission current on laser-on state is enhanced comparing with emission current on laser-off state. At 1 kV bias voltage, the emission current density on laser-on state ($J_{\text{E-on}}$) is 3.78 mA·cm^{-2} while 1.10 mA·cm^{-2} on laser-off state ($J_{\text{E-off}}$). The field emission properties on laser-on state are better than that of properties on laser-off state, as shown in **Figure 13(b)** and **(c)**. **Figure 13(b)** shows the emission current of CNT arrays on fiber diameter of 40 μm on laser-on and laser-off state. **Figure 13(c)** is the field emission results on fiber diameter of 140 μm.

As mentioned above, β and φ of the cathode are two critical factors for the field emission properties. β strongly depends on the cathode morphology. For a given optical fiber substrate, β keeps constant whenever CNT is on laser-on or laser-off states. Thus, the enhanced emission property is attributed to effective φ decreased by photon absorption. As shown in

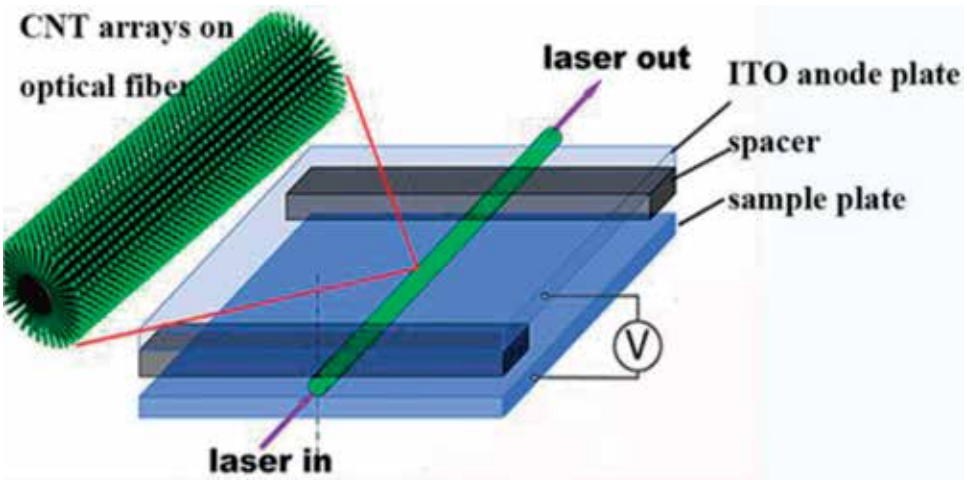

Figure 12. Schematic of laser-induced field emission measurement set-up.

Figure 13(a), when the fiber diameter fixed at 30 μm, β of the CNT arrays cathode is a constant of 4.89 eV. However, the turn-on voltage and emission current density are modulated by introducing laser into the optical fiber. The enhanced property is evaluated by measuring $\Delta\varphi$. According to the F-N plot and Eq.(1), the value of the effectiveφ, $\Delta\varphi$, and β are deduced and listed in **Table 2**. β of the cathode on the optical fiber with diameter of 30 μm is 4672, while that of the cathode on the fiber with diameter of 40 and 140 μm is 2804 and 2526. The different β is attributed to the different curvature of the cathode on fibers with different diameters, agreeing with the above discussion. What we are concerned here is the change of the work function $\Delta\varphi$of the cathode causing by the laser field. From **Table 2**, the work function significantly reduces to 4.14 eV when the fiber substrate diameter is 30 μm on the laser-on state. While the cathodes on fibers with diameters of 40 and 140 μm, the work function reduce to 4.28 and 4.76 eV, respectively.

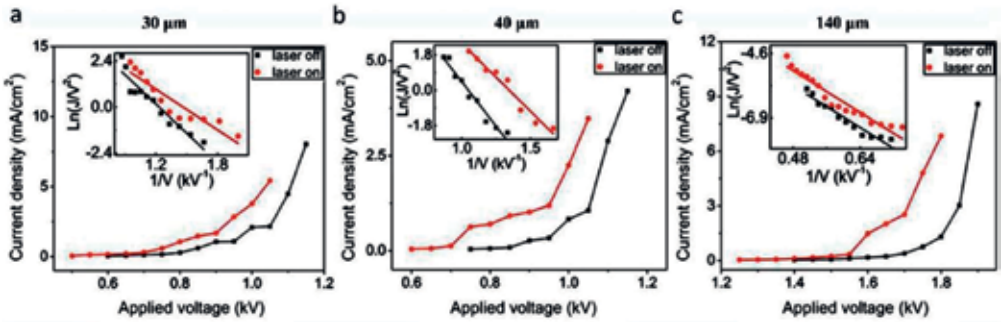

Figure 13. Laser-induced field emission measurement results. (a) The emission current density versus applied field voltage (*J-V*) curves of cathode of CNT arrays on optic fiber with the diameter of 30 μm on laser-on and laser-off cases. Inset is the corresponding F-N plot. (b) Fiber diameter is 40 μm. (c) Fiber diameter is 140 μm.

Diameter	30 μm	40 μm	140 μm
$\varphi_{\text{laser-on}}$	4.14 eV	4.28 eV	4.76 eV
$\Delta\varphi$	0.74	0.49	0.12
β	4672	2804	2526

Table 2. The effective work function φ, $\Delta\varphi=|\varphi_{\text{laser-on}}-\varphi_{\text{laser-off}}|$, and the field enhancement factor β of CNT arrays on fibers substrate with the diameter of 30, 40, and 140 μm on both laser on and off state.

The key factor of influencing φ is the laser field. On the laser-on state, the leakage of laser from the fiber surface is absorbed by CNT cathodes, when laser propagate through the fiber substrate. The electrons are excited to high-energy states and then emit to vacuum on applied voltages. So, the effective work function φ of CNT cathodes should subtract $\Delta\varphi$ (arise from absorbing photons) from 4.89 eV for laser-induced field emission. These results open a new way to improve field emission properties by the work function of cathodes and provide a preparation for realizing pulsed field emission.

5. Pulsed field emission

Illuminating a sharp cathode tip with laser pulses leads to pulsed field emission. A number of studies clarified the intriguing characteristics of the electron emission processes. This part explores pulsed field emission from CNT cathodes.

As mentioned above, the field emission property was modulated by optical field using a continuous wave laser (CW laser) in the laser-induced field emission. Electrons pump up a high-energy state by laser illumination and then tunnel through barrier to emit into vacuum. The emission current is closely related to CW laser field. So, the CW laser is replaced by pulsed laser to desire a discontinuous modulated signal of pulsed emission current. Herein, the pulsed field emission is based on laser-induced field emission. Illuminating CNT arrays with infrared laser pulses leads to pulsed field emission. **Figure 14(a)** shows the experimental set-up of pulsed field emission from CNT cathodes on Si substrate. **Figure 14(b)** shows the

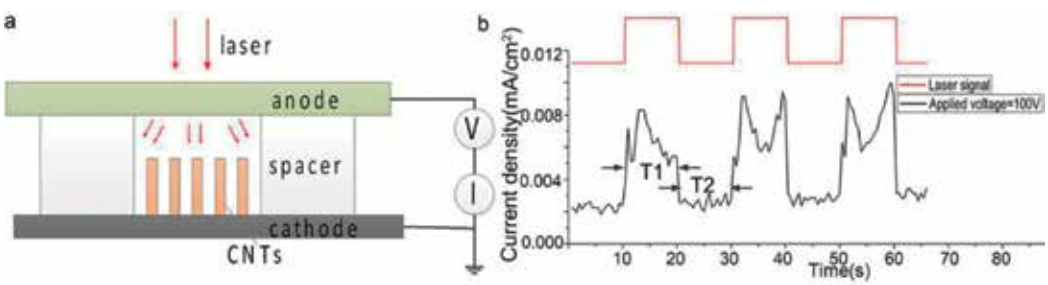

Figure 14. (a) Experimental set-up of pulsed field emission. (b) Electronic pulses from CNT cathodes illuminated by pulsed laser, on applied voltage of 600 V. Laser pulse-on and laser pulse-off are both 10000 ms.

pulsed emission current from CNT cathodes, when the pulse width (Pulse-on denotes the pulse duration expressing by T1) and the trough width (Pulse-off denotes time interval of two pulses expressing by T2) are both 10,000 ms. Importantly, the emission electronic pulses is almost synchronous with laser pulses with the electronic pulse duration of 10,000 ms or so, proving that electron emissions are intensively depended on the condition of laser pulse-on (T1). The average peak value of emission pulses density is 0.0068 mA/cm^2 with a little fluctuation on applied voltage of 600 V. The results demonstrate the realization of emission pulses from CNT cathodes. Besides, the field emission current density is about 0.0023 mA/cm^2 on laser pulse-off, which is much less than the emission current on laser pulse-on. It can be said the emission current can be enhanced by laser field.

Figure 15 shows emission pulses of pulsed field emission from CNT emitters illuminated by laser pulses, on the applied voltage of 100, 300, 500, 700, 900, and 1000 V with the same laser work condition. Increasing applied voltage, the peak value of emission pulses markedly increases on low applied voltage, as shown in **Figure 15(a)–(c)**. Although the peak value of emission pulses increase with the continually increasing applied voltage, the emission pulses trend to decrease on high applied voltage, as shown in **Figure 15(d)–(f)**. **Table 3** demonstrates values of the ratio of $\eta = I_{on}/I_{off}$ on different applied voltage. I_{on} is the average peak value of emission pulses density on pulse-on, and I_{off} is the average trough value of emission current density on pulse-off. The emission pulses are visible on low applied voltages, but the pulses cannot be distinguished on the high voltage of 1000 V ($\eta \approx 1$, that is $I_{on} \approx I_{off}$).

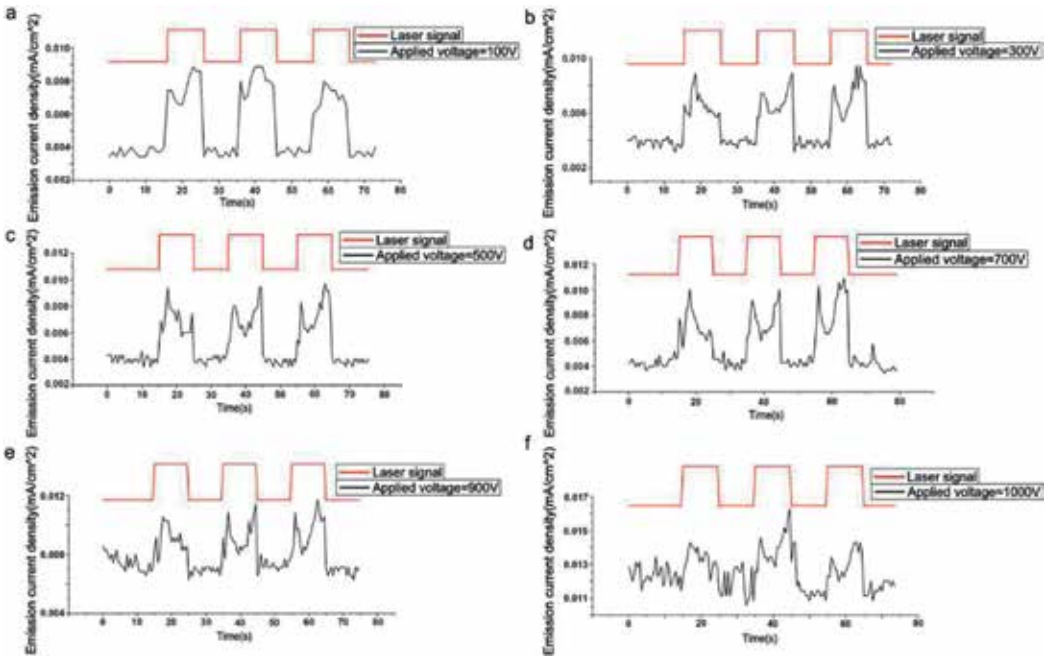

Figure 15. Electronic pulses of pulsed field emission from CNT cathodes illuminated by the same pulsed laser, but on the different applied voltage. Laser pulse-on (T1) and laser pulse-off (T2) are both 10000 ms. (a) on applied voltage of 500 V, (b) 600 V, (c) 700 V, and (d) 800 V.

Voltage (V)	100	200	300	400	500	600	700	800	900	1000
Ratio (mA/cm^2) I_{on}/I_{off}	2.09	2.48	3.53	4.07	5.07	2.09	1.98	1.55	1.39	≈1

I_{on} is the average peak value of emission electronic pulses density on pulse-on, and I_{off} is the average trough value of emission current density on electron pulse-off.

Table 3. The ratio values of $\eta = I_{on}/I_{off}$ on different applied voltage of 100, 200, 300, 400, 500, 600, 700, 800, 900, and 1000 V.

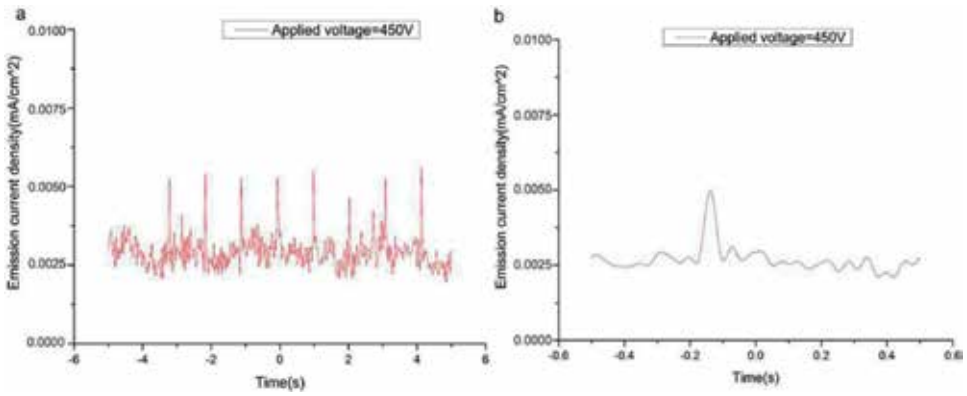

Figure 16. Electronic pulses with width of 50 ms from CNT arrays cathode on applied voltage of 450 V. (a) T1 = 50 ms, T2 = 1000 ms. (b) the detailed information of an electronic pulse.

In fact, emission mechanism is dominated by the electric field on high voltages, while laser field does not play an important role in the emission process. As the applied voltage continuously increases, emission electrons induced by laser pulses can be ignored due to it is too weak comparing with emission current of the field emission, just leading to a fluctuation for emission current. So, the pulsed field emission happens on the low applied voltage, and is greatly depending on the laser pulses. The results explain the emission mechanism and pave a way for realizing pulsed field emission from CNT cathodes.

Shortening the pulse cycle is a conventional method in order to increase the frequency of emission pulses for pulsed field emission. We try to decrease the pulse width to study short electronic pulses from pulsed field emission of CNT cathodes. **Figure 16** shows emission pulses of 50 ms from CNT emitters, on the laser work condition of T1 = 50 ms and T2 = 1000 ms. The results show the width and the time pulse-off of emission pulse is 50 and 1000 ms, synchronously with the laser pulse train. **Figure 16(b)** is the detailed information about an electronic pulse of 50 ms.

However, there is an inevitable problem of thermal effect existing in the pulsed field emission. Laser illumination makes CNT emitters heat up and causes a thermal effect during the emission process. For the further information of the thermal effect, we detect the response time of electronic pulses by oscilloscope with sampling rate of 2.5 GS/s. The results show that the electron emission is not instantaneous with the laser field. The rise and fall time spend more than 2 s on laser pulse-on and pulse-off, as shown in **Figure 17**. Generally, the thermal effect will lead to a response time, but the field emission is instantaneous. For the pulsed field emission, the response time and pulse broadening are the weaknesses causing by thermal effect. Especially, in the short emission electronic pulses, pulse broadening limits the possibility of

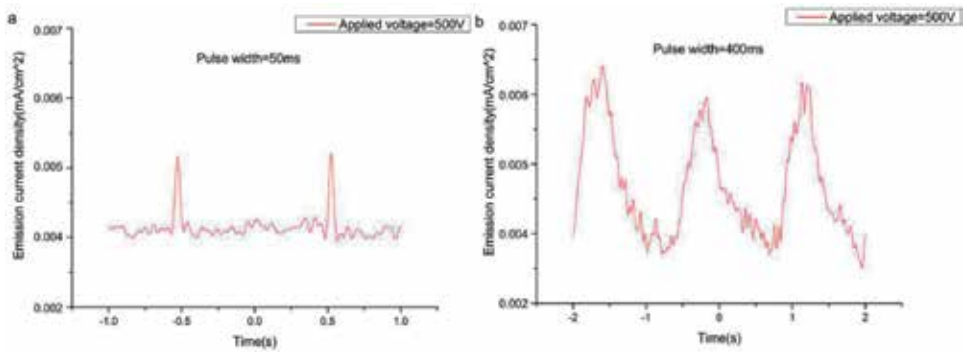

Figure 17. Electronic pulses with width from CNT arrays cathode on applied voltage of 500 V. (a) T1 = 50 ms, T2 = 1000 ms. (b) T1 = 400 ms, T2 = 1000 ms.

the high frequency and short pulse because of the thermal effect, as shown in **Figure 17(b)**. Nevertheless, there is an advantage of enhancing emission current for thermal effect in the pulsed field emission. As shown in **Figure 17**, the peak value of the electronic pulses is quite different on the same work condition but different T1. For **Figure 17(b)**, the emission current is compelled drop down before reach to the peak value of 0.006 mA/cm^2 comparing with **Figure 17(a)**. With the T1 increase, the emission current is enhanced resulting from thermal effect, which is beneficial for the pulsed field emission.

These results show that thermal effect enhances the pulsed field emission of CNT cathodes illuminating by pulsed laser, but emitting short electronic pulses are strongly influenced by thermal effect resulting in pulse broadening. So, the optimum work condition of laser pulse is T2 ≥ T1 for pulsed field emission, especially in realizing ultrashort electronic pulses. It provides a preparation for us studying ultrafast electron source.

Acknowledgements

This work was financially supported by the National Natural Science Foundation of China (Grant Nos. 61,172,040) and Science and Technology Program of Zhejiang Province, China (Grant No. 2017C31087).

Author details

Xianqi Wei[1,2,3*]

*Address all correspondence to: wei.wxq@163.com

1 Science School, HuaiHai Institute of Technology, Lianyungang, Jiangsu, China

2 Department of Microelectronics, School of Electronics and Information Engineering, Xi'an Jiaotong University, Xi'an, Shaanxi, China

3 Research Institute of Xi'an Jiaotong University, Hangzhou City, Zhejiang Province, China

References

[1] Nojeh A. Carbon nanotube electron sources: From electron beams to energy conversion and optophononics. ISRN Nanomaterials. 2014;**2014**(1):879827-879851. DOI: 10.1155/2014/879827

[2] Tian S, Li H, Zhang Y, Liu S, Fu Y. Potential field emitters: HfC nanorods sheathed with a HfO_2 nanoshell. CrystEngComm. 2014;**16**(15):3186-3191. DOI: 10.1039/c3ce42478b

[3] Xu NS, Huq SE. Novel cold cathode materials and applications. Materials Science & Engineering R. 2005;**48**(2-5):47-189. DOI: 10.1016/j.mser.2004.12.001

[4] Wei XQ, Li X, Liu WH, Wang XL. Laser tuned field emission of the car bon nanotube arrays grown on an optical fiber. Science China Technological Sciences. 2014;**57**(10):1936-1940. DOI: 10.1007/s11431-014-5630-1

[5] Krüger M, Schenk M, Hommelhoff P. Attosecond control of electrons emitted from a nanoscale metal tip. Nature. 2011;**475**(7354):78-81. DOI: 1038/nature10196

[6] Vogelsang J, Robin J, Nagy BJ, Dombi P, Rosenkranz D, Schiek M, Grob P, Lienau C. Ultrafast electron emission from a sharp metal nanotaper driven by adiabatic nanofocusing of surface plasmons. Nano Letters. 2015;**15**(7):4685-4691. DOI: 10.1021/acs.nanolett.5b01513

[7] Zhang P, Lau YY. Ultrafast strong-field photoelectron emission from biased metal surfaces: Exact solution to time-dependent Schrödinger equation. Scientific Reports. 2016;**6**:19894-19906. DOI: 10.1038/srep19894

[8] Lyashenko DA, Svirko YP, Petrov MI, Obraztsov AN. The laser assisted field electron emission from carbon nanostructure. Journal of the European Optical Society-Rapid Publications. 2017;**13**(1):4-10. DOI: 10.1186/s41476-017-0033-0

[9] Krüger M, Schenk M, Förster M, Hommelhoff P. Attosecond physics in photoemission from a metal nanotip. Journal of Physics B Atomic Molecular & Optical Physics. 2012;**45**(7):074006-074012. DOI: 10.1088/0953-4075/45/7/074006

[10] Zhang L, Zhang HMDPI. A survey on security and privacy in emerging sensor networks: From viewpoint of close-loop. Sensors. 2016;**16**(4):443-459. DOI: 10.3390/s16040443

[11] Deng JH, Zheng RT, Yang YM, Zhao Y, Cheng GA. Excellent field emission characteristics from few-layer graphene–carbon nanotube hybrids synthesized using radio frequency hydrogen plasma sputtering deposition. Carbon. 2012;**50**(12):4732-4737. DOI: 10.1016/j.carbon.2012.05.065

[12] Chen F, Ji X, Zhang Q. Radial AlN nanotips on carbon fibers as flexible electron emitters. Carbon. 2015;**81**:124-131. DOI: 10.1016/j.carbon.2014.09.037

[13] Kanth SK, Sharma A, Park BC, Kim HS. Multiwalled carbon nanotube field emitter as an electron source for a microcolumn. Journal of Vacuum Science & Technology B. 2016;**34**(1):011805-011811. DOI: 10.1116/1.4939834

[14] Wei X, Zhu Y, Xia X, Wang X, Liu W, Xin L. Carbon nanotube cathodes covered on the cylindrical surface of a fiber. RSC Advances. 2015;**5**(22):17049-17053. DOI: 10.1039/C4RA14537B

[15] Shao X, Srinivasan A, Zhao Y, Khursheed A. A few-layer graphene ring-cathode field emitter for focused electron/ion beam applications. Carbon. 2016;**110**:378-383. DOI: 10.1016/j.carbon.2016.09.048

[16] Xu S, Rezvanian O, Kara P, Zikry MA. Tunneling effects and electrical conductivity of CNT polymer composites. MRS Online Proceedings Library (OPL). 2011;**1304**:6697-6718. DOI: 10.1557/opl.2011.606

[17] Lei W, Zhu Z, Liu C, Zhang X, Wang B, Nathan A. High-current field-emission of carbon nanotubes and its application as a fast-imaging X-ray source. Carbon. 2015;**94**:687-693. DOI: 10.1016/j.carbon.2015.07.044

[18] Wimalasiri Y, Zou L. Carbon nanotube/graphene composite for enhanced capacitive deionization performance. Carbon. 2013;**59**(7):464-471. DOI: 10.1016/j.carbon.2013.03.040

[19] Zhao N, Chen J, Qu K, Khan Q, Zhang X. Stable electron field emission from carbon nanotubes emitter transferred on graphene films. Physica E: Low-Dimensional Systems and Nanostructures. 2015;**72**:84-88. DOI: 10.1016/j.physe.2015.04.024

[20] Deng JH, Zheng RT, Zhao Y, Cheng G. Vapor-solid growth of few-layer graphene using radio frequency sputtering deposition and its application on field emission. ACS Nano. 2012;**6**(5):3727-3733. DOI: 10.1021/nn300900v

[21] Bionta M, Chalopin B, Delmas M, Chatel B. Ultrafast laser-induced field emission from a single carbon nanotube based nanotip. In: Lasers and Electro-Optics (CLEO); 10-15 May 2015; San Jose. USA: IEEE; 2015. pp. 1-2

Chapter 5

Electric Field Induced Alignment of Carbon Nanotubes: Methodology and Outcomes

Ali Mohammad Amani, Seyyed Alireza Hashemi,
Seyyed Mojtaba Mousavi,
Seyyed Milad Abrishamifar and Arash Vojood

Additional information is available at the end of the chapter

http://dx.doi.org/10.5772/intechopen.70481

Abstract

In the current chapter, achievement of aligned carbon nanotube (CNT) network within the matrix via various kinds of electric fields (AC and DC) was evaluated. In this case, alignment mechanism of CNTs within the matrix and two useful techniques for justification of CNT alignment throughout the matrix were examined and presented, respectively. Afterward, effective factors in matter of CNT alignment and applicable procedures for fabrication of nanocomposites containing aligned CNTs were studied and presented, respectively. At the end, significant effects of CNT alignment on overall properties of nanocomposites that include electrical and mechanical properties were evaluated. Achieved results revealed that alignment of CNTs within the matrix can lead to significant improvement in the electrical and mechanical properties of nanocomposites at the same filler loading compared with randomly distribution of CNTs within the matrix, while production steps and conditions can also highly affect the outcome data.

Keywords: carbon nanotube, nanocomposite, electric field, alignment, electrophoresis

1. Introduction

Carbon nanotube (CNT) is a unique material with fantastic electrical, thermal, and mechanical properties, and since its discovery by Iijima in 1991 [1], global attention attracted toward it, and many researchers have evaluated the extraordinary properties of CNTs toward development of nanocomposites and sheets holding highly oriented CNTs with enhanced electrical and mechanical properties [2–7].

Alignment of CNTs within the matrix can boost their properties in various fields include electrical and mechanical properties [2–7]. What is more, alignment of CNTs can be achieved via various methods such as electrical field [2–4, 7, 8], magnetic field [9], shear flow [10, 11], mechanical force [12, 13], and electrospinning [14, 15], which electrical field–induced alignment is the simplest and most manageable method for alignment of CNTs within the matrix.

Besides, exert of electrical field to a matrix containing CNTs can lead to expansion of a highly oriented network from the negative electrode toward the positive electrode, which acting as a pathway for transferring current from the negative electrode toward the positive electrode. In this case, interruption of applied current can lead to collapse of developed network which known as relaxation mechanism [16].

In this chapter, first the alignment mechanism of CNTs within the matrix was evaluated, and thence, useful techniques for justification of CNT alignment in the content of matrix were presented. Afterward, effective techniques for fabrication of nanocomposites containing highly and randomly oriented CNTs were discussed, and effect of alignment on various properties of nanocomposites was examined.

2. Alignment mechanism of CNTs within the matrix

Alignment mechanism of CNTs consisted from four stages [16]. In the first stage, due to the application of electric field, a dipole moment induced at the edges of CNTs resulted in their rotation to a certain angle and thence aligned in the direction of electric field. In the second stage, polarized CNTs attract each other, and head-to-head contact occurs, forming an aggregating in a chain-like structure. In the third stage, CNTs migrate toward and attach to the negative electrode, respectively. When CNTs are close enough to the electrode in order to transfer the charge, they discharge and aggregate onto the electrodes. Attached CNTs to the electrode become sources of high field strength and primary locations for absorption of other CNTs. In the fourth stage, following the connection of the first CNT bundle to the negative electrode, other CNT bundles attached the first bundle, and thence aligned CNT network spans negative-positive electrode spacing. In fact, CNTs form a pathway for transferring the current from the negative electrode toward the positive electrode and if the electric field interrupted during the alignment process, highly oriented network breaks down and CNTs return to their primary locations, this phenomenon is known as relaxation mechanism [16, 17]. Likewise, the translational motion of CNTs toward the negative electrode, justifying the presence of a negative surface charge, is governed by the electrophoretic mobility of charged CNTs. In case of relaxation mechanism, the Brownain diffusion is relevant to the motion and tends to fade of the aligned network, till it returns to the primary randomly distribution situation [18]. In **Figure 1**, alignment process of CNTs within matrix can be seen.

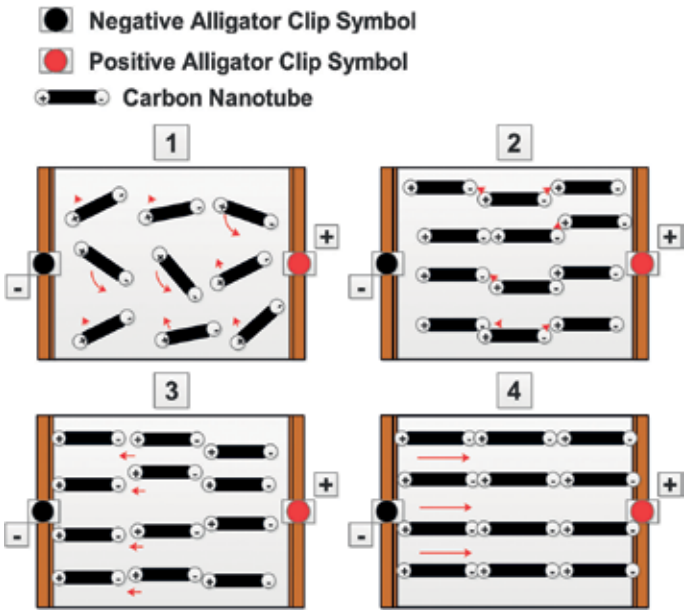

Figure 1. Alignment behavior of CNTs under application of electric field, (1) rotation, (2) head-to-head contact, (3) migration toward the negative electrode and (4) formation of aligned network between electrodes.

3. Justification of CNT alignment

There are several effective techniques for evaluation of CNT alignment within the matrix. In this case, the most common technique is via micro Raman spectroscopy. Raman spectrum of CNT/polymer nanocomposites features two characteristic peaks, namely D-band and G-band. The band at 1350 cm^{-1} is known as D-band and corresponds to overall amount of defects in carbon atom bonds in curved graphene sheets. Therefore, the structural defects including heteroatoms, vacancies, impurities, as well as pentagon-heptagon pairs in helical structures of CNTs can activate the D-band feature. The other strong band observed at 1590 cm^{-1}, called G-band, corresponds to the graphitization/crystallization degree of CNTs. G-band is believed to derive from the stretching of sp^2-hybridized carbon atom bonds along the surface of graphitic CNTs [19–21]. Alignment of CNTs within the polymer matrix has significant effect on both D-band and G-band peaks [22–24]; this introduces Raman spectroscopy as a complementary technique to verify the alignment of SWCNTs within the polymer matrix.

For this purpose, D (G) band intensities obtained parallel and perpendicular to CNT alignment direction are denoted as $D_{\parallel}$ ($G_{\parallel}$) and $D_{\perp}$ ($G_{\perp}$), respectively. Enhancement of $D_{\parallel}/D_{\perp}$ and $G_{\parallel}/G_{\perp}$ values corresponds to improvement of CNT alignment within the matrix, due to higher surface area of aligned CNT projected to applied laser light in parallel direction than perpendicular direction. Abbasi et al. [19] and Arjmand et al. [20, 25, 26] used this technique in order to examine the

alignment degree for compression-molded and injection-molded multi-walled carbon nanotube (MWCNT)/polymer nanocomposites. Their obtained results revealed that alignment of MWCNT via injection molding method had higher $D_{\parallel}/D_{\perp}$ and $G_{\parallel}/G_{\perp}$ values compared to the compression-molded samples, which contain randomly distributed CNTs. They also found out that D-band is more sensitive to MWCNT alignment than G-band; thus, higher values of $D_{\parallel}/D_{\perp}$ than $G_{\parallel}/G_{\perp}$ are expected for the aligned nanocomposites compared to unaligned nanocomposites.

The higher the ratio of $G_{\parallel}/G_{\perp}$ the better the quality of aligned CNT network [27]. In a study by Chapkin et al. [28], they have developed a technique, which has utilized polarized Raman spectroscopy for evaluation of CNT alignment within the polymer matrix under applied electric field. In this case, the effect of electric field strength between range 200 and 1100 V/cm on the degree of alignment and required time for achieving highly oriented CNT network was examined. The Raman scattering intensity is proportional to falling CNTs within the excitation volume of the laser. Increase in the concentration of CNTs within the matrix not only can increase the likelihood of multiple scattering events but also can increase the opacity of the mixture, which can lead to decrease in the penetration depth of the laser. Comparison between intensities of Raman spectra provided by orthogonally polarized incident light in nanocomposites containing well-aligned CNTs is an evaluation method for alignment characterization. Electrostatically aligned network of CNTs can lead to increase in the G-band intensity for parallel polarization direction and decrease for perpendicular direction in comparison to unaligned network. The $G_{\parallel}/G_{\perp}$ ratio indicating the degree of CNT alignment, which increases in this ratio, is the sign of better alignment within the matrix. In an unaligned specimen, this ratio is approximately 1. By applying the electric field between electrodes and alignment of CNTs between them, the intensities related to Raman peaks in the CNT spectrum begin to rise. In this case, the intensity of G-band was increased for the parallel polarization and decreased for the perpendicular polarization than unaligned specimens. Besides, by interruption of electric field, a considerable drop in the normalized G-band intensity was observed which is known as relaxation mechanism [16]. Decrease in the G-band intensity due to interruption of electric field indicating the loss of CNT alignment and collapse of aligned network. Furthermore, viscosity of matrix can highly affect the alignment behavior of CNTs. In this regard, a rapid loss in CNT alignment on the order of tens of milliseconds observed for low viscosity systems by interruption of the electric field [29, 30]. However, it has been observed that the alignment degree of CNTs in a matrix with high viscosity is higher than in a matrix with lower viscosity [31]. Increase in the electric field strength can either improve the $G_{\parallel}/G_{\perp}$ ratio or degree of alignment within the matrix. On the other hand, the polarization of a CNT highly depends on its conductivity [32, 33] and aspect ratio [32]. Conductivity of a CNT is based on its charity and behavior, which could be metallic or semiconducting. It has been proved that metallic CNTs presenting a greater degree of alignment via applied electric field than semiconducting CNTs [28]. Khan et al. [3] and Chen et al [4] have used micro Raman spectroscopy for determining the degree of CNT alignment via applied DC and AC electric fields, respectively.

In addition, Monti et al. [16] and Martin et al. [17] have measured the electrical current during the exertion of electric field as an indicator for formation of a highly oriented network in the area between two opposite electrodes. In fact, when highly oriented CNT network completed, the negative surface charge on the surface of the suspension has become constant, which shows highly oriented network has completed. Moreover, this network is a conductive

http://dx.doi.org/10.5772/intechopen.70481

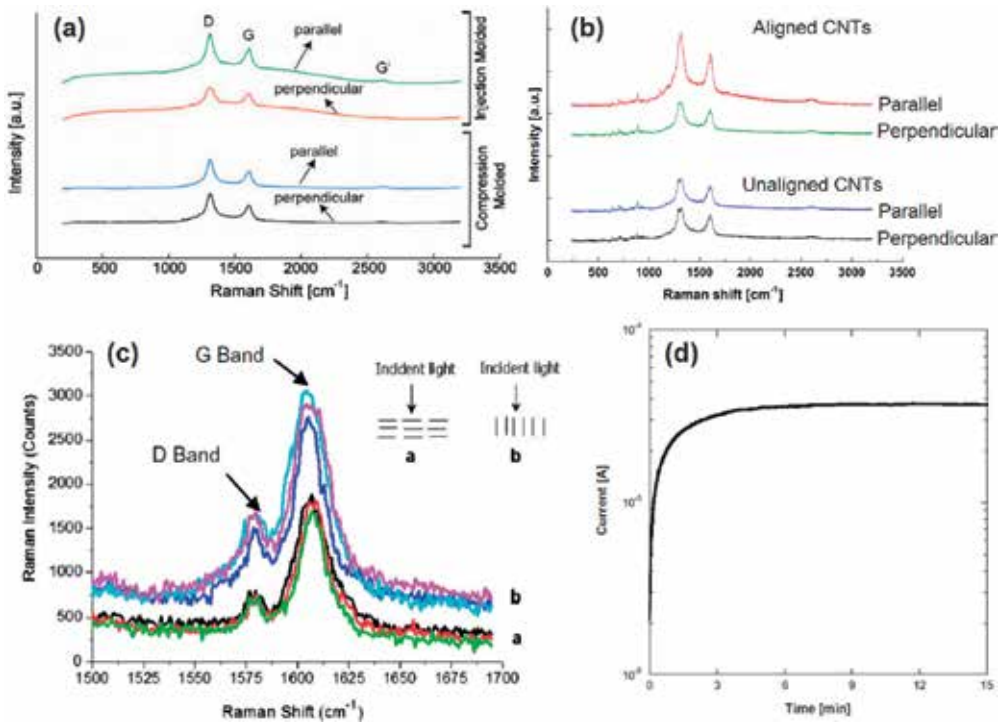

Figure 2. (a–c) Justification of CNT alignment via micro Raman spectroscopy [3, 19, 20], (d) Justification of CNT alignment via constant current on suspension surface [16].

path for transferring the current toward the positive electrode under electrophoresis, which verifying the presence of negative surface charge on CNT surfaces [17]. In **Figure 2**, a view of various justification methods for CNT alignment can be seen.

4. Effective factors on CNT alignment

Many effective factors involved in case of CNT alignment, which evaluation of their effects on aligned network is very essential. Homogenous dispersion of pristine CNT in the matrix is difficult to achieve, which is due to the poor interfacial interaction between CNTs and matrix [34, 35]. What is more, functionalization of CNTs can improve their dispersion within the matrix and enhance the align network. The alignment of CNTs within the matrix has significant effect on overall properties of developed nanocomposites, which are mainly dependent on the degree of CNT dispersion, type of matrix, and interfacial bonds between the matrix and fillers [3]. On the other hand, functionalization of CNTs can improve their dispersion and thus alignment of CNTs within the matrix due to the better interaction with matrix. In fact, functionalization of CNT can change its nature from hydrophobic to hydrophilic [36]. But functionalization of CNTs can increase their resistivity and examination of nanocomposites containing aligned CNTs revealed that highly oriented network consisted form pristine CNTs

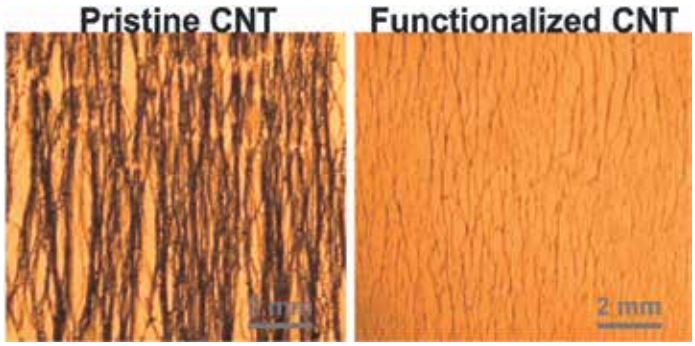

Figure 3. Comparison between performance of pristine and functionalized CNTs for formation of aligned network under application of AC electric field [4].

presenting higher electrical conductivity than functionalized CNTs [8]. A view of aligned CNTs networks containing pristine and functionalized CNTs can be seen in **Figure 3**. As can be seen in this figure, pristine CNTs have formed agglomerated bundles, while functionalized CNTs formed approximately homogenous aligned network.

Furthermore, alignment of CNTs within the matrix can be achieved via both AC and DC electric fields, while behavior of CNTs highly depends on the type of employed electric field and surface charge on the surface of suspension [17, 37]. In regard of DC electric field, migration of CNTs toward the negative electrode is governed by their electrophoretic mobility, which highly depends on the surface charge, while the electrophoretic mobility for AC electric field is zero. This specification of AC electric field can lead to creation of homogenous aligned network within the matrix due to their dielectrophoretic behavior. Likewise, usage of AC electric field found to be more effective compared with DC electric field [4, 17]. Moreover, increase in the electric field voltage can enhance the degree of CNT alignment, while for both AC and DC electric fields, increase in the electric field voltage can increase the aggregation rate, which highlights the requirement for optimization of voltage level [3, 8]. It was revealed that increase in the frequency of AC electric field can enhance the alignment degree and increase the transvers connections between aligned CNT bundles in the direction of electric field [8]. On the other hand, AC electric field presented both better dispersion and alignment within the matrix compared with DC electric field [4]. In **Figure 4**, effect of CNT weight percentage and DC electric field exerting time and strength on the quality of final aligned network can be seen. As can be seen in this figure, increase in CNT weight percentage and voltage can lead to increase in agglomeration rate and creation of robe-like CNT bundles which can be seen in **Figure 4(g)**. Moreover, a view of aligned CNT network in fully cured samples can be seen in **Figure 5**.

In addition, applied voltage and viscosity of matrix can highly affect the alignment process. Increase in the voltage and decrease in the viscosity of matrix can decrease the alignment time. However, unnecessary increase in the electric field voltage can improve the aggregation rate of CNTs and lead to creation of rope-like thick CNT bundles. On the other hand, due to high aspect ratio of CNTs, longitudinal polarization overcomes the transverse polarization. It is worth noting that after completion of the longitudinal polarization, CNTs start to attach each other in the transverse direction, forming transverse crosslinking [3, 16]. In **Figure 6**(**a**–**c**), effect of viscosity

http://dx.doi.org/10.5772/intechopen.70481

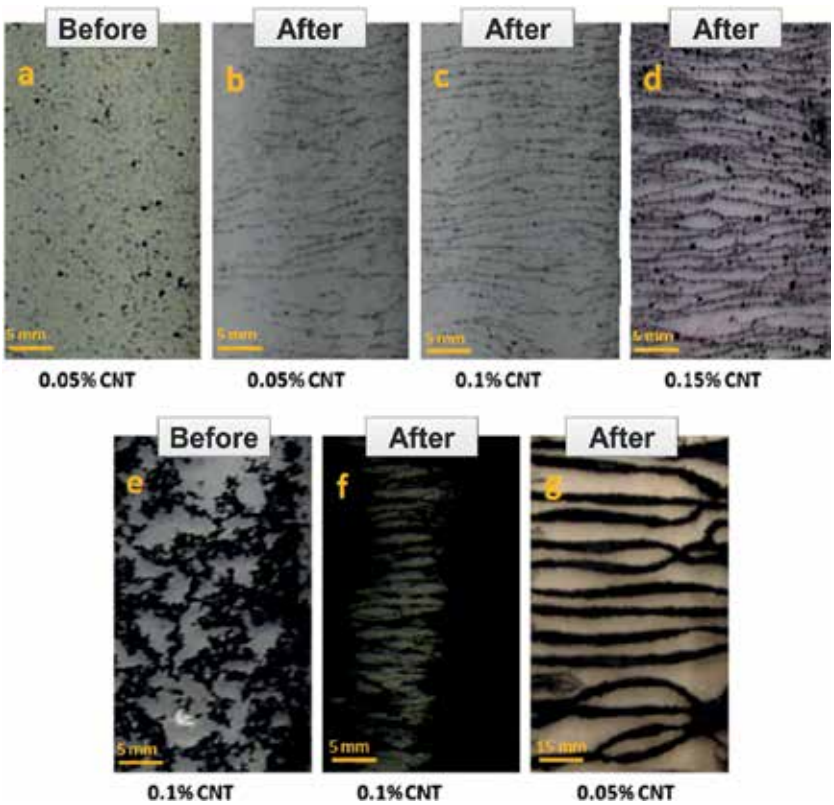

Figure 4. Optical images from aligned CNT networks with respect to their concentration, size and duration which DC electric field was applied between electrodes, (a–f) 100 V/cm for 30 min and (g) 200 V/cm for 30 min [3].

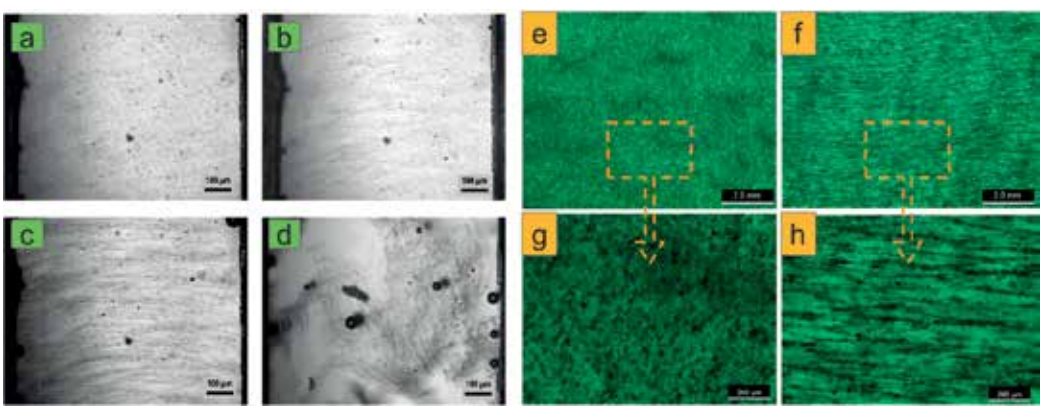

Figure 5. Optical micrographs of suspension containing (a) randomly distributed SWCNTs before the field application, (b) alignment of SWCNTs after 180 s of field application, (c) alignment of SWCNTs after 15 min of field application, (d) a view of relaxation mechanism 10 min after switching the electric field off [16], (e and g) random distribution of MWCNTs within the matrix and (f and h) alignment of MWCNTs within the matrix via DC electric field [3].

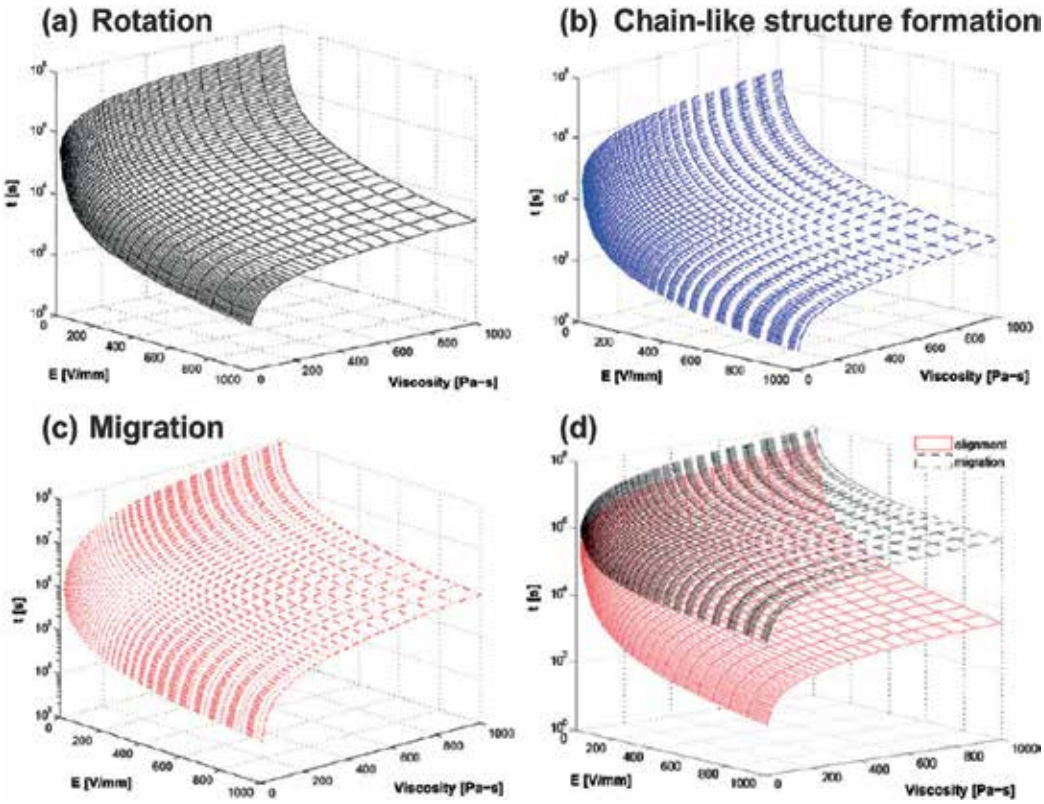

Figure 6. Effect of electric field strength and viscosity of matrix on the required time for (a) rotation, (b) head to head contact and (c) migration, (d) shows comparison between required time for alignment of CNTs within the matrix and migration of CNTs toward negative electrode [16].

and electric field strength on required times for rotation, formation of chain-like structure, and migration can be seen, respectively. Besides, in **Figure 6(d)**, comparison between total alignment time and required time for CNT migration toward negative electrode can be seen.

5. Methodology

In order to achieve a nanocomposite containing highly oriented CNT network with homogenous distribution, development of a practical procedure which has considered all of effective factors in matter of CNT alignment and nanocomposites preparation is essential. In this case, Ma et al. [4] synthesized MWCNTs using chemical vapor deposition (CVD) technique and thence functionalized fabricated MWCNTs using acidic method. In this regard, a mixture of H_2SO_4 and HNO_3 acid (1:1 volume ratio) was prepared, and thereon, MWCNTs were added to the previous solution and heated up to 150°C for 30 min. Then, MWCNTs were rinsed with deionized water till they become chemically neutral. FTIR examination revealed that these MWCNTs have hydroxyl (—OH) and carboxyl (—COOH) functional groups, which

can improve their dispersion within the matrix. Thence, MWCNT/poly methyl meth acrylate (PMMA) composites fabricated using in situ polymerization technique. In this regard, 0.1 wt% 2,2-azobisisobutylonitrile (AIBN) was dissolved in liquid methyl methacrylate (MMA) monomer. Then, desirable weight percentage of MWCNTs added to the MMA/AIBN solution and ultrasonicated for 15 min. In the next step, in order to align MWCNTs in the matrix, AC voltage of 300 Vp-p (peak to peak) at 500 Hz was maintained across the copper electrodes. The resulting nanocomposite was allowed to cure under the AC electric field for 2 h at 70°C.

Zhu et al [7] developed nanocomposites containing aligned MWCNTs within the epoxy resin. In this regard, MWCNTs were synthesized with mean diameter and average length of 20 nm and 10 μm, respectively. Afterward, they have developed two different kinds of MWCNT. For the first MWCNT type, MWCNTs were purified with hydrofluoric acid for 24 h in order to remove impurities and residual catalyst from synthesized MWCNTs. Thence, purified MWCNTs were placed in an oven at 100°C for 24 h, thereby resulting in production of pristine MWCNT. For development of second type of MWCNTs, pristine MWCNTs were added into a solution of H_2SO_4 and HNO_3 (volume ratio 1:1) and resulting suspension heated up to 150°C for 30 min. Thereon, MWCNTs were filtered and rinsed continuously with deionized water in order to make it chemically neutral. This procedure can lead to production of functionalized MWCNTs with carboxyl (–COOH) and hydroxyl (–OH) functional groups. the oxidized MWCNTs were thence refluxed in thionyl chloride at 80°C for 1 h, and residual suspension was distilled and added into a mixture of methylene dichloride, 1,2-ethylenediamine, and triethylamine. Resulting suspension was stirred for 1 h at room temperature. Eventually, MWCNTs were filtrated out, rinsed with deionized water till become chemically neutral, and then dried at 100°C for 24 h to gain amine functionalized MWCNT. In case of matrix, they have used an epoxy resin which could be cured via emission of UV beams and while irradiated by 265-nm UV light, it was fast polymerized within several minutes. In the next stage, specific amount of prepared MWCNTs was poured in the epoxy resin and ultrasonicated for 20 min. Then, 2 mL of the resulting suspension poured into the related mold, and thence, an AC voltage of 2000 Vp-p (peak to peak) at 200 Hz was applied to the suspension for approximately 10 min. Then, UV light was emitted to the suspension for 10 min, which resulted in fast polymerize (cure) of the suspension. A view of their fabrication procedure can be seen in **Figure 7(a)**.

Khan et al. [3] used CVD fabricated MWCNTs for development of nanocomposites containing highly oriented CNTs. For this regard, first MWCNTs were subjected to ultra-violet/ozone (UV-O_3) treatment for 30 min used equipment consisted from a low-pressure mercury vapor grid lamp, which could irradiate UV radiation of 28 W/cm^2 to samples placed 20 mm far from it. This step can change the nature of CNTs from hydrophobic to hydrophilic due to the creation of oxygen-based functional groups on CNT surface, thereby enhancing the interaction between matrix and CNTs. Functionalized MWCNTs sonicated in acetone and Tritone x-100. Thence, epoxy resin was added to the previous suspension and sonicated for further 1 h. Thereon, CNT/epoxy mixture was placed in the vacuum oven for 2 h in order to evaporate acetone from the suspension. For further degassing, suspension was passed through a three-roller mill for six times. Resulting mixture was then degassed for further 20 min to eliminate trapped air bubbles, and thereupon, curing agent triethylenetetramine was added to the epoxy

resin with ratio 12:100. MWCNTs aligned due to application of DC electric field in a place between two aluminum electrodes with 50 mm distance. In this case, 100 or 200 V/cm electric field was applied to the mixture depend on the concentration of MWCNTs. An elevated temperature of 100°C was applied to the mixture after completion of alignment, which resulted in the rapid cure of the mixture. Primary cured composite was then postcured at 120°C for 2 h. A view of their production technique can be seen in **Figure 7(b)**.

On the other hand, despite the fabrication process, which is very important in development of nanocomposites containing aligned CNTs in the direction of electric field, destructive factors such as bubble based voids can also significantly affect the overall properties of nanocomposites includes mechanical and electrical properties [38–43]. Formation of bubble-based voids in the thermoset resins, such as epoxy resin, can highly affect their structural properties

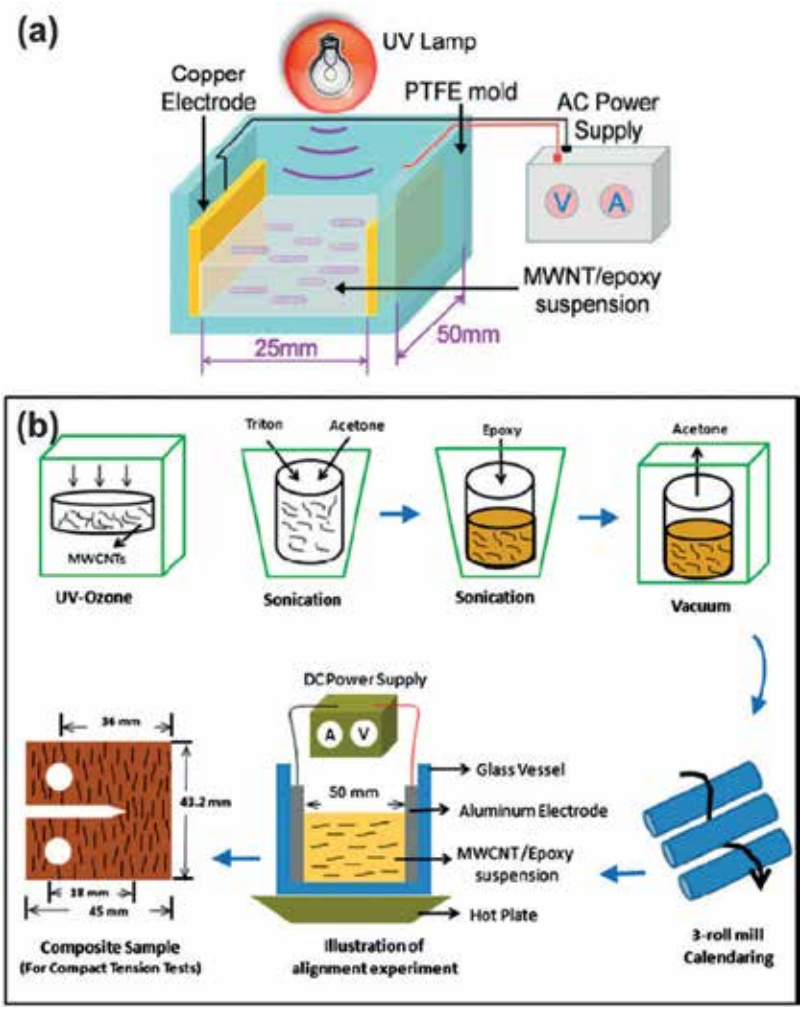

Figure 7. Production procedures presented by (a) Zhu et al. [7] and (b) Khan et al. [3].

and lead creation of stress concentration areas. Bubbles are created due to various factors; diffusion of air into the polymer matrix and amalgamation of small bubbles have the main role in the creation of large bubbles. After completion of matrix-curing steps, the bubbles transform to voids and due to higher internal pressure than pressure in border with matrix and matrix itself, thereby resulting in growth of cracks in radial direction around the void [39, 42, 44]. For this regard, researchers have developed various kind of techniques to minimize the overall amount of bubble based voids, including molecular dispersion of bubbles in the polymer matrix [39], simultaneous usage of vacuum and vibration [45], and vacuum shock technique [42].

Moreover, addition of curing agent to the epoxy resin can lead to generation of a great amount of bubbles throughout the matrix, which is due to the reaction between the resin and the curing agent and can be removed via vacuum shock technique before completion of the first curing step. For instance, the presence of bubble-based voids throughout the epoxy resin with 1.0 wt% randomly oriented single-walled carbon nanotube (SWCNTS) can lead to 63% decrease in EMI shielding (X-band) and significant reduction in the electrical conductivity compared with nanocomposites holding small amount of bubble-based voids (less than 2%) [42]. What is more, creation of moisture throughout the dielectric nanocomposites can lead to significant decrease in both dielectric constant and dielectric loss [46]. Absorbed moisture not only can lead to decrease in the electrical performance but also can deteriorate the reliability of the dielectric materials [47]. Thus, removal of moisture and bubbles from nanocomposites has high level of importance.

6. Outcomes

Alignment of CNTs within the matrix can lead to obvious anisotropy in different directions. In this regard, aligned network presented significant enhancement in mechanical and electrical properties for parallel direction compared to perpendicular direction and randomly distribution of CNTs within the matrix [2–4, 6–8, 13, 20, 35]. Khan et al. [3] achieved remarkably low percolation threshold and significant improvement in mechanical properties of nanocomposites containing aligned MWCNTs. In this case, low percolation threshold of 0.0031 vol% was obtained for parallel direction of CNT alignment, which is one order higher than 0.034 vol% corresponding to the randomly oriented CNTs or that measured in transverse direction of CNT alignment. It is worth noting that the conductivity of developed nanocomposites increased by about four orders of magnitude due to increase in CNT weight percentage from 0.001 to 0.01 wt%, which shows a percolation behavior at even very low weight percentage of CNTs. **Figure 8(a)** shows the effect of CNT alignment on the electrical conductivity of developed nanocomposites containing aligned MWCNTs. As can be seen, alignment of CNTs within the matrix can lead to significant enhancement in the electrical conductivity, which is due to the increase in the interface of CNT bundles that enhanced the contact resistance [27, 48]. This trend for parallel direction is significantly higher than perpendicular direction and randomly distributed CNTs. On application of electric field between electrodes, CNTs immediately align in the direction of electric field to form interconnected bundles even at a very low CNT content, which can lead to achievement of percolation in the direction of CNT alignment, while

the similar trend is not occurred for perpendicular direction of CNT alignment at the same content [3]. Despite CNT content, there are some other effective factors which are also responsible for the anisotropy in percolation include applied voltage, polymerization time (cure time), applied temperature, and viscosity of the matrix [8]. Moreover, it should be mentioned that transverse migration and connection starts once the alignment in the longitudinal direction (parallel direction) completed. In this case, increase in CNT weight percentage can enhance the rate of transverse direction and thus minimize the differences between parallel and perpendicular directions. On the other hand, the same as electrical conductivity, alignment of CNTs within the matrix shows significant improvement in the mechanical properties of nanocomposites include tensile strength, storage modulus, and quasi-static fracture toughness, which indicating the string reinforcing effect of high-modulus CNTs. In this regard, alignment of MWCNTs within the matrix led to 40% and 15% improvement in the Young's modulus for nanocomposites containing 0.3 wt% aligned and unaligned MWCNT, respectively. However, it was observed that by further increase in the CNT concentration beyond 0.3 wt%, overall mechanical properties of developed nanocomposites containing aligned MWCNTs decreased, which is due to the reduction in the degree of alignment at high CNT concentration. In fact, increase in the CNT concentration can lead to significant increase in the viscosity of matrix as well as fillers packing, which can lead to higher resistance and less available free spaces for CNTs in order to move and align in the direction of electric field. In **Figure 8**(**b**–**d**), effect of CNT alignment on storage modulus, Young's modulus, and quasi-static fracture toughness of nanocomposites can be seen [3].

On the other hand, present gaps and pores inside the aligned network due to low-weight percentage of CNTs can increase the contact resistance and thus reduce the electrical conductivity [49, 50]. Alignment of CNTs can lead to significant drop in obtained resistivity for a percolation threshold [51]. Moreover, alignment of CNTs can avoid the entanglement among CNTs in a certain degree, which can avoid creation of the conductive path [31]. It was also reported that alignment of CNTs within the matrix can lead increase in the volume resistivity and thus decrease in the conductivity of matrix [52]. In a work by Gupta et al. [2], they have aligned CNTs with current-assisted technique, which was led to the formation of shortest, continuous path for the flow of electrons, and thus formation of a highly anisotropic conductive path. Obtained results showed that current passage assisted alignment of CNTs can lead to significant 360% improvement in the conductivity for parallel direction than random distribution. However, lower conductivity in transverse direction than randomly distributed structure has been seen, which shows the efficiency of alignment. Despite of that, CNTs are forming a liner path with minimal distance between the electrodes in order to assisting current directly pass through. Electric field–induced alignment recorded 28% increase in the conductivity for parallel direction than randomly distribution, while the transverse direction showed 58% decrease in the electrical conductivity. In fact, current-induced alignment resulted in creation of continuous channels of aligned CNT, where CNTs are contacted end to end with each other and formed and uninterrupted conductive pathway. In this case, electrons will get direct path of flow, which can lead to fantastic enhancement in the electrical conductivity.

Zhu et al. [7] reported that alignment of MWCNTs via AC electric field can lead to significant improvement in the storage modulus and electrical conductivity of developed nanocomposites. Their obtained results revealed that increase in concentration of MWCNTs as well as their alignment can lead significant enhancement in the storage modulus of developed nanocomposites.

http://dx.doi.org/10.5772/intechopen.70481

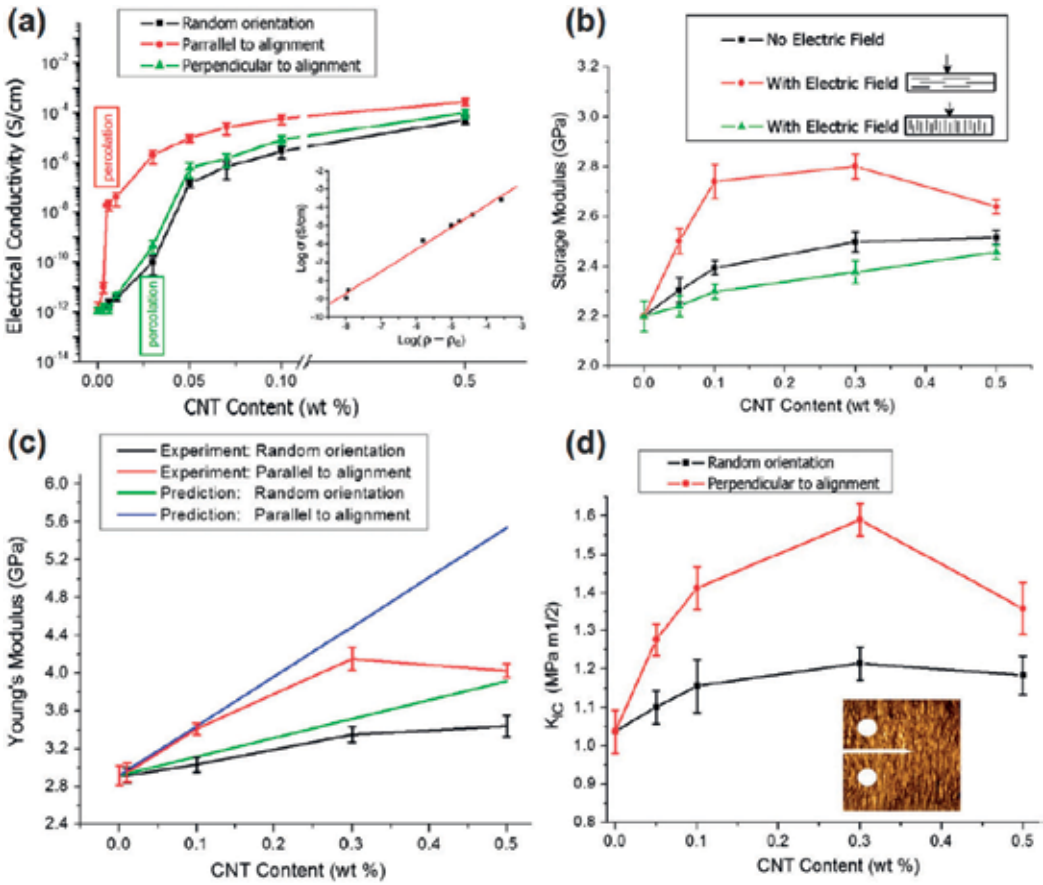

Figure 8. Effect of MWCNT alignment within the epoxy resin on (a) electrical conductivity, (b) storage modulus, (c) Young's modulus, and (d) quasi-static fracture toughness of developed nanocomposites [3].

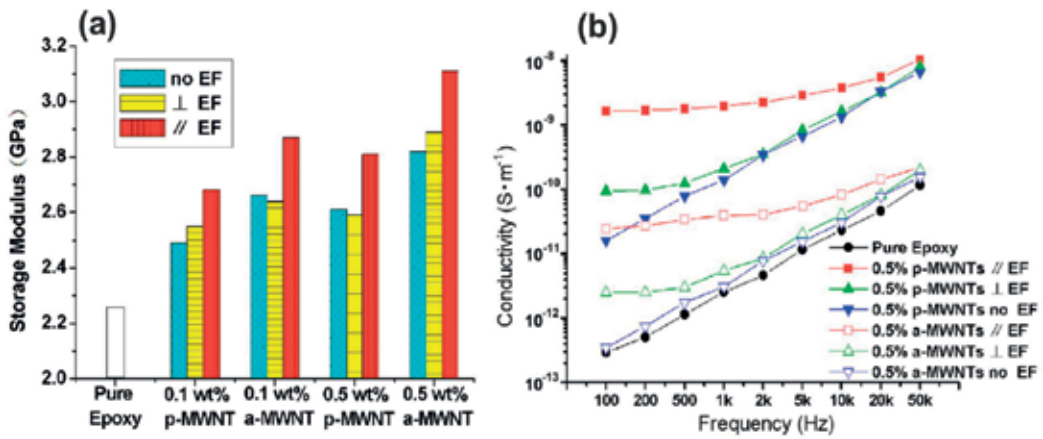

Figure 9. Effect of MWCNT alignment on (a) storage modulus and (b) electrical conductivity of developed nanocomposites [7].

Furthermore, nanocomposites containing amine functionalized MWCNTs (a-MWCNT) have shown higher storage modulus compared to pristine MWCNTs (p-MWCNT), which is due to the better compatibility and interaction between the matrix and a-MWCNTs. Moreover, measured storage modulus of aligned CNTs in parallel direction was greater than perpendicular direction and their randomly distribution within the matrix. On the other hand, nanocomposites containing p-MWCNT were presented higher electrical conductivity compared to a-MWCNT by about two orders of magnitude, which could be due to the decrease in length of a-MWCNT during chemical functionalization and increase in the a-MWCNT resistance. **Figure 9(a)** and **(b)** illustrated the effect of MWCNT alignment within the epoxy resin on storage modulus and electrical conductivity, respectively.

7. Conclusions

CNTs presenting extraordinary mechanical, thermal, and electrical properties, which have reinforcement of nanocomposites with various kinds of CNT, can lead to significant improvement in their overall properties. In this case, application of electric field to the suspension containing CNT at different filler loadings can lead their alignment within the matrix and obvious anisotropy in different directions. In fact, CNTs act as path for transferring current from negative to positive electrode. This phenomenon can boost both electrical and mechanical properties of developed nanocomposites at same filler content. On the other hand, achieved results revealed that the overall properties of nanocomposites include mechanical and electrical properties are higher for parallel direction than perpendicular direction and random distribution of CNTs within the matrix, which is due to the desire of CNTs in formation of longitudinal connections than transverse connections.

Eventually, by alignment of CNTs within the matrix, significant improvement in overall properties of nanocomposites at same filler loadings compared with randomly distribution can be achieved, which is very essential for aerospace and aviation industries that encounter with serious limits in matter of structures' weight.

Author details

Ali Mohammad Amani[1,2], Seyyed Alireza Hashemi[1,2]*, Seyyed Mojtaba Mousavi[1,2], Seyyed Milad Abrishamifar[3] and Arash Vojood[4]

*Address all correspondence to: s.a.hashemi0@gmail.com

1 Department of Medical Nanotechnology, School of Advanced Medical Sciences and Technologies, Shiraz University of Medical Sciences, Shiraz, Iran

2 Pharmaceutical Sciences Research Center, Shiraz University of Medical Sciences, Shiraz, Iran

3 Department of Chemical Engineering, New York International University of Technology and Management, New York, USA

4 Young Researchers and Elite Club, Ardabil Branch, Islamic Azad University, Ardabil, Iran

References

[1] Iijima S. Helical microtubules of graphitic carbon. Nature. 1991;**354**(6348):56

[2] Gupta P, Rajput M, Singla N, Kumar V, Lahiri D. Electric field and current assisted alignment of CNT inside polymer matrix and its effects on electrical and mechanical properties. Polymer. 2016;**89**:119-127

[3] Khan SU, Pothnis JR, Kim JK. Effects of carbon nanotube alignment on electrical and mechanical properties of epoxy nanocomposites. Composites Part A: Applied Science and Manufacturing. 2013;**49**:26-34

[4] Ma C, Zhang W, Zhu Y, Ji L, Zhang R, Koratkar N, Liang J. Alignment and dispersion of functionalized carbon nanotubes in polymer composites induced by an electric field. Carbon. 2008;**46**(4):706-710

[5] Mecklenburg M, Mizushima D, Ohtake N, Bauhofer W, Fiedler B, Schulte K. On the manufacturing and electrical and mechanical properties of ultra-high wt.% fraction aligned MWCNT and randomly oriented CNT epoxy composites. Carbon. 2015;**91**:275-290

[6] Wang Q, Dai J, Li W, Wei Z, Jiang J. The effects of CNT alignment on electrical conductivity and mechanical properties of SWNT/epoxy nanocomposites. Composites Science and Technology. 2008;**68**(7):1644-1648

[7] Zhu YF, Ma C, Zhang W, Zhang RP, Koratkar N, Liang J. Alignment of multiwalled carbon nanotubes in bulk epoxy composites via electric field. Journal of Applied Physics. 2009;**105**(5):054319

[8] Zhang RP, Zhu YF, Ma C, Liang J. Alignment of carbon nanotubes in poly (methyl methacrylate) composites induced by electric field. Journal of Nanoscience and Nanotechnology. 2009:**9**(5):2887-2893

[9] Prolongo S, Meliton B, Del Rosario G, Ureña A. New alignment procedure of magnetite–CNT hybrid nanofillers on epoxy bulk resin with permanent magnets. Composites Part B: Engineering. 2013;**46**:166-172

[10] Hobbie EK, Wang H, Kim H, Han CC, Grulke E, Obrzut J. Optical measurements of structure and orientation in sheared carbon-nanotube suspensions. Review of Scientific Instruments. 2003;**74**(3):1244-1250

[11] Vigolo B, Penicaud A, Coulon C, Sauder C, Pailler R, Journet C, Bernier P, Poulin P. Macroscopic fibers and ribbons of oriented carbon nanotubes. Science. 2000;**290**(5495): 1331-1334

[12] Haggenmueller R, Gommans H, Rinzler A, Fischer JE, Winey K. Aligned single-wall carbon nanotubes in composites by melt processing methods. Chemical Physics Letters. 2000;**330**(3):219-225

[13] Thostenson ET, Chou TW. Aligned multi-walled carbon nanotube-reinforced composites: Processing and mechanical characterization. Journal of Physics D: Applied Physics. 2002;**35**(16):L77

[14] Ko F, Gogotsi Y, Ali A, Naguib N, Ye H, Yang G, Li C, Willis P. Electrospinning of continuous carbon nanotube-filled nanofiber yarns. Advanced Materials. 2003;**15**(14): 1161-1165

[15] Sen R, Zhao B, Perea D, Itkis ME, Hu H, Love J, Bekyarova E, Haddon RC. Preparation of single-walled carbon nanotube reinforced polystyrene and polyurethane nanofibers and membranes by electrospinning. Nano Letters. 2004;**4**(3):459-464

[16] Monti M, Natali M, Torre L, Kenny JM. The alignment of single walled carbon nanotubes in an epoxy resin by applying a DC electric field. Carbon. 2012;**50**(7):2453-2464

[17] Martin C, Sandler J, Windle A, Schwarz MK, Bauhofer W, Schulte K, Shaffer M. Electric field-induced aligned multi-wall carbon nanotube networks in epoxy composites. Polymer. 2005;**46**(3):877-886

[18] Hsu H, Sharma N, Ruoff R, Patankar N. Electro-orientation in particle light valves. Nanotechnology. 2005;**16**(2):312

[19] Abbasi S, Carreau PJ, Derdouri A. Flow induced orientation of multiwalled carbon nanotubes in polycarbonate nanocomposites: Rheology, conductivity and mechanical properties. Polymer. 2010;**51**(4):922-935

[20] Arjmand M, Mahmoodi M, Gelves GA, Park S, Sundararaj U. Electrical and electromagnetic interference shielding properties of flow-induced oriented carbon nanotubes in polycarbonate. Carbon. 2011;**49**(11):3430-3440

[21] Lehman JH, Terrones M, Mansfield E, Hurst KE, Meunier V. Evaluating the characteristics of multiwall carbon nanotubes. Carbon. 2011;**49**(8):2581-2602

[22] Yoo HJ, Lee SY, You NH, Lee DS, Yeo H, Choi YM, Goh M, Park J, Akagi K, Cho JW. Dispersion and magnetic field-induced alignment of functionalized carbon nanotubes in liquid crystals. Synthetic Metals. 2013;**181**:10-17

[23] Sarno M, Sannino D, Leone C, Ciambelli P. CNTs tuning and vertical alignment in anodic aluminium oxide membrane. Journal of Natural Gas Chemistry. 2012;**21**(6):639-646

[24] Han Y, Li S, Chen F, Zhao T. Multi-scale alignment construction for strong and conductive carbon nanotube/carbon composites. Materials Today Communications. 2016;**6**:56-68

[25] Arjmand M, Apperley T, Okoniewski M, Sundararaj U. Comparative study of electromagnetic interference shielding properties of injection molded versus compression molded multi-walled carbon nanotube/polystyrene composites. Carbon. 2012;**50**(14):5126-5134

[26] Mahmoodi M, Arjmand M, Sundararaj U, Park S. The electrical conductivity and electromagnetic interference shielding of injection molded multi-walled carbon nanotube/ polystyrene composites. Carbon. 2012;**50**(4):1455-1464

[27] Han B, Xue X, Xu Y, Zhao Z, Guo E, Liu C, Luo L, Hou H. Preparation of carbon nanotube film with high alignment and elevated density. Carbon. 2017;**122**:496-503

[28] Chapkin WA, McNerny DQ, Aldridge MF, He Y, Wang W, Kieffer J, Taub AI. Real-time assessment of carbon nanotube alignment in a polymer matrix under an applied electric field via polarized Raman spectroscopy. Polymer Testing. 2016;**56**:29-35

[29] Donovan K, Scott K. Transient electric birefringence in suspensions of single-walled carbon nanotubes. Physical Review B. 2005;**72**(19):195432

[30] Robb-Smith T, Donovan K, Scott K, Somerton M. Induced electro-optic effects in single-walled carbon nanotubes. I. Polarizability of metallic nanotubes. Physical Review B. 2011;**83**(15):155414

[31] Cheng J, Pu H. Influences of matrix viscosity on alignment of multi-walled carbon nanotubes in one-dimensional confined space. European Polymer Journal. 2017;**89**:431-439

[32] Blatt S, Hennrich F, Löhneysen HV, Kappes MM, Vijayaraghavan A, Krupke R. Influence of structural and dielectric anisotropy on the dielectrophoresis of single-walled carbon nanotubes. Nano Letters. 2007;**7**(7):1960-1966

[33] Oliva-Avilés A, Avilés F, Sosa V, Seidel G. Dielectrophoretic modeling of the dynamic carbon nanotube network formation in viscous media under alternating current electric fields. Carbon. 2014;**69**:342-354

[34] Ma PC, Siddiqui NA, Marom G, Kim JK. Dispersion and functionalization of carbon nanotubes for polymer-based nanocomposites: A review. Composites Part A: Applied Science and Manufacturing. 2010;**41**(10):1345-1367

[35] Xie XL, Mai YW, Zhou XP. Dispersion and alignment of carbon nanotubes in polymer matrix: A review. Materials Science and Engineering: R: Reports. 2005;**49**(4):89-112

[36] Sham ML, Kim JK. Surface functionalities of multi-wall carbon nanotubes after UV/Ozone and TETA treatments. Carbon. 2006;**44**(4):768-777

[37] Kamat PV, Thomas KG, Barazzouk S, Girishkumar G, Vinodgopal K, Meisel D. Self-assembled linear bundles of single wall carbon nanotubes and their alignment and deposition as a film in a dc field. Journal of the American Chemical Society. 2004;**126**(34):10757-10762

[38] Liu L, Zhang BM, Wang DF, Wu ZJ. Effects of cure cycles on void content and mechanical properties of composite laminates. Composite Structures. 2006;**73**(3):303-309

[39] Li Y, Li Q, Ma H. The voids formation mechanisms and their effects on the mechanical properties of flax fiber reinforced epoxy composites. Composites Part A: Applied Science and Manufacturing. 2015;**72**:40-48

[40] Jongwoo P, Taweeplengsangsuke J, Theis C, Osenbach J. Epoxy adhesive used in optical fiber/passive component: Kinetics voids and reliability. Proceedings 51st Electronic Components and Technology Conference; 2001. pp. 637-644

[41] Hernández S, Sket F, Molina-Aldareguı J, González C, Lorca J. Effect of curing cycle on void distribution and interlaminar shear strength in polymer-matrix composites. Composites Science and Technology. 2011;**71**(10):1331-1341

[42] Hashemi SA, Mousavi SM. Effect of bubble based degradation on the physical properties of single wall carbon nanotube/epoxy resin composite and new approach in bubbles reduction. Composites Part A: Applied Science and Manufacturing. 2016;**90**:457-469

[43] Bodaghi M, Cristóvão C, Gomes R, Correia N. Experimental characterization of voids in high fibre volume fraction composites processed by high injection pressure RTM. Composites Part A: Applied Science and Manufacturing. 2016;**82**:88-99

[44] Nie L, Lee K, Lee S, Shi T, Liao G. Void control in adhesive bonding using thermosetting polymer. Sensors and Actuators A: Physical. 2011;**167**(2):398-405

[45] Muric-Nesic J, Compston P, Noble N, Stachurski Z. Effect of low frequency vibrations on void content in composite materials. Composites Part A: Applied Science and Manufacturing. 2009;**40**(4):548-551

[46] Chao F, Bowler N, Tan X, Liang G, Kessler MR. Influence of adsorbed moisture on the properties of cyanate ester/$BaTiO_3$ composites. Composites Part A: Applied Science and Manufacturing. 2009;**40**(8):1266-1271

[47] Cheng YL, Leon KW, Huang JF, Chang WY, Chang YM, Leu J. Effect of moisture on electrical properties and reliability of low dielectric constant materials. Microelectronic Engineering. 2014;**114**:12-16

[48] Zhao S, Zheng Z, Huang Z, Dong S, Luo P, Zhang Z, Wang Y. Cu matrix composites reinforced with aligned carbon nanotubes: Mechanical, electrical and thermal properties. Materials & Design. 2016;**675**:82-91

[49] Jakubinek MB, Johnson MB, White MA, Jayasinghe C, Li G, Cho W, Schulz MJ, Shanov V. Thermal and electrical conductivity of array-spun multi-walled carbon nanotube yarns. Carbon. 2012;**50**(1):244-248

[50] Miao M. Electrical conductivity of pure carbon nanotube yarns. Carbon. 2011;**49**(12): 3755-3761

[51] Cheng J, Pu H, Du J. A processing method with high efficiency for low density polyethylene nanofibers reinforced by aligned carbon nanotubes via nanolayer coextrusion. Polymer. 2017;**111**:222-228

[52] Li Y, Zhao L, Shimizu H. Electrically conductive polymeric materials with high stretchability and excellent elasticity by a surface coating method. Macromolecular Rapid Communications. 2011;**32**(3):289-294

Chapter 6

Mechanical and Fracture Properties of Carbon Nanotubes

Keiichi Shirasu, Go Yamamoto, Daniel Nelias and Toshiyuki Hashida

Additional information is available at the end of the chapter

http://dx.doi.org/10.5772/intechopen.70578

Abstract

Carbon nanotubes (CNTs) have attracted much interest because of their superior electrical, thermal, and mechanical properties. These unique properties of CNTs have come to the attention of many scientists and engineers worldwide, eager to incorporate these novel materials into composites and electronic devices. However, before the utilization of these materials becomes mainstream, it is necessary to develop protocols for tailoring the material properties, so that composites and devices can be engineered to given specifications. In this chapter, we review our recent studies, in which we investigate the nominal tensile strength and strength distribution of multi-walled CNTs (MWCNTs) synthesized by the catalytic chemical vapor deposition (CVD) method, followed by a series of high-temperature annealing steps that culminate with annealing at 2900°C. The structural-mechanical relationships of such MWCNTs are investigated through tensile-loading experiments with individual MWCNTs, Weibull-Poisson statistics, transmission electron microscope (TEM) observation, and Raman spectroscopy analysis.

Keywords: carbon nanotubes, tensile strength, Weibull-Poisson statistics, structural defects, heat treatment

1. Introduction

Carbon nanotubes (CNTs) have attracted much interest because of their potential application as next-generation electronic and structural materials. In particular, their superior electrical, thermal, and mechanical properties, including high electrical and thermal conductivity [1, 2], negative thermal expansion coefficient [3–10], and high mechanical strength, exceeding 100 GPa [11, 12], make them a candidate material for nano- and microscale composites,

sensors, actuators, and other electronic devices. Additionally, continuous multi-walled CNT (MWCNT) yarns and sheets, which are prepared by directly drawing MWCNTs from spinnable MWCNT arrays, have been developed [13, 14], and new processing methods utilizing MWCNT yarns and sheets have emerged as means of producing preforms and composites with higher MWCNT volume fractions [15–25]. The most recent reviews on these topics were reported by Di et al. [26] and Goh et al. [27].

The Young's modulus and strength of CNTs are well known to depend critically on the structure (e.g., geometry, crystallinity, and defect type and density), which in turn depends on the manufacturing route and subsequent treatment [28–31]. Quantum mechanics calculations [32–36] predict that defect-free single-walled CNTs possess Young's modulus values of ~1 TPa, tensile strengths >100 GPa, and failure strains of ~15–30%, depending on the chirality. However, experimental measurements [29, 37–41], which have all involved MWCNTs, have reported markedly lower values for fracture strengths and failure strains. For example, Ding et al. [40] showed that unpurified arc discharge-grown MWCNTs yielded a mean modulus value of 955 GPa, in good agreement with theory, but mean fracture strengths and failure strains that were only 24 GPa and 2.6%, respectively. Calculations [35] have suggested that defects introduced by oxidative pitting during nanotube purification can markedly reduce fracture strength. Therefore, for the development of basic design concepts for the use of CNTs in nanocomposites that require high strength, experimental evaluation of the mechanical properties of CNTs is crucial.

Several techniques have been developed for exploring the mechanical properties of individual CNTs. One method for measuring the Young's modulus of a CNT is to fabricate a nanotube beam that is clamped at each end to a ceramic membrane (or otherwise supported) and to measure its vertical deflection versus the force applied at a point midway along its length [28]. The atomic force microscope (AFM) is a natural and convenient means for studying the Young's modulus of CNTs, because it allows measurement of the deflection of a sample as a function of applied force when used in contact mode [28, 30, 42–46]. Salvetat et al. [28] deposited a droplet of a MWCNT suspension on a well-polished alumina ultrafiltration membrane and evaluated the Young's modulus using the abovementioned method. They found that MWCNTs grown by catalytic chemical vapor deposition (CVD) have Young's moduli in the range of 12–50 GPa (mean: 27 GPa). These values are considerably lower than the moduli of arc discharge-grown MWCNTs (600–1100 GPa). Recently, Elumeeva et al. [30] investigated the Young's modulus of four types of MWCNTs synthesized by the CVD method followed by a series of high-temperature annealing steps at 2200, 2600, and 2800°C using a method similar to that of Salvetat et al.'s study [28]. The experimental results showed that the Young's modulus increased for the annealed MWCNTs with respect to the as-grown ones. Poncharal et al. presented a vibrating reed technique for testing the bending modulus of MWCNTs [47]. The elastic bending modulus as a function of diameter was found to decrease sharply (from approximately 1 TPa to 100 GPa) with increasing diameter (from 8 to 40 nm), which was attributed to the crossover from a uniform elastic mode to an elastic mode

that involves wavelike distortions in the nanotube. Gaillard et al. [48] also used a similar experimental setup, but their technique is relatively simpler: the resonance frequency of an electrostatically driven MWCNT is determined using a dark-field optical microscope. They found that there was a correlation between the defect density and the bending modulus, which suggests that the bending modulus is relatively more sensitive to wall defects than the nanotube diameter. The other method for evaluation of the tensile strength and Young's modulus of CNTs is the tensile testing method [11, 12, 37–41, 49–51]. Yu et al. [37] measured the stress-strain response and strength at failure of individual arc discharge-grown MWCNTs (~30 μm long) using a manipulator tool operated inside a scanning electron microscope (SEM). They reported measured tensile strengths and Young's moduli of MWCNTs ranging from ~11 to ~63 GPa and from 270 to 950 GPa, respectively. Peng et al. [11] reported that defect-free individual MWCNTs were shown to possess a mechanical strength equivalent to the theoretical value (100 GPa) using a precise in situ transmission electron microscopy (TEM) method with a micro-electromechanical system (MEMS) material testing system. They also performed a study on the effect of electron irradiation parameters on the resulting MWCNT strength. They found that as the irradiation-induced defect density increased, the tensile strength decreased, with that of three nonirradiated samples and a sample irradiated at a higher dose being ~100 GPa on average and 35 GPa, respectively. Yamamoto et al. [29] performed a study of the effect of acid treatment on the tensile strength of CVD-grown MWCNTs (~9 μm long), using a piezo-actuated nanomanipulator. The acid treatment introduced deep nanoscale defects as well as negatively charged functional groups onto the surface of the MWCNTs. The defects in these acid-treated MWCNTs had a channel-like structure, as if a ring of material was cut away from the MWCNT around its circumference [29]. By comparing the SEM images of MWCNTs acquired before and after fracture, it was found that all the nanotubes tested fractured in the so-called *sword-in-sheath failure* mode; the fracture of the acid-treated MWCNTs mostly occurred at the nanodefects. Tensile-loading experiments revealed that the tensile strengths of pristine MWCNTs were in the range of 2–48 GPa (mean, 20 GPa). However, the acid-treated MWCNTs with nanoscale defects possessed a tensile strength of 1–18 GPa (mean, 6 GPa), which is approximately 70% lower than that of the pristine MWCNTs. These results indicated that the channel-like defects associated with the acid etching were typically the weakest points in the acid-treated MWCNT structure and that stress concentration was present at the defect region. In these studies, the tensile strength was calculated from either the fractured cross-sectional area (effective strength) or the cross-sectional area of the outermost layer of the MWCNT. Few research groups have examined the nominal (or *engineering*) strength and its Weibull distribution, which are required for investigations of crack bridging characteristics and mechanical properties of composites reinforced with MWCNTs (a detailed discussion is given in [52]). Yu et al. [37] calculated the nominal tensile strengths to be in the range of 1.4–2.9 GPa, which is much lower than the effective tensile strength (11–63 GPa).

Here, we review our recent studies in which the strength properties of individual MWCNTs synthesized by a CVD method, followed by a series of high-temperature annealing steps that culminate with annealing at 2900°C, are investigated by a manipulator tool operated inside

an SEM [52–54]. The relationship between the MWCNT structure and strength properties of MWCNTs with a significantly different nanostructure is investigated through tensile tests of individual MWCNTs, transmission electron microscope (TEM) observations, and Raman spectroscopy analysis.

2. Structural characterization of carbon nanotubes

MWCNT materials (acquired from Hodogaya Chemical, Japan) synthesized by a catalytic CVD process were thermally annealed in a graphite crucible using a resistance-heated graphite element furnace at 1200, 1800, 2200, and 2600°C under an argon atmosphere [53]. The temperature was raised at a heating rate of approximately 60°C/min to the predetermined temperature and held there for 1 h before cooling to ambient temperature. The average outer diameter, inner diameter, and length of the MWCNTs are approximately 70, 7 nm and 7.8 μm, respectively. **Figure 1** shows typical TEM images of the four types of MWCNTs. At an annealing temperature of 1200°C (**Figure 1a**), the sample consists of turbostratic elementary domains 2–3 graphene layers thick. Each elementary domain is tilted at an angle with respect to the nanotube axis, forming larger wrinkled layers. When the annealing temperature increased to 1800°C (**Figure 1b**), the turbostratic structure disappears, and instead undulated fringes are formed by hooking the adjacent elementary domains together, i.e., both the in-plane and c-axis crystallite sizes appear to increase in this temperature range. For the samples annealed at 2200°C (**Figure 1c**), even though the undulated structure seems to remain unchanged, the graphitic planes become aligned, and the crystallite sizes increase further. With thermal annealing at 2600°C (**Figure 1d**), the undulating structure disappears, and the MWCNTs consist of nested graphitic cylinders that are almost perfectly aligned with the nanotube axis. However, these MWCNTs are observed to possess structural defects such as abrupt structural changes from constant-diameter cylinders and unevenly spaced lattice fringes. Hereafter, these kinds of MWCNTs are referred to as H-MWCNTs.

Spinnable MWCNT arrays were obtained by a thermal CVD method using C_2H_2 and $FeCl_2$ as the base material and the catalyst, respectively. The procedure for the fabrication of the MWCNT arrays follows [55]. The average outer diameter and inner diameter were approximately 40 and 7 nm, respectively, and the length of the MWCNTs was ~700 μm. The MWCNTs were thermally annealed in a graphite crucible (Kurata Giken SCC-U-80/150) using a resistance-heated graphite element furnace at 2000°C in a vacuum, followed by heat treatment at 2400 and 2900°C under an argon atmosphere. **Figure 2** shows TEM images of some of the MWCNTs. The as-grown MWCNTs consist of slightly undulating graphitic cylinders with respect to the nanotube axis (**Figure 2a**). Additionally, these MWCNTs possess several types of structural defects, such as *kinks and bends*, *discontinuous flaws*, and *remnant catalysts* (**Figure 2c–f**). For the samples annealed at 2400°C, the degree of waviness of the nanotube walls seems to decrease. Following thermal annealing at 2900°C (**Figure 2b**), the undulated structure disappears, and the MWCNT consists of nested graphitic cylinders that are almost perfectly aligned with the nanotube axis. However, structural defects such as *discontinuous flaws* and *kinks and bends* are still observed for a subset of the samples. The structural defect densities for the MWCNTs prepared in this study are summarized in **Table 1**. The thermally

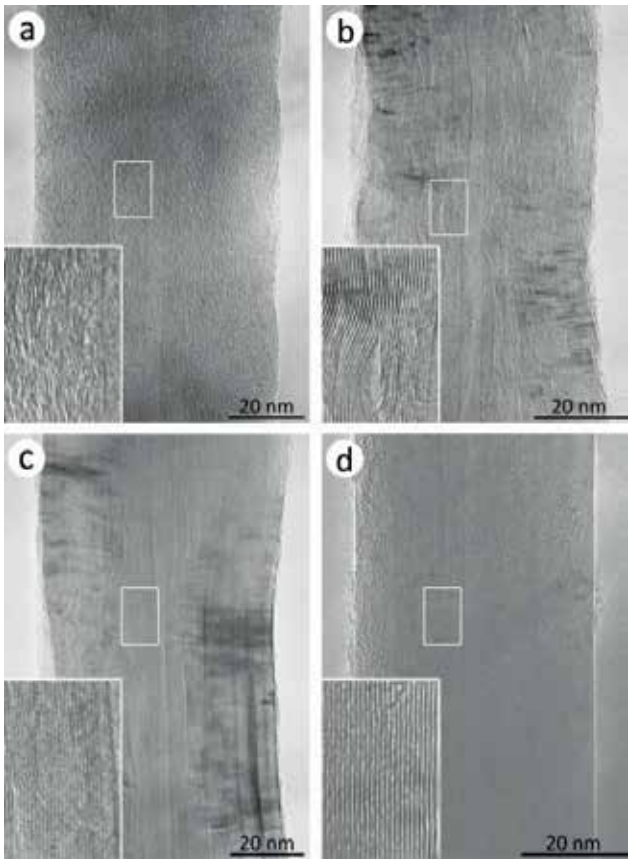

Figure 1. TEM images showing structural evolution of H-MWCNTs [53]. Annealing temperatures are (a) 1200°C, (b) 1800°C, (c) 2200°C, and (d) 2600°C.

annealed MWCNTs possessed a smaller amount of structural defects, characterized by *discontinuous flaws* and *kinks and bends* and no *remnant catalyst* compared with the as-grown MWCNTs. In this chapter, we call these nanotubes S-MWCNTs.

Next, we used Raman spectroscopy to evaluate whether any structural evolution occurs during thermal annealing. The Raman scattering spectrum of the MWCNTs shows a pair of bands around 1360 cm^{-1} (D-band) and 1590 cm^{-1} (G-band) [56]. Thus, the relative intensity ratio of the G-band to D-band peak, i.e., $R = I_G/I_D$, is known to depend on the number of defects in the nanotubes [57]. The Raman intensity ratios (R) of the H-MWCNTs and S-MWCNTs are shown in **Figure 3**. The Raman spectra of the MWCNTs showed a pair of bands near 1360 and 1590 cm^{-1}. The R values of the H-MWCNTs increased from 1.0 to 10.1 with increasing annealing temperature. For the S-MWCNTs, there is no clear difference in the R values between the as-grown MWCNTs and those annealed at 2000°C (R = 3.2 and 3.8), suggesting that both types of MWCNTs have the same degree of crystallinity. On the other hand, the R values increase with increasing annealing temperature over the temperature range 2000–2900°C

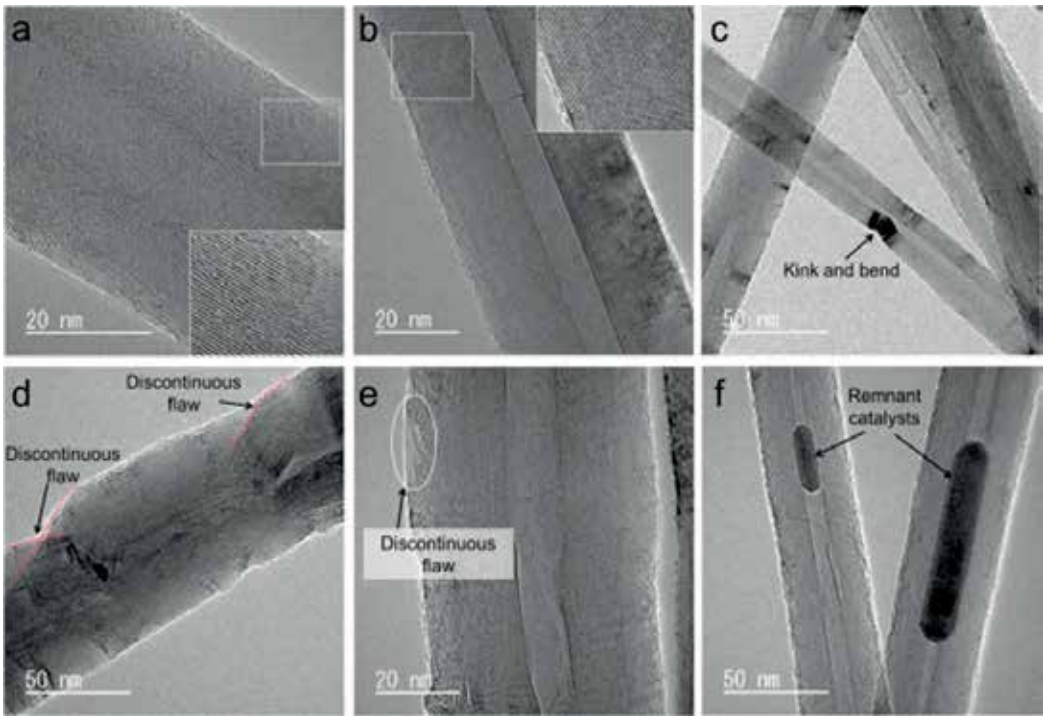

Figure 2. TEM images of the (a, c-f) as-grown S-MWCNTs and (b) MWCNTs thermally annealed at 2900 °C [52]. Arrows indicate the position of structural defects such as (c) *kinks and bends*, (d, e) *discontinuous flaws* (i.e., discontinuity in nanotube layers and *voids and holes*), and (f) *remnant catalyst*.

Annealing temperature (°C)	Kinks and bends (/μm)	Discontinuous flaws (/μm)	Remnant catalysts (/μm)
As-grown	1.9	6.4	1.2
2400	1.1	2.5	0
2900	1.6	1.7	0

Table 1. Structural defect densities for three types of S-MWCNTs [52].

(R = 23.3). This result suggests that defects in the structure of the MWCNTs were removed by annealing to produce a more stable graphite planar structure.

3. Tensile properties

3.1. Fracture behavior

Uniaxial tensile tests on individual MWCNTs were carried out with a manipulator inside the vacuum chamber of a SEM (JEOL JSM6510), as shown in **Figure 4**. Further details of the experimental procedure are described elsewhere [29]. In brief, AFM cantilevers served as

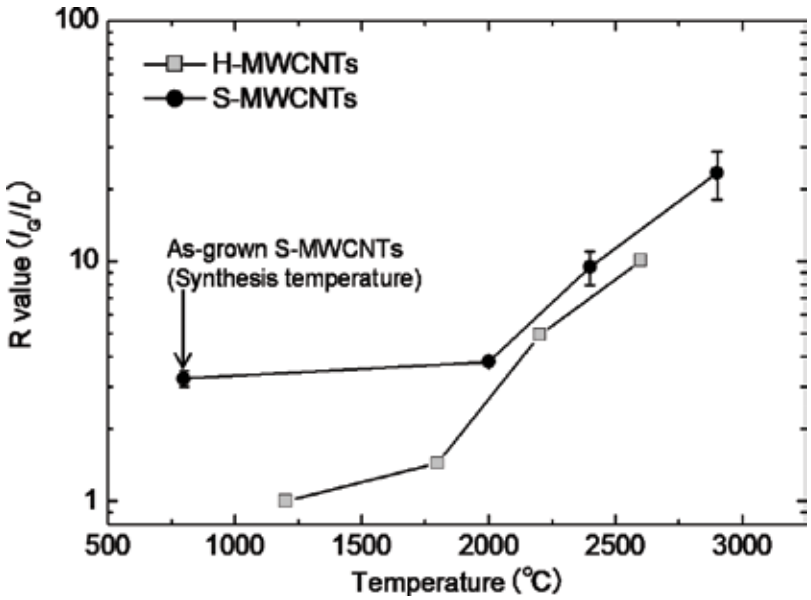

Figure 3. Raman intensity ratio as a function of MWCNT annealing temperature [52, 53].

force-sensing elements, and the force constants of each were obtained in situ prior to the tensile tests using the resonance method developed by Sader et al. [58]. An individual MWCNT was clamped onto the cantilever tip by local electron-beam-induced deposition (EBID) of a carbonaceous material [59]. The applied force can be calculated as follows (**Figure 1d**):

$$F = k(\Delta x - \Delta L) \tag{1}$$

where k is the force constant, Δx is the displacement of the cantilever, and ΔL is the nanotube elongation. The nanotube elongation was determined by counting the number of pixels in the acquired SEM images. The movement rate of the XY motion stage of the manipulator for the tensile tests was approximately 0.1 μm/s. After the MWCNT broke, both cantilevers with attached MWCNT fragments were transferred to a TEM sample stage and examined in the TEM to determine the outer diameters. We measured the full cross-sectional area, including the inner hole of each of the broken MWCNTs, using TEM and used the measured values to calculate the tensile strength.

The fracture morphology of MWCNTs is divided into two groups: the complete fracture of nanotube walls (*clean break* or *sword and sheath failure* mode) and *sword-in-sheath failure* mode, which depends on their crystallinity and existence of structural defects. Two series of SEM and TEM images for each of the two individual H-MWCNTs, captured before and after breaking, are shown in **Figure 5**. In the first series (**Figure 5A1–A5**), a H-MWCNT annealed at 1800°C with a gauge length of 13.1 μm was clamped onto the cantilever and tungsten wire tips by local EBID and then loaded in increments until failure. After breaking, the fragment of the same MWCNT attached to the cantilever tip had a length of 13.3 μm (**Figure 5A2** and **A4**). The other fragment of the same MWCNT attached to the tungsten wire had a length of at least 0.2 μm (**Figure 5A3**

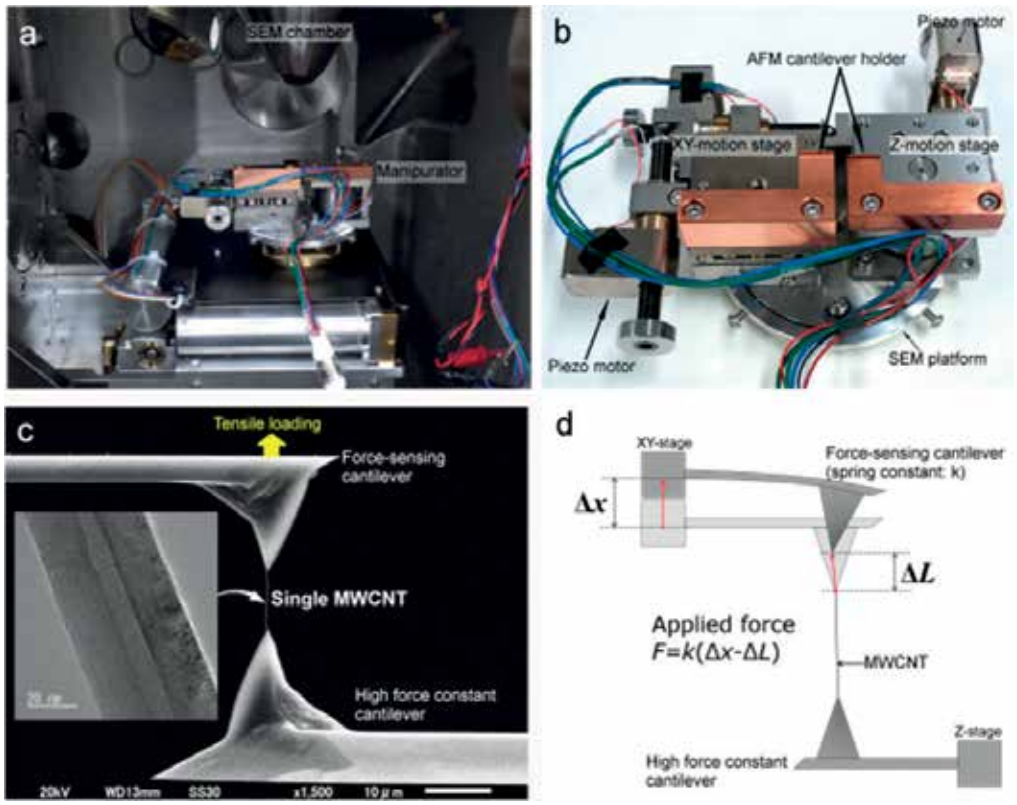

Figure 4. (a, b) Nanomanipulator system used for tensile tests on individual MWCNTs. (c) A SEM image of two AFM cantilever tips holding a MWCNT, which is attached at both ends to the AFM silicon tip surface by electron beam deposition of carbonaceous material. (d) Schematic description of cantilever displacement during the tensile test.

and **A5**), indicating that the MWCNT underwent failure in the so-called clean break manner (**Figure 6A1–A3**), as observed for CVD-grown MWCNTs under tensile loading [38]. Similar *clean break*-type failure was observed for H-MWCNTs annealed at 1200 and 2200°C. In contrast, the H-MWCNTs annealed at 2600°C broke in the outer walls, and the inner core was pulled away from the outer walls (**Figure 5B1–B3**), i.e., they underwent failure in a *sword-in-sheath failure* mode (**Figure 6B1–B3**), as observed for arc discharge-grown MWCNTs under tensile loading [11, 37]. An 11.1-μm-long section of this MWCNT was loaded and fractured in the middle of the gauge length. The resulting fragment attached to the cantilever tip had a length of at least 2.4 μm (**Figure 5B2**), whereas the other fragment on the tungsten wire had a length of at least 10.6 μm (**Figure 5B3**). Thus, the sum of the fragment lengths far exceeded the original section length. This apparent discrepancy can be explained as resulting from a *sword-in-sheath*-type failure.

Next, SEM and TEM images of an individual as-grown S-MWCNT linked between two opposing AFM cantilever tips before and after tensile loading are shown in **Figure 7**. An as-grown S-MWCNT having a gauge length of 3.2 μm was clamped onto the cantilevers and then loaded in increments until failure. After breaking, the fragment of the same MWCNT attached to the high-force constant cantilever tip had a length of 0.5 μm (**Figure 7b1**), while

http://dx.doi.org/10.5772/intechopen.70578

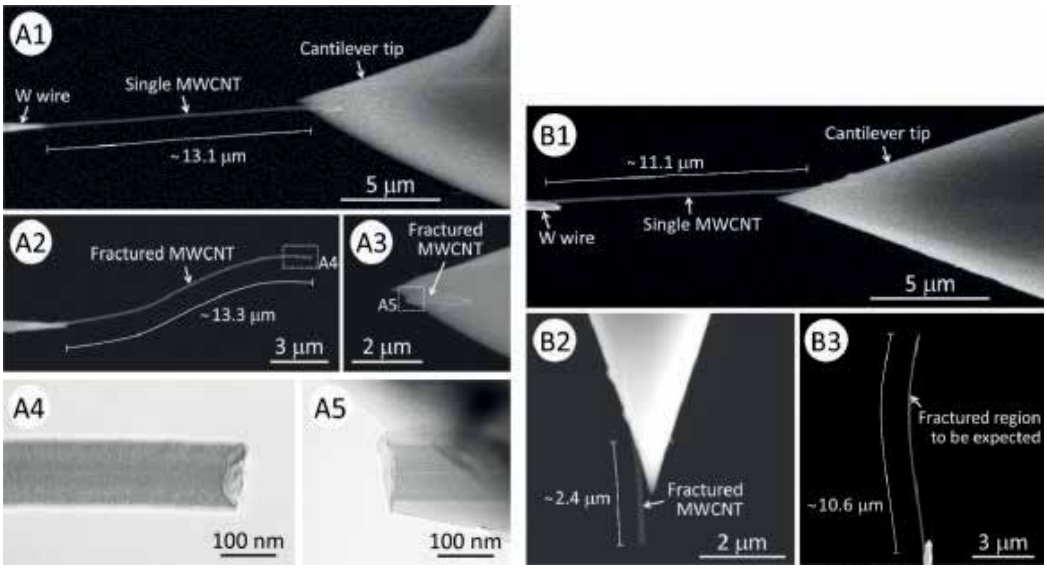

Figure 5. Two series of SEM and TEM images for each of two individual H-MWCNTs, captured before and after their breaking [53]. Annealing temperatures are (A1–A5) 1800°C and (B1–B3) 2600°C.

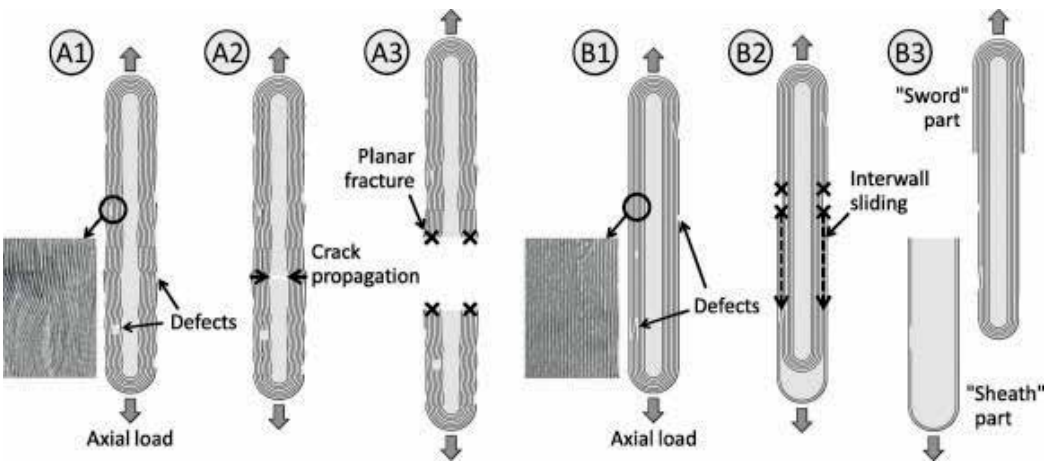

Figure 6. Schematic description of possible fracture mechanisms of MWCNTs annealed at different temperatures [53]. Shown are examples of (A1–A3) *clean break*-type failure and (B1–B3) *sword-in-sheath*-type failure.

the other fragment of the same MWCNT attached to the force-sensing cantilever had a length of approximately 3.8 μm (**Figure 7b2**). Thus, the sum of the fragment lengths (4.3 μm) exceeded the original section length. However, the length of the sword part of the nanotube (1.1 μm, **Figure 7c**) was shorter than that of the MWCNT attached to the high-force constant cantilever tip (1.9 μm). This suggests that the inner walls may break at positions that are far away from the outer walls, as shown in **Figure 7d**. This behavior can explain the *sword and sheath failure*. Of the 23 tested as-grown S-MWCNTs, 9 MWCNTs fractured as a *clean break*, and the remaining 14 MWCNTs failed leaving a *sword and sheath failure*.

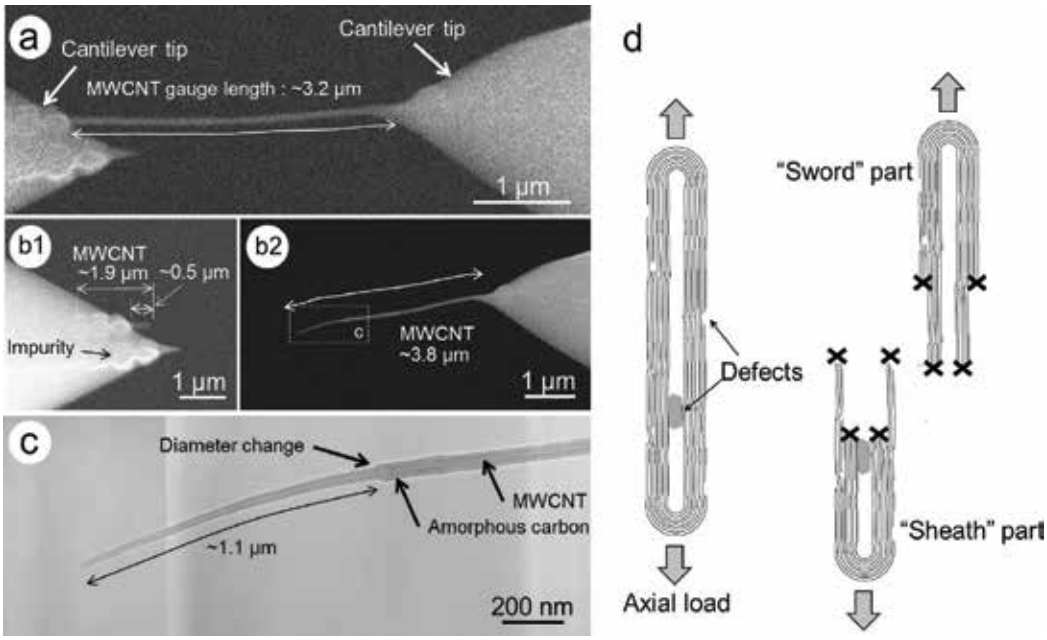

Figure 7. SEM images of S-MWCNT (a) before and (b) after the tensile test [54]. TEM image of the broken MWCNT is indicated in (c). TEM image in (c) shows the tips of the MWCNT that failed leaving the sword and sheath failure. (d) Schematic description of sword and sheath failure.

In addition to the evaluation of the fracture behavior of the MWCNTs mentioned above, we identified the fracture locations of individual S-MWCNTs broken in the uniaxial tensile tests using a piezo manipulator inside the vacuum chamber of the SEM and TEM. Of the five tested MWCNTs, three MWCNTs underwent failure at a *discontinuous flaw*, and the remaining two MWCNTs fractured at a *kink and bend*. A series of TEM images for an individual as-grown S-MWCNT, captured before and after breaking, are shown in **Figure 8**. We found that the fracture of this MWCNT occurred at a *kink and bend* structure and occurred as a *clean break*. **Figure 9** shows the characteristic features observed in a MWCNT, which fractured at a *discontinuous flaw*. The MWCNT fractured leaving a *sword and sheath failure* (**Figure 7d**). Furthermore, this MWCNT featured *hole defects* on the surface of its outer wall and the fracture occurred at a *hole defect*. This finding suggests that the fracture properties of such MWCNTs are dominated by the aforementioned structural defects.

3.2. Mechanical properties

The dependences of the nominal tensile strength upon the fracture cross section ratio and Raman intensity ratio are shown in **Figure 10**. The fracture cross section ratio was calculated by dividing the fractured cross-sectional area by the full cross-sectional area of the MWCNTs, including the inner hole. A higher fracture cross section ratio (for a given outer diameter) means a larger number of fractured walls in the MWCNT. It can

http://dx.doi.org/10.5772/intechopen.70578

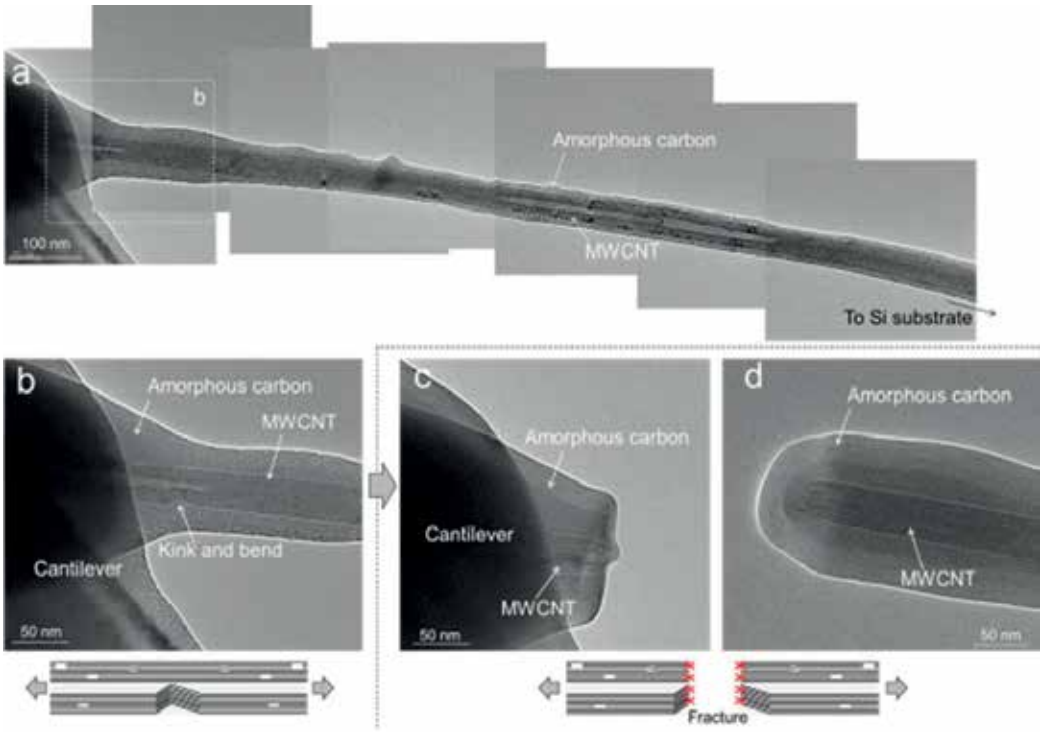

Figure 8. TEM images of S-MWCNT fractured at the *kink and bend* (a, b) before and (c, d) after the tensile test [52].

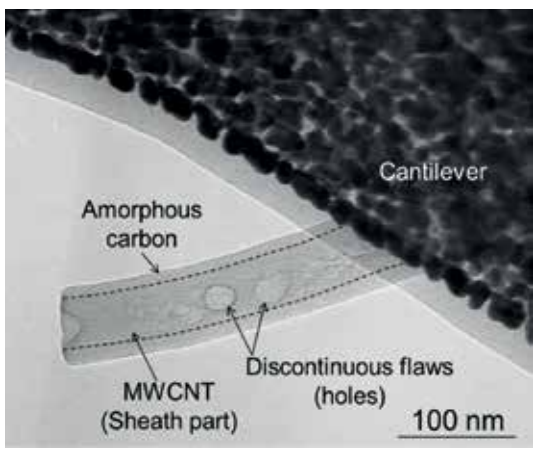

Figure 9. TEM image of S-MWCNT fractured at the *discontinuous flaw* [52].

be seen from **Figure 10a** that the H-MWCNTs annealed at 1800 and 2200°C and the as-grown S-MWCNTs had an intermediate level of crystallinity, as measured from the Raman intensity ratio (R = 1.4–4.9), compared with that of the H-MWCNTs thermally

annealed at 1200 and 2600°C (*R* values of 1.0 and 10.1, respectively). **Figure 10b** shows that the MWCNTs with an intermediate level of crystallinity produced complete fracture of the nanotube walls (*clean break* or *sword and sheath failure*) and exhibited higher nominal tensile strength. The slightly lower value of the fracture cross section ratio of the as-grown S-MWCNTs compared with that of the H-MWCNTs thermally annealed at 1800 and 2200°C was caused by the larger hollow core. Although the H-MWCNTs annealed at 1200°C failed in a *clean break* manner (**Figure 10b**), their nominal tensile strength was observed to be small (~1 GPa) because of their relatively low crystallinity (*R* = 1.0) which reflects their amorphous graphite structure and many defects. The amorphous structure might explain the low load-bearing ability of these MWCNTs. When the annealing temperature was 2600°C, an abrupt decrease in both the nominal tensile strength and the fracture cross section ratio was observed, although the crystallinity considerably increased (*R* = 10.1). This result can be attributed to a decrease in the number of cross-linking defects, i.e., interwall sp^3 bonding, owing to the high-temperature thermal annealing. The removal of cross-linking defects decreases the load transfer from the outer walls to the inner ones, resulting in multiwall-type *sword-in-sheath failure* (i.e., decrease of the fracture cross section ratio) and degradation of the load-bearing ability. These results suggest that improvements to the nominal tensile strength of MWCNTs might be achieved by inducing appropriate interactions between adjacent nanotube walls to enable sufficient load transfer to the MWCNT inner layers. This effect should be balanced to permit an adequate load transfer between the inner and outer walls to give *clean break* fractures. On the other hand, the nominal tensile strength for the thermally annealed S-MWCNTs at 2900°C shows nearly the same value as that

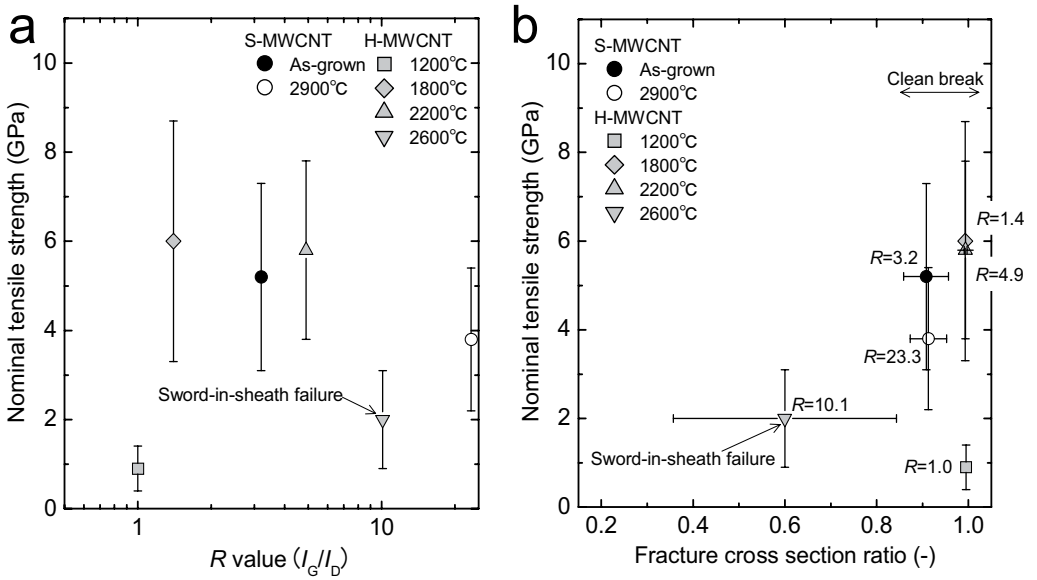

Figure 10. Nominal tensile strength of the MWCNTs as a function of (a) Raman intensity ratio and (b) fracture cross section ratio [52].

of the as-grown S-MWCNTs, even though a slight decrease in the strength is observed for the thermally annealed S-MWCNTs. This result suggests that the structural changes observed over this annealing temperature range may not have a significant impact on the nominal tensile strength of the S-MWCNTs. The H-MWCNTs had small defects, such as vacancies, Stone-Wales defects, or cross-linking defects, but no *discontinuous flaws* and *kinks and bends*, as shown in the S-MWCNTs. As a result, thermal annealing led to a decrease in the small defects with concomitant increases in the nominal tensile strength (0.9 to 5.9 GPa). On the other hand, although the as-grown S-MWCNTs exhibit an intermediate level of crystallinity (R = 3.2), they include structural defects such as *discontinuous flaws* and *kinks and bends*. Such structural defects and *hole defects* were still observed in the thermally annealed S-MWCNTs (**Table 1**). Thus, the annealing treatments led to no major changes in the controlling defects and had no major effects on the fracture morphology and nominal tensile strength of the S-MWCNTs, despite their high crystallinity.

3.3. Weibull distribution

A Weibull plot of the nominal tensile strength of the MWCNTs is shown in **Figure 11**. Supplementing the experimental results of this study, **Figure 11** also gives some results evaluated using data from the literature for previously reported CVD-grown MWCNTs and arc discharge-grown MWCNTs [37, 38, 40, 52, 53]. These nominal values were calculated based on the literature values. **Table 2** shows the outer diameter, nominal tensile strength, and Weibull scale and shape parameters of the MWCNTs. As with other brittle materials, the strength distribution of CNTs does not follow a Gaussian distribution, and failure of nanotubes is described by Weibull-Poisson statistics. If σ_{nom} is the failure strength of a nanotube, the cumulative distribution function $f(\sigma_{nom})$ for the two-parameter Weibull distribution is defined as [39]:

$$f_{(\sigma_{nom})} = 1 - \exp\left[-\left(\frac{\sigma_{nom}}{\alpha}\right)^{\beta}\right] \tag{2}$$

where $f(\sigma_{nom})$ is the probability of failure, α is the scale parameter, and β is the shape parameter. The β values of the MWCNTs are calculated to be in the range of 1.6–3.0. The comparatively low value of the shape parameter for MWCNTs indicates a wide variability in their tensile strength, more so than that of carbon fibers [60] and SiC fibers [61] (β = 15 and 7–11, respectively). This may result from the irregular nanotube structure, which reflects a larger tube defect density relative to carbon fibers and SiC fibers.

4. Conclusions

In this chapter, we reviewed the nominal tensile strength and Weibull scale and shape parameters of the nominal tensile strength distribution of MWCNTs based on our recent previous studies. The comparatively low value of the shape parameter for MWCNTs resulted

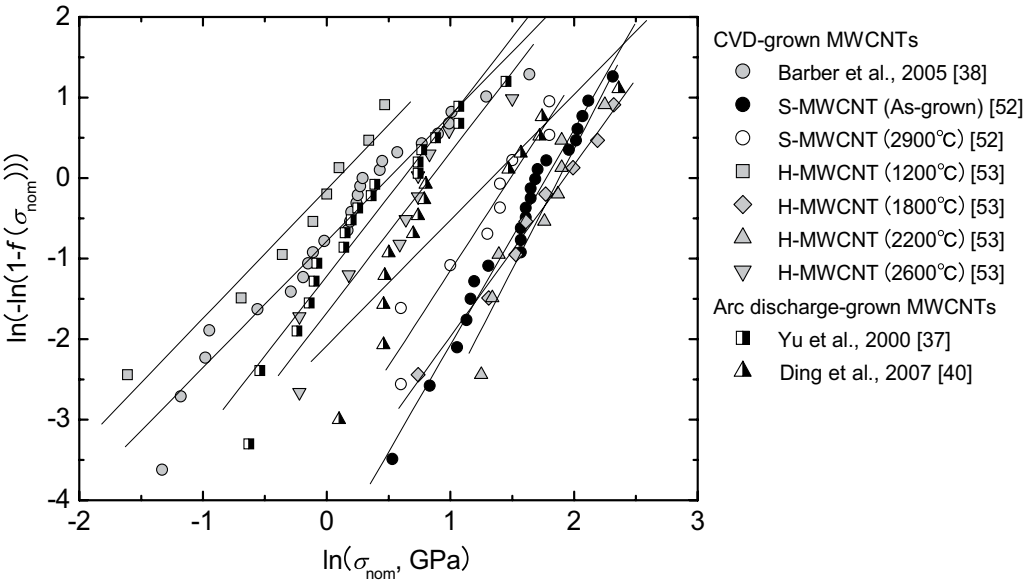

Figure 11. Weibull plot for the nominal tensile strength of MWCNTs [52].

MWCNT type	Outer diameter (nm)	Nominal tensile strength (GPa)	Scale parameter, α (GPa)	Shape parameter, β (–)	Ref.
Arc-discharge-grown	25 ± 7	1.6 ± 1.0	1.9	2.0	[37]
CVD-grown	97 ± 25	1.5 ± 1.1	1.7	1.6	[38]
Arc-discharge-grown	11 ± 3	3.4 ± 2.6	3.8	1.6	[40]
S-MWCNT (CVD, as-grown)	36 ± 7	5.2 ± 2.1	5.9	2.7	[52]
S-MWCNT (CVD, 2900°C)	35 ± 6	3.8 ± 1.6	4.4	2.4	[52]
H-MWCNT (CVD, 1200°C)	90 ± 40	0.9 ± 0.5	1.1	1.6	[53]
H-MWCNT (CVD, 1800°C)	72 ± 21	6.0 ± 2.7	6.8	2.1	[53]
H-MWCNT (CVD, 2200°C)	69 ± 16	5.8 ± 2.0	6.6	3.0	[53]
H-MWCNT (CVD, 2600°C)	67 ± 12	2.0 ± 1.1	2.3	2.0	[53]

Table 2. Measured properties for MWCNTs. Shown are the outer diameter, nominal tensile strength, and Weibull scale and shape parameters. The outer diameter and nominal tensile strength data are presented as average values ± standard deviations.

from the irregular nanotube structure, which reflects a larger tube defect density relative to conventional fiber materials. Nonetheless, the MWCNTs with an intermediate level of crystallinity produced complete fracture of nanotube walls and exhibited higher nominal

tensile strength, suggesting that there is an optimal nanotube defect density for increasing the nominal tensile strength, not too low but also not too high, so as to permit an adequate load transfer between the nanotube walls. To improve the properties of macroscopic CNT composite performance, the structure and properties of MWCNT yarns and sheets must be optimized at all hierarchical levels: from individual MWCNTs to MWCNT bundles, MWCNT networks, and MWCNT yarns and sheets. Future research efforts aimed at each of the following levels should be pursued to improve mechanical properties, particularly the nominal tensile strength of CVD-grown MWCNTs: (1) improved synthesis methods should be developed to reduce structural defects such as *discontinuous flaws* and *kinks and bends*; and (2) the degree of inter-wall cross-linking and load transfer between adjacent nanotube walls should be optimized by posttreatments, such as thermal annealing and electron irradiation. We believe that the above improvements might enable the realization of higher nominal tensile strength. More well-defined CNT architectures should contribute to enhanced mechanical properties as well as improved the electrical and thermal properties of MWCNT yarns and composites.

Acknowledgements

The authors thank Toyo Tanso Co., Ltd. for its technical assistance in thermal annealing of the MWCNTs. The authors acknowledge Prof. Y. Inoue and Prof. Y. Shimamura of Shizuoka University for their useful guidance; Dr. T. Miyazaki of the Technical Division, School of Engineering, Tohoku University, for technical assistance in the TEM analysis; Prof. K. Hirahara of Osaka University and R. Bekarevich of the National Institute for Material Science for technical assistance in the tensile testing; and our colleague, Mr. I. Tamaki of the Fracture and Reliability Research Institute (FRRI), Tohoku University, for helpful discussions. We thank Joshua Green, MS, from Edanz Group (www.edanzediting.com/ac) for editing a draft of this manuscript. This research was supported in part by the Japan Society for the Promotion of Science (JSPS) Core-to-Core Program. This research was partially supported by a Grant-in-Aid for Young Scientists (B) 16 K20904 and a Grant-in-Aid for Young Scientists (A) 15H05502.

Author details

Keiichi Shirasu[1]*, Go Yamamoto[2], Daniel Nelias[3] and Toshiyuki Hashida[1]

*Address all correspondence to: keiichi.shirasu@rift.mech.tohoku.ac.jp

1 Fracture and Reliability Research Institute, Tohoku University, Sendai, Japan

2 Department of Aerospace Engineering, Tohoku University, Sendai, Japan

3 Univ Lyon, INSA-Lyon, Villeurbanne, France

References

[1] Ruoff RS, Lorents DC. Mechanical and thermal properties of carbon nanotubes. Carbon. 1995;**33**:925-930

[2] Ebbesen TW, Lezec HJ, Hiura H, Bennett JW, Ghaemi HF, Thio T. Electrical conductivity of individual carbon nanotubes. Nature. 1996;**382**:54-56

[3] Yoshida Y. High-temperature shrinkage of single-walled carbon nanotube bundles up to 1600 K. Journal of Applied Physics. 2000;**87**:3338-3341

[4] Maniwa Y, Fujiwara R, Kira H, Tou H, Kataura H, Suzuki S, et al. Thermal expansion of single-walled carbon nanotube (SWNT) bundles: X-ray diffraction studies. Physical Review B. 2001;**64**(R):241402

[5] Schelling PK, Keblinski P. Thermal expansion of carbon structures. Physical Review B. 2003;**68**:035425

[6] Kwon YK, Berber S, Tománek D. Thermal contraction of carbon fullerenes and nanotubes. Physical Review Letters. 2004;**92**:015901

[7] Jiang H, Liu B, Huang Y, Hwang KC. Thermal expansion of single wall carbon nanotubes. Journal of Engineering Materials and Technology. 2004;**126**:265-270

[8] Hu N, Jia B, Arai M, Yan C, Li J, Liu Y, Atobe S, Fukunaga H. Prediction of thermal expansion properties of carbon nanotubes using molecular dynamics simulations. Computational Materials Science. 2012;**54**:249-254

[9] Shirasu K, Yamamoto G, Tamaki I, Ogasawara T, Shimamura Y, Inoue Y, Hashida T. Negative axial thermal expansion coefficient of carbon nanotubes: Experimental determination based on measurements of coefficient of thermal expansion for aligned carbon nanotube reinforced epoxy composites. Carbon. 2015;**95**:904-909

[10] Shirasu K, Nakamura A, Yamamoto G, Ogasawara T, Shimamura Y, Inoue Y, Hashida T. Potential use of CNTs for production of zero thermal expansion coefficient composite materials: An experimental evaluation of axial thermal expansion coefficient of CNTs using a combination of thermal expansion and uniaxial tensile tests. Composites Part A: Applied Science and Manufacturing. 2017;**95**:152-160

[11] Peng B, Locascio M, Zapol P, Li S, Mielke SL, Schatz GC, Espinosa HD. Measurements of near-ultimate strength for multiwalled carbon nanotubes and irradiation-induced cross-linking improvements. Nature Nanotechnology. 2008;**3**:626-631

[12] Locascio M, Peng B, Zapol P, Zhu Y, Li S, Belytschko T, Espinosa HD. Tailoring the load carrying capacity of MWCNTs through inter-shell atomic bridging. Experimental Mechanics. 2009;**49**:169-182

[13] Zhang M, Atkinson KR, Baughman RH. Multifunctional carbon nanotube yarns by downsizing an ancient technology. Science. 2004;**306**:1358-1361

[14] Zhang M, Fang S, Zakhidov AA, Lee SB, Aliev AE, Williams CD. Strong, transparent, multifunctional, carbon nanotube sheets. Science. 2005;**309**:1215-1219

[15] Cheng Q, Wang J, Jiang K, Li Q, Fan S. Fabrication and properties of aligned multi-walled carbon nanotube-reinforced epoxy composites. Journal of Materials Research. 2008;**23**:2975-2983

[16] Cheng Q, Bao J, Park JG, Liang Z, Zhang C, Wang B. High mechanical performance composite conductor: Multi-walled carbon nanotube sheet/bismaleimide nanocomposites. Advanced Functional Materials. 2009;**19**:3219-3225

[17] Cheng QF, Wang JP, Wen JJ, Liu CH, Jiang KL, Li QQ, Fan SS. Carbon nanotube/epoxy composites fabricated by resin transfer molding. Carbon. 2010;**48**:260-266

[18] Bradford PD, Wang X, Zhao H, Maria JP, Jia Q, Zhu YT. A novel approach to fabricate high volume fraction nanocomposites with long aligned carbon nanotubes. Composites Science and Technology. 2010;**70**:1980-1985

[19] Cheng Q, Wang B, Zhang C, Liang Z. Functionalized carbon-nanotube sheet/bismaleimide nanocomposites: Mechanical and electrical performance beyond carbon-fiber composites. Small. 2010;**6**:763-767

[20] Ogasawara T, Moon SY, Inoue Y, Shimamura Y. Mechanical properties of aligned multi-walled carbon nanotube/epoxy composites processed using a hot-melt prepreg method. Composites Science and Technology. 2011;**71**:1826-1833

[21] Liu W, Zhang X, Xu G, Bradford PD, Wang X, Zhao H, Zhang Y, Jia Q, Yuan FG, Li Q, Qiu Y, Zhu Y. Producing superior composites by winding carbon nanotubes onto a mandrel under a poly(vinyl alcohol) spray. Carbon. 2011;**49**:4786-4791

[22] Wang X, Bradford PD, Liu W, Zhao H, Inoue Y, Maria JP, Li Q, Yuan FG, Zhu Y. Mechanical and electrical property improvement in CNT/nylon composites through drawing and stretching. Composites Science and Technology. 2011;**71**:1677-1683

[23] Liu W, Zhao H, Inoue Y, Wang X, Bradford PD, Kim H, Qui Y, Zhu Y. Poly(vinyl alcohol) reinforced with large-diameter carbon nanotubes via spray winding. Composites Part A: Applied Science and Manufacturing. 2012;**43**:587-592

[24] Wang X, Yong ZZ, Li QW, Bradford PD, Liu W, Tucker DS, Cai W, Yuan FG, Zhu YT. Ultrastrong, stiff and multifunctional carbon nanotube composites. Materials Research Letters. 2013;**1**:19-25

[25] Mikhalchan A, Gspann T, Windle A. Aligned carbon nanotube-epoxy composites: The effect of nanotube organization on strength, stiffness, and toughness. Journal of Materials Science. 2016;**51**:10005-10025

[26] Di J, Wang X, Xing Y, Zhang Y, Zhang X, Lu W, Li Q, Zhu YT. Dry-processable carbon nanotubes for functional devices and composites. Small. 2014;**10**:4606-4625

[27] Goh PS, Ismail AF, Ng BC. Directional alignment of carbon nanotubes in polymer matrices: Contemporary approaches and future advances. Composites Part A: Applied Science and Manufacturing. 2014;**56**:103-126

[28] Salvetat JP, Kulik AJ, Bonard JM, Briggs GAD, Stöckli T, Méténier K, Bonnamy S, Béguin F, Burnham NA, Forró L. Elastic modulus of ordered and disordered multiwalled carbon nanotubes. Advanced Materials. 1999;**11**:161-165

[29] Yamamoto G, Suk JW, An J, Piner RD, Hashida T, Takagi T, Ruoff RD. The influence of nanoscale defects on the fracture of multi-walled carbon nanotubes under tensile loading. Diamond and Related Materials. 2010;**19**:748-751

[30] Elumeeva KV, Kuznetsov VL, Ischenko AV, Smajda R, Spina M, Forró L, Magrez A. Reinforcement of CVD grown multi-walled carbon nanotubes by high temperature annealing. AIP Advances. 2013;**3**:112101

[31] Kimura T, Suzuki H, Zhang M, Yamamoto G, Hashida T, Motomiya K, Tohji K, Sato Y. Is the tensile strength of carbon nanotubes enhanced by supported materials?: Effect of supported amorphous alumina nanoparticles on the tensile strength of carbon nanotubes. Carbon. 2017;**118**:339-342

[32] Ogata S, Shibutani Y. Ideal tensile strength and band gap of single-walled carbon nanotubes. Physical Review B. 2003;**68**:165409

[33] Ozaki T, Iwasa Y, Mitani T. Stiffness of single-walled carbon nanotubes under large strain. Physical Review Letters. 2000;**84**:1712-1715

[34] Dumitrică T, Belytscko T, Yakobson BI. Bond-breaking bifurcation states in carbon nanotube fracture. Journal of Chemical Physics. 2003;**118**:9485-9488

[35] Mielke SL, Troya D, Zhang S, Li JL, Xiao S, Car R, Ruoff RS, Schatz GC, Belytschko T. The role of vacancy defects and holes in the fracture of carbon nanotubes. Chemical Physics Letters. 2004;**390**:413-420

[36] Troya D, Mielke SL, Schatz GC. Carbon nanotube fracture-differences between quantum mechanical mechanisms and those of empirical potentials. Chemical Physics Letters. 2003;**382**:133-141

[37] Yu MF, Lourie O, Dyer MJ, Moloni K, Kelly TF, Ruoff RS. Strength and breaking mechanism of multiwalled carbon nanotubes under tensile load. Science. 2000;**287**:637-640

[38] Barber AH, Andrews R, Schadler LS, Wagner HD. On the tensile strength distribution of multiwalled carbon nanotubes. Applied Physics Letters. 2005;**87**:213106

[39] Barber AH, Kaplan-Ashiri I, Cohen SR, Tenne R, Wagner HD. Stochastic strength of nanotubes: An appraisal of available data. Composites Science and Technology. 2005;**65**:2380-2384

[40] Ding W, Calabri L, Kohlhaas KM, Chen X, Dikin DA, Ruoff RS. Modulus, fracture strength, and brittle vs. plastic response of the outer shell of arc-grown multi-walled carbon nanotubes. Experimental Mechanics. 2007;**47**:25-36

[41] Zhang B, Zhao L, Cheng Y, Golberg D, Wang MS. Reversible tuning of individual carbon nanotube mechanical properties via defect engineering. Nano Letters. 2016;**16**:5221-5227

[42] Tombler TW, Zhou C, Alexseyev L, Kong J, Dai H, Liu L, Jayanthi CS, Tang M, SY W. Reversible electromechanical characteristics of carbon nanotubes under local-probe manipulation. Nature. 2000;**405**:769-772

[43] Lukić B, Seo JW, Bacsa RR, Delpeux S, Béguin F, Bister G, Fonseca A, Nagy JB, Kis A, Jeney S, Kulik AJ, Forró L. Catalytically grown carbon nanotubes of small diameter have a high Young's modulus. Nano letters. 2005;**5**:2074-2077

[44] Lukić B, Seo JW, Couteau E, Lee K, Gradečak S, Berkecz R, Hernadi K, Delpeux S, Cacciaguerra T, Béguin F, Fonseca A, Nagy JB, Csányi G, Kis A, Kulik AJ, Forró L. Elastic modulus of multi-walled carbon nanotubes produced by catalytic chemical vapour deposition. Applied Physics A. 2005;**80**:695-700

[45] Lee K, Lukić B, Magrez A, Seo JW, Andrew G, Briggs D, Kulik AJ, Forró L. Diameter-dependent elastic modulus supports the metastable-catalyst growth of carbon nanotubes. Nano Letters. 2007;**7**:1598-1602

[46] Duchamp M, Meunier R, Smajda R, Mionic M, Magrez A, Seo JW, Forró L, Song B, Tománek D. Reinforcing multiwall carbon nanotubes by electron beam irradiation. Journal of Applied Physics. 2010;**108**:084314

[47] Poncharal P, Wang ZL, Ugarte D, de Heer WA: Electrostatic deflections and electromechanical resonances of carbon nanotubes. Science. 1999;**283**:1513-1516

[48] Gaillard J, Skove M, Rao AM. Mechanical properties of chemical vapor deposition-grown multiwalled carbon nanotubes. Applied Physics Letters. 2005;**86**:233109

[49] Yu MF, Files BS, Arepalli S, Ruoff RS. Tensile loading of ropes of single wall carbon nanotubes and their mechanical properties. Physical Review Letters. 2000;**84**:5552-5555

[50] Demczyk BG, Wang YM, Cumings J, Hetman M, Han W, Zettl A, Ritchie RO. Direct mechanical measurements of the tensile strength and elastic modulus of multi-walled carbon nanotubes. Material Science and Engineering A. 2002;**A334**:173-178

[51] Wang MS, Golberg D, Bando Y. Tensile tests on individual single-walled carbon nanotubes: Linking nanotube strength with its defects. Advanced Materials. 2010;**22**: 4071-4075

[52] Shirasu K, Tamaki I, Miyazaki T, Yamamoto G, Bekarevich R, Hirahara K, Shimamura Y, Inoue Y, Hashida T. Key factors limiting carbon nanotube strength: Structural characterization and mechanical properties of multi-walled carbon nanotubes. Mechanical Engineering Journal. 2017;**4**:17-00029. DOI: 10.1299/mej.17-00029

[53] Yamamoto G, Shirasu K, Nozaka Y, Sato Y, Takagi T, Hashida T. Structure-property relationships in thermally-annealed multi-walled carbon nanotubes. Carbon. 2014;**66**:219-226

[54] Tamaki I, Shirasu K, Miyazaki T, Yamamoto G, Bekarevich R, Hirahara K, Shimamura Y, Inoue Y, Hashida T. Effects of structural defects on strength and fracture properties of multi-walled carbon nanotubes. Transactions of the JSME (in Japanese). 2017;**83**:16-00283. DOI: 10.1299/transjsme.16-00283

[55] Inoue Y, Kakihata K, Hirono Y, Horie T, Ishida A, Mimura H. One-step grown aligned bulk carbon nanotubes by chloride mediated chemical vapor deposition. Applied Physics Letters. 2008;**92**:213113

[56] Dresselhaus MS, Dresselhaus G, Saito R, Jorio A. Raman spectroscopy of carbon nanotubes. Physics Reports. 2005;**409**:47-99

[57] Kataura H, Kumazawa Y, Maniwa Y, Ohtsuka Y, Sen R, Suzuki S, Achiba Y. Diameter control of single-walled carbon nanotubes. Carbon. 2000;**38**:1691-1697

[58] Sader JE, Chon JWM, Mulvaney P. Calibration of rectangular atomic force microscope cantilevers. Review of Scientific Instruments. 1999;**70**:3967-3969

[59] Ding W, Dikin DA, Chen X, Piner RD, Ruoff RS, Zussman E, Wang X, Li X. Mechanics of hydrogenated amorphous carbon deposits from electron-beam-induced deposition of a paraffin precursor. Journal of Applied Physics. 2005;**98**:014905

[60] Okabe T, Takeda N. Elastoplastic shear-lag analysis of single-fiber composites and strength prediction of unidirectional multi-fiber composites. Composites Part A: Applied Science and Manufacturing. 2002;**33**:1327-1335

[61] Curtin WA, Netravali AN, Park JM. Strength distribution of Carborundum polycrystalline SiC fibres as derived from the single-fibre-composite test. Journal of Materials Science. 1994;**29**:4718-4728

Chapter 7

Charged Carbon Nanotubes

Devashree Atre and Shashank Pant

Additional information is available at the end of the chapter

http://dx.doi.org/10.5772/intechopen.70480

Abstract

As the degree of functionalization on CNTs greatly affects its properties, the structure and dynamics of water confined inside pristine and functionalized/charged carbon nanotubes (CNTs) is of prime importance. The presence of charges on the surface of CNTs results in hydrophobic to hydrophilic transitions which increase its occupancy of the water molecules thereby breaking down 1D water wires, as seen in pristine CNTs.

Keywords: carbon nanotubes, breakdown of 1D water wires, functionalization, confined water, density fluctuations

1. Introduction

1.1. What are carbon nanotubes?

Carbon nanotubes (CNTs) are carbon allotropes having a cylindrical nanostructure. This nanostructure has unusual properties which increases its applications in the field of biology, electronics, water desalination, material science and optics. This material has significantly higher stiffness and exceptional strength. CNTs have been constructed in a wide range of diameter to length ratio [1]. In addition to the mechanical strength and stiffness, it has high thermal conductivity and wide range of electrical properties. Owing to this extremely high strength, CNTs have found a place in the materials used for designing bats, car parts etc. [2, 3]

CNTs belong to the fullerene family and the name is derived from their long and hollow structure where walls are formed by carbon atoms sheets called graphene [4]. These graphene sheets are rolled at a specific angle, which decides the properties of CNTs. Nanotubes can be broadly divided into two types:

1. Single wall carbon nanotubes (SWNTs).
2. Multi wall carbon nanotubes (MWNTs).

Individual CNTs can align themselves by pi-pi stacking and Van der Waals interactions. In more chemical terms, carbon nanotubes bond due to sp2 hybrid carbon atoms. These bonds are stronger than the alkanes and provide CNTs which extremely high in strength. A typical carbon nanotube is show in **Figure 1**.

The wrapping of the graphene sheets is represented by a pair of indices (n,m) where n and m denote the number of unit vector in the crystal structure of graphene as shown in **Figure 2**.

MWNTs can consist of many rolled up graphene sheets and the process can be done either by using concentric single walled nanotubes or by rolling up a single graphene sheet around itself. Recently, many modifications of CNTs morphology have been reported [5–7].

1.2. Application of carbon nanotubes

Owning to its stiffness, mechanical strength, conductivity and structure carbon nanotubes have widespread applications in the area of sports, transistors, material science, biology etc. [8–14]. The Easton-Bell Sports Inc. has been using CNT, in partnership with Zyvex Performance Materials, in designing bicycle components like handlebars, seatposts, crank etc. Owning to the nanometer sized diameter and tunable length which can reach up to a few centimeters CNTs can be a drug vehicle for therapy purposes [15]. The sp2 hybridized orbitals and a large porous surface area can be easily exploited to load large quantity of drugs inside the tube. Not only drug but specific molecules which can increases the targeting ability can be easily loaded in the nanotubes. Drugs like doxorubicin (DOX) can be absorbed on the CNT surface by pi-pi stacking [16], this type of loading is usually pH dependent thus proving a handle to release drugs.

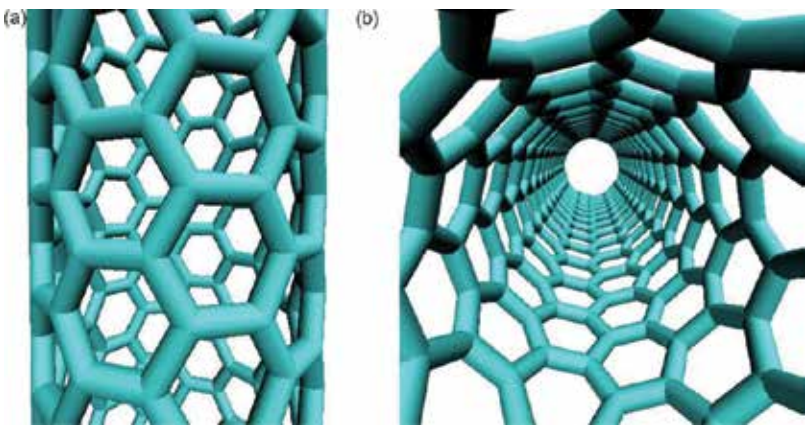

Figure 1. A typical carbon nanotube (a) side view and (b) showing the carbon nanotube pore.

http://dx.doi.org/10.5772/intechopen.70480

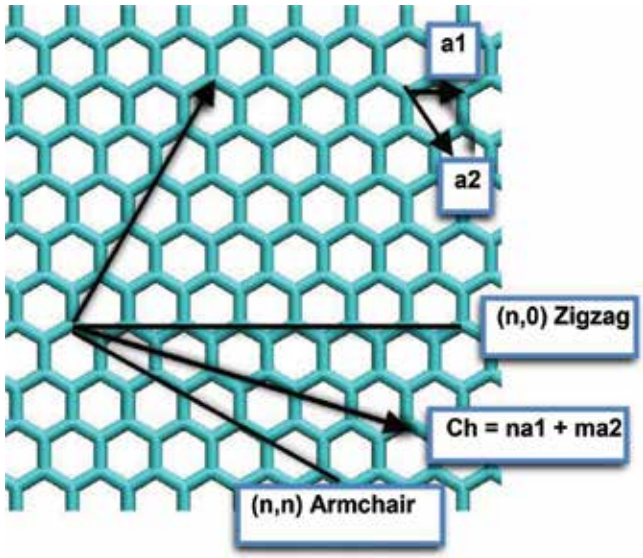

Figure 2. The (n,m) naming scheme of nanotubes can be thought of as a vector C in an infinite graphene sheet; this will describe how to roll up the sheet to form the nanotube. Also, a1 and a2 denotes the unit vector for the graphene.

In addition to the drug delivery the optical properties of CNTs provide NIR (Non Infrared Radiation) region of absorption [17, 18]. In contrast, biological tissues and cells provide maximum transmission in this range, thus making it a suitable candidate for bio-imaging, tracing, diagnosis etc. If chemotherapeutic drugs are combined with CNT optical properties it might increase the treatment effectiveness. The low toxicity of CNTs makes it an utmost important candidate for biomedical applications. We can tune the toxicity of the CNTs by varying the length, aggregation, surface functionalization etc. thus, care must be taken before using them. But the usual MTT assays cannot be used for testing the cytotoxicity of CNTs because MTT-formazan crystals might stick to the surface of the CNTs thereby making it less soluble in isopropanol and DMSO [19].

Carbon nanotubes serve as a robust material for water desalination and in water decontamination. The CNT hollow pores provide frictionless transport of water molecules and the tunable diameter can be used for removing unwanted particles. The functionalized CNTs can also be employed to selectively remove particular particles by specific or non-specific interactions. Thus, CNTs can be used as a "Gate-Keeper" molecule [20–27]. The smooth hydrophobic walls and the pore diameter of CNTs allow ultra-efficient water transport. A prototype of CNT membrane is shown in **Figure 3**.

1.3. Functionalization of carbon nanotubes

The chemical modifications of carbon nanotubes (CNTs) are an emerging area of research as it provides a handle to tune the solubilization [28] of CNTs. The reaction for the modification of CNTs can be broadly divided into two areas:

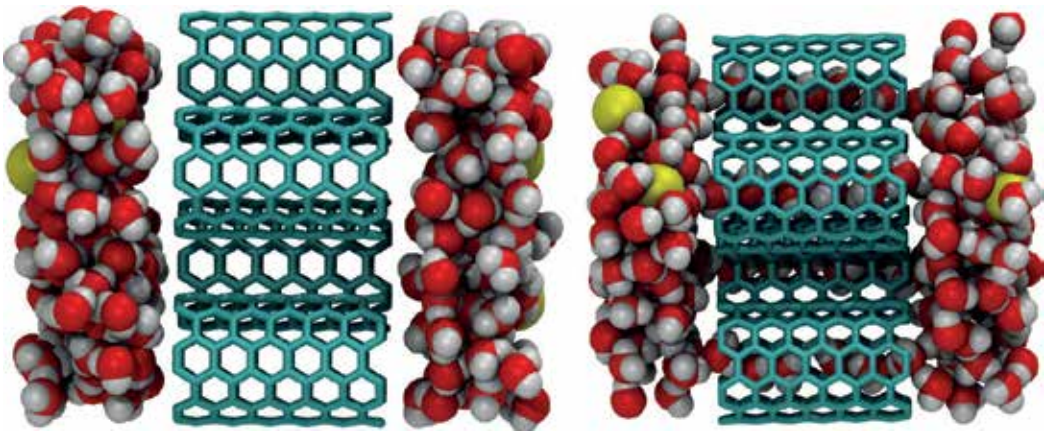

Figure 3. A water desalination setup where 4 CNTs form the membrane, yellow balls represents impurity and red-white molecules are the water. Movement of water through the CNT membrane is seen while impurity does not move through the membrane.

1. Direct attachment of groups on the graphitic carbon atoms.
2. Modifications on the CNT bound- carboxylic acids.

The fluorination [29] of CNTs has been extensively studied and this modification has resulted in the solvated individual CNTs in alcohol type solvents, while the second modification results in changes in the CNT properties as it might lead to the shortening of the nanotubes. Further different methods have been incorporated especially ester modification at the terminal carbon of CNTs. This modification can be easily removed by acid-base chemistry, thus enabling us to get back to the initial state of CNTs.

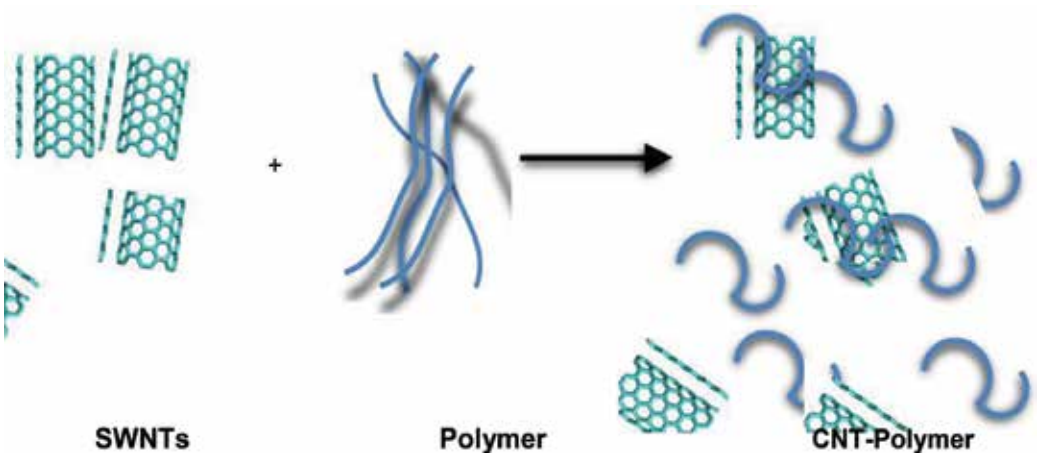

Figure 4. Carbon nanotube modification scheme.

In order, to solubilize CNTs attachment of large chemical group is needed. These larger chemical groups can be certain chemical compounds or can also be certain polymers. These chemical compounds wrap around the CNTs and hinder the formation of CNT bundles in the solvent, thereby solubilizing it in the solvent. The solubility of CNT can be easily modulated by varying the nature of the functional groups. As, the chemical modification [30–35] of CNT greatly alters the chemical and the electronic structure of the nanotubes, good attention has been paid to the non-covalent and non-specific modifications. This type of modification results in almost the same effect without altering the chemical and electronic nature of the nanotube. A typical scheme for modification is shown in **Figure 4**.

2. Properties of solvent inside carbon nanotubes

2.1. Structure of water

Water is ubiquitous yet the most anomalous substance on earth, the origin of its anomalous properties is yet to be fully understood [36–42]. Water is tetrahedral in structure and it forms 4 hydrogen bonds in the fluid state and 6 hydrogen bonds in its solid state i.e. ICE. It is formed by 2 hydrogen and 1 oxygen molecule with the presence of two lone pairs on the oxygen. Due to polarization effect there is a presence of partial positive charge on the hydrogen atoms and partial negative charge on the oxygen atom. Due to its wide range of applications, water is a prime candidate under study for almost all the systems. Its structure along with its dynamic and thermodynamic properties of water confined under nanopores of carbon nanotubes has been widely studied. It has been observed that the properties of confined water are distinctly different from that of bulk or non-confined water. Despite of the hydrophobic nature of carbon nanotubes, it is occupied by 4–5 water molecules. The most interesting feature of water inside the 6,6 pristine CNT is the presence of 1 D water wires (1 dimensional) [43]. The water molecules entering the nanotube channel lose on average two hydrogen bonds and only a fraction of lost energy can be recovered by the VdW interactions between water and the nanotube. The presence of 1D water wire inside pristine 6,6 CNT is shown in **Figure 5**.

Further, extensive amount of work has been put in to study the structure of water confined inside carbon nanotubes. Molecular dynamics simulations suggested the presence of ice like structural ordering of water at room temperature [44–46]. The presence of ice like structures has been quantified by various matrices like the calculation of order parameter, radial distribution curves and snapshots of system. Before moving further, I would like to explain how one of the most important parameter, radial distribution works and what type of information we get from it. Radial distribution function or RDF gives us the structure of the system under study and it works under the assumption that the system should be radially symmetric. It gives us an idea about the variation of the density with respect to the distance. Although, it will not gives us the idea about the instantaneous density of the system but averaged density. In much coarse terms it gives us the probability of finding a particle at a distance of “r” from the central particle.

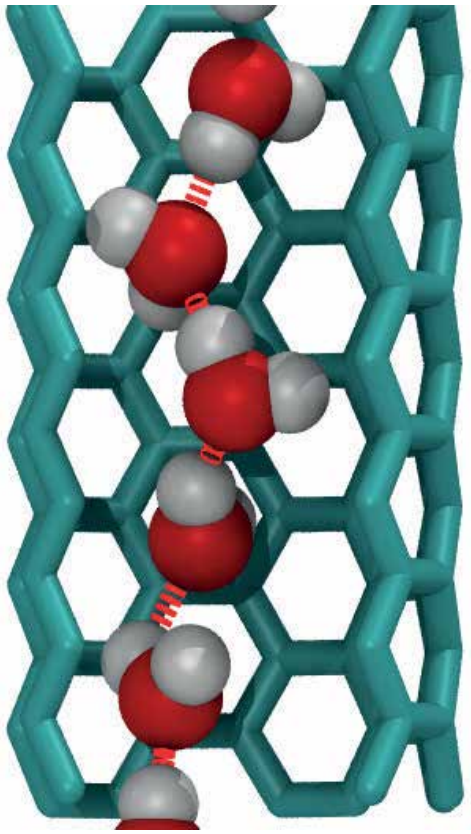

Figure 5. Presence of 1 D water wires inside 6,6 pristine CNT. Hydrogen bonds are shown in black.

The structure (RDF) of confined water is shown in **Figure 6**. The figure clearly shows the presence of peaks at regular intervals which suggest a ordered structure. No such peak was observed in the case of bulk water. A typical snapshot of the simulations performed by Koga et al. is shown in **Figure 6(b)**. The presence of ordered water nanotubes was seen in the simulation at room temperature but under axial pressure, the presence of square, pentagonal and hexagonal water nanotubes was observed in (14, 14), (15,15) and (16,16) nanotubes.

These structural studies suggests the presence of well ordered ice like structure of water inside CNTs at room temperature. Further, this ice-like ordered structures were seen even at a high temperatures like 320 K. Very recently, there has been an effort to study the properties of confined water inside functionalized CNTs. The functionalization was done by incorporating charges on the surface of CNTs i.e. by placing charge on the carbon atoms as shown in **Figure 7**. The presence of charge results in decreasing the ordered ice like structure of water. The main reason for such disordering or absence of an ice-like ordered structure is the hydrophobic to hydrophilic transition in the CNT. Due to the presence of charges on the CNT surface, it does not behave like a hydrophobic wall and there is a loss in the ordering [47–52] as shown in **Figure 8**. It clearly shows the decrease in the peak intensity

http://dx.doi.org/10.5772/intechopen.70480

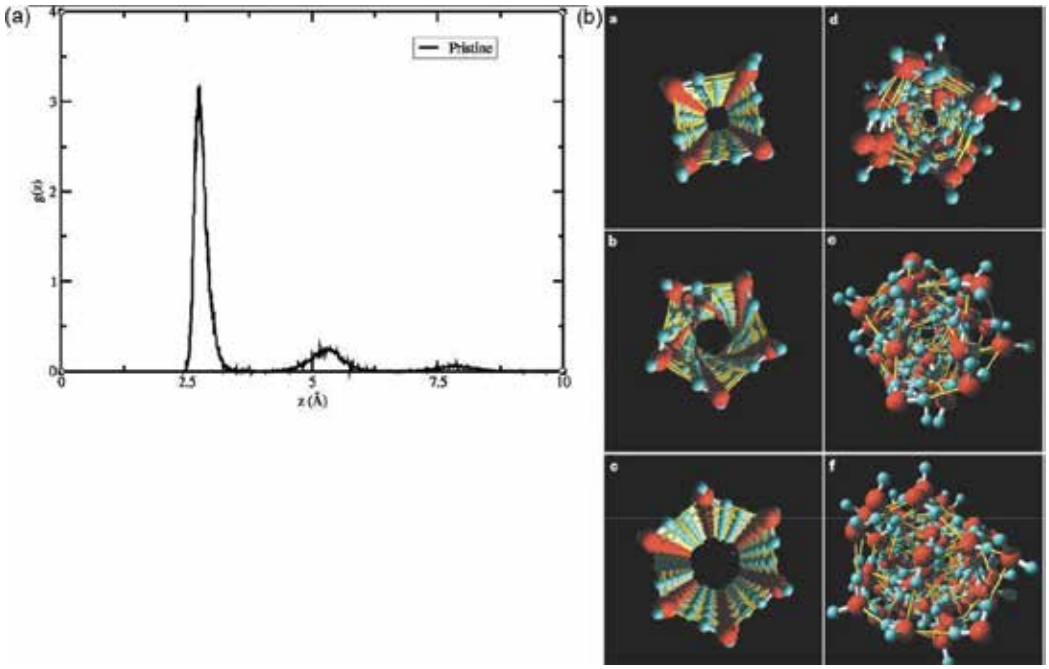

Figure 6. (a) Radial distribution curve along the axis of 6,6 pristine CNT. It shows the presence of regular spaced peaks, (b) snapshots of quenched water co-ordinates in (a) square, (b) pentagonal, (c) hexagonal ice nanotubes in (14,14), (15,15) and (16,16) SWNTs, (d–f) shows the corresponding liquid phase. The ice nanotubes were formed upon cooling under axial pressure of 50 MPa in molecular dynamics simulations. Figure taken from Koga et al. [44].

and the absence of equally spaced peaks. Thus the presence of charge on the CNT surface although increases its solubility in water but greatly affects the properties of confined water.

Now, an interesting question arises on the presence of 1D water wires inside functionalized CNTs. The very first study by Pant et al. clearly shows the breakdown of the 1D water wires rather the presence of 3 linear water wires inside such a confined space was observed as shown in **Figure 9**. The presence of 3 water wires was surprising because earlier the presence

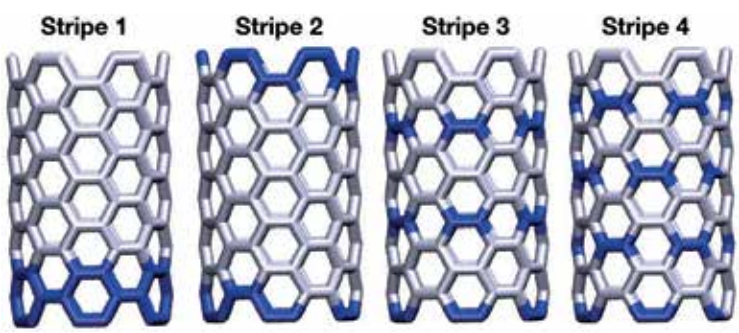

Figure 7. Distribution of charges on CNT. The blue area shows the presence of charged carbon atoms.

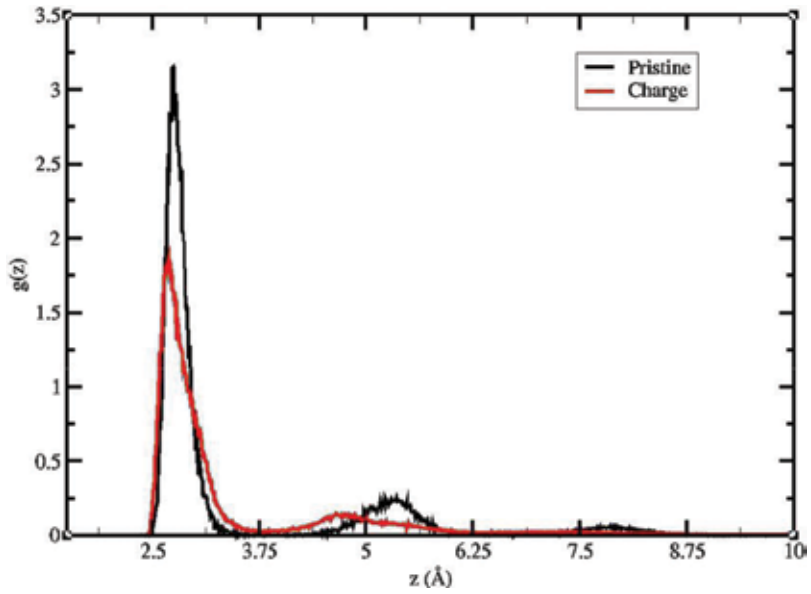

Figure 8. Decrease in the ordering of confined water inside CNT.

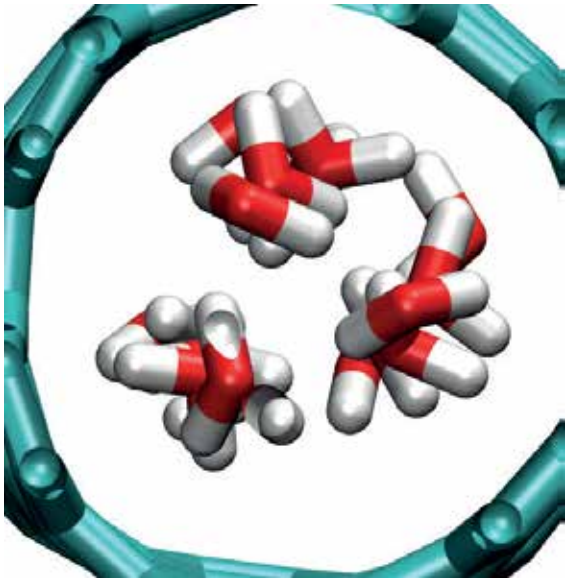

Figure 9. Presence of 3 water wires in functionalized CNT.

of 1D water wire in 6,6 pristine CNT was correlated to the diameter of the CNT and its hydrophobic nature of CNT. Although the functionalization of CNT does not change its diameter but it does changed its hydrophilic nature, thus it suggests the presence of 1D wires in pristine CNT is only dependent on its hydrophobic nature and not on its diameter.

Now, a question arises on how the degree of functionalization affects the confined water? In-order to answer this question we can increase the functionalization and also distribute the functional groups on the CNT surface in the form of various patterns. This can provide us with an easy handle to change the properties of the tube and it can even be use to mimic the properties of complex biological systems like aquaporins [53].

2.2. Permeation, diffusion of water through carbon nanotubes

A single permeation event is considered when a water molecule enters from one of CNT and leaves from the other end. The permeation or flow of water from the CNT has been extensively studied and enhanced water flow was observed. This can be related to the breaking of the hydrogen bonds i.e. in the pristine 6,6 CNT presence of 1D water wires was observed where each water molecule on average forms 1–2 hydrogen bonds which is in contrast with bulk water as it forms 4 hydrogen bonds. Thus the movement of water is less hindered inside the tube and it experiences less resistance from the neighboring water molecules. On, the other hand in the presence of functionalization there is a significant amount of decrease in the water flow. Due to the effect of functionalization, the nature of the tube changes from hydrophobic to hydrophilic and this transitions breaks the formation of 1D water wires, also presence of functional groups on the CNT surfaces results in the formation of hydrophilic-hydrophilic interactions between water and functional groups. These forces results in the decrease of water flow as shown in **Figure 10**.

Figure 11 clearly shows the decrease in the flow rate with the increase in the charge % on the surface of CNT. This can be further explained by the variation of hydrogen bonds between the confined water molecules because in the 6,6 pristine CNT, one water molecule on an average

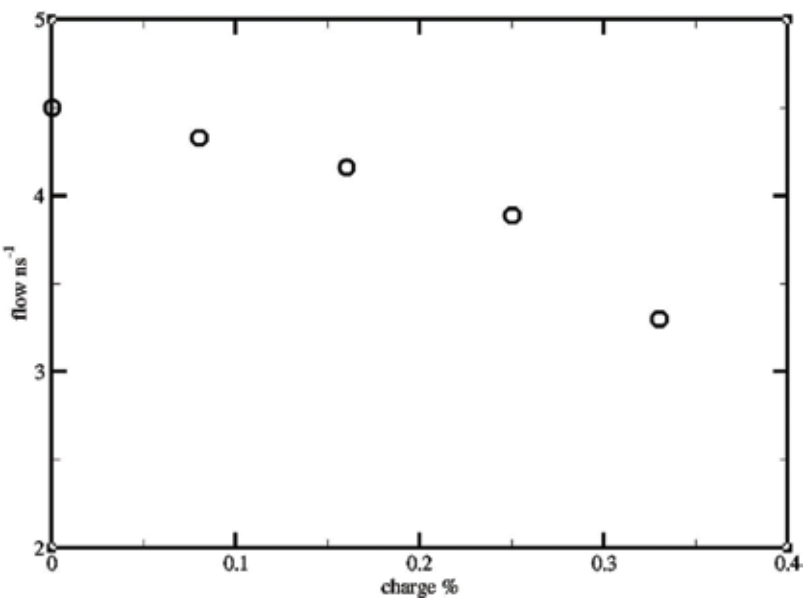

Figure 10. Variation of flow with the charge %.

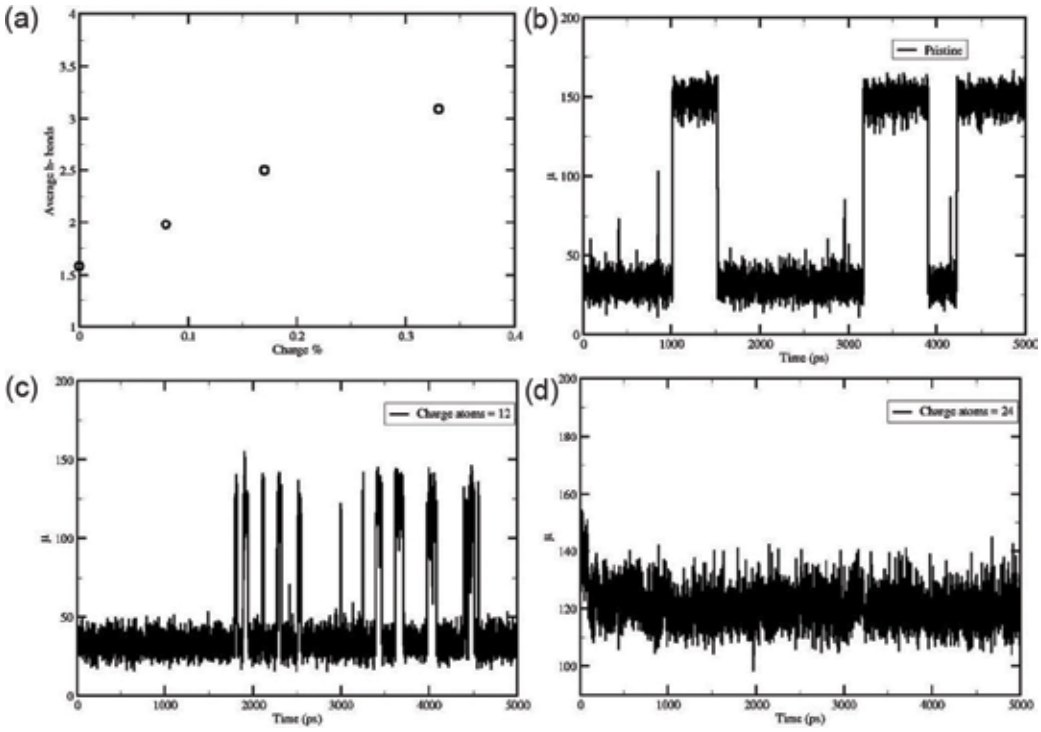

Figure 11. (a) Shows the variation of the hydrogen bonds with the charge %. (b–d) Shows the behavior of the water dipole moment and the decrease in the number of flipping events with the increase in the charge %.

forms 1–2 hydrogen bonds but in the presence of functionalized groups on CNT surface the number of hydrogen bonds almost linearly increases due to the breakdown of 1D water wire as shown in **Figure 11(a)**. This linear increase in the number of hydrogen bonds also prevents the dipole moment of water from flipping inside the CNT as shown in **Figure 11(b)**. A flip event for water is defined if Θ passes through 90°, thus the increase in the number of hydrogen bonds results in a potential barrier for the water's dipole moment to flip. This behavior is only affected by the presence of charges and not on the pattern of charge distribution.

As, we can observe from **Figure 11(a)**, the average number of hydrogen bonds for the highest charged system almost reached 3.5, which matches well with the number of hydrogen bonds in the bulk solvent, thus suggesting that degree of functionalization provides us with a good handle to tune the properties of the system under study.

Now, I would to talk about the macroscopic details of the confined spaces, like pores of carbon nanotubes which can be understood by studying the water density fluctuations. Water density fluctuations gives us the information about the nature of the confined space i.e. it help us to understand if the pore is hydrophobic or hydrophilic in nature. The water density fluctuation can be calculated by the following formula:

$$\kappa = \frac{(\langle N^2 \rangle - \langle N \rangle)}{\langle N \rangle} \tag{1}$$

http://dx.doi.org/10.5772/intechopen.70480

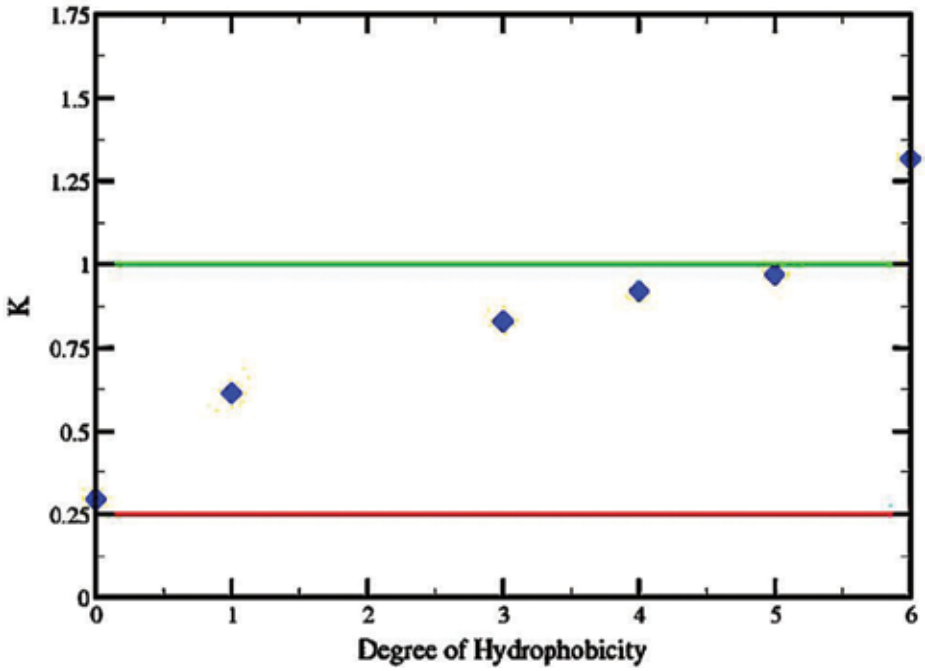

Figure 12. Normalized variance as the function of degree of hydrophobicity.

where K is the variance in the variance in the occupancy of water molecules normalized by its mean value. The ratio of variance and the mean value approaches pk_bTX_t, where X_t is the isothermal compressibility, in macroscopic limits. **Figure 12**, shows fluctuations in the density of confined water inside pristine and functionalized carbon nanotubes. The two horizontal lines indicate two limiting cases for fluctuations in bulk water and in ideal gas. The relative fluctuations in the highest charged CNTs increases by almost 5 times compared to that of pristine CNTs. This suggests that the compressibility of water near the hydrophobic CNTs is more owing to the wet-dry transitions [45, 54].

3. Conclusion

In conclusion charged or functionalized carbon nanotubes behave quite differently compared to pristine CNTs. Functionalization not only affects properties like band gap, conductivity and metallic nature of CNTs but it also greatly affects the properties of confined fluids. The functionalization of CNTs changes the overall nature of the CNTs and increases the hydrophilicity, which varies almost linearly with the degree of functionalization. As the degree of functionalization provides us with a handle on the properties of confined water, it might be interesting to see if we can use carbon nanotubes as a prototype for studying complex biological system like aquaporins.

Author details

Devashree Atre[1] and Shashank Pant[2]*

*Address all correspondence to: pant5@illinois.edu

1 Civil and Environmental Engineering, University of Illinois, Urbana-Champaign, IL, USA

2 Center for Biophysics and Quantitative Biology, University of Illinois, Urbana-Champaign, IL, USA

References

[1] Wang X, Li Q, Xie J, Jin Z, Wang J, Li Y, Jiang K, Fan S. Fabrication of ultralong and electrically uniform single-walled carbon nanotubes on clean substrates. Nano Letters. 2009;**9**(9):3137-3141

[2] Legendary Swords' Sharpness, Strength From Nanotubes, Study Says

[3] Gullapalli S, Wong MS. Nanotechnology: A guide to nano-objects. Chemical Engineering Progress. 2011;**107**(5):28-32

[4] Stankovich S, et al. Synthesis of graphene-based nanosheets via chemical reduction of exfoliated graphite oxide. Carbon. 2007;**45**(7):1558-1565

[5] Gorantla S, et al. In situ observations of fullerene fusion and ejection in carbon nanotubes. Nanoscale. 2017;**2**(10)

[6] Nasibulin AG, et al. A novel hybrid carbon material. Nature Nanotechnology. 2007;**2**(3): 156-161

[7] Nasibulin AG, et al. Investigation of nanobud formation. Chemical Physics Letters. 2007;**446**:109-114

[8] Research and Markets: Opportunities for Nanomaterials in Sporting Applications – 2008-2013: Trend, Forecast and Competitive Analysis

[9] Patel V. Elastomeric Nanocomposites: Tyres spur Nanofillers market growth. Nanotech Insights. 2012;**3**(4):44-48

[10] Baughman RH. Carbon nanotubes — The route towards applications. Science. 2002;**297**: 787-792

[11] Heinze S, et al. Carbon nanotubes as Schottky barrier transistors. Physical Review Letters. 2002;**89**:106801

[12] Thess A, et al. Crystalline ropes of metallic carbon nanotubes. Science. 1996;**273**:483-487

[13] Zhuang L, et al. Carbon nanotubes in biology and medicine: In intro and in vivo detection, imaging and drug delivery. Nano Research. 2009;**2**(2):85-120

[14] Bianco A, et al. Applications of carbon nanotubes in drug delivery. Current Opinion in Chemical Biology. 2005;**9**(6):674-679

[15] Bhirde AA, et al. Targeted killing of cancer cells in vivo and in vitro with EGF-directed carbon nanotube-based drug delivery. Nano Letters. 2009;**3**(2):307-316

[16] Meng L, et al. Single walled carbon nanotubes as drug delivery vehicles: Targeting doxorubicin to tumors. Biomaterials. 2012;**33**:1689-1698

[17] Fisher JW, et al. Photothermal response of human and murine cancer cells to multiwalled carbon nanotubes after laser irradiation. Cancer Research. 2010;**70**:9855-9864

[18] Liu XW, et al. Optimization of surface chemistry on single-walled carbon nanotubes for in vivo photothermal ablation of tumors. Biomaterials. 2011;**32**:144-151

[19] Belyanskaya L, et al. The reliability and limits of the MTT reduction assay for carbon nanotubes-cell interaction. Carbon. 2007;**45**:2643-2648

[20] Bakaji O, et al. Nanofluidic carbon nanotube membranes: Applications for water purification and desalination. In: Savage et al, editors. Willian Andrew Inc. New York: Elsevier; 2009. p. 77-93

[21] Corry B. Designing carbon nanotube membranes for efficient water desalination. The Journal of Physical Chemistry. B. 2008;**112**(5):1427-1434

[22] Corry B. Water and ion transport through functionalised carbon nanotubes: Implicationsfor desalination technology. Energy & Environmental Science. 2011;**4**(3):751-759

[23] Chan WF, et al. Zwitterion functionalized carbon nanotube/ polyamide nanocomposite membranes for water desalination. ACS Nano. 2013;**7**(6):5308-5319

[24] Dai K, et al. NaCl adsorption in multi-walled carbon nanotube/active carbon combination electrode. Chemical Engineering Science. 2006;**61**(2):428-433

[25] Elimelech M, Phillip WA. The future of seawater desalination: Energy, technology, and the environment. Science. 2011;**333**(6043):712-717

[26] Fritzmann C, Löwenberg J, Wintgens T, Melin T. State-of-the-art of reverse osmosis desalination. Desalination. 2007;**216**(1):1-76

[27] Fornasiero F, et al. Ion inclusion by sub-2 nm carbon nanotube pores. Proceedings of the National Academy of Sciences; **105**:17250-17252

[28] Chen J, et al. Solution properties of single-walled carbon nanotubes. Science. 1998;**282**:95-98

[29] Michelson ET, et al. Fluorination of single-wall carbon nanotubes. Chemical Physics Letters. 1998;**296**:188-194

[30] Chen J, et al. Dissolution of full-length single-walled carbon nanotubes. The Journal of Physical Chemistry. B. 2001;**105**:2525-2528

[31] Riggs JE, Guo Z, Carroll DL, Sun Y-P. Strong luminescence of solubilized carbon nanotubes. Journal of the American Chemical Society. 2000;**122**:5879-5880

[32] Riggs JE, Walker DB, Carroll DL, Sun YP. Optical limiting properties of suspended and solubilized carbon nanotubes. The Journal of Physical Chemistry. B. 2000;**104**:7071-7076

[33] Jin Z, Sun X, Xu G, Goh SH, Ji W. Nonlinear optical properties of some polymer/multi-walled carbon nanotube composites. Chemical Physics Letters. 2000;**318**:505-510

[34] Sun Y-P, Huang W, Lin Y, Fu K, Kitaygorodskiy A, Riddle LA, YJ Y, Carroll DL. Soluble dendron-functionalized carbon nanotubes: Preparation, characterization, and properties. Chemistry of Materials. 2001;**13**:2864-2869

[35] Bahr JL, Tour JM. Highly functionalized carbon nanotubes using in situ generated diazonium compounds. Chemistry of Materials. 2001;**13**:3823-3824

[36] Pant S, et al. Effect of attractive interactions on the water-like anomalies of a core-softened model potential. The Journal of Chemical Physics. 2013;**139**:244505

[37] Franks F. Water. A Comprehensive Treatise. New York: Plenum; 1973

[38] Ludwig R. Water: From clusters to the bulk. Angewandte Chemie, International Edition. 2001;**40**:1808-1827

[39] Kell GS, Density, thermal expansivity, and compressibility of liquid water from 0.deg. to 150.deg. Corrections and tables for atmospheric pressure and saturation reviewed and expressed on 1968 temperature scale. J. Chem. Eng. Data, 1975;**20**(1):97-105

[40] Netz PA, Starr FW, Barbosa MC, Stanley HE. Static and dynamic properties of stretched water. The Journal of Chemical Physics. 2001;**115**(1):344-348

[41] de Oliveira AB, Franzese G, Netz PA, Barbosa MC. Waterlike hierarchy of anomalies in a continuous spherical shoulder potential. The Journal of Chemical Physics. 2008;**128**(6): 064901

[42] Pant S, et al. How attractive interaction changes water-like anomalies of a core-softened model potential. AIP Conference Proceedings. 2014;**1591**(1):210-212

[43] Ummer G, et al. Water conduction through the hydrophobic channel of a carbon nanotube. Nature. 2001;**414**:188

[44] Koga K, et al. Formation of ordered ice nanotubes inside carbon nanotubes. Nature. 2001;**412**:802-805

[45] Pant S. Breakdown of 1D water wires inside charged carbon nanotubes. Chemical Physics Letters. 2016;**664**:159-166

[46] Pant S, Ghorai PK. Structural anomaly of core-softened fluid confined in single walled carbon nanotube: A molecular dynamics simulation investigation. Molecular Physics. 2016;**114**(11):1771-1777

[47] Choudhury N. On manifestation of hydrophobicity at nanoscale. The Journal of Physical Chemistry. B. 2008;**112**(20):6296-6300

[48] Pantawane S, Choudhury N. Solvation of fullerenes in coarse- grained water: A molecular dynamics study. AIP Conference Proceedings. 2015;**1665**:040024

[49] Patel AJ, Varily P, Chandler D. Fluctuation of water near hydrophobic and hydrophilic surfaces. The Journal of Physical Chemistry. B. 2010;**114**(4):1632-1637

[50] Choudhury N, Pettitt BM. On the mechanism of hydrophobic association. Journal of the American Chemical Society. 2005;**127**(10):3556-3567

[51] Choudhury N, Pettitt BM. The dewetting transition and the hydrophobic effect. Journal of the American Chemical Society. 2007;**129**(15):4847-4852

[52] Choudhury N, Pettitt BM. Enthalpy-entropy contributions to the potential of mean force of nanoscopic hydrophobic solutes. The Journal of Physical Chemistry. B. 2006;**110**(16): 8459-8463

[53] Tajkhorshid E, et al. Control of the selectivity of the aquaporin water channel family by global orientational tuning. Science. 2002;**296**(5567):525-530

[54] Mittal J, Hummer G. Static and dynamic correlations in water at hydrophobic interfaces. Proceedings of the National Academy of Sciences. 2008;**105**(51):20130-20135

Section 3

State-of-the-Art Nanocomposites

Chapter 8

Highly Anisotropic Polymer Composites Based on Carbon Nanotubes

Geoffrey R. Mitchell, Fred J. Davis,
Saeed Mohan and Meruyert Nazhipkyzy

Additional information is available at the end of the chapter

http://dx.doi.org/10.5772/intechopen.71533

Abstract

Properties of polymers can be optimized through processing methods or by the addition of nanofillers. Carbon nanotubes (CNTs) have gained attention due to their promising behavior. Carbon nanotubes are essentially a sheet of graphene wrapped into a cylindrical shape with either a single or multiple walls. Tube diameters are approximately nanometres, but they can be micrometres in length. Due to the unique properties of nanotubes, they offer promise in composite materials with current research dedicated to embedding them in a polymer matrix. If improvements are to be made , the nanotubes need to be in an aligned configuration. This presents challenges due to the strong intermolecular forces that cause nanotube agglomeration leading to poor quality dispersion and random CNT orientations. Thus, there are two particular challenges to the formation of polymer composites based on CNTs: dispersion and alignment, and these are the focus of this chapter. We consider recent developments in the synthesis of carbon nanotubes and their properties. Next, we detail the challenges of dispersion and alignment that are presented in the preparation of polymer/CNT composites. Finally, we review the literature to identify progress made in preparing high performance polymer/CNT composites and their properties and present one particular solution.

Keywords: composites, alignment, polymer, carbon nanotube

1. Introduction

The properties of polymer-based materials can be substantially modified and enhanced through the inclusion of filler particles. Carbon nanotubes (CNTs) exhibit high flexibility, low mass density and high values of the aspect ratio in excess of 1000. Some types of carbon nanotubes can exhibit metallic or semi-conducting behaviour and coupled to the high

tensile strength and modulus; this combination is ideally suited to their use in composites. The first polymer nanocomposites using CNTs were reported in the 1990s [1] and since then there has been worldwide activity on the methodology to optimise the preparation of such nanocomposites to fully deliver on their promise. Major problems that have been encountered are aggregation of the carbon nanotubes, thereby limiting the full dispersion of the nanoparticles in the polymer matrix, which has a deleterious impact on the properties. Equally the image of a stiff rod embedded in a polymer matrix is far from the reality, and hence carbon nanotubes are often coiled within the polymer matrix and the lack of macroscopic alignment of the tubes severely limits their properties. A wide variety of approaches have been explored including in-situ polymerisation of the matrix, functionalisation of the carbon nanotubes and the use of electric fields to align the carbon nanotubes. This chapter reviews these challenges of dispersion and alignment in the light of recent work both by the authors and that reported in the literature. We identify an approach most likely to succeed.

2. Synthesis-property relationships for carbon nanotubes

The ideal carbon nanotube is a nanoscaled graphene (one leaf of graphite) that is rolled up into a cylindrical shape; structures containing only one wall of cylinder are called single walled carbon nanotubes (SWCNTs), whereas structures with two or more concentric graphene cylinders are termed multi-walled carbon nanotubes (MWCNTs) [2].

Since their discovery in 1991 by Iijima [3], carbon nanotubes have been the subject of a worldwide attention because of their unique properties and associated wide range of applications [4–15]. Over the past two decades, nanotubes have found applications in various areas, such as sources of field emissions, photodetectors, non-volatile memory, ultra-sensitive chemical and transparent conducting membranes, biosensing devices, double layer-type capacitors, transparent electrode films, radio wave absorbents and even in modern electronics.

The most common and widely used nanotube synthesis techniques are arc discharge, chemical vapour deposition and laser ablation [16–21]. CNTs were first produced by arc discharge process or by laser ablation methods; however, recently there has been a significant increase in the synthesis of CNTs by catalytic chemical vapour deposition (CCVD). The catalytic CVD method is an easy and cheap way to produce CNTs at low temperatures and pressures. Compared to the other methods, catalytic CVD provides a higher yield and higher purity of the grown nanotubes and allows control of the parameters of the growth and structure of CNTs.

Hydrocarbons obtained from fossil fuels and the hydrocarbons from plants are the two main sources of carbon for the synthesis of CNTs. There are natural precursors and products containing carboniferous materials. Common fossil fuel CNT precursors are methane, ethylene, acetylene, benzene, xylene and carbon monoxide. There are several reports on the use of natural precursors for synthesis of CNT, such as camphor, turpentine oil, palm oil, etc. Nanoparticles of transition metals (Fe, Ni and Co) are usually used for the catalytic growth of

CNT [22]. Recently, CNT has also been produced from precious novel metal [23–27], catalysts based on ceramic nanoparticles [28, 29] and semiconductor nanostructures [30–33]. This work has led to a new interpretation of the role of the catalyst in growth of nanotubes in which sites of adsorption of carbon are necessary for fixing the nanodimensional curvature. For the growth of CNTs, the formation of nanocrystals of metallic catalysts via CCVD as well as the formation of non-conducting substrates on the surface is necessary. Typical substrates include aluminium oxide, silicon and magnesium oxide. Nevertheless, in spite of the advantages of the CVD method, still there are many problems connected with the growth of high-density CNTs with high purity. Even though many years have passed since the initial discovery of CNTs, it remains challenging to synthesise good quality and high length CNTs because of the many factors that influence the growth process.

There are various ways to use other CVD methods, such as water-assisted CVD [34, 35], oxygen-assisted CVD [36], hot filament CVD [37, 38], microwave plasma CVD [39] or radiofrequency CVD [40]. It is known that the catalysed decomposition of hydrocarbons form carbon fibres as fibrous carbon has been received by a cyanogen transmission on the heated porcelain in 1890 [41]. In 1980, Endo [42] developed the floating catalytic reactor with the use of particles of the catalyst with a diameter of 10 nanometres. This method is a predecessor of the production of CNT widely used today involving an aerosol [43–49] where pyrolysis of hydrocarbons takes place in the presence of a catalyst (Fe, Ni, Co, etc.) generating both MWCNTs and SWCNTs. Key parameters of the growth of CNTs using CVD are the atmosphere, a carbon source, the catalyst and temperature of growth. Low temperatures (300–800°C) lead to the formation of MWCNTs, whereas reaction at high temperatures (600–1150°C) promotes the growth of SWCNTs [50, 51].

The choice of catalyst and catalyst support are very important aspects which affect CNT expansion. Therefore, the preparation stage represents a decisive step in synthesis of CNTs. The influence of the structure and the morphology of the nanoparticles of the catalyst on the growth of CNTs by means of CVD are summarised in the review of Szabo et al. [52]. Flahaut et al. have reported the influence of the conditions of preparation of the catalyst for synthesis of CNTs by means of CCVD using as fuel, urea or citric acid. They have found that the more moderate conditions of burning achieved in the case of citric acid limit the formation of carbon nanofibres or increase the selectivity of the synthesis of CCVD towards CNT with a lower number of walls depending on the catalytic composition.

In order to solve these problems and to improve the main characteristics of CNTs, many miscellaneous fabrication approaches for carbon nanotubes have been considered. For example, Xiang et al. prepared CNT through CCVD using acetylene with a series of catalysts prepared from two-layer double Co/Fe/Al (LDHs) hydroxides. They have noted that the Co content in precursors exerted a noticeable impact on the growth of CNTs. An increase in Co content led to the formation of CNTs with smaller diameters and lower structural frustration [53].

Lyu et al. produced high-quality and high-purity double-walled carbon nanotubes (DWCNTs) by catalytic decomposition of benzene and Fe-Mo/Al_2O_3 as the catalyst at 900°C. They observed DWNT bunches without any amorphous carbon and a low level of defects [54].

Zhang et al. produced MWCNTs with a diameter of 40–60 nanometres by catalytic decomposition of methane at 680°C within 120 minutes together with the use of binary aerogels with nickel oxide as the catalyst [55, 56]. Sano and his colleagues have identified two systems of metal catalyst/source of carbon for growth of CNTs: Ethanol/Co and benzene/Fe. In addition, they investigated two different reactors (the reactor with a gas stream and a liquid reactor) on quality of CNT [57].

Jiang et al. investigated growth of CNT in situ on previously processed graphite electrode (GE) through CCVD with the use of Ni $(NO_3)_2$ as the catalyst [58]. The CNTs prepared with this method had external and internal diameters of 80 and 20, respectively. The length of the CNTs was observed as 200–1000 nanometres; this was attributed to the shorter time of growth. These authors were interested in the concentration of carboxyl and hydroxyl groups on the surface of carbon nanotubes as they are essential features for applications in many fields of science, such as nanomedicine, biosensors or polymeric nanocomposites [58].

A promising one-step method of fabricating carbon nanotubes is flame synthesis. It involves the direct combustion of hydrocarbons in the presence of an oxidiser. The CNTs are normally grown directly on an alloy substrate. The use of metal-organics such as iron pentacarbonyl, ferrocene or metal nitrate dissolved in fuel has been reported. To date, CNTs have only been reported to grow on alloy substrates.

Synthesis using a flame is a very energy efficient process because the fuel is a source of both heat and carbon. The temperatures can reach 1600 K, which is difficult to achieve by means of CVD in a typical furnace. For the synthesis of CNTs over a large area, it is more economic to use a rastering system and a repeated flame for the control of both time and the area of a flame [59]. The higher production efficiency and a lower energy consumption compared to CVD make this method suitable for industrial production. Synthesis using a flame represents a simple single-step method without the need of a substrate. The mechanism of the growth of CNTs in the synthesis of a flame of hydrocarbons can be divided into three main stages. In the first stage of this, hydrocarbon fuel pyrolysis in a previously heated zone results in the formation of hydrocarbon particles which will be a carbon source for CNTs; in second, particles of metal are formed on the surface of the alloy and in final stage, hydrocarbons are absorbed by the catalyst resulting in the growth of CNTs.

Institute of Combustion Problems (ICP), conducts research work on "Synthesis of carbon nanomaterials in flames." We include here one example of report which has been performed in ICP. In this work, oil deposit soot, prepared when burning a propane-butane mixture with the use of electric field, has been chosen among various types of natural materials for preparing porous carbon material (PCM). The PCM is used as the catalyst carrier. We have prepared multiwalled nanotubes (MWNT). We are searching for new methods of creation of catalytic systems (catalyst/carrier), which allow for the control of the structure of carbon particles. This is an important problem, the solution to which can lead to the development of approaches to the synthesis of carbon nanotubes (CNT) with specific functional properties [60]. In addition, ICP has developed a new approach for CNTs synthesis from diatomite. In this work [61], multiwalled nanotubes were obtained using a chemical vapour deposition

method with diatomaceous earth as the substrate and nickel salt as a catalyst. In fact, the catalytic activity of Co and Ni is supported on diatomite and its role in the production of multiwalled carbon nanotubes has been investigated. In this specific example, the diatomite support was prepared by an impregnation method and the CNTs were synthesised on the surface of this as a substrate.

Diatomaceous earth, known as a diatomite, is a soft, powdery, porous and silica-rich mineral, which is found in fossilised deposits near dried up bodies of water. This mineral is the skeletal remains and the result of the accumulation of dead diatoms is found in marine sediments. Diatoms are microscopic single-celled algae that usually have shells that are divided into two halves. The shells of diatoms are hard due to the presence of silica in their cell walls. These silica-rich hard shells are usually found crushed up into tiny, sharp shards, which is the main characteristic of fossilised diatomite. Thanks to having properties, such as low density, high porosity, high surface area, abrasiveness, insulating properties, inertness, absorptive capacity, brightness and high silica content, diatomite has a wide variety of uses, and it is a component in many products. Many different methods of obtaining nanotubes from a variety of materials have been proposed up to this time, but to our knowledge, few have used diatomite.

Figure 1 shows spectra for samples obtained on diatomite at temperatures of 650 and 700°C, peak G is located at 1605 cm^{-1}.

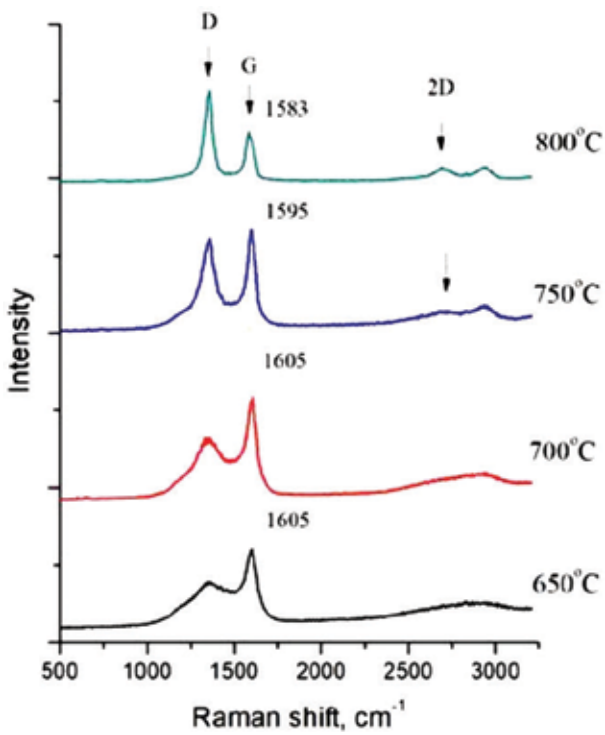

Figure 1. Raman spectra of CNT samples on a diatomite.

The peaks D and G have a large width, which is characteristic of amorphous carbon. There is no clearly expressed second-order peak. These parameters, together with the analysis of SEM images, suggest that at these temperatures, the formation of CNTs on the diatomite does not occur or is weakly expressed [62].

When the synthesis temperature is raised to 750 and 800°C, the width of the peaks is significantly reduced, the position of the main peak G is shifted to the low-frequency region and in the case of 800°C is 1583 cm^{-1}, which is a characteristic value for CNT, graphite and graphene.

There is a manifestation of the 2D peak, which indicates an increase in the degree of crystallinity of the structure and an increase in long-range order and, consequently, an improvement in the quality of CNTs [63].

The peak D arises as a result of defects in graphite structures, and the intensity ratio of the peaks D and G is usually considered an indicator of the quality of CNTs. In the case of CNT synthesised on diatomite, we observe an increase in the intensity of the defect peak with an increase in temperature. This is because an increase in the synthesis temperature makes it possible to reduce the volume of amorphous carbon, but increases the probability of oxidation and the formation of structural defects. In addition, at high synthesis temperatures, nanotubes with a large diameter predominate, which increase the probability of forming knots and strong bends and are manifested in an increase in the D peak intensity in the Raman spectrum.

3. The challenge with polymer nanocomposites: dispersion, alignment and compatibility

To achieve the maximum advantage of carbon nanotubes, they need to be well dispersed, that is not form aggregates. Dispersion is a spatial property. Good dispersion requires the average number density of individual carbon nanotubes to be uniform through the object. Of course, one challenge in this respect is the experimental method requires high magnification and large spatial coverage as highlighted by Li et al. [64], both demanding requirements, moreover there are no standards or commonly accepted procedures to follow although transmission electron micrographs is generally accepted as the gold standard [64].

Achieving good dispersion is experimentally challenging and there is a considerable body of literature on the problem; the reviews of Xie et al. [65], Spitalsky et al. [66], Gkourmpis [67] and Huang and Terentjev [68] cover the key areas. There are many routes to solve basically the same problem. If we start with the situation of traditional thermoplastic polymer, then the basic requirements have been identified and further some simulation of the process achieved [69].

CNTs made by CVD techniques are usually entangled and the first stage of dispersion is to break up these aggregates. Sonication and high shear flow with a high molecular weight

polymer melt are often chosen. However, such treatments may lead to damage or breaking the CNTs into smaller units. These may be advantageous for dispersion but it may at the same time increase the threshold concentration for percolation as the aspect ratio of the tube is lowered. It is common to add surfactants as used in electrospinning of polyethylene oxide with CNTs [70] or to functionalise the CNTs to increase compatibility with the polymer matrix without destroying the electronic properties of the CNTs [71]. Huang and Terentjev [72] studied in detail the use of sonication and melt mixing to disperse CNTs in polymers and they found a critical mixing time, although they indicate that they could not exclude the possibility of small tube clusters persisting after this time.

An alternative approach to that described above is to avoid the problems with the polymer by mixing with a monomer and after mixing carry out the polymerisation process. This is the only route for preparing thermosets containing CNTs, but has also been used to prepare systems with intrinsically conductive polymers such as polyaniline, for example the work of Cochet et al. [73]. Of course, a suitable solvent can be used to generate a uniform dispersion of the CNTs in the solvent and then introduce the polymer. This has been successfully used by a number of authors but of course the removal of the solvent becomes the challenge especially in the industrial production of objects.

A good dispersion of the CNTs is the first step to realise the full potential of CNT-based polymer composites. The second parallel requirement is to fully utilise the anisotropic properties of the CNTs by preparing a common alignment for the CNTs, the alignment depending on the application of the product. A variety of methods have been explored and these have been reviewed by Goh et al. [74], and it is fair to say that many are particularly suited to electronic and other thin film applications. **Figure 2** shows schematically the methodologies for producing a common alignment of CNTs. The introduction of preferred alignment into a polymeric system is usually achieved during processing, for example with fibre spinning [75]. In the case of injection, moulding or other processing, the flow of the polymer melt can be used to induce alignment, and of course in principle, CNTs are straightforward to align due to the high aspect ratio. Zhou et al. [76] have used dissipative particle dynamics to simulate these processes. They find that increasing the volume fraction and the length of CNTs leads to a significant increase in the alignment of the CNTs. The challenge is that the alignment follows the flow in the mould and it requires careful design to achieve the required alignment pattern.

Typically, the CNTs will align parallel to the flow direction, and hence an alignment in a sheet which is normal to the sheet plane is more or less impossible to achieve. The generation of alignment raises the question whether it is possible to prepare patterns of alignment. A number of reports have addressed this area. Goldberg-Oppenheimer et al. [78] used electrohydrodynamic patterning to produce defined patterns on a micrometre scale with the alignment of CNTs within those patterns. Dai has reviewed the use of pyrolytic procedures for large scale production of oriented and micropatterned carbon nanotube arrays normal to a substrate surface which can be transferred onto various substrates of particular interest in either a patterned or non-patterned fashion [79]. The perpendicularly aligned structure is particularly advantageous for surface functionalisation.

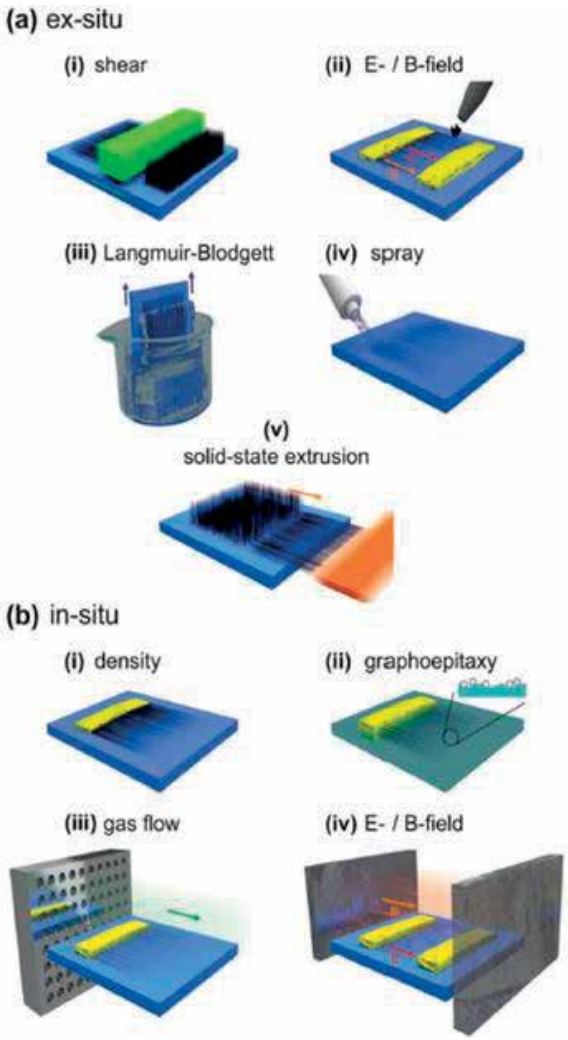

Figure 2. Methodologies for producing a common alignment of CNTs (a) ex situ and (b) in situ (reproduced from Matthew et al. [77], published by The Royal Society of Chemistry).

Alternative methodologies involved the application of electric or magnetic fields. Arguin et al. [80] have used electric fields of 40 kV/m, which can lead to the alignment of MWCNTs in an epoxy resin system. Gupta et al. [81] employed electric field and current-assisted alignment of CNTs in a polyvinylidene fluoride matrix. A promising methodology [82], which is discussed in more detail in Section 5, involves the use of an intermediate state specifically electrospinning. Electrospinning is an old technology which has seen resurgence in the last 10 years. Electrospinning enables the production of nanoscale and microscale fibres from a charged melt of solution [83]. The methodology is to encapsulate the CNTs in polymer nanofibres and deposit this in the sample with a common alignment [70, 82, 84, 85]. The electrospinning process naturally aligns the CNTs within the polymer fibre.

http://dx.doi.org/10.5772/intechopen.71533

4. Some selected recent examples of polymer/CNT composites

Interest in polymer/CNT composites has been particularly inspired by the success of carbon fibre reinforced composites, and as with these, more developed advanced materials with improved mechanical properties are an attractive benefit, but these are potentially combined with advantages of nanocomposites such as a large interfacial area per volume [86]. A review by Coleman et al. neatly sums up the mechanical advantages and point out there is an order of magnitude improvement over carbon nanofibres in terms of modulus [87]. These authors describe the crucial importance of even dispersion; aggregation (for example at high loading) results in a decrease in mechanical properties. Alignment in contrast improves mechanical strength but is less crucial and results in highly anisotropic properties which might be a disadvantage in bulk samples. That being said, in fibres, alignment is easy to achieve and anisotropic properties are unlikely to be a problem. Interestingly, recently Guzman de Villoria et al. have shown that CNTs [88] can be successfully used to bind together weak interfacial layer of reinforced laminate materials; they describe these reinforcing components as nanostitches. Micron diameter pinning techniques reduce some of the advantageous mechanical properties of the composite; in this case, a carbon fibre epoxy prepreg is arranged in layers. Thus, in addition to providing the advantages of highly anisotropic orientation, CNTs can be used to overcome the difficulties associated with this highly directional mechanical behaviour.

Thostenson and Chou [89] examined the benefits of aligned nanofillers on mechanical properties by preparing composites composed of randomly orientated and aligned CNTs in a polystyrene matrix. Samples were prepared at a loading of 5 wt% CNT in the polystyrene matrix. Films of the polystyrene/CNT composite were prepared from solution casting while sonicating. Once dry, the material was heated to 155° C in a microscale compounder with mixing performed at a screw speed of 100 rpm for 3 minutes. The molten material was extruded through a rectangular die and drawn down and passed over a chill roller to solidify, resulting in film thicknesses between 80 and 120 μm depending on the draw ratio. Samples of drawn and non-drawn polystyrene material were also prepared to differentiate between any potential impact on the properties arising from alignment of the polymer chains or the CNT nanofillers. The films produced showed good dispersion due to the mixing process in the compounder and the drawing of the material resulted in an overall alignment of the tubes about a common axis. The sample that had aligned CNTs within the matrix possessed a ~50% improvement to the storage modulus as compared to the bulk material, whereas the sample with randomly orientated CNT filler particles only exhibited a 10% increase. In addition to this, the sample containing the orientated filler showed improvements to the yield and ultimate strengths of the material along the common axis of alignment of the nanotubes, suggesting a load transfer between the polystyrene matrix and the MWCNTs.

Many studies of CNT composites focus on the mechanical advantages but their inclusion of these materials may also benefit the thermal, optical and electrical properties of the nanocomposite material. In a recent review [90], Liu and Kumar have collated the properties of a number of composites. It is clear that both thermal and electrical conductivity depend substantially on the alignment of the CNTs but it does seem that this can vary from one composite

to another. For example, a polypropylene/polyethylene/CNT composite has been found to exhibit a dramatic decrease in conductivity when drawn; in contrast, electrical conductivity of a PVA/SWNT composite showed a fourfold increase when stretched. This is a consequence of the relationship between the electrical conductivity and the percolation network; this network is likely to be distorted by drawing and the consequential change in properties will depend largely upon the loading and dispersion of the CNTs in the original sample.

Dai et al. [91] examined quasi-straight SWCNTs dispersed in a polymethyl methacrylate (PMMA) matrix material. Samples were prepared from solution by taking the SWCNT powder and dispersing it in dimethylformamide (DMF) followed by dissolution of PMMA. Sonication was used for 1 hour before dissolving the PMMA and for another hour after once the PMMA was fully dissolved in order to aid in the nanotube dispersion. The suspension was then air-dried in a fume cupboard until semi-dry, then subjected to a draw ratio of 50 along one direction, folded over and the process was repeated 100 times. The samples were then compressed under 10 MPa at 200°C for 5 minutes with a hydraulic press, transferred to a mould and allowed to dry and cool overnight in a fumehood at 20°C. The drawing method resulted in highly orientated nanotubes within the PMMA matrix. Samples of up to 10 wt% of nanotube loadings were prepared. Strips were cut and heated to 120, 5°C above the polymers glass transition, then a weight applied to act as the deforming force. Mechanical improvements were measured with increases to the draw ratio of the material with increase in loading of the filler particle; however, this was limited to the direction of the tubes long axis alignment. Perpendicular to the common alignment of the tubes long axis, the material exhibited worse draw ratios (weaker mechanical properties), similar to that observed with the SWCNT-epoxy resin composites looked at by Wang et al. [92]. The induced aligned arrays of SWCNTs in the PMMA matrix with the electrical conductivity significantly improved along the draw direction as compared to the perpendicular direction. Electrical conduction of the polymer/CNT nancomposite is possible through the development of an interconnecting CNT network structure within the polymer matrix. Tube contact is a necessary for the transport of electrons across the material, with adequate dispersion of the tubes and a sufficient quantity of CNT within the matrix material being required to make the material conducting throughout. The electrical conductivity of carbon nanotubes displays anisotropic properties, with electron transport more favourable along the tubes axis [93]. Due to this anisotropy in the electrical properties of the CNTs, any composite materials prepared would benefit from alignment of the tubes along a common axis as was demonstrated in this particular study. Dai et al. also measured improved thermal stability of the material with higher loading percentage of the nanofiller, increasing the maximum mass loss temperature of the material compared to pure PMMA alone [91].

Similar electrical and mechanical improvements to a matrix material along the tube orientation direction have been observed by Wang et al. who prepared composite samples of epoxy resin/SWCNTs [92]. The orientation of the SWCNTs was induced through manual stretching of semi-dried composite films with a draw ratio of 50, followed by folding of the sample and repeating the process 100 times. This drawing process resulted in a high degree of orientation of the CNT filler particles. Samples containing different weight percentage

loadings of the filler were prepared and observations on the conductivity and mechanical properties were made. It was observed that the conductivity was significantly better along the direction of common alignment of the tube axis. In this study, composite films that did not undergo stretching were also prepared for comparison purposes. The results showed that the alignment resulted in higher conductivity levels along the stretching direction, for example the 3 wt% loading of SWCNT that had undergone the stretching process had a conductivity of ~1 × 10^{-6} S/cm along the stretching direction (2.8 × 10^{-9} S/cm perpendicular), whereas the unstretched sample had a conductivity of 5 × 10^{-8} S/cm. The addition of 3 wt% of the SWCNTs to the epoxy resin improved the Young's modulus by ~2% and the tensile strength by ~2.6% with respect to the CNTs common axis of alignment; however, at loadings greater than 6 wt%, it was observed that the mechanical properties perpendicular to the tube orientation were lower than the epoxy resin on its own, possibly related to flocculation of the SWCNTs. When compared to the composite samples that had not undergone the stretching procedure, the samples with the aligned filler showed superior mechanical properties along the stretching direction when comparing the values of the Young's modulus and tensile strength to the unstretched samples, however perpendicular to the stretching direction the mechanical properties are not as good as the unstretched samples.

Exposure to an electric field has shown to provide an effective method for the alignment of the carbon nanotubes. Martin et al. have examined the use of both AC and DC fields to aid in the alignment of carbon nanotubes [94]. Low concentrations of CVD-grown MWCNTs were dispersed in an epoxy resin based on bisphenol-A. In the field, it was observed that a fraction of the nanotubes move towards the anode during the epoxy drying stage. These align with the tubes long axis perpendicular to the anode. The tubes themselves then act as a very high field strength at its tip attracting more tubes which form a connecting network between the anode and cathode. The AC field provided a more uniform connecting pathway between the anode and the cathode. Both fields exhibited a concentration of tubes highest at the anode.

Measurements made by Gupta et al. [81] on the electrical conductivity of polyvinylidene fluoride (PVDF), MWCNT composite materials exhibited improved electrical conductivity with improved alignment of the MWCNT filler particles. Five films of the composite materials were prepared with a solution cast method. During casting, two samples were exposed to an alternating voltage at 220 V and 500 V, whereas two others were exposed to alternating pulsed currents from a 220 V and 500 V source. The fifth sample was not exposed to any field resulting in a film that possessed a randomly orientated filler. It was observed that both the alternating voltage and alternating pulsed currents resulted in alignment of the nanotubes within the matrix (with the exception of the sample prepared with an alternating voltage at 220 V). However, differences between the two alignment techniques were observed; the sample exposed to an alternating pulsed current developed conducting channels across the matrix material, where the CNTs joined up in an end-to-end fashion. Meanwhile the films exposed to the alternating voltage resulted in alignment of the CNTs along a common axis, while maintaining their uniform dispersion throughout the matrix. The alternating pulsed current method provided the necessary channels of CNTs for conduction across the matrix, where measurements of the conductivity show a 360% improvement to the electrical conductivity as compared to the sample possessing randomly orientated

CNTs. It was observed that for the sample prepared at 500 V with an alternating pulsed current, the film only exhibited 60% increase in conductivity compared to a randomly orientated sample. Observations of this film during its preparation showed electrical sparking and therefore higher temperatures in areas causing a partial melting and distortion of the film, explaining the drop in conductivity of the film prepared at 500 V compared to the one at 220 V. The conductivity of the nanocomposites was observed to be significantly higher in the direction of the tube alignment compared to perpendicular to the alignment, as would be expected given the anisotropic electrical properties of the CNT filler particles and the channels formed in the material. In addition to the electrical properties, the mechanical properties of the films were measured and showed significant improvements to the Young's modulus and the ultimate tensile strength (180% and 150% respectively) compared to the pure PVDF. However, only slight improvements were measured (26% to the Young's modulus and 30% to the ultimate tensile strength) for the samples possessing the aligned CNT filler when measured along the CNT alignment direction as compared to the samples containing the randomly orientated CNT filler.

More recent developments in alignment of carbon nanotubes involve encapsulation into a narrow fibre using techniques such as electrospinning. Nazhipkyzy et al. have examined [70, 82] electrospun fibres as a potential medium for the encapsulation and alignment of carbon nanotubes. Polyethylene oxide fibres were electrospun from aqueous solution containing different concentrations of nanotubes. To aid in the spinning process, a surfactant, Triton X-100, was added to the solution that greatly aided in the spinning process. Fibres were spun onto a rotating collector that resulted in aligned arrays of parallel fibres. The fibre diameters varied from 100 to 400 nm and TEM images revealed encapsulation of the tubes with the alignment of the CNTS along the electrospun fibres long axis [82].

5. The way forward

The earlier parts of this chapter have identified the critical need for good dispersion and control of alignment of the CNTs. In Section 3, we identified a number of possible routes to achieving a high level of common alignment. However, many of the approaches reviewed were most suited for application with thin films. The authors have recently reported a methodology for preparing CNT-based composites using additive manufacturing technology, and we review this approach here as it underlines the challenges in preparing highly anisotropic CNT-based composites for bulk samples (**Figure 3**).

There has been a huge surge of research in the area of additive manufacturing (AM) over the last few years. The methods used in AM range from thermal extrusion, where a polymer is melted, extruded and deposited in a layer by layer process; granular processing, through melting powder layers using, for example, a laser, and photopolymerisation, where selective areas of a liquid, photocurable polymer are exposed to electromagnetic radiation to induce polymerisation and solidification [71]. Through the use of computer-aided design (CAD), the additive manufacturing technique allows for the manufacturing of complex shaped parts. The methodology which we believe [70, 82] is the best way forward involves

http://dx.doi.org/10.5772/intechopen.71533

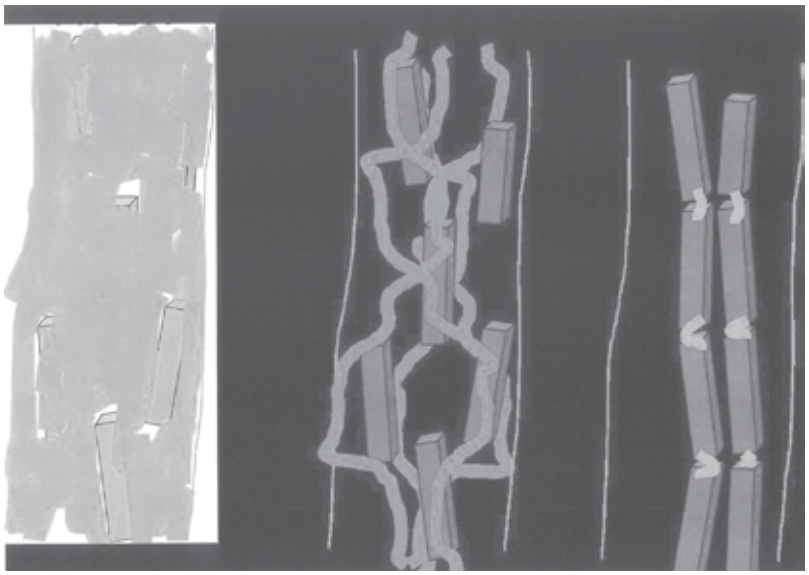

Figure 3. Methodologies for creating fibres from nanoparticles (dark grey). (a) Particles aligned with fibre axis and stabilised in this arrangement by a solid polymer matrix (light grey); (b) particles aligned with fibre axis and stabilised in this arrangement by cross-linking chains which link the particles together; (c) particles aligned with fibre axis and joined end-to-end by short cross-linking chains, which link particles together (reproduced with permission from Mohan et al. [82]).

the encapsulation of the CNTs within a fibrillar structure, where the process of drawing out and enclosing into a narrow diameter fibre can result in the nanoparticles alignment. We use the electrospinning technique to achieve this. During the spinning process, the jet undergoes a shearing force and a narrowing in which the nanoparticulates can be aligned and encapsulated within the fibre as it forms. These fibres themselves have the potential to be used in composite materials to provide mechanical reinforcement; for example, Shinde et al. were able to incorporate electrospun fibres into a resin to improve interlaminar shear stresses of glass fibre composites [95].

The use of layer by layer technology selected by Mohan et al. [82] makes it straightforward to organise the deposition of electrospun fibres, followed by an embedding layer of photocurable resin. The process is completed by photocuring using both UV-visible and IR light [71]. The cycle is then repeated multiple times until the thickness of the object is achieved. Since each layer is deposited sequentially, it is possible to prepare composites with 0 and 90 degree alignment of fibres to prevent defibrillation as might take place in the single orientation case. The use of a low molar mass resin which is then cross-linked means that the resin can flow and wet all fibre surfaces. In the work reported by Mohan et al. [70], the electrospun mean fibre diameter was 360 nm. As the cross-linkable resin is deposited at room temperature, it means that the polymer encapsulation of the CNTs is unaffected by the resin and the spatial distribution remains intact. Thus, this multistep process overcomes both challenges of dispersion and alignment.

6. Summary

In this chapter, we show that CNTs offer some exceptional properties for the design of multi-scale composite materials. In terms of production in bulk, the technology is not quite routine, but clearly promise exists. We have laid out an approach, which we have shown, overcomes the challenges of both dispersion and alignment and deserves wider application.

There are great opportunities for the inclusion of CNTs in the emerging technology of additive or direct digital manufacturing. The future is especially promising in this area.

Acknowledgements

The research work was funded by the Fundação para a Ciencia e a Technologia (Portugal), through the Project reference UID/Multi/04,044/2013 and by the National Agency of Innovation (ANI) (Portugal) through project i.FILM – Multifunctional Films for Intelligent and Active Applications Project Number: 17921.

Author details

Geoffrey R. Mitchell[1]*, Fred J. Davis[2], Saeed Mohan[2] and Meruyert Nazhipkyzy[3]

*Address all correspondence to: geoffrey.mitchell@ipleiria.pt

1 Centre for Rapid and Sustainable Product Development, Institute Polytechnic of Leiria, Rua de Portugal, Marinha Grande, Portugal

2 Department of Chemistry, University of Reading, Whiteknights, UK

3 Institute of Combustion Problems, Almaty, Kazakhstan

References

[1] Ajayan PM, Stephan O, Colliex C, Trauth D. Science. Aligned carbon nanotube arrays formed by cutting a polymer resin-nanotube composite. 1994;**265**:1212-1214

[2] Sinha S, Barjami S, Iannacchione G, Schwab A, Muench G. Off-axis Thermal Properties of Carbon Nanotube Films. Journal of Nanoparticle Research. 2005;**7**:651-657

[3] Iijima S. Nature. Helical microtubules of graphitic carbon. 1991;**354**:56-58

[4] Hong S, Myung S. A flexible approach to mobility. Nanotube Electronics: Nature Nanotechnology. 2007;**2**:207-208

[5] Zeng Y et al. Enhanced adsorption of malachite green onto carbon nanotube/polyaniline composites. Journal of Applied Polymer Science. 2013;**127**:2475-2482

[6] Shao D et al. Polyaniline Multiwalled Carbon Nanotube Magnetic Composite Prepared by Plasma-Induced Graft Technique and Its Application for Removal of Aniline and Phenol. Journal of Physical Chemistry C. 2010;**114**:21524-21530

[7] Ravindran S, Chaudhary S, Colburn B, Ozkan M, Ozkan CS. Covalent Coupling of Quantum Dots to Multiwalled Carbon Nanotubes for Electronic Device Applications. Nano Letters. 2003;**3**:447-453

[8] Novak JP et al. Nerve agent detection using networks of single-walled carbon nanotubes. Applied Physics Letters. 2003;**83**:4026

[9] Niyogi S et al. Chemistry of Single-Walled Carbon Nanotubes. Accounts of Chemical Research. 2002;**35**:1105-1113

[10] Li J et al. Carbon Nanotube Sensors for Gas and Organic Vapor Detection. Nano Letters. 2003;**3**:929-933

[11] Kardimi K et al. Synthesis and characterization of carbon nanotubes decorated with Pt and PtRu nanoparticles and assessment of their electrocatalytic performance. International Journal of Hydrogen Energy. 2012;**37**:1243-1253

[12] Bryning MB et al. Carbon Nanotube Aerogels. Advanced Materials. 2007;**19**:661-664

[13] Bekyarova E et al. Chemically Functionalized Single-Walled Carbon Nanotubes as Ammonia Sensors. The Journal of Physical Chemistry B. 2004;**108**:19717-19720

[14] Saini P. In: Saini P, editor. Fundamentals of Conjugated Polymer Blends, Copolymers and Composites. New Jersey, USA: John Wiley & Sons, Inc.; 2015. p. 449-518. DOI: http://doi.wiley.com/10.1002/9781119137160.ch9

[15] Saini P. In: Mittal V, editor. Thermoset Nanocomposites. Wiley-VCH Verlag GmbH & Co. KGaA; 2013. p. 211-237. DOI: http://doi.wiley.com/10.1002/9783527659647.ch10

[16] Liu J, Fan S, Dai H. Recent advances in methods of forming carbon nanotubes. MRS Bulletin. 2004;**29**(04):244-250

[17] Arepalli S. Laser ablation process for single-walled carbon nanotube production. Journal for Nanoscience and Nanotechnology. Apr. 2004;**4**(4):317-325

[18] Shanov V, Yun Y, Schulz M. Synthesis and characterization of carbon nanotube materials. Journal of the University of Chemical Technology and Metallurgy. 2006;**41**(4):377-390

[19] Öncel Ç, Yürüm Y. Carbon nanotube synthesis via the catalytic CVD method: a review on the effect of reaction parameters, Fullerenes Nanotubes. Carbon Nanostructure. Jun 2006;**14**(1):17-37

[20] Dai H. Carbon nanotubes: synthesis, integration, and properties. Accounts of Chemical Research. Dec 2002;**35**(12):1035-1044

[21] Kingston CT, Simard B. Recent advances in laser synthesis of single-walled carbon nanotubes. Journal of Nanoscience and Nanotechnology. May 2006;**6**(5):1225-1232

[22] Zhou W, Han Z, Wang J, Zhang Y, Jin Z, Sun Z, Zhang Y, Yan C, Li Y. Copper catalyzing growth of single-walled carbon nanotubes on substrates. Nano Letters. 2006;**6**: 2987-2990

[23] Yuan D, Ding L, Chu H, Feng Y, McNicholas TP, Li J. Horizontally aligned single-walled carbon nanotube on quartz from a large variety of metal catalysts. Nano Letters. 2008;**8**:2576-2579

[24] Lee SY, Yamada M, Miyake M. Carbon. Synthesis of carbon nanotubes over gold nanoparticle supported catalysts. 2005;**43**:2654-2663

[25] Yoshihara N, Ago H, Tsuji M. Growth mechanism of carbon nanotubes over gold-supported catalysts. Japanese Journal of Applied Physics. 2008;**47**:1944-1948

[26] Liu H, Takagi D, Ohno H, Chiashi S, Chokan T, Homma Y. Effect of ambient gas on the catalytic properties of Au in single-walled carbon nanotube growth. Applied Physics Express. 2008;**1**:14001-14005

[27] Steiner SA, Baumann TF, Bayer BC, Blume R, Worsley MA, Moberly Chan WJ, Shaw EL, Schlogl R, Hart AJ, Hofmann S, Wardle BL. Nanoscale zirconia as a non-metallic catalyst for graphitization of carbon and growth of single- and multiwall carbon nanotubes. Journal of the American Chemical Society. 2009;**131**:12144-12154

[28] Li WZ, Wen JG, Ren ZF. Straight carbon nanotube Y junctions. Applied Physics Letters. 2001;**79**:1879-1881

[29] Uchino T, Bourdakos KN, de Groot CH, Ashburn P, Kiziroglou ME, Dilliway G, Smith DCD. Metal catalyst-free low-temperature carbon nanotube growth on SiGe islands. Applied Physics Letters. 2005;**86**:233110-233113

[30] Takagi D, Hibino H, Suzuki S, Kobayashi Y, Homma Y. Carbon nanotube growth from semiconductor nanoparticles. Nano Letters. 2007;**7**:2272-2275

[31] Uchino T, Bourdakos KN, Ayre GN, De Groot CH, Ashburn P, Smith DC. In: Chen L-C, Geohegan DB, Robertson J, Wang ZL, editors. Materials Research Society Symposium Proceedings, Warrendale, PA. Vol. 1081. 2008. p. 1-9

[32] Uchino T, Ayre GN, Smith DC, Hutchison JL, de Groot CH, Ashburn P. Growth of single-walled carbon nanotubes using germanium nano-crystals formed by implantation. Journal of the Electrochemical Society. 2009;**156**:K144-K152

[33] Magrez A, Won J, Rita S, Barbara S, Juan K, Andresen C, Mionić M, Casimirius S, Forró L. Low-temperature, highly efficient growth of carbon nanotubes on functional materials by an oxidative dehydrogenation reaction. Materials. 2010;**3**:4871-4891

[34] Patole P, Alegaonkar PS, Lee HC, Yoo JB. Optimization of water assisted chemical vapor deposition parameters for super growth of carbon nanotubes. Carbon. 2008;**46**:1987-1993

[35] Byon HR, Lim H, Song HJ, Choi HC. A synthesis of high purity singlewalled carbon nanotubes from small diameters of cobalt nanoparticles by using oxygen-assisted

chemical vapor deposition process. Bulletin of the Korean Chemical Society. 2007;**28**: 2056-2060

[36] Prasek J, Drbohlavova J, Chomoucka J, Hubalek J, Jasek O, Adam V, Kizek R. Methods for carbon nanotubes synthesis – review. Journal of Materials Chemistry. 2011; **21**:15872-15884

[37] Varshney D, Weiner BR, Morell G. Growth and field emission study of a monolithic carbon nanotube/diamond composite. Carbon. 2010;**48**:3353-3358

[38] Brown B, Parker CB, Stoner BR, Glass JT. Growth of vertically aligned bamboo-like carbon nanotubes from ammonia/methane precursors using a platinum catalyst. Carbon. 2011;**49**:266-274

[39] Xu Y, Dervishi E, Biris AR, Biris AS. Chirality-enriched semiconducting carbon nanotubes synthesized on high surface area MgO-supported catalyst. Materials Letters. 2011;**65**:1878-1881

[40] Dai H. Carbon nanotubes: opportunities and challenges. Surface Science. 2002;**500**: 218-241

[41] Kumar M, Ando Y. Camphor. A botanical precursor producing garden of carbon nanotubes. Diamond and Related Materials. 2003;**12**:998-1002

[42] Endo M. Grow carbon fibres in the vapour phase. ChemTech. 1988;**18**:568-576

[43] Schützenberger P, Acad LCR. History of carbon nanotubes. Science. 1890;**111**:774-778

[44] Grobert N, Mayne M, Terrones M, Sloan J, Dunin-Borkowski RE. Alloy nanowires: inside carbon nanotubes. Chemical Communications. 2001;(5):471-472

[45] Nasibulin AG, Moisala A, Jiang H, Kauppinen EI. Carbon nanotube synthesis from alcohols by a novel aerosol method. Journal of Nanoparticle Research. 2006;**8**:465-475

[46] Ku BK, Emery MS, Maynard AD, Stolzenburg MR, McMurr PH. In situ structure characterization of airborne carbon nanofibres by tandem mobility? Nanotechnology. 2006;**17**:3613-3621

[47] Pinault M, Pichot V, Khodja H, Launois P, Reynaud C, Hermiteet MM. Nano Letters. 2005;**5**:2394-2398

[48] Mayne M et al. Chemical Physics Letters. 2001;**338**:101-107

[49] Reyes-Reyes M, Grobert M, Kamalakaran N, Seegar R, Golberg T, Ruhle D. Chemical Physics Letters. 2004;**396**:167-173

[50] Kamalakaran R, Lupo F, Grobert N, Lozano-Castello D, Jin-Phillipp NY, Ruhle M. In: In-situ formation of carbon nanotubes in an alumina-nanotube composite by spray pyrolysis. Carbon. 2003;**41**:2737-2741

[51] Braidy N, El Khakani MA, Botton Chem GA. Single-wall carbon nanotubes synthesis by means of UV laser vaporization. Physics Letters. 2002;**354**:88-92

[52] Szabo A, Perri C, Csato A, Giordano G, Vuono D, Nagy JB. Synthesis methods of carbon nanotubes and related materials. Materials. 2010;**3**:3092-3140

[53] Xiang X, Zhang L, Hima HI, Li F, Evans DG. Co-based catalysts from Co/Fe/Al layered double hydroxides for preparation of carbon nanotubes. Applied Clay Science. 2009;**42**:405-409

[54] Lyu SC, Liu BC, Lee CJ, Kang HK, Yang CW, Park CY. High quality double-walled carbon nanotubes produced by catalytic decomposition of benzene. Chemistry of Materials. 2003;**15**(20):3951-3954

[55] Zhang DS, Shi LY, Fang JH, Dai K, Li XK. Preparation and desalination performance of multiwall carbon nanotubes. Materials Chemistry and Physics. 2006;**97**(2-3):415-419

[56] Zhang DS, Shi LY, Fang JH, Li XK, Dai K. Preparation and modification of carbon nanotubes. Materials Letters. 2005;**59**(29-30):4044-4047

[57] Sano N, Ishimaru S, Tamaon H. Synthesis of carbon nanotubes in graphite microchannels in gas-flow and submerged-in-liquid reactors. Materials Chemistry and Physics. 2010;**122**(2-3):474-479

[58] Jiang Q, Song LJ, Yang H, He ZW, Zhao Y. Preparation and characterization on the carbon nanotube chemically modified electrode grown in situ. Electrochemistry Communications. 2008;**10**(3):424-427

[59] Yuan L, Li T, Saito K. Synthesis of multiwalled carbon nanotubes using methane/air diffusion flames. Proceedings of the Combustion Institute. 2002;**29**(1):1087-1092

[60] Nazhipkyzy M, Lesbaev BT, Prikhodko NG, Mansurov ZA, Nemkaeva RR. Raman Spectroscopy of Carbon Nanotubes Obtained on the Basis of Oil Sludge and Soot. Universal Journal of Applied Science. 2015;**3**(2):17-20

[61] Zhalgasbaikyzy A, Zhaparova A, Nurgain A, Nazhipkyzy M, Mansurov ZA. Diatomite: an emerging biomaterial with hierarchical porous structure in nanotechnology and its application in synthesis of multiwalled carbon nanotubes by chemical vapor deposition method. IX International Symposium "Combustion and Plasmochemistry", Almaty, Kazakhstan, 2017. p. 63-67

[62] Nazhipkyzy M, Lesbayev BT, Prikhodko NG, Mansurov ZA, Nemkaeva RR. Raman Spectroscopy of Carbon Nanotubes Obtained on the Basis of Oil Sludge and Soot. USA: Universal Journal of Applied Science. 2015;**3**(2):17-20

[63] Ferrari AC. Raman spectroscopy of graphene and graphite: Disorder, electron–phonon coupling, doping and nonadiabatic effects. Solid State Communications. 2007;**143**:47-57

[64] Li X, Zhang H, Jin J, Huang D, Qi X, Zhang Z, Yu D. Quantifying Dispersion of Nanoparticles in Polymer Nanocomposites Through Transmission Electron Microscopy Micrographs. Journal of Micro and Nano-Manufacturing. 2014;**2**:021008. DOI: 10.1115/1.4027339

[65] Xie X-L, Mai Y-W, Zhou X-P. Materials Science and Engineering: Reviews. 2005;**49**:89-112

[66] Spitalsky Z, Tasis D, Papagelis K, Gaaliotis C. Progress in Polymer Science. 2010;**35**:357-401

[67] Gkourmpis T. Electrically conductive polymer nanocomposites. In: Mitchell GR, Tojeira A, editors. Controlling Controlling the Morphology of Polymers: Multiple Scales of Structure and Processing. Switzerland: Springer: 2016. ISBN: 978-3-319-39320-9

[68] Huang YY, Terentjev EM. Dispersion and rheology of carbon nanotubes in polymers. International Journal of Material Forming. 2008;**1**:63-74

[69] Chinesta F, Ammar A, Mackley M, Cueto E, Regnier G, Chatel S. Modeling nanocomposites: from rheology to forming processes simulation. International Journal of Material Forming. 2009;**2**(Suppl 1):141-144

[70] Nazhipkyzy M, Mohan SD, Davis FJ, Mitchel GR. Carbon nanotubes in electrospun polyethylene oxide nanofibres: A potential route to conducting nanofibres. Journal of Physics: Conference Series; 2015;**246**:012007

[71] Bartolo PJ, Mitchell G. Stereo-thermal-lithography: a new principle for rapid prototyping. Rapid Prototyping Journal. 2003;**9**:150-156

[72] Huang YY, Terentjev EM. Dispersion and rheology of carbon nanotubes in polymers. International Journal of Materials Forming. 2008;**1**:63-74

[73] Cochet M, Maser WK, Benitor A, Callejas A, Martinex MT, Benoit JM, Schriber J, Chauvet O. Synthesis of a new polyaniline/nanotube composite: "in-situ" polymerisation and charge transfer through site-selective interaction. Chemical Communications. 2001:1450

[74] Goh PS, Ismail AF, Ng BC. Directional alignment of carbon nanotubes in polymer matrices: contemporary approaches and future advances. Composites: Part A. 2014;**56**:103-126

[75] White JL, Cakmak M. Orientation development and crystallization in melt spinning of fibers. Advances in Polymer Technology. 1986;**6**:295-337. DOI: 10.1002/adv.1986.060060307

[76] Zhou B, Luo W, Yang J, Duan X, Wen Y, Zhou H, Chen R, Shan B. Simulation of dispersion and alignment of carbon nanotubes in polymer flow using dissipative particle dynamics. Computational Materials Science. 2017;**126**:35-42

[77] Matthew TC, Cientanni V, Milne WI. Horizontal carbon nanotube alignment. Nanoscale. 2016;**8**:15836

[78] Goldberg-Oppenheimer P, Eder D, Steiner U. Advanced Functional Materials. Carbon nanotube alignment via electrohydrodynamic patterning of nanocomposites. 2011;**22**: 1895-1901. ISSN 1616-301X

[79] Huang S, Dai L. Microscopic and Macroscopic Structures of Carbon Nanotubes Produced by Pyrolysis of Iron Phthalocyanine. Journal of Nanoparticle Research. 2002;**4**:145-155

[80] Arguin M, Sirois F, Therriault D. Electric Field induced alignment of multiwalled carabon nanotubes in polymers and multiscale composities. Advanced Manufacturing: Polymers & Composite Science. 2015;**1**:16-25

[81] Gupta P, Rajput M, Singla N, Kumar V, Lahiri D. Electric field and current assisted alignment of CNT inside polymer matrix and its effects on electrical and mechanical properties. Polymer. 2016;**89**:119-127

[82] Mohan SD, Nazhipkyzy M, Carreira P, Santos C, Davis FJ, Mateus A, Mitchell GR. Direct digital manufacturing of nanocomposites. Advanced Materials Research in Press. 2017;**12**:304-310

[83] Mitchell GR, Tojeira A, editors. Electrospinning Royal Society of Chemistry. London; 2015

[84] Rakesh GR, Ranjit GS, Karthikeyan KK, Radhakrishnan P, Biji P. A facile route for controlled alignment of carbon nanotube-reinforced, electrospun nanofibers using slotted collector plates. Polymer Letters. 2015;**9**:105-118

[85] Teo WE, Ramakrishna S. A review on electrospinning design and nanofibre assemblies. Nanotechnology. 2006;**17**:R89-106

[86] Vaia RA, Wagner HD. Framework for nanocomposites. Materials Today. 2004;**7**:32-37

[87] Coleman N, Khan U, Blau WJ, Gun'ko YK. Measuring Nanomaterial Release from Carbon Nanotube Composites: Review of the State of the Science. Carbon. 2006;**44**:1624-1652

[88] Guzman de Villoria R, Hallander P, Ydrefors L, Nordin P, Wardle BL. Aligned Carbon Nanotube Film Enables Thermally Induced State Transformations in Layered Polymeric Materials. Composites Science and Technology. 2016;**133**:33-39

[89] Thostenson ET, Chou T-W. Aligned multi-walled carbon nanotube-reinforced composites: processing and mechanical characterization. Journal of Physics D: Applied Physics. 2002;**35**:L77-L80

[90] Liu Y, Kumar S. Enhancing the heat transfer efficiency in graphene–epoxy nanocomposites using a magnesium oxide–graphene hybrid structure. ACS Applied Materials & Interfaces. 2014;**6**:6069-6087

[91] Dai J, Wang Q, Li W, Wei Z, Xu G. Polymer/Carbon Nanotube Nano Composite Fibers–A Review. Materials Letters. 2007;**61**:27-29

[92] Wang Q, Dai J, Li W, Wei Z, Jiang J. The effects of CNT alignment on electrical conductivity and mechanical properties of SWNT/epoxy nanocomposites. Composites Science and Technology. 2008;**68**:1644-1648

[93] de Heer WA, Bacsa WS, Chatelain A, Gerfin T, Humphrey-Baker R, Forro L, Ugarte D. Aligned Carbon Nanotube Films: Production and Optical and Electronic Properties. Science. 1995;**268**:845-847

[94] Martin CA, Sandler JKW, Windle AH, Schwarz M-K, Bauhofer W, Schulte K, Shaffer MSP. Electric field-induced aligned multi-wall carbon nanotube networks in epoxy composites. Polymer. 2005;**46**:877-886

[95] Shinde DK, Kelkar AD. Effect of TEOS Electrospun Nanofiber Modified Resin on Interlaminar Shear Strength of Glass Fiber/Epoxy Composite. World Academy of Science, Engineering and Technology, International Journal of Chemical, Nuclear, Materials and Metallurgical Engineering. 2014;**8**:54

Chapter 9

Recent Progress on Electrochemical Capacitors Based on Carbon Nanotubes

Emilia Grądzka and Krzysztof Winkler

Additional information is available at the end of the chapter

http://dx.doi.org/10.5772/intechopen.71687

Abstract

This review is focused on the theoretical and practical aspects of electrochemical capacitors based on carbon nanotubes. In particular, recent improvements in the capacitance properties of the systems are discussed. In the first part, the charge storage mechanisms of the electrochemical capacitors are briefly described. The next part of the review is devoted to the capacitance properties of pristine single- and multi-walled carbon nanotubes. The major portion of the review is focused on the capacitance properties of modified carbon nanotubes. The electrochemical properties of nanotubes with boron, nitrogen, and other atoms incorporated into the carbon network structure as well as nanotubes modified with different functional groups are discussed. Special attention is paid to the composites of carbon nanotubes and conducting polymers, transition metal oxides, carbon nanostructures, and carbon gels. In all cases, the influences of different parameters such as porosity, structure of the electroactive layer, conductivity of the layer, nature of the heteroatoms, solvent and supporting electrolyte on the capacitance performance of hybrid materials are discussed. Finally, the capacitance properties of different systems containing carbon nanotubes are compared and summarized.

Keywords: carbon nanotubes, carbon nanoparticles, conducting polymers, composites, electrochemical capacitors, charge storage materials

1. Introduction

The last two decades can be considered a nanotechnology revolution. With each passing day, increasing attention is paid to the discovery of new nanoscale materials due to the miniaturization of devices in many areas. Nanomaterials are everywhere, from cosmetics and clothes to medicine and electronic devices. At the same time, the increased development of electronic devices requiring energy storage systems, such as batteries and supercapacitors, is starting to play a crucial role in everyday life. Supercapacitors, also called electrochemical capacitors, are

energy saving units that can provide a huge amount of energy in a short time. Compared with batteries, electrochemical capacitors offer great advantages of high power capability, high rates of charge and discharge, high cycle life, flexible packaging and low weight [1–4].

An interesting class of nanomaterial for storage devices is carbon nanotubes due to their large open surface that is completely exposed to electrolyte ions, good electrical conductivity, high surface area, mechanical strength, good corrosion resistance, chemical stability and low mass density [4–8]. However, so far, pristine CNTs have not met the commercial requirements for energy storage devices applications due to their poor dispersion in solvents, low electrochemical characteristics in the electrolytes, and low specific capacitance [7, 8]. The capacitance properties of carbon nanotubes may be improved by surface functionalization or by the formation of composites with redox-active systems such as conducting polymers or metal oxides. On the other hand, carbon nanotubes are excellent conducting supports to improve the properties of materials with poor conductivity, stability, and capacitance performance. Hence, carbon nanotubes-based nanocomposites or nanohybrids have recently been intensively developed because of their superior properties compared to the individual component alone. Much research on supercapacitors has aimed at increasing power and energy densities as well as lowering fabrication cost [8–18].

The objective of this review is to highlight theoretical and practical aspects of the capacitance properties of carbon nanotubes and their composites. In particular, recent progress in improving the capacitance properties of systems based on carbon nanotubes is discussed. In the first part, the charge storage mechanisms in electrochemical capacitors are briefly described. The next part of the review is devoted to the capacitance properties of pristine carbon nanotubes and carbon nanotubes modified by heteroatoms or functional groups. Special attention is paid to the composites of carbon nanotubes with conducting polymers, carbon nanostructures, transition metal oxides, and carbon gels.

2. Principles and mechanism of charge storage

Electrochemical energy storage may be classified as encompassing either batteries or electrochemical capacitors (ECs), which are also known as supercapacitors, ultracapacitors, electrical double-layer capacitors, pseudocapacitors, gold capacitors or power coaches [19–21]. Supercapacitors fill the gap between batteries that exhibit high energy density and high power density conventional capacitors, covering several orders of magnitude both in energy and in power density. Batteries compared to supercapacitors store and deliver more energy with slower charge and discharge times. In the case of conventional capacitors, they have very high energy density in comparison to supercapacitors. Supercapacitors also exhibit low heating level, safety, long-term operation stability, low weight, and flexible packaging [4, 22, 23]. Due to these properties of semiconductors, they can be applied in many fields of electrotechnology. They can be used in electric and hybrid vehicles [3, 24, 25], high-energy pulsed lasers [26], mobile phones [26–28], laptops [27], and cameras [27, 28].

The charge-storage mechanism of electrochemical capacitors is controlled by two principal mechanisms: (i) a non-Faradaic electrostatic interaction resulting from ion adsorption at the

electrode/electrolyte interface defined as electric-double layer capacitance (EDLC) (**Figure 1a**) and (ii) an electrochemical oxidation/reduction reaction in electroactive materials accompanied with Faradaic charge transfer named pseudocapacitance (**Figure 1b**) [4, 29–32].

Typical supercapacitors consist of two electrodes separated by a dielectric material or electrolyte solution. In the case of EDLC, where the capacitance comes from the electrostatic charge accumulated at the electrode/electrolyte interface and strongly depends on the surface area of the electrode accessible to the electrolyte ions, mostly porous carbons are used as electrode materials due to their low price, facile synthesis, and sustainability. They are prepared by heat treatment and subsequent chemical activation with organic materials or, in the case of "carbide-derived carbons" (CDCs), by extracting metal atoms in metal carbides. More exotic materials, such as carbon nanotubes (CNTs) and graphene, are also being developed for supercapacitor applications. The operating voltage of supercapacitors depends on the solvent and electrolytes separating both electrodes. Tetraethylammonium tetrafluoroborate is often used as the supporting electrolyte in organic solvents. This salt offers a relatively high operating voltage of approximately 2.5 V and a high ionic conductivity of 20–60 mS cm^{-1}. In aqueous solutions, a maximum potential of 1.2 V can be obtained. Moreover, room-temperature ionic liquids with an operating voltage as high as 4 V could also be used as electrolyte systems. However, supercapacitors based on ionic liquids have poor device power performance due to their low ionic conductivity, i.e., below 20 mS cm^{-1} [23, 30, 33].

The specific capacitance for EDLC is assumed to follow that of a parallel-plate capacitor:

$$C = \frac{\varepsilon_r \varepsilon_0}{dA} \tag{1}$$

where ε_r is the electrolyte dielectric constant, ε_0 is the permittivity of vacuum, A is the specific surface area of the electrode, and d is the effective thickness of the EDLC. Depending on the pore size of the electrode material, two models are proposed: an electric double cylinder capacitor (EDCC) model that describes mesoporous carbon electrodes (**Figure 2a**) and an electric

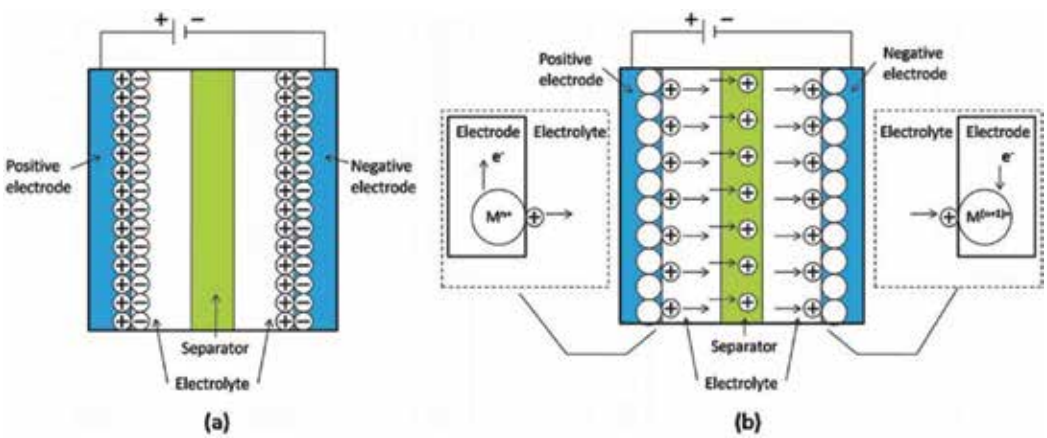

Figure 1. Schematic diagram of supercapacitors: (a) EDLC and (b) pseudocapacitor (M represents the metal atom). Reproduced with permission from Ref. [32]. Copyright 2014 The Royal Society of Chemistry.

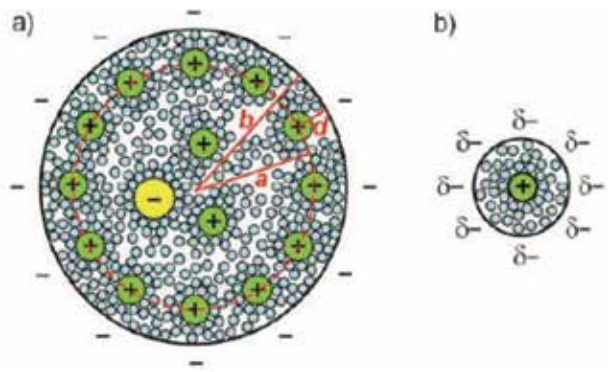

Figure 2. Schematic diagrams (top views) of (a) a negatively charged mesopore with solvated cations approaching the pore wall to form an electric double-cylinder capacitor and (b) a negatively charged micropore of radius b with cations lining up along the pore axis to form an electric wire-in-cylinder capacitor. Reproduced with permission from Ref. [34]. Copyright 2008 Wiley-VCH Verlag.

wire-in-cylinder capacitor (EWCC) model corresponding to microporous carbon electrodes (**Figure 2b**). The equation describing the capacitance in these two models can be written as:

$$C = \frac{\varepsilon_r \varepsilon_0}{b ln\left[\frac{b}{b-d}\right]} A \tag{2}$$

$$C = \frac{\varepsilon_r \varepsilon_0}{b ln\left(\frac{b}{a_0}\right)} A \tag{3}$$

where b is the pore radius, d is the distance of approaching ions to the surface of the carbon electrode, and a_0 is the effective size of counterions. When the pores are large enough and the pore curvature is no longer significant, the EDCC model is reduced to the traditional planar EDLC model described by Eq. (1) [30, 34].

In contrast to EDLC, pseudocapacitance results from faradaic fast reversible redox reactions involving electrode material. During electrochemical reactions, the electrode material is reduced or oxidized and doped with counterions from the electrolyte solution. In this case, conducting polymers and metal oxides or hydroxides as electrode materials are used [30]. High-area carbon electrodes also exhibit a small pseudocapacitance component due to electrochemically active redox functionalities [22]. Pseudocapacitance is described by the following equation:

$$C = \frac{d(\Delta q)}{d(\Delta V)} \tag{4}$$

where Δq is the charge related to the faradaic process in the potential range ΔV. The pseudocapacitance can reach higher values than the EDLC capacitance. However, redox capacitors exhibit lower power density due to poor electrical conductivity and lack of stability during the cycle.

The maximum energy stored in supercapacitors is given by

$$E = \frac{1}{2} C V^2 \tag{5}$$

where C is the capacitance and V is the operating voltage limited by the thermodynamic stability of the electrolyte solution. The total power of a supercapacitor is described by the following equation:

$$P = \frac{V^2}{4R} \tag{6}$$

where R is the internal resistance of the capacitor coming from the various types of resistances associated with the intrinsic electronic properties of the electrode material and electrolyte solution, mass transfer resistance of the ions in the electrode material, and contact resistance between the current collector and the electrode [22, 23, 30, 31].

The electrode is one of the most important components for charge storage and plays a crucial role in determining the energy and power density of supercapacitors [29]. In EDLC, the high surface area resulting from the highly microporous structure of carbon electrode materials such as carbon aerogels, carbon black or carbon cloth is unfavorable for electrolyte wetting and rapid ionic motions, especially at high current loads [22]. The most frequently used activated carbon electrodes exhibit low electrolyte accessibility and poor electrical conductivity. These two effects are responsible for limited energy density and high internal resistance. For this reason, carbon nanotubes (CNTs) with nanoscale size, controllable size distribution, large surface area, high mesoporosity, electrolyte accessibility, and good electrical properties are very promising candidates for replacing carbon materials as the electrode materials in high-performance capacitors. Because of this fact, an extended part of this work will focus on supercapacitors based on carbon nanotubes [4, 29].

3. Capacitance properties of single- and multi-walled carbon nanotubes

Carbon nanotubes exhibit large open surface area, excellent mechanical strength, chemical stability, low mass density, and relatively good electrical conductivity. All these properties make them a very good candidate for the electroactive material in charge storage devices. In these capacitors, the ions of electrolyte are adsorbed on the charged surface of carbon nanotubes, producing a Helmholtz layer. The capacitance properties of these systems depend on the number of graphene walls (single-, double-, or multi-wall), the nature of the electrode material, the composition of the electrolyte solution, and the structure of the carbon nanotube layer. The specific capacitance of pristine CNTs is relatively low and ranges from 2 to 45 F g^{-1} for SWCNTs [35–42] and 3 to 80 F g^{-1} for MWCNTs [36–38, 42–44]. The capacitance properties of thin films of CNTs are collected in **Table 1**.

Such a large scattering of reported specific capacitance values is mainly related to the different procedures of CNT deposition on the conducting electrode surface and, therefore, different structures of CNTs films. Carbon nanotubes can be attached to electrodes by direct growth [45], manual manipulation [46], random spreading [47], deposition in a dc current electric field [48], or gas flow [49]. Specially designed substrates are used for film formation of vertically oriented CNTs [50–53]. Two of the most common orientations of CNTs are displayed schematically in **Figure 3**. In general, films of vertically oriented carbon nanotubes exhibit much better

Carbon nanostructure	Specific capacitance (F g^{-1})	Experimental conditions	Reference
SWCNTs	2	0.1 M Na_2SO_4	[39]
	17	1 M NaCl	[40]
	18	1 M NaCl	[35]
	19	5 M KOH	[35]
	20	6 M KOH	[41]
	21	1 M NaCl	[35]
	24	7 M H_2SO_4	[35]
	40	6 M KOH	[38]
	64	1 M H_2SO_4	[42]
MWCNTs	3	7 M KOH	[43]
	9	7 M KOH	[43]
	14	1 M H_2SO_4	[42]
	14	6 M KOH	[38]
	17	4 M H_2SO_4	[43]
	26	4 M H_2SO_4	[43]
	30	1 M H_2SO_4	[44]
	36	6 M KOH	[38]
	38	1 M Na_2SO_4	[44]
	62	6 M KOH	[38]
	78	1 M H_2SO_4	[38]
	80	6 M KOH	[38]

PC, propylene carbonate.

Table 1. Selected values of specific capacitances obtained for thin films of carbon nanotubes.

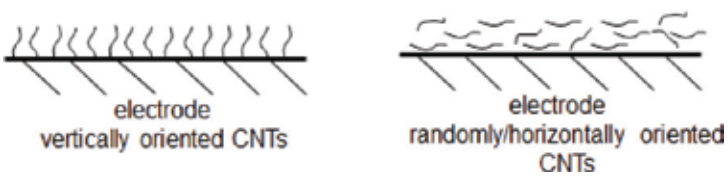

Figure 3. Schematic representation of nanotubes orientation at the electrode surface.

electrical and capacitance properties in comparison to films formed from randomly oriented nanotubes [6, 50, 54–57]. **Figure 4** shows the structure of the SWCNT layer formed under CVD growth procedure. The highest specific capacitance of 52 F g^{-1} and excellent electrochemical stability were reported for such vertical structures of SWCNTs [55].

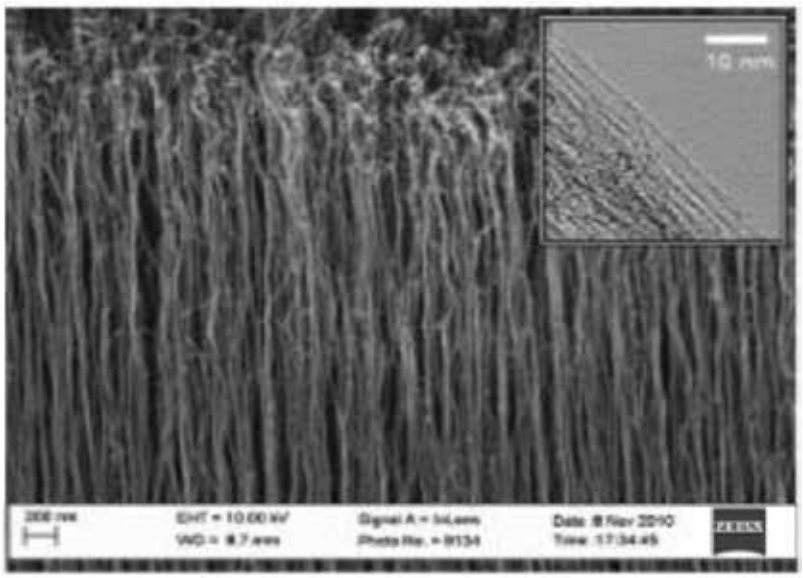

Figure 4. SEM image of the aligned carbon nanotubes formed under CVD procedure. Reproduced with permission from Ref. [6]. Copyright 2011 American Chemical Society.

4. Covalent modification of carbon nanotubes and their capacitance properties

The covalent functionalization of carbon nanotubes provides modification of their physicochemical properties. Insertion of functional groups to the carbon network solves the problem of their poor dispersion capability. Stable dispersions of modified carbon nanotubes are particularly important in the formation of thin films of capacitors or capacitive devices. Moreover, tethering electron-donating or electron-withdrawing groups on CNT surfaces changes their electronic properties by the doping effect [22, 58–62]. Such groups exhibit electrochemical activity resulting in a pseudo-Faradaic capacitance effect.

Park and co-workers showed the relationship between the electrochemical activity of functional groups attached to the CNT surface and their capacitive characteristics [58]. They found that MWCNTs covalently functionalized by carboxylic, sulfonic, and amine groups (**Figure 5**) showed a two- to fourfold increase in capacitance over that of pristine MWCNTs due to pseudocapacitive charging-discharging arising from the presence of functional groups. Functionalized CNTs also form more stable dispersions in deionized water and polar organic solvents. Such dispersions can be used in the formation of mechanically stable and uniform capacitor films. Functionalized CNTs, however, exhibit a lower surface area due to the reduction in the average pore size as a consequence of the presence of surface functional groups [58].

Figure 6 shows the effect of the addition of oxygen redox-active molecules on the electrochemical performance of CNTs. Nanotubular materials can be treated (CNTs-T) chemically [62–70],

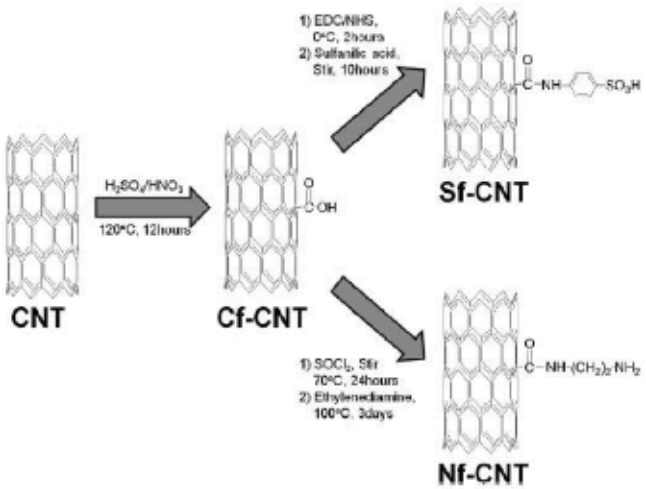

Figure 5. Schematic illustration of the covalent functionalization of CNTs. Reproduced with permission from Ref. [58]. Copyright 2013 The Royal Society of Chemistry.

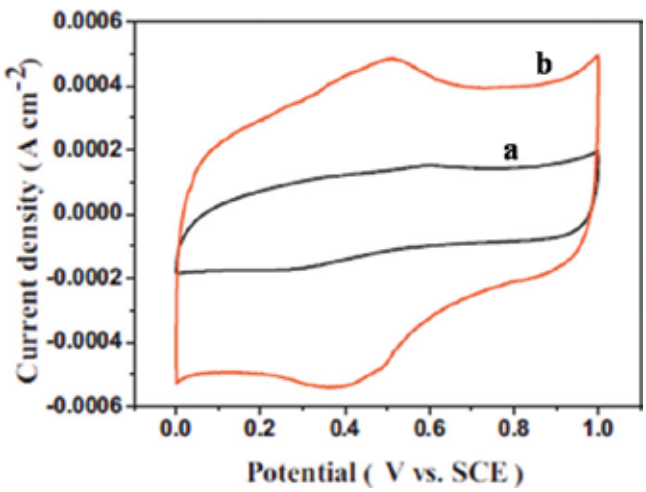

Figure 6. Cyclic voltammograms of (a) raw CNTs and (b) CNTs-T electrodes in 1 M H_2SO_4. Reproduced with permission from Ref. [62]. Copyright 2014 Elsevier.

electrochemically [59, 71, 72], photochemically [73, 74], and using plasma-induced techniques [75, 76]. The chemical modifications are usually performed in concentrated nitric acid or in a mixture of nitric and sulfuric acids. Cyclic voltammograms recorded for raw CNTs exhibit pseudorectangular cathodic and anodic profiles, which are the characteristics of ideal capacitors. In the case of CNTs-T, a pair of voltammetric peaks is observed. They are related to the redox reactions of functional groups on the CNTs-T surface:

$$>C\text{-}OH \rightleftharpoons >C{-}O + H^{+} + e^{-} \quad (7)$$

$$>C{=}O + e^{-} \rightleftharpoons >C\text{-}O^{-} \quad (8)$$

$$\text{-}COOH \rightarrow CO_2 + H^{+} + e^{-} \quad (9)$$

A higher current observed for CNTs-T suggests that their surface area is larger compared to that of raw CNTs. The surface of oxygen-containing functional groups also decreases surface resistivity and enhances surface wettability, offering more accessible sites for the physisorption of electrolyte ions and increasing the ionic conductivity at the electrode/electrolyte interface. In the procedure proposed by Wang and co-workers [62], the specific capacitance was increased from 28 F g^{-1} for raw CNTs to 85 F g^{-1} for CNTs-T in H_2SO_4 solution. Changing the electrolyte to H_2SO_4/hydroquinone mixture provides a drastic improvement of the specific capacitance to 508 and 3199 F g^{-1} for CNTs and CNTs-T, respectively [62].

The distribution and type of oxygen-containing functional groups depend on the type (**Figure 7a**) and concentration (**Figure 7b**) of the oxidizing agent [66, 67].

The oxidation of CNTs is a principle reaction for further functionalization of the carbon network. The combination of CNTs with graphene oxide in a lamellar graphene-CNT structure, r[GO/CNT], shown in **Figure 8** causes an increase in the electrolyte-accessible surface area due to the intercalation of CNTs between the stacked GO sheets with associated large electrochemical active sites, thus improving conductivity through the formation of a 3D network aided by CNTs. Such a covalently linked CNTs-graphene system exhibits capacitance performance much superior than that of other carbon-based electrodes [77].

The high specific capacitance of CNTs could also be obtained with the incorporation of heteroatoms such as N [61, 78–87], B [86–89], P [86, 90], and F [91]. The type of defect created by the heteroatom influences the kind of conduction generated ranging from n-type transport

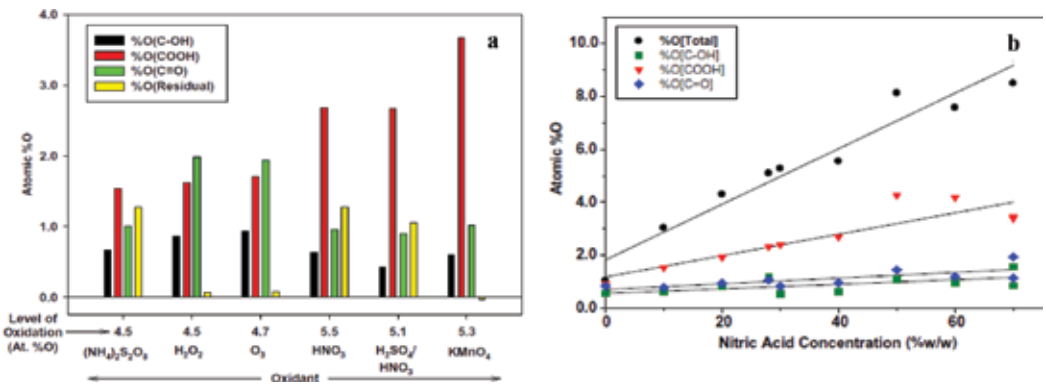

Figure 7. (a) Influence of the oxidant on the distribution of oxygen-containing functional groups, measured on MWCNTs. (b) Influence of % w/w HNO_3 on the level of oxidation, as well as the distribution of oxygen-containing functional groups. Reproduced with permission from Ref. [66]. Copyright 2011 Elsevier.

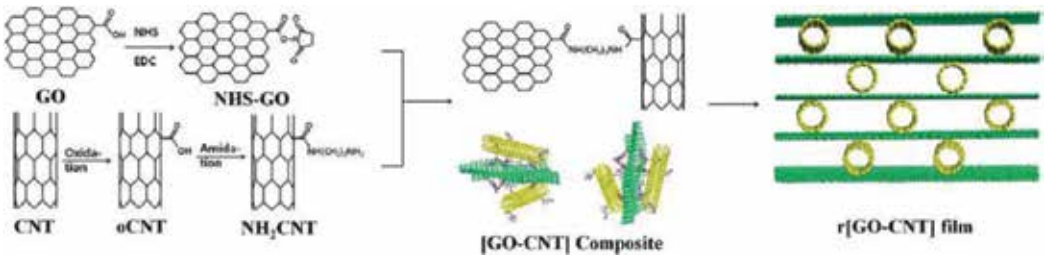

Figure 8. Synthesis scheme depicting the reaction between a GO layer and a CNT and a view of the fabricated r[GO-CNT] film. Reproduced with permission from Ref. [77]. Copyright 2013 Wiley-VCH Verlag.

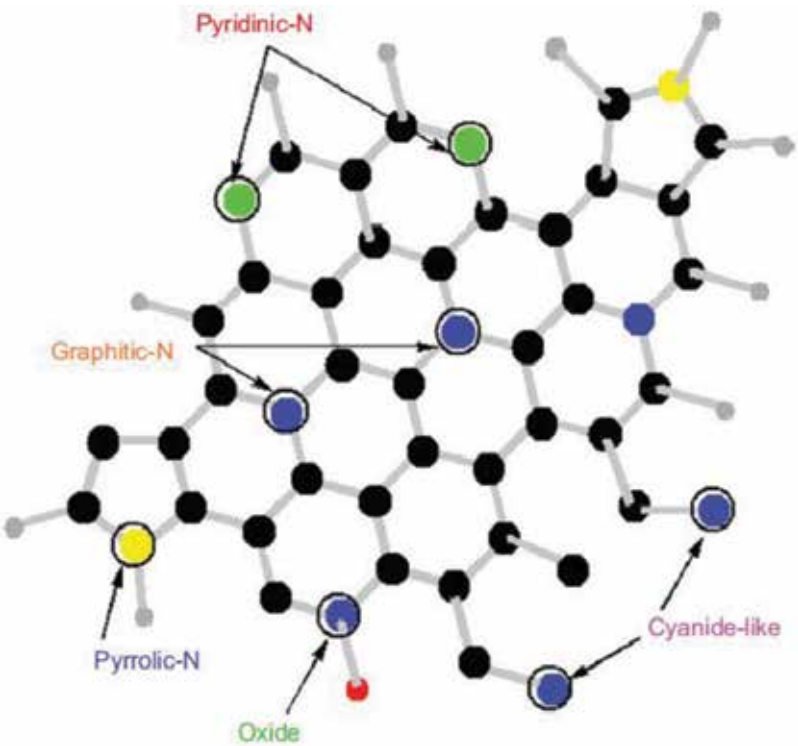

Figure 9. Schematic representation of N doping in the carbon nanomaterial. Reproduced with permission from Ref. [92]. Copyright 2013 De Gruyter.

(N substitution doping) to p-type conduction (B substitution of boron in lattice) [92]. The existence of heteroatoms significantly enhances the specific capacitance values of carbon materials by the pseudocapacitance effect [83, 88]. Gueon and co-workers found that nitrogen-doped carbon nanotubes have a specific capacitance three times higher compared to undoped carbon nanomaterial [79]. Nitrogen-containing pentagons (**Figure 9**) can induce strong bending of the nanotubes and affect the alignment of the CNT lattice, resulting in the creation of donor states near the Fermi level and hence the specific capacitance [79, 80]. The effect of B-doping on the

capacitance can be explained by modification of the space charge layer in carbon. The presence of boron leads to the enhancement of the space-charge layer capacitance through increasing the number of holes as a charge carrier or the DOS change at the Fermi level [88].

Thermal oxidation [88] or acid treatment [81] of doped CNTs improves the specific surface area and, as a consequence, the capacitance due to the tube end opening process. Coaxial supercapacitors based on hollow carbon nanotubes synthesized by chemical vapor deposition (CVD) exhibit high rate capacitance, long cycle life, and good flexibility [93].

The combination of synergetic effects in boron carbonitride nanotubes (BCNs) resulting from the combined co-doping of B and N in CNTs and their well-aligned vertical structure (VA) also provides a significant enhancement of specific capacitance performance. Vertically aligned boron carbonitride nanotubes (VA-BCNs) were synthesized on a Ni-Fe-coated SiO_2/Si substrate using the chemical vapor deposition method with a melamine diborate precursor. In this case, nitrogen atoms are bonded to carbons in both graphitic and pyridinic forms, and the resultant VA-BCNs show high specific capacitance (321 F g^{-1}) with an excellent rate capability and high durability compared to nonaligned BCNs (167 F g^{-1}) and undoped multi-walled carbon nanotubes (117 F g^{-1}) [94].

5. Hybrid materials of carbon nanotubes for energy storage

Carbon nanotubes are combined with carbon nanostructures, conducting polymers or metal oxides to form nanocomposite materials that display favorable electronic and mechanical properties [95]. Composites containing carbon nanotubes and an electroactive phase exhibit pseudocapacitive properties like metal oxide or conducting polymers and represent an important breakthrough for developing a new generation of supercapacitors based on three reasons: (i) the percolation of the electroactive particles is more efficient with nanotubes than with other carbon materials; (ii) the open mesoporous network formed by the entanglement of nanotubes allows ions to diffuse easily to the active surface of the composite components; and (iii) since the nanotubular materials are characterized by a high resiliency, the composite electrodes can easily adapt to the volumetric changes during the charging/discharging process, which improves drastically the cycling performance [22]. However, capacitors fabricated from inorganic pseudocapacitive materials typically suffer from higher internal resistance and lower lifetimes. The combination of carbon nanotubes with other carbon nanostructures results in an enhancement of energy density and lowering of the internal resistance [96].

5.1. Capacitors based on carbon nanotubes and different carbon nanostructures

The continued technological progress has led to the miniaturization of electronic devices with large volumetric energy densities. Most fabricated micro-supercapacitors based on carbon nanostructures exhibit excellent rate capabilities and stability, but low volumetric energy density. In general, increased volumetric energy density is obtained by the application of porous conductive electrode materials with sufficiently high packing density. The most popular electrode material is graphene sheets because of their ultrahigh surface area and excellent

conductivity as well as high mechanical and chemical stability. However, various interesting structures of graphene, such as one-dimensional fibers, two-dimensional films, and three-dimensional foams, in spite of high gravimetric capacitance exhibit poor volumetric performance due to strong intersheet π-π interactions, which, while increasing the packing density, do not allow high ion accessibility. To solve this problem, the synergistic effect of graphene and carbon nanotubes is utilized by the preparation of graphene-carbon nanotubes composites. In most cases, graphene oxide is used due to its hydrophilic character. However, its conductivity is low, and hence, it is doped by carbon nanotubes with very high conductivity [97]. Numerous synthesis methods have been used and a large family of hybrid composites based on graphene oxide and carbon nanotubes with the specific capacitance in the range of 120–222 F g^{-1} depending on the preparation procedure has been discovered [77, 98–104].

Ternary carbon composites containing carbon nanotubes, graphene, and activated carbon exhibit much better capacitance performance. Such systems have specific capacitances several times higher than those of their components (**Figure 10a**). The excellent electrochemical properties of ternary composites can be attributed to the high surface area and low equivalent series resistance, demonstrating that they improve the electrochemical performance for supercapacitor applications [97]. Among the multicomponent composites, a novel type of highly flexible and all-solid state supercapacitor utilizing hybrid aerogels exhibits promising properties (**Figure 10b**) [105].

Recently, much attention has been paid to 3D pillared vertically aligned carbon nanotubes (VACNTs)—graphene architectures with a controllable nanotube length (PL)/intertube distance (MIPD) as electrode materials for energy-related devices (**Figure 11**). Theoretical

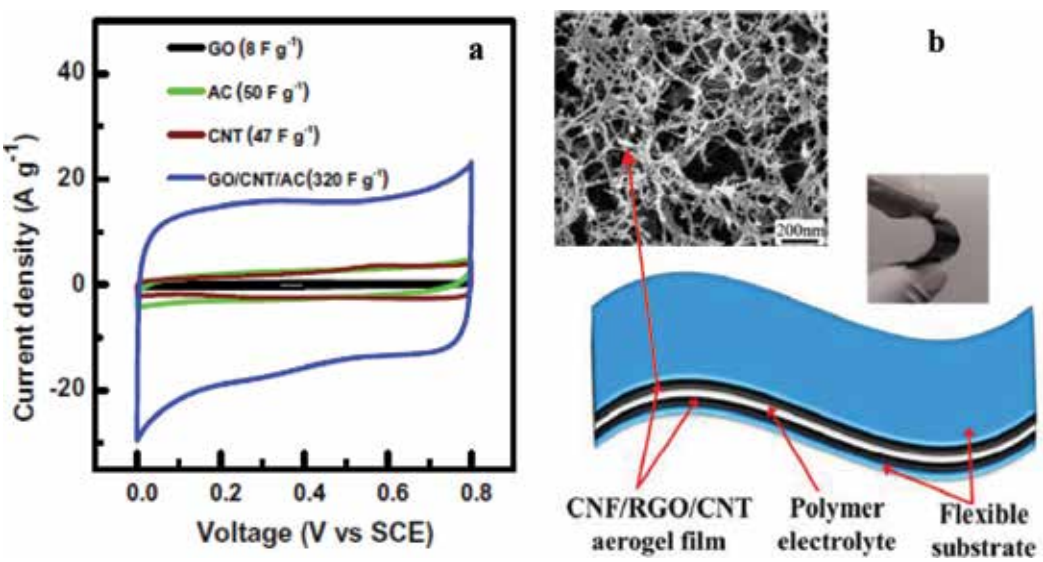

Figure 10. (a) Cyclic voltammograms of different carbon particles (GO, CNT, AC) and their composite recorded in 1 M H_2SO_4. Reproduced with permission from Ref. [97]. Copyright 2017 Elsevier. (b) Schematic diagram of the all-solid-state supercapacitor where the polymer-gel electrolyte serves as the electrolyte and the separator. Insets show the flexibility of the device and SEM image of aerogel hybrid film. Reproduced with permission from Ref. [105]. Copyright 2015 American Chemical Society.

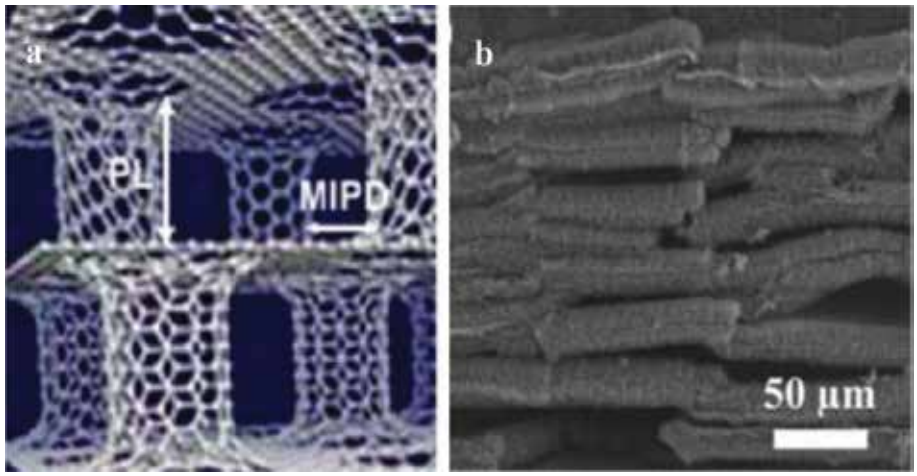

Figure 11. (a) Schematic diagram of a 3D pillared VACNT graphene nanostructure. (b) SEM images of the 3D pillared VACNT graphene architectures. Reproduced with permission from Ref. [102]. Copyright 2011 American Chemical Society.

studies have indicated that 3D pillared architectures, consisting of parallel graphene layers supported by vertically aligned carbon nanotubes (VACNTs) in between, possess desirable out-of-plane transport and mechanical properties while maintaining the excellent properties of their building blocks [102].

An ultrafast compact capacitor based on free-standing, flexible, and highly conducting films consisting of stacked nanoporous graphene layers pillared with single-walled carbon nanotubes (SWCNTs) was obtained by Pham and co-workers [109]. **Figure 12** shows the carbon nanotube (CNT)-bridged graphene 3D building blocks via the Coulombic interaction between positively charged CNTs grafted by cationic surfactants and negatively charged graphene oxide sheets, followed by KOH activation. Such a structure enhances the accessible surface area and allows for fast ion diffusion. Due to this unique 3D porous structure, a remarkable electrochemical performance with a maximum capacitance as high as 199 F g^{-1} was achieved [99].

The electrodeposition of nickel hydroxide on such hybrid nanostructures results in pseudocapacitance due to the Faradaic reaction associated with the $Ni(OH)_2$ coating. The specific capacitance is increased from 110 F g^{-1} obtained for VACNT-graphene architectures to 1384 F g^{-1} for $Ni(OH)_2$-coated VACNT graphene electrode [102].

Pristine carbon nanotubes usually provide unsatisfactory specific capacitance due to their relatively low surface area, which still needs to be enhanced. Composites containing hollow carbon nanospheres anchored to the surface of carbon nanotubes, CNT-HCS, (**Figure 13**) are synthesized via the hard template method following this trend. Disordered pores (~2 nm) observed in the shells of the carbon spheres facilitate the penetration of electrolyte ions and favor the rapid charge propagation during the charge/discharge process [106]. The electrochemical performance of capacitors based on the composites of carbon nanotubes and different carbon nanostructures are collected in **Table 2**.

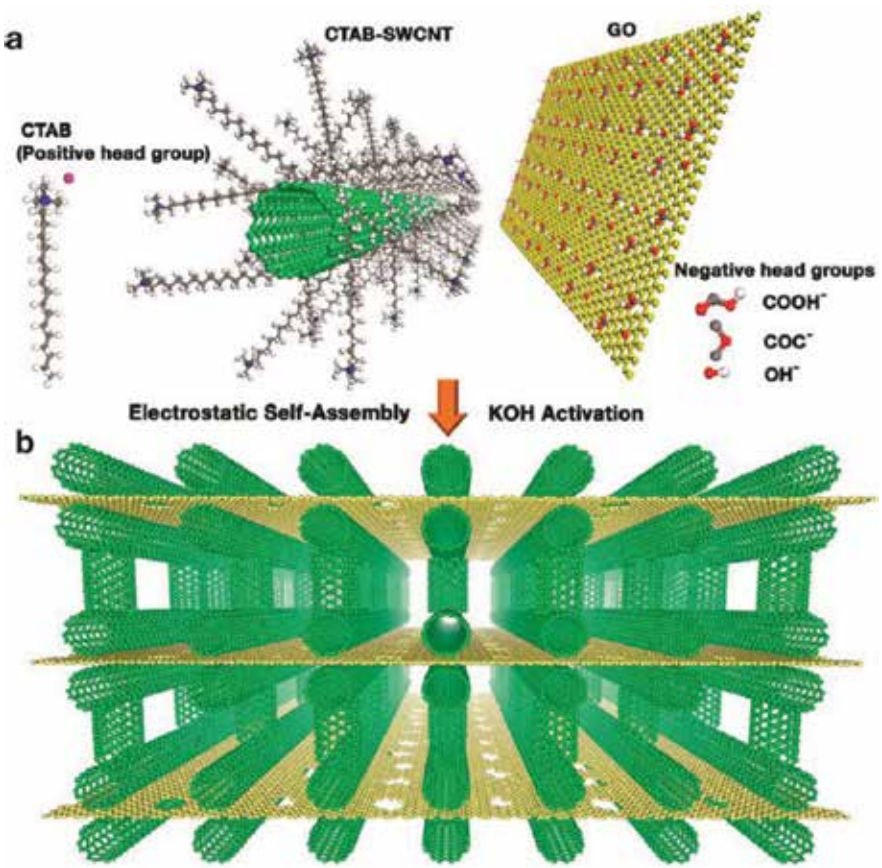

Figure 12. Schematic for fabricating the ac-Gr/SWCNT hybrid nanostructure. (a) The CTAB-grafted SWCNTs are positively charged, and the GO layers are negatively charged due to their functional groups. (b) Schematic of the 3D SWCNT-bridged graphene block. Reproduced with permission from Ref. [99]. Copyright 2015 American Chemical Society.

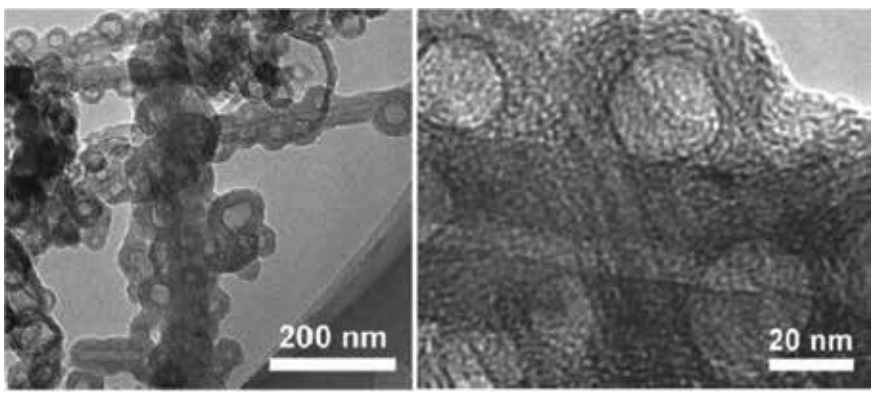

Figure 13. TEM images of CNT-HCS composite with different magnifications. Reproduced with permission from Ref. [106]. Copyright 2013 Elsevier.

Composite	Specific capacitance ($F\ g^{-1}$)	Capacitance	Power density	Energy density	Capacitance retention	Reference
CNF/rGO/CNT	252	216 mF cm^{-2}	9.5 mW cm^{-2}	28.4 mW cm^{-2}	99.5%	[105]
HCS/CNT	201.5	30.1 F cm^{-3}	11.8 kW kg^{-1}	11.3 Wh kg^{-1}	90%	[106]
SWCNT/GO	–	305 F cm^{-3}	1.085 mW cm^{-3}	6.3 mWh cm^{-3}	93%	[98]
SWCNT/GO	199	211 mF cm^{-3}	400 kW kg^{-1}	110.6 Wh kg^{-1}	98.2%	[99]
GO/CNT/AC	636	–	550 W kg^{-1}	16 Wh kg^{-1}	99.8%	[97]
Graphene/CNT	–	3.93 mF cm^{-3}	115 W cm^{-3}	2.42 mWh cm^{-3}	86%	[107]
SWCNT/CNH	43	–	3.50 kW kg^{-1}	6.03 Wh kg^{-1}	–	[96]

CNF, carbon nanofibril; rGO, reduced graphene oxide; HCS, hollow carbon spheres; AC, activated carbon; CNH, carbon nanohorns.

Table 2. Selected values of electrochemical performance of capacitors based on composites of carbon nanotubes and different carbon nanostructures.

5.2. Capacitors based on carbon nanotubes and conducting polymers

Composites of conducting polymers with carbon nanotubes are promising electrode materials as supercapacitors because of their good conductivity, high surface area, and excellent ability to store energy [7, 108–117]. The composites combine the large pseudocapacitance of conducting polymers with the fast charging/discharging double-layer capacitance and excellent mechanical properties of carbon nanotubes [118]. In **Scheme 1**, the properties of carbon nanostructures, conducting polymers, and the composite materials are compared.

CNTs/conducting polymer composites can be prepared by chemical [7, 13, 108, 113, 114, 118–121] or electrochemical [14, 16, 95, 110–112, 115, 118, 119, 121] polymerization. This process can be carried out on pristine CNTs or CNTs modified with functional groups or heteroatoms as a non-covalent deposition polymeric layer onto the nanotubular surface or covalent functionalization of carbon walls by polymeric chains. In the case of covalent functionalization, two approaches can be used: first, when the monomer is attached to CNTs and, in the next step, when it is polymerized via chemical or electrochemical methods [122, 123], and second, in situ chemical polymerization in the presence of dopant and self-organizing agent [7, 124]. For noncovalently modified CNTs with polymers, several strategies have been developed. Currently, they involve physical mixing in solution, in situ polymerization of monomers in the presence of CNTs, surfactant- and template-assisted processing of composites, chemical functionalization of the incorporated nanotubular material, and electrochemical polymerization carried out on an electrode surface modified with carbon nanostructures or electrochemical co-polymerization [118, 125, 126]. In **Figure 14**, exemplary procedures of nanocomposites formation are schematically presented. In most cases, electrochemical synthesis provides homogenous films [16, 118]. However, chemical polymerization generates polymers with a more porous morphology [118, 127].

Figure 15 shows the SEM images of SWCNTs/PPy composites prepared by deposition of PPy on pristine SWCNTs (**Figure 15a**) and on functionalized SWCNTs (**Figure 15b**). In the case of functionalized SWCNTs, an incomplete coverage of SWCNTs by PPy is observed [14].

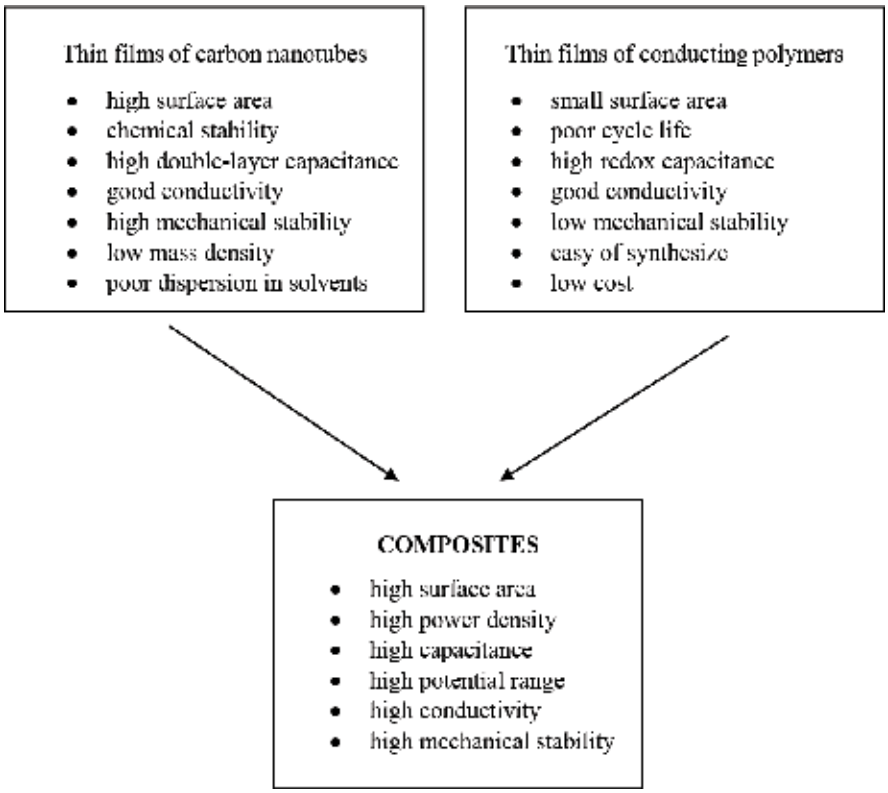

Scheme 1. Properties of carbon nanostructures, conducting polymers and the composite materials.

A comparison of the electrochemical behavior of PPy, SWCNTs/PPy, and PPy/functionalized SWCNTs composites is shown in **Figure 16**. PPy films at a low scan rate exhibits a rectangular shape, which indicates an ideal capacitance behavior, while for higher scan rates, the curves are not rectangle-shaped, which indicates resistance-like electrochemical behavior due to the slow doping/dedoping process of the compact PPy layer. However, a pseudorectangular shape of the recorded cyclic voltammograms in all of the scan rates (up to 200 $mV \cdot s^{-1}$) is observed for the composites based on pristine SWCNTs (**Figure 16b**) and functionalized SWCNTs (**Figure 16c**). The PPy/functionalized SWCNTs composite exhibits also better capacitance properties compared to PPy/SWCNTs and pristine PPy (**Figure 17**).

Another way to form composites based on CNTs and conducting polymers is covalent functionalization of CNTs with monomeric units. In the next step, the composite is obtained by copolymerization of the monomer with monomer units grafted on the CNTs surface using controlled potential electrolysis. **Figure 18a** shows the electrochemical behavior of polypyrrole/CNTs (PPY/CNTs) composites obtained at different charge densities. The broad peaks observed in the voltammograms are related to the redox process within the polypyrrole component. The composites exhibit higher currents than the pure polymeric material due to higher porosity (**Figure 18c**) compared to pristine PPy (**Figure 18b**) and as a consequence of the higher capacitance of PPy/CNTs [122].

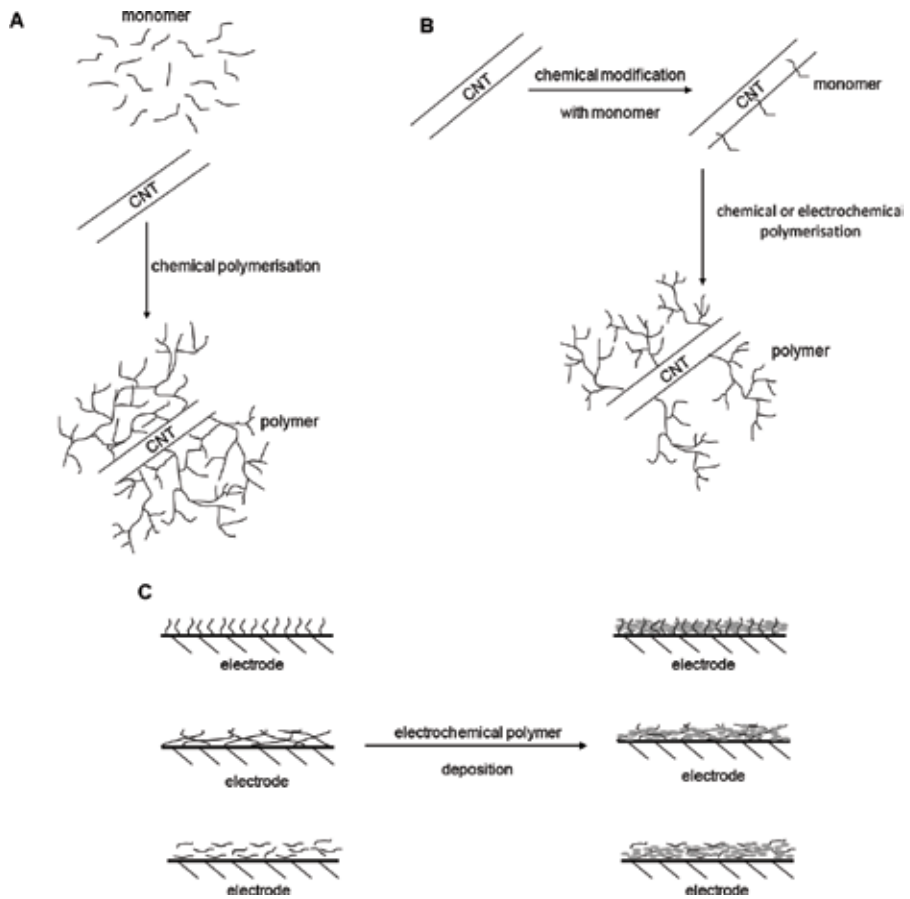

Figure 14. A schematic representation of exemplary procedures of nanocomposites formation for electrochemical measurements. (A) *in situ* chemical polymerization, (B) chemical polymerization of monomers attached to carbon nanostructure, (C) electrochemical polymerization carried out on an electrode surface modified with carbon nanostructures.

The presence of CNT components results in an increase in the practical range of electrical conductivity of the material. For example, C_{60}-Pd polymer demonstrates pseudocapacitance behavior due to faradaic reduction of C_{60} in the negative potential range (**Figure 19a**); at potentials lower than this threshold, the material exhibits very high resistance. In the CNTs/C_{60}Pd composite, the potential range of electrochemical activity increases. At negative potentials, the pseudocapacitive behavior of the polymeric component is still observed. However, the material also shows double-layer capacitance, mainly attributed to the conducting CNTs, in a less negative potential range (**Figure 19b**). Composites based on C_{60}-Pd polymers and SWCNTs or MWCNTs exhibit specific capacitance equal to 994 F g^{-1} or 758 F g^{-1} for SWCNTs/C_{60}-Pd and MWCNTs/C_{60}-Pd composites, respectively [119].

A very promising energy storage behavior was reported for 3D structure composite based on aligned carbon nanotubes (ACNTs) offering a large specific surface area, superior electronic transfer ability through individual nanotubes, and chemical inertness [95]. Three-dimensional

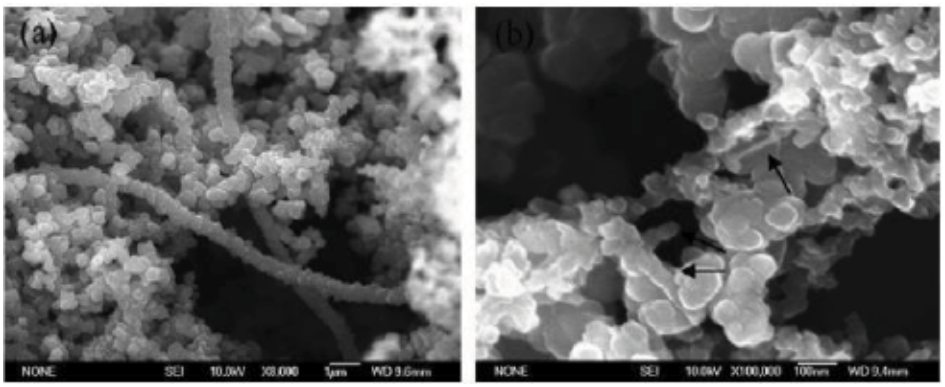

Figure 15. SEM images of (a) SWCNTs/PPy and (b) functionalized SWCNTs/PPy. Reproduced with permission from Ref. [14]. Copyright 2007 Elsevier.

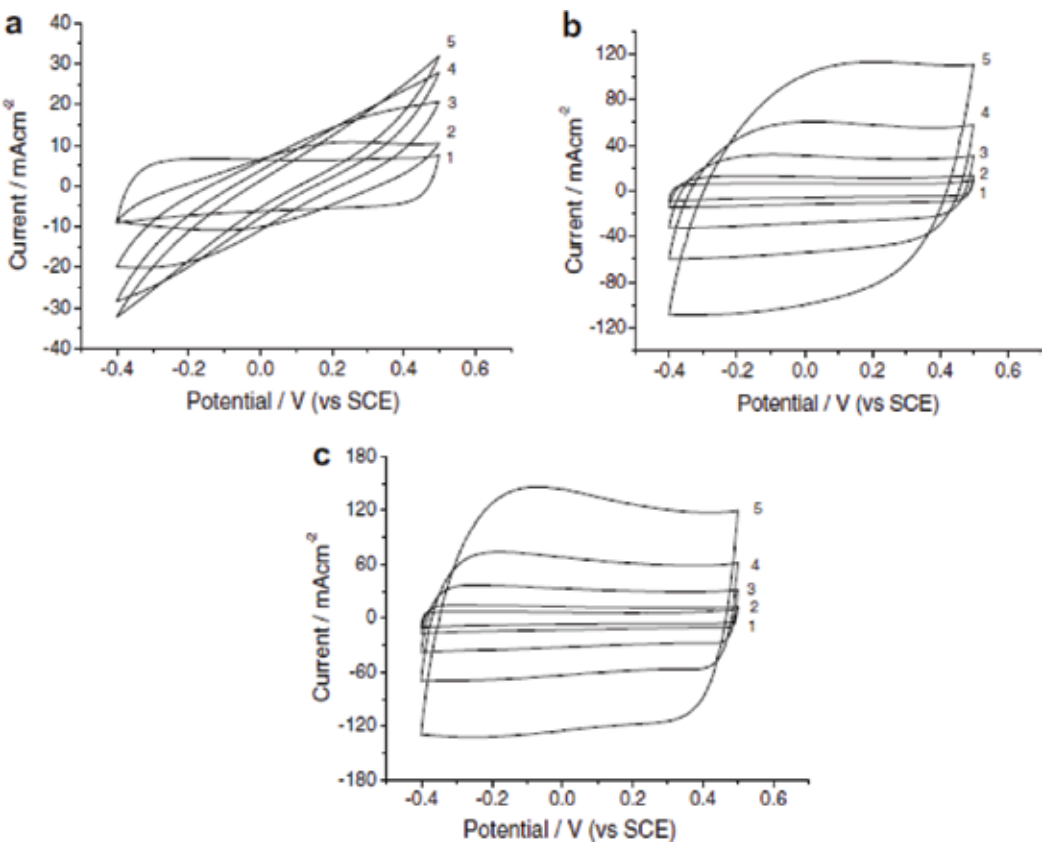

Figure 16. Cyclic voltammograms recorded for pristine (a) PPy, (b) SWCNTs/PPy and (c) functionalized SWCNTs/PPy composite films at different scan rates: (1) 10, (2) 20, (3) 50, (4) 100 (5) 200 mV s^{-1} in 1M KCl solution. Reproduced with permission from Ref. [14]. Copyright 2007 Elsevier.

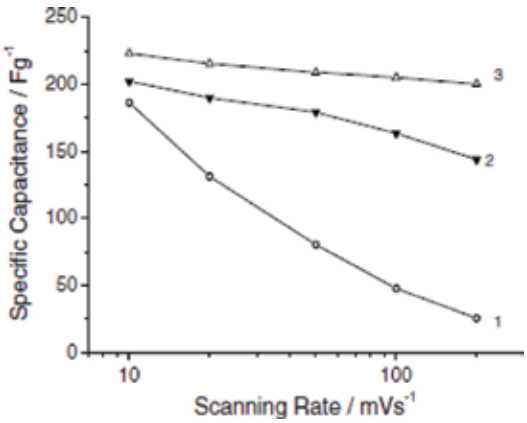

Figure 17. The specific capacitance of (1) pristine PPy film, (2) PPy/SWCNTs composite film and (3) PPy/functionalized SWCNTs composite film at various scanning rates solution. Reproduced with permission from Ref. [14]. Copyright 2007 Elsevier.

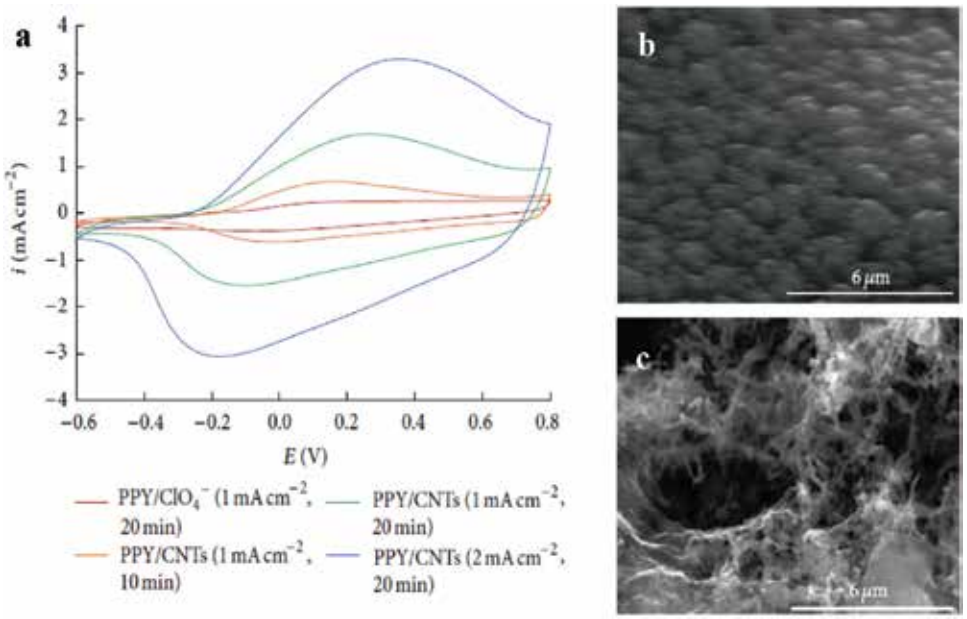

Figure 18. (a) Cyclic voltammograms recorded in propylene carbonate containing 0.1 M $LiClO_4$ for the PPY/CNTs composite films and pure polypyrrole obtained in galvanostatic conditions at different charge densities. SEM images of (b) PPY and (c) PPY/CNTs composite. Reproduced with permission from Ref. [122]. Copyright 2013 Hindawi.

hybrid composite material composed of 2D fish scale-like polyaniline nanosheet arrays on graphene oxide sheets and carbon nanotubes exhibiting high specific capacitance of 589 F g^{-1} compared to 397 F g^{-1} for pristine PANI was also investigated [18]. Moreover, ternary composite systems containing carbon nanotubes, graphene, and conducting polymers were also

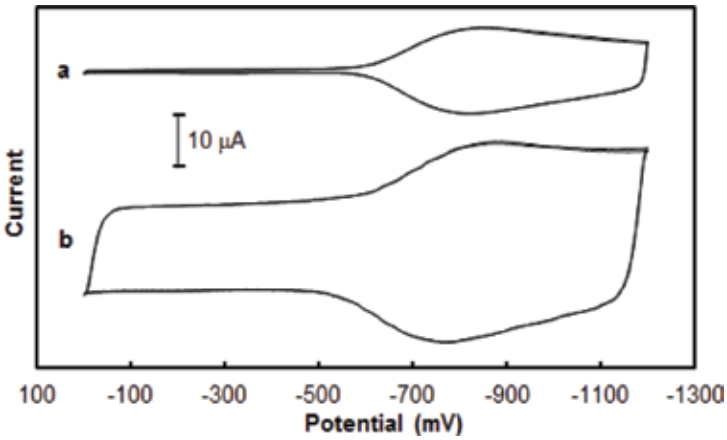

Figure 19. Cyclic voltammogram of (a) C_{60}-Pd polymer and (b) MWCNT/C_{60}-Pd composite at 100 mV/s in acetonitrile containing 0.1 M (n-$C_4H_9)_4NClO_4$. Reproduced with permission from Ref. [119]. Copyright 2013 Elsevier.

Carbon nanostructure	Composite	Specific capacitance (F g^{-1})	Reference
SWCNT	SWCNT/PPy	200	[14]
	SWCNT/PPy	305	[132]
	SWCNT/PANI	247	[129]
	SWCNT/PANI	485	[111]
	SWCNT/PANI	707	[133]
	SWCNT/PANI	1000	[134]
	SWCNT/C_{60}-Pd	994	[119]
MWCNT	MWCNT/PANI	50	[120]
	MWCNT/PANI	500	[112]
	MWCNT/PANI	670	[130]
	MWCNT/PPy	70	[120]
	MWCNT/PPy	268	[7]
	MWCNT/PPy	243	[16]
	MWCNT/PPy	506	[130]
	MWCNT/PPy	554	[126]
	MWCNT/C_{60}-Pd	758	[119]
	MWCNT/PEDOT:PSS	30	[120]
	MWCNT/PEDOT	237	[126]
Graphene/CNT	Graphene/CNT/PPy	453	[132]
GO/CNT	GO/CNT/PANI	413	[18]

Table 3. Capacitance properties of selected composites containing carbon nanostructure and conducting polymer.

investigated [128, 131]. The capacitance properties of selected composites of carbon nanotubes and conducting polymers are reported in **Table 3**.

5.3. Composites containing carbon nanotubes and metal oxides

To overcome the low energy density of supercapacitors, pseudocapacitors based on transition metal oxides have been developed [135]. The most promising among them is manganese dioxide MnO_2 because of its low cost, environmental compatibility, natural abundance, high energy density, and excellent capacitive performance in aqueous electrolytes [32, 135–143]. In aqueous electrolytes, the charging mechanism of MnO_2 may be described by the following reaction:

$$MnO_2 + M^+ + e \rightleftharpoons MnOOM \tag{10}$$

where M represents protons (H^+) and/or alkali cations such as K^+, Na^+, and Li^+. The charge storage is based either on the adsorption of cations at the surface of the electrode material or on the intercalation of cations in the bulk of the electrode material. However, the reported specific capacitance values for the various structures of MnO_2 electrodes are still far from the theoretical one [144], which may be attributed to the intrinsically poor electronic conductivity of MnO_2. To improve the capacitive performance of MnO_2, composites with carbon nanotubes characterized by high conductivity and high surface area are formed [143]. The surface morphology of CNTs/MnO_2 composite and its components is shown in **Figure 20**. **Figure 21a**

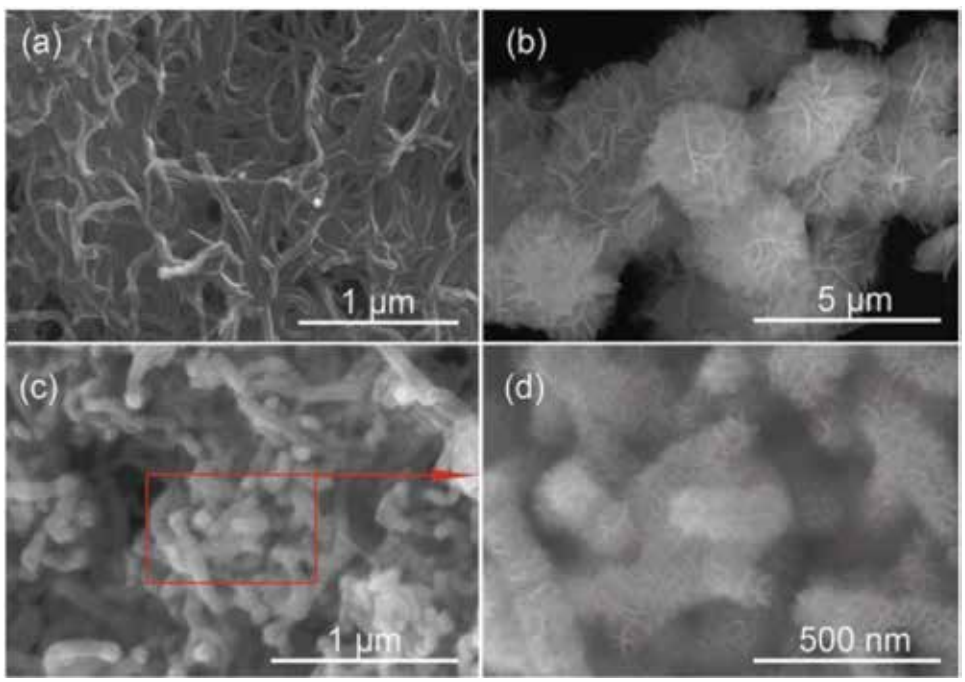

Figure 20. SEM images of (a) pristine CNTs, (b) flower-like MnO_2, (c and d) MnO2/CNT nanocomposite. Reproduced with permission from Ref. [143]. Copyright 2012 Springer.

shows the comparison of the specific capacitances of pristine CNTs, pure MnO_2 and a composite where CNTs are decorated by MnO_2 nanoflakes. CNTs exhibit the best rate capability, but their capacitance is the lowest due to the charge storage mechanism typical for double layer capacitors. The low rate capability of MnO_2 is associated with its poor electronic conductivity and low specific surface area. The combination of MnO_2 and CNTs provides the formation of a MnO_2/CNT nanocomposite exhibiting good rate capability and high specific capacitance. The results obtained by electrochemical impedance spectroscopy (**Figure 21b**) show that the MnO_2/CNT composite has a much lower diffusive resistance compared to pure MnO_2 because the slope of the low-frequency straight line representing the diffusive resistance of electrolyte in the electrode pores and cation diffusion in the host materials is similar to the line obtained for the CNTs but much larger than that of the pure MnO_2. Additionally, the charge transfer resistance, R_{ct}, localized between R_{ct} observed for CNTs and MnO_2 suggests high specific surface area for the unique hierarchy architecture of the CNTs/MnO_2 composite where the 3D electron path network constructed by the CNT cores and the nanoporous sheath composed of tiny MnO_2 nanoflakes facilitate fast electron and ion transport [143].

Apart from MnO_2 [9, 17, 135, 136, 143, 145–150], other metal oxides such as hydrous RuO_2 [151–154], NiO [155, 156], Fe_2O_3 [157], Co_3O_4 [158], MoO_3 [10, 135, 159], V_2O_5 [160], CeO_2 [161], and $NiCo_2O_4$ [162], In_2O_3 [149], TiO_2 [153], SnO_2 [153], and (Sn + Mn)O_x [163] are also utilized for the formation of composite electrodes. In the case of the expensive hydrous ruthenium oxide ($RuO_2 \cdot xH_2O$) exhibiting excellent capacitance performance [164], relatively high conductivity and exceptional electrochemical reversibility, composites based on carbon nanotubes are formed to reduce its cost and enhance its capacitance properties [151–154].

So far, most studies have been devoted to the deposition of the pseudocapacitance phase onto carbon nanostructures. However, it is also possible to encapsulate metal oxides with CNTs. The MnO_2@CNTs material exhibits a significantly higher specific capacitance compared to MnO_2 outside of carbon nanotubes (**Table 4**). The difference in the electrochemical behaviors of MnO_2 enclosed in CNTs (MnO_2-*in*-CNT) and MnO_2 deposited on CNTs surface (MnO_2-*out*-CNT) is

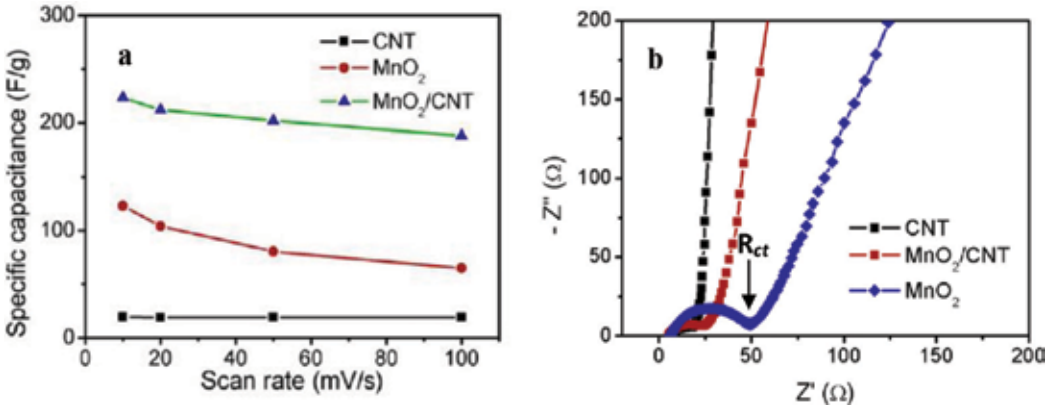

Figure 21. (a) Dependence of specific capacitance on the sweep rate and (b) Nyquist plots for pristine CNTs, pure MnO_2, and MnO_2/CNT nanocomposite electrodes. Reproduced with permission from Ref. [143]. Copyright 2012 Springer.

shown in **Figure 22**. In such a system, the former stores charge electrostatically, and the latter stores charge in virtue of highly reversible redox reactions of MnO_2. The broad anodic peak at 0.72–0.84 and 0.59–0.80 V for the samples MnO_2-*in*-CNT and MnO_2-*out*-CNT, respectively, is associated with the oxidation process of Mn(III) to Mn(IV) according to the reaction:

$$MnO_2 + 4H^+ + e \rightleftharpoons Mn^{3+} + 2H_2O \quad (11)$$

The oxidation potential of MnO_2-*in*-CNT is shifted to higher values compared to that of MnO_2-*out*-CNT because CNT-confined manganese oxide particles can easily form lower oxidation-state species compared to exterior particles. The double-layer capacitance of MnO_2-*in*-CNT is increased due to both the formation of Mn(IV)/Mn(III) redox couple and the desolvation of electrolyte ions inside the channels of CNTs blocked by MnO_2 nanoparticles [9].

Carbon nanostructure	Composite	Specific capacitance (F g^{-1})	Reference
SWCNT	SWCNT/In_2O_3	201	[149]
	SWCNT/MnO_2	253	[149]
	SWCNT/NiC_2O_4	1642	[162]
MWCNT	MWCNT/MoO_3	70	[159]
	MWCNT/MoO_3	178	[10]
	MWCNT/MnO_2	250	[147]
	MWCNT/MnO_2	944	[145]
	MWCNT/RuO_2	138	[153]
	MWCNT/RuO_2	953	[151]
	MWCNT/RuO_2	1050	[154]
	MWCNT/SnO_2	93	[153]
	MWCNT/NiO	160	[155]
	MWCNT/NiO	523	[156]
	MWCNT/TiO_2	160	[153]
	MWCNT/Co_3O_4	201	[158]
	MWCNT/(Sn+Mn)O_x	337	[163]
	MWCNT/MC/MnO_2	351	[165]
	MWCNT@MnO_2@PPy	273	[12]
CNT	MnO_2-*out*-CNT	790	[9]
	MnO_2-*in*-CNT	1250	[9]
	CNT/MnO_2	199	[150]
	CNT/MnO_2	214	[148]

MC, mesoporous carbon.

Table 4. Capacitance properties of selected composites containing carbon nanostructure and metal oxide.

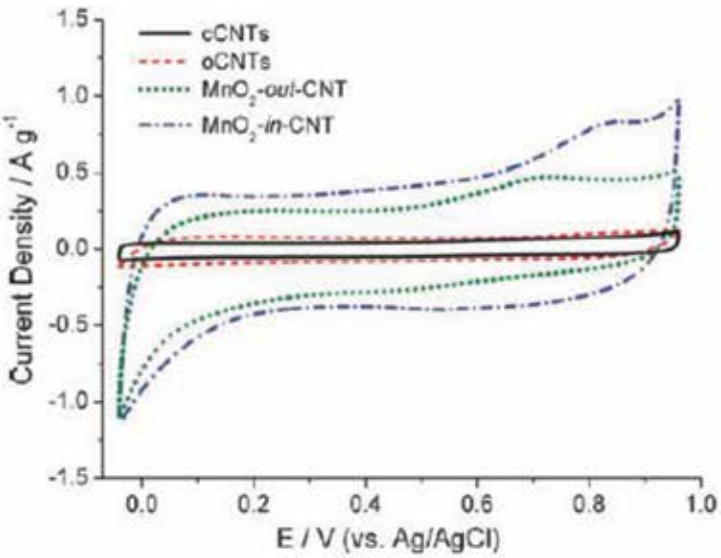

Figure 22. Cyclic voltammogram of blank cCNTs (CNTS with closed tips), oCNTs (CNTs with open tips), MnO_2-*out*-CNT and MnO_2-*in*-CNT in 1 M Na_2SO_4. Reproduced with permission from Ref. [9]. Copyright 2010 The Royal Society of Chemistry.

Moreover, hybrid materials such as carbon nanotubes/mesoporous carbon/MnO_2 [165], carbon nanotubes/3D graphene/MnO_2 [11], and carbon nanotube@MnO_2@polypyrrole [12] have been developed. **Table 4** shows the capacitance of exemplary composites based on carbon nanostructures and metal oxides.

5.4. Capacitors based on carbon nanotubes and carbon gels

Recently, much attention has been paid to novel ultralight mesoporous carbon materials named carbon aerogels (CAGs) [15, 166–173] or carbon xerogels [8, 174–178]. Carbon aerogels exhibit many interesting properties such as low mass density, continuous porosity, high surface area, and high electrical conductivity. These properties are characteristic of the aerogel microstructure, which is a network of interconnected primary particles with diameters between 3 and 25 nm (**Figure 23a**). However, aerogels consist of agglomerate particles linked by covalent bridges with a ladder structure. The contact between these particles and the space due to the pores unfortunately introduces a high internal resistance within the aerogel which limits their practical applications. To overcome this problem, composites of carbon aerogels with carbon nanotubes are formed (**Figure 23b**). CNTs with their high electrical conductivity work as nanopathways for charges and thus improve the intrinsic conductivity of the CAGs and their mechanical integrity as well [166].

The main problem in the case of composite formation is the agglomeration of carbon nanotubes within the CAG's pore network. A very useful approach for the formation of binderless carbon nanotube aerogel (CNAG) composites proposed by Bordjiba and co-workers [166, 172] provides a significant improvement in the dispersion of carbon nanotubes within the aerogel matrix and

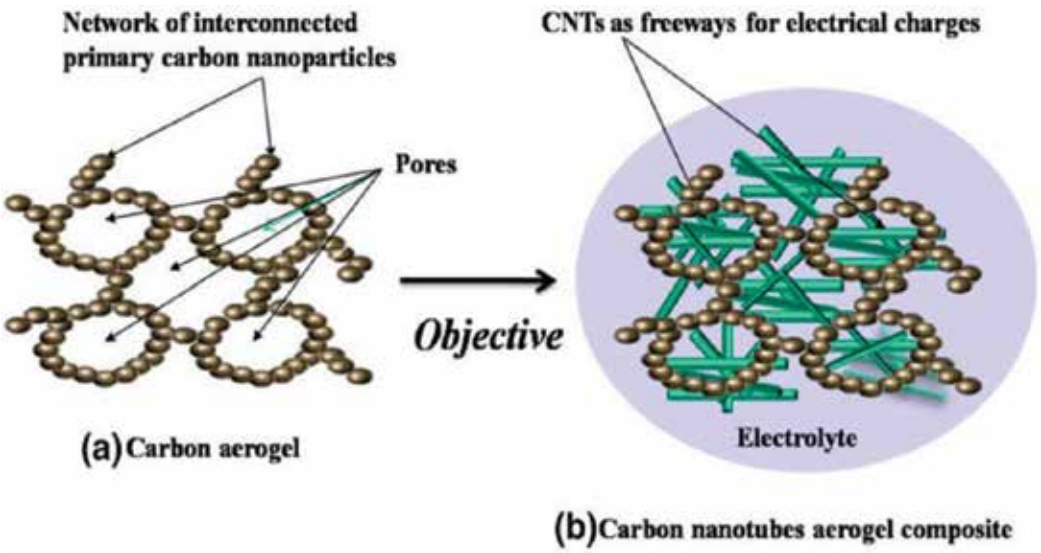

Figure 23. (a) Representation of the carbon aerogel internal structure and (b) targeted carbon nanotube aerogel composite. Reproduced with permission from Ref. [166]. Copyright 2011 Springer.

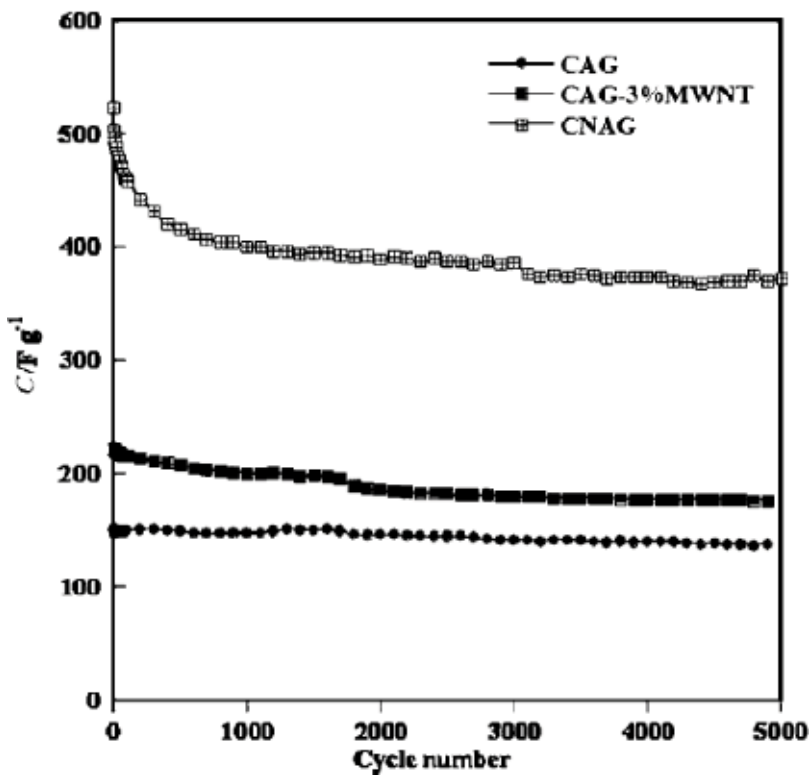

Figure 24. Cycle life of CAG, CAG-3%MWNT and CNAG composites in 5 M KOH. Reproduced with permission from Ref. [166]. Copyright 2011 Springer.

better interfacial coating. The CNAG material was prepared by a molding procedure, i.e., synthesis by a chemical vapor deposition method to grow carbon nanotubes directly onto a microfibrous carbon paper substrate. In the next step, the carbon aerogel was synthesized on the carbon nanotubes. The key feature of this method is eliminating the need to control the carbon nanotube concentration, which permits optimized dispersion processes to reinforce the aerogel's networks. The CNAG electrode delivered very high specific capacitances equal to 524 F g^{-1}. Furthermore, better integration of carbon nanotubes in the matrix of carbon aerogel improves its resistance to attack by the electrolyte and assures excellent cycle life. Such a system exhibits significantly higher capacitance and stability compared to the composite processed from the dispersion of its components in liquid phase, CAG-3%MWNT (**Figure 24**). Apart from the capacitance performance, binderless nanostructured electrodes also reduce the cost of manufacturing and avoid complicated interferences of the binders and conductivity enhancers used in practical electrodes [166, 172].

The research on CNTs and carbon aerogel composites is relatively new because their very promising properties are still being developed. The composites that have been prepared so far exhibit excellent capacitance properties [8, 166, 170–172, 177, 178]. A large progress in this area of study can be expected in the near future.

6. Conclusion and outlook

Supercapacitors have been developed to close the gap between conventional capacitors and batteries because of their high energy density and power density. In the development of electrochemical capacitors, carbon nanotubes and their composites have been widely used as electrode materials. The specific capacitance of pristine carbon nanotubes is relatively low and depends on many factors such as the kind of carbon nanotubular material, i.e., single- or multi-walled, its orientation, i.e., open or closed tips, surface area, synthesis method, solvent and supporting electrolyte. Compared with pristine carbon nanotubes, functionalized carbon nanotubes by heteroatoms or functional groups attached to nanotubes walls are expected to display improved capacitance performance. The formation of composites based on carbon nanotubes provides especially high surface area due to the presence of CNTs which is very important in the case of storage systems. Moreover, it enhances the properties of both the carbon nanotubes and the second component. Apart from the improvement in capacitance performance, the addition of CNTs reduces cost compared to metal oxide, improves stability compared to conducting polymers which exhibit rapid degradation in performance after repetitive cycles because of their swelling and shrinking, and improves the poor volumetric performance of supercapacitors based on other carbon nanomaterials. The capacitance properties strongly depend on the localization of the redox system. It was found that encapsulation of the redox phase inside a nanotubular material provides higher specific capacitance compared to a redox system situated outside of carbon nanotubes. Recently, a new generation of cheap storage systems based on mesoporous carbon aerogels was discovered. However, in this case, there is a problem with the non-homogeneous spread of carbon nanotubes within the whole network of carbon aerogel. Hence, increasing

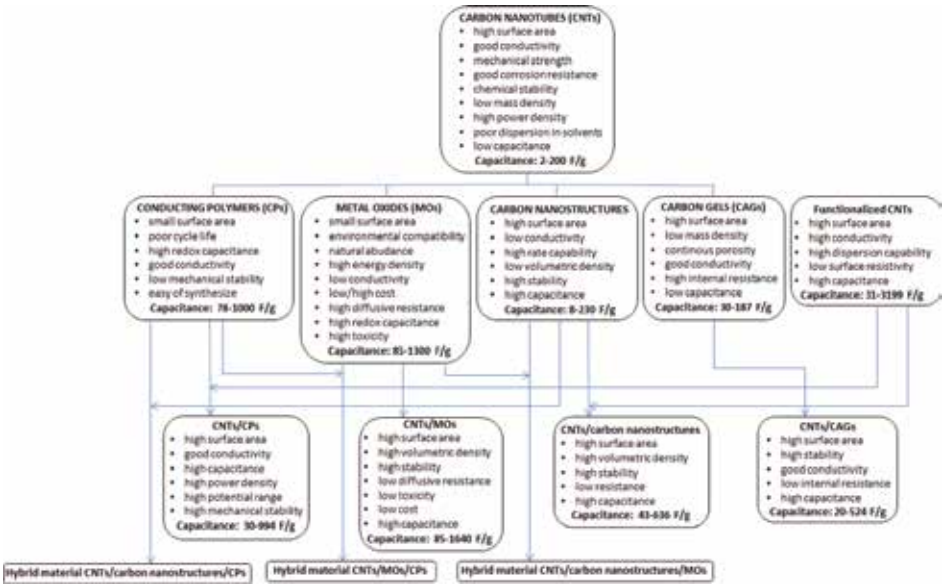

Scheme 2. Comparison of properties of composites based on carbon nanotubes and their components.

attention is needed to solve this problem because this system could be the future for storage devices. A very promising system seems to be the attachment of redox-active nanoparticles to carbon nanotubes. Compared to bulk materials, they exhibit unique properties arising from their nanoscale sizes, such as high electrical conductivity, large surface area, short path lengths for the transport of ions and high electrochemical activity. Ultrafast compact capacitors based on 3D hybrid structures that increase the accessible surface area and allow fast ion diffusion are introducing a new class of electrode materials for storage devices. A comparison of the properties of composites based on carbon nanotubes and their components is summarized in **Scheme 2**.

Acknowledgements

The authors acknowledge the National Center of Science (project No. 2016/21/B/ST5/02496 to KW) for a financial support.

Author details

Emilia Grądzka* and Krzysztof Winkler

*Address all correspondence to: emilia@uwb.edu.pl

Institute of Chemistry, University of Bialystok, Poland

References

[1] Kandalkar SG, Gunjakar JL, Lokhande CD. Preparation of cobalt oxide thin films and its use in supercapacitor application. Applied Surface Science. 2008;**254**:5540-5544. DOI: 10.1016/j.apsusc.2008.02.163

[2] Chen GZ. Supercapacitor and supercapattery as emerging electrochemical energy stores. International Materials Reviews. 2017;**62**:173-202. DOI: 10.1080/09506608.2016.1240914

[3] Garcia P, Torreglosa JP, Fernandez LM, Jurado F. Control strategies for high-power electric vehicles powered by hydrogen fuel cell, battery and supercapacitor. Expert Systems with Applications. 2013;**40**:4791-4804. DOI: 10.1016/j.eswa.2013.02.028

[4] Li J, Cheng X, Sashurin A, Keidar M. Review of electrochemical capacitors based on carbon nanotubes and graphene. Graphene. 2012;**1**:1-13. DOI: 10.4236/graphene.2012.11001

[5] Du R, Zhao Q, Zhang N, Zhang J. Marcoscopic carbon nanotube-based 3D monoliths. Small. 2015;**11**:3263-3289. DOI: 10.1002/smll.201403170

[6] In JB, Grigoropoulos CP, Chernov AA, Noy A. Growth kinetics of vertically aligned carbon nanotube arrays in clean oxygen-free conditions. ACS Nano. 2011;**5**:9602-9610. DOI: 10.1021/nn2028715

[7] Reddy RK, Alonso-Marroquin F. Polypyrrole functionalized with carbon nanotubes as an efficient and new electrodes for electrochemical supercapacitors. AIP Conference Proceedings. 2017;**1856**:020002-1-020002-4. DOI: 10.1063/1.4985553

[8] Fathy NA, Annamalai KP, Tao Y. Effects of phosphoric acid activation on the nanopore structures of carbon xerogel/carbon nanotubes hybrids and their capacitance storage. Adsorption. 2017;**23**:355-360. DOI: 10.1007/s10450-017-9860-y

[9] Chen W, Fan Z, Gu L, Bao X, Wang C. Enhanced capacitance of manganese oxide via confinement inside carbon nanotubes. Chemical Communication. 2010;**46**:3905-3907. DOI: 10.1039/c000517g

[10] Shakir I, Sarfraz M. Evaluation of electrochemical charge storage mechanism and structural changes in interwined MoO_3-MWCNTs composites for supercapacitor applications. Electrochimica Acta. 2014;**147**:380-384. DOI: 10.1016/j.electacta.2014.09.073

[11] Pan Z, Liu M, Yang J, Qiu Y, Li W, Xu Y, Zhang X, Zhang Y. High electroactive material loading on a carbon nanotube@graphene aerogel for high-performance flexible all-solid-state asymmetric supercapacitors. Advanced Functional Materials. DOI: 10.1002/adfm.201701122

[12] Pequeno de Oliveira AH, Ferreira Nascimento ML, Pequeno de Oliveira H. Carbon nanotube@MnO_2@polypyrrole composites: Chemical synthesis, characterization and application in supercapacitors. Materials Research. 2016;**19**(5):1080-1087. DOI: 10.1590/1980-5373-MR-2016-0347

[13] Mi H, Zhang X, Xu Y, Xiao F. Synthesis, characterization and electrochemical behavior of polypyrrole/carbon nanotube composites using organometallic-functionalized carbon nanotubes. Applied Surface Science. 2010;**256**:2284-2288. DOI: 10.1016/j.apsusc.2009.10.053

[14] Wang J, Xu Y, Chen X, Sun X. Capacitance properties of single wall carbon nanotube/polypyrrole composite films. Composites Science and Technology. 2007;**67**:2981-2985. DOI: 10.1016/j.compscitech.2007.05.015

[15] Worsley MA, Satcher JH, Baumann T. Synthesis and characterization of monolithic carbon aerogel nanocomposites containing double-walled carbon nanotubes. Langmuir. 2008;**24**:9763-9766. DOI: 10.1021/la8011684

[16] Sun X, Xu Y, Wang J, Mao S. The composite film of polypyrrole and functionalized multi-walled carbon nanotubes as an electrode material for supercapacitors. International Journal of Electrochemical Science. 2012;**7**:3205-3214

[17] Cheng Q, Ma J, Zhang H, Shinya N, Qin LC, Tang J. Electrodeposition of MnO_2 on carbon nanotube thin films as flexible electrodes for supercapacitors. Transactions of the Materials Research Society of Japan. 2010;**35**(2):369-372

[18] Ning G, Li T, Yan J, Xu C, Wei T, Fan Z. Three-dimensional hybrid materials of fish scale-like polyaniline nanosheet arrays on graphene oxide and carbon nanotube for high-performance ultracapacitors. Carbon. 2013;**54**:241-248. DOI: 10.1016/j.carbon.2012.11.035

[19] Kotz R, Carlen M. Principles and applications of electrochemical capacitors. Electrochimica Acta. 2000;**45**:2483-2498. DOI: 10.1016/S0013-4686(00)00354-6

[20] Zhang Y, Feng H, Wu X, Wang L, Zhang A, Xia T, Dong H, Li X, Zhang L. Progress of electrochemical capacitor electrode materials: A review. International Journal of Hydrogen Energy. 2009;**34**:4889-4899. DOI: 10.1016/j.ijhydene.2009.04.005

[21] Yamada H, Bandaru PR. Limits to the magnitude of capacitance in carbon nanotube array electrode based electrochemical capacitors. Applied Physics Letters. 2013;**102**:173113-1-173113-4. DOI: 10.1063/1.4803925

[22] Pan H, Li J, Feng YP. Carbon nanotubes for supercapacitor. Nanoscale Research Letters. 2010;**5**:654-668. DOI: 10.1007/s11671-009-9508-2

[23] Forse AC, Merlet C, Griffin JM, Grey CP. New perspectives on the charging mechanisms of supercapacitors. Journal of the American Chemical Society. 2016;**138**:5731-5744. DOI: 10.1021/jacs.6b02115

[24] Karden E, Ploumen S, Fricke B, Miller T, Snyder K. Energy storage devices for future hybrid electric vehicles. Journal of Power Sources. 2007;**168**:2-11. DOI: 10.1016/j.jpowsour.2006.10.090

[25] Thounthong P, Rael S, Davat B. Control strategy of fuel cell/supercapacitors hybrid power sources for electric vehicle. Journal of Power Sources. 2006;**158**:806-814. DOI: 10.1016/j.jpowsour.2005.09.014

[26] Ghosh S, Inganas O. Conducting polymers hydrogels as 3D electrodes: Applications for supercapacitors. Advanced Materials. 1999;**11**:1214-1218. DOI: 10.1002/(SICI)1521-4095(199910)11:14<1214::AID-ADMA1214>3.0.CO;2-3

[27] Fic K, Lota G, Meller M, Frackowiak E. Novel insight into neutral medium as electrolyte for high-voltage supercapacitors. Energy & Environmental Science. 2012;**5**:5842-5850. DOI: 10.1039/c1ee02262h

[28] Reddy ALM, Amitha FE, Jafri I, Ramaprabhu S. Asymmetric flexible supercapacitor stack. Nanoscale Research Letters. 2008;**3**:145-151. DOI: 10.1007/s11671-008-9127-3

[29] Chen T, Dai L. Carbon nanomaterials for high-performance supercapacitors. Materials Today. 2013;**16**:272-280. DOI: 10.1016/j.mattod.2013.07.002

[30] Zhang LL, Zhao XS. Carbon-based materials as supercapacitor electrodes. Chemical Society Reviews. 2009;**38**:2520-2531. DOI: 10.1039/b813846j

[31] Zhang LL, Zhou R, Zhao XS. Graphene-based materials as supercapacitor electrodes. Journal of Materials Chemistry. 2010;**20**:5983-5992. DOI: 10.1039/c000417k

[32] Shi F, Li L, Wang XL, Gu CD, Tu JP. Metal oxide/hydroxide-based materials for supercapacitors. RSC Advances. 2014;**4**:41910-41921. DOI: 10.1039/c4ra06136e

[33] Lu W, Qu L, Henry K, Dai L. High performance electrochemical capacitors from aligned carbon nanotube electrodes and ionic liquid electrolytes. Journal of Power Sources. 2009;**189**:1270-1277. DOI: 10.1016/j.jpowsour.2009.01.009

[34] Huang J, Sumpter BG, Meunier V. A universal model for nanoporous carbon supercapacitors applicable to diverse pore regimes, carbon materials, and electrolytes. Chemistry A European Journal. 2008;**14**:6614-6626. DOI: 10.1002/chem.200800639

[35] Barisci JN, Wallace GG, Baughman RH. Electrochemical studies of single-wall carbon nanotubes in aqueous solutions. Journal of Electroanalytical Chemistry. 2000;**488**:92-98. DOI: 10.1016/S0022-0728(00)00179-0

[36] Li J, Cassell A, Delzeit L, Meyyappan M. Novel three-dimensional electrodes: Electrochemical properties of carbon nanotube ensembles. Journal of Physical Chemistry B. 2002;**106**:9299-9305. DOI: 10.1021/jp021201n

[37] Pumera M. Electrochemical properties of double wall carbon nanotube electrodes. Nanoscale Research Letters. 2007;**2**:87-93. DOI: 10.1007/s11671-006-9035-3

[38] Frackowiak E, Jurewicz K, Delpeux S, Beguin F. Nanotubular materials for supercapacitors. Journal of Power Sources. 2001;**97-98**:822-825. DOI: 10.1016/S0378-7753(01)00736-4

[39] Krivenko AG, Matyushenko VI, Stenina EV, Sviridova LN, Krestinin AV, Zvareva GI, Kurmaz VA, Ryabenko AG, Dmitriev SN, Skuratov VA. Peculiarities of the electrochemical behavior of modified electrodes containing single-wall carbon nanotubes. Elecrochemistry Communications. 2005;**7**:199-204. DOI: 10.1016/j.elecom.2004.12.009

[40] Oh J, Kozlov ME, Kim BG, Kim H-K, Baughman RH, Hwang YH. Preparation and electrochemical characterization of porous SWNT–PPy nanocomposite sheets for supercapacitor applications. Synthetic Metals. 2008;**158**:638-641. DOI: 10.1016/j.synthmet.2008.04.007

[41] Liu CG, Fang HT, Li F, Liu M, Cheng HM. Single-walled carbon nanotubes modified by electrochemical treatment for application in electrochemical capacitors. Journal of Power Sources. 2006;**160**:758-761. DOI: 10.1016/j.jpowsour.2006.01.072

[42] Vivekchand SRC, Rout CS, Subrahmanyam KS, Govindaraj A, Rao CNR. Graphene-based electrochemical supercapacitors. Journal of Chemical Sciences. 2008;**120**:9-13. DOI: 10.1007/s12039-008-0002-7

[43] Jurewicz K, Babeł K, Pietrzak R, Delpeux S, Wachowska H. Capacitance properties of multi-walled carbon nanotubes modified by activation and ammoxidation. Carbon. 2006;**44**:2638-2375. DOI: 10.1016/j.carbon.2006.05.044

[44] Deng L, Hao Z, Wang J, Zhu G, Kang L, Liu Z-H, Yang Z, Wang Z. Preparation and capacitance of graphene/multiwall carbon nanotubes/MnO_2 hybrid material for high-performance asymmetrical electrochemical capacitor. Electrochimica Acta. 2013;**89**:191-198. DOI: 10.1016/j.electacta.2012.10.106

[45] Valentini L, Armentano I, Kenny JM. Sensors for sub-ppm NO_2 gas detection based on carbon nanotube thin films. Applied Physics Letters. 2003;**82**:961-963. DOI: 10.1063/1.1545166

[46] Rueckes T, Kim K, Joselevich E, Tseng GY, Cheung C-L, Lieber CM. Carbon nanotube—Based nonvolatile random access memory for molecular computing. Science. 2000;**289**:94-97. DOI: 10.1126/science.289.5476.94

[47] Martel R, Schmidt T, Shea HR, Hertel T, Avouris P. Single- and multi-wall carbon nanotube field-effect transistors. Applied Physics Letters. 1998;**73**:2447-2449. DOI: 10.1063/1.122477

[48] Kamat PV, Thomas KG, Barazzouk S, Girishkumar G, Vinodgopal MD. Self-assembled linear bundles of single wall carbon nanotubes and their alignment and deposition as a film in a dc field. Journal of the American Chemical Society. 2004;**126**:10757-10762. DOI: 10.1021/ja0479888

[49] Xin H, Woolley AT. Directional orientation of carbon nanotubes on surfaces using a gas flow cell. Nano Letters. 2004;**4**:1481-1484. DOI: 10.1021/nl049192c

[50] Wang D, Song P, Liu C, Wu W, Fan S. Highly oriented carbon nanotube papers made of aligned carbon nanotubes. Nanotechnology. 2008;**19**:1-6. DOI: 10.1088/0957-4484/19/7/075609

[51] Wang Y, Iqbal Z. Vertically oriented single-wall carbon nanotube/enzyme on silicon as biosensor electrode. JOM. 2005;**34**:27-29. DOI: 10.1007/s11837-005-0132-z

[52] Cao A, Ajayan PM, Ramanath G, Baskaran R, Turner K. Silicon oxide thickness-dependent growth of carbon nanotubes. Applied Physics Letters. 2004;**84**:109-111. DOI: 10.1063/1.1636826

[53] Liu Z, Shen Z, Zhu T, Hou S, Ying L. Organizing single-walled carbon nanotubes on gold using a wet chemical self-assembling technique. Langmuir. 2000;**16**:3569-3573. DOI: 10.1021/la9914110

[54] Taurino I, Carrara S, Giorcelli M, Tagliaferro A, De Micheli G. Comparison of two different carbon nanotube-based surfaces with respect to potassium ferricyanide electrochemistry. Surface Science. 2012;**606**:156-160. DOI: 10.1016/j.susc.2011.09.001

[55] Azam MA, Fujiwara A, Shimoda T. Significant capacitance performance of vertically aligned single-walled carbon nanotube supercapacitor by varying potassium hydroxide concentration. International Journal of Electrochemical Science. 2013;**8**:3902-3911

[56] Luo Y, Li X, Gong Z, Sheng Z, Peng X, Mou Q, He M, Li X, Chen H. Aligned carbon nanotubes array by DC glow plasma etching for supercapacitor. Journal of Nanomaterials. DOI: 10.1155/2013/270289

[57] Izadi-Najafabadi A, Futaba DN, Iijima S, Hata K. Ion diffusion and electrochemical capacitance in aligned and packed single-walled carbon nanotubes. Journal of the American Chemical Society. 2010;**132**:18017-18019. DOI: 10.1021/ja108766y

[58] Park SK, Mahmood Q, Park HS. Surface functional groups of carbon nanotubes to manipulate capacitive behaviors. Nanoscale. 2013;**5**:12304-12309. DOI: 10.1039/c3nr04858f

[59] Balasubramanian K, Burghard M. Electrochemically functionalized carbon nanotubes for device applications. Journal of Materials Chemistry. 2008;**18**:3071-3083. DOI: 10.1039/b718262g

[60] Tasis D, Tagmatachris N, Bianco A, Prato M. Chemistry of carbon nanotubes. Chemical Reviews. 2006;**106**:1105-1136. DOI: 10.1021/cr050569o

[61] Zhou Z, Zhang Z, Peng H, Qin Y, Li G, Chen K. Nitrogen- and oxygen-containing activated carbon nanotubes with improved capacitive properties. RSC Advances. 2014;**4**:5524-5530. DOI: 10.1039/c3ra45076g

[62] Wang G, Liang R, Liu L, Zhong B. Improving the specific capacitance of carbon nanotubes-based supercapacitors by combining introducing functional groups on carbon nanotubes with using redox-active electrolyte. Electrochimica Acta. 2014;**115**:183-188. DOI: 10.1016/j.electacta.2013.10.165

[63] Mombeshora ET, Ndungu PG, Jarvis ALL, Nyamori VO. Oxygen-modified multiwalled carbon nanotubes: Physicochemical properties and capacitor functionality. International Journal of Energy Research. 2017;**41**:1182-1201. DOI: 10.1002/er.3702

[64] Tian Y, Amal R, Wang D-W. An aqueous metal-ion capacitor with oxidized carbon nanotubes and metallic zinc electrodes. Frontiers in Energy Research. 2016;**4**:1-14. DOI: 10.3389/fenrg.2016.00034

[65] Smith B, Wepasnick K, Schrote KE, Bertele AR, Ball WP, O'melia C, Fairbrother DH. Colloidal properties of aqueous of acid-treated multi-walled carbon nanotubes. Environmental Science & Technology. 2009;**43**:819-825. DOI: 10.1021/es802011e

[66] Wepasnick KA, Smith BA, Schrote KE, Wilson KH, Diegelmann SR, Fairbrother DH. Surface and structural characterization of multi-walled carbon nanotubes following different oxidative treatments. Carbon. 2011;**49**:24-36. DOI: 10.1016/j.carbon.2010.08.034

[67] Wepasnick KA, Smith BA, Botter JL, Fairbrother DH. Chemical and structural characterization of carbon nanotube surfaces. Analytical and Bioanalytical Chemistry. 2010;**396**:1003-1014. DOI: 10.1007/s00216-009-3332-5

[68] Smith B, Wepasnick K, Schrote KE, Cho H-H, Ball WP, Fairbrother DH. Influence of surface oxides on the colloidal stability of multi-walled carbon nanotubes: A structure-property relationship. Langmuir. 2009;**25**(17):9767-9776. DOI: 10.1021/la901128k

[69] Datsyuk V, Kaylva M, Papagelis K, Parthenios J, Tasis D, Siokou A, Kallitsis I, Galiotis C. Chemical oxidation of multiwalled carbon nanotubes. Carbon. 2008;**46**:833-840. DOI: 10.1016/j.carbon.2008.02.012

[70] Li M, Boggs M, Beebe TP, Huang CP. Oxidation of single-walled carbon nanotubes in dilute aqueous solutions by ozone as affected by ultrasound. Carbon. 2008;**46**:466-475. DOI: 10.1016/j.carbon.2007.12.012

[71] Komarova NS, Krivenko AG, Stenina EV, Sviridova LN, Mironovich KV, Shulga YM, Krivchenko VA. Enhancement of the carbon nanowall film capacitance. Electron transfer kinetics on functionalized surfaces. Langmuir. 2015;**31**:7129-7137. DOI: 10.1021/acs.langmuir.5b00391

[72] Ye JS, Liu X, Cui HF, Zhang W-D, Sheu F-S, Lim TM. Electrochemical oxidation of multi-walled carbon nanotubes and its application to electrochemical double layer capacitors. Electrochemistry Comunications. 2005;**7**:249-255. DOI: 10.1016/j.elecom.2005.01.008

[73] Jang IY, Lee SH, Park KC, Wongwiriyapan W, Kim C, Teshima K, Oishi S, Kim YJ, Endo M. Effect of photochemically oxidized carbon nanotubes on the deposition of platinum nanoparticles for fuel cells. Electrochemistry Comunications. 2009;**11**:1472-1475. DOI: 10.1016/j.elecom.2009.05.036

[74] Lee SH, Jung YC, Kim YA, Muramatsu H, Teshima K, Oishi S, Endo M. Optical spectroscopic studies of photochemically oxidized single-walled carbon nanotubes. Nanotechnology. 2009;**20**:1-5. DOI: 10.1088/0957-4484/20/10/105708

[75] Zschoerper NP, Kotzenamier V, Vohrer U, Haupt M, Oehr C, Hirth T. Analytical investigation of the composition of plasma-induced functional groups on carbon nanotube sheets. Carbon. 2009;**47**:2174-2185. DOI: 10.1016/j.carbon.2009.03.059

[76] Yang D-Q, Sacher E. Strongly enhanced interaction between evaporated Pt nanoparticles and functionalized multiwalled carbon nanotubes via plasma surface modifications: Effects of physical and chemical defects. Journal of Physical Chemistry C. 2008;**112**:4075-4082. DOI: 10.1021/jp076531s

[77] Jung N, Kwon S, Lee D, Yoon D-M, Park YM, Benayad A, Choi J-Y, Park JS. Synthesis of chemically bonded graphene/carbon nanotube composites and their application in large volumetric capacitance supercapacitors. Advanced Materials. 2013;**25**:6854-6858. DOI: 10.1002/adma.201302788

[78] Xu D, Ding B, Nie P, Shen L, Wang J, Zhang X. Porous nitrogen-doped carbon nanotubes derived from tubular polypyrrole for energy-storage applications. Chemistry A European Journal. 2013;**19**:12306-12312. DOI: 10.1002/chem.201301352

[79] Gueon D, Moon JH. Nitrogen-doped carbon nanotube spherical particles for supercapacitor applications: Emulsion-assisted compact packing and capacitance enhancement. ACS Applied Materials & Interfaces. 2015;**7**:20083-20089. DOI: 10.1021/acsami.5b05231

[80] Karakaya M, Zhu J, Raghavendra AJ, Podila R, Parler SG, Kaplan JP, Rao AM. Roll-to-roll production of spray coated N-doped carbon nanotube electrodes for supercapacitors. Applied Physics Letters. 2014;**105**:263103-1-263103-4. DOI: 10.1063/1.4905153

[81] John AR, Arumugam P. Open ended nitrogen-doped carbon nanotubes for the electrochemical storage of energy in a supercapacitor electrode. Journal of Power Sources. 2015;**277**:387-392. DOI: 10.1016/j.jpowsour.2014.11.151

[82] Liao L, Pan C. Enhanced electrochemical capacitance of nitrogen-doped carbon nanotubes synthesized from amine flames. Soft Nanoscience Letters. 2011;**1**:16-23. DOI: 10.4236/snl.2011.11004

[83] Yun YS, Park HH, Jin H-J. Pseudocapacitive effects of N-doped carbon nanotube electrodes in supercapacitors. Materials. 2012;**5**:1258-1266. DOI: 10.3390/ma5071258

[84] Dubal DP, Chodankar NR, Caban-Huertas Z, Wolfart F, Vidotti M, Holze R, Lokhande CD, Gomez-Romero P. Synthetic approach from polypyrrole nanotubes to nitrogen doped pyrolyzed carbon nanotubes for asymmetric supercapacitors. Journal of Power Sources. 2016;**308**:158-165. DOI: 10.1016/j.jpowsour.2016.01.074

[85] Ayala P, Arenal R, Rummeli M, Rubio A, Pichler T. The doping of carbon nanotubes with nitrogen and their potential applications. Carbon. 2010;**48**:575-586. DOI: 10.1016/j.carbon.2009.10.009

[86] Mousavi-Khosedel SM, Jahanbakhsh-bonab P, Targholi E. Structural, electronic properties, and quantum capacitance of B, N and P-doped armchair carbon nanotubes. Physics Letters A. 2016;**380**:3378-3383. DOI: 10.1016/j.physleta.2016.07.067

[87] Terrones M, Souza Filho AG, Rao AM. Doped Carbon Nanotubes: Synthesis, Characterization and Applications. In: Jorio A, Dresselhaus G, Dresselhaus MS, editors. Topics in Applied Physics. Berlin, Heidelberg: Springer-Verlag Berlin Heidelberg; 2008. pp. 531-566. DOI: 10.1007/978-3-540-72865-8_17

[88] Siraishi S, Kibe M, Yokoyama T, Kurihara H, Patel N, Oya A, Kaburagi Y, Hishiyama Y. Electric double layer capacitance of multi-walled carbon nanotubes and B-doping effect. Applied Physics A. 2006;**82**:585-591. DOI: 10.1007/s00339-005-3399-6

[89] Yeh M-H, Lin L-Y, Li T-J, Leu Y-A, Chen G-L, Tien T-C, Hsieh C-Y, Lo S-C, Huang S-J, Chiang W-H, Ho K-C. Synthesis of boron-doped multi-walled carbon nanotubes by an ammonia-assisted substitution reaction for applying in supercapacitors. Energy Procedia. 2014;**61**:1764-1767. DOI: 10.1016/j.egypro.2014.12.207

[90] Patino J, Lopez-Salas N, Gutierrez MC, Carriazo D, Ferrer ML, del Monte F. Phosphorous-doped carbon-nanotube hierarchical monoliths as true three-dimensional electrodes in supercapacitor cells. Journal of Materials Chemistry A. 2016;**4**:1251-1263. DOI: 1039/C5TA09210H

[91] Lee JY, An KH, Heo JK, Lee YH. Fabrication of supercapacitor electrodes using fluorinated single-walled carbon nanotubes. Journal of Physical Chemistry B. 2003;**107**:8812-8815. DOI: 10.1021/jp034546u

[92] Majeed S, Zhao J, Zhang L, Anjum S, Liu Z, Xu G. Synthesis and electrochemical applications of nitrogen-doped carbon nanomaterials. Nanotechnology Reviews. 2013;**2**(6): 615-635. DOI: 10.1515/ntrev-2013-0007

[93] Zang X, Xu R, Zhang Y, Li X, Zhang L, Wei J, Wang K, Zhu H. All carbon coaxial supercapacitors based on hollow carbon nanotube sleeve structure. Nanotechnology. 2015;**26**:1-8. DOI: 10.1088/0957-4484/26/4/045401

[94] Iyyamperumai E, Wang S, Dai L. Vertically aligned BCN nanotubes with high capacitance. ACS Nano. 2012;**6**:5259-5265. DOI: 10.1021/nn301044v

[95] Xu Y, Zhyang SQ, Zhang XY, He PG, Fang YZ. Configuration and capacitance properties of polypyrrole/aligned carbon nanotubes synthesized by electropolymerization. Chinese Science Bulletin. 2011;**56**:3823-3828. DOI: 10.1007/s11434-011-4745-z

[96] Hiralal P, Wang H, Unalan HE, Liu Y, Rouvala M, Wei D, Andrew P, Amaratunga AJ. Enhanced supercapacitors from hierarchical carbon nanotube and nanohorn architectures. Journal of Materials Chemistry. 2011;**21**:17810-17815. DOI: 10.1039/c1jm12156a

[97] Tran M-H, Jeong HK. Ternary carbon composite films for supercapacitor applications. Chemical Physics Letters. 2017;**684**:1-7. DOI: 10.1016/j.cplett.2017.06.025

[98] Yu D, Goh K, Wang H, Wei L, Jiang W, Zhang Q, Dai L, Chen Y. Scalable synthesis of hierarchically structured carbon nanotube–graphene fibers for capacitive energy storage. Nature Nanotechnology. 2014;**9**:555-562. DOI: 10.1038/NNANO.2014.93

[99] Pham DT, Lee TH, Luong DH, Yao F, Ghosh A, Le VT, Kim TH, Li B, Chang J, Lee YH. Carbon nanotube-bridged graphene 3D building blocks for ultrafast compact supercapacitors. ACS Nano. 2015;**9**:2018-2027. DOI: 10.1021/nn507079x

[100] Yu D, Dai L. Self-assembled graphene/carbon nanotube hybrid films for supercapacitors. The Journal of Physical Chemistry Letters. 2010;**1**:467-470. DOI: 10.1021/jz9003137

[101] Jha N, Ramesh P, Bekyarova E, Itkis ME, Haddon RC. High energy density supercapacitor based on a hybrid carbon nanotube-reduced graphite oxide architecture. Advanced Energy Materials. 2012;**2**:438-444. DOI: 10.1002/aenm.201100697

[102] Du F, Yu D, Dai L, Ganguli S, Varshney V, Roy AK. Preparation of tunable 3D pillared carbon nanotube-graphene networks for high-performance capacitance. Chemistry of Materials. 2011;**23**:4810-4816. DOI: 10.1021/cm2021214

[103] Huang Z-D, Zhang B, S-W O, Zheng Q-B, Lin X-Y, Yousefi N, Kim J-K. Self-assembled reduced graphene oxide/carbon nanotube thin films as electrodes for supercapacitors. Journal of Materials Chemistry. 2012;**22**:3591-3599. DOI: 10.1039/c2jm15048d

[104] Byon HR, Gallant BM, Lee SW, Shao-Horn Y. Role of oxygen functional groups in carbon nanotube/graphene freestanding electrodes for high performance lithium batteries. Advanced Functional Materials. 2013;**23**:1037-1045. DOI: 10.1002/adfm.201200697

[105] Zheng Q, Cai Z, Ma Z, Gong S. Cellulose nanofibril/reduced graphene oxide/carbon nanotube hybrid aerogels for highly flexible and all-solid-state supercapacitors. ACS Applied Materials & Interfaces. 2015;**7**:3263-3271. DOI: 10.1021/am507999s

[106] Wang Q, Yan J, Wang Y, Ning G, Fan Z, Wei T, Cheng J, Zhang M, Jing X. Template synthesis of hollow carbon spheres anchored on carbon nanotubes for high rate performance supercapacitors. Carbon. 2013;**52**:209-218. DOI: 10.1016/j.carbon.2012.09.022

[107] Lin J, Zhang C, Yan Z, Zhu Y, Peng Z, Hauge RH, Natelson D, Tour JM. 3-dimensional graphene carbon nanotube carpet-based microsupercapacitors with high electrochemical performance. Nano Letters. 2013;**13**:72-78. DOI: 10.1021/nl3034976

[108] Sivakkumar SR, Kim WJ, Choi J-A, MacFarlane DR, Forsyth M, Kim D-W. Electrochemical performance of polyaniline nanofibres and polyaniline/multi-walled carbon nanotube composite as an electrode material for aqueous redox supercapacitors. Journal of Power Sources. 2007;**171**:1062-1068. DOI: 10.1016/j.jpowsour.2007.05.103

[109] Ghosh A, Lee YH. Carbon-based electrochemical capacitors. Chemistry & Sustainability Energy & Materials. 2012;**5**:480-499. DOI: 10.1002/cssc.201100645

[110] Peng C, Jin J, Chen GZ. A comparative study on electrochemical co-deposition and capacitance of composite films of conducting polymers and carbon nanotubes. Electrochimica Acta. 2007;**53**:525-537. DOI: 10.1016/j.electacta.2007.07.004

[111] Gupta V, Miura N. Polyaniline/single-wall carbon nanotube (PANI/SWCNT) composites for high performance supercapacitors. Electrochimica Acta. 2006;**52**:1721-1726. DOI: 10.1016/j.electacta.2006.01.074

[112] Zhang J, Kong L-B, Wang B, Luo Y-C, Kang L. In-situ electrochemical polymerization of multi-walled carbon nanotube/polyaniline composite films for electrochemical supercapacitors. Synthetic Metals. 2009;**159**:260-266. DOI: 10.1016/j.synthmet.2008.09.018

[113] Canobre SC, Almeida DAL, Fonseca CP, Neves S. Synthesis and characterization of hybrid composites based on carbon nanotubes. Electrochimica Acta. 2009;**54**:5383-6388. DOI: 10.1016/j.electacta.2009.06.002

[114] Paul S, Lee Y-S, Choi J-A, Kang YC, Kim D-W. Synthesis and electrochemical characterization of polypyrrole/multi-walled carbon nanotube composite electrodes for supercapacitor applications. Bulletin of the Korean Chemical Society. 2010;**31**:1228-1323. DOI: 10.5012/bkcs.2010.31.5.1228

[115] Branzoi V, Branzoi F, Pilan L. Electrochemical fabrication and capacitance of composite films of carbon nanotubes and polyaniline. Surface & Interface Analysis. 2009;**42**:1266-1270. DOI: 10.1002/sia.3387

[116] Chen X, Paul R, Dai L. Carbon-based supercapacitors for efficient energy storage. National Science Review. 2017;**4**:1-37. DOI: 10.1093/nsr/nwx009

[117] Teresawa N, Asaka K. High-performance PEDOT:PSS/single-walled carbon nanotube/ionic liquid actuators combining electrostatic double-layer and faradaic capacitors. Langmuir. 2016;**32**:7210-7218. DOI: 10.1021/acs.langmuir.6b01148

[118] Peng C, Zhang S, Jewell D, Chen GZ. Carbon nanotube and conducting polymer composites for supercapacitors. Progress in Natural Science. 2008;**18**:777-788. DOI: 10.1016/j.pnsc.2008.03.002

[119] Grądzka E, Winkler K, Borowska M, Plonska-Brzezinka ME, Echegoyen L. Comparison of the electrochemical properties of thin films of MWCNTs/C_{60}-Pd, SWCNTs/C_{60}-Pd and ox-CNOs/C_{60}-Pd. Electrochimica Acta. 2013;**96**:274-284. DOI: 10.1016/j.electacta.2013.02.035

[120] Lee KYT, Shi HTH, Lian K, Naguib HE. Flexible multiwalled carbon nanotubes/conductive polymer composite electrode for supercapacitor applications. Smart Materials and Structures. 2015;**24**:1-17. DOI: 10.1088/0964-1726/24/11/115008

[121] Kausar A. Performance of polyaniline doped carbon nanotube composite. American Journal of Polymer Science and Engineering. 2017;**5**:43-54

[122] Raicopol M, Pruna A, Pilan L. Supercapacitance of single-walled carbon nanotubes-polypyrrole composites. Journal of Chemistry. 2013:1-7. DOI: 10.1155/2013/367473

[123] Maubane M, Mamo MA, Nxumalo EN, van Otterlo WAL, Coville NJ. Tubular shaped composites made from polythiophene covalently linked to Prato functionalized N-doped carbon nanotubes. Synthetic Metals. 2012;**162**:2307-2315. DOI: 10.1016/j.synthmet.2012.10.020

[124] Wei D, Kvarnstrom C, Lindfors T, Ivaska A. Electrochemical functionalization of single walled carbon nanotubes with polyaniline in ionic liquids. Electrochemistry Communications. 2007;**9**:206-210. DOI: 10.1016/j.elecom.2006.09.008

[125] Angeles Herranz M, Martin N. Noncovalent functionalization of carbon nanotubes. In: Guldi DM, Martin N, editors. Carbon Nanotubes and Related Structures. Synthesis, Characterization, Functionalization, and Application. Weinheim: Wiley-VCH Verlag GmbH & Co. KgaA 2010. P. 103-134. DOI: 10.1002/9783527629930.ch5

[126] Liu L, Yoo S-H, Park S. Composite materials with MWCNTs and conducting polymer nanorods and their application as supercapacitors. Journal of Electrochemical Science and Technology. 2010;**1**:25-30. DOI: 10.5229/JECST.2010.1.1.025

[127] Frackowiak E, Khomenko V, Jurewicz K, Lota K, Beguin F. Supercapacitors based on conducting polymers/nanotubes composites. Journal of Power Sources. 2006;**153**:413-418. DOI: 10.1016/j.jpowsour.2005.05.030

[128] Cheng Q, Tang J, Shinya N, Qin L-C. Polyaniline modified graphene and carbon nanotube composite electrode for asymmetric supercapacitors of high energy density. Journal of Power Sources. 2013;**241**:423-428. DOI: 10.1016/j.jpowsour.2013.04.105

[129] Plonska-Brzezinska ME, Breczko J, Palys B, Echegoyen L. The electrochemical properties of nanocomposite films obtained by chemical in situ polymerization of aniline and carbon nanostructures. A European Journal of Chemical Physics and Phyical Chemistry. 2013;**14**:116-124. DOI: 10.1002/cphc.201200759

[130] Khomenko V, Frackowiak E, Beguin F. Determination of the specific capacitance of conducting polymer/nanotubes composite electrodes using different cell configurations. Electrochimica Acta. 2005;**50**:2499-2506. DOI: 10.1016/j.electacta.2004.10.078

[131] Aphale A, Maisuria K, Mahapatra MK, Santiago A, Singh P, Patra P. Hybrid electrodes by in-situ integration of graphene and carbon-nanotubes in polypyrrole for supercapacitors. Scientific Reports. 2015;**5**(14445):1-8. DOI: 10.1038/srep14445

[132] Zhou C, Kumar S, Doyle CD, Tour JM. Functionalized single wall carbon nanotubes treated with pyrrole for electrochemical supercapacitor membranes. Chemistry of Materials. 2005;**17**:1997-2002. DOI: 10.1021/cm047882b

[133] Liu J, Sun J, Gao L. A promising way to enhance the electrochemical behavior of flexible single-walled carbon nanotube/polyaniline composite films. Journal of Physical Chemistry C. 2010;**114**:19614-19620. DOI: 10.1021/jp1092042

[134] Mikhaylova AA, Tusseeva EK, Mayrova NA, Rychagov AY, Volfkovich YM, Krestinin AV, Khazova O. Single-walled carbon nanotubes and their composites with polyaniline. Structure, catalytic and capacitive properties as applied to fuel cells and supercapacitors. Electrochimica Acta. 2011;**56**:3656-3665. DOI: 10.1016/j.electacta.2010.07.021

[135] Yang P, Chen Y, Yu X, Qiang P, Wang K, Cai X, Tan S, Liu P, Song J, Mai W. Reciprocal alternate deposition strategy using metal oxide/carbon nanotube for positive and negative electrodes of high-performance supercapacitors. Nano Energy. 2014;**10**:108-116. DOI: 10.1016/j.nanoen.2014.08.018

[136] Wu M-S. Electrochemical capacitance from manganese oxide nanowire structure synthesized by cyclic voltammetric electrodeposition. Applied Physics Letters. 2005;**87**:153102-1-153102-3. DOI: 10.1063/1.2089169

[137] Devaraj S, Munichandraiah N. Effect of crystallographic structure of MnO_2 on its electrochemical capacitance properties. Journal of Physical Chemistry C. 2008;**112**:4406-4417. DOI: 10.1021/jp7108785

[138] Jiang H, Zhao T, Ma J, Yan C, Li C. Ultrafine manganese dioxide nanowire network for high-performance supercapacitors. Chemical Communications. 2011;**47**:1264-1266. DOI: 10.1039/c0cc04134c

[139] Yan J, Khoo E, Sumboja A, Lee PS. Facile coating of manganese oxide on tin oxide nanowires with high-performance capacitive behavior. ACS Nano. 2010;**4**:4247-4255. DOI: 10.1021/nn100592d

[140] Jiang R, Huang T, Liu J, Zhuang J, Yu A. A novel method to prepare nanostructured manganese dioxide and its electrochemical properties as a supercapacitor electrode. Electrochimica Acta. 2009;**54**:3047-3052. DOI: 10.1016/j.electacta.2008.12.007

[141] Beadrouet E, Le Gal La Salle A, Guyomard D. Nanostructured manganese dioxides: Synthesis and properties as supercapacitor electrode materials. Electrochimica Acta. 2009;**54**:1240-1248. DOI: 10.1016/j.electacta.2008.08.072

[142] Wei W, Cui X, Chen W, Ivey DG. Electrochemical cyclability mechanism for MnO_2 electrodes utilized as electrochemical supercapacitors. Journal of Power Sources. 2009;**186**:843-550. DOI: 10.1016/j.jpowsour.2008.10.058

[143] Xia H, Wang Y, Lin J, Lu L. Hydrothermal synthesis of MnO_2/CNT nanocomposite with a CNT core/porous MnO_2 sheath hierarchy architecture for supercapacitors. Nanoscale Research Letters. 2012;**7**(33):1-10. DOI: 10.1186/1556-276X-7-33

[144] Kang J, Hirata A, Kang L, Zhang X, Hou Y, Chen L, Li C, Fujita T, Akagai K, Chen M. Enhanced supercapacitor performance of MnO_2 by atomic doping. Angewandte Chemie. 2013;**125**:1708-1711. DOI: 10.1002/ange.201208993

[145] Yan J, Fan Z, Wei T, Cheng J, Shao B, Wang K, Song L, Zhang M. Carbon nanotube/MnO_2 composites synthesized by microwave-assisted method for supercapacitors with high power and energy densities. Journal of Power Sources. 2009;**194**:1202-1207. DOI: 10.1016/j.jpowsour.2009.06.006

[146] Ma S-B, Nam K-W, Yoon W-S, Yang X-Q, Ahn K-Y, Oh K-H, Kim K-B. A novel concept of hybrid capacitor based on manganese oxide materials. Electrochemistry Communications. 2007;**9**:2807-2811. DOI: 10.1016/j.elecom.2007.09.015

[147] Xie X, Gao L. Characterization of a manganese dioxide/carbon nanotube composite fabricated using an in situ coating method. Carbon. 2007;**45**:2365-2373. DOI: 10.1016/j.carbon.2007.07.014

[148] Jin X, Zhou W, Zhang S, Chen GZ. Nanoscale microelectrochemical cells on carbon nanotubes. Small. 2007;**3**:1513-1517. DOI: 10.1002/smll.200700139

[149] Chen P-C, Shen G, Shi Y, Zhou C. Preparation and characterization of flexible asymmetric supercapacitors based on transition-metal-oxide nanowire/single-walled carbon nanotube hybrid thin-film electrodes. ACS Nano. 2010;**4**:4403-4411. DOI: 10.1021/nn100856y

[150] Zhang H, Gao G, Wang Z, Yang Y, Shi Z, Gu Z. Growth of manganese oxide nanoflowers on vertically-aligned carbon nanotube arrays for high-rate electrochemical capacitive energy storage. Nano Letters. 2008;**8**:2664-2668. DOI: 10.1021/nl800925j

[151] Bi R-R, X-L W, Cao F-F, Jiang L-Y, Guo Y-G, Wan L-J. Highly dispersed RuO_2 nanoparticles on carbon nanotubes: Facile synthesis and enhanced supercapacitance performance. Journal of Physical Chemistry C. 2010;**114**:2448-2451. DOI: 10.1021/jp9116563

[152] Chen P, Chen H, Qiu J, Zhou C. Inkjet printing of single-walled carbon nanotube/RuO_2 nanowire supercapacitors on cloth fabrics and flexible substrates. Nano Research. 2010;**3**:594-603. DOI: 10.1007/s12274-010-0020-x

[153] Reddy ALM, Ramaprabhu S. Nanocrystalline metal oxides dispersed multiwalled carbon nanotubes as supercapacitor electrodes. Journal of Physical Chemistry C. 2007;**111**:7727-7734. DOI: 10.1021/jp069006m

[154] Yan S, Wang HW, Qu P, Zhang Y, Xiao Z. RuO_2/carbon nanotubes composites synthesized by microwave-assisted method for electrochemical supercapacitor. Synthetic Metals. 2009;**159**:158-161. DOI: 10.1016/j.synthmet.2008.07.024

[155] Lee JY, Liang K, An KH, Lee YH. Nickel oxide/carbon nanotubes nanocomposite for electrochemical capacitance. Synthetic Metals. 2005;**150**:153-157. DOI: 10.1016/j.synthmet.2005.01.016

[156] Gao B, Yuan B-Z, L-H S, Chen L, Zhang X-G. Nickel oxide coated on ultrasonically pretreated carbon nanotubes for supercapacitor. Journal of Solid State Electrochemistry. 2009;**13**:1251-1257. DOI: 10.1007/s10008-008-0658-4

[157] Zhao X, Johnston C, Grant PS. A novel hybrid supercapacitor with a carbon nanotube cathode and an iron oxide/carbon nanotube composite anode. Journal of Materials Chemistry. 2009;**19**:8755-8760. DOI: 10.1039/b909779a

[158] Shan Y, Gao L. Formation and characterization of multi-walled carbon nanotubes/Co_3O_4 nanocomposites for supercapacitors. Materials Chemistry and Physics. 2007;**103**:206-210. DOI: 10.1016/j.matchemphys.2007.02.038

[159] Aravinda LS, Nagaraja KK, Udaya Bhat K, Bhat BR. Magnetron sputtered MoO_3/carbon nanotube composite electrodes for electrochemical supercapacitor. Journal of Electroanalytical Chemistry. 2013;**699**:28-32. DOI: 10.1016/j.jelechem.2013.03.022

[160] Sathiya M, Prakash AS, Ramesha K, Tarascon J-M, Shukla AK. V_2O_5-anchored carbon nanotubes for enhanced electrochemical energy storage. Journal of the American Chemical Society. 2011;**133**:16291-16299. DOI: 10.1021/ja207285b

[161] Enterria M, Goncalves AG, Pereira MFR, Martins JI, Figueiredo JL. Electrochemical storage mechanisms in non-stoichiometric cerium oxide/multiwalled carbon nanotube composites. Electrochimica Acta. 2016;**209**:25-35. DOI: 10.1016/j.electacta.2016.05.036

[162] Wang X, Han X, Lim M, Singh N, Gan NS, Jan M, Lee PS. Nickel cobalt oxide-single wall carbon nanotube composite material for superior cycling stability and high-performance supercapacitor application. Journal of Physical Chemistry C. 2012;**116**:12448-12454. DOI: 10.1021/jp3028353

[163] Chiang DNK, Lim SS, Peng C. Novel bimetallic tin-manganese oxides/carbon nanotube nanocomposite and their charge storage properties. Journal—the Institution of Engineers, Malysia. 2014;**75**(1):24-39

[164] Jang JH, Kato A, Machida K, Naoi K. Supercapacitor performance of hydrous ruthenium oxide electrodes prepared by electrophoretic deposition. Journal of the Electrochemical Society. 2006;**153**:A321-A328. DOI: 10.1149/1.2138672

[165] Tao T, Zhang L, Jiang H, Li C. Functional carbon nanotube/mesoporous carbon/MnO_2 hybrid network for high-performance supercapacitors. Journal of Nanomaterials. 2014;**2014**:1-6. DOI: 10.1155/2014/568561

[166] Bordjiba T, Mohamedi M. Molding versus dispersion: Effect of the preparation procedure on the capacitive and cycle life of carbon nanotubes aerogel composites. Journal of Solid State Electrochemistery. 2011;**15**:765-771. DOI: 10.1007/s10008-010-1155-0

[167] Kim SJ, Hwang SW, Hyun SH. Preparation of carbon aerogel electrodes for supercapacitor and their electrochemical characteristics. Journal of Materials Science. 2005;**40**:725-731. DOI: 10.1007/s10853-005-6313-x

[168] Kim C-Y, Jang AR, Cho Y. Optimization of pore structures and supercapacitor properties of carbon aerogel electrodes. Asian Journal of Chemistry. 2012;**24**:4205-4212

[169] Macias C, Rasines G, Garcia TE, Zafra MC, Lavela P, Tirado JL, Ania CO. Synthesis of porous and mechanically compliant carbon aerogels using conductive and structural additives. Gels. 2016;**2**:1-16. DOI: 10.3390/gels2010004

[170] Bordjiba T, Mohamedi M, Dao LH. Novel binderless nanostructured carbon nanotubes —carbon aerogel composites for electrochemical double layer capacitors. ECS Transactions. 2008;**6**:183-189. DOI: 10.1149/1.2943237

[171] Bordjiba T, Mohamedi M, Dao LH. Charge storage mechanism of binderless nanocomposite electrodes formed by dispersion of CNTs and carbon aerogels. Journal of the Electrochemical Society. 2008;**155**:A115-A124

[172] Bordjiba T, Mohamedi M, Dao LH. Synthesis and electrochemical capacitance of binderless nanocomposite electrodes formed by dispersion of carbon nanotubes and carbon aerogels. Journal of Power Sources. 2007;**172**:991-998. DOI: 10.1016/j.jpowsour.2007.05.011

[173] Hao P, Zhao Z, Li L, Tuan C-C, Li H, Sang Y, Jiang H, Wong PC, Liu H. The hybrid nanostructure of $MnCo_2O_{4.5}$ nanoneedle/carbon aerogel for symmetric supercapacitors with high energy density. Nanoscale. 2015;**7**:14401-14412. DOI: 10.1039/c5nr04421a

[174] Annamalai KP, Fathy NA, Tao Y. Synthesis and capacitance performance of phosphorous-enriched carbon xerogel. Journal of Sol-Gel Science and Technology. DOI: 10.1007/s10971-017-4452-6

[175] Lufrano F, Staiti P, Calvo EG, Juarez-Perez EJ, Menendez JA, Arenillas A. Carbon xerogel and manganese oxide capacitive materials for advanced supercapacitors. International Journal of Electrochemical Science. 2011;**6**:596-612

[176] Liu X, Li S, Mi R, Liu L-M, Cao H, Lau W-M, Liu H. Porous structure design of carbon xerogels for advanced supercapacitor. Applied Energy. 2015;**153**:32-40. DOI: 10.1016/j.apenergy.2015.01.141

[177] Ordenanan-Martinez AS, Rincon ME, Vargas M, Estrada-Vargas A, Casillas N, Barcena-Sato M, Ramos E. Carbon nanotubes/carbon xerogel-nafion electrodes: A comparative study of preparation methods. Journal of Solid State Electrochemistry. 2012;**16**:3777-3782. DOI: 10.1007/s10008-012-1819-z

[178] Fernandez PS, Castro EB, Real SG, Visintin A, Arenillas A, Calvo EG, Juarez-Perez EJ, Menendez AJ, Martins ME. Electrochemical behavior and capacitance properties of carbon xerogel/multiwalled carbon nanotubes composites. Journal of Solid State Electrochemistry. 2012;**16**:1067-1076. DOI: 10.1007/s10008-011-1487-4

Chapter 10

Studies of Nanocomposites of Carbon Nanotubes and a Negative Dielectric Anisotropy Liquid Crystal

Parvathalu Kalakonda and Germano S Iannacchione

Additional information is available at the end of the chapter

http://dx.doi.org/10.5772/intechopen.73391

Abstract

The complex specific heat is reported over a wide temperature range for a negative dielectric anisotropy alkoxyphenylbenzoate liquid crystal (9OO4) and carbon nanotube (CNT) composites as a function of carbon nanotube concentration. It has been observed that the combination of nanotubes (CNT) and liquid crystal (LC) provides a very useful way to align CNTs and also dramatically increases the order in the liquid crystal performance, which is useful in liquid display technology (LCD). The calorimetric scans were performed between 25 and 95°C temperatures, first allowed cooling and then heating for CNT concentration ranging from φ_w = 0 to 0.2 wt%. All 9OO4/CNT composite mesophases have transition temperatures about 1 K higher and a crystallization temperature 4 K higher as compared to the pure 9OO4 liquid crystal. A strongly first-order specific heat feature is observed, which is 0.5 K higher than in the pure 9OO4. The transition enthalpy for the composite mesophases is observed 10% lower than the pure liquid crystal. We interpret that these results arising from the LC-CNT surface interaction lead to pinning orientational order uniformly along the CNT, without pinning the position of the 9OO4 molecule. These effects of incorporating CNTs with LC are likely due to elastic coupling between CNT and LC. These effects of incorporating CNTs into LCs are likely due to an "anisotropic orientational" coupling between CNT and LC, the change in the elastic properties of composites and thermal anisotropic properties of the CNTs.

Keywords: carbon nanotubes, liquid crystal, chirality

1. Introduction

Composites of nanoparticles with liquid crystal represent a unique physical system, where properties of the constituents fully mix and may lead to show new behavior. As of now,

traditional composites are well understood, the superposition of component of the composites interfacial interactions play a very important role in holding the composite together. As the filler size shrink, the surface area begins to dominate, leading to unique behavior of the composites. Carbon nanotubes (CNT) and liquid crystals (LC) are good examples of such components. For large number of applications, the challenge lies in the alignment and ordering of CNTs to take advantages of their highly anisotropic thermal characteristics. Carbon nanotubes have emerged as a new category of nanosized particles for incorporation into different liquid crystal systems, attracting favorable interest from both basic level science research and industrial applications [1]. As a result of the exceptional properties of carbon nanotubes, the novel materials can be envisioned that exhibit property enhancements at lower concentration than in conventional composite technology [2]. In the research area of polymer nanocomposites, reported property enhancements include enhanced mechanical performance [3, 4], higher thermal and electrical conductivity [5–7], and increased property of crystallization rate [8–12]. In addition to CNT's thermal, mechanical, and magnetic properties [13–22], their unique electrical properties make them potentially very useful materials for making nanoflexible electronic devices [2, 23–26]. Liquid crystals [27–29] are anisotropic fluids that exhibit thermodynamically stable phases between an isotropic liquid and a full, three-dimensionally ordered solid. In the nematic (N) phase, LCs show orientational order, and in the smectic-A (SmA) phase, the rod-like molecules are arranged in layers with their long axes on average, normal to the layer planes. They show both orientational and partial translational order characterized by a quasi-1-d density wave. The smectic phases incorporate the structures of materials with diverse symmetry groups [30], such as that of smectic-C (SmC), which has the layer tilting away from the director. In smectic-B (SmB) phase, the molecules show short-range hexagonal ordering within the layers but not from layer to layer, and it shows a short or long-range translational order. Higher order, lower symmetry, liquid crystalline materials have been studied because three of their industrial applications as well as important physical models of self-assembly [29, 30]. When CNTs are dispersed in a liquid crystal, they can modify the physical properties and hence the phase behavior of the nanocomposite. Due to the specific surface anchoring between nanoparticle and LC, the nanoparticles can act either as nucleation sites for a given type of order or as disordering sites that stabilize the isotropic phase [31, 32]. However, if the local ordering effects of CNT surfaces are randomly arranged, this can lead to a random-field effect [33] and an overall disordering of the composites. Investigations have been made on liquid crystal nanocomposites using optical microscopy and differential scanning calorimetry (DSC), finding an enhancement of the isotropic to nematic phase transition temperature and revealing a "chimney type" phase diagram over a narrow range of CNT weight percent between 0.001 and 0.002 wt% [34]. In fact, researchers found that the addition of CNT into LC increases the clearing point of LCs because of the strong attraction of CNT and LC [35]. However, other studies have found disordering effects of CNT on LC phase transitions [31]. Other work has shown improved electro-optical switching properties of nanocomposites in thermotropic or lyotropic liquid crystals and CNTs [36–41]. In liquid crystals, the effect of carbon nanotubes on the phase ordering of LC/CNT composites depends on the surface coupling of the molecule and graphene surface, as well as the distribution of those surfaces. In fact, it is also observed that aligned CNTs can cause an increase of the orientational order in the LC [42, 43]. Such composites have been proposed as memory devices

by exploiting their nanoelectromechanical properties [44, 45]. Recently, investigations on LC/CNT composites have shown that the CNTs can induce chirality in the bulk LC [46–48]. Most of the recent studies were focused on the nematic ordering and the isotropic (I) to nematic (N) phase transition behavior in LC/CNT composite scaffolds. In this study, we focus the phase transition behavior of the liquid crystal alkoxyphenylbenzoate (9OO4) doped with multiwall carbon nanotubes as a function of CNT weight percent. The incorporation of nanotubes in pure 9OO4 reveals that all mesophase transition temperatures and the crystallization transition temperatures shift upward. These results suggest that the interactions between molecular structure, dipole moment of liquid crystal, and graphene-like surface can allow the random dispersion of CNTs to promote both orientational and positional order. We interpret this effect in terms of pinning the director at the CNT surface with bulk-like scalar order parallel to the CNT long axis over distances that span multiple nematic domains while allowing the LC molecule to slide along the surface, accommodating four various positional orders. Our presentation is organized as follows: Following this introduction, Section 2 describes the preparation of the sample and modulated differential scanning calorimetry procedure, as well as the electroclinic procedure. Section 3 describes the calorimetric and electroclinic results of all phase transitions in the 9OO4/CNT system, Section 4 provides a discussion, and Section 5 provides conclusions of our work and future directions.

2. Methodology

2.1. Material and sample preparation

The liquid crystal 9OO4 is a phenyl benzoate containing an oxoester linkage group with two alkoxy end groups (see **Figure 1**). The molecular mass for 9OO4 is Mw = 424.66 g/mol with an extended molecular structure approximately 4 nm long and 0.8 nm wide. For 9OO4, modeling suggests that due to the carbon = oxygen double bond in the oxoester linking group, the effective dipole moment of 9OO4 is approximately perpendicular to the long axis and average plane of the phenyl rings. The multiwall CNTs were obtained from Nanostructured and Amorphous Materials, Inc., and have an average outer diameter of 8–15 nm, an inner diameter 3–5 nm, a length of 500–2000 nm, and a distribution of different chiral structures [46]. To reduce aggregation, a small amount of CNTs were dispersed first in acetone and shaken using a mixer for 30 min, followed by sonication for 3 hours. The 9OO4 was added to the acetone + CNT mixture to

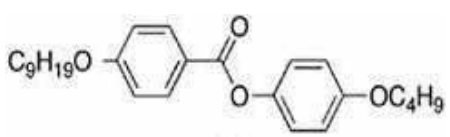

Figure 1. The member of the 4-n-alkoxy phenyl-40-m-alkoxy benzoate homolog series denoted nOOm. In this study, n = 9 and m = 4 (9OO4). Note that the negative dielectric anisotropy is due to the O-C=O group in the benzoate group linking the two phenyl rings. Molecular modeling suggests that the effective dipole moment of about 2.5 is pointing approximately perpendicular to the twisted phenyl rings, essentially out of the page [58].

achieve the desired final weight percent φ_w of CNTs. The mixture was then sonicated for 3 hours to facilitate good dispersion. Finally, the acetone was evaporated slowly and then allowed to degass under a modest vacuum in the isotropic phase of 9OO4 at ~364 K (or 90°C) for about 2 hours. Microbalance is used to mass the mixture of composites to ensure complete removal of acetone before sealed in the experimental sample cell. This process was continuously repeated to prepare 0 (pure 9OO4), 0.008, 0.010, 0.025, and 0.200 wt% CNT samples and tested uniform dispersion with the help of microscopy. On cooling, pure 9OO4 exhibits the phase sequence I - 87 - N - 73 - SmA - 62 - SmC - 50 - SmB - 35 - K (crystal), where temperatures are in Celsius; while on heating, melting occurs nearly 25 K higher, which is followed by a specific heat peak almost 2 K higher than the melting peak before entering the SmA phase. Further heating yields the N and I phases. Based on the imaginary specific heat $\Delta C''_p$ behavior, the I-N transition is weakly first order, the N-SmA is continuous, the SmA-SmC is continuous, the SmC-SmB is first order, and the SmB-K is strongly first order. The initial melting from crystal is strongly first order followed by a second, weakly first order, Cp feature that indicates the presence of a narrow temperature range having a smectic-like texture, as seen under polarizing microscopy (labeled SmX) between the K and SmA phase on heating [49]. Unfortunately, the polarizing microscope images could not distinguish which type of smectic is the SmX region.

2.2. Modulated differential scanning calorimetry (MDSC)

Modulated differential scanning calorimetry (MTDSC/MDSC) allows for the simultaneous measurement of the evolution of both the heat flow and heat capacity. It is essentially the combination of traditional ac-calorimetry and DSC. This method allows for measuring the total heat flow of material, as well as its nonreversible and reversible heat capacities. A detailed description of the MDSC method can be found elsewhere [50–57]. MDSC experiments were performed using a Model Q200 from TA Instruments, USA. Prior to all measurements, temperature calibration was done with a sapphire disc, under the same experimental conditions used for all 9OO4/CNT samples. The analysis method used to extract the complex specific heat is based on linear response theory [50, 58]. In general, a temperature oscillation is described as $T(t) = T_0 + T'_0\, t + A_T \sin(\omega t)$, where T_0 is the initial temperature at time t = 0, T indicates the absolute temperature at time t, T'_0 represents the baseline temperature scan rate, A_T is the temperature amplitude, and ω ($\omega = 2\pi f$) is the angular frequency of the temperature modulation. The rate of temperature is also time dependent and is given by equation $T'(t) = dT/dt = T'_0 + Aq\cos(\omega t)$, where Aq represents the amplitude of temperature modulation r ($Aq = \omega AT$). Since the applied temperature rate consists of two components, T_0 the underlying rate and $Aq\cos(\omega t)$ the periodic rate. The measured heat flow H_F can also be separated into two components in response to these temperature rates. The periodic component can be described by $HFq = A_{HF} \cos(\omega t - \phi)$, where A_{HF} represents the amplitude of the heat flow and ϕ is the phase angle between heat flow and temperature rate. The absolute value of the complex specific heat is written as $C * p = A_{HF}/mAq$, where 'm' is the mass of the sample. The phase angle ϕ requires a small calibration to account for finite six thermal conductivities of the sample and cell, see Ref. [57]. The real part of specific $C'p$ and imaginary part of specific heat C''_p are then given by $C' p = C * p \cos(\phi)$ and $C''p = C * p \sin(\phi)$, which allows for a consistent definition for the complex specific heat. Typically, under equilibrium conditions, $C'' p = 0$ after ϕ calibration. The appearance of a peak-like nonzero C''_p feature commensurate with

a peak in the real part of the specific heat indicates that this feature is a first-order transition and involves a latent heat. The excess specific heats were determined in order to isolate the contribution from the various transitions. A linear baseline was used over the entire temperature scan range in order to determine $\Delta Cp = C_p - C_{baseline}$ for both the real and imaginary parts of specific heat components, though C″p always exhibited a very shallow linear baseline that was very close to zero, indicating near equilibrium conditions for the experimental parameters used in this work. For specific heat features that are close in temperature, the wing of one peak is subtracted from the lower specific heat peak in order to isolate the excess specific heat of the lower temperature transition, denoted as $\delta Cp = \Delta Cp - C_{wing}$, where C_{wing} is a mimic function (polynomial) of the underlying wing. This calculation was only applied to the real component of the specific heat. The particular transition enthalpy component is simply the integration of the excess specific heat component over a consistent temperature range. Finally, for first-order transitions, the transition temperature (T_{IN}, T_{CB}, T_{BK}, T_{KX}, and T_{XA}) is determined as the highest temperature of the two-phase coexistence region indicated by the onset of nonzero values of ΔC″ p. For continuous transitions, the transition temperature is taken as the ΔC′ p peak temperature. We have tested quasi-equilibrium parameter such as scan rate, temperature amplitude, and modulation time period by varying different values above and below specified values of nearly equilibrium.

2.3. Electroclinic measurements

Details of the electroclinic effect experimental set up are described elsewhere [59]. Briefly, a cell of thickness $d = 7.7 \pm 0.1$ μm was constructed from a pair of indium-tin-oxide–coated glass slides covered with a rubbed polyimide alignment layer. The cell was filled with 0.05 wt% CNT in 9OO4, which aligned in the planar direction. Light polarized at 22.5° relative to the director orientation was incident on the cell, subsequently passing through the cell, an analyzer, and into a detector. On applying an ac-electric field E at frequency f = 25 Hz across the cell, the director rotated in the cell's plane by an angle θ [$\propto$ E], resulting in an ac intensity component Iac at frequency f, as measured by a lock-in amplifier. It can be shown [59] that the ratio Iac/4Idc corresponds to the spatially averaged rms director rotation θ, where Idc is the dc intensity measured at the detector. At each temperature, the electric field was ramped from 0 to 2.6 × 106 V/m (rms) over a time 450 s, and the results were fitted to a straight line. The electroclinic coefficient is defined as $ec \equiv d\theta/dE$.

3. Results

For the pure 9OO4, calorimetry shows that the I-N phase transition occurs at T_{IN} = 86.23°C, the N-SmA phase transition at T_{NA} = 71.49°C, the SmA-SmC phase transition at T_{AC} = 61.5°C, the SmC-SmB phase transition at T_{CB} = 49.38°C, and SmB-Cry phase transition at TBK = 35.3°C in good agreement with literature values [49]. All the phase transitions are characterized by a distinct C_p peaks at a nearly equilibrium scan rate of ±0.3 K/min (**Figures 2–6**). The strongly first-order melting followed by a second first-order C_p feature indicates the presence of an intermediate phase (labeled SmX) between K and SmA on heating. The transition temperatures and enthalpies of pure 9OO4 on cooling and heating are presented in **Tables 1** and **2**.

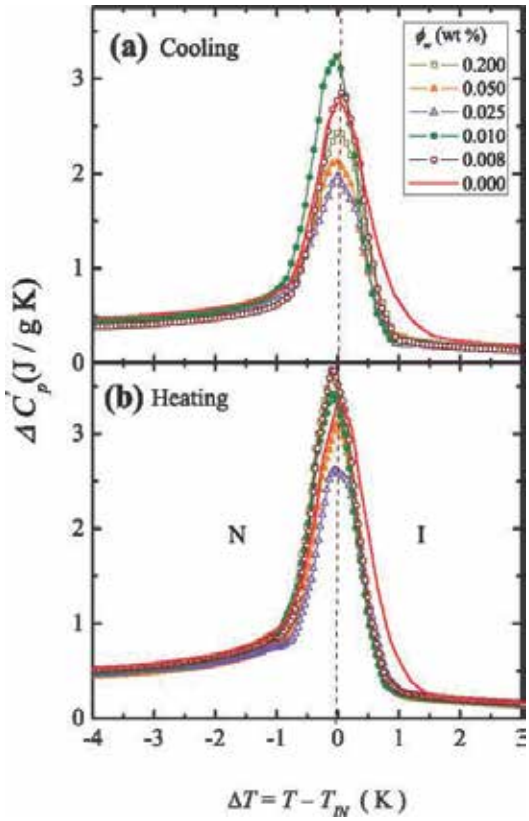

Figure 2. (a) Excess real part specific heat associated with the I-N phase transition as function of temperature about T_{IN} on cooling. The definitions of the symbols are indicated in the inset. (b) Excess real part of specific heat associated with the I-N phase transition as function of temperature about T_{IN} on heating.

For the I-N phase transition, the excess real specific heat signatures as a function of temperature about T_{IN} for pure 9OO4 and 9OO4/CNT composite samples are shown in **Figure 2**. The ΔC'p of 9OO4/CNT for the I-N transition phase is steeper and narrower than in the pure 9OO4, with the peak maximum nearer the high-temperature side of the coexistence region. The ΔC'p and C"p behavior are consistent on heating and cooling, as well as being reproducible after multiple thermal cycles. The ΔC'p wings above and below the I-N transition match each other and that in pure 9OO4 on heating and cooling. The ΔC'p peak height for cooling and heating scans within the two-phase I + N coexistence region is about the same as that in pure 9OO4 up to φ_w = 0.010, decreasing markedly for the 0.025 sample and then rising with increasing φ_w up to the highest CNT content sample of 0.20 wt% studied.

For the N-SmA phase transition, the specific heat δC'p on cooling and heating as a function of temperature about T_{NA} is shown in **Figure 3** for bulk 9OO4 and 9OO4/CNT composite samples. For all samples, the N-SmA phase transition does not exhibit any special feature in the case of imaginary specific heat, indicating an apparent absence of latent heat, and indicates the continuous nature of the transition. The δC'p of the N-SmA transition for the composite 9OO4/CNT

http://dx.doi.org/10.5772/intechopen.73391

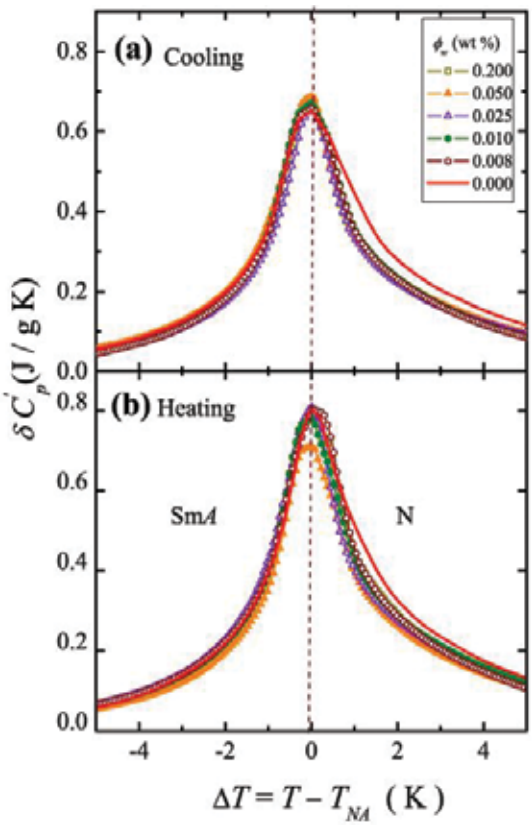

Figure 3. (a) The excess real part of specific heat associated with the N-SmA phase transition as function of temperature about T_{NA} on cooling. (b) The excess real part specific heat associated with the N-SmA phase transition as function of temperature about T_{NA} on heating. The definitions of the symbols are indicated in the inset.

samples overlay each other for all CNT concentrations φ_w and for bulk 9OO4 on the SmA side while are systematically below bulk 9OO4 on the nematic side of the transition. The δC′p behavior does not show any features as a function of φ_w, and no power-law fits were attempted.

For the SmA-SmC phase transition, the excess specific δC′p as the function of temperature for pure 9OO4 and 9OO4/CNT composite samples is shown in **Figure 4**. The observed shape and continuous nature of the δC′p peak for pure 9OO4 are consistent with a Landau (mean-field) second-order transition [30] with no observed signature in C″p. The δC′p (AC) for the 9OO4/CNT samples, heights are the same as pure 9OO4 up to 0.025 wt% and then decrease for the 0.05 and 0.20 wt% samples. The step in δC′p (AC) on the SmC-side for below T_{AC} is 0.025 J/gK for pure 9OO4 and all 9OO4/CNT samples, independent of φw.

The tilt susceptibility at the SmA-SmC transition was examined by measuring the electroclinic effect [59] in the LC/CNT mixtures. In the past, it has been shown that there is a nonzero enantiomeric excess for these CNTs, as well as a net chirality for CNTs from four other manufacturers [43]. When dissolved in a liquid crystal, the CNT imparts a net chiral environment to the

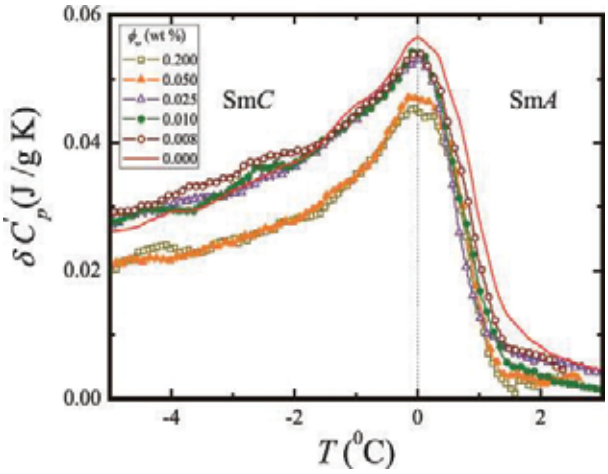

Figure 4. Excess real specific heat associated with the SmA-SmC phase transition as function of temperature about TAC on cooling for different CNT content sample. The definition of the symbols is given in the inset.

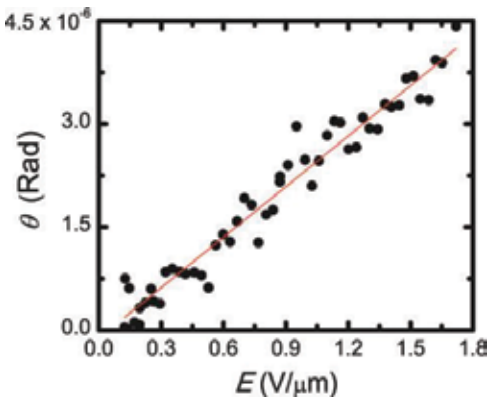

Figure 5. Electroclinic response is a function of electric applied field (E). Data collected at temperature 63.2°C, approximately 1.2°C above SmA-SmC transition. Field was ramped over approximately 5 min.

liquid crystal in the vicinity of the CNT surface. On application of an electric field, a surface electroclinic effect obtains, which requires the presence of a chiral symmetry environment and in which the director rotates by an angle $\theta \propto E$. Because of the sufficiently high concentration of CNTs, the polarized light "sees" an average rotation of the liquid crystal director for the entire sample. **Figure 5** shows the director rotation at temperature 63°C as the function applied filed.

The inverse electroclinic coefficient e_c^{-1} is shown as a function of temperature for the 0.05 wt% 9OO4/CNT sample in **Figure 6**, approaching the SmC phase from the SmA. A three parameter (amplitude, T_{AC}, and susceptibility exponent) power-law fit of e_c^{-1} versus temperature resulted in $\gamma = 0.99 \pm 0.06$. Despite the localization of the chirality induced in the liquid crystal to within a few nanometers of the CNT surface [58], the susceptibility exponent clearly is mean-field-like and apparently unaffected by the presence of the nanotubes. This result suggests that the

http://dx.doi.org/10.5772/intechopen.73391

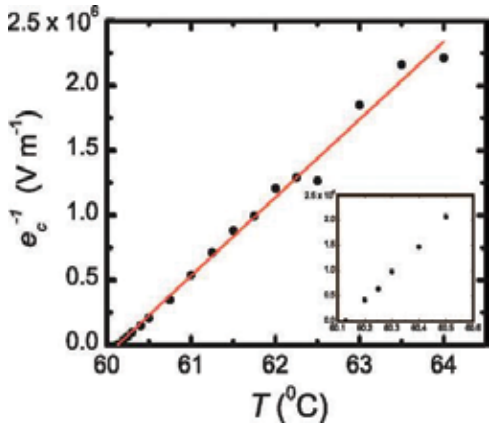

Figure 6. The inverse electroclinic coefficient $e - 1$ c is shown as a function of temperature for an applied electric field at frequency 25 Hz across the cell containing a 0.05 wt% 9OO4/CNT sample. The results were fitted a 3-parameter power law and resulted in a susceptibility exponent $\gamma = 0.99 \pm 0.06$. Inset shows an expanded view of the inverse electroclinic coefficient for low temperature range.

	T_{IN}(C)	T_{NA}(C)	T_{AC}(C)	T_{CB}(C)	T_{BK}(C)	T_{KX}(H)	T_{KA}(H)	T_{NA}(H)	T_{IN}(H)
0.000	86.19	71.27	61.10	49.38	35.00	60.96	63.55	71.46	86.48
0.008	87.13	72.68	62.49	50.33	39.16	61.36	64.24	72.72	87.27
0.010	87.14	72.69	62.50	50.26	39.34	61.45	64.34	72.85	87.27
0.025	87.37	72.52	62.53	50.25	39.66	61.49	64.06	72.45	87.10
0.050	86.92	72.50	62.28	50.17	39.85	61.42	64.00	72.62	87.35
0.200	86.88	72.48	62.27	50.13	39.56	61.37	63.98	72.51	87.27

CNT weight percent φ_w, the *I*-*N* transition temperature $T_{IN,}$ the *N*-Sm*A* transition temperature T_{NA}, the *K*-Sm*X* transition temperature T_{KX}, the Sm*X*-Sm*A* transition temperature T_{XA}, the Sm*A*-Sm*C* transition temperature T_{AC}, the SmC-Sm*B* transition temperature T_{CB}, and the Sm*B*-*K* transition temperature T_{BK} are shown. All temperatures are given in Celsius.

Table 1. Summary of the transition temperatures for pure 9OO4 and all 9OO4/CNT samples on cooling (C) and heating (H).

director rotation extends a length scale ξ, comparable to the SmC correlation length, into the bulk liquid crystal from the narrow chiral region immediately surrounding the CNTs, which is the region that responds directly to the applied field. As an aside, we note that although T_{AC} was obtained for this concentration of nanotubes, it is not possible to compare it with the transition temperature in the absence of nanotubes, for which chirality would be absent, and no electroclinic effect would be present.

For the SmC-SmB-K phase transition sequence on cooling, the ΔC′p and C″ p signatures for pure 9OO4 and 9OO4/CNT composite samples over a range from +4 to −10 K about T_{CB} are shown in **Figure 7**. All peak signatures remain sharp, while the peak height of the SmC-SmB phase transition decreases with increasing φ_w. The SmC-SmB transition is marked by a strongly first-order specific heat signature at T_{CB} = 49.38°C, with the imaginary part being much larger than the real part. The total transition enthalpy ΔH_{CB} decreases slightly, while ΔH_{BK} increases

φ_w	δH^*_{IN}(C)	$\delta H''_N$C)	δH_{NA}(C)	ΔH_{CB}(C)	ΔH_{BK}(C)	ΔH_T	ΔH_{KX}(H)	ΔH_{KA}(H)	ΔH_{NA}(H)	ΔH_{IN}H)	ΔH_T
0.000	3.9	0.95	3.1	35.9	35.9	80.2	72.0	32.0	3.0	4.9	83.4
0.008	3.8	0.99	2.6	38.9	38.9	84.1	69.2	17.1	2.9	5.1	85.7
0.010	4.3	0.96	2.6	39.7	39.7	84.4	67.4	13.6	2.9	4.8	83.9
0.025	3.2	0.69	2.6	29.1	29.1	70.1	67.8	10.5	2.9	4.2	75.0
0.050	3.4	1.01	2.8	31.2	31.2	72.4	61.9	10.3	2.8	4.4	85.3
0.200	3.6	1.03	2.7	27.4	27.4	70.0	62.0	12.7	2.9	5.0	74.6

CNT weight percent φ_w, the *I*-*N* transition δH^*_{IN} real enthalpy, imaginary enthalpy $\delta H''_{IN}$, the *N*-Sm*A* transition enthalpy δH_{NA}, the *K*-Sm*X* total transition enthalpy ΔH_{KX}, the Sm*X*-Sm*A* total transition enthalpy ΔHXA, the Sm*C*-Sm*B* total transition enthalpy ΔH_{CB}, and the Sm*B*-*K* total transition enthalpy ΔH_{BK} are shown. All enthalpies are given in joules per gram. The cumulative sum of all total transition enthalpies ΔH_T on cooling (C) and heating (H) is also shown.

Table 2. Summary of the transition enthalpies for pure 9OO4 and all 9OO4/CNT samples on cooling and heating.

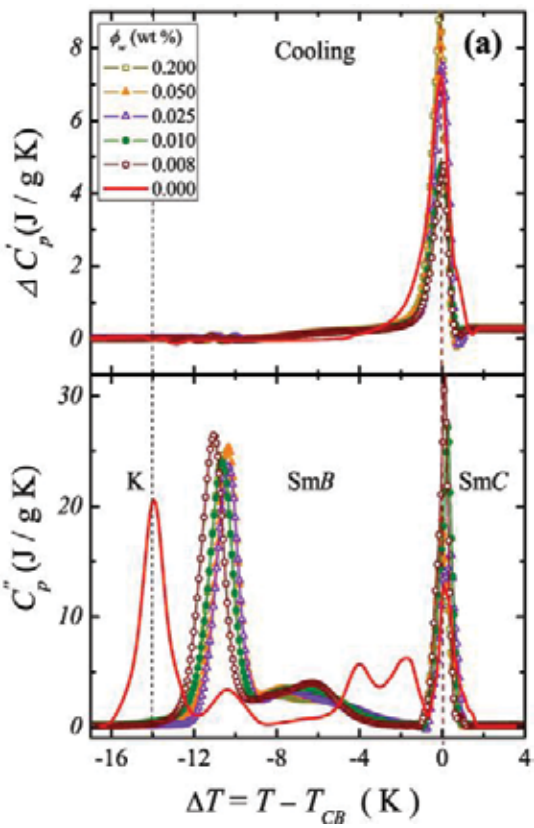

Figure 7. (a) Excess real specific heat associated with the SmC-SmB phase transition as function of temperature about T_{CB} on cooling. The definition of the symbols is given in the inset. (b) Imaginary specific heat as function of temperature about T_{CB} on cooling.

http://dx.doi.org/10.5772/intechopen.73391

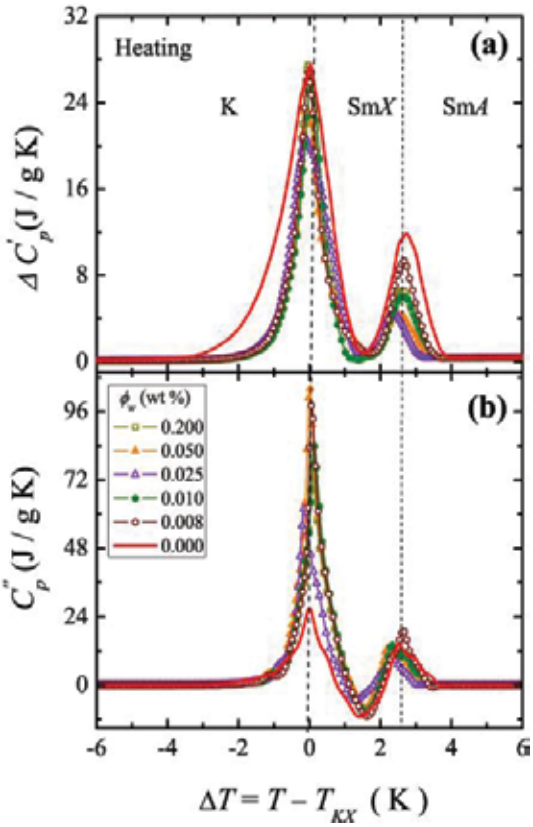

Figure 8. (a) Excess real-specific heat associated with the *K*-SmX-SmC phase transition as function of temperature about T_{XA} on heating. The definition of the symbols is given in the inset. (b) Imaginary specific heat as function of temperature about T_{XA} on heating.

slightly with increasing φ_w. Similarly, the imaginary part is much larger than the nearly non-existent ΔC′p for the SmB-K transition. This is consistent with both the SmC-SmB and SmB-K phase transitions being strongly first order, as expected. Note that the C″p behavior observed in the SmB phase are due to a very slow phase conversion to the SmB from the SmC.

For all samples, upon heating under continuous quasi-equilibrium conditions, the crystal phase superheats slightly until a strongly first-order specific heat feature is observed. Upon further heating, a second first-order feature is seen before the SmA phase appears. **Figure 8** shows pure 9OO4 and 9OO4/CNT composite samples over a range from −6 to +6 K about T_{XA}. The K-SmX ΔC_p peak is narrower for composite samples, except for the φ_w = 0.025 wt% sample, as compared to the pure 9OO4. The melting ΔC′p peak generally decreases in amplitude with an increase in the C″p peak. The total transition enthalpy of ΔH_{KX} = 72 J/g for pure 9OO4 decreases slightly for the 9OO4/CNT samples with increasing φ_w. The ΔH_{XA} = 32 J/g and strongly decreases with φ_w. Interestingly, the second feature specific heat peak height decreases with increasing φ_w and suggests that this feature is not due to residual crystal melting. Because

of the magnitude of the enthalpy involved, it is possible that this feature is a transition into an intermediate smectic phase before heating into the SmA phase. We denote this phase as SmX and are unclear from polarizing microscopy image as to whether this phase is SmB or SmC-like, since the melting occurs very near T_{AC} on cooling.

While the calorimetric and electroclinic behavior of the phases and phase transitions for the 9OO4/CNT samples are clearly retaining the character found in pure 9OO4, the phase boundaries have more shrinking changes due to the CNT. The transition temperature changes from pure 9OO4 for all 9OO4/CNT samples are shown in **Figure 9**. On cooling, the I-N transition temperature in the 9OO4/CNT samples shift upward by nearly a constant +1.18 K compared to that in pure 9OO4, while the two-phase I + N coexistence width shrink with a constant

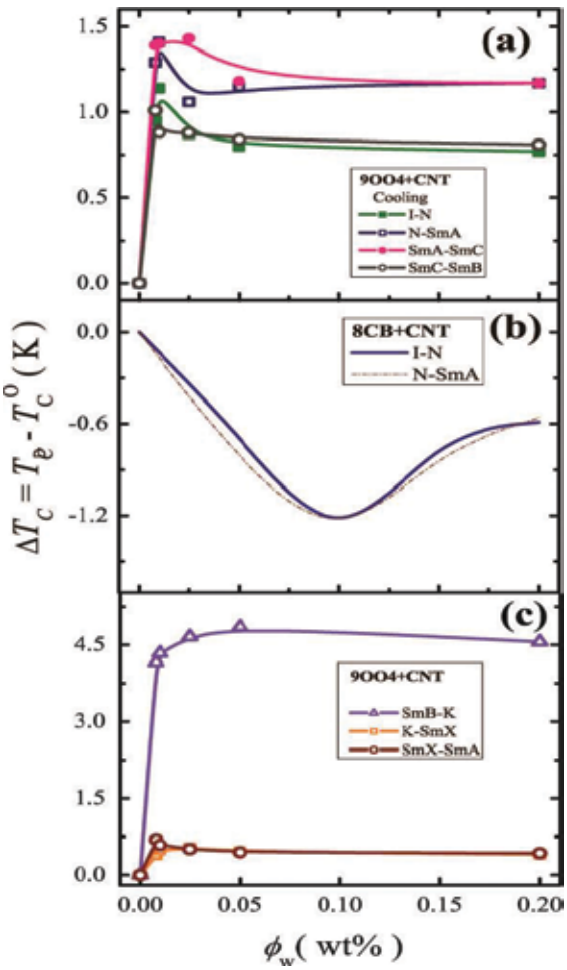

Figure 9. (a) The phase transition temperature shifts for the *I-N* (•), *N*-SmA (▫), SmA-SmC (•), and SmC-SmB (°) in 9OO4/CNT samples and the *I-N* (–). (b) *N*-SmA (– – –) transition temperature shift for 8CB/CNT as a function of *φw*. (c) The phase transition temperature shifts of the SmB-*K* (Δ), K-SmX (▫), and SmX-SmA (°) for the 9OO4/CNT samples as a function of *φw*.

~1.5 K in 9OO4/CNT over this range of φ_w. For the N-SmA, transition temperature in 9OO4/CNT shifts upward by +1.31 K compared to pure 9OO4, shrinking the nematic temperature range $\Delta T_{nem} = T_{IN} - T_{NA}$ by +0.3 K for all φ_w. The SmA-SmC transition temperature in 9OO4/CNT shifts upward by about +1.4 K, widening the SmA range by +0.4 K for all φw. The SmC-SmB transition temperature shifts upward by +1.01 K, widening the SmC range slightly for all φ_w studied. Finally on cooling, the SmB-K crystallization shifted upward by the largest, +4 K for all φw, narrowing the SmB range by 3 K. On heating, the K-SmX melting superheats an additional +0.4 K, similarly for the SmX-SmA boundary compared to pure 9OO4 for all φw samples. The T_{NA} on heating is +1.2 K, and the TIN is +0.8 K higher than in pure 9OO4, narrowing the nematic range ΔT_{nem} by 0.4 K, similar to that seen on cooling.

4. Discussion

It is useful to compare these results with another high-resolution phase transition study on 8CB/CNT nanocomposites, which also used near equilibrium calorimetric conditions and identical mixing method of CNTs from the same source [31]. The 8CB is a typical rod-like molecule, with biphenyl core, to which an aliphatic tail and a polar cyano head group are attached, whereas 9OO4 has a benzoate group, linking the two phenyl rings and having alkoxy end tails (see **Figure 1**). The transition temperatures and enthalpies of the isotropic to nematic and nematic to smectic-A phase transitions in 9OO4/CNT and 8CB/CNT systems [31] are shown in **Figures 9** and **10**. In the 8CB/CNT system, both transition temperatures shift downward by ~1.5 K with increasing φw, with a nonlinear φ_w dependence, while ΔTnem remains constant as seen by the dashed and dash-dotted lines in panel (a) of **Figure 9**. Clearly, the same surface and distribution of CNTs for 8CB produce disordering effects on orientational order shifting both the I-N and N-SmA transitions. The transition enthalpies of the I-N and N-SmA phase transitions in the 8CB/CNT system increase over a broad range of φ_w and then remain constant for higher φ_w. The total transition enthalpy of 8CB/CNT system has been interpreted as the sum of the pure transition contribution and a random field induced distortion energy. Apparently, given the near constant decrease of the enthalpy of the 9OO4/CNT, the ordering is bulk like with a reduction perhaps due to suppression of long-wavelength director fluctuations. If the enthalpy suppression of the I-N and N-SmA in 9OO4/CNT was due to surface pinning, it should scale with CNT surface area, approximately linear in φ_w for these low concentrations, which is not observed. This suggests a different surface interaction for the 9OO4 than 8CB molecule with the CNT. The electroclinic effect result suggests that the director rotation θ extends a length scale ξ, comparable to the SmC correlation length, into the bulk liquid crystal forming a chiral region immediately surrounding the CNTs. This chiral region responds to the applied field, resulting in a tilt over the entire SmC correlation region. On cooling, the 9OO4/CNT SmB-K phase transition temperature increases 4 K, and K-SmX phase transition temperature increases 0.5 K on heating for all φw, while the total transition enthalpy remains constant on heating and cooling (see **Figures 9** and **10**). It is important to note that all experimental results presented here are reproducible over repeated scans.

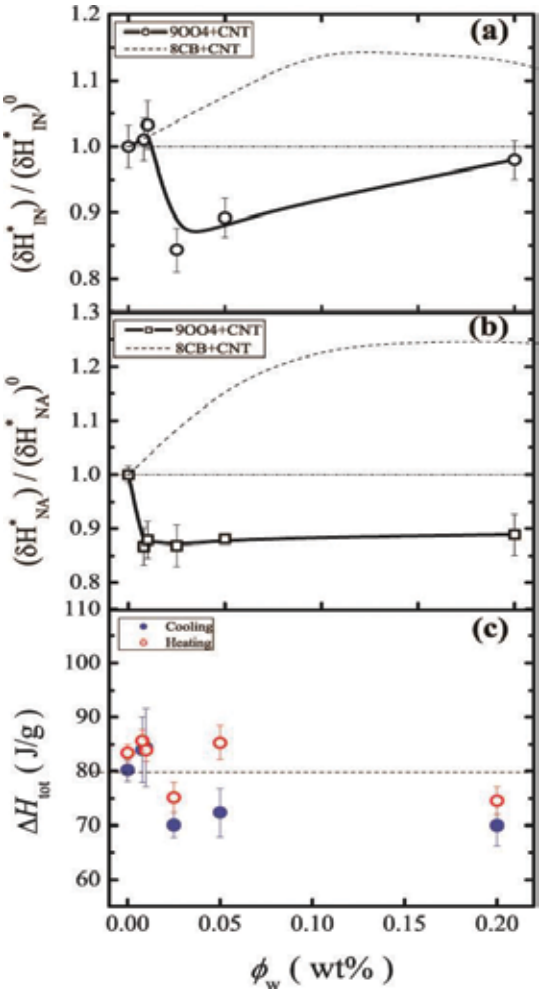

Figure 10. (a) The *I-N* average fractional effective transition enthalpy for 9OO4/CNT (°) and 8CB/CNT (– – –) as a function of φw. (b) The *N*SmA average fractional effective transition enthalpy for 9OO4 (▫) and 8CB (– – –) nanocomposites as a function of φw. (c) The effective total transition enthalpy on heating (°) and cooling (•) for the 9OO4/CNT samples as the function of φw.

From the calorimetric observations presented here, the effect of CNTs on the phase transitions of 9OO4 apparently enhances orientational order and is compatible with various positional orders of all the higher order phases (broken symmetries) up to and including the crystal phase. This is despite the globally random dispersion of CNTs in these nanocomposites and in contrast to the disordering effects observed in the 8CB/CNT system [31]. Clearly, at such low concentrations with random CNT distribution, the specific CNT- LC boundary condition must play an important role along with the ultra-high aspect ratio (string-like structure) of the CNT nanoparticles.

To account for the opposing the behavior of the I-N transition between 9OO4/CNT and 8CB/CNT given the similar chemical nature of both liquid crystals and common graphene surface, the CNT may promote nematic order in both liquid crystals but with different correlation lengths

of the local anchoring field. For 8CB/CNT system, the nucleated local director for 8CB varies in orientation along the long-axis of the CNT creating a surface paranematic layer while further away from the CNT surface, ˆn becomes aligned parallel to the CNT strands [31]. This would mean that the local anchoring field direction varies along the CNT strands over a distance comparable to or shorter than the ˆn correlation length, leading to quenched random-field disordering effects [33]. For 9OO4/CNT system, the surface anchoring orientation correlation length must be larger than the ˆn correlation length of the LC, likely parallel to the CNT long axis with essentially no distortion (elastic strain) of ˆn further away from the strand surface. This would yield a quenched locally nonrandom field that spans more than one nematic domain, while still possessing a global (macroscopic) random distribution. This is consistent with the observed ECE in 9OO4/CNT and not in 8CB/CNT [46, 47], which would also account for the suppression of smectic order in the 8CB/CNT system as the pinned surface para-nematic layer would further disorder any positional ordering. In 9OO4/CNT, the local field spans multiple nematic domains and would actually suppress director fluctuations and so promote smectic ordering.

However, the observed enhancement of the higher order smectic phases as well as the crystal phase implies that the uniform surface orientational anchoring is not accompanied by positional pinning along the CNT for the 9OO4 molecule. This degree of freedom of the LC molecule to essentially slide along the surface and each other parallel to the CNT long-axis is needed to accommodate all the higher positional ordering (broken symmetries) in pure 9OO4, yielding the observed bulk-like behavior and phase boundary enhancement in this work. The origin of these two different behaviors between 9OO4 and 8CB with CNT is not immediately known but may be due to either the negative dielectric anisotropy of 9OO4 as opposed to that in 8CB or the different commensurate surface packing of the phenyl rings onto the graphene surface by these two LCs.

5. Conclusions

We have presented a detailed calorimetric study on the effect of carbon nanotubes on phase transitions of the 9OO4/CNT nanocomposites as a function of CNT concentration. The complex specific heat was measured over a wide range of temperature for negative dielectric anisotropy alkoxyphenylbenzoate liquid crystal (9OO4)/carbon nanotube (CNT) composites as a function of CNT concentration. The thermal scans were performed between 25 and 95°C, first cooling followed by heating scans, as the function of CNT concentration ranging from 0 to 0.2 wt%. All mesophases have transition temperatures 1 K higher and a crystallization temperature 4 K higher than that of the pure 9OO4. The crystal phase superheats until a strongly first-order specific heat feature is observed, indicating melting 0.5 K higher than in the pure 9OO4. The enthalpy change associated with I-N and N-SmA phase transitions is only slightly changed with increasing φ_w but are generally lower than pure 9OO4. The total transition enthalpy associated with the all transitions is independent on the CNT concentration and thermal treatment. The bulk or pure-like behavior of the phase transitions is supported by the bulk-like 9OO4 ECE behavior of the SmA-SmC for the 0.05 wt% sample. We interpret that these results as arising from the LC-CNT surface interaction breaking orientational symmetry uniformly over a distance along the CNT greater than the nematic correlation length but allowing the LC to slide essentially freely on the CNT surface to accommodate various

translational symmetries, leading to a net ordering effect for all transitions. These results suggest that the interactions between molecular structure, dipole moment of liquid crystal, and graphene-like surface can allow a random dispersion of CNT to promote both orientational and positional order depending on the length scale of the local order and the degree of surface freedom. The observed effects are incorporating CNTs with LC likely due to elastic coupling between CNT and LC and this leads to change in the elastic properties of composites. Continued experimental efforts probing the homogeneity of the sample, frequency-dependent dynamics, smectic structures via X-ray scattering, and elastic behavior via light scattering of the homogeneous sample as a function of CNT concentration and temperature would be particularly important and interesting.

Acknowledgements

The authors are grateful to Robert P. Lemieux for providing the 9OO4 liquid crystal. This work was supported at WPI by the Department of Physics and a grant from the NSF award DMR-0821292(MRI). At CWRU, this work was supported by the National Science Foundation's Condensed Matter Physics and Solid State and Materials Chemistry Programs under grant DMR-1065491.

Author details

Parvathalu Kalakonda* and Germano S Iannacchione

*Address all correspondence to: parvathalu.k@gmail.com

Department of Physics, Worcester Polytechnic Institute, Worcester, Massachusetts, USA

References

[1] Iijima S. Nature. 1991;**354**:56

[2] Thostenson ET, Ren ZF, Chou TW. Composites Science and Technology. 2001;**61**:1899

[3] Coleman JN, Khan U, Gun'ko YK. Advanced Material. 2006;**18**:689

[4] Coleman JN, Khan U, Blau WJ, Gun'ko YK. Carbon. 2006;**44**:1624

[5] Gojny FH, Wichmann MHG, Fiedler B, Kinloch IA, Bauhofer W, Windle AH, Schulte K. Polymer. 2006;**47**:2036

[6] Qunaies Z, Park C, Wise KE, Siochi EJ, Harrison JS. Composites Science and Technology. 2003;**63**:1637

[7] Haggenmueller R, Guthy C, Lukes JR, Fischer JE, Winey KI. Macromolecules. 2007;**40**:2417

[8] Bhattacharyya AR, Sreekumar TV, Liu T, Kumar S, Ericson LM, Hauge RH, Smalley RE. Polymer. 2003;**44**:2373

[9] Assouline E, Lustiger A, Barber AH, Cooper CA, Klein E, Wachtel E, Wagner HD. Journal of Polymer Science Part B: Polymer Physics. 2003;**41**(520)

[10] Sandler JKW, Pegel S, Cadek M, Gojny FH, Es MV, Lohmar J, Blau WJ, Schulte K, Windle AH, Shaffer MSP. Polymer. 2004;**45**:2001

[11] Potschke P, Fornes TD, Paul DR. Polymer. 2002;**43**:3247

[12] Kharchenko SB, Douglas JF, Obrzut J, Grulke EA, Migler KB. Nature Material. 2004;**3**(564)

[13] Poncharal P, Wang ZL, Ugarate D, de Heer WA. Science. 1999;**283**:1513

[14] Wang L, Dang ZM. Applied Physics Letters. 2005;**87**:042903

[15] Xu Y, Zhang Y, Suhir E. Journal of Applied Physics. 2006;**100**:113524

[16] Zhao GL, Bagayoko D, Yang L. Journal of Applied Physics. 2006;**99**:114311

[17] Sinha S, Barjami S, Iannacchione G, Schwab A, Muench G. Journal of Nanoparticle Research. 2005;**7**:651

[18] Stephan O, Taverna D, Kociak M, Suenaga K, Henrard L, Colliex C. Physical Review B. 2002;**66**:155422

[19] Madarhri A, Pecastings G, Carmona F, Achour ME. Journal of Microwave Optoelectronics. 6, 36 15. 2007

[20] Sato Y, Terauchi M, Saito Y, Saito R. Journal of Electron Microscopy. 2006;**55**:137

[21] Potschke P, Dudkin SM, Alig I. Polymer. 2003;**44**:5023

[22] Ahmad K, Pan W, Shi SL. Polymer. 2006;**55**:133122

[23] Baughman RH, Zakhidov AA, de Heer WA. Science. 2002;**297**:787

[24] Collins PG, Avouris P. Scientific American. 2000;**283**:62

[25] Javey A, Wang Q, Urai A, Li Y, Dai H. Nano Letters. 2002;**2**:929

[26] Martel R, Schmidt T, Shea HR, Hertel T, Avouris P. Applied Physics Letters. 1998;**73**:2447

[27] Goodby JW, Waugh, Stein SM, Chin E, Pindak R, Patel JS. Nature. 1989;**337**:449

[28] Chandrashekhar S. Liquid Crystals. England: Cambridge University Press; 1992

[29] Demus D, Goodby JW, Gray G, Spiess H, Vill V, editors. Handbook of Liquid Crystals. Canada: Wiley-VCH; 1998

[30] de Gennes PG, Prost J. The Physics of Liquid Crystals. Clarendon, Oxford, England: Oxford University Press; 1993

[31] Sigdel KP, Iannacchione GS. European Physical Journal E. 2011;**34**:11034

[32] Iannacchione GS, Park S, Garland CW, Birgeneau RJ, Leheny RL. Physical Review E. 2003;**67**:011709

[33] Iannacchione GS. Fluid Phase Equilibria. 2004;**222/223**:177

[34] Duran H, Gazdecki B, Yamashita A, Kyu T. Liquid Crystals. 2005;**32**:815

[35] Ji Y, Huang YY, Terentjev EM. Langmuir. 2011;**27**:13254

[36] Somoza AM, Sagui C, Roland C. Physical Review B. 2001;**63**, 081403(R)

[37] Song W, Windle AH. Macromolecules. 2005;**38**:6181

[38] Song W, Kinloch IA, Windle AH. Science. 2003;**302**:1363

[39] Zhang S, Kumar S. Small. 2008;**4**:1270

[40] Chen HY, Lee W, Clark NA. Applied Physics Letters. 2007;**90**:033510

[41] Chen HY, Lee W. Optical Review. 2005;**12**:223

[42] Basu R, Iannacchione GS. Physical Review E. 2010;**81**:051705

[43] Basu R, Boccuzzi KA, Ferjani S, Rosenblatt C. Applied Physics Letters. 2010;**97**:21908

[44] Basu R, Iannacchione G. Journal of Applied Physics. 2009;**106**:124312, 16

[45] Basu R, Chen CL, Rosenblatt C. Journal of Applied Physics. 2011;**109**:083518

[46] Basu R, Pendery JS, Petschek RG, Lemieux RP, Rosenblatt C. Physical Review Letters. 2011;**104**:237804

[47] Basu R, Rosenblatt C, Lemieux RP. Liquid Crystals. 2012;**39**:199

[48] P. Kalakonda and G. S. Iannacchione, to be submitted (2013)

[49] Schawe JEK. Thermochimica Acta. 1995;**260**:1

[50] Coleman NJ, Craig DQM. International Journal of Pharmaceuticals. 1996;**135**:13

[51] Hutchinson JM, Montserrat S. Journal of Thermal Analysis. 1996;**47**:103

[52] Hensel A, Dobbertin J, Boller A, Schawe JEK. Journal of Thermal Analysis. 1996;**46**:935

[53] Wunderlich B. Journal of Thermal Analysis. 1997;**48**:207

[54] Aubuchon SR, Gill PS. Journal of Thermal Analysis. 1997;**49**:1039

[55] Weyer S, Hensel A, Schick C. Thermochimica Acta. 1997;**304/305**:267

[56] Schawe JEK. Thermochimica Acta. 1996;**271**:127

[57] Garoff S, Meyer RB. Physical Review Letters. 1977;**38**:848

[58] Berardi R, Kuball HG, Memmer R, Zannon C. Journal of the Chemical Society, Faraday Transactions. 1998;**94**:1229

[59] Molecular modeling was done using Avogadro: An open-source molecular builder and visualization tool. Version 1.XX. http://avogadro.openmolecules.net/. 17

Section 4

State-of-the-Art Electrochemical

Chapter 11

Applications of Carbon Nanotubes to Flexible Transparent Conductive Electrodes

Bu-Jong Kim and Jin-Seok Park

Additional information is available at the end of the chapter

http://dx.doi.org/10.5772/intechopen.72002

Abstract

Transparent conductive electrodes (TCEs) have attracted great interest because of their wide range of applications in solar cells, liquid crystal displays (LCDs), organic light-emitting diodes (OLEDs), and touch screen panels (TSPs). Indium-tin-oxide (ITO) thin films as TCEs possess exceptional optoelectronic properties, but they have several disadvantages such as a brittle nature due to their low fracture strain and lack of flexibility, a high processing temperature that damages the flexible substrates, low adhesion to polymeric materials, and relative rarity on Earth, which makes their price unstable. This has motivated several research studies of late for developing alternative materials to replace ITO such as metal meshes, metal nanowires, conductive polymers, graphene, and carbon nanotubes (CNTs). Out of the abovementioned candidates, CNTs have advantages in chemical stability, thermal conductivity, mechanical strength, and flexibility. However, there are still several problems yet to be solved for achieving CNT-based flexible TCEs with excellent characteristics and high stability. In this chapter, the properties of CNTs and their applications especially for flexible TCEs are presented, including the preparation details of CNTs based on solution processes, the surface modification of flexible substrates, and the various types of hybrid TCEs based on CNTs.

Keywords: carbon nanotubes, flexible transparent conductive electrodes, solution processes, hybrid-type electrodes, PEDOT:PSS, metal meshes, transmittance, reflectance, color properties

1. Introduction

Transparent conductive electrodes (TCEs) are thin films of optically transparent and electrically conductive materials. Indium tin oxide (ITO) has been the most widely used TCEs in rigid electronics due to its exceptional electrical and optical properties. Recently, flexible

TCEs fabricated by solution processes, which have some advantages such as simple and continuous process and relatively low costs, have attracted enormous interest because of their wide range of applications in flexible devices such as displays, touch screen panels (TSPs), sensors, film heaters that can attach to the skin, fabrics, and papers [1, 2]. However, ITO has disadvantages in the application fields where flexibility is ensured due to its brittle nature because of its low fracture strain and absence of flexibility, a high processing temperature that damages the flexible substrates, low adhesion to polymeric materials, and their relative rarity on Earth, which makes their price unstable [3]. Therefore, this has recently motivated various researches to discover alternative materials to replace ITO films, which include metal meshes, silver nanowires, conductive polymers, graphene, and carbon nanotubes (CNTs) [4, 5]. Also, for the flexible applications, the TCEs are required to be deposited on polymer substrates such as polyethylene terephthalate (PET), polypropylene (PP), and polydimethylsiloxane (PDMS).

Metal meshes and nanowires have excellent electrical properties, but they also have some problems such as visibility due to the reflectivity of metals and reliability for oxidation of metals [6]. Additionally, for metal nanowires, high contact resistances between individual nanowires have critical issues [7]. The conductive polymers, graphene, and CNTs have great advantages such as high mechanical flexibility and low processing costs because they can utilize solution processes [8]. Conductive polymers, however, are generally known to be not good enough at stability in an ambient atmosphere. Also, the poly(3, 4-ethylene-dioxythiophene):poly(styrenesulfonate) (PEDOT:PSS), which may be the most widely used conductive polymers, is tinged with the color blue, which may cause the problem of patterns of electrodes being revealed in TSPs [9]. Graphene has also been reported to be synthesized using solution processes such as the chemical reduction of exfoliated graphite oxide [10]. However, a thermal treatment at high temperature is needed for achieving high transparency and conductivity of graphene, which may restrict the use of flexible substrates.

CNTs, which have potential in chemical stability, thermal and electrical conductivity, mechanical strength, and flexibility, may be the best alternative material for applications in flexible TCEs. Actually, CNTs in some applications, which have low conductivity regardless of transmittance, are being commercialized. The rough surface of CNT films due to their tubular structures brings about a serious problem in the application of organic light-emitting diodes (OLEDs) [11]. In CNTs, furthermore, a relatively high contact resistance of the tube-tube junction may lead to insufficient sheet resistance [12]. Regarding this issue, the separation method of metallic and semiconducting components in CNTs by controlling the diameter and chirality of CNTs has been introduced in the literature [13]. The perfect separation technology, however, has not been realized yet as such a process is very complex. In addition, the chemical doping technology that lowers the sheet resistance has been introduced [14], but effectively controlling the defects in the CNTs is still difficult. As another method of improving the electric characteristics of CNTs, studies on the manufacturing of hybrid-type transparent electrodes have been attempted by several research groups.

In this chapter, the properties of CNTs and their applications especially for flexible TCEs are presented. First, the preparation details of CNTs based on solution processes are introduced, including purification and dispersion of CNT suspension, spray coating of CNTs,

and posttreatment of CNTs. Then, the surface modification of flexible substrates for enhancing the adhesion between CNTs and flexible substrates, which can eventually improve the flexibility of CNT-based TCEs, is discussed. Also, the effects of PEDOT:PSS coating on the electrical characteristics and color properties (e.g., redness, yellowness) of CNT-based TCEs are described, where the various methods for PEDOT:PSS coating, such as spin coating and electrophoretic deposition (EPD), are introduced and compared. Finally, the hybrid-type TCEs, which are fabricated by coating metal meshes with CNTs, are presented along with their characteristics as flexible TCEs.

2. Preparation of CNTs

2.1. Purification and dispersion of CNT suspension

Figure 1(a) shows the procedures for production of CNT suspension, including purification and dispersion processes. The synthesized CNTs necessarily contain metal catalyst and carbonaceous substances, including amorphous carbon, fullerenes, and graphite particles [15]. Therefore, to obtain high purity CNTs, the purification processes have to be conducted prior to the deposition of CNTs. Here, the chemical method induces the oxygenated functional group on CNTs, which causes damage to the surface of CNTs and eventually leads to an increase in the sheet resistance of CNTs. This indicates that it is important to determine the appropriate purification time when the chemical method is used.

After purification, the CNTs have to be properly dispersed since the van der Waals attraction forces between CNTs and the poor solubility of CNTs result in the formation of bundles and agglomerates [16]. There are several approaches for the dispersing of CNTs such as chemical modification (i.e., covalent approach), mechanical treatment, using of surfactants (i.e., noncovalent approach), and so on [17]. The chemical modification improves the solubility of CNTs

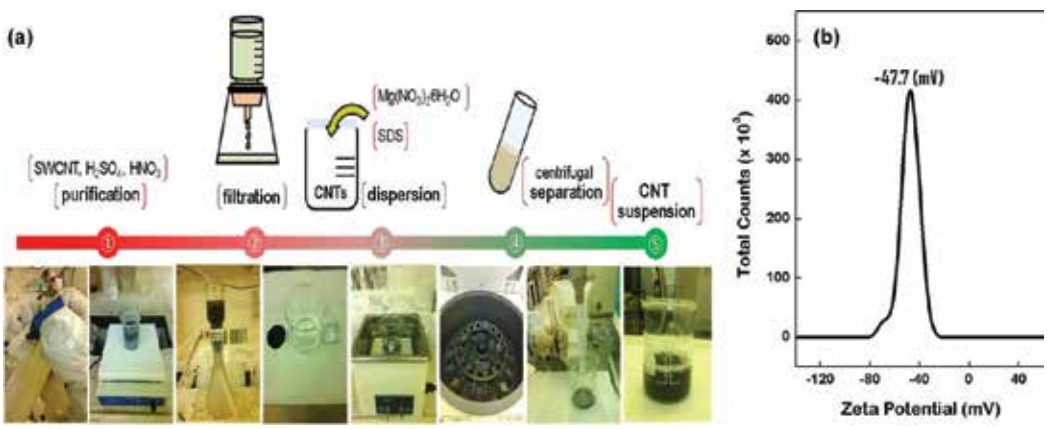

Figure 1. (a) The procedures for production of CNT suspension, including purification and dispersion processes and (b) the zeta potential measured from the prepared CNT suspension.

in solvent by attaching the various moieties and functional groups. However, the chemical method may also affect the electrical properties of CNTs. For the mechanical treatment, the applied high power can effectively separate CNTs, but it can also cause shortening of the CNTs.

In contrast to the chemical and mechanical approaches, the use of surfactants is based on the adsorption of chemical moieties onto the CNTs' surface without damaging the inherent properties of CNTs. Here, the dispersion method for achieving the stable CNT suspension using surfactant is introduced. The purified CNTs are filtered out using the vacuum filtering system, and the dispersion process is carried out for about 30 min in the ultrasonic generator after adding the anionic surfactant of sodium dodecyl sulfate (SDS, $NaC_{12}H_{25}SO_4$, 40 mg) together with deionized water (50 ml). Finally, only the dispersed supernatant is extracted by using the centrifugal separator with the speed of 4000 rpm for 30 min. The actual photo of the CNT suspension produced in this manner is also shown in **Figure 1(a)**. To confirm that the CNT suspension is well dispersed, the zeta potential of the CNT suspension is measured. Generally, the stable state of CNT suspension has a zeta potential of ±40 mV or higher. **Figure 1(b)** shows the zeta potential measured with the CNT suspension of **Figure 1(a)** and it was about 47.7 mV, indicating that the CNT suspension was well dispersed.

2.2. Solution-based deposition of CNTs

Recently, solution-based processes have been increasingly adopted in the deposition of thin films since they have several advantages over the vacuum deposition system such as low fabrication cost, simple process, and massive scalability. To deposit CNTs on the flexible substrates, various methods have been developed, including spray coating, dip coating, bar coating, and inkjet printing [18, 19]. Among them, the spray coating method has the advantage that the thickness of deposited CNTs can be controlled precisely. Here, the CNT-TCEs, fabricated by depositing the CNTs on the polyethylene terephthalate (PET) substrates via spray coating, are presented. The process conditions are controlled by varying the spraying time from 10 to 80 s and by fixing the other process variables such as the injection pressure of 0.2 MPa, the injection amount of 2 ml/min, and the hotplate temperature of 100°C. **Figure 2(a)** indicates the schematic of the spray coating system used in this study and **Figure 2(b)** shows the photo of the surface morphology of CNTs, deposited on the PET substrate via spray coating, obtained using the field-emission scanning electron microscope (FE-SEM).

2.3. Posttreatment of CNTs

After the deposition of CNTs, the surfactant (e.g., SDS) may still remain in the CNTs and serves as an insulating layer, which may disturb the effective electrical contact of the CNTs. Therefore, the posttreatment for removing the remaining surfactant has to be conducted. Several posttreatment methods have been adopted to remove surfactants [20]. Here, the posttreatment of CNTs using nitric acid (HNO_3) is introduced. **Figure 3(a)** compares the sheet resistances and transmittances of CNTs before and after the HNO_3 posttreatment. After the HNO_3 posttreatment, the sheet resistance of CNTs was decreased. This was because the surfactant was removed. **Figure 3(b)** shows the change in the relative percentage of the chemical components incorporated in the CNTs due to the HNO_3 posttreatment, which was estimated

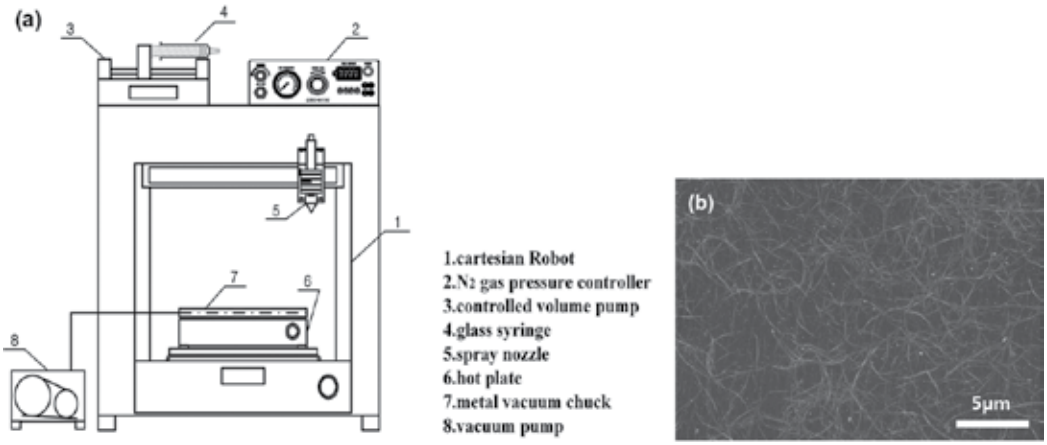

Figure 2. (a) The schematic of the spray coating system and (b) the FE-SEM image indicating the surface morphology of CNTs deposited on the PET substrate via spray coating.

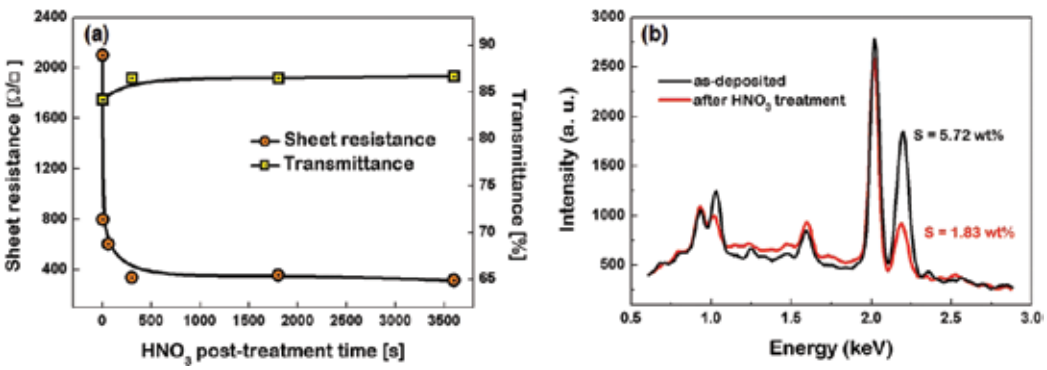

Figure 3. (a) The sheet resistances and transmittances of CNTs before and after HNO_3 posttreatment and (b) the EDS results indicating the change of the chemical components incorporated in the CNTs due to the HNO_3 posttreatment.

by using the energy dispersive X-ray spectroscopy (EDXS). The amount of sulfur (S) element in the CNTs was decreased after the HNO_3 posttreatment, which was resulted from the removal of the surfactant. Meanwhile, the transmittance of the CNTs slightly increased after the HNO_3 posttreatment, as also shown in **Figure 3(a)**. This was because some of the CNTs together with the surfactant were peeled off during the HNO_3 posttreatment.

3. CNT-TCEs fabricated on corona-treated flexible substrates

For depositing CNTs on flexible substrates, various solution-based methods have been utilized. However, these methods have common problems regarding the weak adhesion between the flexible substrates and the CNTs. Generally, the most widely used method is surface modification of substrate to improve the adhesion by using plasma treatment [21, 22]. This method

is a chemical modification that can be formed on polar groups on the surface of substrate before film deposition and also includes the physical changes, which can increase the surface area by generating nanoscratches. However, most of these methods have several problems such as low working pressures, long treatment times, and high processing temperatures. Therefore, corona pretreatment has also been suggested because it can be carried out at atmospheric pressure and room temperature. During the corona treatment, corona energy breaks molecular bonds on the surface of nonpolar substrates, and the broken bonds then recombine with free radicals in the corona environment to form polar groups on the film surface [23]. Namely, the surface of flexible substrate can be changed from hydrophobic to hydrophilic through the corona treatment.

In Section 3, the experimental results that regard the surface modification of PET substrates through corona treatment before the deposition of CNTs and the effects of such surface modification on the properties of the CNTs as flexible TCEs are presented. The changes in the surface roughness, contact angle, and surface energy of the PET substrates due to the corona treatment are characterized in terms of the applied corona energies, PET feeding directions, and treatment times.

3.1. Surface modification of PET substrates via corona treatment

For surface modification, the PET substrates were treated using corona discharge prior to the deposition of CNTs. **Figure 4(a)** shows the schematic of the corona discharge system. **Figure 4(b)** and **(c)** illustrates the corona treatment methods, including the feeding directions of the PET substrates and the numbers of treatment (e.g., 2-times and 4-times for the single-directional treatment and [1 + 1]-times and [2 + 2]-times for the mutually vertical bidirectional treatment). The corona discharge was generated by applying 8 kV voltage to the corona electrode. The PET substrate was fed between the two electrodes (i.e., the corona electrode and the grounded electrode) at the various feeding speeds. The corona energy densities (E_{cor}) were controlled to be increased from 149 to 5263 kJ/m^2 by decreasing the PET feeding speed from 17 to 0.5 m/min.

The surface images and roughness of PET substrates were measured by atomic force microscope (AFM) as shown in **Figures 5(a)**, **(b)**, and **(c)** for nontreated, 4-times single-directionally corona treated, and [2 + 2]-times bidirectionally corona treated, respectively. The

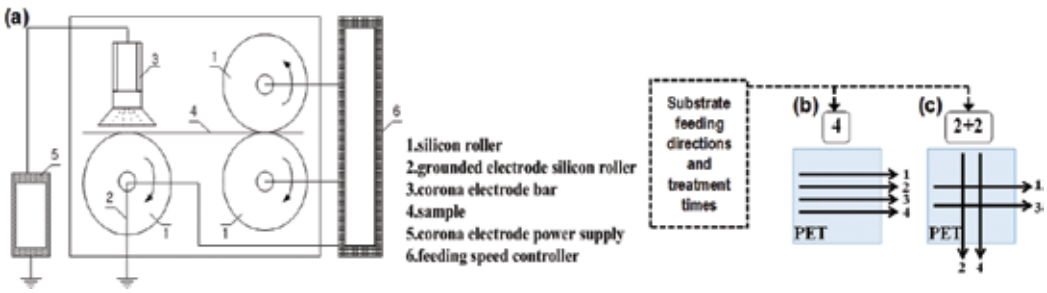

Figure 4. (a) The schematic diagram of the corona discharge system used in this study. The corona treatment methods such as (b) 4-times single-directionally corona treated and (c) [2 + 2]-times bidirectionally corona treated.

http://dx.doi.org/10.5772/intechopen.72002

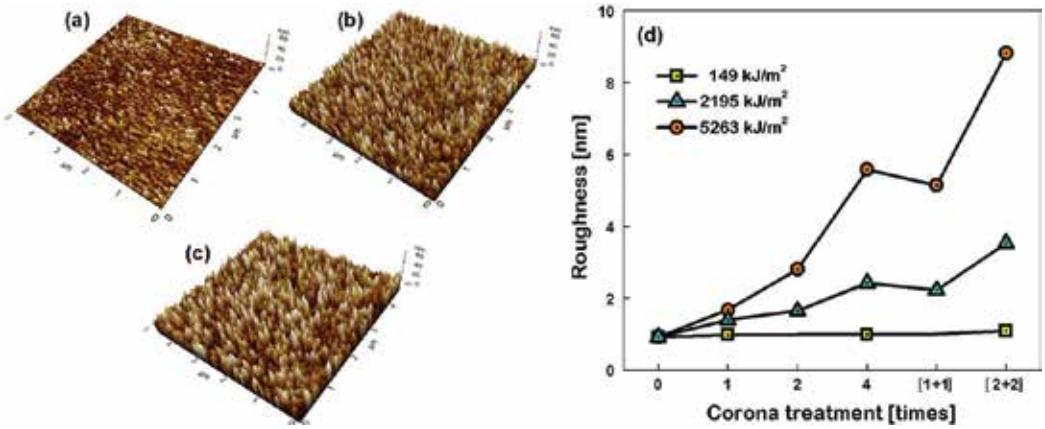

Figure 5. The AFM measurement data such as surface images and roughness for the various PET substrates: (a) nontreated, (b) 4-times corona treated, and (c) [2 + 2]-times corona treated. (d) The surface roughness indicated for three different corona energy densities in terms of feeding directions and the numbers of treatment.

root-mean-square surface roughness (σ_{rms}) was estimated, which is plotted in **Figure 5(d)**, in terms of the substrate feeding directions and the numbers of corona treatment. When the surface modification was performed at the low E_{cor} (149 kJ/m^2), the change in σ_{rms} of the PET substrates appeared to have been negligibly small, regardless of the treatment manner. In contrast, when the PET substrates were treated at the higher E_{cor} (2195 or 5263 kJ/m^2), the σ_{rms} values significantly increased as the treatment number increased. Also, the degree of the increase in σ_{rms} value due to the corona treatment was seen to have been bigger in the cases of the bidirectional treatment than in the cases of the single-directional treatment. For instance, the PET substrate that was bidirectionally [2 + 2]-times treated showed the σ_{rms} value of approximately 8.82 nm, whereas the PET substrate that was single-directionally treated 4-times yielded the σ_{rms} value of approximately 5.58 nm. This indicates that the bidirectionally treated method can effectively increase the surface area.

The contact angles (θ_c) of the PET substrates were measured from liquid drop images and compared in **Figure 6**, according to feeding directions and the numbers of treatment. In the θ_c measurement, two kinds of liquids were used such as water as a polar liquid (**Figure 6(a)–(d)**) and diiodomethane as a nonpolar or dispersive liquid (**Figure 6(e)–(h)**). As the number of corona treatment increased, the θ_c values based on water monotonically decreased, but the θ_c values based on diiodomethane continuously increased.

From the estimated θ_c results, the surface energies of the PET substrates were also calculated using the formula in the Owens-Wendt model [24]. **Figure 6(i)** shows the polar components (E_P) calculated from the water-based θ_c values, the dispersive components (E_D) obtained from the diiodomethane-based θ_c values, and the total surface energy (E_S) obtained from the sum of the E_P and E_D. The E_S value was observed to have increased as the number of the corona treatment increased in the single-direction (i.e., once and 4-times corona treated). Also, the higher E_S value was observed for the PET substrate that was [2 + 2]-times treated, compared with the PET substrate that was 4-times treated. These results indicate that the changes in the

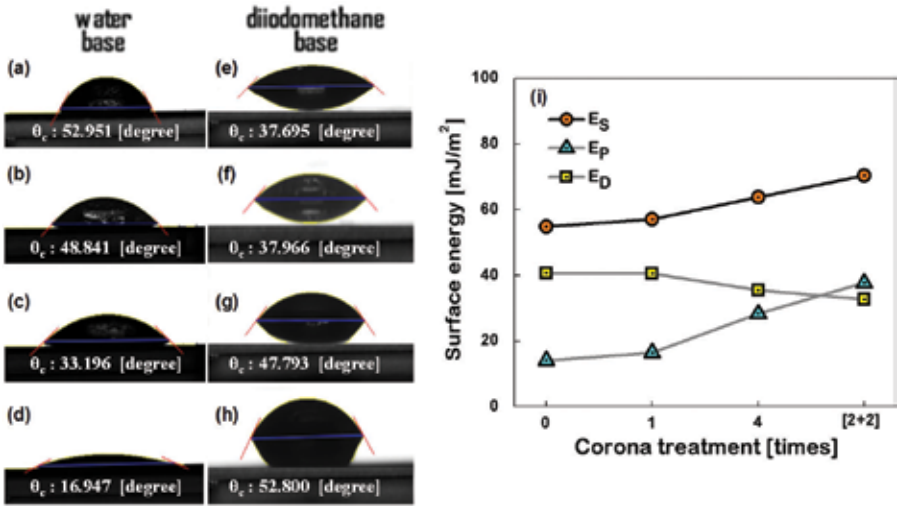

Figure 6. [(a)–(h)] The liquid drop images pictured from the PET substrates: (a) and (e) for nontreated, (b) and (f) for once corona treated, (c) and (g) for 4-times corona treated, (d) and (h) for [2 + 2]-times corona treated, and (i) the estimated E_S along with E_P and E_D components in terms of the PET feeding directions and the numbers of treatment.

E_S values of the PET substrates due to the corona treatment may cause the change of surface chemistries. Also, the results may confirm that the E_S of the PET substrates is closely related to the surface roughness.

It is known that the electrons, ions, and activated neutrons and protons produced from corona discharge react with the oxygen in the air to produce functional groups that contain oxygen, such as the COH and C═O groups, on the PET substrate surface [25]. The X-ray photoelectron spectroscopy (XPS) spectra of the carbon (C) 1*s*–state were measured for both nontreated and corona-treated PET substrates to investigate the changes in the surface chemistries of the PET substrates due to the corona treatment. For the nontreated PET substrate, three distinguishable peaks were observed and assigned to the aromatic hydrocarbons (284.7 eV), aliphatic esters (CH_2O, 286.3 eV), and carboxyl component (C–O–C═O, 288.7 eV) [26], as shown in **Figure 7**. In contrast, additional oxygen polar groups [27], such as phenolic-OH (286.5 eV), C═O (287.5 eV), and carboxyl acid (COOH, 289.2 eV), were observed for the corona-treated PET substrates. The relative contributions of each chemical group in the XPS spectra are summarized in **Table 1**, according to the corona treatment conditions. The relative contents of the oxygen polar groups increased by increasing the number of repetitions of the corona treatment and were larger especially for the bidirectionally corona-treated PET substrates.

It was also discovered that the PET's surface chemistry was changed from a hydrophobic nature to a hydrophilic nature after the corona treatment. It has been known that CNTs refined using acids such as HNO_3 may possess oxygen-related functional groups (e.g., carboxyl groups) on their outer walls [28], and also on the corona-treated PET substrate via a hydrogen bond [29]. This indicates that the adhesive force between the PET substrate and the CNTs can be enhanced by corona treatment of the PET substrate.

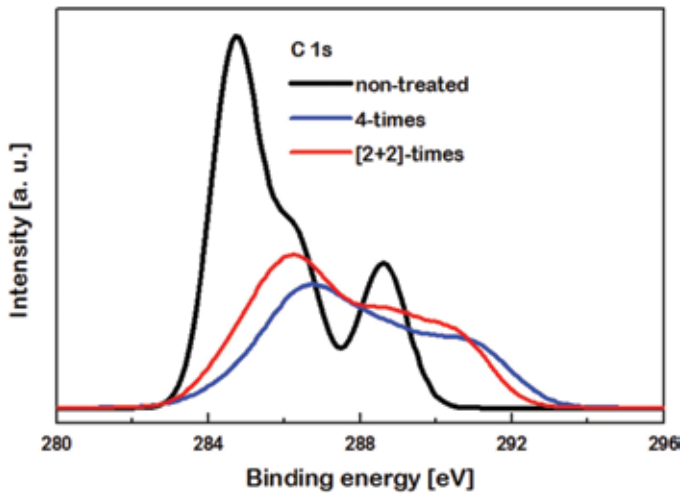

Figure 7. The XPS spectra for carbon (C 1s-state) measured for the nontreated and corona-treated PET substrates.

Assignment	Binding energy (eV)	Content (%)		
		Nontreated	Corona treated	
			4-times	[2 + 2]-times
Aromatic C–C	284.70	53.98	12.31	7.72
CH_2O	285.82–286.68	24.65	18.53	18.71
Phenolic-OH	288.34–288.93	21.37	19.59	18.11
C═O	286.50	—	11.23	10.64
C–O–C═O	287.51–287.67	—	20.11	22.10
COOH	288.88–289.03	—	18.23	22.72

Table 1. The binding energies and relative contents of the chemical bonds observed in the XPS spectra for the nontreated and corona-treated PET substrates.

3.2. The effect of corona treatment on the flexibility of CNT-TCEs

The effect of corona treatment of PET substrates on the flexibility CNT-TCEs has been investigated by measuring the changes in the CNTs' sheet resistance ($R_{\square}$) due to repetitive bending. Two bending tests such as outer bending and inner bending were carried out with a bending radius of 12 mm and a bending speed of 40 mm/s at an ambient temperature and pressure, as displayed in the insets of **Figure 8(a)** and **(b)**, respectively. For all of the PET substrates that were nontreated or corona treated, the average $R_{\square}$ value of the CNTs was observed to have been approximately 350 ± 10 Ω/□ before the bending test was conducted. As shown in **Figure 8(a)**, the $R_{\square}$ value of the CNTs deposited on the nontreated PET substrate significantly increased as the bending times increased, such that the $R_{\square}$ value after

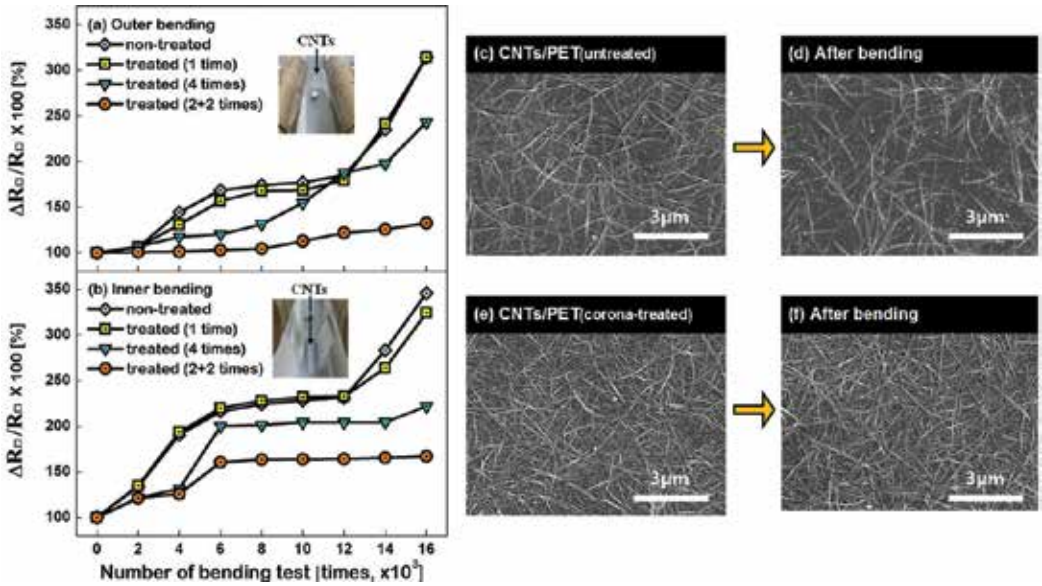

Figure 8. The changes in $R_{\square}$ of CNTs during bending: (a) for outer bending and (b) for inner bending. [(c)–(f)] The comparison of FE-SEM images for the CNTs before and after bending. The photos (c) and (d) indicate the CNTs deposited on the nontreated PET substrates. The photos (e) and (f) indicate the CNTs deposited on the [2+2]-times corona-treated PET substrates.

16,000 times bending was almost more than 300% larger than the initial $R_{\square}$ value before the bending. The increase in the CNTs' $R_{\square}$ value due to bending may be attributed to the weak adhesion between the CNTs and the PET substrate. In contrast, the increase in the $R_{\square}$ due to bending was observed to have been substantially alleviated for the CNTs that were deposited on the corona-treated PET substrates. As shown in **Figure 8(b)**, the similar results were observed in the case of the inner bending test. For both bending tests, the increase in $R_{\square}$ after 16,000 bending repetitions was observed to have been minimal when the CNTs were deposited on the PET substrates that were [2 + 2]-times corona treated. Accordingly, the results shown in **Figure 8** confirm that the corona pretreatment improved the adhesion of the CNTs to the PET substrate.

Figure 8(c) and **(e)** shows the FE-SEM surface morphologies of the CNTs before they were bent, and **Figure 8(d)** and **(f)** displays the surface morphologies of the CNTs after they underwent bending. As shown in **Figure 8(d)**, the repetitive bending caused the marked reduction in the CNTs' density for the CNTs deposited on the untreated PET substrate. In contrast, as shown in **Figure 8(f)**, the CNTs deposited on the [2 + 2]-times corona-treated PET substrate revealed insignificant changes in the surface morphology even after the bending of 16,000 times. As a result, the higher surface roughness, the greater contact angles, and the higher surface energies, which the corona-treated PET substrates revealed, indicated that the surfaces of the PET substrates became hydrophilic from hydrophobic and thereby led to the improvement of adhesion between the CNTs and the PET substrates.

http://dx.doi.org/10.5772/intechopen.72002

4. CNT-TCEs coated with PEDOT:PSS

Of the aforementioned in Section 1, CNTs have potential advantages such as chemical stability, thermal and electrical conductivity, mechanical strength, flexibility, solution processability, and low cost production. CNTs, however, still do not satisfy the electrical characteristics required for TCEs due to the uniform coating caused by their tubular structure and the large contact resistance at their tube-tube junction. To improve the electrical characteristics of CNTs, it was recently reported [30] that hybrid-type electrodes were introduced by combining CNTs with polymers via solution processes such as spray coating and spin coating. Adding the conductive polymers to the CNTs led to the decrease in the sheet resistance of CNTs; however, the electrical properties of the hybrid-type electrodes were sensitive to the deposition methods and combination conditions used to produce the electrodes. Furthermore, for the application of some devices such as display and TSPs, a neutral color of electrodes is required to prevent the distortion of the image color. However, the conductive polymer material is generally known to be tinged with the color blue, which may cause the problem that patterns of electrodes are revealed. Therefore, there is a necessity of studying how the chromaticity characteristic of CNTs changes or can be effectively adjusted according to the mixture with other materials (e.g., conductive polymers) for producing the hybrid-type electrodes.

In this section, hybrid-type transparent electrodes with characteristics desirable for flexible TCEs are introduced by coating CNTs with PEDOT:PSS via various methods such as spin coating, electrophoretic deposition (EPD), and electropolymerization. Their surface morphologies, sheet resistances, visible transmittances, and color properties have been characterized as functions of their preparation conditions. Also, to identify the flexible capabilities of the PEDOT:PSS-coated hybrid-type CNT-TCEs, the changes in their sheet resistances due to repetitive bending (up to 30,000 times) have been measured and compared with the results measured from the CNT-TCEs.

4.1. PEDOT:PSS coating via spin coating

For manufacturing hybrid-type CNT-TCEs, the CNTs were deposited on the PET substrates via spray coating by varying the spraying time from 10 to 80 s. Then, PEDOT:PSS layers were deposited on the CNTs via spin coating (for 1 min) by changing the spin speed within the range of 200–1500 rpm. The PEDOT:PSS-coated CNTs were dried in the oven for 5 min at 100°C and atmospheric pressure. The hybrid-type CNT-TCEs with various thickness combinations of CNTs and PEDOT:PSS layers were manufactured by controlling the spray time (for CNTs) and the spin speed (for PEDOT:PSS).

Figure 9(a) and **(c)** displays the electrical sheet resistances ($R_{\square}$) and visible range transmittances (T_{vis}) for CNTs (C_x) according to the increased spray time from 20 (C_1) to 80 s (C_7) and for PEDOT:PSS films (P_y) according to the decreased spin speed from 1500 (P_1) to 200 rpm (P_7), respectively. For the CNTs, both $R_{\square}$ and T_{vis} monotonically decreased (e.g., $R_{\square}$ from 3035 to 379 Ω/□ and T_{vis} from 93.2 to 80.4%) as the spray time increased. Therefore, there is a trade-off between $R_{\square}$ and T_{vis}. For the PEDOT:PSS films, the similar trends in $R_{\square}$ and T_{vis} appeared

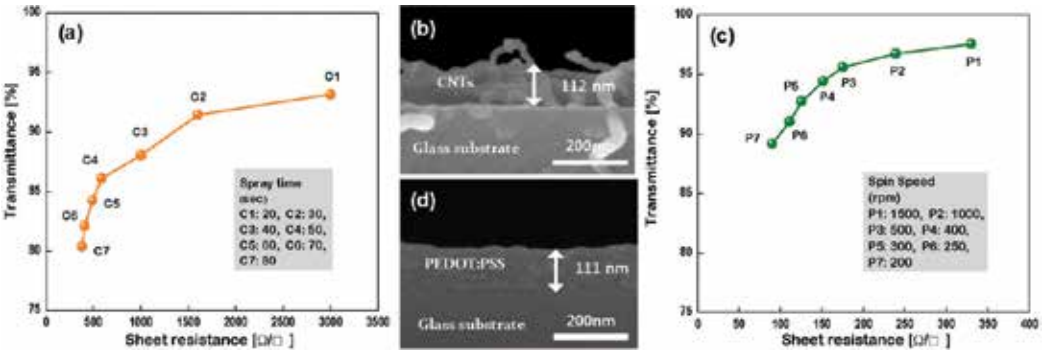

Figure 9. The sheet resistance and transmittance measured from the (a) CNTs and (c) PEDOT:PSS according to deposition thickness. The FE-SEM images (b) and (d) indicate the cross-sectional morphology of the CNTs specimen of C_7 and PETOD:PSS specimen of P_7.

(e.g., $R_□$ from 330 to 90 Ω/□ and T_{vis} from 97.5 to 89.2%) as the spin speed decreased. Also, the FE-SEM cross-sectional morphology of the CNTs and PEDOT:PSS electrodes are displayed in the inset of **Figure 9(b)** and **(d)**. The thickness of CNTs increased from 40.5 to 112 nm by increasing the spraying time from 20 to 80 s and the thickness of PEDOT:PSS films increased from 28.4 to 111 nm by decreasing the spinning speed from 1500 to 200 rpm. Accordingly, the decrease of T_{vis} as shown in **Figure 9(a)** and **(c)** was attributed to the increase in the thicknesses of CNTs and PEDOT:PSS layers.

For the hybrid electrodes (S_z), the $R_□$ and T_{vis} were also measured and the results are shown in **Figure 10(a)**. Here, the hybrid electrodes were fabricated by depositing the CNTs via spray coating under the same condition as the specimen C_3 and coating them with PEDOT:PSS by decreasing the spinning speed from 1500 (S_1) to 200 rpm (S_5) via spin coating. For the hybrid-type specimens (S_z), both $R_□$ and T_{vis} decreased (e.g., $R_□$ from 298 to 73.49 Ω/□ and T_{vis} from 87.52 to 78.84%) as the spinning speed decreased because the thickness of the PEDOT:PSS films increased from 28.4 to 114.9 nm with a decrease in the spinning speed from 1500 to 200 rpm. It was observed that the decrease in the T_{vis} due to the coating of the PEDOT:PSS films was trivial, while the $R_□$ of CNTs was substantially reduced by the coating of PEDOT:PSS. For instance, the hybrid electrode of S_1, which was fabricated by coating the CNTs (C_3) with the PEDOT:PSS film at the spinning speed of 1500 rpm, had an $R_□$ of approximately 298 Ω/□ and a T_{vis} of 87.52%, whereas the CNTs (C_3) showed a much higher $R_□$ (959.3 Ω/□) and a slightly higher T_{vis} (88.80%). This was because the PEDOT:PSS particles filled up the voids between the tubes in the CNTs as shown in **Figure 10(e)** and thereby formed a conduction bridge for electron transfer, inducing a decrease in the tube-tube junction resistance and the percolation threshold, eventually enhancing the conductivity of the hybrid electrodes [31].

In addition to low electric sheet resistance and high transmittance, TCEs should also satisfy the chromatic characteristics approaching no color. Generally, the chromaticity of a TCE can be determined by using the three-dimensional color space (namely, L*, a*, and b*) where each coordinate axis expresses specific color components [32], as shown in **Figure 11(a)**. Here, L* means brightness having the numerical value between 0 (lowest) and 100 (highest). The a*

http://dx.doi.org/10.5772/intechopen.72002

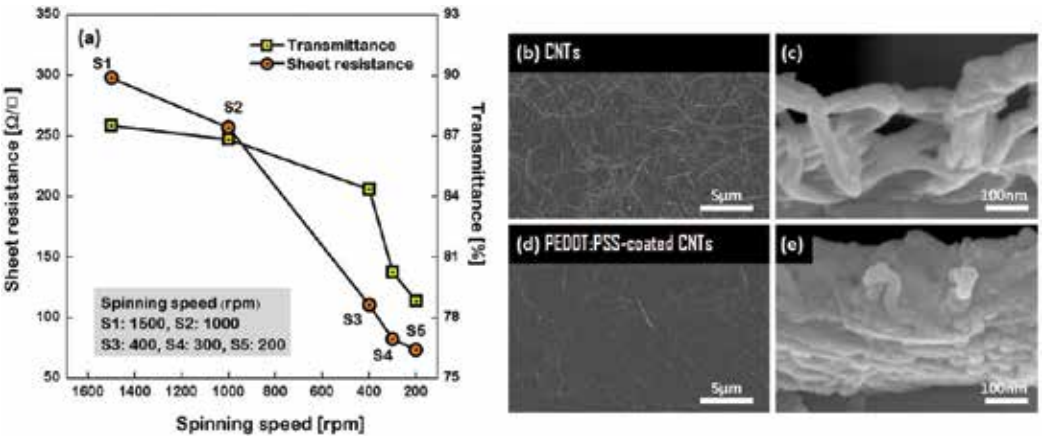

Figure 10. (a) The sheet resistance and average transmittance measured from the PEDOT:PSS-coated CNTs hybrid electrodes as a function of the spinning speed used to coat the PEDOT:PSS films via spin coating. The FE-SEM surface and cross-sectional images: (b) and (c) for CNTs, (d) and (e) for PEDOT:PSS-coated CNTs.

(redness) value is the positive definiteness (+) that is close to the color red as it increases and it is close to the color green as it increases with the negative definiteness (−). Also, the b* (yellowness) value is close to yellow color as it increases with the positive definiteness and it appears to be blue color as it increases with the negative definiteness.

Figure 11(b)–(d) shows the measured results of chromaticity characteristics for three kinds of TCEs such as (b) CNTs, (c) PEDOT:PSS, and (d) PEDOT:PSS-coated CNTs. For the CNTs, the b* gradually increased in the negative direction of sign from about 0.58 to 1.58 as the spraying time increased, whereas the a* showed neighboring zero regardless of the spraying time. For the PEDOT:PSS films, both a* and b* monotonically increased in the negative direction of

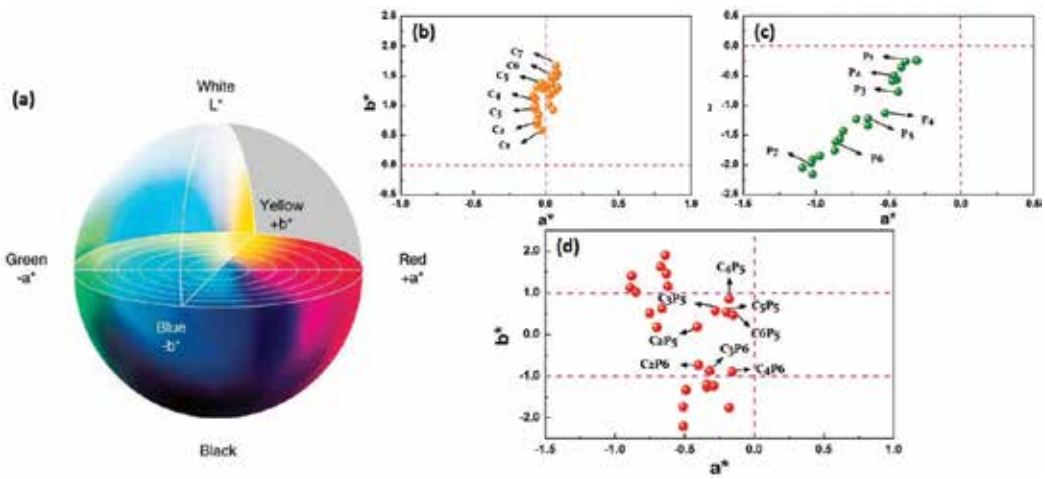

Figure 11. (a) Color space (L*, a*, and b*). [(b)–(d)] The measured chromatic parameters (a* and b*) for various electrodes: (b) for CNTs (C_x), (c) for PEDOT:PSS (P_y), and (d) for PEDOT:PSS-coated CNTs (C_xP_y).

sign as the spinning speed decreased (e.g., the a* from −0.31 to −1.09 and the b* from −0.24 to −2.05). Namely, increasing the thicknesses of CNTs and PEDOT:PSS layers led to the decrease in their sheet resistances, but it resulted in the deterioration of their chromaticity characteristics, especially for the yellowness. Here, it should be noted that the b* values of the CNTs and PEDOT:PSS layers changed in the mutually opposite directions of sign according to the thicknesses of CNTs and PEDOT:PSS layers. **Figure 11(d)** displays the measured results of characteristic values of a* and b* of the PEDOT:PSS-coated CNTs manufactured by variously combining the deposition conditions of CNTs (i.e., the spraying times) and the coating conditions of PEDOT:PSS (i.e., the spinning speeds). For the C_3P_5 specimen, the a* value of −0.28 was located between those of CNTs and PEDOT:PSS (i.e., −0.08 for C_3 and −0.64 for P_5) and the b* value of 0.57 was also between those of CNTs and PEDOT:PSS (i.e., 0.96 for C_3 and −1.22 for P_5). This indicates that hybrid-type electrodes with CNTs and PEDOT:PSS combined) can possess the better color properties compared with those of single electrodes (e.g., CNTs or PEDOT:PSS) due to their complementary color relation.

4.2. PEDOT:PSS coating via electrophoretic deposition (EPD)

The coating of CNTs with PEDOT:PSS films via EPD was performed using a mixed solution of PEDOT:PSS (5 ml) and isopropyl alcohol (IPA, 100 ml). In the EPD process, the PEDOT:PSS films were deposited on the anode electrode where the spacing between the anode (i.e., CNTs) and the cathode (i.e., Cu) was kept at 10 mm and the DC bias voltage of 100 V was applied during the changing of the process time within the range of 20–40 s.

For the hybrid electrodes (E_z) which were fabricated by coating the CNTs (C_3) with the PEDOT:PSS films via the EPD method, the $R_{\square}$ and T_{vis} were measured. The results are shown in **Figure 12(a)**, according to the increase in the EPD time from 20 (E_1) to 40 s (E_5). **Figure 12(a)** shows the relationships between the $R_{\square}$ and T_{vis} measured from the two different hybrid electrodes such as the S_z specimens fabricated by coating the CNTs (C_3) with the PEDOT:PSS films

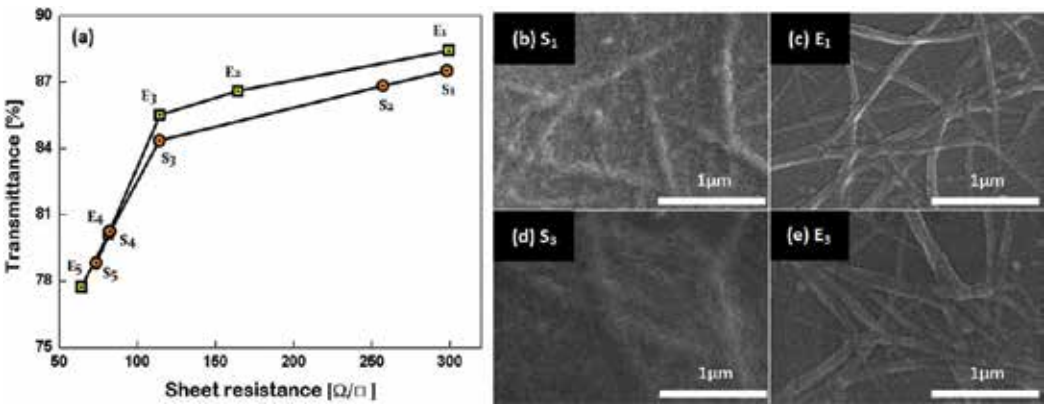

Figure 12. (a) The sheet resistances and average transmittances of the hybrid electrodes, where the PEDOT:PSS films were coated on the CNTs via spin coating (i.e., the specimens denoted as S_z) or EPD (i.e., the specimens denoted as E_z), along with the FE-SEM images of the S_1 and E_1 specimens. [(b)–(e)] The surface morphologies of the specimens (b) S_1, (c) E_1, (d) S_3, and (e) E_3.

via spin coating and the E_z specimens fabricated by coating the CNTs (C_3) with the PEDOT:PSS films via EPD. For the hybrid electrodes E_z (i.e., using EPD), the changes in the $R_□$ and T_{vis} were observed to have been similar to those of the hybrid electrodes S_z (i.e., using spin coating). Here, it may be noted that the T_{vis} of the hybrid electrode E_3 was measured as 85.52%, slightly higher than that (84.36%) of the hybrid electrode S_3, whereas both hybrid electrodes had almost the same $R_□$ values such as approximately 114.4 Ω/□ for E_3 and 110.5 Ω/□ for S_3. The similar trend was also observed for the hybrid electrodes of S_1 and E_1.

Generally, the film deposition via EPD is generally achieved by the motion of the charged particles that are dispersed in a suitable solvent toward an electrode under an applied electric field [33]. Accordingly, the results of **Figure 12(a)** can be explained by comparing the surface morphologies of the hybrid electrodes, which are shown in **Figure 12(b)–(e)**. It was observed from the surface images of **Figure 12(b)** and **(d)** (i.e., the hybrid electrodes of S_1 and S_3) that the PEDOT:PSS layer was deposited not only on the region where the CNTs existed but also on the region where no CNTs existed. On the other hand, the surface images of **Figure 12(c)** and **(e)** (i.e., the hybrid electrodes of E_1 and E_3) showed that most of the PEDOT:PSS layer covered the area near the CNTs. Therefore, the observation that the sample E_1 (or E_3) displayed the higher transmittance as compared to the sample S_1 (or S_3) was because there were regions where the PEDOT:PSS films were hardly coated.

To compare the flexibility of the CNTs and the hybrid electrodes (i.e., PEDOT:PSS-coated CNTs either using EPD (E_z) or spin coating (S_z)), the bending tests were analyzed, and the results are shown in **Figure 13(a)** as functions of the number of bending tests (up to 30,000). In the case of the CNTs, the $R_□$ increased continuously as the number of bending times increased and appeared to almost have doubled after the completion of the bending test. On the contrary, the increase in the $R_□$ was mitigated for the hybrid electrodes, indicating an improvement in flexibility. The flexibility-enhancement effect was higher by increasing the thickness of the coated PEDOT:PSS layer (i.e., from S_1 to S_3 or from E_1 to E_3). This may be because the PEDOT:PSS film induced the physical gripping of the CNTs to enable them to adhere better to the underlying PET substrate [34]. This may also be due to the chemical bonds between the PEDOT:PSS film and the corona-treated PET substrate or between the PEDOT:PSS film and the acid-treated CNTs [35].

Figure 13(b)–(g) shows the changes of FE-SEM surface morphologies due to bending, measured from the electrodes of CNTs (C_3) and hybrids (S_3 and E_3). **Figure 13(b)**, **(c)**, and **(d)** indicates their images measured before bending and **Figure 13(e)**, **(f)**, and **(g)** shows images measured after bending of 30,000 times. For the C_3 electrode (CNTs), the density of the CNTs was significantly decreased from about 1.97 to 1.52 tubes/μm^2 after bending. On the contrary, the density of the CNTs in the S_3 and E_3 electrodes (hybrid) hardly changed after bending. This may confirm that the hybrid electrodes have more potential in flexibility as compared to the CNTs. In addition, the hybrid electrode fabricated via spin coating showed less change in resistance than the hybrid electrode fabricated via EPD. The deposition of PEDOT:PSS occurs mainly on the surface of the CNTs in EPD, whereas in spin coating, the deposition of PEDOT:PSS occurs not only on the CNTs' surface but also on the PET substrate where no CNTs exist. In the case of the EPD-produced hybrid electrodes, accordingly, if the CNTs are

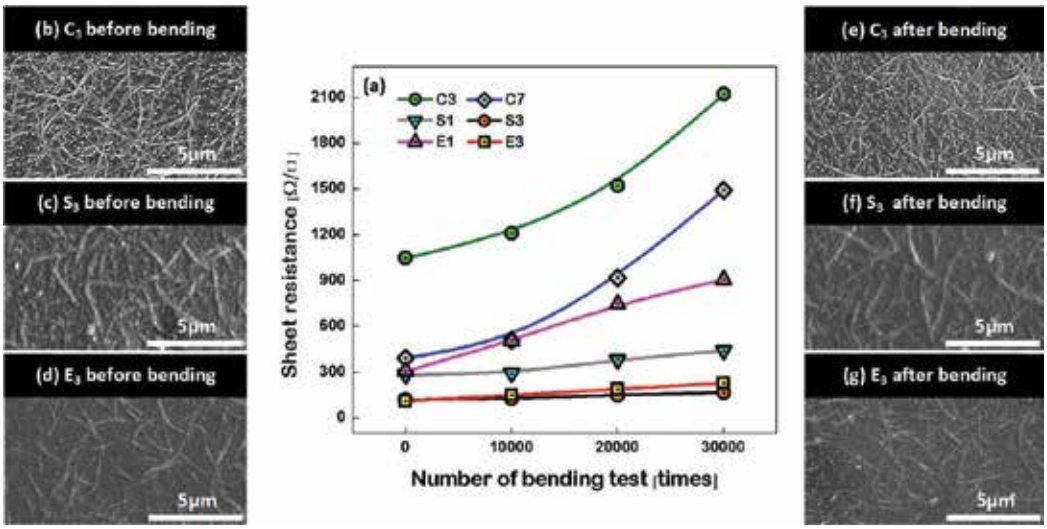

Figure 13. (a) The changes in the sheet resistances due to bending tests (up to 30,000 times), measured from the various electrodes such as CNTs (i.e., C_3 and C_7) and PEDOT:PSS-coated CNTs (i.e., S_1, S_3, E_1, and E_3). [(b)–(g)] The changes of FE-SEM surface morphologies due to bending, measured from the electrodes of CNTs (C_3) and hybrids (S_3 and E_3). Here, (b), (c), and (d) indicate their images obtained before bending (left photos), and (e), (f), and (g) obtained after bending (right photos) of 30,000 times.

detached during the bending test, then the PEDOT:PSS layer on the CNTs is also detached and thus, the resistance of the electrodes will inevitably increase. In contrast, in the case of the hybrid electrodes fabricated via spin coating, the increase in resistance may be insignificant even if they experience the detachment of CNTs due to bending because the conductive PEDOT:PSS layers still remain.

5. Effects of CNT-coating and washing on properties of copper meshes

Metal meshes have been developed as the alternative transparent electrodes to replace the conventional ITO due to their low electric sheet resistance and high visible transmittance. However, metal meshes have a relatively high reflectance generated by metals, and several metals, such as gold (Au) and copper (Cu), are generally tinged with specific colors, leading to a visibility problem. The most commonly used materials for the metal-based TCEs are silver (Ag) and Cu. Compared with Ag, Cu is more abundant and less expensive, but it has higher resistivity. Also, Cu is generally tinged with a red-orange color [36], requiring it to be coated with black materials capable of absorbing light effectively. CNTs are known as excellent absorbers of visible light [37] and have advantages in terms of chemical stability, thermal and electric conductivity, mechanical strength, and flexibility. To improve the visibility of metal mesh electrodes, the authors recently introduced hybrid-type TCEs fabricated via the combination of metal meshes with CNTs [38].

Cu films were deposited on glass substrates (Corning, Eagle 2000, 3 × 3 cm^2) at room temperature via RF sputtering at 80 W power and 30 mTorr working pressure. Cu meshes were formed via lithography to produce a 200 μm line spacing and a 10 μm line width. Single-walled CNT powder (NanoAmor 1284YJ, 15 mg) was placed in a mixture of H_2SO_4 (20 ml) and HNO_3 (10 ml) at a 2:1 volume ratio and was ultrasonicated for 30 min to eliminate the impurities such as the metal catalysts and amorphous carbons. The CNT solution was dispersed for 15 min using an ultrasonic generator after adding a dispersant of magnesium nitrate ($Mg(NO_3)_26H_2O$, 15 mg) and isopropyl alcohol (IPA, 100 ml). CNTs were deposited on the Cu meshes via the EPD process, conditions of which were previously reported in the authors' recent paper. The thickness of the CNTs was controlled by varying the EPD time from 5 to 15 s. Finally, for post-washing, the CNT-coated Cu meshes were dipped in deionized water by varying the post-washing time from 0 to 30 s.

Figure 14(a) and **(b)** displays the FE-SEM photos of the fabricated Cu mesh and the CNT-coated Cu mesh along with the enlarged photo of the surface morphology of the CNT coating layer, respectively. It can be clearly seen that CNTs were used to selectively coat only the surfaces where the Cu mesh patterns had been formed. The thickness profiles of the CNT-coated Cu meshes measured before and after post-washing are shown in the inset of **Figure 14(c)**. The thickness of the Cu mesh was approximately 106 nm, and it was increased to approximately 913 nm after the Cu mesh was coated with CNTs via the 15 s EPD process. Meanwhile, the thickness of the CNT-coated Cu mesh was considerably decreased as the post-washing process progressed, and it was approximately 237 nm after 30 s post-washing, as shown in **Figure 14(c)**. This was because some of the CNTs were detached from the Cu mesh during the washing process. All of the Cu mesh specimens considered in this study are summarized in **Table 2**.

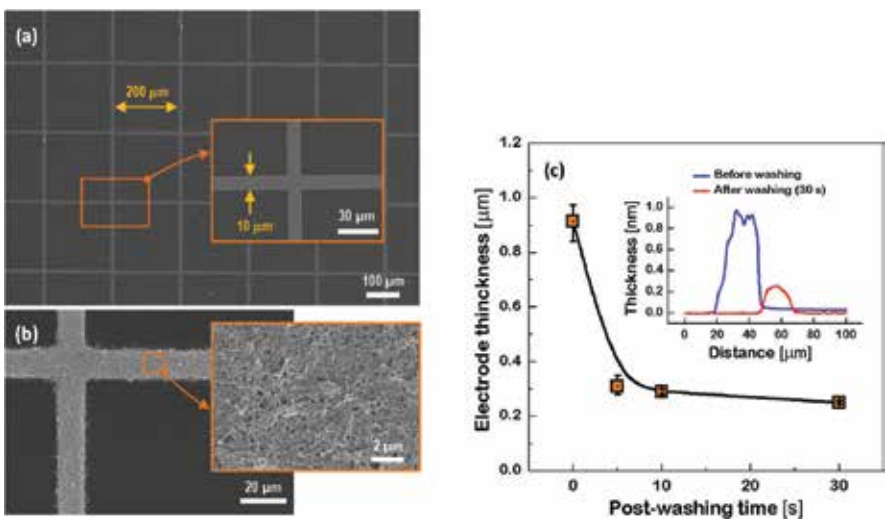

Figure 14. [(a) and (b)] The FE-SEM photos for a pristine Cu mesh with a 200 μm line spacing and a 10 μm line width and a CNT-coated Cu mesh including the surface morphology of the CNT coating layer. (c) The change in the thickness of the CNT-coated Cu mesh as a function of the post-washing time and the thickness profiles (inset) of the CNT-coated Cu meshes measured before and after post-washing (30 s).

Sample	EPD time (min)	Washing time (s)	Thickness of CNTs (nm)	T_{vis} (%)	R_{vis} (%)	a*	b*
Cu(p)	—	—	106.3	90.71	11.83	1.91	1.92
CCu-1	5	—	323.6	90.24	8.91	1.54	1.88
CCu-2	10	—	546.2	89.80	8.44	1.15	1.61
CCu-3	15	—	807.0	89.79	7.89	0.88	1.13
W-CCu-1	5	30	95.6	90.18	8.51	1.44	1.51
W-CCu-2	10	30	110.9	89.98	7.79	0.96	0.58
W-CCu-3	15	30	130.7	89.83	7.37	0.16	−0.55

Table 2. The sample ID's considered in this study, along with their preparation conditions and the summary of measured quantities.

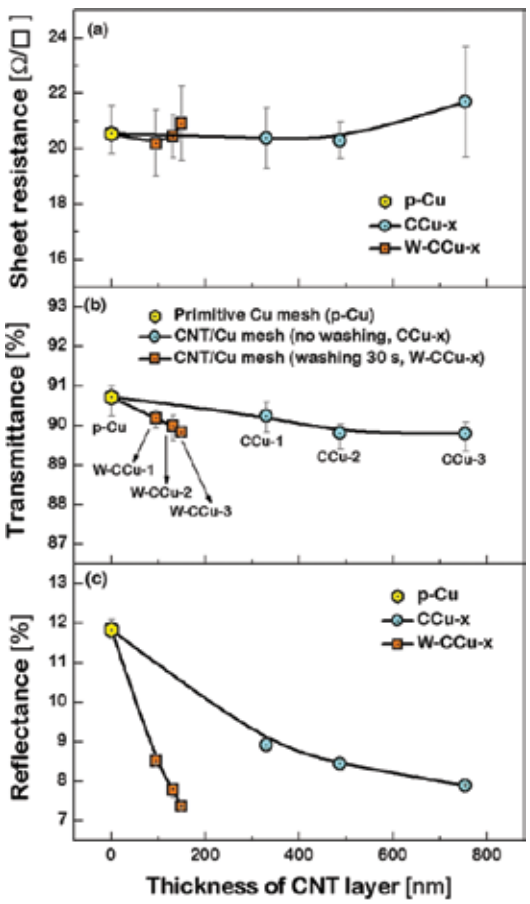

Figure 15. (Left) The results of: (a) sheet resistance, (b) transmittance, and (c) reflectance, measured from pristine Cu mesh (denoted by "p-Cu"), and CNT-coated Cu-meshes before washing and after 30 s post-washing (denoted by "CCu-x" and "W-CCu-x" ("x" = 1, 2, and 3), respectively), in terms of the CNT's thicknesses.

http://dx.doi.org/10.5772/intechopen.72002

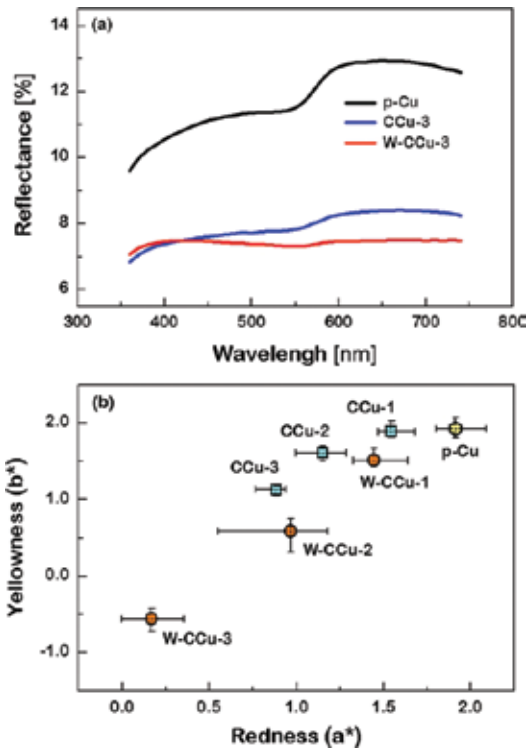

Figure 16. (Right) (a) The reflectance spectra of primitive Cu-mesh (p-Cu), and CNT-coated Cu meshes before washing (CCu-3) and after washing (W-CCu-3). (b) The estimated chromatic parameters of redness (a*) and yellowness (b*) for all the specimens fabricated in this study.

Figure 15(a)–(c) shows the results of the sheet resistance, transmittance, and reflectance measured from the pristine Cu mesh and the CNT-coated Cu meshes before and after post-washing, in terms of the CNT's thicknesses. The sheet resistance and transmittance of the Cu meshes were hardly affected by the CNT coating and the CNT's thickness, and was also marginally changed by post-washing. For all of the specimens, their sheet resistance and transmittance values were in the range of 20.2–21.5 Ω/□ and 89.8–90.7%, respectively. On the other hand, the reflectance of the Cu mesh was significantly reduced by the CNT coating. This indicated that the CNT coating layer played the role of suppressing the visible light reflected from the Cu mesh. In **Figure 15(c)**, it is noted that the reflectance of the CNT-coated Cu mesh was further reduced after it underwent post-washing (e.g., 7.89% for C-Cu-3 and 7.37% for W-CCu-3, respectively).

Generally, the color property of a metal mesh is closely related to its reflectance spectrum, from which the chromatic parameters, redness (a*) and yellowness (b*), can be determined. Both the a* and b* components being closer to zero indicate that the metal mesh appears nearly colorless. **Figure 16(a)** shows the reflectance spectra measured from the p-Cu, CCu-3, and W-CCu-3 specimens, and **Figure 16(b)** shows the redness and yellowness values estimated from all of the specimens. The pristine Cu mesh revealed a stair-like spectrum where the level of reflectance was demarcated at a wavelength of around 560 nm, and its redness

and yellowness values were approximately 1.91 and 1.92, respectively. This may be the cause of the red-orange tint of the pristine Cu mesh. In contrast, such disparity in reflectance nearly disappeared when the Cu meshes were coated with CNTs, and the flat-type spectra with much lower reflectance levels were observed for the CNT-coated Cu meshes. Both a* and b* values considerably decreased as the CNT's thickness was increased, and further decreased when the CNT-coated Cu meshes underwent post-washing. For instance, the a* and b* values of the CCu-3 mesh were approximately 0.88 and 1.13, respectively, and those of the W-CCu-3 mesh were approximately 0.16 and −0.55, respectively.

In order to discover why the CNT-coated Cu meshes exhibited such lower reflectance and smaller a* and b* after they underwent post-washing, the changes in their atomic components and surface chemistry were investigated. **Figure 17(a)** and **(b)** shows the Auger electron spectroscopy (AES) measurement results, which indicate the relative atomic contents of C, O, Mg, and Cu for the CNT-coated Cu meshes before and after post-washing, respectively, as a function of the sputtering time (0–25 min) used for the AES analysis. For the CCu-3 specimen as shown in **Figure 17(a)**, the C atom content was always greater than the Cu atom content, while for the W-CCu-3 specimen as shown in **Figure 17(b)**, the Cu atom content exceeded the C atom content as the sputtering time was around 15 min, indicating that the layer was changed from a CNT region to a Cu mesh region. This was attributed to the decrease in the Cu mesh's thickness due to the detachment of the CNTs after post-washing. It was also observed that the CCu-3 specimen contained the Mg atoms with an atomic content higher than about 10%. This was because magnesium nitrate ($Mg(NO_3)_2 6H_2O$) was

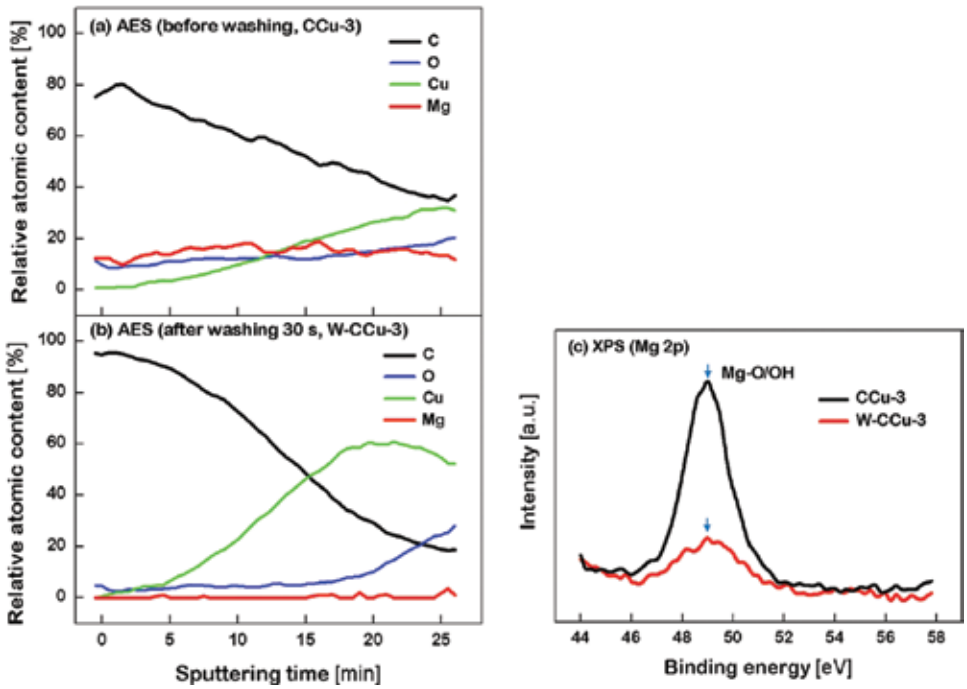

Figure 17. The relative atomic contents (measured by AES) of C, O, Mg, and Cu incorporated in the CNT-coated Cu mesh: (a) before washing (CCu-3) and (b) after washing (W-CCu-3). (c) The XPS Mg 2p spectra for CCu-3 and W-CCu-3 specimens.

used as the dispersant for the CNT suspension. On the other hand, it was discovered that the Mg content was almost negligible in the W-CCu-3 specimen, indicating that most of the Mg atoms were removed by post-washing. **Figure 17(c)** compares the XPS Mg 2p spectra of the CCu-3 and W-CCu-3 specimens. The XPS peak corresponding to Mg-O/OH [39] was observed at around 49 eV, and the peak intensity of the W-CuC-3 specimen was much smaller than that of the CuC-3 specimen, indicating that the Mg component was removed by post-washing. Accordingly, it was suggested that the lower reflectance and the smaller chromatic parameters, which were observed when the CNT-coated Cu meshes underwent post-washing, resulted from the removal of the residual Mg element.

6. Conclusion

CNTs have excellent chemical stability, thermal and electrical conductivity (high intrinsic conductivity), mechanical strength, flexibility, solution processability, and potential for production at a low cost. Based on these advantages, the CNT-based TCEs are presented. In Section 3, it was illustrated that the adhesion of the CNTs was remarkably improved after the surface modification via corona pretreatment of the PET substrates. Then, in Sections 4 and 5, the hybrid-type TCEs, which can be commercialized in various applications, were fabricated and their characteristics were demonstrated. In particular, the studies about improving the electrical conductivity and transmittance of CNTs-TCEs may warrant increased interest. Finally, in Section 5, the metal-based TCEs coated with CNTs were considered as an effective structure to resolve the high reflectance generated by the intrinsic properties of metals. Until now, the TCEs fabricated using only CNTs had insufficient properties for applications to electronic devices. Various hybrid-types of CNT-based TCEs, however, could have potential in the application to next-generation flexible and stretchable electronics to overcome various issues.

Author details

Bu-Jong Kim and Jin-Seok Park*

*Address all correspondence to: jinsp@hanyang.ac.kr

Department of Electronic Systems Engineering, Hanyang University, Ansan, Gyeonggi-do, Republic of Korea

References

[1] Cann M, Large MJ, Henley SJ, Milne D, Sato T, Chan H, Jurewicz I, Dalton AB. High performance transparent multi-touch sensors based on silver nanowires. Materials Today Communications. 2016;**7**:42-50. DOI: 10.1016/j.mtcomm.2016.03.005

[2] Lordan D, Burke M, Manning M, Martin A, Amann A, O'Connell D, Murphy R, Lyons C, Quinn AJ. Asymmetric pentagonal metal meshes for flexible transparent electrodes and heaters. ACS Applied Materials & Interfaces. 2017;**9**:4932-4940. DOI: 10.1021/acsami.6b12995

[3] Parkb J-M, Wang Z-J, Kwon D-J, Ga-Young G, Lawrence DeVries K. Electrical properties of transparent CNT and ITO coatings on PET substrate including nano-structural aspects. Solid-State Electronics. 2013;**79**:147-151. DOI: 10.1016/j.sse.2012.05.037

[4] Song C-H, Ok K-H, Lee C-J, Kim Y, Kwak M-G, Han CJ, Kim N, Byeong-Kwon J, Kim J-W. Intense-pulsed-light irradiation of Ag nanowire-based transparent electrodes for use in flexible organic light emitting diodes. Organic Electronics. 2015;**17**:208-215. DOI: 10.1016/j.orgel.2014.12.015

[5] Highly conductive PEDOT:PSS transparent electrode prepared by a post-spin-rinsing method for efficient ITO-free polymer solar cells. Solar Energy Materials & Solar Cells. 2016;**144**:143-149. DOI: 10.1016/j.solmat.2015.08.039

[6] Mallikarjuna K, Hwang H-J, Chunga W-H, Kim H-S. Photonic welding of ultra-long copper nanowire network for flexible transparent electrodes using white flash light sintering. RSC Advances. 2016;**6**:4770-4779. DOI: 10.1039/c5ra25548a

[7] Hajimammadov R, Csendes Z, Ojakoski J-M, Lorite GS, Mohl M, Kordas K. Nonlinear electronic transport and enhanced catalytic behavior caused by native oxides on Cu nanowires. Surface Science. 2017;**663**:16-22. DOI: 10.1016/j.susc.2017.04.011

[8] Jung S-G, Lee HJ, Hwang JH, Shim YS, Kim KN, Park CH, Park YW, Byeong Kwon J. Tungsten oxide buffer layer on silver nanowires for electrically stable, flexible, transparent hybrid electrodes using solution process. Late-News Poster. 2015;**46**(1):1386-1387. DOI: 10.1002/sdtp.10133

[9] Park S, Vosguerichian M, Bao Z. A review of fabrication and applications of carbon nanotube film-based flexible electronics. Nanoscale. 2013;**5**:1727-1752. DOI: 10.1039/c3nr33560g

[10] Akimitsu Narita, editor. Bottom-Up Synthesis of Chemically Precise Graphene Nanoribbons. Japan; 2013. 280 p

[11] Ok K-H, Kim J, Park S-R, Kim Y, Lee C-J, Hong S-J, Kwak M-G, Kim N, Han CJ, Kim J-W. Ultra-thin and smooth transparent electrode for flexible and leakage-free organic light-emitting diodes. Scientific reports. 2015;**5**:9464. DOI: 10.1038/srep09464

[12] Blackburn JL, Barnes TM, Beard MC, Kim Y-H, Tenent RC, McDonald TJ, Bobby T, Coutts TJ, Heben MJ. Transparent conductive single-walled carbon nanotube networks with precisely tunable ratios of semiconducting and metallic nanotubes. ACS Nano. 2008;**2**(6):1266-1274. DOI: 10.1021/nn800200d

[13] Feng Y, Miyata Y, Matsuishi K, Kataura H. High-efficiency separation of single-wall carbon nanotubes by self-generated density gradient ultracentrifugation. Journal of Physical Chemistry C. 2011;**115**:1752-1756. DOI: 10.1021/jp1100329

[14] Chandra B, Afzali A, Khare N, El-Ashry MM, Tulevski GS. Stable charge-transfer doping of transparent single-walled carbon nanotube films. Chemistry of Materials. 2010;**22**:5179-5183. DOI: 10.1021/cm101085p

[15] Hou P-X, Liu C, Cheng H-M. Purification of carbon nanotubes. Carbon. 2008;**46**:2003-2025. DOI: 10.1016/j.carbon.2008.09.009

[16] Park T-J, Banerjee S, Hemraj-Benny T, Wong SS. Purification strategies and purity visualization techniques for single-walled carbon nanotubes. Journal of Materials Chemistry. 2006;**16**:141-154. DOI: 10.1039/b510858f

[17] Rastogi R, Kaushal R, Tripathi SK, Sharma AL, Kaur I, Bharadwaj LM. Comparative study of carbon nanotube dispersion using surfactants. Journal of Colloid and Interface Science. 2008;**328**:421-428. DOI: 10.1016/j.jcis.2008.09.015

[18] Jang EY, Kang TJ, Im H, Baek SJ, Kim S, Jeong DH, Park YW, Kim YH. Macroscopic single-walled-carbon-nanotube fiber self-assembled by dip-coating method. Advanced Materials. 2009;**21**:4357-4361. DOI: 10.1002/adma.200900480

[19] Chatzikomis C, Pattinson SW, Kozio KKK, Hutchings IM. Patterning of carbon nanotube structures by inkjet printing of catalyst. Journal of Materials Science. 2012;**47**:5760-5765. DOI: 10.1007/s10853-012-6467-2

[20] Sung WY, Lee SM, Kim WJ, Ok JG, Ho YL, Kim YH. New approach to enhance adhesions between carbon nanotube emitters and substrate by the combination of electrophoresis and successive electroplating. Diamond & Related Materials. 2008;**17**:1003-1007. DOI: 10.1016/j.diamond.2008.03.001

[21] Urbaniak-Domagala W. Pretreatment of polypropylene films for the creation of thin polymer layers, part 1: The use of chemical, electrochemical, and UV methods. Journal of Applied Polymer Science. 2011;**122**:2071-2080. DOI: 10.1002/app.34301

[22] Liua X-D, Shenga D-K, Gaoa X-M, Tong-Bing L, Yang Y-M. UV-assisted surface modification of PET fiber for adhesion improvement. Applied Surface Science. 2013;**264**:61-69. DOI: 10.1016/j.apsusc.2012.09.107

[23] Gorenšek M, Gorjanc M, Bukošek V, Kovac J, Jovancić P, Mihailović D. Functionalization of PET fabrics by corona and nano silver. Textile Research Journal. 2010;**80**(3):253-262. DOI: 10.1177/0040517509105275

[24] Owens DK, Wendt RC. Estimation of the surface free energy of polymers. Journal of Applied Polymer Science. 1969;**13**:1741-1747. DOI: 10.1002/app.1969.070130815

[25] Park S-J, Jin J-S. Effect of corona discharge treatment on the dyeability of low-density polyethylene film. Journal of Colloid and Interface Science. 2001;**236**:155-160. DOI: 10.1006/jcis.2000.7380

[26] O'Hare L-A, Smith JA, Leadley SR, Parbhoo B, Goodwin AJ, Watts JF. Surface physico-chemistry of corona-discharge-treated poly(ethylene terephthalate) film. Surface and Interface Analysis. 2002;**33**:617-625. DOI: 10.1002/sia.1429

[27] Jacobs T, Carbone E, Morent R, De Geyter N, Reniers F, Leys C. Surfacemodification of polymer films with a remote atmospheric pressure d.C. glow discharge: Influence of substrate location. Surface and Interface Analysis. 2010;**42**:1316-1320. DOI: 10.1002/sia.3319

[28] Jia H, Lian Y, Ishitsuka M, Nakahodo T, Yutaka M, Tsuchiya T, Wakahara T, Akasaka T. Centrifugal purification of chemically modified single-walled carbon nanotubes. Science and Technology of Advanced Materials. 2005;**6**:571-581. DOI: 10.1016/j.stam.2005.08.004

[29] Sahoo NG, Cheng HKF, Bao H, Pan Y, Li L, Chan SH. Covalent functionalization of carbon nanotubes for ultimate interfacial adhesion to liquid crystalline polymer. Soft Matter. 2011;**7**:9505-9514. DOI: 10.1039/c1sm05360d

[30] Zhang J, Gao L, Sun J, Liu Y, Wang Y, Wang J. Incorporation of single-walled carbon nanotubes with PEDOT/PSS in DMSO for the production of transparent conducting films. Diamond & Related Materials. 2012;**22**:82-87. DOI: 10.1016/j.diamond.2011.12.008

[31] Xiao G, Ye T, Jianping L, Zhang Z. Highly conductive and transparent carbon nanotube composite thin _lms deposited on polyethylene terephthalate solution dipping. Thin Solid Films. 2010;**518**:2822-2824. DOI: 10.1016/j.tsf.2009.11.021

[32] Hecht DS, Thomas D, Liangbing H, Ladous C, Lam T, Park Y, Irvin G, Drzaic P. Carbon-nanotube film on plastic as transparent electrode for resistive touch screens. Journal of the SID. 2009;**17**(11):941-946. DOI: 10.1889/JSID17.11.941

[33] Boccaccini AR, Cho J, Roether JA, Thomas BJC, Jane Minay E, Shaffer MSP. Electrophoretic deposition of carbon nanotubes. Carbon. 2006;**44**:3149-3160. DOI: 10.1016/j.carbon.2006.06.021

[34] Kiefera R, Temmer R, Tamm T, Travas-Sejdic J, Kilmartin PA, Aabloo A. Conducting polymer actuators formed on MWCNT and PEDOT-PSS conductive coatings. Synthetic Metals. 2013;**171**:69-75. DOI: 10.1016/j.synthmet.2013.03.017

[35] Koidis C, Logothetidis S, Kapnopoulos C, Karagiannidis PG, Laskarakis A, Hastas NA. Substrate treatment and drying conditions effect on the properties of roll-to-roll gravure printed PEDOTPSS thin films. Materials Science and Engineering B. 2011;**176**:1556-1561. DOI: 10.1016/j.mseb.2011.03.007

[36] Jin Y, Li Q, Chen M, Li G, Zhao Y, Xiao X, Wang J, Jiang K, Fan S. Large area nanoscale metal meshes for use as transparent conductive layers. Nanoscale. 2015;**7**:16508-16515. DOI: 10.1039/c5nr04528b

[37] Sun T, Akinoglu EM, Guo C, Paudel T, Gao J, Wang Y, Giersig M, Ren Z, Kempa K. Enhanced broad-band extraordinary optical transmission through subwavelength perforated metallic films on strongly polarizable substrates. Applied Physics Letters. 2013;**102**:101114. DOI: 10.1063/1.4795151

[38] Mizuno K, Ishii J, Kishida H, Hayamizu Y, Yasuda S, Futaba DN, Yumur M, Hata K. A black body absorber from vertically aligned single-walled carbon nanotubes. PNAS. 2009;**106**:6044-6047. DOI: 10.1073/pnas.0900155106

[39] Fotea C, Callaway J, Alexander MR. Characterisation of the surface chemistry of magnesium exposed to the ambient atmosphere. Surface and Interface Analysis. 2006;**38**: 1363-1371. DOI: 10.1002/sia.2463

Chapter 12

Production of Water Dispersible Carbon Nanotubes and Nanotube/Cellulose Composite

Kazi Hanium Maria and Tetsu Mieno

Additional information is available at the end of the chapter

http://dx.doi.org/10.5772/intechopen.70543

Abstract

Polymer wrapping methods have been used to disperse carbon nanotube (CNT) by using gelatin, an environment-friendly and easily decomposable biopolymer. The amino acid chain of gelatin becomes immobilized by the physical adsorption in the side wall of the CNTs through hydrophobic-hydrophobic interaction and results in the untangling of the CNT bundles. The dispersed solution remains stable for more than a month. Furthermore, this technique does not affect the physical properties of CNTs while enabling their dispersion in aqueous solutions. In addition, gelatin can be easily removed from the nanotubes after the dispersion of nanotubes by heating in water and filtration. Gelatin-dispersed CNTs are homogeneously mixed with the cellulose suspension and dried at room temperature to produce CNT/cellulose composite paper sheet. Adding multiwalled carbon nanotubes (MWNTs) in composite improves the mechanical, thermal, and electrical properties of cellulose. SEM investigation confirms the homogeneous distribution of MWNTs in the cellulose, which can be attributed to the improvement of its characteristics. Both sides of the CNT/cellulose sheet show uniform electrical conductivity, which is enhanced by increasing the MWNTs' content. IR image of the sheet clearly shows the temperature homogeneity of the surface. Thermal stability and the flame retardancy of the sheet are also found to be improved. The sheet has also strong absorbing of electromagnetic waves, which make them important for microwave technology applications.

Keywords: carbon nanotube, polymer wrapping, water dispersibility, gelatin, CNT/cellulose composite

1. Introduction

Carbon nanotubes (CNTs) are realized to have a tremendous potential in many fields of applications because of their associated admirable chemical and physical properties [1, 2]. These molecular-scale

tubes of graphitic carbon are among the stiffest and strongest fibers known and have remarkable optical, electronic, and mechanical properties and many other unique characteristics [3]. For these reasons, there are already many studies using CNTs for electronic devices, including the use of CNTs as transistor channels, electrical wiring for lighting solutions industries (LSIs), and electron emitters [4–8]. Nevertheless, the as-produced material is extremely difficult to process. CNTs have a tendency to aggregate owing to the van der Waals attractive interaction between their sidewalls [9]. This tube-to-tube contact results in the hydrophobic nature of CNTs, which is responsible for their poor solubility in water and also incompatibility with a majority of solvents [10]. As a result, CNTs are precipitated in solvent. This lack of solubility and the difficulty of manipulating them in solvents limit the development of CNT-based devices or composites of interest for new applications. In order to obtain fine dispersion in the selected solutions, especially water, it is important to break the cohesion of aggregated CNTs. Development of efficient processes and chemical treatments that are able to control the quality of the CNT samples and to induce both their dispersion and partial or complete de-bundling remains highly challenging. Chemical modifications are the well-established method up to now, though this method modifies the desirable properties of CNTs [11]. On the other hand, polymer wrapping methods can preserve the intrinsic properties of CNTs. Usually, polymers and surfactants wrap the nanotube surface to enable the CNT dispersion in aqueous solutions [12, 13]. Also, this method produces impurity in the sample because wrapped polymers and surfactants become stuck in the sample after dispersion. Therefore, to overcome this problem, easily decomposable polymer should be considered for the dispersion of the CNTs. Here, in this chapter, various dispersion methods will be reviewed and an efficient procedure for the water dispersion will be reported by using gelatin, an environment-friendly material to wrap the surface of single walled carbon nanotubes (SWNTs) enabling their dispersion in water.

Next-generation computer devices, consumer electronics, wireless LAN devices, wireless antenna systems, cellular phone systems, high-performance sportswear, wearable displays, new classes of portable power, and embedded health monitoring devices are few portable device applications that have attracted a large interest in the scientific community because of their remarkable utilities [4–8]. The design of soft portable electronic equipment requires the development of a new class of materials with an array of novel functionalities, such as flexibility, stretch ability, and light-weight. Generally, this new class of material is termed as composites, which allow for many applications and designs previously impossible with traditional electronics technology. Nowadays, composites based on carbon nanotubes (CNTs) are very promising for the continuous growth of telecommunication market due to their many unique chemical and physical properties. Here, we introduced a convenient production method for the CNT composite, where cellulose is employing with multiwalled carbon nanotube (MWNTs) to enlarge the cellulose functionalities. This approach is illustrated by the blending of CNT with cellulose and characterization studies show that CNTs enable them to show outstanding electrical properties and thermal stabilities.

2. Water dispersibility of CNTs

Because of strong van der Waals attraction, the CNTs pack into bundles that aggregate into tangled networks, and thus do not disperse well in the water in their pristine state [9]. For optimal performance in most applications, the CNT should be separated into individual tubes

or bundles of only a few tubes. Dissolution of CNT in water has been facilitated by suitable enhancement of the surface of the nanotubes.

Generally, there are two mechanisms to disperse nanotube. In the mechanical mechanism, nanotube disentanglement is done by sonication and high-shear mixing. Sonication cut the longer nanotube into pieces to disperse CNT easily into water. As a result, the aspect ratio of nanotube also decreases in this way. Besides this, the stability of the dispersion is poor. Nevertheless, the chemical mechanism incorporates both covalent and non-covalent methods. In covalent functionalization, chemical modifications can be performed at the sidewall site, which causes the transformation of sp^2 into sp^3 hybridized carbon atoms [14] or at the defect sites via amidation or esterification reactions of carboxylic residues obtained on CNTs [15]. Usually, this sidewall modification or defect functionalization are the continuation of CNT treatment with strong acid such as HNO_3, H_2SO_4 or a mixture of them, or with strong oxidants such as $KMnO_4$, ozone, and reactive plasma, which open the tubes and consequently produce oxygenated functional groups such as carboxylic acid, ketone, alcohol, and ester groups. Therefore, they produce different types of chemical moieties onto the ends and defect sites of these tubes, which in turn significantly change the mechanical properties of CNTs by destroying the perfect structure of CNTs as well as disruption of π electron system in nanotubes, which is detrimental to transport properties of CNTs. Furthermore, strong oxidants or concentrated acids are environmentally unfriendly, which are often used for CNT functionalization. **Figure 1** shows the different kinds of CNT functionalizations.

A non-covalent mechanism associated with the adsorption of the chemical moieties onto the nanotube surface, either via π–π stacking interaction such as in DNA, uncharged surfactants, etc., or through coulomb attraction in the case of charged chemical moieties [16]. Compared to covalent functionalizations, non-covalent functionalizations are more capable of preserving

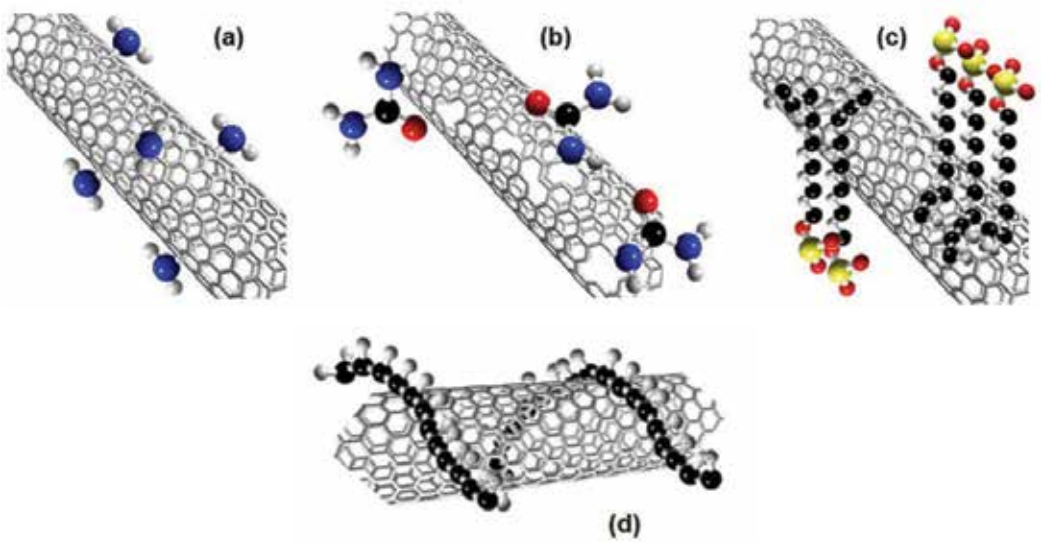

Figure 1. Different type of functionalization possibilities of CNTs: (a) covalent sidewall functionalization, (b) covalent defect sidewall functionalization, (c) non-covalent adsorption of surfactants, and (d) wrapping of polymers. Adapted from Ávila-Orta et al. [16].

intrinsic properties of CNTs when improving exfoliation and interfacial bonding. Though, the concern of this approach is the presence of physically bound modifier molecules on the surface, such anomalies can be removed easily by washing. Besides, this method increases the solubility of CNTs, making them less toxic and preserving the electrical properties of CNTs. Polymer wrapping method are widely used non-covalent approach that attributed to the physical association of polymers with CNTs. Polymers can wrap around CNTs, forming supramolecular complexes and most of the nanotubes are found as single tubes associated with at most a single layer of polymer. A smaller number of aggregates consisting of more than one nanotube are also remained at the dispersion. The advantage is that a stable suspension is observed for months. Stabilizing dispersions of carbon nanotubes (CNTs) is a major challenge, since it is a prerequisite to high performance of CNT in a large field of applications.

3. Methodology of gelatin-wrapped CNTs

Water dispersible CNTs without changing their physical properties are a significant challenge and a prerequisite for their applications [4–8]. For this reasons, polymer wrapping method can be the best option for CNT dispersion, because, in this method, polymer and surfactants are used to exfoliate the nanotube from the nanotube bundles by wrapping the individual nanotube surface while enabling their dispersion in aqueous solutions [12, 13]. As a result of polymer wrapping, polymers and surfactants stay in the sample synchronously to intact the physical properties of CNTs. The remaining polymers and surfactants create impurity in the samples, which in turn influence the CNT application. Therefore, easily decomposable polymer can be used to get rid of this issue as well as to produce safe nanotube materials for the nano-bioscience and technology. Here, we used the biocompatible, non-immunogenic gelatin to wrap the surface of CNTs enabling their dispersion in water [17]. Moreover, gelatin is an environment-friendly material and easy to remove from the CNTs by heating in water and filtering. This method is safe compared to the other methods available in the literature, as no hazardous reagents are used here.

3.1. Molecular structure of gelatin

Gelatin has a noticeable property of forming elastic gels at room temperature for relatively low concentrations (a few per cent of gelatin in water). It is a denatured collagen and contains different amino acid content. Collagen, which is the major protein present in animal bones, skin, and connective tissue, consists of rigid bar-like molecules that arranged in fibers are interconnected by covalent bonds. These molecules have three polypeptide chains such as glycine, proline, and 4-hydroxyproline, and they are arranged in a triple helix that is stabilized by hydrogen and hydrophobic bonds. Gelatin is a mixture of α-chains (one polymer/single chain), β-chains (two α-chains covalently cross-linked), and γ-chains (three covalently cross-linked α-chains) [18]. Gelatin also has a mixture of single and double unfolded chains of hydrophilic character. The physical properties of gelatin depend on amino acid compositions, relative content of α-chains, β- or γ-components, and higher molecular weight aggregates. A typical structure of gelatin is -Ala-Gly-Pro-Arg-Gly-Glu-4Hyp-Gly-Pro- which is shown in **Figure 2**.

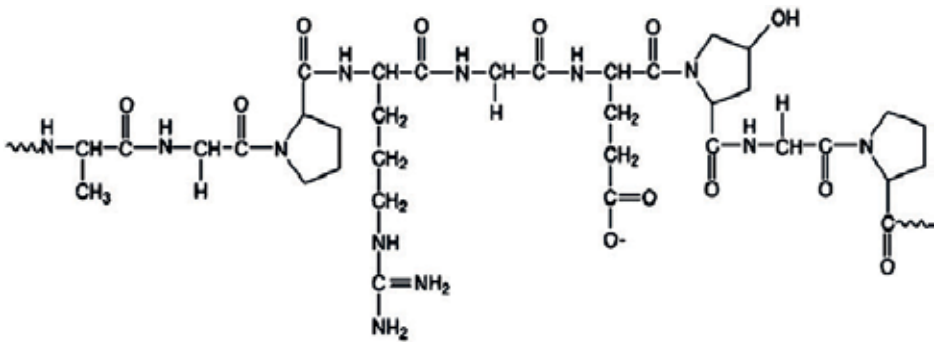

Figure 2. A typical Structural unit of gelatin. Adapted from Ref [18].

There are two types of gelatin depending on acid or alkaline treatment. Type A gelatin (isoionic point of 6–9) is collected from acid-treated collagen, whereas alkali-treated precursor is responsible for manufacture type B (isoionic point of 5) gelatin. Usually type A gelatin and type B gelatin are successively extracted from pigskin and beef skin [19].

3.2. Properties of gelatin

The properties of gelatin are influenced by the intrinsic factors such as the source, age of the animal, and type of collagen. Gelatins produced from cattle and pigs' bones and skins are mostly used in commercial. Recently, gelatin from fish and poultry has received considerable attention and may serve as important commercial gelatin sources into the future [20]. This is because proteins derived from these sources may possess similar functional properties like mammalian. Moreover, fish gelatin is free from bovine spongiform encephalopathy (BSE) which is commonly called mad cow disease and more religiously acceptable.

Gelatin macromolecules can display a wide variety of conformations under specific conditions such as temperature, solvent, and pH. It can form a physical thermos-reversible gel at room temperature or below 40°C for relatively low concentrations. If the temperature is raised, the gel "melts," becoming liquid again [19]. This reversible conformational nature of gelatin makes it a suitable dispersing agent of carbon nanotube dispersion, which can be removed thermally.

Gelatin has different amino acid composition and the molecular weight distribution based on their type. The gel strength, viscosity, pH, and melting point of gelatin depend on their structure and the amino acid chain [18–20]. Generally, gelatin with the higher number of amino acids chains have higher gel strength, which in turn increases the melting point. Over a wide range of pH values, gelatin behaves like polyampholyte, where the gelatin macromolecule has mixed anion and cation character, which also has uncharged hydrophilic and hydrophobic groups [20]. This in turn makes gelatin molecules soluble in water but may also cause them to be adsorbed at charged or hydrophobic surfaces.

3.3. Preparation of gelatin dispersed CNTs

Pristine SWNT powder (Nanostructure & Amorphous Materials Inc., diameter = 1–2 nm, length = 5–30 μm, purity = 90%), MWNTs (Sigma-Aldrich, outer diameter = 10–30 nm, inner

diameter = 3–10 nm, length = 1–10 μm, purity >90%), and geletin (Wako 1st Grade, appearance: yellowish-brown and crystalline powder) are used as received to prepare the mixture and the mixture is observed to check the dispersion ability. 5 mg raw carbon soot and 20 mg gelatin were mixed with 20 ml of pure water (Wako Pure Chemical Industries Ltd.). Both MWNT and SWNT soot was used with gelatin to prepare the mixture. An ultrasonic homogenizer equipped with a microtip sonotrode (VC 130, Vibra Cell, Sonics & Materials Inc., f = 20 kHz, 6 mmϕ probe) was intermittently operated to stir the mixture. The input power of homogenizer was always kept at 20 W and the mixing was for 60 min, where the duty ratio was 60%. The collected gelatin-SWNT and gelatin-MWNT dispersion last above a month at room temperature.

4. Evaluation of dispersibility of the CNTs with gelatin

The CNTs have a tendency to aggregate owing to the attractive interaction between their sidewalls. CNTs can be hydrated by gelatin, which can wrap around their sidewalls [17], as schematically shown in **Figure 3**.

4.1. Visual inspection of gelatin-CNT dispersibility

The resulting hydrophobic nature is responsible for their poor solubility in water, and CNTs are precipitated in water as shown in **Figure 4(a)** and **(b)**. Most polymer wrapping methods depend on the physical adsorption of the polymer on the surface of the CNTs to increase the solubility of the nanotubes.

Gelatin is a natural water-soluble biopolymer that is composed of 18 types of amino acid chains [21, 22]. The amino acid chains of the gelatin wrap around the sidewalls of the CNTs through a hydrophobic-hydrophobic interaction [17, 21, 23]. Gelatin has zwitterionic structure and the amino acid chain of the gelatin has hydrophobic nature. CNTs' surfaces are also hydrophobic. This hydrophobic-hydrophobic interaction may include a hydrophilic group to the CNTs' surface, which in turn disperses CNT into water, as shown in **Figure 4(c)** and **(d)**. The CNT dispersion is found to last over a month.

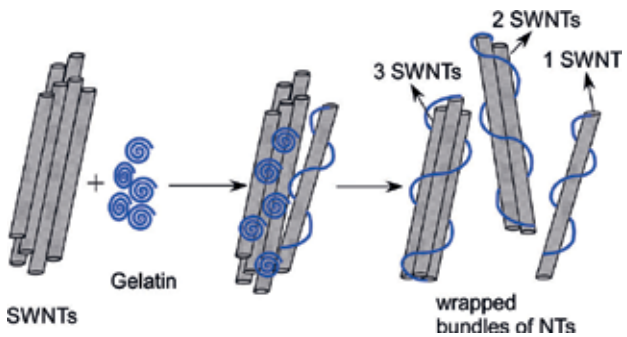

Figure 3. Schematic showing wrapping of SWNTs with gelatin. Adapted from Maria and Mieno [17].

Figure 4. Photographs of (a) SWNT dispersion in water immediately after sonication, (b) SWNT precipitate in water after a few hours, (c) SWNT dispersion in gelatin-water solution immediately after sonication, and (d) stable SWNT-gelatin dispersion after 1 month.

4.2. TEM observation of gelatin-CNT dispersion

To observe the dispersion state of the wrapped CNTs in water, one drop of the solution is placed on a copper grid coated with a collodion film for the image observation from the transmission electron microscope (TEM, JEOL JEM1400, accelerating voltage 100 kV). **Figure 5** is a typical TEM image where it is shown that the CNTs are well wrapped with gelatin. It is seen that the gelatin uniformly wrapped around the entire surface of tubes making the SWNTs opaque and surfaces rough as compared with unwrapped SWNTs. The wrapping mechanism of polymer is believed to be driven largely by thermodynamics to eliminate hydrophobic interface between the tubes and the aqueous medium. In case of growth technique of NT, metal particle is used in the electrode as a catalyst to grow SWNTs and then remain attached to the SWNTs as impurity. Usually, amorphous carbon and metal nanoparticles are produced

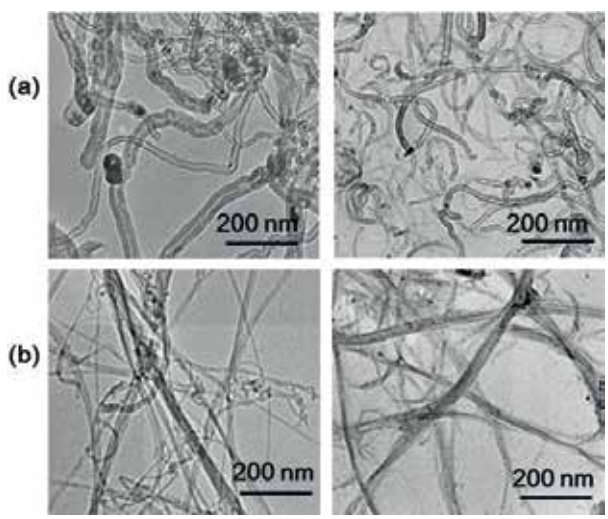

Figure 5. Typical TEM images of (a) pure MWNTs and (b) pure SWNTs. Left side shows the pristine nanotubes and right side shows the dispersed nanotube bundles in aqueous gelatin solution.

with the SWNTs as byproducts. These byproducts can be dispersed by gelatin also and can be removed from SWNTs dispersion by filtration. Another worth mentioning advantage of using gelatin as a dispersing agent is that dried gelatin-wrapped CNTs are easily re-dissolved in water with sonication.

4.3. Investigation by UV–visible spectrometer

A UV–visible spectrometer (JASCO Co., V-630) was used to examine the dispersion stability of the dispersed solution. For this experiment, 1 mg of raw soot and 5 mg of gelatin were mixed with 10 ml of pure water to make the sample. The sample was placed in a quartz cuvette (1.0 × 1.0 × 4.5 cm^3) and time variation of absorbance (Abs) at a wavelength of 233 nm was measured for 4 h. Here, the wavelength was chosen corresponding to the maximum absorbance region of the UV–visible spectra. **Figure 6** shows the time variation of absorption spectrum for gelatin-SWNT dispersing liquid at a wavelength of 233 nm. It is noticed that the absorbance started to decrease for more than 1 h and then shows a stable nature with the increase of time, which indicates the stability of gelatin-SWNT dispersion.

From the above analysis, it is found that the gelatin-CNT dispersion is very stable and CNTs do not precipitate in water. Therefore, it can claim that the gelatin molecules wrap around CNTs and CNTs are separated and dispersed in water. This easy way to make dispersed solution of CNT has great impact on the application field. CNT composite material can be made by using this gelatin-CNT dispersion as gelatin can be easily removed by heating and filtration.

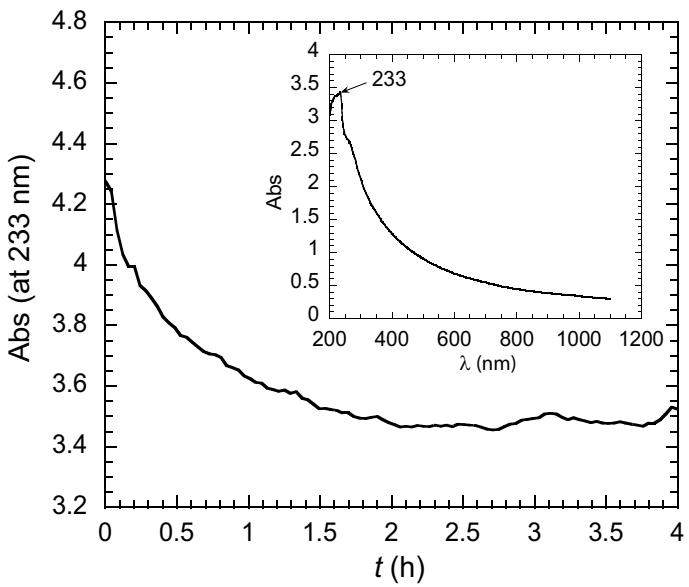

Figure 6. Absorbance vs. time at λ = 233 nm to measure the stability of the gelatin-SWNT dispersion. Inset shows the UV absorption spectrum of the solution.

5. CNT/polymer composites

Generally, composites are composed of two or more materials, which exhibit the unique properties of combined materials. These composites, such as polymer composites, have enhanced mechanical properties because they combine the properties of high modulus carbon fibers and polymer [24]. The additive has great effect in polymer composites because the modulus, strength, and high-fracture toughness of composites are built upon on the nature of additive. By employing the nanoscale CNT into a polymer system results in very short distance between the fillers; thus, the properties of composites can be largely modified even at an extremely low content of filler. Thus, CNT/polymer composites, consisting of CNT as additives and polymer matrices, are considered to be an important group of relatively inexpensive materials for many engineering applications. In order to successfully introduce CNTs in large-scale industrial applications, they need to be homogeneously embedded into light-weight polymer to make nanocomposites. The combination of mechanical and electrical properties of individual nanotubes makes them the ideal reinforcing agents in a number of applications. CNT-polymer composites are promising as new generation materials, and the importance for nanocomposites will increase as miniaturization becomes more important in areas, such as computing, sensors, biomedical, and many other applications [25]. Therefore, CNT/polymer nanocomposites are one of the utmost investigated composite because of the easy fabrication of polymer matrix without damaging CNTs. Another advantage is the low cost of polymer for which mass production of nanocomposites would be possible in the future.

5.1. Objective of CNT/cellulose composite

Recently, the rapid development of portable device hardware has aroused huge demand for lighter and more efficient heat-transfer materials [25]. As the overweighted heat-transfer materials have delayed the development of portable device hardware, it is required to develop light, flexible, inexpensive, and even roll up or wearable devices for multifunctional portable electronics [6, 26, 27]. In this case, composite materials consisting of carbon nanotubes and cellulose can be the ideal solution [28, 29], because nanocomposites have the potential to significantly surpass the properties of conventional bulk materials. The difficulties in developing such nanocomposites are dispersion of nanotubes, CNT-polymer interactions, manufacturing cost, and performance of the composite. Cellulose have attracted great attention with expertise in diverse areas [30, 31] as a renewable source-based biodegradable polymer and becomes a major medium for displaying and transmitting information owing to its potential compostibility, mechanical stability under atmospheric conditions, and ability to absorb ink [32]. Carbon nanotubes (CNTs) are regarded as one of the most versatile additives of composites because it can improve mechanical and electrical characteristics of cellulose [33]. Especially, homogeneous distribution of CNTs in the cellulose matrix has predominantly contributed to improve its characteristics. CNT forms a conducting network using its electron donating and accepting ability in the composite [6, 34–36]. These CNT/cellulose composite materials have some outstanding properties such as being highly strong, electrically

and thermally conductive, and the usage of these materials have been widely investigated [35–38]. CNT/pulp has been prepared by a paper making process, which is a fast, simple, robust, low-cost, and readily scalable process. The properties of the resulting CNT/cellulose paper sheet are also identified and reported here.

5.2. Fabrication of CNT/cellulose composites

The most important part of preparation of CNT/cellulose composites is to improve the interaction between the pulp fibers, gelatin and multiwalled carbon nanotubes (MWNTs) to optimize the paper making process for CNT/cellulose composites. MWNTs and geletin are purchased from Sigma-Aldrich and Wako Pure Chemical, respectively, which are used as received. Cellulose fibers used here are obtained directly from manufacturing facility, where cellulose is processed with a beater to get uniform pulp in the sheet.

At first, the cellulose suspension is made by soaking the fibers into pure water and blended for 20 min. 10 mg of MWNTs (outer diameter = 10–30 nm, inner diameter = 3–10 nm, length = 1–10 μm, purity >90%) and 30 mg of gelatin are sonicated with 10 ml of pure water by using a supersonic homogenizer (Sonic vibra cell, VC 130, Sonic & Materials Inc., f = 20 kHz, 6 mmφ probe) at an input power of 20 W for 60 min. Then, 300 mg of cellulose suspension is added to the CNT dispersion and blended for 20 min. The final solution is poured into a tray dish and dried at room temperature to get a paper sheet. A possible paper making process is schematically shown in **Figure 7**. The obtained paper sheets have a thickness of about 0.2–0.4 mm. **Figure 8** shows the image of the cellulose pulp, SEM image of the pulp, and CNT/cellulose coposit sheet.

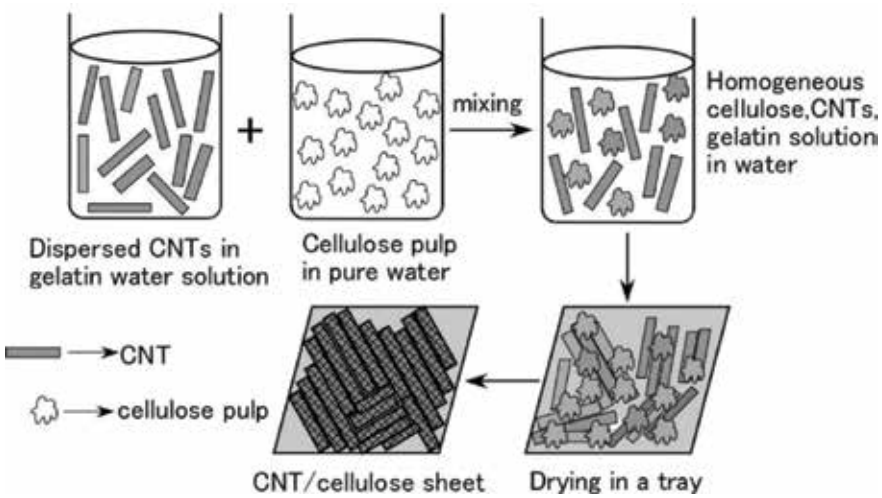

Figure 7. A schematic of the paper making process for the fabrication of CNT/cellulose composite sheets. Adopted from Maria and Mieno [37].

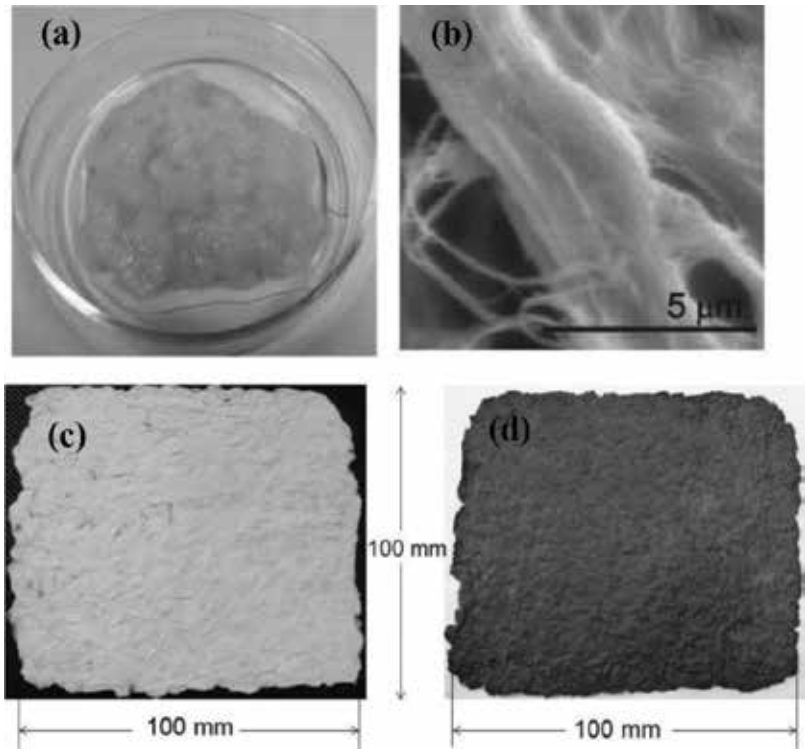

Figure 8. (a) Image of the cellulose pulp that used for making the sheet, (b) SEM image of the pure cellulose pulp at low magnification (×5000), (c) photographs of a pure cellulose sheet (left), and (d) a CNT/cellulose sheet (right).

5.3. Presence of CNTs on the composite sheet

The image of the uniform distribution of MWNTs in the CNT/cellulose composite is taken by a SEM (JEOL JSM 6510LV, operating voltage of 10 kV) to observe the morphology of the sheet as well as the presence of CNT into the composites. It is observed from **Figure 9** that CNTs cover surface of almost all fibers of the sheet. Some CNTs seem to form bridge-like structure with paper fibers. The SEM images clearly reveal that the interconnected networks established by the individual CNTs so that numerous electrical paths can be formed. In contrast with the SEM observation, Raman measurement (JASCO NR-1800, using a laser for excitation, λ = 532 nm) also confirmed the presence of CNTs in the paper sheets. It is observed that Raman peaks of both G-band and D-band and radial breathing modes generated from CNTs, as shown in **Figure 10**.

5.4. Properties of CNT/cellulose composites

5.4.1. Electrical properties of the CNT/cellulose composite sheet

As CNT forms the conducting paths into the cellulose sheet, composites shows considerable resistance. Resistance is measured of 10 randomly chosen measuring points on both sides (A side and B side) of

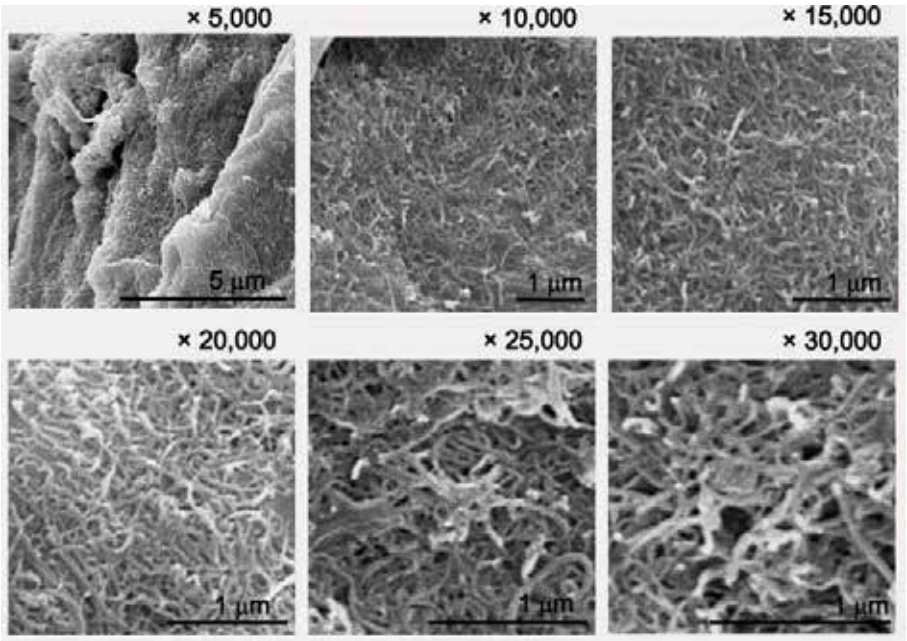

Figure 9. SEM images of the CNT-paper sheet at different magnifications taken at an operating voltage of 10 kV.

a CNT/cellulose paper sheet by the needle-electrodes, and the distance between needle-electrodes are kept constant at 20 mm. The distributions of the resistances are shown as histograms in **Figure 11**.

It is found that the electrical conductivity of the CNT/cellulose paper sheets is highly uniform. In case of 5 mg MWNTs added sheet, the A side has resistance, R = 2.61 MΩ (standard deviations, s = ±0.08, electrical conductivity, σ = 1.91 mS/m) and the B side has resistance, R = 2.60 MΩ (standard deviations, s = ±0.05, electrical conductivity, σ = 1.92 mS/m). When 10 mg of MWNTs are added, the A side has resistance, R = 1.14 MΩ (standard deviations, s = ±0.04, electrical

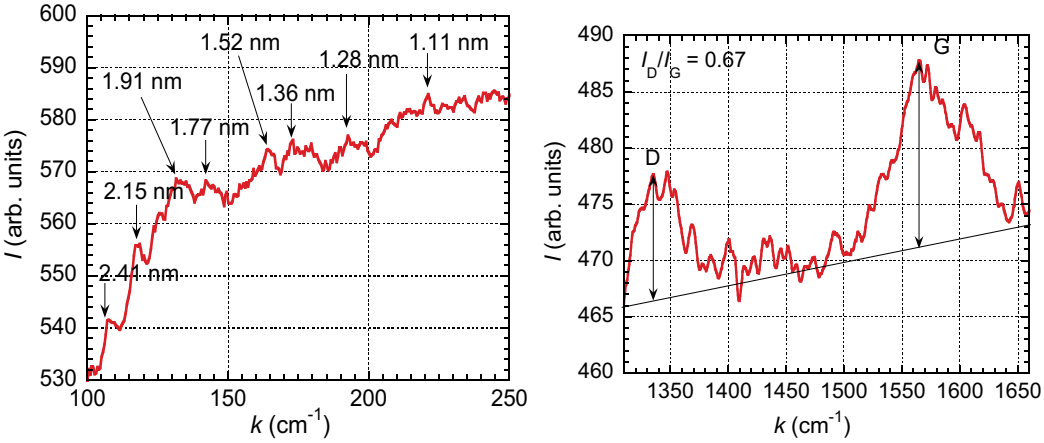

Figure 10. Raman spectra of the CNT/cellulose paper sheet. RBM modes are shown on the left side and the G and D bands are shown on the right side.

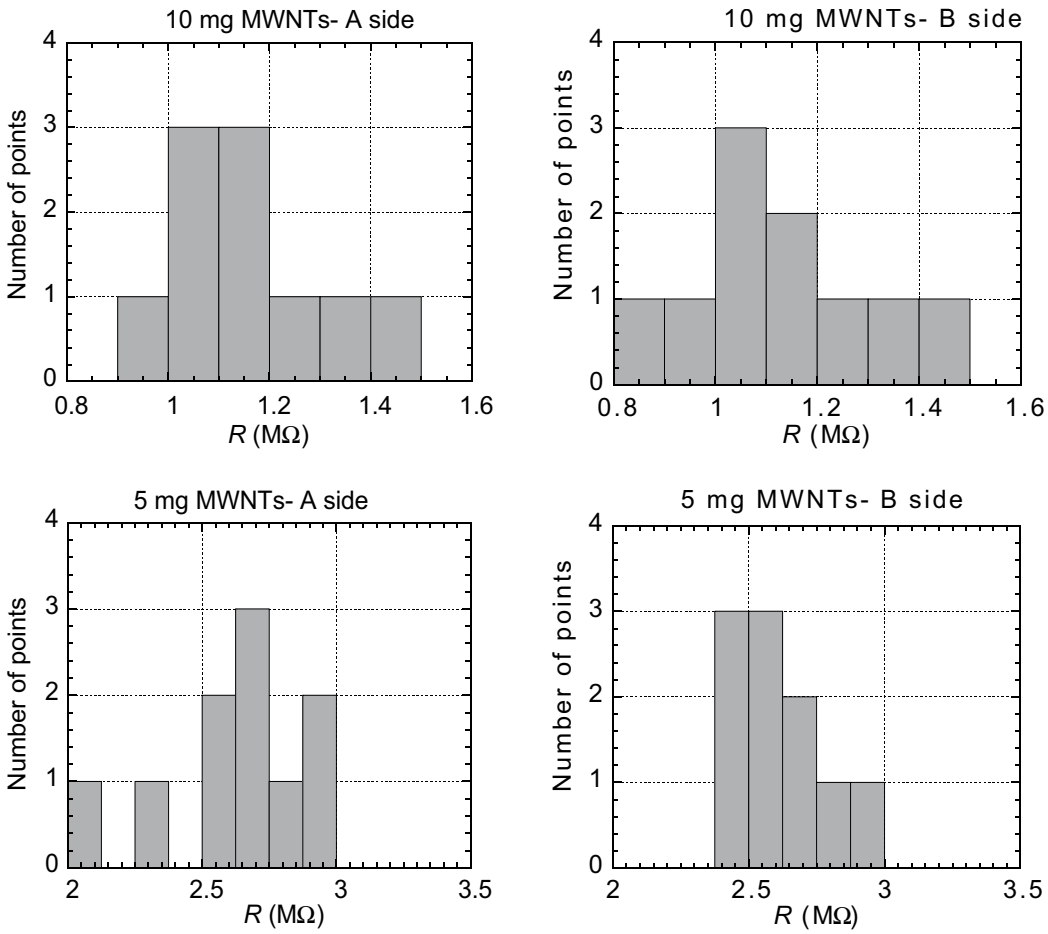

Figure 11. Histograms of measured resistance on the both sides of the CNT/cellulose paper sheet. Resistances are decreased with the increase of MWNTs content.

conductivity, σ = 4.38 mS/m) and the B side has resistance, R = 1.103 MΩ (standard deviations, s = ±0.05, electrical conductivity, σ = 4.53 mS/m). Therefore, it is noticed that the conductivity can be improved by increasing the amount of CNTs added to the cellulose [37]. I-V_{in} characteristic curve shows the ohmic conduction on the paper sheet as shown in **Figure 12**.

5.4.2. Thermal properties of the CNT/cellulose composite sheet

TG/DTA (Rigaku Thermoplus Analyzer, TG8120) experiments for the cellulose sheet and the CNT/cellulose sheet are carried out at a heating rate of 10°C/min from room temperature to 800°C and the curves are shown in **Figure 13**. DTA curves show that the thermal degradation of the both sheets occurs in two different steps in air atmosphere. In the first step of degradation, the cellulose sheet and the CNT/cellulose sheet begin to lose weight at 332 and 355°C, respectively, and the final combustion in second step occurs at 409 and 507°C, respectively. The final combustion of the CNT/cellulose sheet delayed by ca. 100°C is clearly observed from

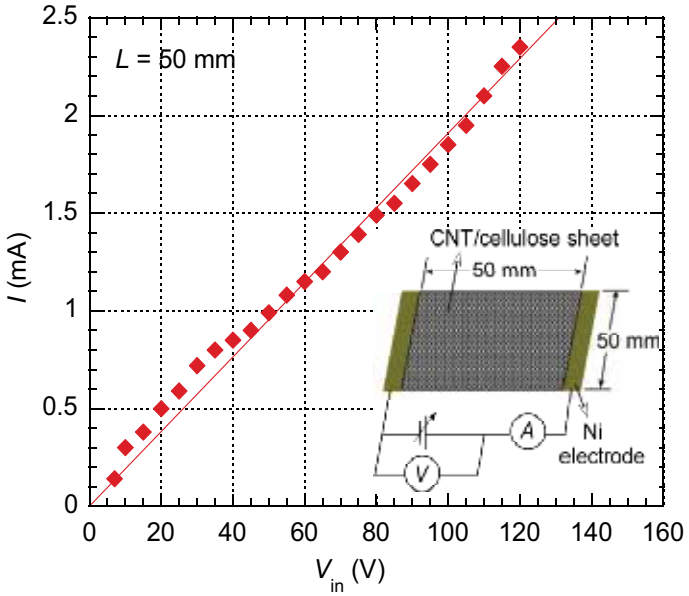

Figure 12. I-V_{in} curve for L = 50 mm showing the linear conduction (inset: Schematic of the I-V_{in} characteristic measurement setup).

the DTA curves, which indicate that cellulose sheets losses weight faster than CNT/cellulose sheet. From the TG curves, it is observed that the combustion rate of CNT/cellulose sheet is 22% less than that of the pure cellulose sheet. This result signifies that the thermal stability

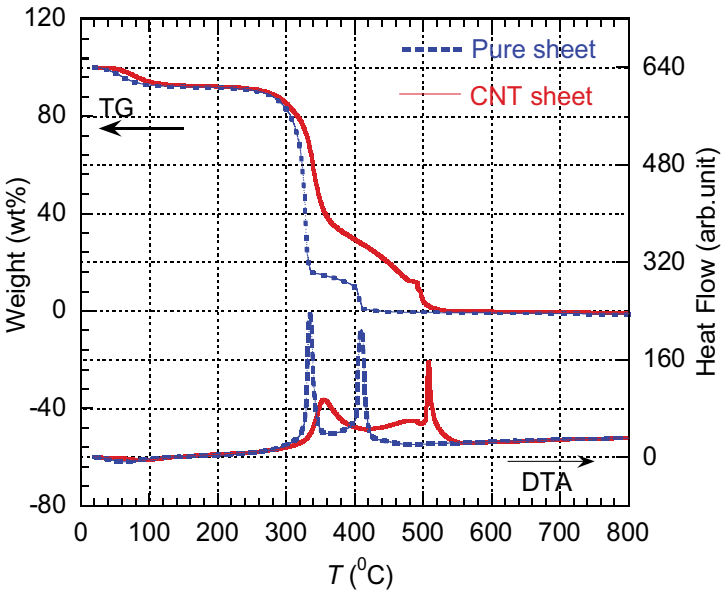

Figure 13. TG/DTA curves for the pure cellulose sheet (dotted line) and the CNT/cellulose sheet solid line).

of the sheet is improved by adding MWNTs [35, 37, 39]. There is also an additional peak at 477°C on the CNT/cellulose curve before the final combination peak, which corresponds to the combustion of the gelatin.

The flame retardancy test is carried out for both the cellulose and CNT/cellulose sheets. The combustion process is shown in **Figure 14**. Both the sheets are hanged on a metal supporter and ignited simultaneously by a gas flame. It is observed that the cellulose sheet burns quickly to ashes completely within 20 s, but the CNT/cellulose takes more than half minutes to burn and turns to charcoal, which indicates that added MWNTs improved the flame retardancy of the sheet [37].

Figure 15(b) and **(c)** shows the temperature vs. time curves of the CNT/cellulose sheet by a thermocouple and by an IR camera during heating and cooling process. The schematic of the measurement are shown in **Figure 15(a)**. The experiment is carried out by measuring the variation in the temperature under the applied voltage, V_{in} = 80–220 V. Three layers of CNT/cellulose sheet has been used for reducing resistance low enough by which the passage of an electric current through a CNT/cellulose sheet releases heat due to Joule heating process [40]. Heating and cooling temperatures of the sheet are measured at the center of the sheet. It is observed that the heat starts to increase with time by applying a DC voltage and radiate from the sheet. The surface of the CNT/cellulose sheet reached above a maximum temperature of 120°C within 5 min depending on the applied voltage and become saturate at that maximum

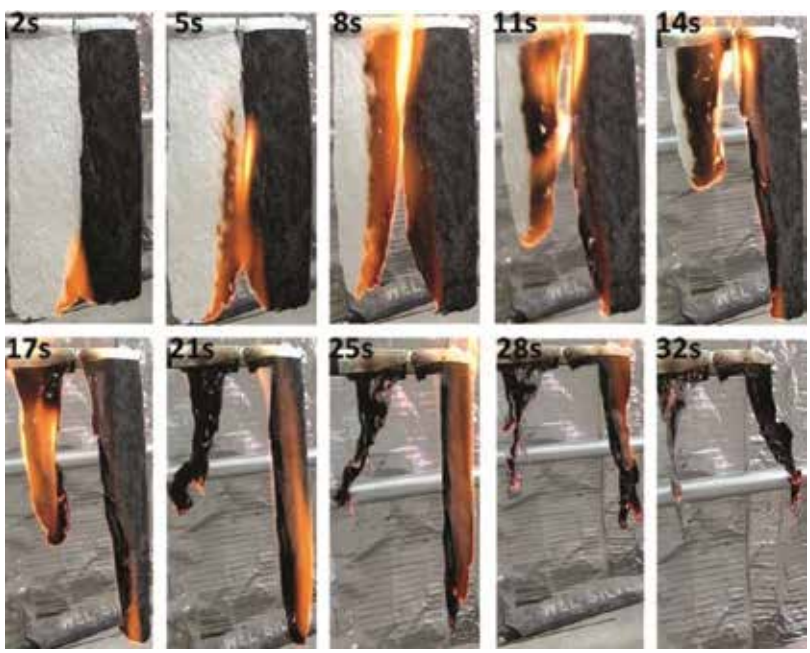

Figure 14. Photographs of flame retardancy test for the pure cellulose sheet (left-white sample) and CNT/cellulose sheet (right-black sample). At t = 0 s, a flow is added on the bottom of the samples.

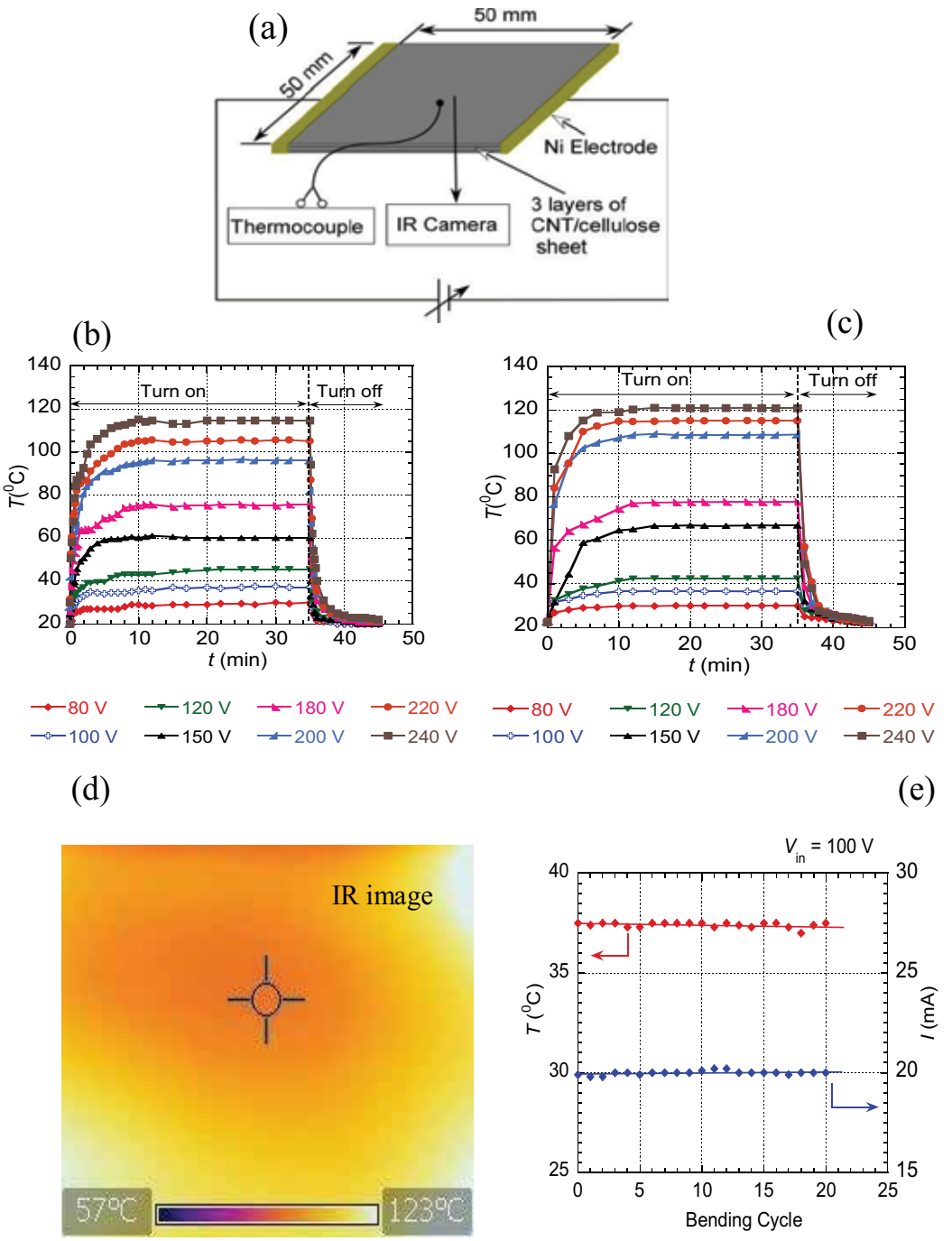

Figure 15. (a) Schematic of the heating test measurement of the CNT/cellulose sheet by a thermocouple and an IR camera. Temperature vs time curves during heating and cooling of the CNT/cellulose sheet measured (b) by a thermocouple and (c) by an IR camera. (d)Thermal image at *V*in = 220 V showing the uniform heating of the sheet where the temperature scales shown at the bottom part. (e) Variation of temperature and current after repeated bending, where the input voltage V_{in} = 100 V.

temperature. Much higher temperature can be obtained by increasing the layers of the CNT/cellulose sheet and the sheet could be used as a flat-type electric heater.

During the test, all the samples are heated to maximum equilibrium temperature and then cooled naturally, and this heat releasing ability of the sheets is also measured. It is observed that temperature decreases exponentially to the room temperature within few minutes. Thermocouple-based measurements show a little lower value of temperature than the infrared-based measurements. This difference arises from the slow response of the thermocouple due to the slow heat propagation [41]. The IR image of the CNT/cellulose sheet as shown in **Figure 15(d)** indicates the uniformity of the heat dissipation. It is clearly shows that high temperature area (glow area) is located at the center of the sheet. To study the flexibility of the CNT/cellulose sheet, the temperature and current are also measured by bending the sheet more than 90° for 20 times and the total time elapsed for the whole process is 80 min. **Figure 15(e)** shows the flexible nature of the paper sheet, because repeated bending of paper sheet does not make any significant change of the current conduction through the paper sheet, and temperature also remains almost constant. These results mentioned above indicate that CNT/cellulose sheet can be used as an electrothermal heating element [37].

5.4.3. Absorbing properties of the composite sheet

A gun-diode microwave transmitter and a recorder (Pasco Scientific WA-9314B, $P_{\mu} = 10$ mW) of 10.5 GHz with horn antenna are used to measure the microwave absorption properties of the sheet. For this experiment, a size of 100 × 100 × 0.3 mm^3 of the both CNT/cellulose sheet and pure cellulose sheet are made for comparison. The pure cellulose sheet and the CNT/cellulose sheet are placed on a plastic substrate during the experiment. A schematic representation of the measurement of microwave absorption ability is shown in **Figure 16(a)**.

In this absorption ability experiment, the incident microwave is divided into two parts: the transmitted microwave and the absorbed one. To determine the reflection ability of the sheet, transmitter and receiver is set in such a way that the incident and reflected wave makes equal angles to the surface normal, as shown in **Figure 16(b)**. The experimental result of the absorption and transmission ability vs. the content of MWNTs of the CNT/cellulose sheet is shown in **Figure 17(a)**. The sheet with low content of MWNTs shows weak absorbing ability and the absorption increases with the increase of MWNTs content [37].

The absorption test is also carried out with the increase of thickness of the sheet as shown in **Figure 17(b)**. Few sheets of same thickness and same content of MWNTs (30 mg) are used for this experiment. During the experiment, thickness is increased by putting the sheet one after one on the plastic sheet. Absorption ability is found to increase with the increase of thickness as well as MWNTs content. This increase of absorption may occur due to the increase of conductivity with the increase of MWNTs content [37].

The CNT/cellulose sheets exhibit very small reflection and the reflections slightly improve with the increase of MWNTs content as shown in **Figure 18**. It is conjectured that interfacial electric polarization improves with the increase of MWNTs content due to the interaction of

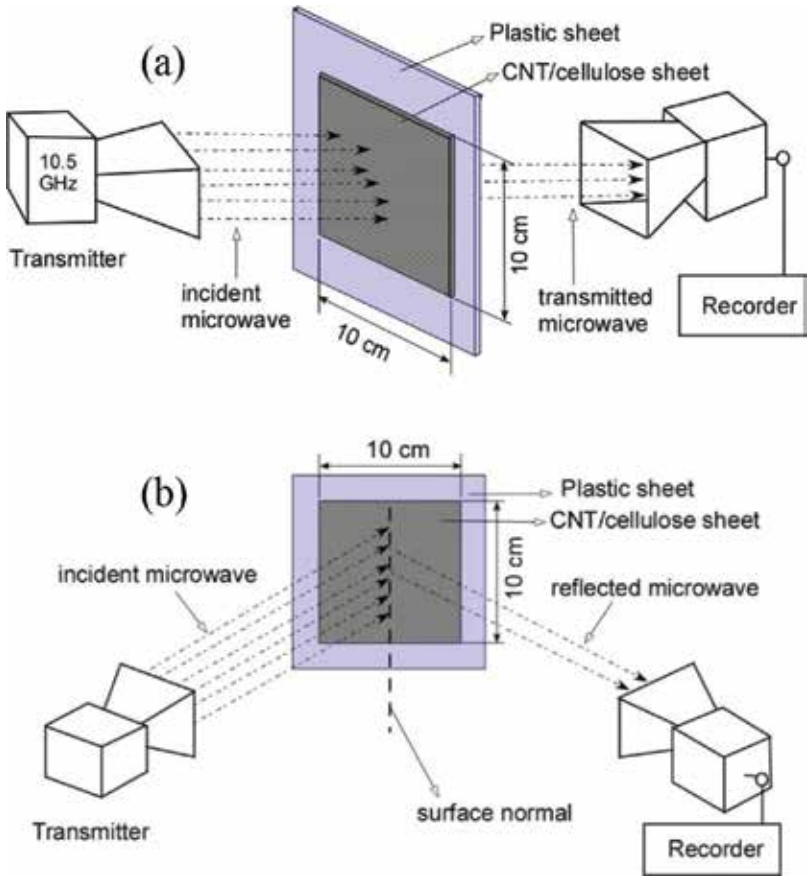

Figure 16. Schematic representation of the (a) microwave absorption measurement and (b) reflection measurement of CNT/cellulose sheet.

microwave radiation with the large number of charge multipoles between the MWNTs and cellulose, which causes reflection rather absorption as shown in **Figure 18(b)**. The results can be comparable with the previous examinations with the other composites of MWNT [42]. This means, there are several considerable factors, like the MWNTs content, thickness of sheet, the interfacial electric polarization, etc. to design a microwave absorbing material [37, 43]. It is also found that a zigzag setup of four sheets of same dimensions, each contains 30 mg MWNTs can absorb about 50% of the incident microwave. Therefore, this composite sheet may have great potential for microwave absorbing applications taking into account all the above results.

5.4.4. Aqueous absorption speed of CNT/cellulose composites

Generally, cellulose sheets have high absorption speed, which in turn degrades their functional, structural, and mechanical properties. CNT/cellulose composite shows the significant improvement on the aqueous absorption properties without degradation resulted from the

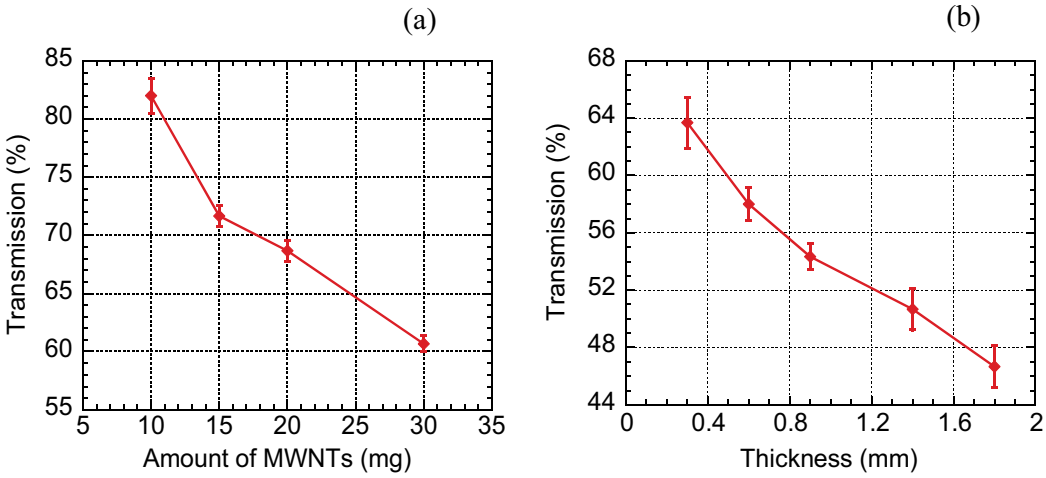

Figure 17. Variation of transmission property of the CNT/cellulose sheet (a) with the increase of MWNT content and (b) with the thickness, where MWNT content increases with the thickness.

addition of carbon nanotubes in the cellulose. The pure cellulose sheet and CNT/cellulose sheet are prepared with a size of 100 × 20 × 0.3 mm^3 for this experiment. In this experiment, the samples are immersed in color and saline. Both the cellulose and CNT/cellulose sheets start to absorb aqueous solution immediately after the immersion and keep the sheets in the solution until they get wet completely. The schematic of the absorption speed measurement is shown in **Figure 19(a)**. The absorption speed, weight changes of the CNT/cellulose sheets are measured from this experiment and compared with the pure cellulose sheet. Absorbed amount of saline by the sheets are calculated by measuring the weight changes of the sheets after the experiment.

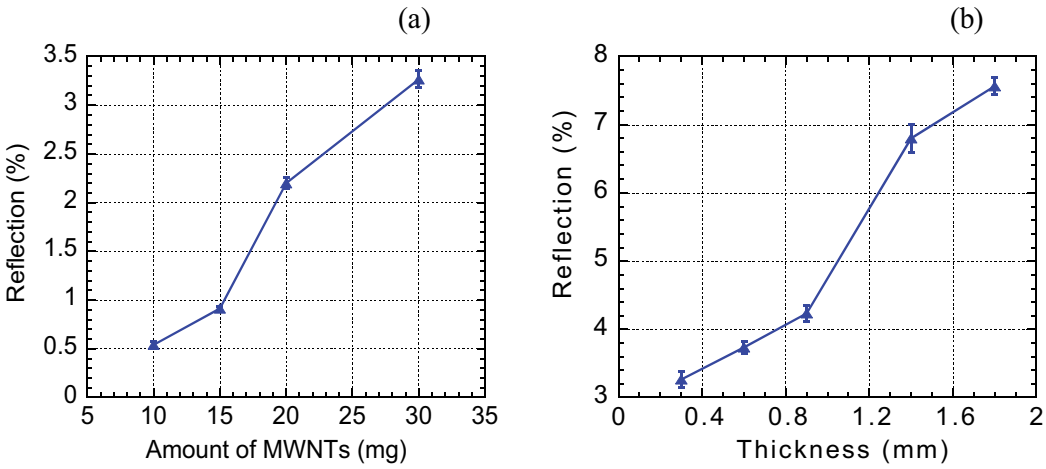

Figure 18. Variation of reflection property of the CNT/cellulose sheet (a) with the increase of MWNT content and (b) with the thickness, where MWNT content increases with the thickness.

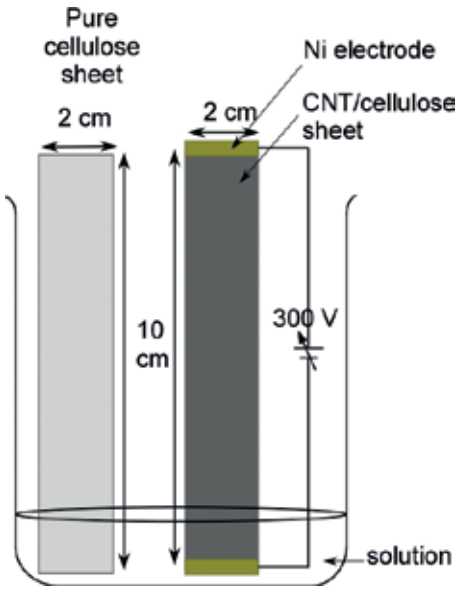

Figure 19. (a) Schematic of the absorption speed measurement of the CNT/cellulose sheet. (b) Absorption speed of the cellulose sheet and CNT/cellulose sheet in different solutions and conditions.

Figure 19(b) shows that the absorption speed of the cellulose sheet is very high in both color and saline. On the other hand, the CNT/cellulose sheet has low absorption speed. A high voltage, ~300 V, is applied through Ni electrode to the CNT/cellulose sheet to investigate the changes in speed, and it is found that the absorption speed increases significantly in both color and saline.

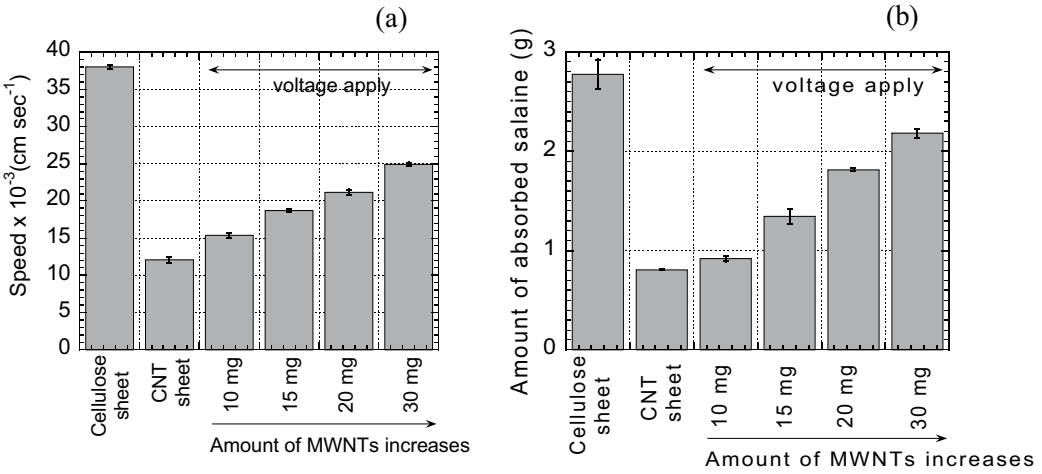

Figure 20. (a) Absorption speed of the cellulose sheet and CNT/cellulose sheet with the increase of MWNT content, (b) amount of absorbed saline with the increase of MWNT content.

The high voltage is also applied by changing the polarity and it does not have any noticeable effect in absorption speed. It is also evident from **Figure 20** that absorption speed and absorbed amount increases with the increase of MWNT content and by applying voltage. This may indicate that the absorption speed and absorbed aqueous amount of the CNT/cellulose sheet is controlled by the MWNT loading [37]. Addition of MWNTs in the sheet or and high voltage may responsible to increase the diffusive energy of the aqueous molecule to penetrate through the sheet. Absorption speed is also governed by other factors, for example cellulose pulp content, dispersion of MWNT, and homogeneous mixing of MWNT with the cellulose in the sheet. This increasing behavior of absorption speed of the composite sheet indicates the mechanical reliability of the composite.

6. Summary

This work provides a simple and effective method for dispersing CNTs in water by using gelatin in order to broaden the application of CNTs. Gelatin wraps the surface of the nanotube to form a stable dispersion, which remains stable for more than a month. This wrapping method does not affect the physical properties of the nanotube. In addition, it can be easily removed from the nanotubes after the dispersion of nanotubes by heating in water and filtration.

The applications of CNTs as composites offer new opportunities to produce cost-effective electronics. CNT-based sheet has been prepared by using a paper making process. MWNTs improve the mechanical, thermal, and electrical properties of cellulose. SEM investigation confirms the homogeneous distribution of MWNTs in the cellulose, which can be attributed to the improvement of its characteristics. Both sides of the CNT/cellulose sheet show uniform electrical conductivity, which is enhanced by increasing the MWNTs content. IR image of the sheet clearly shows the temperature homogeneity of the surface. Thermal stability and the flame retardancy of the sheet are also found to be improved. The sheet has also strong absorbing of electromagnetic waves, which makes them important for microwave technology applications. These electrically conductive and electromagnetic-wave-absorption properties can be useful in radar wave absorbing, electro thermal heating elements, and 2D electric circuit applications, electromagnetic shields, etc.

Acknowledgements

This study was supported by the Promotion of Nano-Biotechnology Research to Support Aging, Welfare Society from Ministry of Education, Culture, Sports, Science and Technology, Japan. TEM, SEM, and TG/DTA measurements were done at Research Institute of Green Science & Technology, Shizuoka University. Raman measurement was done at Research Institute of Electronics, Shizuoka University.

Author details

Kazi Hanium Maria[1,2]* and Tetsu Mieno[2,3]

*Address all correspondence to: kazimaria@du.ac.bd

1 Department of Physics, University of Dhaka, Dhaka, Bangladesh

2 Graduate School of Science and Technology, Shizuoka University, Shizuoka, Japan

3 Department of Physics, Shizuoka University, Shizuoka, Japan

References

[1] Endo M, Strano MS, Ajayan PM. Potential applications of carbon nanotubes. In: Jorio A, Dresselhaus G, Dresselhaus MS, editors. Carbon Nanotubes-Topics in Applied Physics. Heidelberg: Spinger; 2008. p. 13-26

[2] Iijima S. Helical microtubules of graphitic carbon. Nature. 1991;**354**:56-58. DOI: 10.1038/354056a0

[3] Baughman HR, Zakhidov AA, de Heer WA. Carbon nanotubes—The route toward applications. Science. 2002;**297**:787-792. DOI: 10.1126/science.1060928

[4] Yan XB, Tai XZ, Chen JT, Xue JQ. Fabrication of carbon nanofiber–polyaniline composite flexible paper for supercapacitor. Nanoscale. 2010 Nov 8;**3**:212-216. DOI: 10.1039/c0nr00470g

[5] Chen C, Yang QH, Yang Y, Lv W, Wen Y, Hou PX, Wang M, Cheng HM. Self-assembled free-standing graphite oxide membrane. Advanced Materials. 2009 Apr 20;**21**:3007-3011. DOI: 10.1002/adma.200803726

[6] Nishide H, Oyaizu K. Toward flexible batteries. Science. 2008 Feb 8;**319**:737-738. DOI: 10.1126/science.1151831

[7] Brosseau C, Boulic F, Queffelec P, Bourbigot C, YLe M, Loaec J, Beroual A. Dielectric and microstructure properties of polymer carbon black composites. Journal of Applied Physics. 1997;**81**:882-891

[8] Mdarhri A, Carmona F, Brosseau C, Delhaes P. Direct current electrical and microwave properties of polymer-multiwalled carbon nanotubes composites. Journal of Applied Physics. 2008;**103**:054303-054309

[9] Fei B, Lu H, Hu Z, Xin JH. Solubilization, purification and functionalization of carbon nanotubes using polyoxometalate. Nanotechnology. 2006 Feb 21;**17**:1589-1593. DOI: 10.1088/0957-4484/17/6/010

[10] Krueger A. Carbon nanotubes. In: Carbon Materials and Nanotechnology. Weinheim: Wiley-VCH; 2010. p. 123-281. DOI: 10.1002/9783527629602.ch3

[11] Zimmerman JL, Bradley RK, Huffman CB, Hauge RH, Margrave JL. Gas-phase purification of single-wall carbon nanotubes. Chemistry of Materials. 2000;**12**:1361-1366. DOI: 10.1021/cm990693m

[12] O'Connell MJ, Boul P, Ericson LM, Huffman C, Wang Y, Haroz E, Kuper C, Tour J, Ausman KD, Smalley RE. Reversible water-solubilization of single-walled carbon nanotubes by polymer wrapping. Chemical Physics Letters. 2001;**342**:265-271. DOI: 10.1016/S0009-2614(01)00490-0

[13] Hill DE, Lin Y, Rao AM, Allard LF, Sun YP. Functionalization of carbon nanotubes with polystyrene. Macromolecules. 2002;**35**:9466-9471. DOI: 10.1021/ma020855r

[14] Dang ZM, Wang L, Zhang LP. Surface functionalization of multiwalled carbon nanotube with trifluorophenyl. Journal of Nanomaterials. 2006;**2006**:1-5. Article ID: 83583. DOI: 10.1155/JNM/2006/83583

[15] Kim WJ, Nairs N, Lee CY, Strano MS. Covalent functionalization of single-walled carbon nanotubes alters their densities allowing electronic and other types of separation. The Journal of Physical Chemistry C. 2008;**112**:7326-7331. DOI: 10.1021/jp710919b

[16] Ávila-Orta CA, o González- Morones P, Espinoza-González CJ, Martínez-Colunga JG, Neira-Velázquez MG, Sáenz-Galindo A, López-López LT. Toward greener chemistry methods for preparation of hybrid polymer materials based on carbon nanotubes. In: Suzuki S, editor. Syntheses and Applications of Carbon Nanotubes and their Composites. Intech; 2013. p. 167-192. DOI: 10.5772/51257

[17] Maria KH, Mieno T. Effect of gelatin on the water dispersion and centrifugal purification of single-walled carbon nanotubes. Japanese Journal of Applied Physics. 2015;**55**:01AE04. DOI: 10.7567/JJAP.55.01AE04

[18] Elzoghby AO: Gelatin-based nanoparticles as drug and gene delivery systems: Reviewing three decades of research. Journal of Controlled Release. 2013;**172**:1075-1091. DOI: http://dx.doi.org/10.1016/j.jconrel.2013.09.019

[19] Aramwit P, Jaichawa N, Ratanavaraporn J, Srichana T. A comparative study of type a and type B gelatin nanoparticles as the controlled release carriers for different model compounds. Materials Express. 2015;**5**:241-248. DOI: 10.1166/mex.2015.1233

[20] Kozlov PV, Burdygina GI. The structure and properties of solid gelatin and the principles of their modification. Polymer Reviews. 1983;**24**:651-666. DOI: 0032-2861/83/060651

[21] Zheng W, Zheng YF. Gelatin-functionalized carbon nanotubes for the bioelectrochemistry of hemoglobin. Electrochemistry Communications. 2007;**9**:1619-1623. DOI: 10.1016/j.elecom.2007.03.007

[22] Kim Y, Minami N, Kazaoui S. Highly polarized absorption and photoluminescence of stretch-aligned single-wall carbon nanotubes dispersed in gelatin films. Applied Physics Letters. 2005;**86**:073103. DOI: 10.1063/1.1863448

[23] Djabourov M, Papon P. Influence of thermal treatments on the structure and stability of gelatin gels. Polymer. 1983;**24**:537. DOI: 0032-3861/83/050537

[24] Rogers JA, Someya T, Huang YG. Materials and mechanics for stretchable electronics. Science. 2010;**327**:1603-1607. DOI: 10.1126/science.1182383

[25] Hu LB, Pasta M, FLa M, Cui LF, Jeong S, Deshazer HD, Choi JW, Han SM, Cui Y. Stretchable, porous, and conductive energy textiles. Nano Letters. 2010;**10**:708-714. DOI: 10.1021/nl903949m

[26] Yan XB, Tai XZ, Chen JT, Xue JQ. Fabrication of carbon nanofiber–polyaniline composite flexible paper for supercapacitor. Nanoscale. 2010;**3**:212-216. DOI: 10.1039/c0nr00470g

[27] Li X, Rong J, Wei B. Electrochemical behavior of single-walled carbon nanotube supercapacitors under compressive stress. ACS Nano. 2010;**4**(10):6039-6049. DOI: 10.1021/nn101595y

[28] Tanaka T, Sano E, Imai M, Akiyama K. Electrical conductivity of carbon-nanotube/cellulose composite paper. Journal of Applied Physics. 2010;**107**:054307. DOI: 10.1063/1.3319675

[29] Yun S, Kim J. Multi-walled carbon nanotubes–cellulose paper for a chemical vapor sensor. Sensors and Actuators, B: Chemical. 2010;**150**:308-313. DOI: 10.1016/j.snb.2010.06.068

[30] Klemm D, Heublein B, Fink HP, Bohn A. Cellulose: Fascinating biopolymer and sustainable raw material. Angewandte Chemie, International Edition. 2005;**44**:3358-3393. DOI: 10.1002/anie.200460587

[31] Kim J, Yun S, Ounaies Z. Discovery of cellulose as a smart material. Macromolecules. 2006;**39**:4202-4206. DOI: 10.1021/ma060261e

[32] Turner MB, Spear SK, Holbrey JD, Rogers RD. Production of bioactive cellulose films reconstituted from ionic liquids. Biomacromolecules. 2004;**5**:1379-1384. DOI: 10.1021/bm049748q

[33] Ebbesen TW, Lezec JH, Hiura H, Bennett WJ, Ghaemi FH, Thio T. Electrical conductivity of individual carbon nanotubes. Nature. 1996;**382**:54-56. DOI: 10.1038/382054a0

[34] Kashiwagi T, Du F, Douglas JF, Winey KI, Harris RH Jr, Shields JR. Nanoparticle networks reduce the flammability of polymer nanocomposites. Nature Materials. 2005;**4**:928-933. DOI: 10.1038/nmat1502

[35] Rahman MJ, Mieno T. Conductive cotton textile from safely functionalized carbon nanotubes. Journal of Nanomaterials. 2015;**2015**:978484-1-978484-10. DOI: 10.1155/2015/978484

[36] Fugetsu B, Sano E, Sunada M, Sambongi Y, Shibuy T, Wang X, Hiraki T. Electrical conductivity and electromagnetic interference shielding efficiency of carbon nanotube/cellulose composite paper. Carbon. 2008;**46**:1256-1258. DOI: 10.1016/j.carbon.2008.04.024

[37] Maria KH, Mieno T. Production and properties of carbon nanotube/cellulose composite paper. Journal of Nanomaterials. 2017;**2017**:6745029-1-6745029-11. DOI: 10.1155/2017/6745029

[38] Beneventi D, Alila S, Boufi S, Chaussy D, Nortier P. Polymerization of pyrrole on cellulose fibres using a $FeCl_3$ impregnation- pyrrole polymerization sequence. Cellulose. 2006;**13**:725-734. DOI: 10.1007/s10570-006-9077-9

[39] Ceylan O, Landuyt LV, Rahier H, De Clerck K. The effect of water immersion on the thermal degradation of cotton fibers. Cellulose. 2013;**20**:1603-1612. DOI: 10.1007/s10570-013-9936-0

[40] Ragab T, Olsson C. Joule heating in single-walled carbon nanotubes. Journal of Applied Physics. 2009;**106**:063705. DOI: 10.1063/1.3204971

[41] Kang J, Kim H, Kim KS, Lee SK, Bae S, Ahn JH, Kim YJ, Choi JB, Hong BH. High-performance graphene-based transparent flexible heaters. Nano Letters. 2011;**11**:5154-5158. DOI: 10.1021/nl202311v

[42] Nwigboji IH, Ejembi JI, Wang Z, Bagayoko D, Zhao GL. Microwave absorption properties of multi-walled carbon nanotube (outer diameter 20-30 nm) epoxy composites from 1 to 26.5 GHz. Diamond and Related Materials. 2014;**52**:66-71. DOI: 10.1016/j.diamond.2014.12.008

[43] Fan Z, Luo G, Zhang Z, Zhou L, Wei F. Electromagnetic and microwave absorbing properties of multi-walled carbon nanotubes/polymer composites. Materials Science and Engineering B. 2006;**132**:85-89. DOI: 10.1016/j.mseb.2006.02.045

Section 5

State-of-the-Art Energy

Chapter 13

The Porous Carbon Nanotube-Cellulose Papers as Current Collector and Electrode for Lithium Ion Battery and Supercapacitor Applications

Xiaogang Sun, Manyuan Cai, Long Chen,
Zhiwen Qiu, Jie Wang, Xu Li and Wei Chen

Additional information is available at the end of the chapter

http://dx.doi.org/10.5772/intechopen.71916

Abstract

Lithium ion batteries (LIB) and supercapacitors (electric double-layer capacitors (EDLCs) and lithium ion capacitors (LIC)) are the most energy storage service for mobile application. Lithium ion batteries are currently the most popular type of battery for powering portable electronic devices and are growing in popularity for defense, automotive and aerospace applications. The investigation of supercapacitors (SCs) has also achieved significant progresses. Although they have shown remarkable commercial successes, the electrodes and their constituent materials are still the subject of intensive research. Our research focused on a new type of carbon nanotube-cellulose composite materials as current collector of LIBs and as electrodes of SCs for improving and enhancing the energy/power density and cyclic performance of them. Carbon nanotubes (CNTs) have been widely used as conductive agent for both anodes and cathodes to replace super carbon black to satisfy the multifunctional requirements for LIBs.

Keywords: carbon nanotube, cellulose, lithium ion battery, collector, paper, supercapacitor

1. Applications of carbon nanotubes (CNTs) in lithium ion battery and supercapacitor

Lithium ion batteries (LIBs) and supercapacitors (SCs) are considered to be the most promising energy storage devices because of their relatively high energy density, good cycle

performance, power performance, longer service life, and green environmental characteristics. LIBs have a broad application prospects in portable electronic equipment, electric vehicles, and hybrid vehicles [1, 2].

The electrodes of LIB commonly use copper foil or aluminum foil as a current collector, and the active material is coated on the current collector. Carbon nanotubes (CNTs) have unique features of one-dimension, large surface area and high conductivity, which contribute to electrochemical performance of LIBs and SCs [3–5]. Thus, many investigations in terms of electrode materials are focused on CNTs. Compared with aluminum foil or copper foil, metal-free current collector is a research hotspot, CNT film or cellulose papers used as negative electrode, or anode current collector was applied in flexible lithium ion battery in many researches [6, 7]. CNT-cellulose papers (CNTCPs) are very good host for activated materials, which have a porous structure, easy formability, flexibility, and excellent physical and chemical properties. The porous CNTCP has excellent flexibility and conductivity. It has a broad application prospect for LIB applications including lithium-sulfur battery [1–15], Nano-SnO_2 anode [16–43], silicone anode [44–56], Li/CFx battery [57–63], and supercapacitors [64–80]. In this paper, we report the porous CNTCP applications as current collector and electrode for lithium ion battery and supercapacitor, respectively. Moreover, the CNTs used in this study are whisker multiwalled carbon nanotubes.

The fabrication process of the papers is simple and scalable, similar to those technology widely used for paper making in industry. The porous CNTCP with interconnected channel has high surface area and high electrical conductivity. It was considered as potential current collector and electrode for LIBs and SCs.

2. Fabrication and characterization of CNTs and CNTCPs

The synthesis of CNTs in the present investigation was synthesized in a vertical tubular reactor. An organic-metallic compound (ferrocene) was used as catalyst precursor, toluene as carbon feedstock, sulfur as growth promotion agent, and hydrogen as carrier gas.

The microfeed pump was used to feed the toluene solution and organic metal compound into reactor at a rate of 30 ml/min. The mass flow instrument was used to add hydrogen to the reactor at a rate of 40 ml/min. The generation temperature of CNTs is about 1200°C. The graphitization treatment of CNTs was operated in graphite resistance furnace.

CNTCPs were prepared by the following process: The CNT powders were dispersed by sonication and high speed cutting in distilled water for 2 h, respectively. The surfactant of polyvinylpyrrolidone (PVP) was added to improve the dispersion performance. Cellulose fibers were prepared through smashing napkins by high-speed shearing for 3 h. Both were fully dispersed and mixed by high-speed shear and sand milling in deionized water to form a suspension with a ratio of 1:1. The mixed slurry of CNTs and cellulose fibers was infiltrated by vacuum filtration, and the as-produced CNT paper (AMP) was obtained by peeling it off from the filter paper after drying at 60°C for 12 h. A randomly interwoven fiber mats were peeled from filter cloth and carbonized at 1460°C in vacuum condition. **Figure 1(a, b)** shows the SEM and HRTEM images of CNTs, and **Figure 1(c, d)** shows the SEM images of CNTCP and FCNT.

http://dx.doi.org/10.5772/intechopen.71916

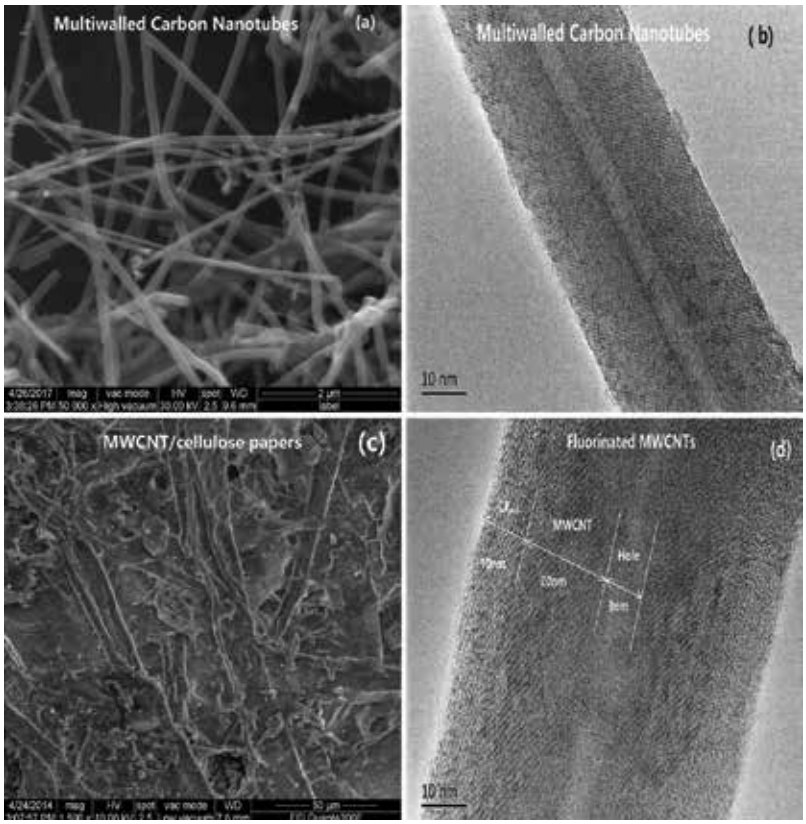

Figure 1. (a) SEM of CNTs, (b) HRTEM of CNT, (c) SEM of CNTCP, and (d) FCNT.

The CNTs were characterized by field-emission scanning electron microscopy (FE-SEM, JSM-6701F), transmission electron microscopy (TEM, JEOL JEM-2010FEF), X-ray diffraction (XRD, DI SYSTEM), Raman spectrometry (SENTERRA), and thermogravimetry (TGA, PYRIS DIAMOND). The microstructure of the electrodes was investigated by scanning electron microscopy (FE-SEM, JSM-6701F). Fourier transformation infrared spectra (FTIR, Nicolet 5700) were recorded. Electrical conductivity was measured by the conventional four-probe DC method (St2258C four-point probe meter).

3. The CNTCP used as current collector and electrode for LIBs and SCs application

3.1. CNTCP used to replace aluminum foils for Li-S cells

3.1.1. Experiment

3.1.1.1. Preparation of composite host

CNTs were synthesized by chemical vapor deposition and treated at a high temperature of 3000°C for graphitization. The CNTs powder was dispersed in deionized water with a dispersant

of sodium dodecylsulfate (SDS) ($CH_3(CH_2)_{11}OSO_3Na$). The paper cellulose is made of soaked soft wood pulp in deionized water. The CNTs dispersion liquid and the cellulose pulp were mixed by high-shear emulsifier to form suspension for 3 h. The suspension liquid of cellulose and CNTs pulp was infiltrated by vacuum filtration. A randomly interwoven fiber mat was obtained. The paper was rolled and tailored as current collector for activated materials.

3.1.1.2. Preparation of sulfur electrodes

Sulfur and conductive additive of carbon black (CB) were mixed by balling for 2 h at 230 r/min. Then, the slurry of sulfur and CB was prepared by ultrasonication and high-shear process with N-methyl-2-pyrrolidone (NMP) as solution and PVDF as binder. The ratio of S:CB:PVDF = 36:54:10. The blended slurry was coated on to aluminum foils (S-Al electrode) and porous composite host (S-CNTs/CP electrode). The electrodes were dried under vacuum at 60°C for 24 h.

3.1.1.3. Assembling of cell and electrochemical measurements

The tailored of S-Al electrode and S-CNTs/CP electrode were respectively used as working electrodes. Li metal foils were used as the counter electrodes, and Celgard 2300 was used as the separator. CR2025 coin-type cells were assembled in an Ar-filled glove box (MBRAUN LABSTAR, Germany). The electrolyte was prepared by dissolving lithium bistrifluoromethane sulfonylimide (LITFSI) and lithium nitrate ($LiNO_3$) in 1,2-dimethoxyethane (DME) and 1,3-dioxolane (DOL) (1:1 ratio, by volume). The electrochemical characterization of the cells was measured by a cell tester (CT-3008 W-5V5mA-S4). Electrochemical impedance spectroscopy (EIS) and cyclic voltammetry (CV) were performed within a potential window of 1.8–2.6 V by an electrochemical workstation (CHI 660B). The specific capacity was calculated according to the mass of the sulfur in the host. The charge and discharge current density was set at 0.05 C to 2C.

3.1.2. Results and discussion

SEM image in **Figure 2(a)** shows that the CNTs have a distinct one-dimension line structure and were not entangled. They can be more easily dispersed than common carbon nanotubes (CCNTs). TEM image of the CNTs is shown in **Figure 2(b)**. It can be observed that the CNTs have a straight and clear texture with high crystallinity.

Figure 3(a) shows SEM image of top surface of as-produced CNTs/CP host with a random-in-plane web-like network structure. The CNTs/CP host demonstrated homogenous incorporation of CNTs in the cellulose fibers network. **Figure 3(b)** shows the cross-section image of CNTs/CP host. The figures clearly displayed porous network structure which provided sufficient void space for loading a large amount of sulfur and accommodating the volume expansion of sulfur during cycles. The coarse surface and interconnected channel permit good penetration of the electrolyte and sulfur. The pore size distribution of as-produced CNTs/CP host is shown in **Figure 3(c)**. From the picture, we can see that the host has big porosity. The special surface area of the host reached 25.6 m^2/g.

http://dx.doi.org/10.5772/intechopen.71916

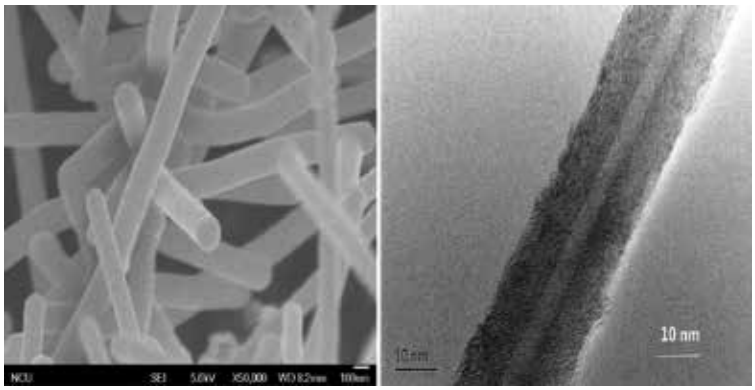

Figure 2. SEM (a) and TEM (b) images of CNTs.

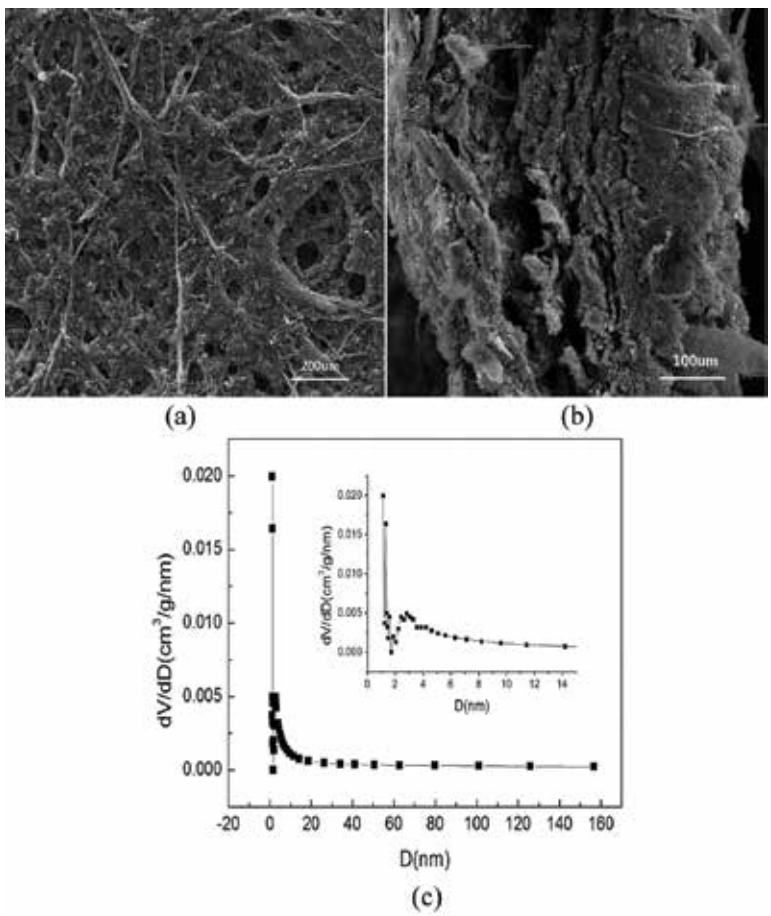

Figure 3. SEM images of CNTs/CF host (a) surface, (b) cross-section, and (c) pore size distribution.

It was known that a sufficient amount of electrolyte is especially required for a high sulfur-loaded cathode during the electrochemical transformation between sulfur and polysulfides [81, 82]. Therefore, the superior electrolyte absorbability of the S-CNTs/CP contributes to stabilized electrochemical reactions in high sulfur-loaded electrodes. S-CNTs/CP can also suppress the diffusion of polysulfides, which resulted in superior cycling stability.

Figure 4(a) shows the cross-section images of S-CNTs/CP electrode. It can be observed that sulfur embedded into micropores of host has a uniform distribution. This made an intimate contact between sulfur and host. The interfacial contact area enhanced and interface resistance decreased substantially, which are highly desirable for high rate charge-discharge cycles. The energy dispersive spectra (EDS) of cross-section of S-CNTs/CP electrode (**Figure 5**) further demonstrate that sulfur embedded into CNTs/CP host which was attributed to good cycle stability. **Figure 4(b)** shows the cross-section images of S-Al electrode. It can also be observed

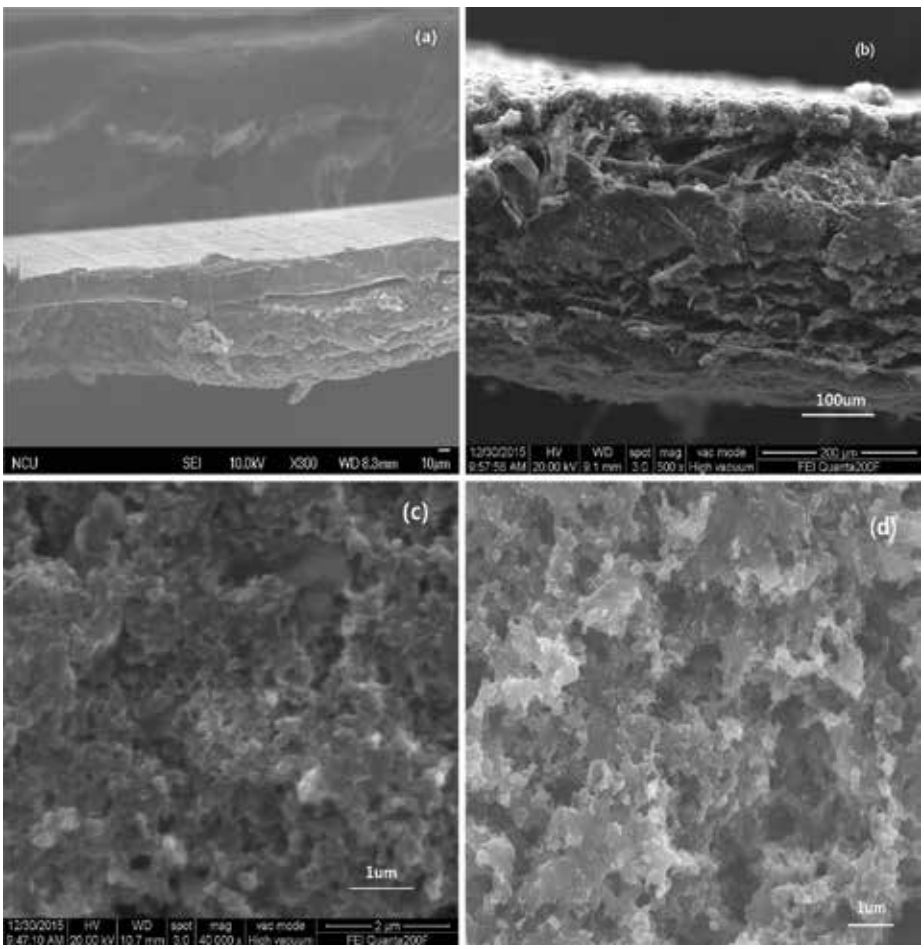

Figure 4. SEM of CNTs/CP and Al foil loaded with sulfur (a) S-Al cross section, (b) S-CNTs/CP cross section, (c) S-Al top after cycles, (d) S-CNTs/CP top after cycles.

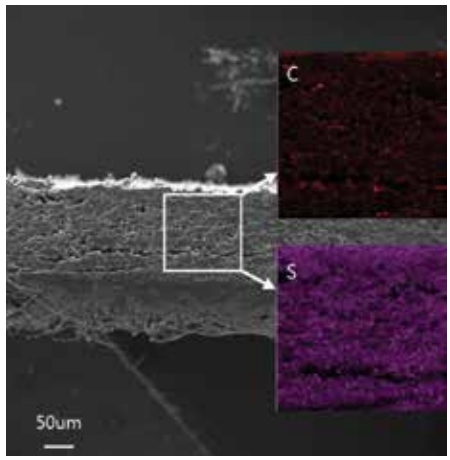

Figure 5. The EDS images of cross section of S-CNTs/CP electrode.

that there will be visible pores between the interface of sulfur and Al foil, which resulted in increasing interface resistance. **Figure 4** shows the morphologies of two electrodes of S-Al electrode (c) and S-CNTs/CP electrode (d) after 60 cycles. It was observed that S-CNTs/CP electrode maintains a smooth and unbroken surface, while the S-Al electrode shows an uneven surface. Due to weak binding force and low affinity between sulfur and Al foil, sulfur was exfoliated from Al foil during cycles. **Figure 6** shows the first three cyclic voltammetry (CV) curve of the S-CNTs/CP electrode at a scan rate of 0.05 mV /S in the voltage range of 1.8–2.6 V. In the first electrode scan, two characteristic reduction peaks at 2.29 and 1.99 V can be observed. The reduction peak at about 2.3 V belongs to the reduction of element sulfur to long-chain LiPSs (Li_2S_n, 4<n<8). The peak at 2.0 V indicated the reduction of lithium polysulfide to short-chain lithium sulfide (Li_2S_2, (Li_2S) [81–84]. The two oxidation peaks were

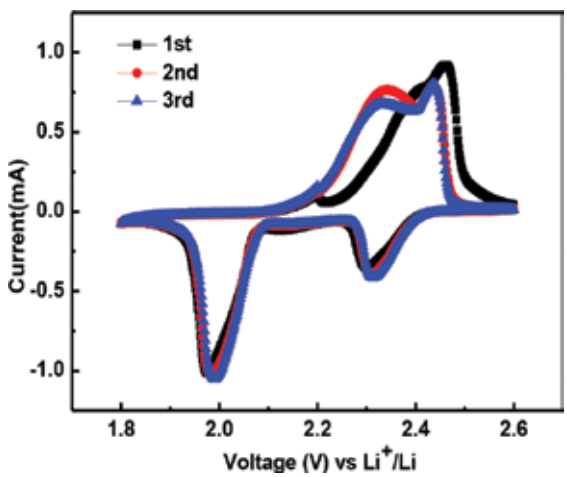

Figure 6. The first three cycles of CV curves of S-CNTs/CP electrode.

represented at 2.3 and 2.4 V. Li_2S_n (n > 2) was formed at 2.3 V, and elemental sulfur was generated at 2.4 V. The electrodes displayed the almost identical CV curves from beginning of the second cycle. The overlap of subsequent oxide and reduction peaks suggested that the electrodes have high electrochemical stability and good reversibility. It also indicated that the interconnected porous 3D structure is a quite good support of sulfur to prevent shuttle effect and maintain high utilization of sulfur.

Figure 7(a) shows the discharge-charge curves of S-Al electrode at first, second, and 10th at the current rate of 0.05 C, respectively. It can be seen that there are two plateaus for each discharge curve at 2.3 and 2.1 V, respectively. The plateaus of 2.3 V represented the formation of long-chain polysulfides (Li_2Sn, 4<n<8) with shorter flat range. The plateaus of 2.1 V represented conformation of short-chain sulfides of Li_2S_2 and Li_2S [13] with longer flat range. The first discharge specific capacity reached around 1085 mAh/g, which represented a 64.7% utilization of sulfur (1675 mAh/g). But the capacity rapidly faded to 884.5 mAh/g at second cycle. The capacity only maintained at 714 mAh/g after 10th cycle, which is only 65.8% of first discharge capacity. The utilization of sulfur was also declined to 42.6%.

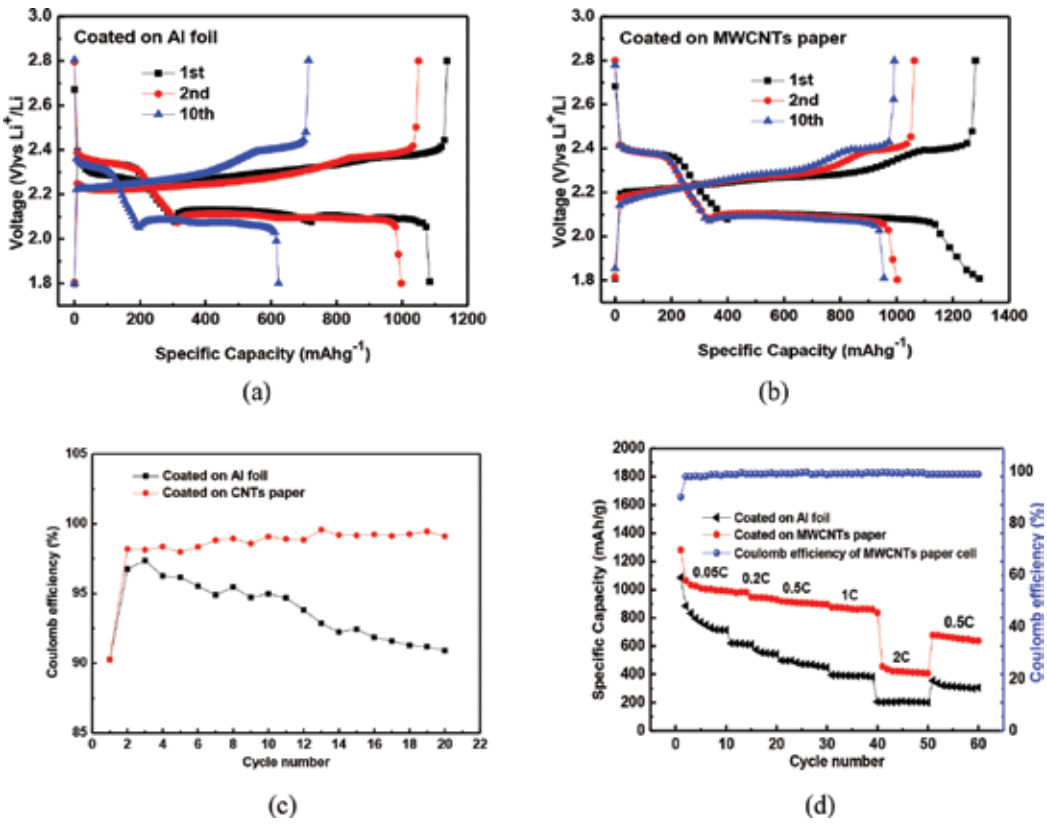

Figure 7. Charge/discharge of S-Al electrode (a) and S-CNTs/CP electrode (b), coulombic efficiency (c), cycle and rate performance of (d).

Figure 7(b) shows the discharge-charge curves of S-CNTs/CP electrode. The galvanostatic discharge-charge profiles displayed a similar curve as S-Al electrode. These plateaus are also consistent well with the current peaks in the CV curves (**Figure 6**). But the discharge profiles of S-CNTs/CP electrode displayed highly overlapped voltage plateaus at 2.1 V. It was considered that the short-chain sulfides taken place in almost same potential upon cycling, which revealed little kinetic barriers for conformation of short-chain sulfides [85–87]. The first discharge specific capacity of S-CNTs/CP electrode reached around 1282 mAh/g, which represented a 76.5% utilization of sulfur (1675 mAh/g). The capacity still maintained at 991.7mAh/g after 10 cycles, which is 77.3% of first discharge capacity. The Coulombic efficiency maintained over 98% from second cycle beginning (**Figure 7c**). After 20 cycles, the Coulombic efficiency of S-Al electrode dropped sharply to 90%, while S-CNTs/cellulose electrode still held 98%. The S-CNTs/cellulose electrode achieved better electrochemical performance than S-Al electrode. The cycle and rate performance of the both electrodes were shown in **Figure 7(d)**. It was shown that the discharge capacity of S-Al electrode declined rapidly. The capacity only maintained around 180 mA/g at the rate of 2C after 50 cycles, while S-CNTs/CP electrode exhibited a stabile discharge capacity of 400mAh/g at 2C. When the charge-discharge rate returned to 0.5C, the discharge capacity recovered to 600mAh/g with a Coulombic efficiency of 97.5%, which suggested excellent redox stability of the S-CNTs/CP electrode. The excellent electrochemical performance of S-CNTs/CP electrode could be ascribed to its good conduction, abundant active interface, and porous interconnected structure. The unique structure can not only increase the absorption of electrolyte and loading of sulfur but also provide stable transfer channels for ions and electrons. The diffusion of LiPSs also was confined effectively.

Figure 8 illustrates the electrochemical impedance analyses of the S-CNTs/cellulose and S-Al electrode before cycles and after cycles, respectively. The experimental data demonstrated that the electrochemical impedance spectra of the two electrodes consist of a single-depressed

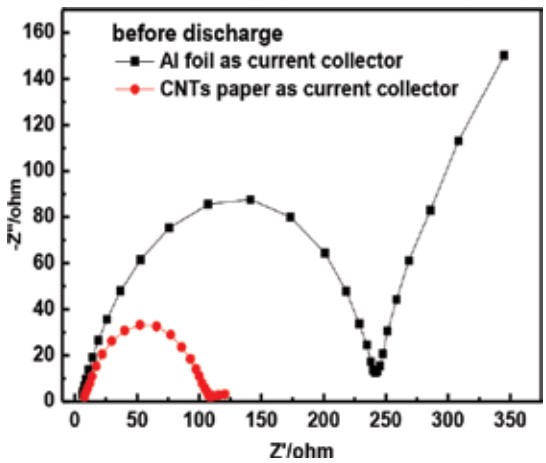

Figure 8. The electrochemical impedance spectra before (a) and after (b) cycles.

semicircle in the high-to-medium frequency region and an inclined line at low frequencies. Before cycle, the charge-transfer resistance of S-CNTs/CP electrode reached 110 Ω, which is lower than 240 Ω of S-Al electrode. After 60 cycles, the charge-transfer resistance of S-CNTs/CP electrode declined to 60 Ω, while the charge-transfer resistance of S-Al electrode only reduced to 210 Ω (**Figure 8b**). This can be attributed to the porous structure of the electrode and 3D conductive network of the electrode, which provides good electrolyte wetting and infiltrating and fast charge transport channel. The polysulfides in the S-CNTs/CP electrode suffer from less dissolution in the electrolyte due to the confinement which prevent and relieve shuttle effect. EDS (**Figure 5**) also identify that sulfur was well distributed in S-CNTs/CP electrode. The strong interaction between sulfur encapsulated in the micropores of the electrode and CNTs is beneficial to improve the electron transfer. The electrolyte and sulfur incorporated in the interconnected channel of porous electrode enhanced the mobility of lithium ions for the electrochemical reaction. The novelty host can also accommodate the volume change of sulfur and alleviate stress generated by volume expansion during cycling.

3.1.3. Conclusions

The S-CNTs/CP electrode with high porosity and interconnected channel was fabricated as host of sulfur for Li-S batteries. This unique hierarchical porous structure with 3D electric conductive network formed by CNTs can provide good path for the penetration of electrolyte and sulfur. The conduction of ions and electrons also were significantly improved. The unique architecture can trap elemental sulfur and LiPSs to suppress shuttle effect. The dissolution and diffusion of LiPSs were effectively checked during cycles. S-CNTs/CP electrode also demonstrated an excellent electrolyte uptake characteristic with four times higher than S-Al electrode. The high electrolyte absorbability of S-CNTs/CP electrode improved the utilization of sulfur. The porous structure can accommodate the volumetric expansion of sulfur during lithiation and alleviate stress generated by volume expansion [88]. This work provided a facile and environment-friendly technology for fabricating high-performance Li-S batteries and exhibited a promising future for practical applications.

3.2. CNTCP used to replace aluminum foils as collector and scaffold for nano-SnO_2 anode

3.2.1. Experiment

3.2.1.1. Preparation of electrode pieces anodes

The nanosized tin oxide (SnO_2) and carbon nanotubes (CNTs) were milling in a ball mill (250 r/min) for about 1 h. Solvent 1-methyl-2-pyrrolidone (NMP) and binder (PVDF) was wetted ball mill for 2 h to obtain a negative electrode slurry. Solid content is about 50 vol%. The ratio of SnO2: CNT: PVDF = 1.8 g: 0.6 g: 0.3 g was uniformly coated to a 3 μm copper foil and approximately 100 μm of CNT conductive paper, respectively. Then, drying at 60°C in vacuum atmosphere cut into φ14mm pole pieces. The tin oxide lithium battery pole piece was prepared.

3.2.1.2. Assembling of cell

The tailored CNT papers were used as working electrodes, and Li metal plate was used as the counter electrode. CR2025 coin-type cells were assembled in an Ar-filled glove box (MBRAUNLABSTAR, Germany) by stacking a porous polypropylene separator. The liquid electrolyte was 1 M LiPF6 dissolved in a mixture of ethylene carbonate (EC) and dimethyl carbonate (DMC) (1:1 in weight).

3.2.1.3. Electrochemical measurements

The electrochemical characterization of the cells was measured by a cell tester (CT-3008 W-5V5mA-S4). Electrochemical impedance spectroscopy (EIS) and cyclic voltammetry (CV) were performed by an electrochemical workstation (CHI 660B). The specific capacity was calculated according to the total mass of the CNT and SnO_2.

3.2.2. Results and discussion

The morphology and microstructures of SnO_2/CNT/Cellulose electrodes were examined by scanning electron microscopy (SEM) and transmission electron microscopy (TEM).

Figure 9(a) shows cross-sectional area of CNT paper. It was exhibited that the CNT papers have a random-in-plane web-like network structure with interconnected channel. The Hierarchical open channel can store a large of SnO_2 to increase energy density. The porous paper has high special surface and can increase interface contact area of SnO_2 and support to reduce interface resistance. **Figure 9(b)** shows the SnO_2 has an average diameter of 60 nm and similar ball structure. **Figure 9(c,d)** exhibits the morphology of CNTs. It can be observed the CNTs have line structure and good aligned carbon atoms.

The electrochemical process can be summarized as following in charge-discharge for the SnO_2/CNT electrode:

Discharge and charge for CNTs.

$$\text{Discharge}: 6C + xLi^+ + xe^- \rightarrow Li_xC_6 \quad (1)$$

$$\text{Charge}: Li_xC_6 \rightarrow 6C + xLi^+ + xe^- \quad (2)$$

Discharge and charge for SnO_2.

$$\text{Discharge}: SnO_2 + 4Li^+ + 4e^- \rightarrow 2Li_2O + Sn \quad (3)$$

$$Sn + xLi^+ + xe^- \rightarrow Li_xSn\ (0 \leq x \leq 4.4) \quad (4)$$

$$\text{Charge}: Li_xSn \rightarrow Sn + xLi^+ + xe^-\ (0 \leq x \leq 4.4) \quad (5)$$

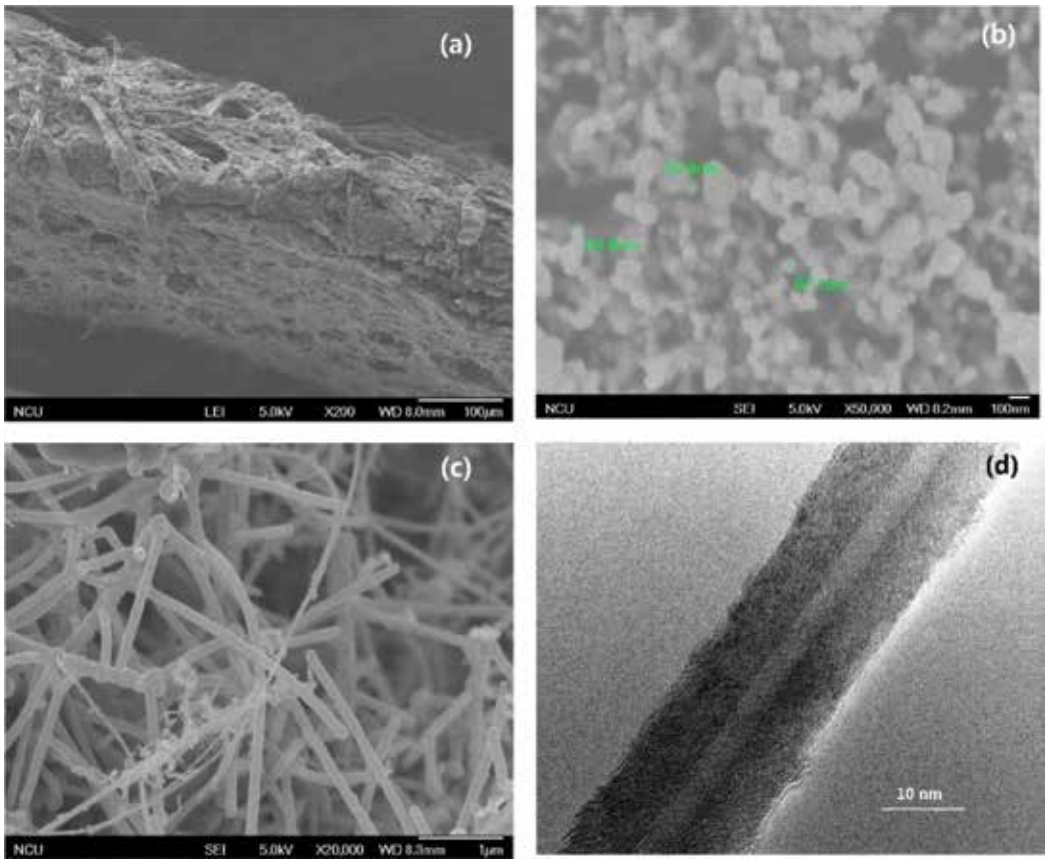

Figure 9. SEM images of porous collector (a), SnO_2 (b), CNTs (c), and HRTEM image of CNTs (d).

Cyclic voltammetry curves were recorded for SnO_2/CNT electrodes as shown in **Figure 10(a)**. The first cycle curve in the anodic sweep is substantially different from the subsequent curves. During the first oxidation scan, three characteristic oxidation peaks were observed at 0.3, 0.5, and 1.3 V. The strong peak at 0.3 V can be ascribed to lithium insertion into CNTs (Eq.(1)), which have been treated at 3000°C and obtained at very high crystallinity degree [89]. The strong peak at 0.5 V was corresponding to alloying process for forming Li_xSn alloy (Eq. (4)) [90]. The broad peak at 1.3 V can be considered to be the partly reversible reaction representing the conversion of Sn to SnO_2 (Eq. (3)) [91]. In first cathodic sweep process, sharp characteristic peaks were observed at 0.65 V. The sharp peak at 0.65 V can be ascribed to the formation of the solid electrolyte interphase (SEI) film on surface of CNTs and SnO_2 [92]. The irreversible transformation of SnO_2 to Sn was also contributed to the prominent reduction peak (Eq. (3)) [92]. The sharp reduction peak only appeared in first discharge cycle, which was originated from the initial irreversible capacity [92]. During subsequent 2nd and 3rd cycles, the CV curves were overlapped fully. This implied that the reactions in Eqs. (3) and (4) are highly reversible.

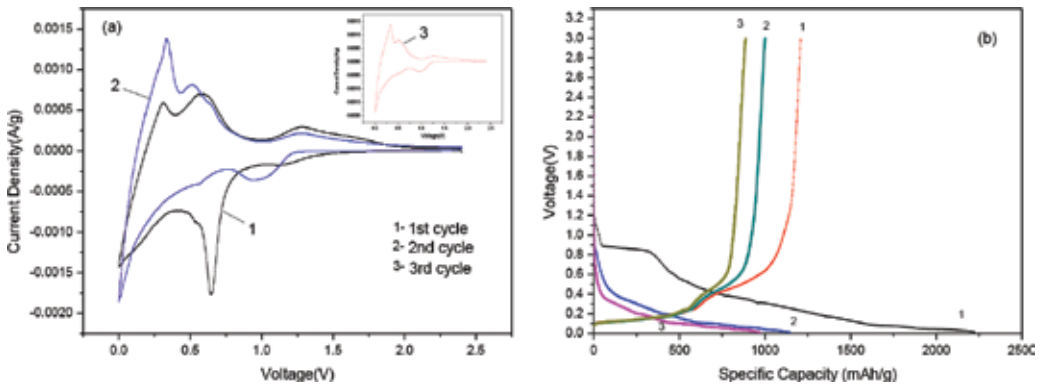

Figure 10. (a) Cyclic voltammetry curves at a scan rate of 0.1 mV/s over the potential window of 0–2.4 V. (b) the initial three galvanostatic discharge and charge profiles of the SnO_2/CNT electrode at current density of 100 mA/g.

Figure 10(b) shows the initial three galvanostatic discharge and charge profiles of the SnO_2/CNT electrode at current density of 100 mA/g. The first discharge and charge capacity reached around 2240 and 1250 mAh/g, respectively, with first coulombic efficiency of 56%. A voltage plateau at around 0.90 V can be noticed in the initial discharge process, which is attributed to the formation of Sn and Li_2O [28]. Moreover, the initial discharge capacities of 2240 mAh/g are higher than the theoretical capacity of SnO_2 (1494 mAh/g) [93], which can be attributed to CNTs that have a specific capacity of 200–3000mAh/g [94], and the oxygen containing functional groups reacted with lithium ions to exhibit certain capacity and the irreversible formation of the SEI layer [95]. A discharge capacity of 1140 and 1000 mAh/g was achieved in the 2nd and 3rd cycle. With the increase of the cycle numbers, the capacity fades very slowly.

The electrochemical performances of pure SnO_2 and CNT porous composite electrode were evaluated (**Figure 11**). The pure SnO_2 and slurry (1.8 g SnO_2: 0.6 g CNT: 0.3 g PVDF) were coated on copper foil and CNT paper collector, respectively. The charge-discharge current was hold at 100 mA/g. **Figure 11** shows the capacity of pure SnO_2 cathode exhibited abrupt capacity fading at the initial stage of cycling. After 20 cycles, the capacity almost faded away completely. The cathode-doped CNTs coated on copper foil collector maintained a capacity of 200mAh/g after 20 cycles. The cathode with CNT paper as collector exhibited excellent performance. The capacity was tend to stabilization after 6 cycles and still holds a capacity of about 600mAh/g after 20 cycles. The result suggested that the porous CNT paper collector is beneficial to enhance the kinetics of electrochemical reactions between SnO_2 and lithium ions with more interface areas.

The SnO_2/CNT paper electrode presents the excellent electrochemical performance. **Figure 12(a)** shows the rate capabilities of SnO_2/CNT paper electrode at various current densities from 100 mA/g to 500 mA/g. It exhibits a first discharge capacity of 1218 100mAh/g compared with a first discharge capacity of 1050mAh/g of copper foil collector. SnO_2/CNT/cellulose electrode showed remarkably enhanced rate capability, and much better capacity retention was attained, particularly at high current densities during charging. The capacity retention holds 680 mAh/g

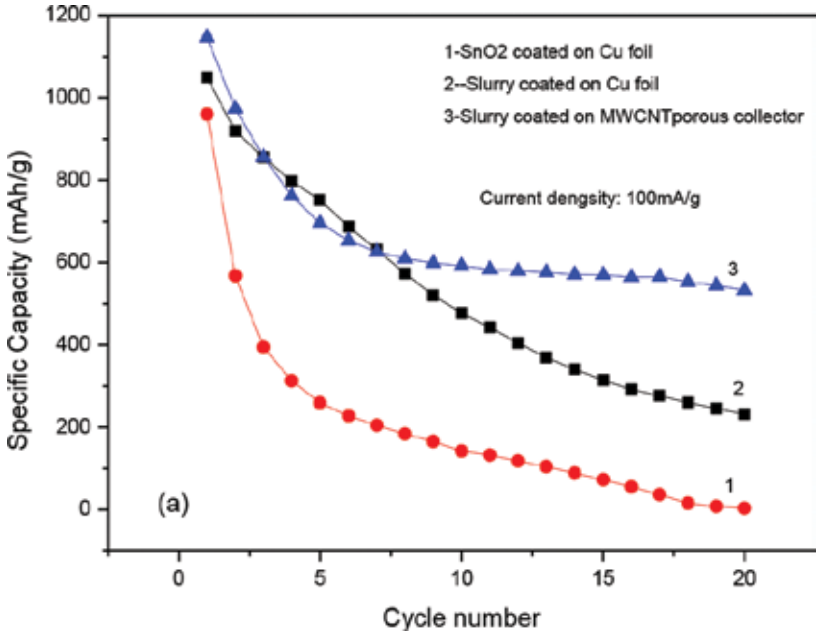

Figure 11. Cycling performance of SnO_2 coated on different collector.

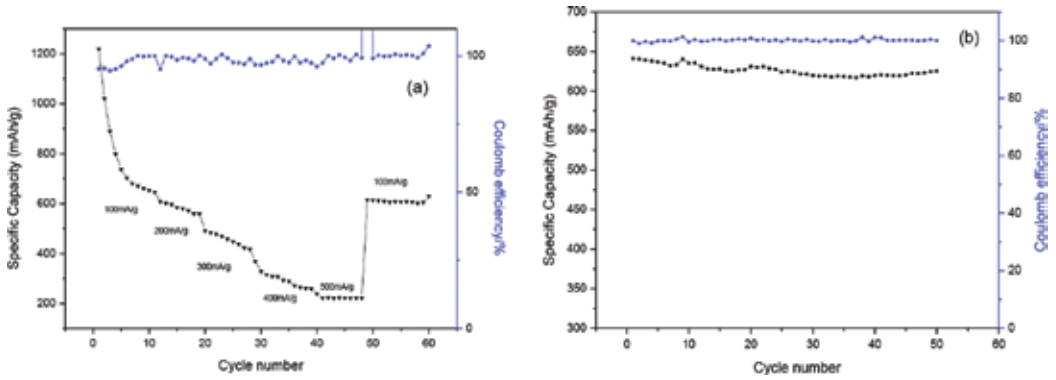

Figure 12. Cycling and rate performance of SnO_2 coated on CNT porous collector.

at 100 mA/g, 580 mAh/g at 200 mA/g, 420 mAh/g at 300 mA/g, 310 mAh/g at 400 mA/g, and 220 mAh/g at 500 mA/g. When the current density returned to 100 and 50 mA/g, respectively, the discharge capacity was recovered to 610 and 620 mAh/g in spite of subjecting to cycling at high current densities. The outstanding rate retention identified that the composite electrode is robust and highly stable even so high rate charge-discharge was tested.

The cycling performance and coulombic effect of SnO_2/CNT electrode were evaluated at 200 mA/g. As presented in **Figure 12(b)**, the capacity of electrode reduces rapidly during first

6 cycles. After then, the capacity fading was quite gentle. It should be noted that the retained capacity of the electrode was approximately 500 mAh/g after 100 cycles, which is much higher than that of the commercial graphite electrode. Furthermore, the CNT electrode maintained a stable coulombic efficiency of over 98%. This suggested the SnO_2/CNT/cellulose can bear big current shock and maintain good cycle performance.

Figure 13 illustrates the electrochemical impedance analyses of the SnO_2/CNT/cellulose electrode before cycles and after cycles, respectively. The experimental data show that the electrochemical impedance spectra of the electrodes consist of a single depressed semicircle in the high-to-medium frequency region and an inclined line at low frequencies. Before cycles, the charge-transfer resistance of the electrode reached 260 Ω. But after 100 cycles, the charge-transfer resistance of the electrode drastically declined to 60 Ω. This can be attributed to the porous structure of the electrode and 3D conductive network formed in the electrode by CNTs, which provide good electrolyte wetting and infiltrating and fast charge transport channel. The porous collector provides a large of space for storage of SnO_2, and reduced element Sn can be dispersed and infiltrated into the space of the collector. This resulted in the increase of contact interface areas for activated materials and collector. The Sn (SnO_2) encapsulated in the micropores of the electrode enhanced effectively the electron transfer. This can account for the decline of charge-transfer resistance after charge/discharge cycles.

Figure 14(a) shows top surface images of SnO_2/CNT/cellulose electrodes. It can be observed that SnO_2 was embedded into micropores of CNT/cellulose electrodes. This made an intimate contact between SnO_2 and CNTs and increases interfacial contact areas. The interface electrical resistance decreased substantially, which are beneficial to high-rate charge-discharge cycles. **Figure 14(b)** shows the morphologies of SnO_2/CNT/cellulose electrodes after cycles. A smooth layer on the surface can be observed. The SnO_2 nanoparticles do not show obvious aggregation. **Figure 14(c, d)** shows the image of cross section of both electrodes. **Figure 14(c)**

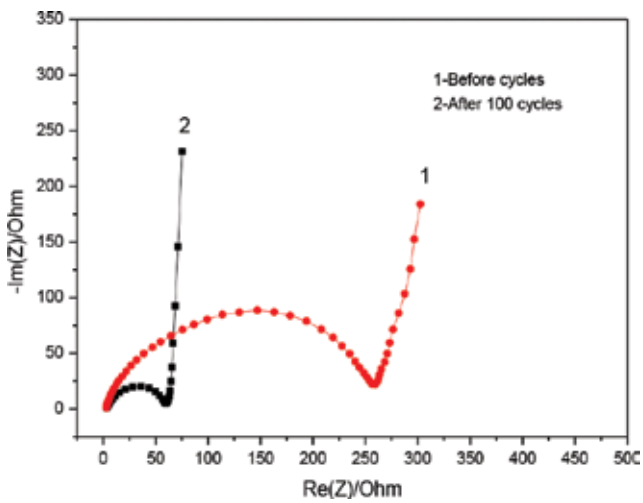

Figure 13. EIS of SnO_2 coated on CNT collector.

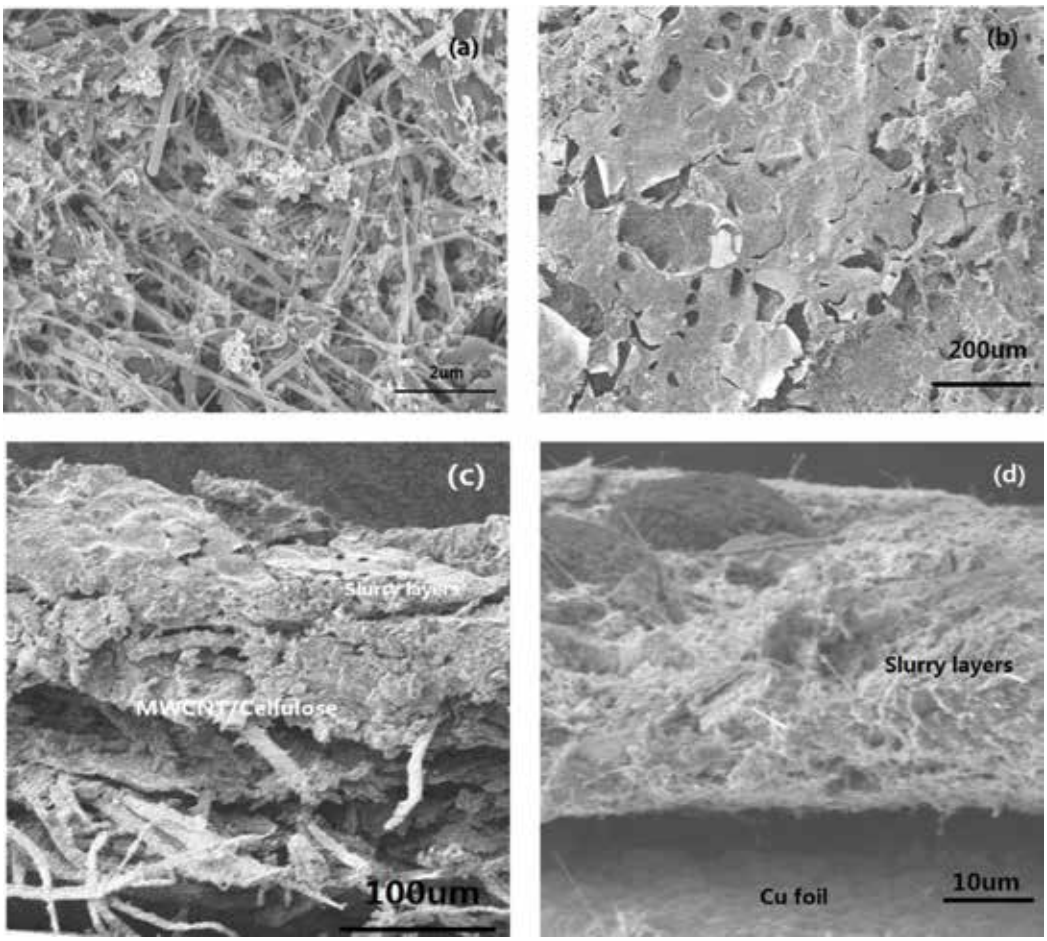

Figure 14. SEM images of SnO_2/CNT/cellulose electrodes (a) top surface before cycles, (b) top surface after cycles, (c) cross section after cycles, and (d) SnO_2/copper foil electrode cross section after cycles.

demonstrates that SnO_2 and CNT/Cellulose collector have close combination, and no cracks can be observed on interface of both after cycles. **Figure 14(c)** further revealed that SnO_2 was embedded into CNT/cellulose collector and made an intimate contact which was attributed to good cycle stability. However, SnO_2/copper foil electrode shows an obvious crack and pores on interface after cycles. It can also be observed that SnO_2 and Cu foil collector have not good affinity, and there can be visible interface pores which resulted in the decreasing contact interface. This sharply increasing of interface resistance will result in rapid fading of capacity.

Figure 15(a) shows that SnO_2 was only observed on the top of CNT porous collector. After charge-discharge cycles, SnO_2 intercalated into the interior of CNT collector and fully dispersed in the collector (**Figure 15(b)**). This can be attributed to the special interconnected channel of the CNT collector which provided and enhanced diffusion of nano-tin reduced from SnO_2 in discharging process. The homogeneous diffusion of tin increased effectively

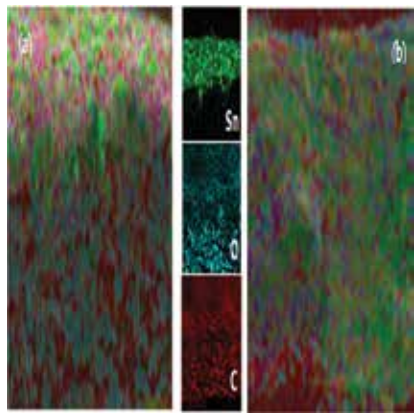

Figure 15. EDS of SnO_2/CNT porous electrodes (a) before and (b) after cycles.

contact interface areas of collector and tin dioxide and lowed interface electrical resistance. This is in full accord with EIS spectra (**Figure 13a**), which indicated that the charge transfer resistance became smaller after cycles. The diffusion also improved reversible capacity and maintained a good cycle stability from beginning of 40th cycles.

3.2.3. Conclusion

In summary, we have demonstrated a porous CNT/cellulose host to support SnO_2 as positive electrode for lithium ion battery electrode. The 3D structure with interconnected channel can load ultrahigh SnO_2 for high energy density battery. The hierarchical pores and channels can accommodate the big expansion of SnO_2 during charge/discharge and maintain a good cycle stability. SnO_2/CNT/ cellulose electrode showed remarkably enhanced rate capability and much better capacity retention. The capacity retention holds 680 mAh/g at 100 mA/g and 220 mAh/g at 500 mA/g. When the current density returned to 100 mA/g, the discharge capacity was recovered to 610 mAh/g. This suggested that the SnO_2/CNT/cellulose can bear big current shock and maintain good cycle performance. The CNT electrode also shows a stable coulombic efficiency of over 98%.

3.3. CNTCP used to replace aluminum foils as collector and scaffold for nanosilicon anode

3.3.1. Experiment

3.3.1.1. Raw materials

Commercial nanosilicon powders (purity: 99.0%, average diameter: 100 nm) and cellulose fibers were purchased in market. CNTs were synthesized by floating reactant method in a vertical tubular reactor. Benzene was used as carbon feedstock, organic-metallic compound (ferrocene) as a catalyst precursor, thiophene as growth promotion agent, and hydrogen as

carrier gas. The reaction temperature is around 1200°C. The following thermal treatment of CNTs was carried out at 3000°C for 20 h using a graphite-resistance furnace operating in a vacuum atmosphere.

3.3.1.2. Preparation of ternary electrodes

The CNTs powder was dispersed in deionized water with a surfactant of polyvinylpyrrolidone (PVP). The paper cellulose is made of napkins in deionized water. The CNTs dispersion liquid and the cellulose pulp were mixed by acute stirring. The mixed slurry of nanosilicon, CNTs, and cellulose fibers was infiltrated by vacuum. A porous mats of CNTs and cellulose fibers embedded with nanosilicon were obtained for anode applications.

3.3.1.3. Characterizations and testing

The CNTs were characterized by scanning electron microscopy (SEM), transmission electron microscopy (TEM), X-ray diffraction (XRD), Raman spectrometry, and thermogravimetry (TGA). Nanosilicon and the microstructure of the electrodes were observed by SEM.

The CR2025 coin-type cells were assembled in an Ar-filled glove box with a metallic lithium foil as the counter electrode. The electrochemical performance was measured by a cell tester with 1 M $LiPF_6$ in a mixture of ethylene carbonate (EC) and diethyl carbonate (DEC) as electrolyte. The galvanostatic charge-discharge was tested within a cut-off voltage window from 0 to 3.0 V at a current density of 80 mA/g.

3.3.2. Results and discussion

Figure 16a, b shows the morphology and structure of nanosilicon and composite anode of Si/CNT. The SEM image exhibits that the nanosilicon powders behave a polyhedral structure and an average diameter distribution of about 100 nm.

Figure 16b shows that nanosilicon is uniformly embedded in the network of CNTs. **Figure 17a** shows the morphology and structure of CNTCP with rough and porous surface. CNTs is uniformly dispersed and attached on paper fiber (**Figure 17b**). A good three-dimensional conductive network was constructed with cellulose fiber as the framework. **Figure 18** shows the galvanostatic charge-discharge curves of the Si/CNT composite anode at a current density of 80 mA/g with current collector of copper foil (CF) and CNTCP, respectively. It can be seen that CF electrode exhibited an initial discharge and charge specific capacity of 1020 mAh/g and 817 mAh/g, respectively (**Figure 18a**). The capacity rapidly faded with cycling. The capacity dropped to less than 200 mAh/g after 30 cycles. It was very evident that CF electrode exhibited very high irreversible capacity loss in cycles. The irreversible capacity is mainly from the growth of solid-electrolyte interface (SEI) films on surface of nanosilicon. The lithiation of silicon, which resulted in accumulation of Li + in silicon matrix to form Li_xSi alloy, also contributes to the big irreversible capacity. Further, owing to big volume change over 400% and press [96–98] during lithium ion insertion and extraction, the nanosilicon crystals were cracked and pulverized by press. Those produce new interface for forming SEI film. The pulverization of nanosilicon will also result in incomplete dealloying [99, 100]. The phase change of crystalline nanosilicon into amorphous state also caused

http://dx.doi.org/10.5772/intechopen.71916

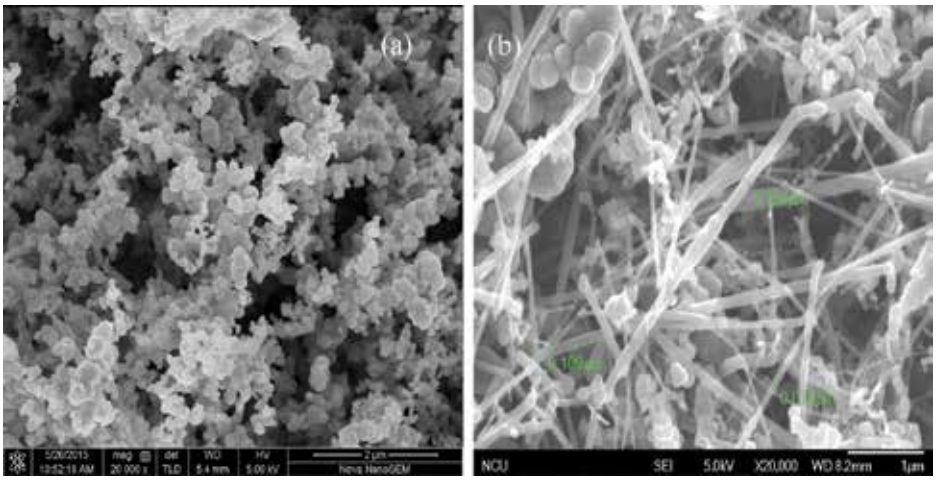

Figure 16. SEM images of nanosilicon (a) and composite Si/CNT anode (b).

some irreversible capacity loss. All those resulted in continuous capacity loss in cycles [101–103]. **Figure 18a** also exhibits an obvious charge voltage plateau at 0.5 V in first 10 cycles, which was connected to the characteristic of dealloying of Li/Si alloy. **Figure 18b** shows the discharge and charge profile of CNTCP electrode. The first discharge capacity and Coulomb efficiency of CNTCP electrode reached 2107mAh/g and 85%, respectively, which are 106 and 6% higher than those of CF electrode. CNTCP electrode becomes stable after 3 cycles, and Coulomb efficiency is closed to 100%. After 30 cycles, the specific capacity still maintained 1000mAh/g compared with only 180mAh/g of CP electrode. The cycling performances of both electrodes are showed in **Figure 18**. CNTCP electrode exhibited a 1000, 900, 500, and 200 mAh/g at a current density of 80, 200, 1000, and 2000 mA/g, respectively. When the current density reduced to 200 mA/g, the specific capacity restored 850 mAh/g after 160 cycles, which illustrated the highly reversible electrochemical behavior of CNTCP electrode. As a contrast, the capacity of CF electrode rapidly faded during cycles. The capacity declined to around 200 mAh/g at a current density of 80 mA/g after 30 cycles. The capacity

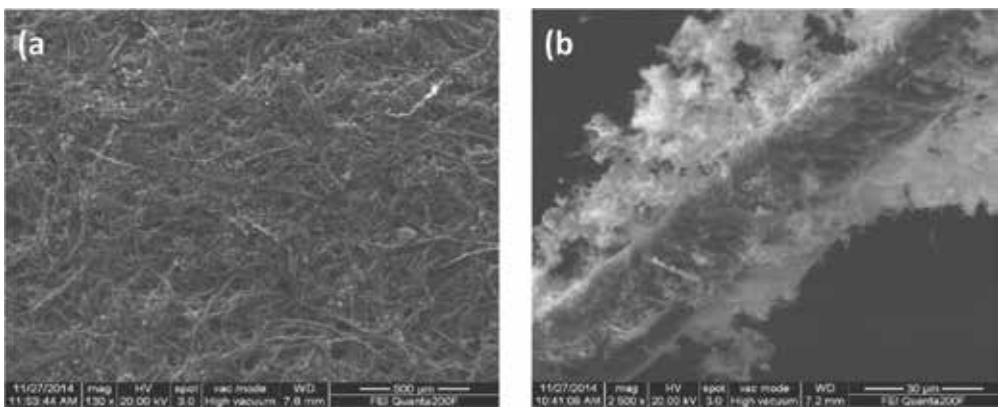

Figure 17. SEM images of CNT paper (a) top and (b) single cellulose fiber coated by MWCNTs.

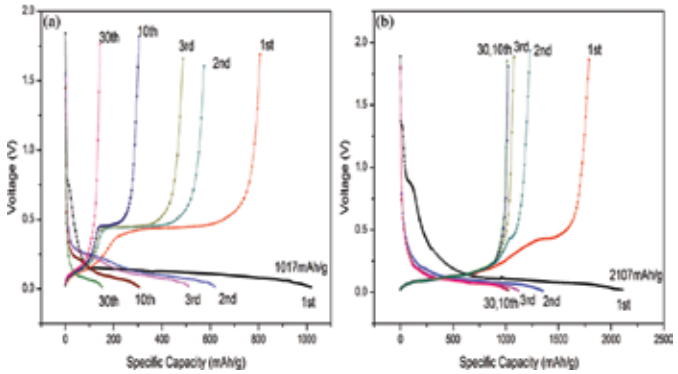

Figure 18. Discharge and charge curves of (a) copper foil cell and (b) CNT paper cell.

lowered to around 100 mAh/g after 69 cycles at a current density of 200 mA/g (**Figure 19**). The rapid decay of capacity of CF electrode was ascribed to the cracking and pulverization of silicone, which resulted in more SEI forming on interface and inefficacy of silicone, owing to big volume change and high press cannot be buffered on copper foil current collector. **Figure 20a** and **b** shows the cross-section images of CF electrode and CNTCP electrode. It can be observed in **Figure 20a** that Cu foil collector has no good affinity and nanosilicon easily produces pores on interface and big interface resistance. The sharply increasing of interface resistance will result in rapid fading of capacity. The CNTCP collector has high-porous structure and interconnected channel. Carbon and cellulose fiber have intrinsic affinity with activated materials. Nano-Si was embedded into surface

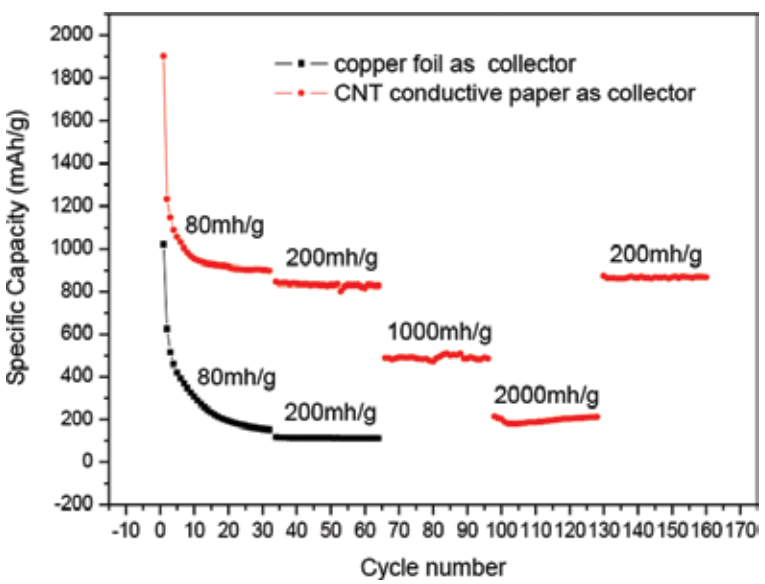

Figure 19. Cycle performance in different rate of copper foil cell and CNT paper cell.

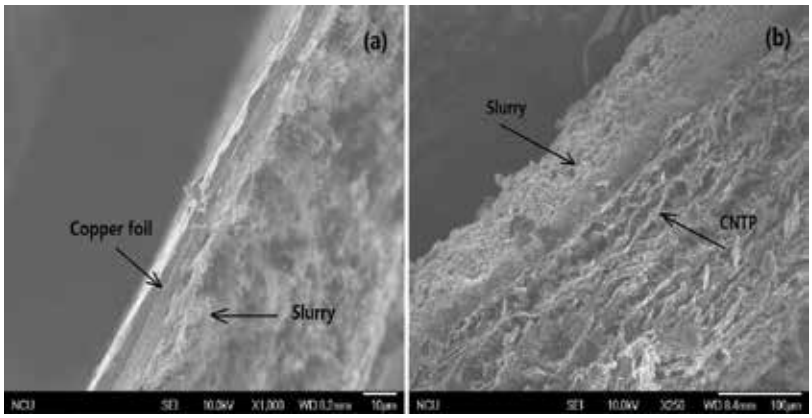

Figure 20. SEM image of interface of copper foil electrode (a), CNT paper electrode (b).

pores of CNTCP, which contributes to the low interface resistance and fast transfer of electrons and ions. The rate performance and utilization ratio of the active material were further improved.

To better understand the volume change and the stability of SEI layer, the impedance analysis was performed. All the EIS curves (**Figure 21**) show a depressed semicircle in the high frequency region and an oblique line in the low frequency domain. The CF electrode and CNTCP electrode exhibited a charge -transfer resistance 820 Ω (**Figure 21a**) and 580 Ω (**Figure 21c**) respectively. CNTCP electrode decreased by 29% than CF electrode because nano-Si was embedded into CNTCP host and effectively reduced the resistance of the coated activated material. After 30 cycles, the CNTCP electrode demonstrated significantly superiority than CF electrode. Owing to excellent accommodation of volume expansion and electrolyte absorptivity of CNTCP electrode, the charge-transfer resistance of CNTCP electrode decreased to around 30 Ω (**Figure 21c**). On the contrary, the charge-transfer resistance of CF electrode rapidly increased to around 2000 Ω (**Figure 21d**). This may be ascribed to the exfoliation of activated materials from copper collector owing to big volume expansion of silicone in cycles.

Here, CNTCP not only was used as current collector but also provides the battery with a certain capacity. **Figure 22b** revealed that CNTCP contributes 200mAh/g reversible capacity, while CF only provides a capacity of 45mAh/g [100, 104–117]. The CNTCP also consumes an irreversible capacity of 170 mAh/g (**Figure 22a**).

3.3.3. Conclusions

In the summary, the porous CNTCP was used as host of nano-Si for high-performance Li-ion battery. The CNTCP exhibited high conduction and excellent absorptivity of electrolyte. Nano-Si penetrated into the network of CNTCP to achieve a low interface resistance for high rate performance. The porous CNTCP with interconnected channel can absorb an amount of electrolyte and was wetted fully by electrolyte. All those contribute to the electrochemical performance of CNTCP electrode. The CNTCP electrode obtained a reversible capacity, as high as 1000mAh/g after 50 charge-discharge cycles. The good cycle performance is ascribed to

the accommodation and buffering effect to huge volume expansion of silicone during cycles. Therefore, the author believes that CNTCP has a good application prospect as current collector for silicon-based lithium ion batteries.

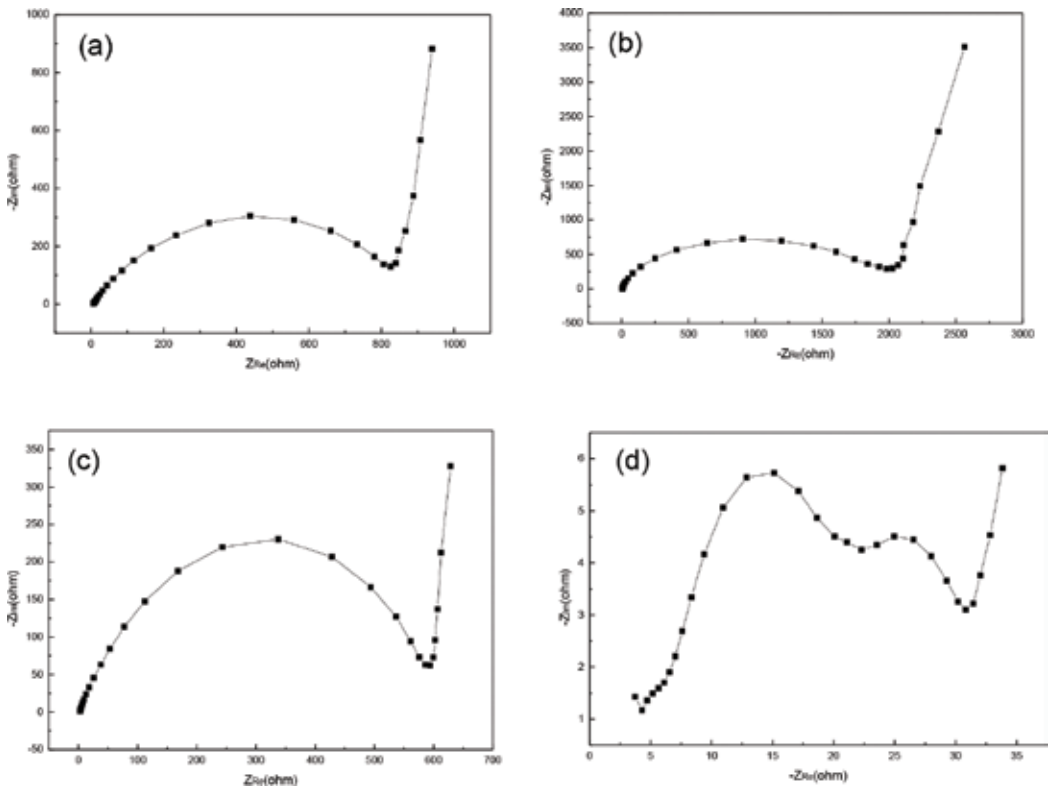

Figure 21. Impedance spectra of CF and CNT electrodes (a) fresh CF electrode (b) CF electrode after 30 cycles (c) fresh CNT electrodes (d) CNT electrodes after 30 cycles.

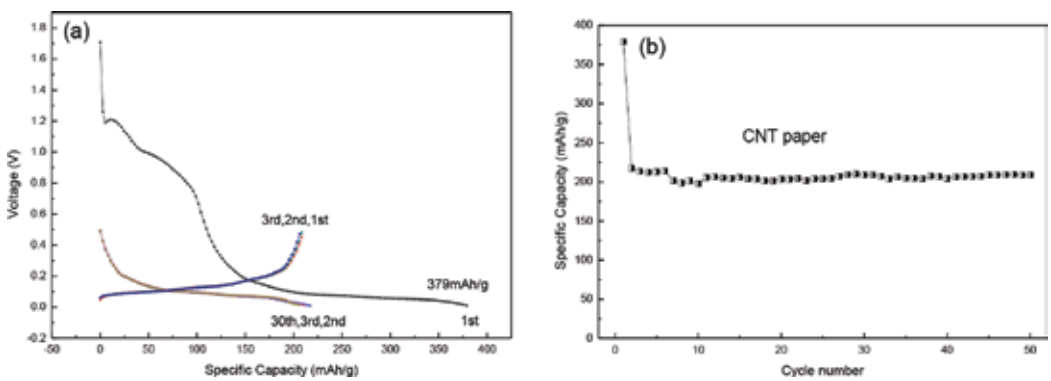

Figure 22. (a) First 30 discharge and charge curves and (b) cycle performance of CNTCP.

3.4. Primary battery based on fluorinated CNTs as cathode with CNTCP collector

3.4.1. Experimental

3.4.1.1. Fluorination of multiwalled carbon nanotubes

Three samples of fluorinated CNTs (FCNTs) were synthesized by direct fluorination of multiwalled carbon nanotubes [118]. The fluorination temperature was set at around 400°C. F/C ratio was adjusted to 0.28, 0.59, and 0.81. The FCNTs maintained a core-shell-hole structure after fluorination. The core still maintained pristine MWCNT structure with high electric conductivity and outer layers formed the structure of fluorinated carbon.

3.4.1.2. Physical characterization

Scanning electron microscopy (SEM) and high-resolution transmission electron microscopy (HRTEM) were performed to observe the core-shell-hole structure of FCNTs and analyzed their composition (EDX). F/C ratio was obtained by chemical titration method and EDX spectrometry. The change of atomic and electronic structures of FCNTs was investigated using X-ray photoelectron spectroscopy (XPS). The thermal stability of the FCNTs was investigated by thermogravimetric analysis (TGA). The weight loss of the material under argon atmosphere was recorded, while it was heated at a rate of 10°C/min from ambient temperature to 900°C. X-ray diffraction (XRD) and Raman were performed to identify the structure of FCNTs and primary CNTs.

3.4.1.3. Primary Li/CFx assemble and electrochemical characterization

The primary Li/CFx (x = 0.81) batteries were assembled with FCNTs as cathode against Li foil as anode. The electrochemical performance of the batteries was measured by cell tester (CT-3008 W-5V5mA-S4). Electrochemical impedance spectroscopy (EIS) measurements were performed on a CHI660B electrochemical workstation.

3.4.2. Results and discussion

SEM and HRTEM images of the FCNTs ($CF_{0.81}$) are presented in **Figure 23a** and **b**, respectively. After fluorination, the FCNTs exhibited a classic core-shell-hole structure. **Figure 24** shows the microstructure of FCNTs ($CF_{0.81}$). It can be clearly observed that the outer layers of CNTs were inserted by fluorine to form fluorinated carbides and inner layers hold pristine highly crystallized structure of CNTs. The exterior shell thickness of carbon fluorides ($CF_{0.81}$) was around 12 nm and internal layers of CNTs retained pristine graphitized structure with a thickness around 10 nm. The novel structure suggested that FCNTs still hold good interior electron conduction channel, even though exterior CNTs transformed into electrical insulator of carbon fluorides ($CF_{0.81}$). The central hole of CNT still remained with a diameter of 6 nm. The core-shell-hole structure means that the FCNTs maintained better electric conductivity than those of FG which is electric insulator. The central holes were contributed to the absorption of electrolyte and the diffusion of lithium ions. The novel structure can improve the conduction of both electrons but ions.

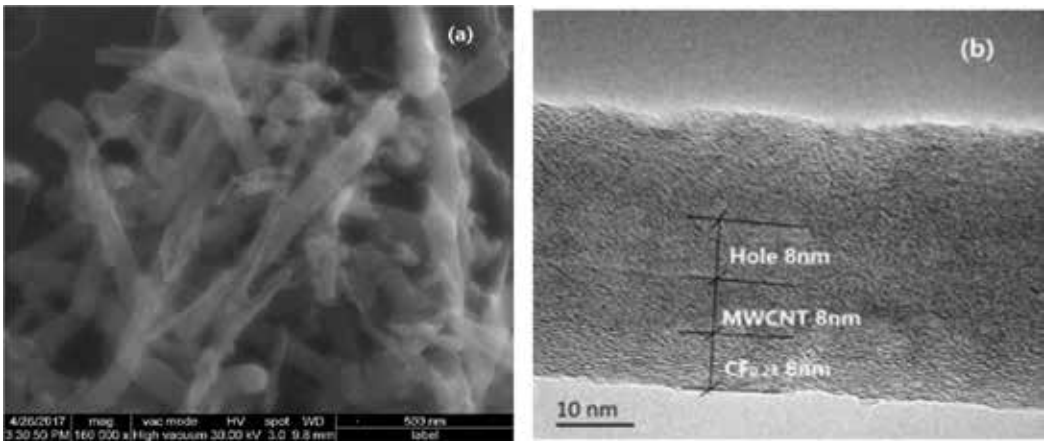

Figure 23. SEM and HRTEM of FCNTs ($CF_{0.28}$).

Carbon fluorides (CF*x*) are a type of nonstoichiometric compounds, whose thermal stability depends on the content of fluorine, the nature of carbon precursor, and the method of synthesis [8, 9]. The TGA of pristine CNTs and three FCNTs ($CF_{0.28}$,$CF_{0.56}$, and $CF_{0.81}$) are shown in **Figure 24**. It was founded that there is little loss for MWCNTs before 700°C. The weight loss of CNTs slowly began at 700°C and only has a weight loss of 10.6% at 900°C. It suggested a high heat stability of CNTs which have been treated at a temperature of 3000 and obtained very high crystallinity over 90%. The three FCNTs maintained stable before 460°C. But they began to decompose slowly when the temperature continues to increase. The decomposing of FCNTs accelerated at 500°C and terminated basically at 620°C. The primary volatile products of the thermal decomposition of the FCNTs contained CF_4 and C_2F_4, which are formed through a fluorocarbon radical process [119, 120]. It can be concluded that the $CF_{0.28}$, $CF_{0.56}$, and $CF_{0.81}$ contained around 40, 55, and 70 wt% fluorinated carbons. The following loss of

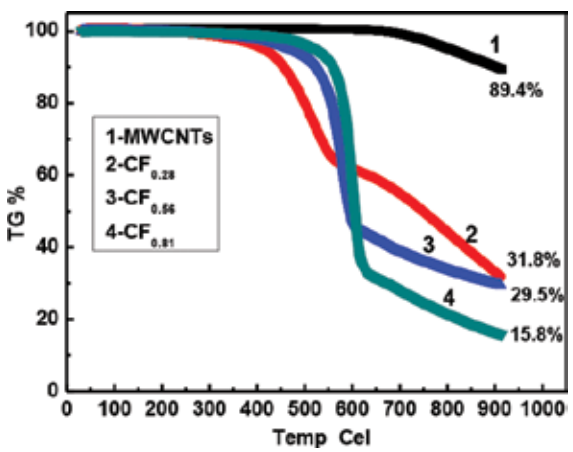

Figure 24. TGA curves of CNTs and FCNTs ($CF_{0.28}$, $CF_{0.56}$, $CF_{0.81}$) in nitrogen atmosphere from room temperature to 900°C.

weight can be ascribed to the forming of gaseous carbon-nitrogen compounds ($(CN)_x$, etc.) at temperature from 620–900°C [1]. The last remaining weight of four samples hold 89.4, 31.8, 29.5, and 15.8%, respectively, at 900°C. XRD patterns are shown for CNTs and FCNTs ($CF_{0.28}$, $CF_{0.56}$, $CF_{0.81}$) in **Figure 25a** and **b**, respectively. The stronger graphite peak (002) is observed at around 26.5° for CNTs (**Figure 25a**). But the graphite peak of FCNTs gradually weaken and finally disappeared with the enhancing fluorination of CNTs (**Figure 25a**). The outer layer structure of CNTs was destroyed with the formation of FCNTs. Fluorination only affects the outer layers of the CNTs which was resulted in destruction of graphite structure. The FCNT inner layers maintained graphite structure (**Figure 23b**). **Figure 25b** shows the Raman spectra of CNTs and FCNTs respectively. The characteristic D, G, and 2D bands are seen in two samples. Each spectrum consists of a distinctive pair of broadband at 1580 cm^{-1} (G band) and 1360 cm^{-1} (D band). The Raman peaks correspond to sp2 and sp3 carbon stretching modes, respectively. The intensity ratio of the G-band to the D-band (I_G/I_D) can be used to evaluate the graphitized degree of the samples [121, 122]. The I_G/I_D ratio of the CNTs reaches 4.3, which means a very high crystallinity. The ratio of I_G/I_D was seen to decrease to 0.66 for the FMWCNTs, as fluorine atoms are incorporated into the sp2 carbon lattice of outer layers to form amorphous sp3 structure in fluorination progresses. These results are in good agreement with XRD (**Figure 25a**).

The X-ray photoelectron spectroscopy (XPS) of the CNTs were obtained with a MultiLab 3000 spectrometer. The spectra were analyzed in order to investigate the nature of FCNTs. XPS of pure CNTs and FCNT samples are plotted in **Figure 26a**. The distinct carbon peaks of spectra were around 285.0 eV. The fluorine peaks in FCNTs were also found around 687.7 eV. With the fluorination enhanced, the F1 s peak was increased, while the intensity of the C1s peak was decreased. The detailed features for C1s peak are shown in **Figure 26b**. The peak at a binding energy (284.6 eV) in C1s spectra was assigned to sp2 hybridized carbon in CNTs. To format C-F bonds as a result of fluorination, the peak at a binding energy (289.4 eV) was assigned to sp3 hybridized carbon [118]. The peak (sp2) becomes broader and finally faded away, while the peak (sp3) was strengthened as the fluorination progresses [123]. Based on EDAX data, the four samples have been identified as $CF_{0.28}$, $CF_{0.56}$, $CF_{0.81,}$ and pure CNTs.

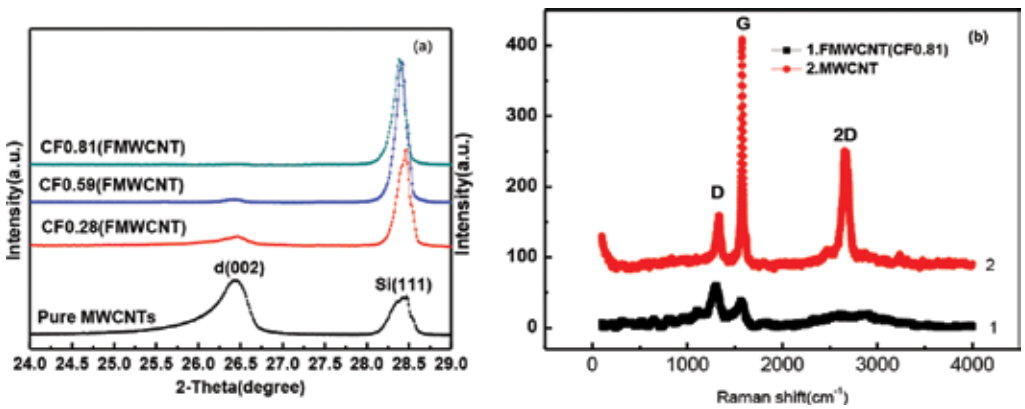

Figure 25. (a) XRD of CF0.28, CF0.59, CF0.81 and CNT and (b) Raman of CF0.81 and CNT.

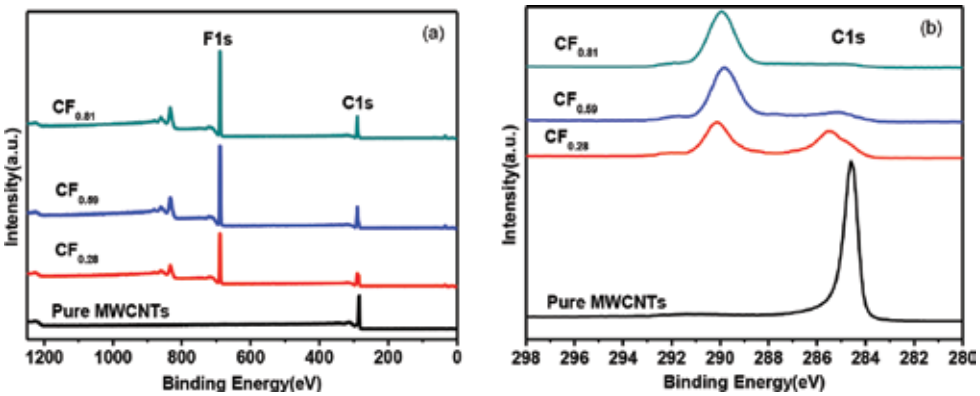

Figure 26. (a) XPS showing both F1 s and C1s peaks for pristine and FCNTs (b) detailed features for C1s peak.

The discharge profile of FG (Li/CF_1, theoretic capacity: 864mAh/g) cells is shown in **Figure 27a**. The discharge capacity reached 840 mAh/g (0.05 C), 744 mAh/g (0.1 C), 663 mAh/g (0.5 C), and 520 mAh/g (1 C). The graphite monofluoride exhibited the characteristic voltage plateau around 2.5 V at 0.05 C rate. The discharge plateau slowly dropped to about 2.0 V at discharge rate of 1 C. **Figure 27b** shows the discharge curves of FCNTs ($Li/CF_{0.81}$). The discharge starts at a higher voltage of about 3.2 V and then drops to about 2.7 V at discharge rate of 0.05 C. The discharge plateau maintained at 2.7 V with a specific capacity of 782mAh/g, which reached 98.7% of theoretic capacity of FCNT (792mAh/g for $CF_{0.81}$). The discharge plateau dropped to 2.45 V, when the discharge rate increased to 1 C from 0.05 C with a capacity of 620 mAh/g. The discharge efficiency lowered to 78.28% of theoretic capacity for carbon fluorides ($CF_{0.81}$) (**Figure 27**).

Electrochemical impedance spectroscopy (EIS) measurements were conducted in the frequency range of 100 kHz to 0.01 Hz at an excitation amplitude of 5 mV (**Figure 28**). The

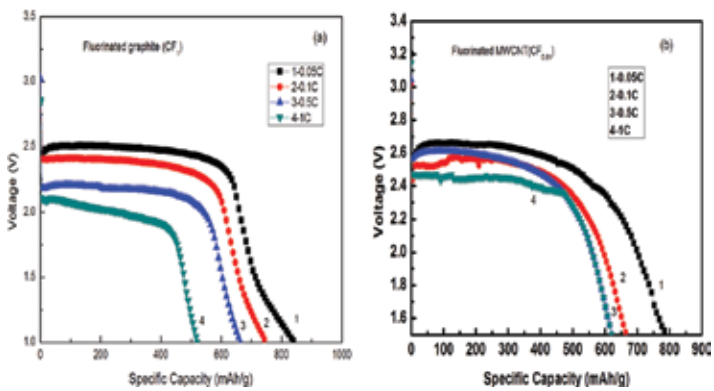

Figure 27. Discharge profile of FG and three FCNT electrodes at different rates.

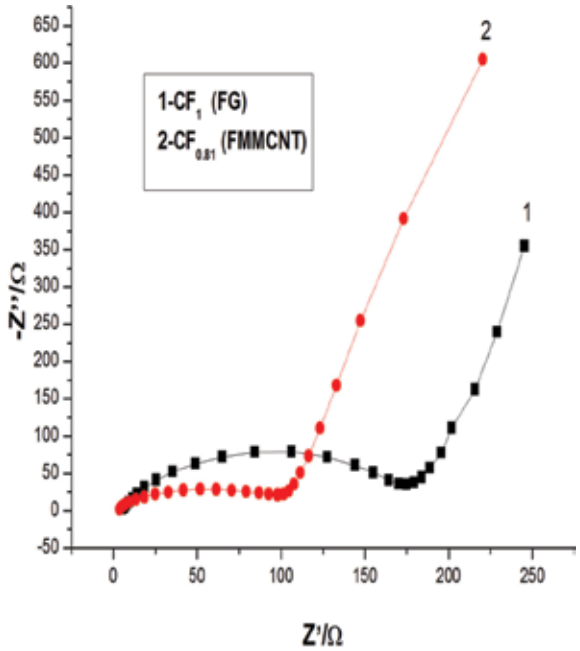

Figure 28. Electrochemical impedance spectroscopy (EIS) of $CF_{0.28}$, $CF_{0.56}$, $CF_{0.81}$ and CF_1.

Nyquist plots are composed of a semi-circle at high frequency and a linear line at low frequency. The intersection with the x-axis was corresponded to the charge-transfer resistance of the electrode with 100 and 180 Ω for $CF_{0.81}$ electrode and CF_1 electrode, respectively. It was noteworthy that the charge-transfer resistance of the electrodes increased with the increasing content of fluorine. The higher ratio of fluorine/carbon provided more activated points for the reduction of carbon fluorides to lithium fluorides and resulted in higher discharge capacity [124–128].

3.4.3. Conclusions

FCNTs exhibits a classic core-shell-hole structure. The outer layers of CNTs were Fluorinated and inner layers still maintained pristine graphitized structure integrity. The FCNTs hold good interior electron conduction channel, even though exterior CNTs transformed into electrical insulator. The core-shell-hole structure means that the FCNT maintained better electric conductivity than those of FG. FCNT exhibited better electrochemical performance than those of FG. The discharge plateau of FCNT maintained at 2.7 V (0.05C) with a specific capacity of 782 mAh/g, which reached 98.7% of theoretic capacity of FCNT (792mAh/g for $CF_{0.81}$). The discharge plateau still maintained 2.45 V at 1 C with a capacity of 620 mAh/g, and the discharge efficiency reached 78.28% compared with FG of 2 V, 520 mAh/g, and 60%, respectively. FCNTs were considered as a promise cathode materials for high performance of lithium fluoride battery.

3.5. CNTCP used as electrodes for supercapacitors

3.5.1. Experiment

3.5.1.1. Synthesis of multiwalled carbon nanotubes (CNTs)

CNTs were synthesized by floating reactant method in a vertical tubular reactor (**Figure 29**). Benzene was used as carbon feedstock, organic-metallic compound (ferrocene) as a catalyst precursor, thiophene as growth promotion agent, and hydrogen as carrier gas. The reaction temperature is around 1200°C. The following thermal treatment of CNTs was carried out at 3000°C for 10 h using a graphite resistance furnace operating in a vacuum atmosphere.

3.5.1.2. Preparation of electrodes

The CNTs powder was dispersed in deionized water with a surfactant of polyvinylpyrrolidone (PVP). The paper cellulose is made of napkins in deionized water. The CNTs dispersion liquid and the cellulose pulp were mixed by acute stirring. A vacuum filtration was used to infiltrate the mixed slurry of CNTs and cellulose fiber. Then, the formed CNTCP was carbonized at 1460°C in vacuum condition.

3.5.1.3. Material characterizations

The electrochemical characterization of the supercapacitors was measured by a cell tester (CT-3008 W-5V5mA-S4). Electrochemical impedance spectroscopy (EIS) was tested by electrochemical workstation (PARSTAT4000). Cyclic voltammetry (CV) was performed by an electrochemical workstation (CHI 660B).

3.5.1.4. Assembling of supercapacitors and testing

The tailored CNT-cellulose papers were used as the electrodes for symmetric electrochemical supercapacitors. CR2025 coin-type cells were assembled in an Ar-filled glove box (MBRAUNLABSTAR, Germany) by stacking a porous polypropylene separator. The liquid

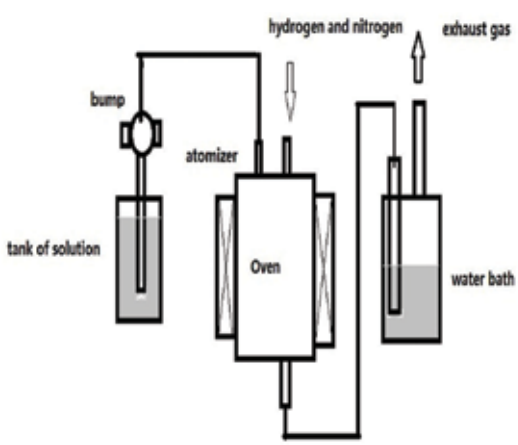

Figure 29. Schematic diagram of the setup for synthesis of CNTs.

electrolyte was 1 M LiPF6 dissolved in a mixture of ethylene carbonate (EC) and dimethyl carbonate (DMC) (1:1 in weight).

3.5.2. Results and discussion

The SEM (**Figure 30a**) images show that the CNTs have a distinct one-dimension line structure and were not entangled. They can be more easily dispersed than common carbon nanotubes (CCNTs). TEM image of the CNTs is shown in **Figure 30(b)**. It can be observed that the MWCNTs have a straight and clear texture with high crystallinity. The Raman spectra is demonstrated in **Figure 31a**. The intensity ratio of G and D band presents the degree of graphitization [121]. The I_G/I_D ratio of graphitized-CNTs was 1.81, which means a higher degree of graphitization than the raw CNTs with a 0.67 ratio of I_G/I_D. The XRD pattern (**Figure 31b**) shows the degree of graphitization as 97.25%.

The CNTCP papers are shown in **Figure 32(a, b)** and presented an obvious structure of fibers network with a 50 wt% CNT addition. **Figure 32(c, d)** shows the SEM images of carbonized CNTCP papers (CNT/CCP). It can be seen that carbonized paper fibers were coated with multiwalled carbon nanotubes. CNTs were uniformly dispersed on the surface of paper fibers.

There are five strong bands in the Raman spectra (**Figure 33**) of CNT/CP; the bands of 1100 and 2900 cm^{-1} represented the cellulose characteristic band and the bands of 1350, 1580, and 2700 cm^{-1} corresponded to the D band, G band, and 2D band of CNTs, respectively. The G band presents the ordered carbon, and D band presents the disordered carbon. The ratio of I_G/I_D was 1.18, which means CNTs have a high degree of graphitization. The CNT/CCP only has three bands of D, G, and 2D, which can be related to the reason of carbonization. The ratio of I_G/I_D was decreased to 1.02 due to higher amorphous carbon content [121, 129, 130].

Both of the CNT/CP and CNT/CCP electrodes exhibited a good layered porous structure (**Figure 34**). Most of the pore size is distributed in 2–4 nm, and CNT/CP has a much smaller pore size than CNT/CCP. Nanopores can improve the specific surface area of two papers but also conducive to the absorption of electrolytes to form electric double layer. More importantly, nanopores have played a role in helping the diffusion of electrolyte. Resulting in charged ions can pass through the 3D porous electrode, which can greatly reduce the charge transfer resistance.

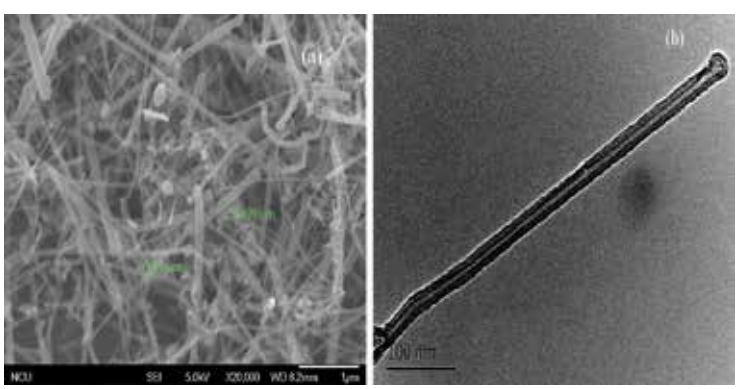

Figure 30. SEM and TEM images of CNTs.

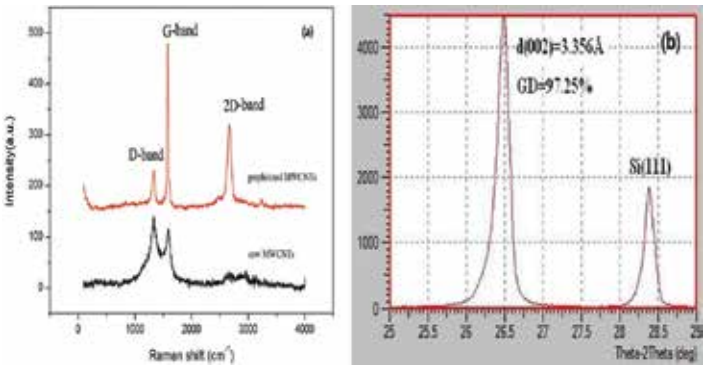

Figure 31. XRD pattern and Raman spectrometry of CNTs.

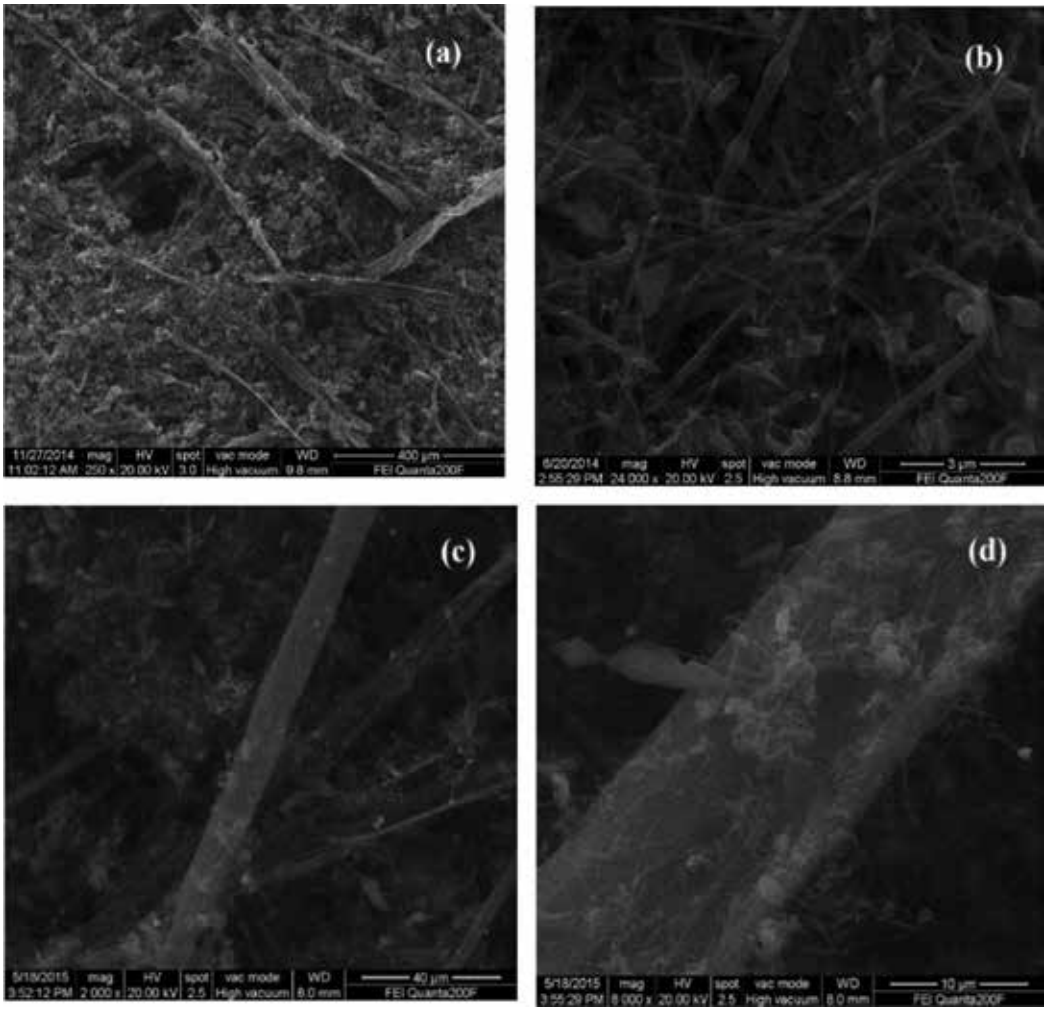

Figure 32. SEM images of (a,b) CNT/CP and (c,d) CNT/CCP electrodes.

http://dx.doi.org/10.5772/intechopen.71916

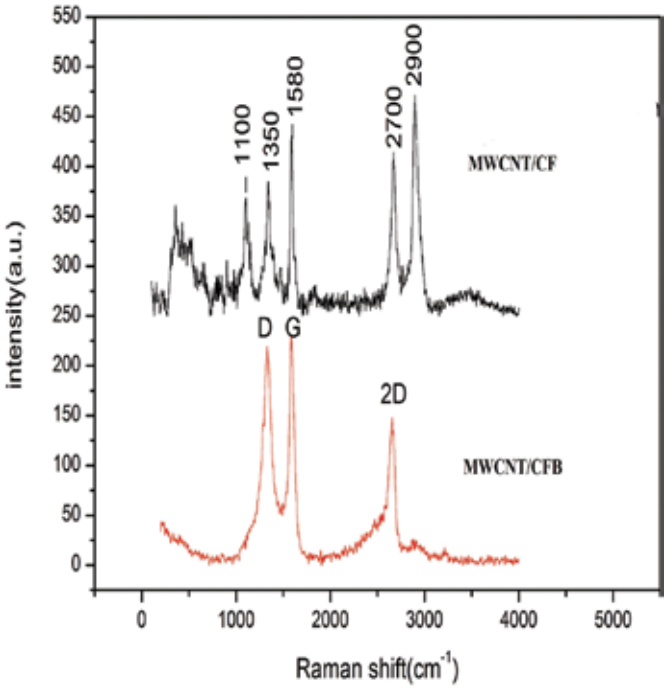

Figure 33. Raman spectra of CNT/CP and CNT/CCP electrodes.

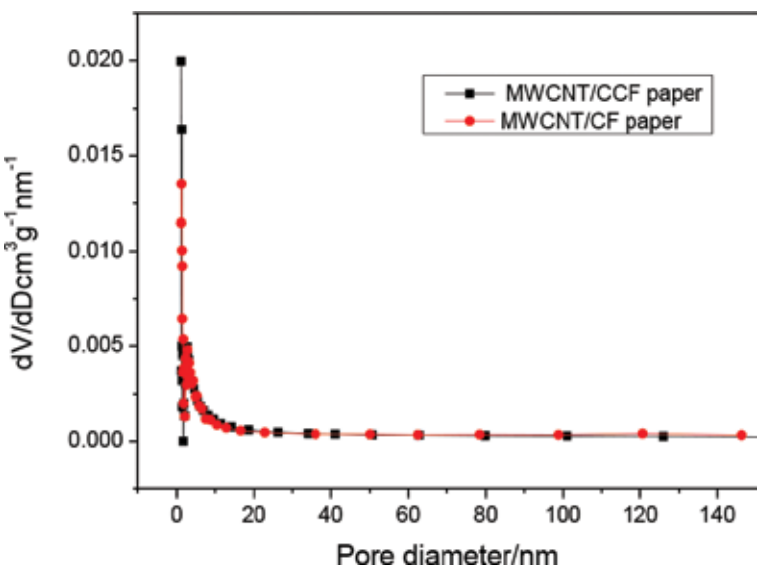

Figure 34. Pore diameter distribution for the CNT/CP and the CNT/CCP.

The electrochemical performance of the electrodes has been investigated by cyclic voltammetry (CV) (**Figure 35a,b**) with the voltage range of 0–2.5 V at four different scan rates of 5, 30, 50, and 100 mV/s. The CV curve of electric double layer capacitor is rectangular [131, 132].

However, the CV curve of CNT/CP (**Figure 35a**) electrodes presented a reduction peak without oxidation peak. The reduction reaction was related to the iron-based catalyst metals and reaction of lithium ions in electrolyte. Moreover, the irreversible redox reaction of iron and irreversible capacity of CNTs contributed to the absence of oxidation peak [121, 133–135]. The CV curve of CNT/CCP (**Figure 35b**) electrodes presented a perfect redox peak, which was related to faraday reaction. The no-carbon elements of CNT/CCP electrodes were evaporated in the process of carbonization. This is beneficial to the intercalate and de-intercalate of lithium ions in amorphous carbon particles [64, 131–136].

Specific capacitance and scan rate curves of CNT/CP and CNT/CCP are shown in **Figure 36**. The specific capacitance (Cscv) of the symmetric supercapacitor was calculated according to the following equation: Cscv = 2S/[(U2-U1) mν]. Cscv is the specific capacitance of the capacitor in F/g, S is the total voltammetric sweeps area during CV, (U2–U1) is the range of voltage, m is the active material mass per electrode, and ν is the scan rate.

With the increase of scan rate, the capacity of supercapacitor was decreased. The capacitance of MWCNT/CF electrode was 24 and 4.55 F/g at a scan rate 5 and 100 mV/s, respectively. By contrast, the capacitance of CNT/CCF electrode corresponds to 43 and 26 F/g at a scan rate 5 and 100 mV/s, respectively. The results show that carbonized electrode (CNT/CCF) exhibited a better capacitance performance than uncarbonized electrodes (CNT/CF).

Figure 37 shows the electrochemical impedance spectroscope (EIS) of the supercapacitors, and the EIS was measured at the same open circuit potential of 2.5 V. The interception of the real axis represents the solution resistance. The solution resistance of the supercapacitor is 16 Ω. The semicircle in the high frequency region presented the charge transfer resistance of electrode. The charge transfer resistance of carbonized electrode (CNT/CCF) is only 3 Ω, which suggested an excellent transfer resistance performance. The impedance curves showed a straight line slopes at low frequency region, which also suggested a good capacitive performance of carbonized electrodes. Absence of semicircle at low frequency means low contact resistance between collector and electrode plates [9]. The electrical conductivity of CNT/CCF electrode was tested by four-point probe resistance meter. The electrical conductivity was obviously raised from 714.3 to 325.1 S/m after carbonization.

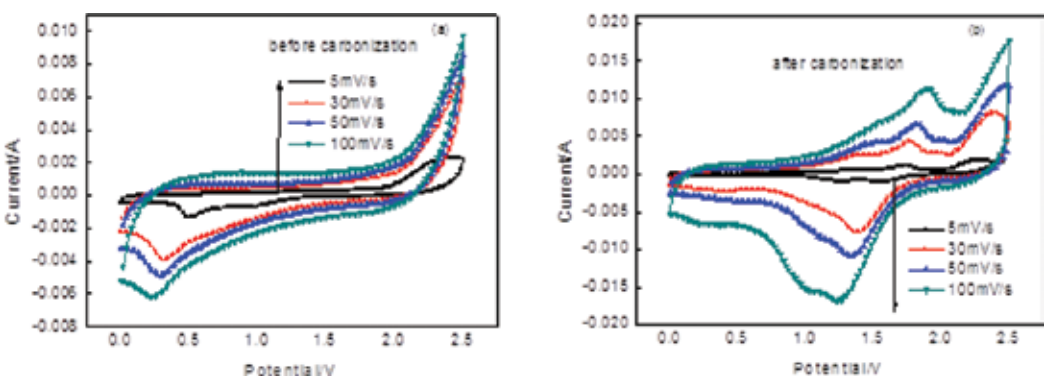

Figure 35. Cyclic voltammetry curves of (a) CNT/CP and (b) CNT/CCP electrodes.

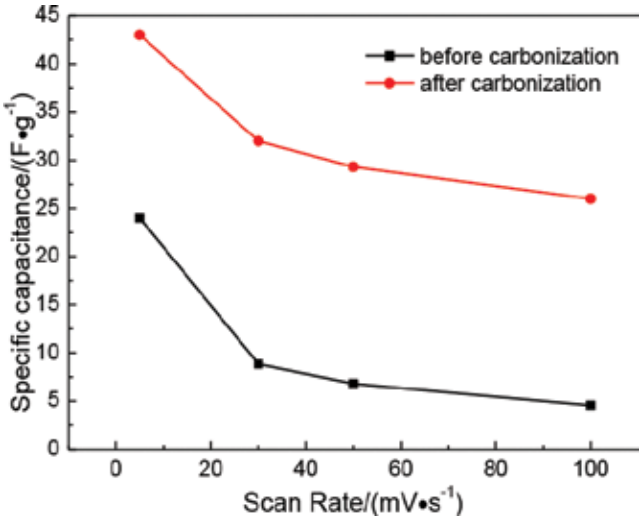

Figure 36. The specific capacitance of the supercapacitors vs. scan rate for CNT/Cp electrode and CNT/CCp electrode.

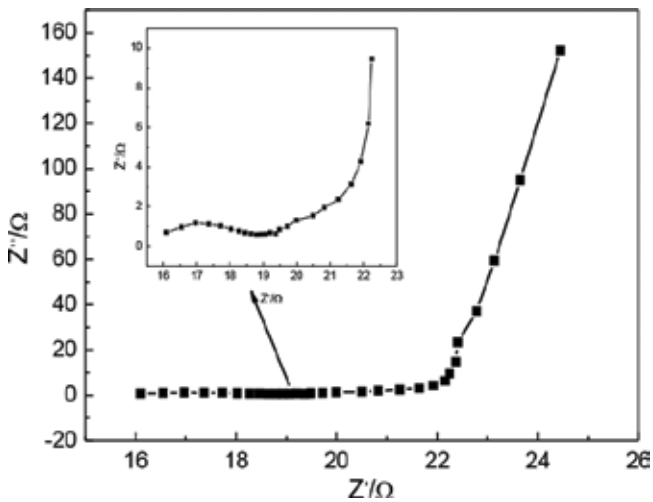

Figure 37. Electrochemical impedance spectroscope (EIS) of supercapacitor with carbonized electrode.

The specific capacitance (Cscv) of the two capacitors was calculated based on the charge/discharge profiles according to the following equation: Cscd = [2I]/[m(dV/dt)], where Cscd is the specific capacitance of the capacitors in F/g, I is the current in A, m is the mass of the active material in the capacitors in gram, and dV/dt is the slope of the discharge curve after the IR drop.

The charge/discharge curves of the CNT/CF and CNT/CCF electrodes were compared using different current density of 50, 100, 200, and 400 mA/g (**Figure 38**). The Cscd decreased as the current density increased. For CNT/CF electrode (**Figure 38a**), the capacity decreased from 17

F/g (50 mA/g), 12.8 F/g (100 mA/g), and 13 F/g (200 mA) to 12 F/g (400 mA/g). For CNT/CCF electrode (**Figure 38b**), the capacity decreased from 39 F/g (50 mA/g), 38 F/g (100 mA/g), 38 F/g (200 mA/g), 32.9 F/g (400 mA/g) to 29.2F/g (800 mA/g). The testing results indicated that the performance of supercapacitor was greatly improved after carbonization of electrodes. The curves of charge/discharge are not straight lines due to Faraday reaction.

Continuous charge-discharge was carried out for the CNT/CCP supercapacitor at constant current of 400 mA/g for 500 cycles (**Figure 39**). **Figure 39** shows the change in specific capacitance in 500 cycles. The CNT/CCP supercapacitor showed a progressive decrease in cycles. The specific capacitance still holds 74.6% after 500 cycles, which may be contributed to good wetting of electrolyte to electrodes and big interface areas between electrodes and electrolyte.

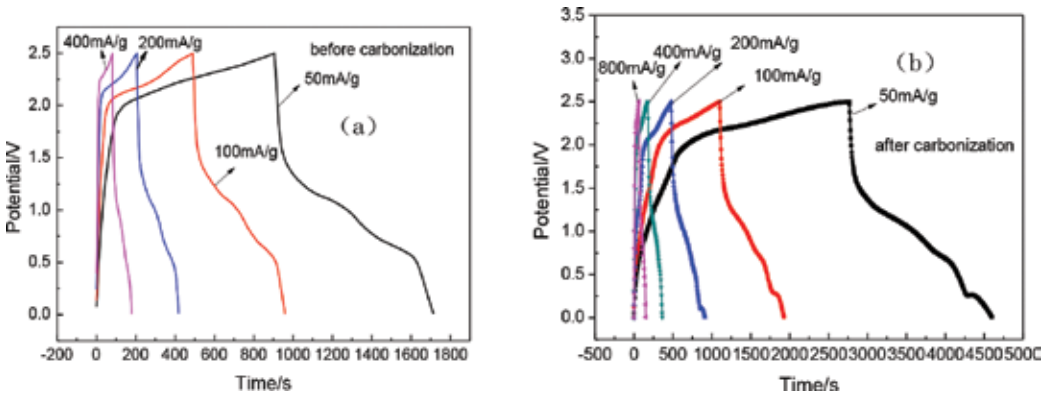

Figure 38. Galvanostatic charge/discharge curves of (a) CNT/CF and (b) CNT/CCP electrodes.

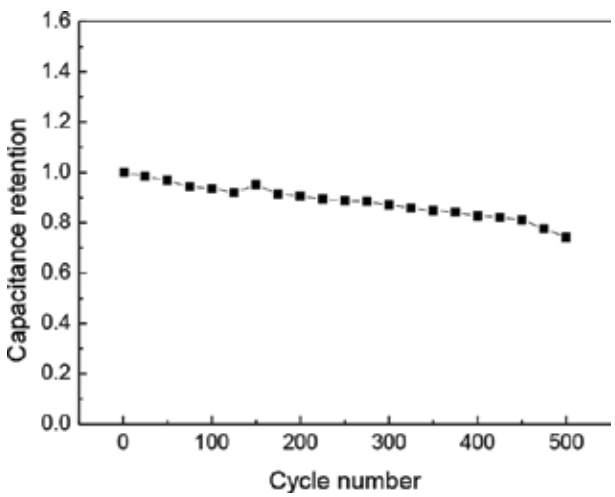

Figure 39. Capacitance retention of the carbonized CNT/CCP electrodes.

3.5.3. Conclusions

MWCNT/cellulose fiber electrodes provide 3D porous network structure and large interfacial area between electrode and electrolyte. Capacitance performance could be improved by the electrode and electrolyte's intimate contact. After carbonization treatment, the CNT/CCP electrodes have a higher performance of capacitance. The improvement is contributed to a better absorption of electrolyte, lower resistance of carbonized electrodes, and increase of effective interface area for forming of double layers. When the current density is 50 mA/g, the maximum specific capacitance of a unit capacitor reached 39 F/g by galvanization charge/discharge measurement, while the minimum specific capacitance of unit capacitor reached 24 F/g at a scan rate 5 mV/s of cyclic voltammetry measurement. The capacitance holds 74.6% after 500 cycles at a current density of 400 mA/g.

4. Outlook for CNTs and CNTCP in primary/second batteries and capacitors

In summary, our researches were reported of CNTs and CNTCP for primary/second batteries and supercapacitors applications. It has a great potential application value for the porous carbon nanotube-cellulose papers as current collectors and electrodes in lithium ion battery and supercapacitors. However, there are still some problems to be solved. The pore size and porosity and carbonization process of CNTCPs needed to be innovated to improve the strength and electrical conductivity. New high flexibility and strength of nanofibers need to be developed to adapt to electrolytes, as the cellulose papers are easily destroyed in liquid. The further investigations need to be done to overcome technological barriers for industrial applications of CNTCP in LIBs and SCs.

Author details

Xiaogang Sun*, Manyuan Cai, Long Chen, Zhiwen Qiu, Jie Wang, Xu Li and Wei Chen

*Address all correspondence to: xiaogangsun@163.com

School of Mechatronics Engineering, Nanchang University, Nanchang, China

References

[1] Zhang Y, Zhao Y, Konarov A, et al. Effect of mesoporous carbon microtube prepared by carbonizing the poplar catkin on sulfur cathode performance in Li/S batteries. Journal of Alloys and Compounds. 2015;**619**:298-302

[2] Liang J, Sun ZH, Li F, et al. Carbon materials for Li–S batteries: Functional evolution and performance improvement. Energy Storage Materials. 2015;**2**:76-106

[3] Wang C, Chen JJ, Shi YN, et al. Preparation and performance of a core–shell carbon/sulfur material for lithium/sulfur battery. Electrochimica Acta. 2010;**55**(23):7010-7015

[4] Li Y, Zhan H, Liu S, et al. Electrochemical properties of the soluble reduction products in rechargeable Li/S battery. Journal of Power Sources. 2010;**195**(9):2945-2949

[5] Jin S, Xin S, Wang L, et al. Covalently connected carbon nanostructures for current hosts in both the cathode and anode of Li-S batteries. Advanced Materials. 2016:**28**(41)

[6] Zhang J, Yang N, Yang X, et al. Hollow sulfur@graphene oxide core–shell composite for high-performance Li–S batteries. Journal of Alloys and Compounds. 2015;**650**:604-609

[7] Stoeck U, Balach J, Klose M, et al. Reconfiguration of lithium sulphur batteries: "Enhancement of Li–S cell performance by employing a highly porous conductive separator coating". Journal of Power Sources. 2016;**309**:76

[8] Wu Y, Gao M, Li X, et al. Preparation of mesohollow and microporous carbon nanofiber and its application in cathode material for lithium–sulfur batteries. Journal of Alloys and Compounds. 2014;**608**(10):220-228

[9] Choi S, Kim J, Eom M, et al. Application of a carbon nanotube (CNT) sheet as a current host for all-solid-state lithium batteries. Journal of Power Sources. 2015;**299**:70-75

[10] Hu L, Liu N, Eskilsson M, et al. Silicon-conductive nanohost for Li-ion batteries. Nano Energy. 2013;**2**(1):138-145

[11] Fang J, Qin F, Li J, et al. Improved performance of sulfur cathode by an easy and scale-up coating strategy. Journal of Power Sources. 2015;**297**:265-270

[12] Lee SK, Oh SM, Park E, et al. Highly cyclable lithium-Sulfur batteries with a dual-type Sulfur cathode and a lithiated Si/SiOx nanosphere anode. Nano Letters. 2015;**15**(5)

[13] Zhe Y, Peng HJ, Huang JQ, et al. Hierarchical free-standing carbon-nanotube host electrodes with ultrahigh Sulfur-loading for lithium–sulfur batteries. Advanced Functional Materials. 2014;**24**(39):6105-6112

[14] Wei W, Wang J, Zhou L, et al. CNT enhanced sulfur composite cathode material for high rate lithium battery. Electrochemistry Communications. 2011;**13**(5):399-402

[15] Chen JJ, Jia X, She QJ, et al. The preparation of nano-sulfur/MWCNTs and its electrochemical performance. Electrochimica Acta. 2010;**55**(27):8062-8066

[16] Waag W, Käbitz S, Sauer DU. Experimental investigation of the lithium-ion battery impedance characteristic at various conditions and aging states and its influence on the application. Applied Energy. 2013;**102**(2):885-897

[17] Lou X, Wang Y, Yuan C, et al. Template-free synthesis of SnO_2 hollow nanostructures with high lithium storage capacity. Advanced Materials. 2006;**18**(17):2325-2329

[18] Wang Y, Zeng H, Lee J. Highly reversible lithium storage in porous SnO_2, nanotubes with coaxially grown carbon nanotube Overlayers. Advanced Materials. 2006;**18**(5):645-649

[19] Li L, Yin X, Liu S, et al. Electrospun porous SnO_2, nanotubes as high capacity anode materials for lithium ion batteries. Electrochemistry Communications. 2010;**12**(10): 1383-1386

[20] Chen JS, Yan LC, Chen YT, et al. SnO_2 nanoparticles with controlled carbon Nanocoating as high-capacity anode materials for lithium-ion batteries. Journal of Physical Chemistry C. 2009;**113**(47):20504-20508

[21] Wang MS, Lei M, Wang ZQ, et al. Scalable preparation of porous micron-SnO_2/C composites as high performance anode material for lithium ion battery. Journal of Power Sources. 2016;**309**:238-244

[22] Xia G, Li N, Li D, et al. Graphene/Fe_2O_3/SnO_2 ternary nanocomposites as a high-performance anode for lithium ion batteries. ACS Applied Materials & Interfaces. 2013;**5**(17): 8607-8614

[23] Srinivasan NR, Mitra S, Bandyopadhyaya R. Improved electrochemical performance of SnO_2-mesoporous carbon hybrid as a negative electrode for lithium ion battery applications. Physical Chemistry Chemical Physics PCCP. 2014;**16**(14):6630-6640

[24] Yang L, Chen K, Dong T, et al. One-pot synthesis of SnO_2/C Nanocapsules composites as anode materials for lithium-ion batteries. Journal of Nanoscience and Nanotechnology. 2016;**16**(2):1768-1774

[25] Han F, Li WC, Li MR, et al. Fabrication of superior-performance SnO_2@C composites for lithium-ion anodes using tubular mesoporous carbon with thin carbon walls and high pore volume. Journal of Materials Chemistry. 2012;**22**(19):9645-9651

[26] Yao J, Shen X, Wang B, et al. In situ, chemical synthesis of SnO_2 –graphene nanocomposite as anode materials for lithium-ion batteries. Electrochemistry Communications. 2009;**11**(10):1849-1852

[27] Zhou X, Wan LJ, Guo Y. Binding SnO_2, Nanocrystals in nitrogen-doped Graphene sheets as anode materials for lithium-ion batteries. Advanced Materials. 2013;**25**(15):2152-2157

[28] Song H, Li X, Cui Y, et al. Controllable lithium storage performance of tin oxide anodes with various particle sizes. International Journal of Hydrogen Energy. 2015;**40**(41): 14314-14321

[29] Han S, Jang B, Kim T, et al. Simple synthesis of hollow tin dioxide microspheres and their application to lithium-ion battery anodes. Advanced Functional Materials. 2005;**15**(11): 1845-1850

[30] Park M-S, Wang G-X, Kang Y-M, et al. Preparation and electrochemical properties of SnO_2 nanowires for application in lithium-ion batteries. Angewandte Chemie. 2007; **119**(5):764-767

[31] Yang Z, Du G, Feng C, et al. Synthesis of uniform polycrystalline tin dioxide nanofibers and electrochemical application in lithium-ion batteries. Electrochimica Acta. 2010;**55**(19):5485-5491

[32] Park M-S, Kang Y-M, Wang G-X, et al. The effect of morphological modification on the electrochemical properties of SnO_2 Nanomaterials. Advanced Functional Materials. 2008;**18**(3):455-461

[33] Wang C, Zhou Y, Ge M, et al. Large-scale synthesis of SnO_2 Nanosheets with high lithium storage capacity. Journal of the American Chemical Society. 2009;**132**(1):46-47

[34] Yu Y, Chen CH, Shi Y. A tin-based amorphous oxide composite with a porous, spherical, multideck-cage morphology as a highly reversible anode material for lithium-ion batteries. Advanced Materials. 2007;**19**(7):993-997

[35] Wu GT, Wang CS, Zhang XB, et al. Lithium insertion into cu O/carbon nanotubes. Journal of Power Sources. 1998;**75**(1):175-179

[36] Cui G, Hu Y-S, Zhi L, et al. A one-step approach towards carbon-encapsulated hollow tin nanoparticles and their application in lithium batteries. Small. 2007;**3**(12):2066-2069

[37] Derrien G, Hassoun J, Panero S, et al. Nanostructured Sn–C composite as an advanced anode material in high-performance lithium-ion batteries. Advanced Materials. 2007; **19**(17):2336-2340

[38] Jung YS, Lee KT, Ryu JH, et al. Sn-carbon Core-Shell powder for anode in lithium secondary batteries. Journal of the Electrochemical Society. 2005;**152**(7):A1452-A1457

[39] Marcinek M, Hardwick LJ, Richardson TJ, et al. Microwave plasma chemical vapor deposition of nano-structured Sn/C composite thin-film anodes for Li-ion batteries. Journal of Power Sources. 2007;**173**(2):965-971

[40] Lee KT, Jung YS, Oh SM. Synthesis of tin-encapsulated spherical hollow carbon for anode material in lithium secondary batteries. Journal of the American Chemical Society. 2003;**125**(19):5652-5653

[41] Hassan FM, Chen Z, Yu A, et al. Sn/SnO_2, embedded in mesoporous carbon nanocomposites as negative electrode for lithium ion batteries. Electrochimica Acta. 2013;**87**(1): 844-852

[42] Iijima S. Helical microtubules of graphitic carbon. Nature. 1991;**354**(6348):56-58

[43] Landi BJ, Dileo RA, Schauerman CM, et al. Multi-walled carbon nanotube paper anodes for lithium ion batteries. Journal of Nanoscience and Nanotechnology. 2009;**9**(6):3406-3410

[44] Wang CS, Wu GT, Li WZ. Lithium insertion in ball-milled graphite. Journal of Power Sources. 1998;**76**(1):1-10

[45] de las Casas C, Li W. A review of application of carbon nanotubes for lithium ion battery anode material. Journal of Power Sources. 2012;**208**:74-85

[46] Holzapfel M, Buqa H, Hardwick LJ, et al. Nano silicon for lithium-ion batteries. Electrochimica Acta. 2006;**52**(3):973-978

[47] Liang B, Liu Y, Xu Y. Silicon-based materials as high capacity anodes for next generation lithium ion batteries. Journal of Power Sources. 2014;**267**:469-490

[48] Huggings RA, Cui YI. High-performance lithium battery anodes using silicon nanowires. Materials for sustainable energy: A collection of peer-reviewed research and review articles from nature publishing group. 2011;**187**

[49] Zhang Y, Zhang XG, Zhang HL, et al. Composite anode material of silicon/graphite/carbon nanotubes for Li-ion batteries. Electrochimica Acta. 2006;**51**(23):4994-5000

[50] Khomenko VG, Barsukov VZ. Characterization of silicon-and carbon-based composite anodes for lithium-ion batteries. Electrochimica Acta. 2007;**52**(8):2829-2840

[51] Kim T, Mo YH, Nahm KS, et al. Carbon nanotubes (CNTs) as a buffer layer in silicon/CNTs composite electrodes for lithium secondary batteries. Journal of Power Sources. 2006;**162**(2):1275-1281

[52] Zhou Z, Xu Y, Liu W, et al. High capacity Si/DC/MWCNTs nanocomposite anode materials for lithium ion batteries. Journal of Alloys and Compounds. 2010;**493**(1):636-639

[53] Luo Z, Fan D, Liu X, et al. High performance silicon carbon composite anode materials for lithium ion batteries. Journal of Power Sources. 2009;**189**(1):16-21

[54] Zuo P, Yin G, Yang Z, et al. Improvement of cycle performance for silicon/carbon composite used as anode for lithium ion batteries. Materials Chemistry and Physics. 2009; **115**(2):757-760

[55] Khomenko VG, Barsukov VZ, Doninger JE, et al. Lithium-ion batteries based on carbon–silicon–graphite composite anodes. Journal of Power Sources. 2007;**165**(2):598-608

[56] Dimov N, Xia Y, Yoshio M. Practical silicon-based composite anodes for lithium-ion batteries: Fundamental and technological features. Journal of Power Sources. 2007;**171**(2):886-893

[57] Lam P, Yazami R. Physical characteristics and rate performance of (CF x) n (0.33< x< 0.66) in lithium batteries. Journal of Power Sources. 2006;**153**(2):354-359

[58] Dose WM, Donne SW. Optimising heat treatment environment and atmosphere of electrolytic manganese dioxide for primary Li/MnO_2 batteries. Journal of Power Sources. 2014;**247**:852

[59] Nakajima T. Fluorine compounds as energy conversion materials. Journal of Fluorine Chemistry. 2013;**149**:104-111

[60] Eweka EI, Giwa CO, Mepsted GO, Green K, Scattergood D. Development of high energy density small flat spiral cells and battery pack based on lithium/ carbon monofluoride (Li/CFx). Journal of Power Sources. 2006;**162**:841

[61] Zhang Q, D'Astorg S, Xiao P, Zhang X, Lu L. Carbon-coated FG for high energy and high power densities primary lithium batteries. Journal of Power Sources. 2010;**195**:2914

[62] Zhang SS, Foster D, Read J. Enhancement of discharge performance of Li/CFx cell by thermal treatment of CFx cathode material. Journal of Power Sources. 2009;**188**:601

[63] Dubois M, Guérin K, Zhang W, et al. Tuning the discharge potential of fluorinated carbon used as electrode in primary lithium battery. Electrochimica Acta. 2012;**59**(4):485-491

[64] Pasta M, Mantia FL, Hu L, et al. Aqueous Supercapacitors on conductive cotton. Nano Research. 2010;**3**(6):452-458

[65] Kang YJ, Chung H, Kim W. 1.8-V flexible supercapacitors with asymmetric configuration based on manganese oxide, carbon nanotubes, and a gel electrolyte. Synthetic Metals. 2013;**166**(4):40-44

[66] Zhu Z, Hu Y, Hao J, et al. A three-dimensional ordered mesoporous carbon/carbon nanotubes nanocomposites for supercapacitors. Journal of Power Sources. 2014;**246**(3):402-408

[67] Chuang, Peng, Shengwen, et al. Carbon nanotube and conducting polymer composites for supercapacitors. Progress in Natural Science. 2008;**18**(7):777-788

[68] Chao, Zheng, Weizhong, et al. Carbon nanotubes for supercapacitors: Consideration of cost and chemical vapor deposition techniques. Journal of Natural Gas Chemistry. 2012;**21**(3):233-240

[69] Yin Y, Liu C, Fan S. A new type of secondary hybrid battery showing excellent performances. Nano Energy. 2015;**12**:486-493

[70] Ruch PW, Kötz R, Wokaun A. Electrochemical characterization of single-walled carbon nanotubes for electrochemical double layer capacitors using non-aqueous electrolyte. Electrochimica Acta. 2009;**54**(19):4451-4458

[71] Wang G, Ling Y, Qian F, et al. Enhanced capacitance in partially exfoliated multi-walled carbon nanotubes. Journal of Power Sources. 2011;**196**(11):5209-5214

[72] Yun TG, Oh M, Hu L, et al. Enhancement of electrochemical performance of textile based supercapacitor using mechanical pre-straining. Journal of Power Sources. 2013;**244**(4): 783-791

[73] Kötz R, Carlen M. Principles and applications of electrochemical capacitors. Electrochimica Acta. 2000;**45**(15-16):2483-2498

[74] Wang H, Cheng P, Feng P, et al. Facile synthesis of MnO 2 /CNT nanocomposite and its electrochemical performance for supercapacitors. Materials Science and Engineering B. 2011;**176**(14):1073-1078

[75] Smithyman J, Liang R. Flexible supercapacitor yarns with coaxial carbon nanotube network electrodes. Materials Science and Engineering B. 2014;**184**(5):34-43

[76] Ge D, Yang L, Fan L, et al. Foldable supercapacitors from triple networks of macroporous cellulose fibers, single-walled carbon nanotubes and polyaniline nanoribbons. Nano Energy. 2015;**11**:568-578

[77] Youn HC, Park SH, Roh KC, et al. Highly dispersible surface-unzipped multi-walled carbon nanotubes as binder-free electrodes for supercapacitor applications. Current Applied Physics. 2015;**15**:S21-S26

[78] Wang G, Liang R, Liu L, et al. Improving the specific capacitance of carbon nanotubes-based supercapacitors by combining introducing functional groups on carbon nanotubes with using redox-active electrolyte. Electrochimica Acta. 2014;**115**(3):183-188

[79] Portet C, Taberna PL, Simon P, et al. Influence of carbon nanotubes addition on carbon–carbon supercapacitor performances in organic electrolyte. Journal of Power Sources. 2005;**139**(1-2):371-378

[80] Zheng C, Qian W, Wei F. Integrating carbon nanotube into activated carbon matrix for improving the performance of supercapacitor. Materials Science and Engineering B. 2012;**177**(13):1138-1143

[81] Fang R, Zhao S, Hou P, et al. 3D interconnected electrode materials with ultrahigh areal Sulfur loading for Li-S batteries. Advanced Materials. 2016;**28**(17):3374-3382

[82] Chen SR, Zhai YP, Xu GL, et al. Ordered mesoporous carbon/sulfur nanocomposite of high performances as cathode for lithium–sulfur battery. Electrochimica Acta. 2011;**56**(26):9549-9555

[83] Zhu Y, Xu G, Zhang X, et al. Hierarchical porous carbon derived from soybean hulls as a cathode matrix for lithium-sulfur batteries. Journal of Alloys and Compounds; 2016

[84] Ghazi ZA, Zhu L, Wang H, et al. Efficient polysulfide chemisorption in covalent organic frameworks for high-performance lithium-Sulfur batteries. Advanced Energy Materials. 2016

[85] Fang R, Zhao S, Pei S, et al. Toward More Reliable Lithium–Sulfur Batteries: An all-Graphene cathode structure. Acs Nano. 2016;**10**(9):8676-8682

[86] Liu X, Zhang Q, Zhang S, et al. Hierarchical nanostructured composite cathode with carbon nanotubes as conductive scaffold for lithium-sulfur batteries. Journal of Energy Chemistry. 2013;**22**(2):341-346

[87] Zheng W, Liu YW, Hu XG, et al. Novel nanosized adsorbing sulfur composite cathode materials for the advanced secondary lithium batteries. Electrochimica Acta. 2006;**51**(7):1330-1335

[88] Nazar LF, Cuisinier M, Pang Q. Lithium-sulfur batteries. MRS Bulletin. 2014;**39**(5 (Lithium Batteries and Beyond)):436-442

[89] Tessonnier JP, Rosenthal D, Hansen TW, et al. Analysis of the structure and chemical properties of some commercial carbon nanostructures. Carbon. 2009;**47**(7):1779-1798

[90] Zhu X, Zhu Y, Murali S, et al. Reduced graphene oxide/tin oxide composite as an enhanced anode material for lithium ion batteries prepared by homogenous coprecipitation. Journal of Power Sources. 2011;**196**(15):6473-6477

[91] Miao C, Liu M, He YB, et al. Monodispersed SnO_2 nanospheres embedded in framework of graphene and porous carbon as anode for lithium ion batteries. Energy Storage Materials. 2016;**3**:98-105

[92] Wen Z, Zheng F, Liu K. Synthesis of porous SnO_2, nanospheres and their application for lithium-ion battery. Materials Letters. 2012;**68**(2):469-471

[93] Hu R, Sun W, Zhu M. Microstructure and Composition Tuning: Enhancing Reversibility of SnO_2 based anodes and reducing their initial capacity loss. The Electrochemical Society. 2014;(2):386-386

[94] Wang Y, Su D, Wang C, et al. SnO_2 @MWCNT nanocomposite as a high capacity anode material for sodium-ion batteries. Electrochemistry Communications. 2013;**29**(10):8-11

[95] Meng FL, Li HH, Kong LT, et al. Parts per billion-level detection of benzene using SnO_2/graphene nanocomposite composed of sub-6 nm SnO_2, nanoparticles. Analytica Chimica Acta. 2012;**736**(14):100

[96] Deshpande R, Cheng YT, Verbrugge MW. Modeling diffusion-induced stress in nanowire electrode structures. Journal of Power Sources. 2010;**195**(15):5081-5088

[97] Pushparaj VL, Shaijumon MM, Kumar A, et al. Flexible energy storage devices based on nanocomposite paper. Proceedings of the National Academy of Sciences. 2007; **104**(34):13574-13577

[98] Gohier A, Laïk B, Kim KH, et al. High-rate capability silicon decorated vertically aligned carbon nanotubes for Li-ion batteries. Advanced Materials. 2012;**24**(19):2592-2597

[99] Lee JH, Kim WJ, Kim JY, et al. Spherical silicon/graphite/carbon composites as anode material for lithium-ion batteries. Journal of Power Sources. 2008;**176**(1):353-358

[100] Chen S, Shen L, Peter A, et al. Dual-functionalized double carbon shells coated silicon nanoparticles for high performance lithium-ion batteries. Advanced Materials. 2017:1605650

[101] Yang X, Wen Z, Zhang L, et al. Synthesis and electrochemical properties of novel silicon-based composite anode for lithium-ion batteries. Journal of Alloys and Compounds. 2008;**464**(1):265-269

[102] Yoon S, Lee S, Kim S, et al. Carbon nanotube film anodes for flexible lithium ion batteries. Journal of Power Sources. 2015;**279**:495-501

[103] Song B, Fang H, Yang J, et al. Intercalation and diffusion of lithium ions in a carbon nanotube bundle by ab initio molecular dynamics simulations. Energy & Environmental Science. 2011;**4**(4):1379-1384

[104] Gao H, Hou F, Zheng X, et al. Electrochemical property studies of carbon nanotube films fabricated by CVD method as anode materials for lithium-ion battery applications. Vacuum. 2015;**112**:1-4

[105] Ni JF, Zhou HH, Chen JT, et al. Study of current collectors for Li-ion batteries. Battery Bimonthly. 2005;**2**:128-130

[106] Gao L, Liu S, Dougal RA. Dynamic lithium-ion battery model for system simulation. IEEE Transactions on Components and Packaging Technologies. 2002;**25**(3):495-505

[107] Armand M, Tarascon JM. Building Better Batteries. Nature. 2008;**451**(7179):652-653

[108] Lee SW, Gallant BM, Lee Y, et al. Self-standing positive electrodes of oxidized few-walled carbon nanotubes for light-weight and high-power lithium batteries. Energy & Environmental Science. 2012;**5**(1):5437-5444

[109] Zheng D, Wu C, Li J, et al. Chemically shortened multi-walled carbon nanotubes used as anode materials for lithium-ion batteries. Physica E: Low-dimensional Systems and Nanostructures. 2013;**53**:155-160

[110] Scrosati B, Garche J. Lithium batteries: Status, prospects and future. Journal of Power Sources. 2010;**195**(9):2419-2430

[111] Marom R, Amalraj SF, Leifer N, et al. A review of advanced and practical lithium battery materials. Journal of Materials Chemistry. 2011;**21**(27):9938-9954

[112] Kwon YK, Tomanek D. Electronic and structural properties of multiwall carbon nanotubes. Physical Review B. 1998;**58**(24):16001-16004

[113] Ajayan PM. Nanotubes from carbon. Chemical Reviews. 1999;**99**(7):1787-1800

[114] Dai HJ. Carbon nanotubes: Opportunities and challenges. Surface Science. 2002;**500**(1-3): 218-222

[115] Baughman RH, Zakhidov AA, De Heer WA. Carbon nanotubes–the route toward applications. Science. 2002;**297**(5582):787-792

[116] Salajkove M, Valentini L, Zhou Q, et al. Tough nanopaper structures based on cellulose nanofibers and carbon nanotubes. Composites Science and Technology. 2013;**87**: 103-110

[117] Cheng Q, Song Z, Ma T, et al. Folding paper-based lithium-ion batteries for higher areal energy densities. Nano Letters. 2013;**13**(10):4969-4974

[118] Lee YS. Syntheses and properties of fluorinated carbon materials. Journal of Fluorine Chemistry. 2007;**128**(4):392-403

[119] Nobili L, Guglielmini A. Thermal stability and mechanical properties of fluorinated diamond-like carbon coatings. Surface and Coatings Technology. 2013;**219**:144-150

[120] Jayasinghe R, Thapa AK, Dharmasena RR, et al. Optimization of multi-walled carbon nanotube based CF x, electrodes for improved primary and secondary battery performances. Journal of Power Sources. 2014;**253**(5):404-411

[121] Ouyang Y, Cong LM, Chen L, et al. Raman study on single-walled carbon nanotubes and multi-walled carbon nanotubes with different laser excitation energies. Physica E: Low-dimensional Systems and Nanostructures. 2008;**40**(7):2386-2389

[122] Groult H, Nakajima T, Perrigaud L, et al. Surface-FG anode materials for Li-ion batteries. Journal of Fluorine Chemistry. 2005;**126**(7):1111-1116

[123] Mar M, Ahmad Y, Guérin K, et al. Fluorinated exfoliated graphite as cathode materials for enhanced performances in primary lithium battery. Electrochimica Acta. 2016

[124] Li Y. The improved discharge performance of Li/CFx batteries by using multi-walled carbon nanotubes as conductive additive. Journal of Power Sources. 2011;**196**(196): 2246-2250

[125] Nagasubramanian G, Sanchez B. A new chemical approach to improving discharge capacity of Li/(CF x) n, cells. Journal of Power Sources. 2007;**165**(2):630-634

[126] Pang C, Ding F, Sun W, et al. A novel dimethyl sulfoxide/1,3-dioxolane based electrolyte for lithium/carbon fluorides batteries with a high discharge voltage plateau. Electrochimica Acta. 2015;**174**:230-237

[127] Xu Y, Zhan L, Wang Y, et al. Fluorinated graphene as a cathode material for high performance primary lithium ion batteries. Carbon. 2015;**86**(1):79-85

[128] Wu C, Wang H, Liao C, et al. Enhanced performance of Li-O_2, battery based on CF x /C composites as cathode materials. Electrochimica Acta. 2015;**186**:631-641

[129] Guo W, Li X, Xu J, et al. Growth of highly nitrogen-doped amorphous carbon for Lithium-ion battery anode. Electrochimica Acta. 2015;**188**:414-420

[130] Delhaes P, Couzi M, Trinquecoste M, et al. A comparison between Raman spectroscopy and surface characterizations of multiwall carbon nanotubes. Carbon. 2006;**44**(14):3005-3013

[131] Yang C, Chen C, Pan Y, et al. Flexible highly specific capacitance aerogel electrodes based on cellulose nanofibers, carbon nanotubes and polyaniline. Electrochimica Acta. 2015;**182**:264-271

[132] Zhang J, Gao L. Dispersion of multiwall carbon nanotubes by sodium dodecyl sulfate for preparation of modified electrodes toward detecting hydrogen peroxide. Materials Letters. 2007;**61**(17):3571-3574

[133] Ng SH, Wang J, Guo ZP, et al. Single wall carbon nanotube paper as anode for lithium-ion battery. Electrochimica Acta. 2005;**51**(1):23-28

[134] Eom JY, Kwon HS, Liu J, et al. Lithium insertion into purified and etched multi-walled carbon nanotubes synthesized on supported catalysts by thermal CVD. Carbon. 2004; **42**(12):2589-2596

[135] Sivakkumar SR, Pandolfo AG. Carbon nanotubes/amorphous carbon composites as high-power negative electrodes in lithium ion capacitors. Journal of Applied Electrochemistry. 2014;**44**(1):105-113

[136] Morris RS, Dixon BG, Gennett T, et al. High-energy, rechargeable Li-ion battery based on carbon nanotube technology. Journal of Power Sources. 2004;**138**(1-2):277-280

Chapter 14

Potential Application of Photo-thermal Volumetric Ignition of Carbon Nanotubes in Internal Combustion Engines

Antonio Paolo Carlucci, Bruce Chehroudi, Antonio Ficarella, Domenico Laforgia and Luciano Strafella

Additional information is available at the end of the chapter

http://dx.doi.org/10.5772/intechopen.70887

Abstract

In internal combustion engines, an ignition source is required to initiate the combustion process. This is commonly obtained either through an electric spark generation or by physical act of compression-ignition. In order to improve performance and lower pollutants levels, researchers have proposed alternatives to conventional ignition or combustion processes, such as homogeneously-charge compression-ignition (HCCI) combustion, whose critical operational requirement is precise control of the autoignition timing within the engine operating cycle. In this work, an innovative volumetrically-distributed ignition approach is proposed to control the onset of the autoignition process, by taking advantage of the optical ignition properties of carbon nanotubes when exposed to a low-consumption light source. It is shown that this ignition method enhanced the combustion of methane, hydrogen, LPG, and gasoline (injected to chamber in liquid phase). The results for this new ignition method show that pressure gradient and combustion efficiency are increased, while combustion duration and ignition delay time are decreased. A direct observation of the combustion process indicates that these benefits are due to the spatially-distributed ignition followed by a faster initial consumption of the air/fuel mixture. The use of this ignition system is therefore proposed as a promising technology for the combustion management in internal combustion engines, specifically for the HCCI engines.

Keywords: carbon nanotubes, combustion control, internal combustion engines, metal nanoparticles, photo-thermal ignition, HCCI, autoignition, photo-ignition

1. Introduction

The system for triggering and controlling the ignition process is the heart of the robust and effective combustion process in internal combustion engines (ICEs).

The electric spark used in gasoline engines generates a relatively slow flame front, which then propagates burning the air/fuel mixture. This ignition system is, by its nature, a single point ignition system and is characterized by a relatively high energy input. The benefits of having multiple ignition nuclei and ability to vary their positions on the fuel conversion efficiency and reduction of pollutants levels have been demonstrated in the literature at different operating conditions. However, the practical applications have been limited to a few points, that is, a maximum of two spark plugs per cylinder in automotive engines.

In diesel engines, on the other hand, the ignition is achieved through the compression process, realized by the piston movement during the compression stroke. The compression ignition process, being sensitive to operating conditions such as ambient temperature and pressure, affects the following combustion development, characterized by two different burning phases. The first phase is a fast-burning combustion of the injected liquid fuel that was previously atomized, vaporized, and mixed with air during the ignition delay period, called premixed phase, which is followed by a second phase, characterized by a much slower mixture burning rate called the mixing-controlled or diffusive combustion.

In the literature, the potentials of a third combustion mode, called homogeneous-charge compression-ignition (HCCI), in simultaneously reducing fuel consumption and pollutant emissions are extensively documented. HCCI is an alternative combustion mode for ICE, in which a premixed homogeneous mixture of fuel and oxidizer (auto-)ignites, ideally all at the same time. In this manner, the combustion process instantly involves the entire mixture trapped inside the cylinder, leading to a remarkable reduction in fuel consumption [1]. The ignition (or autoignition) process in the HCCI engines exhibits multiple ignition points distributed throughout the combustion chamber. This, when combined with the combustion of a lean premixed air/fuel mixture, lowers burned-gas temperatures, which prevents the formation of nitrogen oxides (NO_x). Furthermore, combustion of premixed lean mixtures forms virtually no soot. However, the HCCI combustion mode, simple from a conceptual point of view, is hard to be implemented. In gasoline engines, waste thermal energy contained in exhaust gases and coolant, hot residuals, and internal exhaust gas recirculation (EGR) have been demonstrated to be effective ways to heat the intake air and hence initiate mixture autoignition. In this way, and under HCCI combustion mode, it is possible to achieve a reduction of the fuel consumption up to 50%, a reduction of two orders of magnitude of NO_x, comparable levels of carbon monoxide (CO), and an acceptable increase in hydrocarbons (HC)—that can be eliminated by means of an already mature technology such as the three-way catalyst—compared to conventional gasoline spark ignition engines [2].

In diesel engines, on the other hand, the critical issue is represented by the preparation of a homogeneous mixture. In this view, port injection as well as the number and timing of injections and spray and combustion chamber shape can help obtaining a more homogeneous air/fuel

mixture into the combustion chamber. The greatest benefits were reductions of NO_x and soot. However, there were little or no reductions in fuel consumption and increases in CO and HC emissions [2].

Finally, in natural gas engines, the HCCI combustion mode can be reached by increasing the intake temperature, boost pressure, and compression ratio, or varying the fuel composition (e.g., by adding n-butane).

In order to implement the above techniques, substantial modifications have been necessary on the air, exhaust, and fuel paths, as well as on the engine structure and layout. Most of all, the critical requirement for the proper operation of the HCCI engines was found to be a precise control of the autoignition process, namely, the control of the time at which autoignition of the gaseous air/fuel mixture takes place inside the combustion chamber [2, 3]. Using a variety of complex control systems, based on parameters influencing the beginning of the autoignition process, it is possible to efficiently operate a HCCI engine. However, these controlling systems are still extremely complex, expensive, and onerous [2, 4]. This stems from the fact that the onset of autoignition for premixed air/fuel mixtures is very sensitive to engine operating and design parameters. Unfortunately, the ignition processes initiated by conventional sources of external energy are sensitive to surrounding environmental conditions and generally not suitable for the HCCI engines.

Therefore, an innovative light-activated approach has been proposed by Chehroudi [3] in order to obtain a volumetrically distributed ignition. This approach, which takes advantage of the optical ignition properties of carbon nanotubes (CNTs), is based on the observation that carbon nanotubes, bounded with other nanoenergetic materials (nEMs), that is, metallic nanopowders, ignite collectively and burn when exposed to low-consumption short-duration light sources. Therefore, they could act as autoignition nuclei when mixed with a homogenous fuel/oxidizer mixture and exposed to a pulsed light source, such as an ordinary camera flash. This phenomenon is usually referred to as "photo-thermal ignition" (PTI).

A CNT is a hollow nanostructure like a hollow cage, essentially consisting of a graphitic plane rolled into a thin tube, both ends of which can be closed by a fullerene-type dome structure. The existence of CNTs was originally discovered by Iijima [5]. Since their discovery, CNTs have been a subject of intense study: this material, in fact, exhibits various interesting mechanical, thermal, optical, and electrical properties. Many of these properties have been proposed for countless applications, for example, for the hydrogen storage, as additives in structural materials and for the production of ad-hoc biosensors for the diagnosis of diseases. There are two forms of carbon nanotubes, namely single-walled carbon nanotube (SWCNT) consisting of a single layer of graphene rolled into a tube whose diameter depends on the chirality of the nanotube, and multi-walled carbon nanotube (MWCNT) that can appear in a coaxial assembly of SWCNT similar to a coaxial cable, or as a single sheet of graphite rolled into the shape of a scroll.

The mechanism by which CNTs bonded with nEMs' photo-ignite is difficult to analyze and has not been fully explained. However, there are some theories based on experimental observations. The first observation of this phenomenon was documented by Ajayan et al. [6].

They suggested that the optically black SWCNT fibers absorbed visible and infrared light and transmitted that energy as heat to Fe (iron) nanoparticle sites (leftovers from the SWCNT growth phase), which subsequently gained enough activation energy to oxidize and support a combustion reaction with the surrounding air. Tseng et al. [7] proposed that the photo-acoustic and ignition effects are attributable to rapid increase in temperature over 457°C (ignition point of Ferrocene, Fc), resulting from both absorption of the light flash by CNTs and the presence of catalyst particles in fluffy SWCNTs, generating an acoustic wave and oxidation of the CNTs. Bockrath et al. [8] showed that the phenomenon is not isolated to SWCNTs but, in fact, other carbonaceous compounds synthesized on metal catalysts can ignite upon exposure to a flash lamp. Braidy et al. [9] not only confirmed the flash ignition effect on SWCNTs but also reported the presence of iron oxide particles in the combustion by-products. In [10], the authors concluded that the metal nanoparticle impurities in the SWCNT samples are responsible for the photo-ignition phenomenon.

Despite the intensive analysis of the PTI phenomenon, few applications have been proposed so far. Among them, the idea of igniting various fuel/oxidizer mixtures through PTI has rather been investigated. For example, Berkowitz et al. [11] introduced and mixed SWCNTs (containing 70% iron by weight) in an air/ethylene mixture inside a combustion chamber and exposed them to the camera flash, triggering in this way the combustion process. Another application was proposed by Manaa et al. [12] who demonstrated that the flash ignition and initiation of explosive-nanotubes mixture—SWCNTs with at least 29% by weight of iron impurity—in solid fuels are possible. However, in order to attain SWCNTs-nEMs mixture photo-ignition in liquid fuels, the CNTs-nEMs must be separated from the liquid until the moment of ignition. Badakshan et al. [13] have encapsulated a small sample of SWCNTs and solid additives—aluminum nanoparticles and ammonium perchlorate as solid oxidizers—inside a gelatin capsule through which they have been flashed. It was observed that the photo-ignition of nanopowder speeded up the combustion process of hexane + acetone as fuels (50% each). Furthermore, the authors have also tested PTI of simulated solid rocket fuel as an alternative to classic electric ignition. These tests essentially showed a great potential for obtaining the volumetrically distributed ignition of liquid and solid fuels.

A further application was first pioneered by Chehroudi [14], who studied the PTI of liquid fuels with CNTs, was limited to atmospheric conditions. Chehroudi [15–20] believes that this phenomenon could be used to ignite multiple points in an air/fuel mixture simultaneously, for example in ICE, and hence realizing the so-called volumetrically-distributed ignition for HCCI combustion.

The use of PTI system would lead to the following advantages compared to the other ignition systems:

- the ignition could be achieved remotely and timely; and
- the volume where ignition takes place can be adjusted to achieve both localized or volumetrically distributed ignition.

A first investigation in this direction has been described in [21, 22], where the combustion process initiated by CNT and nEMs, collectively referred to as nanoignition agents (nIAs),

when exposed to a light source, was compared with the one obtained with a conventional spark plug ignition system (SI), limiting the analysis only to air/methane mixtures. For all air/fuel ratios (AFRs) tested, it was demonstrated that the combustion triggered by PTI of the MWCNTs with Fc (i.e., Ferrocene) was characterized by a higher combustion pressure gradient and a higher peak pressure than the one started by the SI. Moreover, a volumetrically distributed combustion process was observed instead of the classic flame front propagation seen in conventional gasoline engines. Therefore, in this chapter, the application of "CNT bounded with nEMs powders," collectively referred here as nanoignition agents (nIAs), for the ignition of different fuels such as methane (CH_4), liquified petroleum gas (LPG), hydrogen (H_2), and gasoline, inside a constant volume chamber is described. A constant volume chamber was used to simulate the combustion chamber of an ICE, highlighting the benefits, in terms of reduction of combustion duration and its completeness, compared with the combustion triggered by a conventional SI system.

2. Experimental setup

A system was designed and realized on purpose to demonstrate volumetric ignition of gaseous fuels (methane, hydrogen, and LPG) and gasoline through PTI of MWCNTs with 75% by weight of Fc (it was demonstrated in [23] that this composition had the lowest power density required for ignition). MWCNTs and Fc properties are reported, respectively, in **Table 1**. A schematic diagram of the complete experimental layout for both air/gaseous fuel mixtures and air/gasoline mixtures is shown in **Figure 1**.

	MWCNTs	**Fc**
Purity	≥98%	98%
Form, color	Powder, black	Powder, yellow-orange
O.D. × I.D. × L.	10 nm ± 1 nm × 4.5 nm ± 0.5 nm × 3–6 μm	–
Density	~2.1 g/mL at 25°C (lit.)	1.49 g/cm^3
Bulk density	0.068 g/cm^3	–
Surface area	280–350 m^2/g	–
Melting point	3652–3697°C (lit.)	172–175°C (lit.)
Specific heat (~300 K)	242 kJ/kg	344 kJ/kg
Autoignition point	–	>150°C
Boiling point	–	249°C (lit.)
Vapor pressure	–	0.03 mmHg (40 °C)
Absorption	–	λ_{max} = 358 nm

Table 1. Properties of MWCNTs and ferrocene.

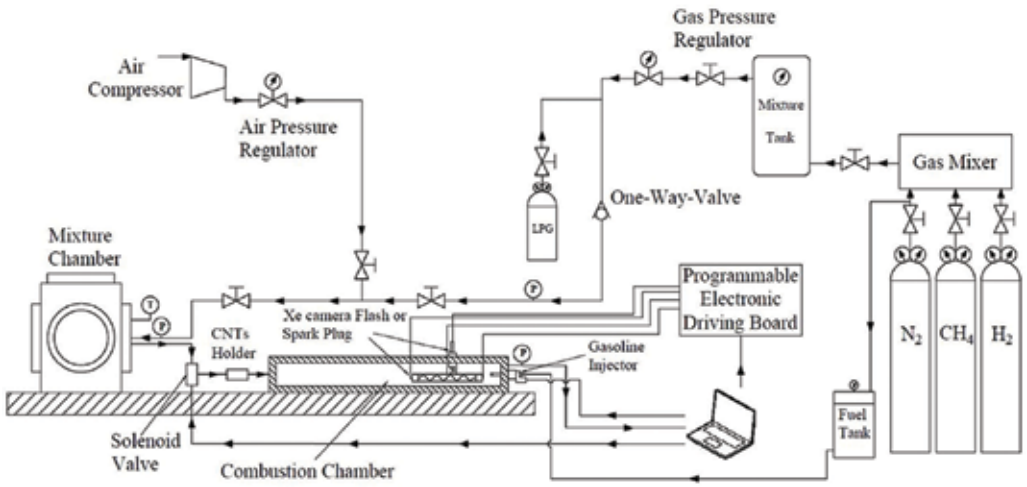

Figure 1. Schematic diagram of the experimental apparatus used during air/gaseous fuels and air/gasoline tests. Reprinted from [24], with permission from Elsevier.

The experimental setup was designed for performing a single combustion event at a time; the procedure for charging the air/fuel mixture as well as the ignition agents, therefore, must be repeated for each test, as detailed in the following. The constant volume combustion chamber is made of low-carbon steel and has a cylindrical shape with inner diameter of 53 mm and length of 270 mm. The chamber was equipped with a piezoresistive pressure sensor (KELLER type PA-21Y 0–200 bar). Pressure signal has been sampled at 2.5 kHz using a NI cDAQ 9178 acquisition board with a NI 9205 AI module. A longitudinal quartz rectangular optical window (172 mm length × 37 mm height × 20 mm thickness) was mounted along the side of the combustion chamber to allow visual access. By using a CCD Memrecam GX-1F High Speed framing camera, positioned in front of the quartz optical access, images of the ignition and burning processes have been acquired with a frame rate of 2.5 kHz.

An automotive spark plug (NGK model 4983 DCPR7E-N-10) and a Xe camera flash (Linear Xenon Flash Tubes model FT-L4040 for air/gaseous fuel tests, and a Linear Xenon Flash Tubes model FT-L6085 for air/gasoline tests) have been placed at appropriate locations inside the combustion chamber. In this manner, the combustion process via SI can be compared with that obtained through PTI of MWCNTs/nEMs mixed with air/fuel mixture. Both ignition methods have been activated by a relay, remotely controlled by means of a DIO 5 Volt TTL High Speed NI 9401 module. Once the desired pressure of 3 bar is reached in the combustion chamber, the solenoid valve automatically closes and, after a constant delay, a TTL signal is generated for activating either the camera flash or the spark plug. The maximum energy that can be released by Xe flash lamps used for photo-ignition is respectively 50 J for tests with gaseous fuels and 120 J for tests with gasoline since, supposedly, tests with gasoline would require more energy for nIAS ignition.

In order to run the experiments for air/gaseous fuel mixtures, air and gaseous fuel are separately introduced into the mixture chamber through different ducts. The amount of gaseous

http://dx.doi.org/10.5772/intechopen.70887

fuels used in each case is determined in order to ensure a final pressure of 6 bar in the mixture chamber while at the same time achieve a desired air/gaseous-fuel mass ratio. From the mixture chamber, the air/gaseous-fuel mixture is introduced into the combustion chamber. A solenoid valve is used to determine the amount of air/gaseous fuel mixture introduced into the combustion chamber in order to reach a desired pressure of 3 bar at the onset of the experiment. Passing through the solenoid valve, the mixture flow also picks up and carries with it a desired amount of MWCNTs/nEMs (nIAs) into the combustion chamber previously introduced in the CNTs holder, see **Figure 1**.

For the experiments carried out with air and gasoline, a liquid fuel injection system composed of a fuel tank pressurized with an inert gas (nitrogen) to a value equal to 4.5 bar is used for all tests. The fuel injection system is composed of a traditional automotive gasoline injector and a module to control the injector opening. In order to run the experiments, air and gasoline are separately introduced into the combustion chamber. The amount of the gasoline introduced into the combustion chamber is determined in order to ensure a desired value of the air/gasoline mass ratio and this is realized through on the pulse width applied to the electronics associated with the injector control system. Once the gasoline is injected into the combustion chamber, the air, at a pressure of 6 bar in the mixture chamber, is introduced into the combustion chamber by means of a solenoid valve. In this case too, the amount of air introduced into the combustion chamber is controlled by the opening time of the solenoid in order to reach the desired pressure of 3 bar for each test. Tests with the gasoline fuel were conducted by varying an additional parameter, that is, the "residence time" of the liquid gasoline injected into the combustion chamber before it is mixed with the air coming from the mixture chamber carrying the nIAs. Because the photo-ignition could possibly be negatively impacted due to wetting of the nIAs by the injected liquid gasoline spray, the effects of this residence time should offer a preliminary data as to the impacts of such a wetting process. The residence time is the time between the end of liquid fuel injection and the air solenoid valve opening time. Two different residence times have been tested: 0 and 500 ms, representing the lower and upper bounds for this parameter used in this study.

For each test, as described previously, once the desired pressure (3 bar) was reached in the combustion chamber, the solenoid valve was automatically closed and, after a constant delay, a TTL signal was generated for activating either the camera flash or the spark plug. Furthermore, the energy released by the flash unit was about 5 J for air-methane fuel tests (this value was assumed to be constant and taken as a reference for all air-gaseous fuel tests), 8 J for air-gasoline tests, while the energy released by the spark plug was about 20 J for all tests.

Before each test, the combustion chamber was thoroughly purged with fresh air. In all the tests, nIAs sample, each consisting of 20 mg of MWCNTs with 75% of Fc by weight were used. The minimum amount of nanoparticles was obtained as in [22], which corresponds to a nIAs concentration of 159 ppmv in the combustion chamber. Out of 158 ppmv, 139 represented by the MWCNTs and 19 ppmv by the Fc, corresponds to an overall energy equal to 6.3 J, of which 1.1 J come from MWCNTs and 5.2 J from Fc (which collectively are less than 1% of the overall thermal energy released by the fuels).

For experiments with both ignition systems, tests were conducted by varying the relative air/fuel ratio, λ, defined as:

$$\lambda = \frac{(A/F)_{act}}{(A/F)_{st}} \tag{1}$$

where $(A/F)_{act}$ is the ratio between air (A) and fuel (F) mass actually fed into the combustion chamber, and $(A/F)_{st}$ is the stoichiometric amount of air for the type of the fuel per unit amount of fuel used. Based on this definition, $\lambda = 1$ represents an actual stoichiometric mixture, while $\lambda > 1$ indicates a mixture leaner than the stoichiometric as λ exceeds unity. In this work, $(A/F)_{st}$ for methane, hydrogen, LPG, and gasoline were assumed equal to 17.4, 34, 15.5, and 14.7, respectively. The air/fuel ratio, λ, was varied within an interval ranging from 1 to 3.5 and was estimated considering both the mixture composition in the mixture chamber and the filling process of the combustion chamber described earlier.

The ignition and combustion characteristics were analyzed through measurement of the combustion chamber pressure. In fact, for a constant volume chamber and under the hypotheses of homogeneous system and negligible wall heat transfer, the first law of thermodynamics allows the estimation of the heat release rate (*HRR*) by the fuel combustion as:

$$HRR(t) = \frac{dQ}{dt} = \frac{1}{\gamma - 1} V \frac{dp}{dt} \tag{2}$$

where Q is the heat released by the fuel during combustion (on first approximation, it is proportional to the fuel burned), γ is the mixture-specific heat ratio (assumed constant and equal to 1.38), V is the combustion chamber volume, and p is the pressure measured in the combustion chamber. Using the *HRR*, it is also possible to estimate the cumulative thermal energy released within a time interval between the start of combustion ($t_{ignition}$) and any time t later as follows:

$$cumHRR(t) = \int_{t_{ignition}}^{t} HRR\,dt \tag{3}$$

The maximum value of the *cumHRR(t)* is obtained by integrating the *HRR* between $t_{ignition}$ and the time t_{pmax}, which corresponds to the maximum pressure reached in the combustion chamber. This value is an indicator of the total heat released. Furthermore, knowing *cumHRR(t)*, it is also possible to estimate the combustion efficiency, here defined as:

$$\eta_b = \frac{\int_{t_{ignition}}^{t_{p_{max}}} HRR\,dt}{\left(m_{fuel} * H_{i,fuel}\right) + \left(m_{nIAs} * H_{i,nIAs}\right)} \tag{4}$$

in which the numerator is equal to the total heat released during combustion, while the denominator is equal to the thermal energy supplied to the system in the form of liquid or gaseous fuels. The contribution of the nanoparticles combustion energy in the denominator is equal to 6.3 J, which is less than 0.3% for each condition tested, and has been neglected.

Figure 2 shows *cumHRR* traces of the fuel burning process when initiated through the ignition of nIAs via a flash and a spark plug in an air/methane mixture at a λ value of 1.6. It is possible to see that, after the trigger signal (flash or spark activation), both curves exhibit a rising phase due to the heat released by the fuel during the combustion and reach a peak value when all the fuel is fully oxidized. Afterward, the pressure, and *cumHRR* as a consequence, slowly

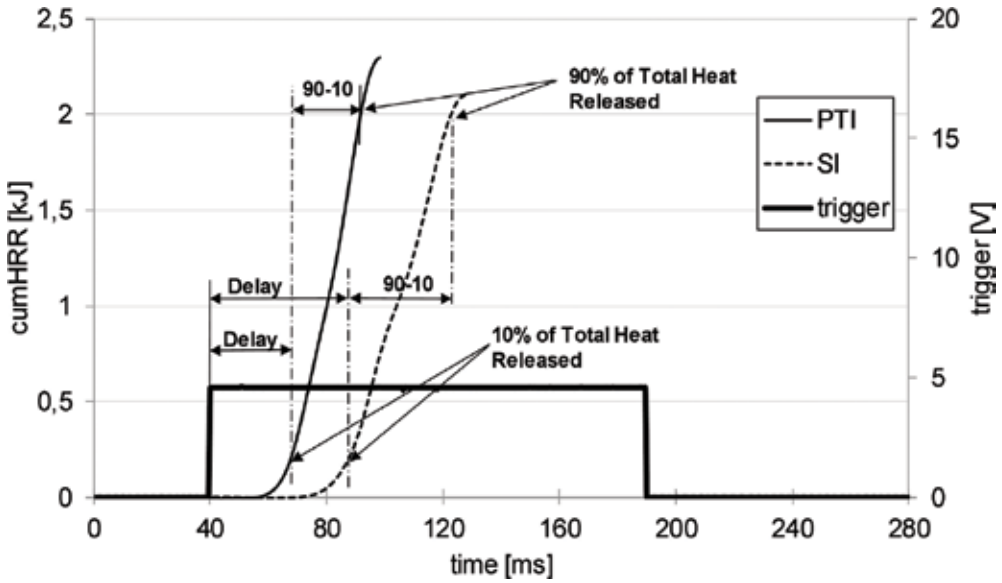

Figure 2. *cumHRR(t)* traces for PTI and SI ignition approaches using air/methane mixture at $\lambda = 1.6$. Reprinted from [24], with permission from Elsevier.

decreases (not shown in **Figure 2**) due to cooling of the exhaust gases through heat exchange with the chamber walls. Therefore, the portion of the *cumHRR(t)* curve useful for the combustion analysis is only the rising one as shown.

From the *cumHRR(t)* curve, it was possible to estimate the following parameters:

- the *ignition delay*, defined as the difference between the time when the amount of heat released had reached a value equal to 10% of total heat released and the time when the trigger has been activated;
- the *combustion duration*, defined as the difference between the time instants when the heat released had reached 90% and 10% of the total heat released. Note that the "total" combustion period is the sum of ignition delay and combustion duration.

3. Performance of PTI combustion

3.1. Air/gaseous fuel mixtures

In **Figure 3**, the *cumHRR(t)* curves related to PTI (a, a′, and a″) and SI (b, b′, and b″) combustion processes are shown. **Figure 3** also separates results for methane, LPG, and hydrogen for different values of λ. **Table 2** shows percentages of CNT and Fc for different fuels and different values of λ in the tests.

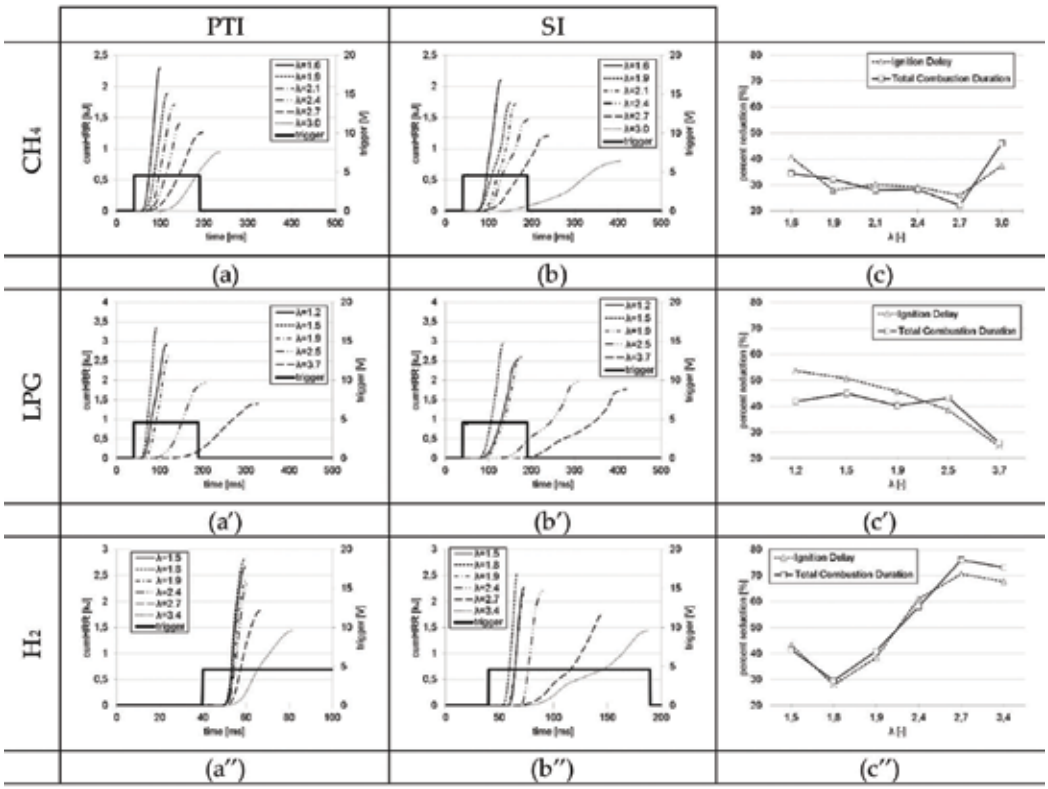

Figure 3. Plots of *cumHRR(t)* for PTI (a, a′, and a″) and SI (b, b′, and b″) ignition methods are shown. Plots in (c, c′, and c″) show percent reductions of ignition delay and total combustion duration for the PTI approach with respect (or reference) to the SI method for different values of λ. Results for methane, LPG, and hydrogen are shown. PTI and SI stand for photo-thermal ignition and spark ignition. Reprinted from [24], with permission from Elsevier.

Comparing the results for PTI column with those for SI column in **Figure 3**, it can be observed that the combustion initiated by the photo-thermal ignition of nIAs releases a total heat higher than the case in which the mixture is ignited by a spark plug. This effect is thought to be due to two reasons. On one hand, the wall heat transfer is expected to play a role in SI due to longer combustion duration. On the other hand, from the analysis of combustion process images (results are presented in the following section), the combustion triggered by the PTI involves the entire mixture in the combustion chamber when compared to the SI case. It is therefore expected that for the PTI case, the mixture at the peripheral areas of the combustion chamber (i.e., near-wall regions) is more easily reached and burned. While for the SI combustion, this would be unlikely because the propagating flame front cools as it approaches the walls of the chamber. Moreover, comparing results in PTI and SI columns in **Figure 3**, it can also be argued that, with PTI, both ignition delay and combustion duration are shortened. This conclusion is confirmed by results reported in **Figure 3(c)**, (**c**′), and (**c**″) for methane, LPG, and hydrogen, respectively, which show percent relative reductions in ignition delay and total combustion duration using PTI as compared to the SI approach. The same trend has also been reported in [11] where the authors have tested the photo-induced

	Methane						LPG					Hydrogen					
λ [–]	1.6	1.9	2.1	2.4	2.7	3.0	1.2	1.5	1.9	2.5	3.7	1.5	1.8	1.9	2.4	2.7	3.4
Air [g]	1.73	1.75	1.76	1.77	1.77	1.78	1.79	1.80	1.806	1.82	1.83	1.44	1.49	1.52	1.57	1.59	1.64
Fuel [g]	0.06	0.05	0.05	0.04	0.04	0.03	0.09	0.08	0.06	0.05	0.03	0.03	0.03	0.02	0.02	0.02	0.01
% CNT	0.28	0.28	0.28	0.28	0.28	0.28	0.27	0.27	0.27	0.27	0.27	0.34	0.33	0.32	0.31	0.31	0.30
% Fc	0.84	0.83	0.83	0.83	0.83	0.82	0.8	0.8	0.8	0.8	0.8	1.00	0.99	0.97	0.95	0.93	0.90

Table 2. Air, gaseous fuel, CNT and Fc quantities used for each test. Percentages are on mass basis.

http://dx.doi.org/10.5772/intechopen.70887

ignition of quiescent air/fuel mixtures containing suspended photo-sensitive nanomaterials. SWCNTs with 70% Fe impurity by weight were suspended in air/ethylene mixtures in a static combustion chamber and exposed to a camera flash to cause ignition of the mixture. For comparison purposes, traditional automotive spark ignition experiments were also carried out for air-ethylene mixtures.

Still referring to **Figure 3**, and for all gaseous fuel tests, increasing λ, the maximum *cumHRR(t)* decreases and is delayed. In fact, the combustion processes are limited in their heat capacity by the amount of air mixed with the gaseous fuel. Therefore, the maximum gaseous fuel amount is determined based on the maximum amount of air that the system is capable of handling. It is possible to note that the maximum *cumHRR(t)* value is higher at the near-stoichiometric ratio and decreases at higher λ values. This is because the amount of air to complete the combustion process is more than that necessary for the stoichiometric AFR (λ = 1). For all conditions tested, the combustion process with hydrogen is much faster, more intense, and shows a shorter ignition delay and combustion duration compared to other two gaseous fuels. This is mainly due to its laminar flame burning speed, being higher than that of methane and LPG (see data reported in **Table 3**), and more intense because the lower heating value (LHV) of hydrogen is higher than that of methane and LPG. Finally, the ignition delay is shorter because the minimum ignition energy required to ignite hydrogen is ≈0.02 mJ, while those for the methane and LPG are 0.3 and 0.26 mJ, respectively.

From **Figure 3(c)**, (**c**'), and (**c**''), it can be seen that in all cases, the ignition delay period is reduced when combustion was initiated using the PTI approach. Interestingly, it can also be observed that, for the methane and LPG, the advantage (in terms of % reduction in ignition delay period and total combustion duration) of PTI declines as the mixture AFR increases toward the leanest mixture. There is an exception in the case of methane and for the leanest mixture tested where this percent reduction actually increases substantially (from λ of 2.7–3.0). One sees a completely different trend for hydrogen, where the advantage of the photo-ignition continuously increases as the mixture is leaned out. The comparison of the percent reductions in ignition delay period to those for the total combustion duration indicates that the two values are generally very close to each other. This suggests that the benefits of PTI are primarily at the ignition delay phase of the combustion. However, one can see a slightly larger difference between the two values for LPG and only for the lowest values of the λ.

	Hydrogen	**Methane**	**LPG**
LHV [mJ/kg]	119.9	50.0	46.2
Flammability limit	2.9–76%	5.3–15%	1.7–9.5%
Flash point [°C]	585	540	480
Minimum ignition energy [mJ]	0.02	0.30	0.26
Laminar flame speed [m/s]	2.7–3.3	0.3–0.4	0.3–0.4

Table 3. Physical properties of tested gaseous fuels.

The combustion peak pressures reached inside the combustion chamber, using both the PTI and SI methods, are reported in **Figure 4(a)**, (**b**), and (**c**), for methane, LPG, and hydrogen, respectively. Also, the total combustion duration and ignition delay times are shown in **Figure 4(a′)**

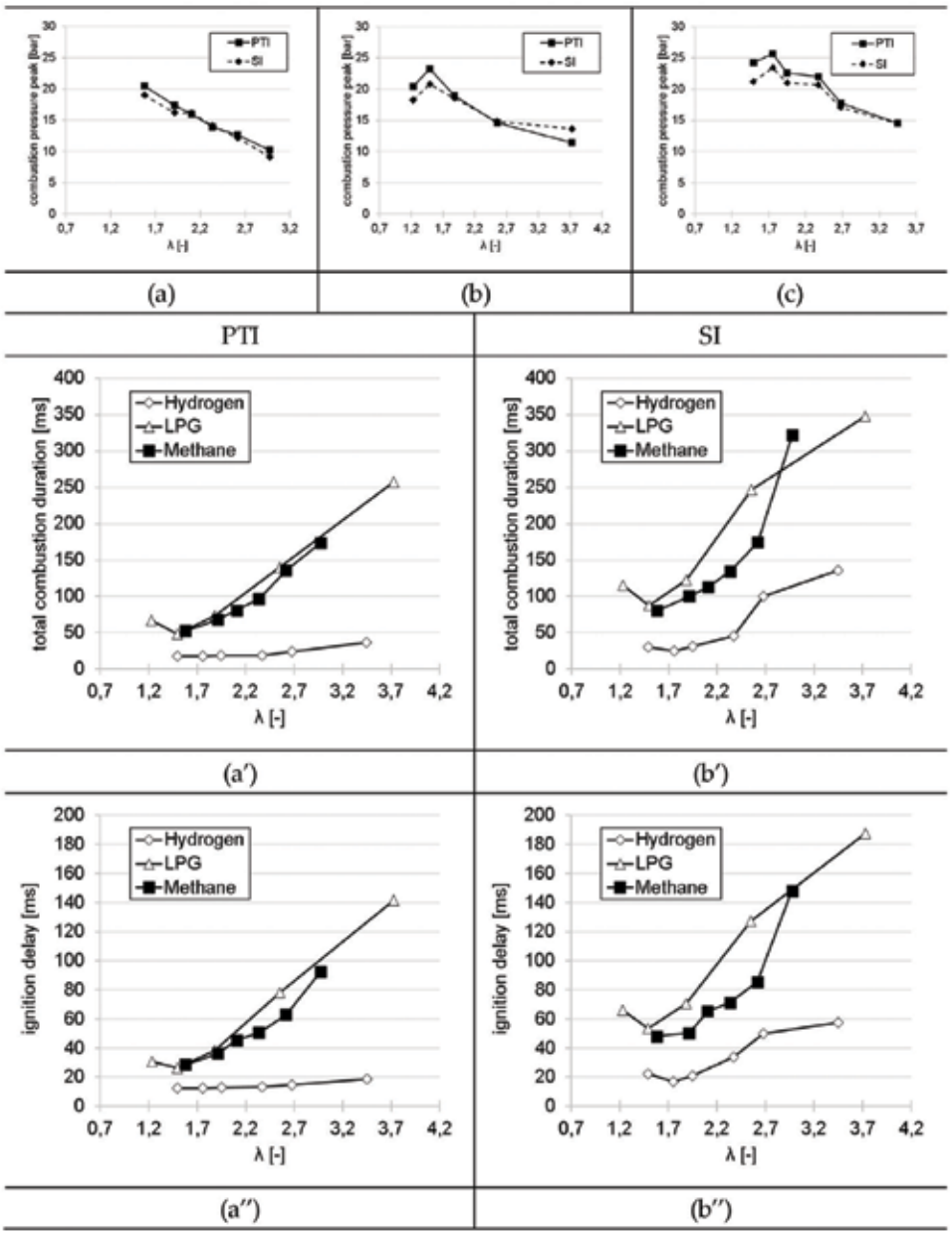

Figure 4. Comparison of the peak pressures a, b, and c for CH_4, LPG, and H_2, respectively. Total combustion duration (a′) and ignition delay (a″) with PTI and total combustion duration (b′) and ignition delay (b″) with SI for different values of λ are shown for the gaseous fuels used in this study. Reprinted from [24], with permission from Elsevier.

and (**a**″) for the PTI and **Figure 4(b′)** and (**b**″), for the SI approaches. In this way, differences between the three gaseous fuels are highlighted.

In summary, rapid rise of pressure and, therefore, a shorter pressure rise time, as well as a higher total heat released are seen in **Figure 3**. Also, mostly higher peak pressures were observed for the PTI approach as seen in **Figure 4**. This is due to the fact that the ignition of the mixture by flash exposure of the MWCNTs/nEMs leads to numerous ignition nuclei, burning "simultaneously," and hence speeding up the heat release during the combustion process. However, with the spark plug approach, as it is well known, the combustion process is triggered in only one point (i.e., within the spark plug gap) and then proceeds with the propagation of a flame front. The fuel mixture burning process is therefore too far from burning simultaneously as it is almost the case for the PTI.

This spatially-distributed ignition of the air/fuel mixture has been confirmed by observing the combustion process directly. **Figure 5** shows consecutive frames of the combustion process evolution in time. Two series of pictures related to the combustion process with PTI (left column) and spark plug (right column) are reported. Data refer to λ = 2.10 for air/methane mixture, and the time interval between two consecutive frames is equal to 5 ms. It is clearly visible that, with PTI process, the combustion is faster and the combustion chamber is entirely illuminated starting from the fifth frame indicating spatial burning. On the contrary, in the SI case, the propagation of a flame front is recognized in all the pictures. Moreover, the light radiated by the flame is weaker.

Finally, in **Figure 6**, the combustion efficiency η_b with PTI and SI is reported for different values of λ for CH_4, LPG, and H_2. It is possible to note that, for each gaseous fuel tested, the

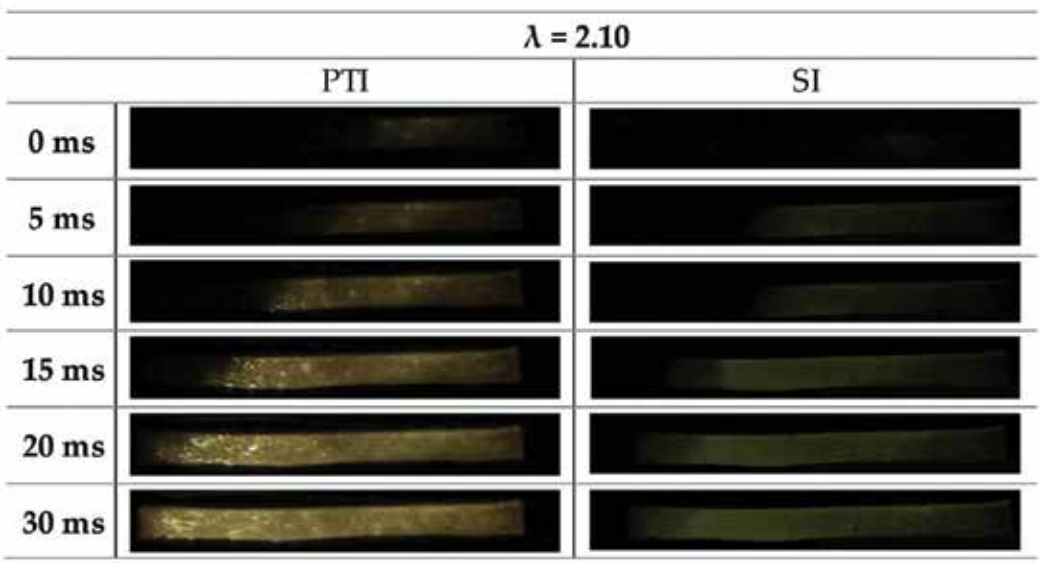

Figure 5. Pictures of the combustion process of an air/methane mixture with λ = 2.10; comparison between PTI and SI. Reprinted from [21], with permission from Elsevier.

http://dx.doi.org/10.5772/intechopen.70887

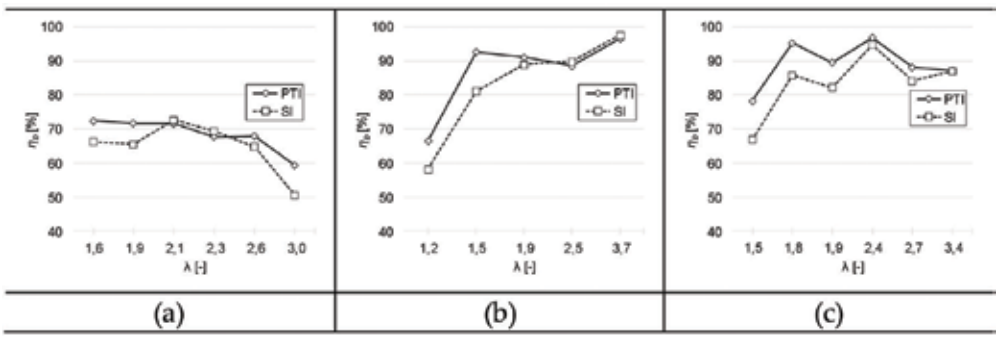

Figure 6. Comparison of combustion efficiency with PTI and SI at different values of λ and for (a) CH_4, (b) LPG, and (c) H_2.

combustion efficiency obtained with the combustion process triggered by the PTI process is slightly higher or comparable to that observed using the spark plug.

3.2. Air/gasoline mixtures

For the first time, the feasibility of igniting air/gasoline mixtures by means of PTI has been demonstrated in a constant volume combustion chamber. The combustion process has been compared with the one obtained by a traditional SI system. For these tests too, the amounts of air and gasoline as well as the CNT and Fc as percentages of the fuel mass in the mixture have been calculated, and are reported in **Table 4**.

Figure 7(a) and (**b**) show *cumHRR(t)* traces for tests with liquid gasoline fuel injection by using PTI and SI approaches, respectively. Results for the percent reduction of combustion duration and ignition delay time using PTI as compared to SI approach are also shown in **Figure 7(c)** and (**c**′). Data shown in **Figure 7(a)**, (**b**) and (**c**) are related to tests when the residence time of gasoline fuel inside the combustion chamber (before mixing with the incoming air through the solenoid valve) was equal to 0 ms. On the other hand, results reported in **Figure 7(a′)**, (**b**′) and (**c**′) refer to tests with the residence time 500 ms. In the first set of tests, the liquid fuel, after injection into the combustion chamber, was immediately mixed

λ [–]	Air [g]	Gasoline [g]	% CNT	% Fc
0.4	1.97	0.34	0.22	0.65
0.5	1.97	0.26	0.22	0.67
0.8	1.97	0.16	0.23	0.70
1.2	1.97	0.11	0.24	0.72
2.2	1.97	0.06	0.25	0.74
2.7	1.97	0.05	0.25	0.74

Table 4. Air, gasoline, CNT and Fc quantities used of each test. Percentages are on mass basis.

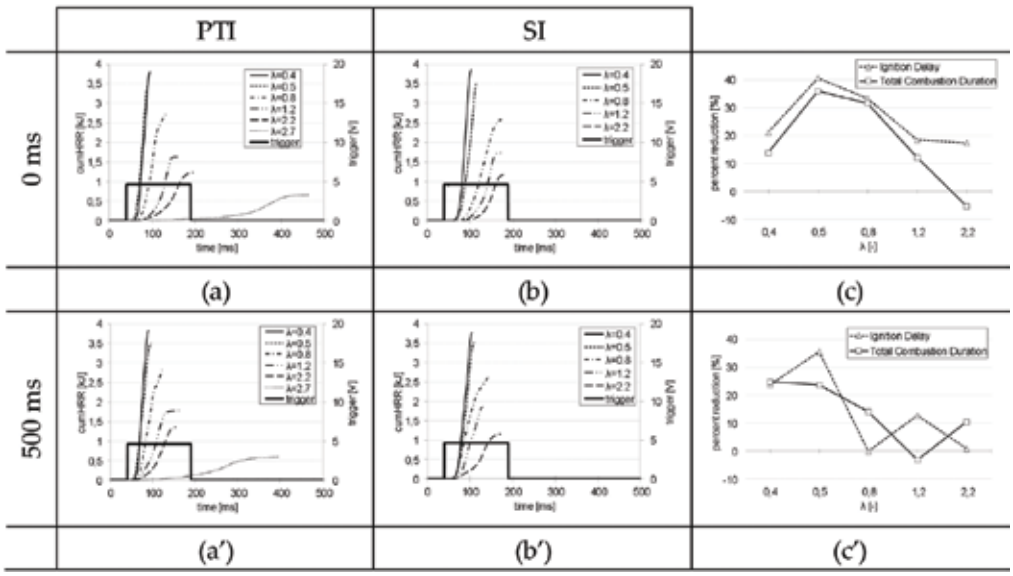

Figure 7. *cumHRR(t)* for combustion of liquid gasoline injection into the chamber initiated with PTI (a, a′) and SI (b, b′) for different values of λ and at two residence times of 0 and 500 ms. Percent reduction of the ignition delay and total combustion duration (c, c′) with PTI as compared to the SI approach for different values of λ and at two residence times of 0 ms and 500 ms are shown. Reprinted from [24], with permission from Elsevier.

with the air coming from the mixture chamber. In the second set of tests, the mixing process inside the combustion chamber took place after a fuel residence time equal to 500 ms before the air from the mixture chamber is brought into the combustion chamber. Note that because the gasoline is injected into the combustion chamber in liquid phase, the case with zero residence time implies ignition in the presence of fuel which is predominantly in liquid phase. The case with 500 ms attempts to allow time for more vaporization/mixing to approach a more homogenous mixture. However, the degree of mixing and homogeneity cannot be fully verified at this time.

Also in tests with the liquid fuel, it was observed that the combustion process triggered by the photo-thermal ignition system exhibited the same trend seen when gaseous fuels were used. That is, the combustion process triggered by the PTI generated higher or comparable *cumHRR* to that observed with the spark plug ignition system. Increasing λ, i.e., burning leaner mixtures, the peak *cumHRR* decreases and is delayed. Furthermore, it is seen in **Figure 7(c)** and (**c′**) that with PTI, both ignition delay and total combustion duration are shorter than those calculated when SI is used.

From **Figure 7**, it can also be noted that the combustion process for a very lean condition, that is, a λ value equal to 2.7, has occurred only for the photo-thermal ignition process, while a misfire took place when combustion was initiated by the spark plug system. This misfire could be either due to an excess of air in the air/fuel mixture or the nature of the SI process. Because the spark plug can only provide ignition at a single point, it is intrinsically incapable of initiating and sustaining the flame front under such a highly lean condition.

http://dx.doi.org/10.5772/intechopen.70887

From **Figure 8**, it is possible to note that the combustion efficiency obtained with the combustion process triggered by photo-thermal ignition is slightly higher or comparable to that observed using the spark plug, for both residence times used in this study.

Figure 9 shows (a) peak pressure, (b) ignition delay, (c) combustion duration, and (d) combustion efficiency, for different values of λ and for the two residence times tested. Generally, it is seen that the combustion process generated for the longer residence time exhibits a higher peak of combustion pressure. The ignition delay for the tests with 500 ms residence time seems to be equal or less than the ones with 0 ms case. However, both ignition delay and combustion duration with 500 ms residence time are shorter compared to those at 0 ms. Furthermore, it was possible to note a slight improvement of the combustion efficiency and the total heat released (THR) for the tests carried out igniting the mixtures where the fuel has had a higher residence time before mixing with the air. This behavior could be due to more time for evaporation of the gasoline fuel droplets in the combustion chamber after liquid injection, leading to a more homogeneous and distributed air/fuel mixture inside the combustion chamber. This could facilitate the ignition process and cause a faster consumption of the air/gasoline mixture with a consequent increase of the combustion peak pressure and efficiency.

Finally, in each test with PTI, shorter pressure rise times and higher peaks of *cumHRR* and combustion pressures were observed because the ignition of the mixture was by a large number of ignition nuclei which occurred "simultaneously," thereby speeding up the combustion process. With the spark plug ignition system, combustion is initiated at single point and hence proceeds with flame propagation mechanism. The burning process is therefore far from being "simultaneous." This behavior has been confirmed by observing the combustion process through high-speed imaging. **Figure 10** shows high-speed images of a single combustion event in each case, initiated by the two ignition systems. Two series of pictures related to the combustion process with PTI (left column) and SI (right column) are reported. It is possible to note that even from the first frame an instantaneous and spatially

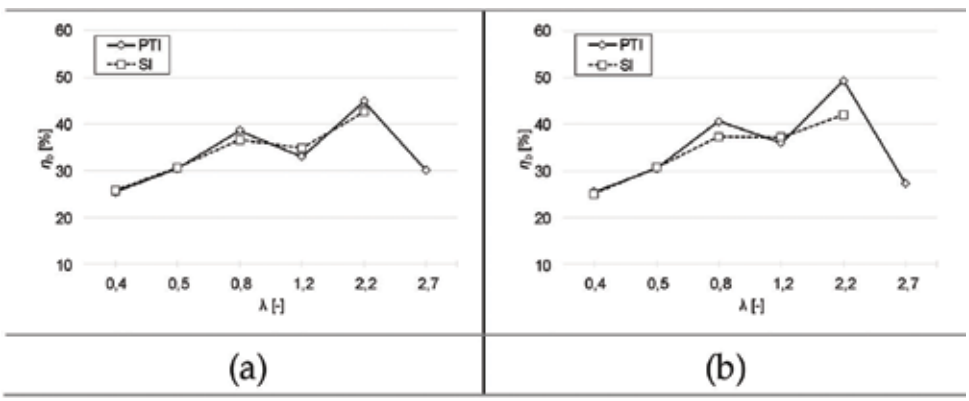

Figure 8. Combustion efficiency with PTI and SI for different values of λ and for tests carried out with a residence time equal to 0 ms (a) and 500 ms (b).

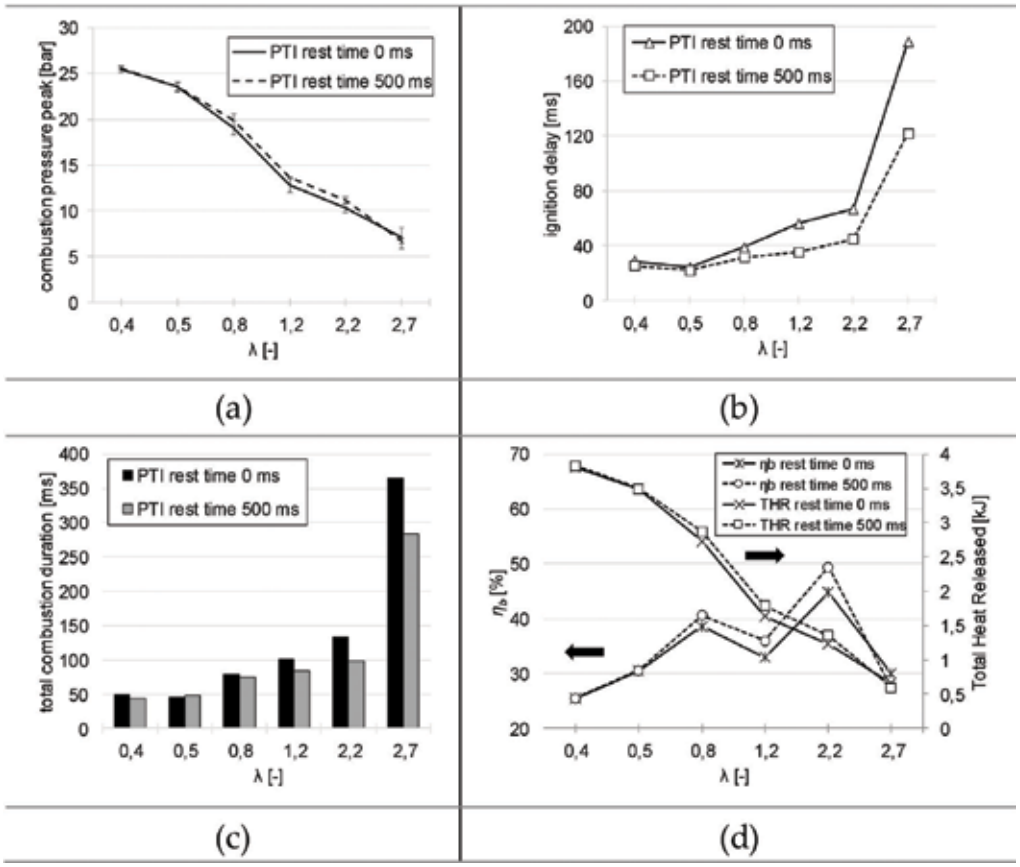

Figure 9. Comparison of (a) peak pressure, (b) ignition delay, (c) total combustion duration, (d) combustion efficiency, and total heat released with PTI for different values of λ and for tests carried out with a residence time equal to 0 and 500 ms are shown.

distributed MWCNTs/nEMs particles ignition is occurring during the flash exposure, which leads to ignition of the entire charge in the combustion chamber. Indeed, the combustion chamber is fully illuminated starting from the third frame. The light radiated by the burning process is distributed throughout the entire chamber until the combustion process is completed. This could be due to the fact that the nanoignition agents, being spatially distributed inside the chamber, are able to ignite the mixture away from the actual location of the flash lamp ignition source. On the other hand, the combustion process triggered by the spark plug exhibits an ignition phase that is longer and filled by the presence of flame starting from the 5th to 6th frame. It initially involves only a small fraction of the charge within the chamber (i.e., near the spark plug electrodes) with the high-intensity areas located close to the trigger point (i.e., spark plug). The spark ignition process forms a flame kernel which subsequently propagates and consumes the fuel at the burning speed of the flame. Note that the air/gasoline ratio for **Figure 10** is at a rich mixture condition because it generates a much better contrast. However, images under lean condition also exhibited very similar burning behavior explained here.

http://dx.doi.org/10.5772/intechopen.70887

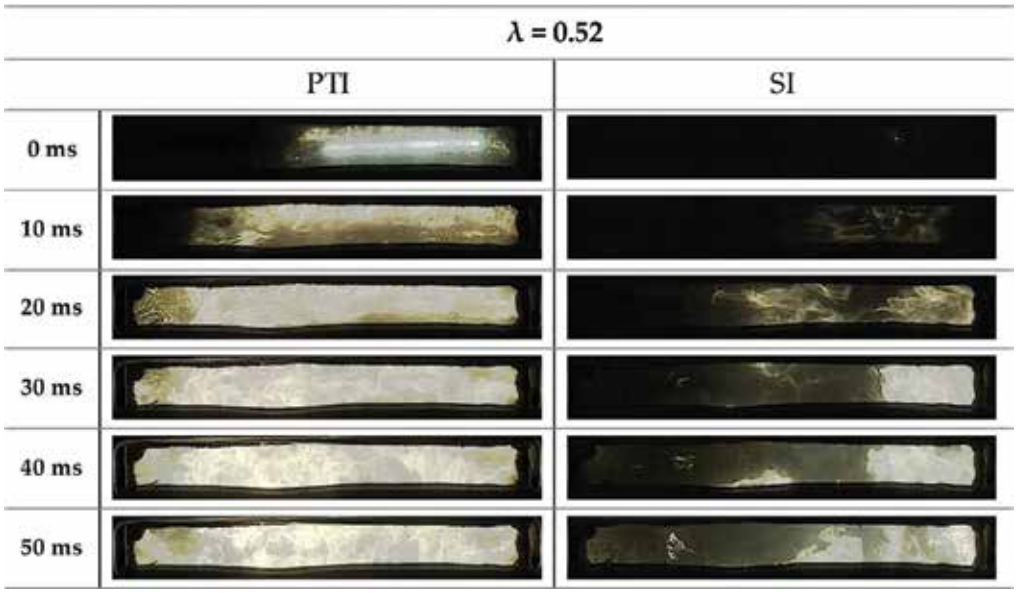

Figure 10. Pictures of the combustion process at λ = 0.52; comparison between MWCNTs/nEMs PTI and SI for air/gasoline mixture.

4. Nanostructured materials for automotive propulsion

Preliminary results from the PTI approach shows a potential for volumetrically distributed ignition of the fuels. However, the next step is to demonstrate the same results in a real engine. Indeed, the fact that a very small amount of energy (such as that emitting from an ordinary camera flash) is able to bring about volumetric ignition in a lean air/fuel mixture could lead to substantial improvements of engine performance. There are several ways the nanostructured materials could be introduced into the engine, for example, either by powder injection into the intake port or through mixing it with the fuel. A system of fiberoptic cables and flash lamp could be used to direct the flash energy into the combustion chamber.

But the main issue is possible environmental impacts of nanometric carbonaceous structures in the combustion process due to possible creation of condensation nuclei for further particulate formation in the engine and from some nanostructured materials escaping the combustion process, which can end up in the atmosphere. The potential impact of combustion products on health and environment cannot be easily predicted at the present stage of the research. In fact, it is expected that the in actual application, a more precise control of ignition timing and a shorter combustion would allow more flexibility to redesign the engine in terms of geometric as well as control parameters. This could have direct implications on the raw pollutant levels. Special concern exists because of emission of particles or particulate matters. On the other hand, many direct injection engines currently present on the market are already equipped with filtering systems, like diesel particulate filter, for the particulate abatement.

5. Conclusions

The presented data here demonstrate the feasibility of a new ignition concept for initiating the combustion process of several air/fuel mixtures. The new ignition concept is called photo-thermal ignition (PTI) and consists of flashing a nanoenergetic material with a light flash. The results from the PTI approach were compared with those obtained using a traditional spark plug system, showing great potential for future applications in combustion processes, especially for implementing the HCCI combustion mode in internal combustion engines.

In this chapter, the promising results in enhancing the combustion of methane, hydrogen, LPG, and gasoline applying this novel approach to initiate combustion are shown. In particular, the abovementioned fuels have been mixed with air in a constant volume vessel and ignited with nanopowder or a conventional spark ignition system.

The new light-activated distributed ignition demonstrated superior performance, which includes a shorter combustion duration, a shorter ignition delay period, an increased pressure peak, and improved combustion efficiency. A direct observation of the combustion process has established that benefits shown here are due to the fact that photo-thermal ignition system establishes a spatially distributed ignition, which consequently leads to a faster consumption of the air/fuel mixture in the test vessel. Higher pressure peaks and shorter rapid rising period are achieved by the fact that the new ignition system leads to numerous ignition nuclei that burn near-simultaneously, hence contributing to a volumetrically distributed combustion process in the combustion chamber. This is drastically different than the flame front propagation observed with the spark ignition.

Moreover, it was demonstrated for the first time that the proposed ignition system is able to ignite air/gasoline mixtures when liquid gasoline fuel is injected into the chamber, without isolating/encapsulating the nanoenergetic material.

Furthermore, a combustion process triggered by the photo-thermal ignition was possible even at a relative air/fuel ratio of 2.7. Ignition at this relative air/fuel ratio was impossible with the conventional spark-plug ignition system used here.

High-speed camera images acquired during the combustion process indicate that photo-thermal ignition resulted in volumetrically distributed quasi-homogeneous ignition followed by a better and faster consumption of the air/fuel mixture with no discernible flame front. This behavior is in contrast to what observed with the spark ignition, namely a single ignition point followed by a flame propagation across the combustion chamber.

The use of the photo-thermal ignition system is therefore a promising technology for the combustion management in internal combustion engines because it is characterized by the following advantages compared to the other ignition systems:

- the ignition could be achieved remotely and distributed spatially at a large number of locations; and
- the volume where ignition takes place could be adjusted to achieve both localized and volumetrically distributed ignition.

These results are considered to be of scientific and practical importance because the combustion process, initiated in mixtures with extremely lean air/fuel ratios of interest in lean-burn HCCI engines, would allow substantial reductions of fuel consumption, nitrogen oxides, and soot emissions.

Author details

Antonio Paolo Carlucci[1]*, Bruce Chehroudi[2], Antonio Ficarella[1], Domenico Laforgia[1] and Luciano Strafella[1]

*Address all correspondence to: paolo.carlucci@unisalento.it

1 Department of Engineering for Innovation, University of Salento, Lecce, Italy

2 Department of Mechanical Engineering, Arkansas Tech University, Russellville, Arkansas, USA

References

[1] Yao M, Zheng Z, Liu H. Progress and recent trends in homogeneous charge compression ignition (HCCI) engines. Progress in Energy and Combustion Science. 2009;**35**:398-437

[2] Zhao H, editor. HCCI and CAI Engines for the Automotive Industry. Woodhead Publishing in Mechanical Engineering and CRC Press; 2007. p. 557

[3] Chehroudi B. Activation and control of autoignition in HCCI engines using volumetrically-distributed ignition of as-produced single-walled carbon nanotubes. In: SAE Technical Paper. 2012. DOI: 10.4271/2012-01-1691

[4] Johansson B. Homogeneous charge compression ignition: the future of IC engines?. International Journal of Vehicle Design. 2007;**44**:1-19

[5] Iijima S. Helical microtubules of graphitic carbon. Nature. 1991;**354**:56-58

[6] Ajayan PM, Terrones M, de la Guardia A. Nanotubes in a flash-ignition—Ignition and reconstruction. Science 2002;**296**:705

[7] Tseng S, Tai N, Hsu W, Chen L, Wang J, Chiu C. Ignition of carbon nanotubes using a photoflash. Carbon. 2007;**45**(5):958-964

[8] Bockrath B, Johnson JK, Sholl DS, Howard B, Matragna C, Shi W. Ignition nanotubes with a flash. Science. 2002;**297**(5579):192-193

[9] Braidy N, Botton GA, Adronov A. Oxidation of Fe nanoparticles embedded in single-walled carbon nanotubes by exposure to a bright flash of white light. Nano Letters. 2002;**8**:1277-1280

[10] Smits J, Wincheski B, Namkung M, Crooks R, Louie R. Response of Fe powder, purified and as-produced HiPco single-walled carbon nanotubes to flash exposure. Materials Science and Engineering: A (Structural Materials: Properties, Microstructure and Processing). 2003;**358**:384-389

[11] Berkowitz A, Oehlschlaeger M. Photo-induced ignition of quiescent ethylene/air mixtures containing suspended carbon nanotubes. Proceedings of the Combustion Institute. 2011;**33**(2):3359-3366

[12] Manaa R, Mitchell A, Garza R. Flash ignition and initiation of explosives nanotubes mixture. Journal of the American Chemical Society. 2005;**127**:13786-13787

[13] Badakhshan A, Danczyk SA, Wirth D, Pilon L. Ignition of liquid fuel spray and simulated solid rocket fuel by photo-ignition of carbon nanotubes utilizing a camera flash. In: JANNAF-Liquid Propulsion Conference 2011; December 5-9; Huntsville, Alabama. 2011

[14] Chehroudi B. Nanotechnology and applied combustion: Use of nanostructured materials for light-activated distributed ignition of fuels with propulsion applications. Recent Patents on Space Technology. 2012;**1**(2):107-122

[15] Chehroudi B, Vaghjiani GL, Ketsdever A. Method for distributed ignition of fuels by light sources. US Patent 7517215 B1. 2009

[16] Chehroudi B, Vaghjiani GL, Ketsdever A. Apparatus for distributed ignition of fuels by light sources. US Patent 7665985 B1. 2010

[17] Chehroudi B, Badashan A, Danczyk SA, Morgan C. Ignition characteristics of Single-Walled Carbon Nanotubes (SWCNTs) utilizing a camera flash for distributed ignition of liquid sprays. In: Joint Army-Navy-NASA-Air Force (JANNAF) Propulsion Meeting (JPM) and 6th Modeling and Simulation/4th Liquid Propulsion/3ed Spacecraft Propulsion Joint Sub-committee Meeting; December 8-12; Orlando, Florida. 2008

[18] Chehroudi B, Danczyk SA. A novel distributed ignition method using single-walled carbon nanotubes (SWCNTs) and a low-power flash light. In: Global Powertrain Congress, World Powertrain Conference & Exposition; September 19-21; Novi, Michigan. 2006

[19] Chehroudi B, Danczyk SA, Ketsdever A, Vaghjiani GL. A low power, novel ignition of fuels using Single-Walled Carbon Nanotubes (SWCNTs) and a camera flash. In: 53ed JANNAF Interagency Propulsion Committee Meeting, 2nd Liquid Propulsion, 1st Spacecraft Propulsion Subcommittee; December 5-8; Monterey, California. 2005

[20] Chehroudi B, Danczyk SA. An innovative ignition method using SWCNTs and a camera flash. In: Nano Science and Technology Institute (NSTI), Nanotechnology Conference and Trade Show; May 8-12; Anaheim, California. 2005. p. 226-229

[21] Carlucci AP, Stafella L. Air-methane mixture ignition with Multi-Walled Carbon NanoTubes (MWCNTs) and comparison with spark ignition. Energy Procedia. 2015; **82**:915-920

[22] Carlucci AP, Ciccarella G, Strafella L. Multi-Walled Carbon Nanotubes (MWCNTs) as ignition agents for air/methane mixtures. IEEE Transactions on Nanotechnology. 2016;**15**(5):699-704

[23] Visconti P, Primiceri P, Longo D, Strafella L, Carlucci AP, Lomascolo M, et al. Photo-ignition process of multiwall carbon nanotubes and ferrocene by continuous wave Xe lamp illumination. Beilstein Journal of Nanotechnology. 2017;**8**:134-144. DOI: 10.3762/bjnano.8.14

[24] Ficarella A, Carlucci AP, Chehroudi B, Laforgia D, Strafella L. Multi-Walled Carbon Nanotubes (MWCNTs) bonded with Ferrocene particles as ignition agents for air-fuel mixtures. Fuel. 2017;**208**:734-745. DOI: https://doi.org/10.1016/j.fuel.2017.07.052

Chapter 15

Reversible and Reproducible Hydrogen Storage in Single-Walled Carbon Nanotubes Functionalized with Borane

Duraisamy Silambarasan, Velappa Jayaraman Surya, Veerapandy Vasu and Kombiah Iyakutti

Additional information is available at the end of the chapter

http://dx.doi.org/10.5772/intechopen.75763

Abstract

In this chapter, commercial single-walled carbon nanotubes (SWCNTs) were purified by standard methods and functionalized with borane (BH_3). The morphology, presence of elements and vibrations of different functional groups are probed by transmission electron microscopy (TEM), energy dispersive (ED) spectroscopy, and Fourier transform infrared spectroscopy (FTIR), respectively. A Sievert-like hydrogenation setup has been designed and is employed for hydrogenating the functionalized SWCNTs for different time durations. The amount of hydrogen stored in the functionalized SWCNTs has been quantified using elemental analysis, carbon, hydrogen, nitrogen, sulfur (CHNS) combined with thermal (TG/TDS) measurements. A maximum of 4.77 wt.% of hydrogen has been stored at 50°C and the samples become dehydrogenated in the temperature range 90–125°C. From the experiments, it has been found that the amount of hydrogen stored in functionalized SWCNTs increases with increasing hydrogenation duration. Moreover, the entire hydrogenation and dehydrogenation process was examined by Raman, thermal, and elemental analyses together. During the experiments, hydrogenation and dehydrogenation processes were stabilized and were found to be repeatable. Overall, the achieved hydrogen storage capacity of SWCNTS functionalized with BH_3 is close to the US DOE target.

Keywords: single-walled carbon nanotubes, functionalization, borane, density functional theory, hydrogen storage capacity, dehydrogenation

1. Introduction

Hydrogen is evolving as a green fuel for transportation purposes [1, 2]. In recent times, the storage and transport of hydrogen remains a subject of scientific importance. Storage of hydrogen in the form of gas and liquid needs high pressurized environment and cryogenic temperatures which has general problems associated with leakage, safety, and storage capacity. Therefore, storage in solid-state materials provides an appropriate choice. However, the interaction between hydrogen and the host material is either strong (covalent or ionic) or weak (van der Waals forces). For instance, metal hydrides, metal organic frameworks, clathrates, and other nanostructures cannot provide synergic advantages of high gravimetric storage capacity, reliability, and suitable kinetics for applications [3–6]. Carbon-based nanostructures have attracted the scientific community as one of the promising materials for hydrogen storage [7–10]. Among them, carbon nanotubes (CNTs) are widely reported to be potential materials for hydrogen storage [11–17]. CNTs possess unique properties such as hollowness, cylindrical shape, interstitial sites, nanometer scale diameter, and porosity that make them as one of the viable candidates for hydrogen storage [17]. An attempt of hydrogen storage in SWCNT bundles made by Dillon et al. [18] has led to broad investigation on CNTs for hydrogen storage. Further experimentations on hydrogen storage in CNTs indicated that bare CNTs are not suitable material for the storage of hydrogen [19–23]. This is because of the weak interaction (van der Waals interaction) between hydrogen molecules and CNTs; hence, more hydrogen can be stored only at lower temperatures through physisorption. Functionalization of CNTs by the addition of atoms or molecules enhances the interaction between hydrogen and CNTs which results in higher storage capacity [24–29]. Moreover, the functionalization of SWCNTs with transition-metal atoms itself occupies more weight percentage on SWCNTs [30]; and also they form strong metal hydrides while hydrogenation which inturn obviously reduce the space for hydrogen storage [31, 32].

In this chapter, a hydrogen storage medium (HSM) based on SWCNTs, capable of storing and delivering hydrogen in the temperature range suitable for fuel cell applications has been developed. Here, the SWCNTs are modified by means of functionalizing them with BH_3. Our earlier computational studies [27] based on density functional theory (DFT) exhibited that functionalization of SWCNTs with BH_3 increases the binding energy of hydrogen molecules, thereby improving the storage capacity too. The theoretical results inspired us to choose BH_3 for functionalization of SWCNTs, experimentally. Moreover, it was pre-determined to carry out the hydrogenation experiments just above room temperature. This was due to the fact that hydrogen storage at very lower temperature and pressure conditions is not feasible for mobile applications. Hydrogenation of the functionalized SWCNTs has been performed for different time durations. Further, the hydrogenated samples were annealed to check the desorption of hydrogen. The amount of hydrogen uptake and desorption temperature range have been calculated. The binding energy of hydrogen and the nature of hydrogen binding were estimated based on the characterization results. Both hydrogenation and dehydrogenation experiments were repeated to examine the reproducibility.

http://dx.doi.org/10.5772/intechopen.75763

2. Theoretical background

To understand the hydrogen storage behavior of CNT and the mechanism of hydrogen binding, we have investigated the hydrogen storage capacity of CNT (10, 0) functionalized with BH_3 using DFT calculations implemented in VASP (Vienna Ab-initio Simulation Package). **Figure 1** shows the front and top views of CNT (10, 0). CNT (10, 0) is an achiral type of zigzag nanotube, whose mirror image has an identical structure to the original one. The shape of the cross section is trans-type. The radius of the tube is 3.96 Å and it has 20 hexagons and 40 carbon atoms per unit cell.

2.1. Computational details

Ultra-soft pseudopotentials treating the electronic states as valence C: $2s^2\ 2p^2$; B: $2s^2\ p^1$; H: $1s^1$ were used. The local density approximation (LDA) was adopted for the exchange-correlation functional. Two unit cells of (10, 0) were taken in a super cell of geometry $28 \times 28 \times 7.92$ Å. The super cell was taken to be large enough since the periodic repetitions do not lead to any effective interactions between neighboring tubes. The super cell of the tube has 20 half and full hexagons. The energy cutoff for the plane wave basis set was 287 eV. The Brillouin zone was sampled by $1 \times 1 \times 8$ mesh points with Monkhorst-pack *k*-point scheme [33]. Twenty BH_3 molecules were attached on 20 full hexagons around the CNT; this corresponds to the full coverage case. The structures were optimized using conjugate gradient algorithm. Convergence was achieved when the energy was less than 1×10^{-5} eV/atom and 0.5×10^{-5} eV/Å. The hydrogen molecules were attached to the SWCNT–BH_3 complex with a bond length of 0.74 Å parallel to the tube axis. The binding energy of the BH_3 molecule was calculated as

$$E_B\,(BH_3) = [E_T\,(\text{SWCNT} - 20BH_3) - E_T\,(\text{SWCNT}) - 20E_T\,(BH_3)]/m \quad (1)$$

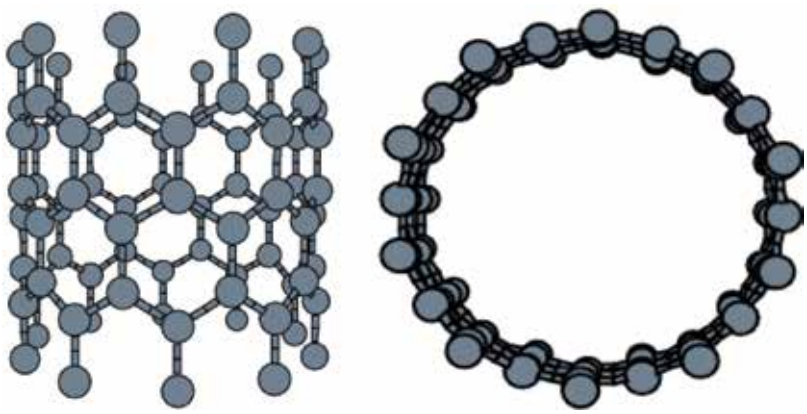

Figure 1. Front and top views of CNT (10, 0).

In a similar way, the binding energy per H_2 molecule was calculated as

$$E_B\,(H_2) = [E_T\,(\mathrm{SWCNT} - 20BH_3 + mH_2) - E_T\,(\mathrm{SWCNT} - 20BH_3) - m \times E_T\,(H_2)]/m \quad (2)$$

where E_T denotes the total energy of the respective systems. The integer m represents the number of H_2 molecule adsorbed on the surface.

2.2. Functionalization

Being light weight and hydrogen rich, BH_3 is able to adsorb H_2 molecules as adsorbates on the surface of CNT. Two unit cells of CNT (10, 0) contain 20 complete hexagons. It is reported that the center of a hexagon is the most stable state for adsorbates [34]. We have attached a single BH_3 on the center of each hexagon at a distance of 2 Å from the surface of the tube. The system $C20BH_3$ refers to CNT (10, 0) + $20BH_3$ complex. After relaxation, the equilibrium position of BH_3 occurs at 2.6 Å from the surface of the tube with an increased bond length of 1.2 Å and an average bond angle of 119°. **Figure 2a** and **b** shows the structure of $C20BH_3$ before and after relaxation, respectively. The binding energy per BH_3 is 3.98 eV. In the figures, gray, parrot green and white color balls represent the carbon, boron, and hydrogen atoms, respectively.

2.3. Hydrogenation

2.3.1. C20(BH_3 + H_2)

A single H_2 molecule is attached to each BH_3 at 2 Å distance from the surface of the tube in the relaxed structure of $C20BH_3$. This complex C20(BH_3 + H_2) is relaxed and the H_2 close to BH_3 has been displaced. Now the distance between BH_3 and H_2 reduces to 1.47 Å. After relaxation, the bond length of H_2 molecule has been increased from 0.74 to 0.9 Å. The relaxed structure of the system C20(BH_3 + H_2) is shown in **Figure 3a**. The binding energy of a single H_2 molecule is 0.86 eV, the storage capacity is 3.16 wt%, and the desorption temperature is 1100 K.

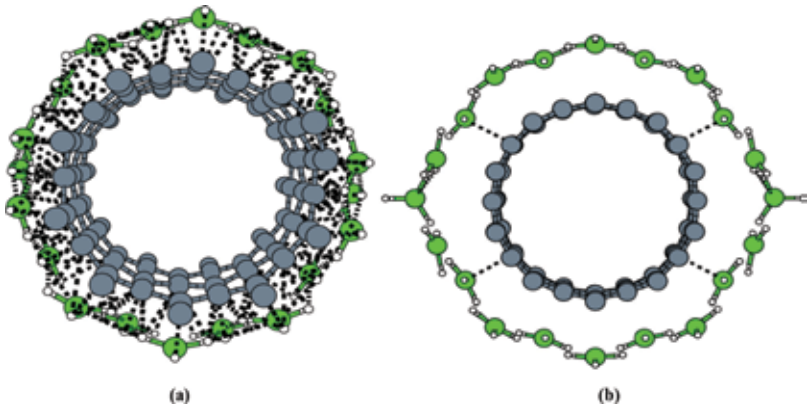

Figure 2. Structure of $C20BH_3$ before relaxation and after relaxation.

http://dx.doi.org/10.5772/intechopen.75763

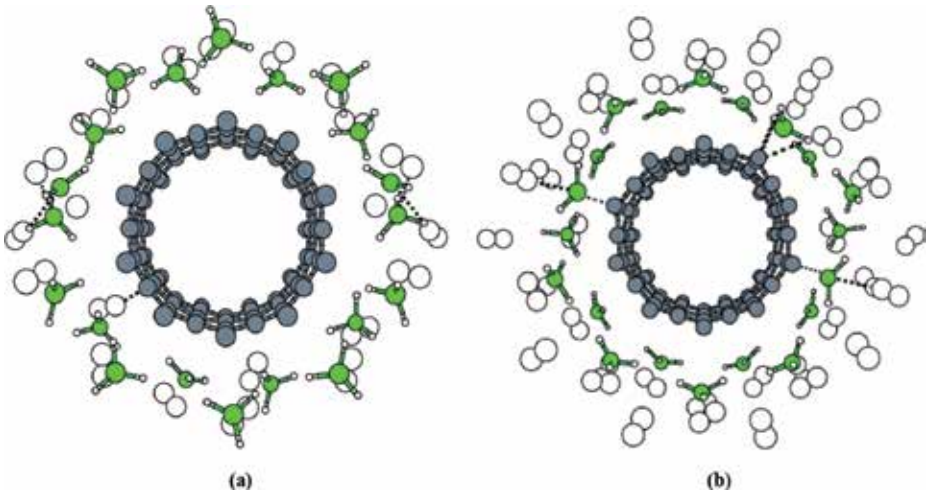

Figure 3. (a) Relaxed structure of C20(BH_3 + H_2) (b) relaxed structure of C20(BH_3 + $2H_2$).

2.3.2. C20(BH_3 + $2H_2$)

Another H_2 molecule is attached to each BH_3. The C20(BH_3 + $2H_2$) structure is relaxed and the H_2 has been displaced from the distance of 2 to 4 Å. After relaxation, the bond length of H_2 molecule has been increased from 0.74 to 0.78 Å. The relaxed structure of the system C20 (BH_3 + $2H_2$) is shown in **Figure 3b**. The binding energy of a H_2 molecule is 0.38 eV, the hydrogen storage capacity is 6.12 wt%, and the desorption temperature is calculated as 486 K.

2.3.3. C20(BH_3 + $3H_2$)

The binding energy of the system C20(BH_3 + $2H_2$) lies in the range of ideal binding energy 0.2–0.4 eV. Hence, the system can adsorb more number of hydrogen. The third H_2 adsorbed on BH_3 is moved away from the BH_3 after relaxation. It is adsorbed at 3.42 Å and the bond length of H_2 molecule has been increased from 0.74 to 0.83 Å. The relaxed structure of the system C20 (BH_3 + $3H_2$) is shown in **Figure 4a**. The binding energy of a H_2 molecule is 0.24 eV, the storage capacity of the system is 8.9 wt%, and the desorption temperature is 307 K.

2.3.4. C20(BH_3 + $4H_2$)

Another H_2 molecule is added to each BH_3. This structure is relaxed and the H_2 has been adsorbed at a distance of 3.39 Å. After relaxation, the bond length of H_2 molecule has been increased from 0.74 to 0.83 Å. The relaxed structure of the system C20(BH_3 + $4H_2$) is shown in **Figure 4b**. In this case, the H_2 molecules are weakly bound, and the binding energy is found to be 0.16 eV, which lies below the ideal binding energy of H_2.

All H_2 are molecularly physisorbed through BH_3 and oriented randomly on CNT. The binding energy of H_2, storage capacity, and desorption temperature of all the systems are given in **Table 1**. The electrostatic interaction is responsible for the binding of H_2 on the (CNT + BH_3)

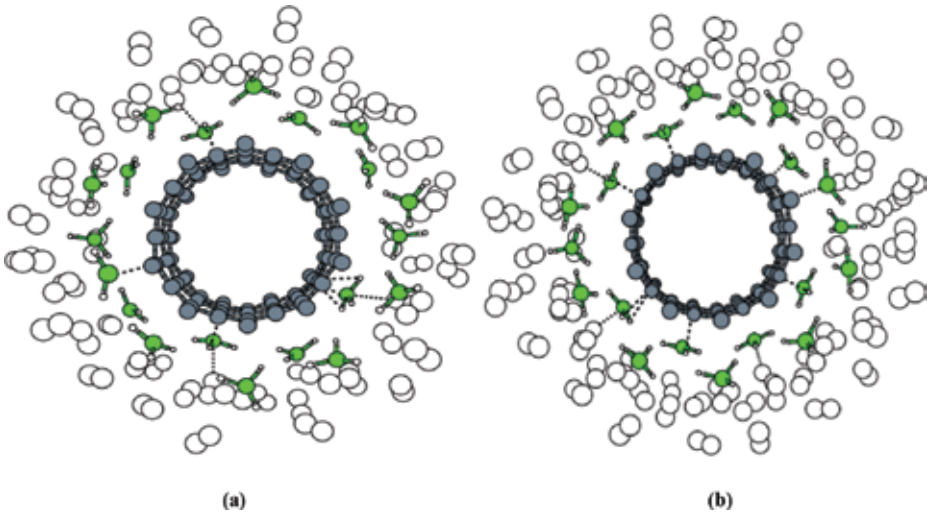

Figure 4. (a) Relaxed structure of C20(BH_3 + $3H_2$) (b) relaxed structure of C20(BH_3 + $4H_2$).

System	Binding energy/H_2 (eV)	Desorption temperature (K)	Storage capacity (wt%)
CNT20(BH_3 + H_2)	0.86	1100	3.16
CNT20(BH_3 + $2H_2$)	0.38	486	6.12
CNT20(BH_3 + $3H_2$)	0.24	307	8.90
CNT20(BH_3 + $4H_2$)	0.16	208	11.5

Table 1. Storage capacities for system C20(BH_3 + nH_2) (n = 1–4).

complex. Since the binding energy of BH_3 is higher than the H_2 binding energy range, only H_2 molecules will be released during desorption and not the BH_3 molecules.

3. Experimental

3.1. Materials

SWCNTs were purchased from Sigma Aldrich with a purity of >98% and purified using acid treatment. $LiBH_4$ was purchased from Sigma Aldrich with an assay of >95%. The other reagents and chemicals used for experiments were purchased from Merck with 99% purity. Alumina substrates of dimension 19 × 19 × 0.65 mm were used. The substrates were cleaned with chromic acid, acetone, and distilled water by means of sonication for 30 minutes (alumina substrates were taken as they are stable at higher temperatures).

3.2. Purification of SWCNTs

Generally, commercial CNTs contain a major component of CNTs along with amorphous carbon structures and metal catalyst impurities (that might be used during the synthesis

process) in few proportions. Hence, it is essential to purify the CNTs before conducting experiments. The purification steps involved heating at 300°C for 1 hour, acid treatment, and repeated washing.

3.3. Designing of hydrogen storage setup

A chamber made up of stainless steel has been designed for our hydrogen storage experiments and is named as hydrogen storage setup. The length of the chamber is about 45 cm with a diameter about 10 cm. The thickness of the stainless sheet is about 0.5 cm. The schematic diagram of the hydrogen storage setup is shown in **Figure 5**. In the figure, the size of the gas inlet valve is large compared to the gas outlet valve. This has been made intentionally to make some amount of gas exist in the chamber to react with samples during the hydrogenation experiment. Moreover, the sample is placed in the path of gas outlet. This is because of the reason that; the gas should meet the sample before leaving the chamber. The sample holder is also made up of stainless steel sheet. Commercial hydrogen gas (purity >90%) cylinders has been used for the experiments.

3.4. SWCNT deposition and functionalization

A well dispersed solution of SWCNTs was deposited on alumina substrates and a subsequent heating up to 200°C was done. $LiBH_4$ (the precursor for BH_3) was mixed with diethyl ether ($(C_2H_5)_2O$) in a ratio of 25 mg/ml, and it was drop casted over the surface of SWCNTs. Then the substrates were heated to 275°C (decomposition temperature of $LiBH_4$) for 1 hour, which yields borane. The released BH_3 reacts with SWCNTs and forms a complex, SWCNT + BH_3. This complex acts as an HSM.

3.5. Hydrogenation

The functionalized samples were loaded in the hydrogenation setup and hydrogenated as detailed in this section. Initially, we would like to know whether the functionalized SWCNTs exhibit hydrogen storage capability at a temperature around 100 or 50°C. For that, the functionalized samples were maintained at a particular temperature and the hydrogen gas was allowed to flow for some time interval at a known flow rate and then the samples were left in the chamber to attain room temperature. After hydrogenation, the hydrogen content present in the samples was again estimated using CHNS-elemental analysis. The initial hydrogenation results we got were encouraging. The results are presented in **Table 2**. After the confirmation of the hydrogen storage ability of functionalized SWCNTs, we improved our hydrogenation setup by introducing a few controlled valves to reduce the leakage of hydrogen gas. The

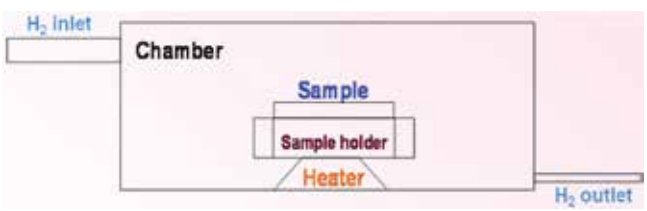

Figure 5. Schematic diagram of hydrogen storage setup.

Substrate temperature (°C)	Flow rate (liter/min)	Flow duration (min)	Storage capacity (wt.%)
100	1	4	0.68
100	1	20	0.87
50	3	20	1.50

Table 2. Initial hydrogenation results.

Sample index	Flow rate (liter/min)	Flow duration (min)	Storage capacity (wt.%)
CBH1	0.5	30	3.27
CBH2	0.5	35	3.78
CBH3	0.5	40	4.35
CBH4	0.5	45	4.77

CBH1–4 represents four different hydrogenated samples.

Table 3. Optimized hydrogenation results.

functionalized samples were loaded in the hydrogenation setup and hydrogenated for different time durations by maintaining the substrate temperature at 50°C and the hydrogen flow rate at ~0.5 liter/minute. The storage capacities were calculated as the difference of hydrogen content in the samples before and after the hydrogenation experiment and the results are presented in **Table 3**.

3.6. Dehydrogenation

Thermal annealing was used to stimulate the dehydrogenation from the hydrogenated samples. The hydrogenated samples were annealed at 200°C for 1 hour. The temperature was controlled by a digital proportional-integral-derivative (PID) controller. After annealing, the samples were left in the furnace to reach room temperature and then characterized.

3.7. Characterizations

The morphology of SWCNTs was analyzed by transmission electron microscope (TEM) imaging using a JEOL JEM 2100 model unit with an accelerating voltage of 200 kV. The energy dispersive (ED) spectrum of SWCNTs was recorded using the JEOL model 6390 unit with an accelerating voltage of 5 kV. Infrared (IR) spectrum was recorded over the range 4000–450 cm^{-1} using a Shimadzu model (FTIR-8400S, CE) spectrometer at room temperature with a resolution of 1 cm^{-1}. X-ray photoelectron spectroscopy (XPS) measurements were taken using a Scienta ESCA3000 model spectrometer. Raman measurements were carried out using a Labram HR800 model spectrometer. The samples were excited with a 17 mW (~633 nm) He–Ne laser. Before taking measurements, the spectrometer was calibrated using a silica wafer. An Elementar Vario EL III model analyzer was used for CHNS-elemental analysis. A Perkin Elmer-Diamond model unit was used to study the thermal response of the samples.

http://dx.doi.org/10.5772/intechopen.75763

4. Results and discussion

4.1. Morphology, elemental and functional group analyses

Figure 6(a) shows the TEM image of SWCNTs. The image reveals the good distribution and separation of SWCNTs with an average diameter of 2–4 nm. The ED spectrum of SWCNTs shown in **Figure 6(b)** displays the existence of carbon and oxygen in the sample along with copper resulting from the supporting grid. The functional groups present in the functionalized SWCNTs are determined from the bands appearing in the IR spectrum. **Figure 7** shows the IR spectrum of the functionalized SWCNTs. Absorption peaks at 1608, 1027, and 729 cm^{-1} correspond to C=C stretching, C–C stretching, and skeleton vibrations of carbon atoms in CNTs, respectively. The electrostatic interaction between BH_3 and CNT caused the deformation [35] and asymmetric stretching [36] of B–H bonds; the resultant respective peaks are observed at 1260 and 2350 cm^{-1}. On the other hand, the appearance of a peak at 1430 cm^{-1} is due to C–H asymmetric deformation vibrations of the dissociative adsorption of BH_3 on CNT. The results of the IR study authenticate that the SWCNTs functionalized with BH_3 is stable and is agreed with the theoretical results [25].

The composition of elements present in the functionalized sample is found from the X-ray photoelectron spectroscopy (XPS) spectrum. The full survey spectrum of the functionalized sample is shown in **Figure 8**. The de-convoluted XPS spectra of the individual components, such as C, Li, B, and O are shown in **Figure 9(a)–(d)**, respectively. The C 1s component at 286.3 eV is assigned to C–O or C–OH bond [37] and a small peak at 290.9 eV is due to Li_2CO_3. The peak at 56.7 eV is attributed to Li. The lower binding energy component (188.9 eV) is assigned to boron atoms bonded only to the other boron atoms [38, 39], whereas the higher energy component (193.8 eV) represents the oxidized boron [40, 41]. The main O 1s component is assigned to boron oxide [39]. The weight percentages are 44.7, 15.4, 7.1, and 28.7 for the elements C, B, Li, and O, respectively. From the XPS studies, it is observed that the incorporation of

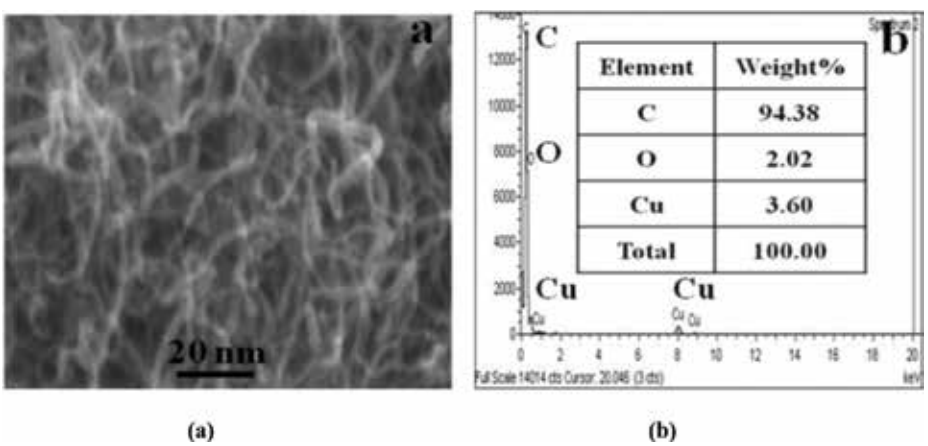

Figure 6. (a) TEM image and (b) ED spectrum of SWCNTs.

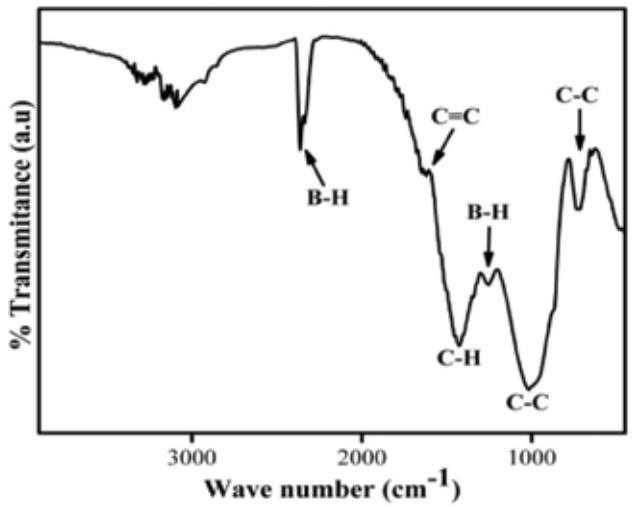

Figure 7. IR spectrum of functionalized SWCNTs.

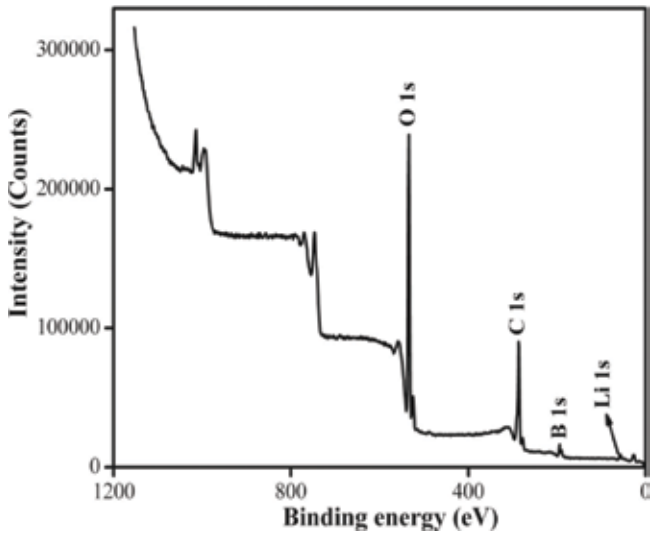

Figure 8. XPS survey spectrum of functionalized SWCNTs.

oxygen present in the functionalized sample is ~30 wt%. This incorporation may be due to the deposition of samples carried out in open atmosphere.

4.2. Hydrogenation analyses

The quantity of hydrogen stored in the functionalized samples is measured from the CHNS-elemental analysis. The hydrogenation results are shown in **Tables 2** and **3**. The storage capacity at this temperature (50°C) of the designed storage medium is much higher than the

http://dx.doi.org/10.5772/intechopen.75763

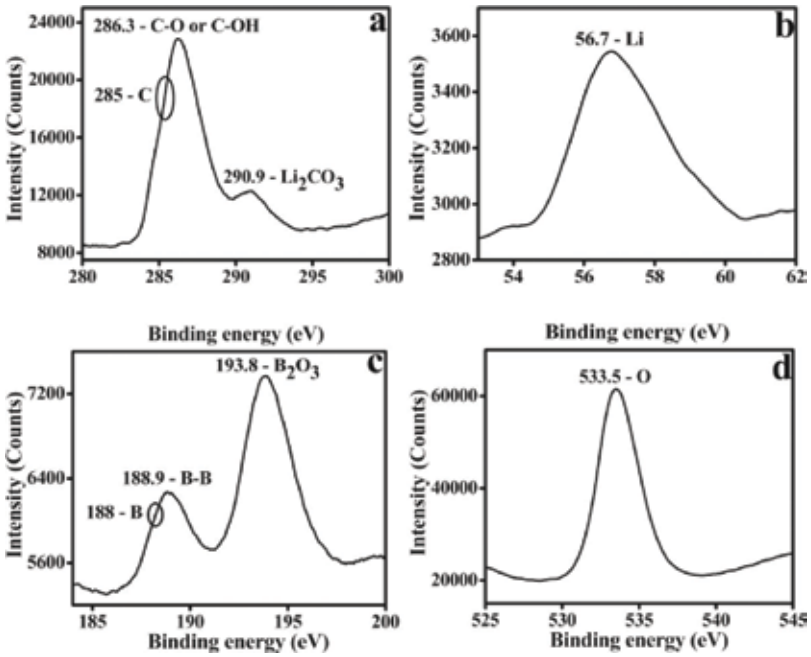

Figure 9. De-convoluted XPS spectra of (a) carbon, (b) Lithium, (c) boron and (d) oxygen.

values reported by Ioannatos et al. [1], Im et al. [39], and Li et al. [42]. **Figure 10** shows the Raman spectra of SWCNTs (C), SWCNTs functionalized with BH_3 (CB), and hydrogenated functionalized SWCNTs (CBH). In the entire spectrum, the D and G bands appeared around 1350 and 1570 cm^{-1}, respectively. The defect concentration in CNT can be measured by calculating the intensity ratio of the D to G band. As the defect density increased for the samples from SWCNTs, functionalized SWCNTs to hydrogenated SWCNTs, the corresponding D/G ratio has also increased from 0.08, 0.21, to 0.59. The Raman and CHN-elemental analyses are together used to probe dehydrogenation (the dehydrogenated sample and is designated as DCB). The hydrogenation and dehydrogenation experiments are repeated a number of times and the corresponding D/G ratio is also measured. The deterioration level of the functionalized SWCNTs after repeated hydrogenation and dehydrogenation is only about 2.3%. A similar change of 3% was reported by Zhang et al. [43]. The hydrogen storage capacity varies 5% about the mean value.

4.3. Desorption analyses

Figure 11 shows the TG spectra of all hydrogenated samples CBH1, CBH2, CBH3, CBH4 and **Figure 12** shows the region associated with hydrogen desorption. The spectrum for the sample CBH1 shows a weight loss of about 3.27 wt% in the temperature range 105–140°C and it corresponds to the desorption of stored hydrogen from the sample. The desorption profile shown in **Figure 12** exactly measures the starting and end temperatures of the desorption. The primary weight loss is attributed to hydrogen desorption since the desorption of borane starts above 275°C. The findings obtained from TG analysis are in line with Raman results.

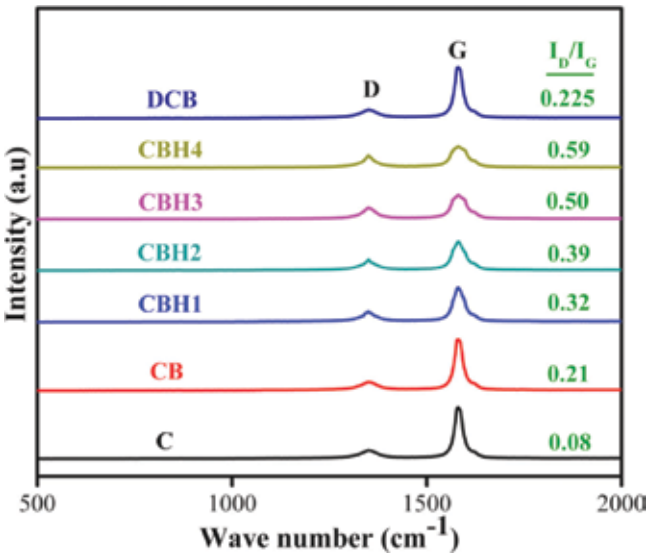

Figure 10. Raman spectra of all the samples.

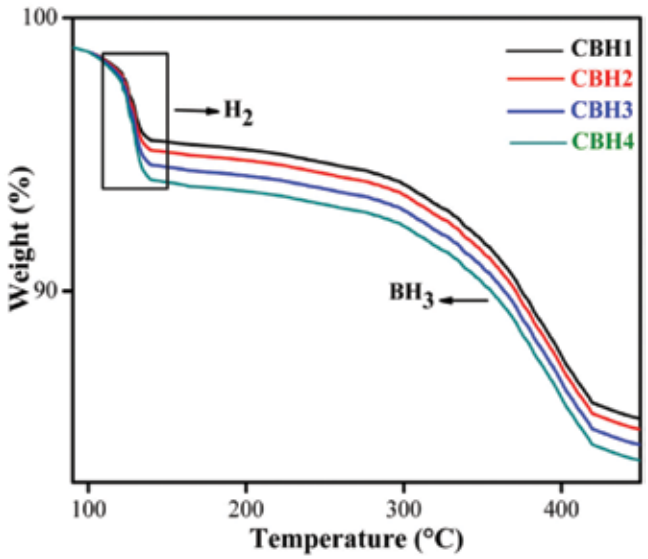

Figure 11. TG spectra of all the hydrogenated samples.

The activation energy of desorption, E_d can be calculated from the maximum desorption peak using the following Equation [1],

$$\ln\left(T_m{}^2/\beta\right) = E_d/R{*}T_m \tag{3}$$

where T_m is the temperature at maximum peak (121°C), β is the heating rate (10°C/min), and R is the universal gas constant. The calculated activation energy of desorption for the sample

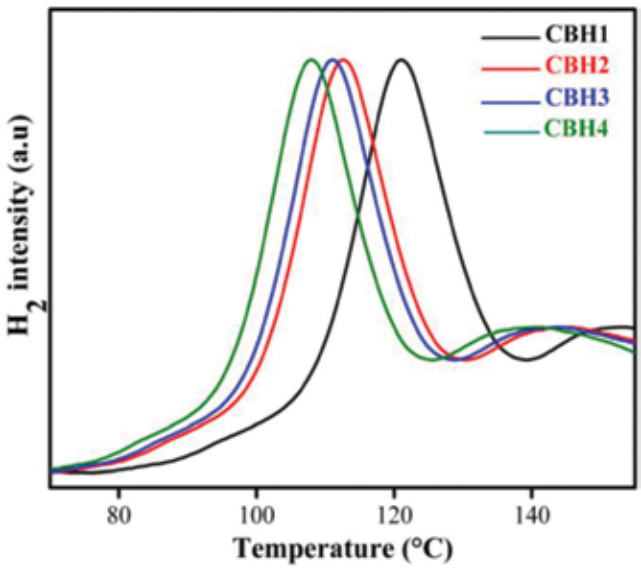

Figure 12. Desorption spectra of all the hydrogenated samples.

Sample index	H_2 (wt.%)	T_m (°C)	E_d (kJ/mol)	E_B (eV)
CBH1	3.277	121	20.66	0.310
CBH2	3.785	113	20.11	0.302
CBH3	4.345	111	19.97	0.300
CBH4	4.770	107	19.69	0.287

Table 4. Hydrogen desorption characteristic parameters.

CBH1 is 20.66 kJ/mol. Van't Hoff Equation [2] is applied to estimate the binding energy (E_B) of hydrogen,

$$E_B = T * K_B\ (\Delta S/R) \tag{4}$$

where T is the desorption temperature, K_B is Boltzmann's constant and ΔS is change in entropy. The estimated binding energy value is 0.31 eV per H_2 for the temperature 121°C. The various factors found from the hydrogenation and dehydrogenation studies are presented in **Table 4**. From the desorption profile, it is apparent that the desorption peak temperature reduces with the increase in hydrogen storage capacity.

The obtained binding energy values fall in the weak chemisorption region, and is in the suggested region (0.2–0.4 eV) for a practical hydrogen storage medium [7]. The functionalized SWCNTs and hydrogen interact through a combination of inductive, covalent, and electrostatic charge transfer mechanisms [7, 25] amidst CNTs and hydrogen, borane anchored as a bridge. The composition presence of hydrogen measured from CHNS analysis is equivalent to

the weight lost in the thermogravimetric study, i.e., the quantity of hydrogen desorbed is equal to the quantity of hydrogen adsorbed. Thus, our system exhibits 100% desorption in the temperature range 90–140°C, which may be more suitable for vehicular-based fuel cells than the desorption temperature reported by Arellano et al. [21] and Lee et al. [44]. This observation reveals that the adsorption sites on CNTs surface are relatively uniform and that there are no sites which form very weak or very strong adsorption bonds [1]. On the whole, the present investigation reveals the ability of reversible hydrogen uptake by the functionalized SWCNTs.

5. Summary

In this chapter, the hydrogenation and dehydrogenation studies of SWCNTs functionalized with BH_3 are presented. The SWCNTs are successfully functionalized with BH_3 using $LiBH_4$ as the precursor. The deposition process involves a simple drop casting method. The presence of BH_3 in the functionalized sample is confirmed using IR study. From XPS study, apart from C, the presence of Li, B, and O are also observed in the functionalized sample. Then, the functionalized samples are hydrogenated for different time durations. A maximum storage capacity of 4.77 wt% is achieved at 50°C, which is close to the U.S. DOE target of 5.5 wt% for an HSM to be used for on-board applications. Based on thermal annealing, a systematic investigation of desorption of hydrogen is carried out. The evidences for desorption is provided by Raman, CHNS-elemental, and TG measurements. The results show that thermal annealing treatment induces desorption of hydrogen from the hydrogenated functionalized SWCNTs. The stored hydrogen is released over the temperature range 90–140°C. The deterioration level of the sample is also checked using Raman analysis. Overall, this investigation shows that the SWCNTs functionalized with BH_3 may be a suitable reversible hydrogen storage system that is capable of storing and releasing hydrogen under optimum conditions over repeated cycles suitable for hydrogen-based fuel cells used in vehicular applications.

Author details

Duraisamy Silambarasan[1,2]*, Velappa Jayaraman Surya[3,4], Veerapandy Vasu[1] and Kombiah Iyakutti[3]

*Address all correspondence to: simbuphysics@yahoo.com

1 School of Physics, Madurai Kamaraj University, Madurai, Tamil Nadu, India

2 PG and Research Department of Physics, The MDT Hindu College, Tirunelveli, Tamil Nadu, India

3 Department of Physics and Nanotechnology, SRM University, Kattankulathur, Tamil Nadu, India

4 SRM Research Institute, SRM University, Kattankulathur, Tamil Nadu, India

References

[1] Ioannatos GE, Verykios XE. H_2 storage on single- and multi-walled carbon nanotubes. International Journal of Hydrogen Energy. 2010;**35**:622-628. DOI: 10.1016/j.ijhydene.2009.11.029

[2] Durgun E, Ciraci S, Yildirim T. Functionalization of carbon-based nanostructures with light transition-metal atoms for hydrogen storage. Physical Review B. 2008;**77**:085405-085409. DOI: 10.1103/PhysRevB.77.085405

[3] Orimo S, Nakamori Y, Eliseo JR, Züttel A, Jensen CM. Complex Hydrides for Hydrogen Storage. Chemical Review. 2007;**107**:4111-4132. DOI: 10.1021/cr0501846

[4] Zhang J, Hu YH. Intermediate species and kinetics of lithium imide decomposition. International Journal of Hydrogen Energy. 2012;**37**:10467-10472. DOI: 10.1016/j.ijhydene.2011.12.061

[5] Hu YH, Zhang L. Hydrogen storage in metal-organic frameworks. Advanced Materials. 2010;**22**:E117-E130. DOI: 10.1002/adma.200902096

[6] Murray LJ, Dinca M, Long JR. Hydrogen storage in metal-organic frameworks. Chemical Society Review. 2009;**38**:1294-1314. DOI: 10.1039/B802256A

[7] Lochan RC, Head-Gordon M. Computational studies of molecular hydrogen binding affinities: The role of dispersion forces, electrostatics, and orbital interactions. Physical Chemistry Chemical Physics. 2006;**8**:1357-1370. DOI: 10.1039/b515409j

[8] Li J, Terumi F, Hajime G, Toshiyuki O, Yoshiya F, Sidney Y. Theoretical evaluation of hydrogen storage capacity in pure carbon nanostructures. Journal of Chemical Physics. 2003;**119**:2376-2385. DOI: 10.1063/1.1582831

[9] Duplock EJ, Scheffler M, Lindan PJD. Hallmark of perfect graphene. Physical Review Letters. 2004;**92**:225502–1–225502-4. DOI: 10.1103/PhysRevLett.92.225502

[10] Zuttel A, Sudan P, Mauron P, Kyobayashi T, Emenenrgger C, Schlapbach L. Hydrogen storage in carbon nanostructures. International Journal of Hydrogen Energy. 2002;**27**: 203-212. DOI : S0360-3199(01)00108-2

[11] Zhao M-W, Xia Y-Y, Ma Y-C, Ying M-J, Liu X-D, Mei L-M. Tunable adsorption and desorption of hydrogen atoms on single-walled carbon nanotubes. Chinese Physics Letters. 2002;**19**:1498-1500. DOI: cpl.iphy.ac.cn/Y2002/V19/I10/01498

[12] Okati A, Zolfaghari A, Hashemi FS, Anousheh N, Jooya H. Hydrogen Physisorption on stone-Wales defect-embedded single-walled carbon nanotubes. Fullerenes, Nanotubes, and Carbon Nanostructures. 2009;**17**:324-335. DOI: 10.1080/15363830902776599

[13] Muniz AR, Meyyappan M, Maroudas D. Effects of hydrogen chemisorption on the structure and deformation of single-walled carbon nanotubes. Applied Physics Letters. 2009;**95**:163111–1–163111-3. DOI: 10.1063/1.3095923

[14] Rzepka M, Lamp P, de la Casa-Lillo MA. Physisorption of hydrogen on microporous carbon and carbon nanotubes. The Journal of Physical Chemistry. B 1998;**102**:10894-10898. DOI:10.1021/jp9829602

[15] Lee SM, An KH, Lee YH, Seifert G, Frauenheim T. A hydrogen storage mechanism in single-walled carbon nanotubes. Journal of American Chemical Society. 2001;**123**:5059-5063. DOI: 10.1021/ja003751+

[16] Darkrim FL, Levesque D. Monte Carlo simulations of hydrogen adsorption in single-walled carbon nanotubes. Journal of Chemical Physics. 1998;**109**:4981-4984. DOI: 10.1063/1.477109

[17] Cheng JR, Yuan XH, Zhao L, Huang DC, Zhao M, Dai L, Ding R. GCMC simulation of hydrogen physisorption on carbon nanotubes and nanotube arrays. Carbon. 2004;**42**:2019-2024. DOI: 10.1016/j.carbon.2004.04.006

[18] He Z, Wang S, Wang X, Iqbal Z. Hydrogen storage in hierarchical nanoporous silicon–carbon nanotube architectures. International Journal of Energy Research. 2013;**37**:754-760. DOI: 10.1002/er.2979

[19] Dillon AC, Jones KM, Bekkendahl TA, Kiang CH, Bethune DS, Heben MJ. Storage of hydrogen in single-walled carbon nanotubes. Nature. 1997;**386**:377-379. DOI: 10.1038/386377a0

[20] Ye Y, Ahn CC, Witham C, Fultz B, Liu J, Rinzler AG, Colbert D, Smith KA, Smalley RE. Hydrogen adsorption and cohesive energy of single-walled carbon nanotubes. Applied Physics Letters. 1999;**74**:2307-2309. DOI: 10.1063/1.123833

[21] Arellano JS, Molina LM, Rubio A, MJ L'p, Alonso JA. Interaction of molecular and atomic hydrogen with (5,5) and (6,6) single-wall carbon nanotubes. Journal of Chemistry Physics. 2002;**117**:2281-2288. DOI: 10.1063/1.1488595

[22] Sudan P, Zuttel A, Mauron P, Emmenegger C, Wenger P, Schlapbach L. Physisorption of hydrogen in single-walled carbon nanotubes. Carbon. 2003;**41**:2377-2383. DOI: 10.1016/S0008-6223(03)00290-2

[23] Tibbetts GG, Meisner GP, Olk CH. Hydrogen storage capacity of carbon nanotubes, filaments, and vapor-grown fibers. Carbon. 2001;**39**:2291-2301. DOI: 10.1016/S0008-6223(01)00051-3

[24] Wu XM, Wang Y, Dong KM, Zhou JM, Lin GD, Zhang HB. Study of storage and adsorption/desorption characteristics of H_2 on MWCNTs modified by metal potassium. Acta Chimica Sinica. 2005;**63**:484-490

[25] Surya VJ, Iyakutti K, Rajarajeswari M, Kawazoe Y. Functionalization of single-walled carbon nanotube with borane for hydrogen storage. Physica E: Low-dimensional Systems and Nanostructures. 2009;**41**:1340-1346. DOI: 10.1016/j.physe.2009.03.007

[26] Liu W, Zhao YH, Li Y, Jiang Q, Lavernia EJ. Enhanced hydrogen storage on Li-dispersed carbon nanotubes. Journal of Physical Chemistry C. 2009;**113**:2028-2033. DOI: 10.1021/jp8091418

[27] Surya VJ, Iyakutti K, Venkataramanan NS, Mizuseki H, Kawazoe Y. Single walled carbon nanotubes functionalized with hydrides as potential hydrogen storage media: A survey of intermolecular interactions. Physical Status Solidi B. 2011;**248**:2147-2158. DOI: 10.1002/pssb.201046532

[28] Reyhani A, Mortazavi SZ, Mirershadi S, Moshfegh AZ, Parvin P, Nozad Golikand A. Hydrogen storage in decorated multiwalled carbon nanotubes by Ca, co, Fe, Ni, and Pd nanoparticles under ambient conditions. Journal of Physical Chemistry C. 2011;**115**:6994-7001. DOI: 10.1021/jp108797p

[29] Reddy ALM, Ramaprabhu S. Hydrogen adsorption properties of single-walled carbon nanotube-Nanocrystalline platinum composites. International Journal of Hydrogen Energy. 2008;**33**:1028-1034. DOI: 10.1016/j.ijhydene.2007.11.005

[30] Iyakutti K, Kawazoe Y, Rajarajeswari M, Surya VJ. Aluminum hydride coated single-walled carbon nanotube as a hydrogen storage medium. International Journal of Hydrogen Energy. 2009;**34**:370-375. DOI: 10.1016/j.ijhydene.2008.09.086

[31] Yildirim T, Ciraci S. Titanium-decorated carbon nanotubes as a potential high-capacity hydrogen storage medium. Physical Review Letters. 2005;**94**:175501-1-175501-4. DOI: 10.1103/PhysRevLett.94.175501

[32] Jianwei R, Shijun L, Junmin L. Hydrogen storage of multiwalled carbon nanotubes coated with Pd-Ni nanoparticles under moderate conditions. Chinese Science Bullettin. 2006;**51**: 2959-2963. DOI: 10.1007/s11434-006-2216-8

[33] Monkhorst HJ, Pack JD. Special points for Brillouin-zone integrations. Physical Review B. 1976;**13**:5188-5192

[34] Iyakutti K, Rajarajeswari M, Dharmawardhana MWC. The interaction of nitrogen molecules with (4,0) single-walled carbon nanotube: Electronic and structural effects. Nanotechnology 2008;**19**:185704–185701–185704-4. DOI:10.1088/0957-4484/19/18/185704

[35] Kaldor A, Porter RF. Infrared spectra of the pyrolysis products of Borane carbonyl in an argon matrix. Journal of American Chemical Society. 1971;**93**:2140-2145

[36] Nakamoto K. Infrared and Raman Spectra of Inorganic and Coordination Compounds: Part A: Theory and Applications in Inorganic Chemistry. 6th ed. Newyork: Wiley; 1978. DOI: 10.1002/9780470405840

[37] Vickerman JC. Surface Analysis - The Principle Techniques. 2nd ed. Chichester: Wiley; 1997. DOI: 10.1002/9780470721582

[38] Guo L, Singh RN, Kleebe HJ. Growth of boron-rich nanowires by chemical vapor deposition (CVD). Journal of Nanomaterials. 2006;**2006**:58237-1-58237-6. DOI: 10.1155/JNM/2006/58237

[39] Ong CW, Huang H, Zheng B, Kwok RMW, Hui YY, Lau WM. X-ray photoemission spectroscopy of nonmetallic materials: Electronic structures of boron and BxOy. Journal of Applied Physics. 2004;**95**:3527-3534. DOI: 10.1063/1.1651321

[40] Xu TT, Zheng JG, Wu NQ, Nicholls AW, Roth JR, Dikin DA, Ruoff RS. Crystalline boron Nanoribbons: Synthesis and characterization. Nano Letters. 2004;**4**:963-968. DOI: 10.1021/nl0498785

[41] Im JS, Yun J, Kang SC, Lee JK, Lee Y-S. Hydrogen adsorption on activated carbon nanotubes with an atomic-sized vanadium catalyst investigated by electrical resistance measurements. Applied Surface Science. 2012;**258**:2749-2756. DOI: 10.1016/j.apsusc.2011.10.126

[42] Li B, Huang X, Gong R, Ma M, Yang X, Liang L, Tan B. Catalyzed hydrogen spillover for hydrogen storage on microporous organic polymers. International Journal of Hydrogen Energy. 2012;**37**:12813-12820. DOI: 10.1016/j.ijhydene.2012.05.106

[43] Zhang G, Qi P, Wang X, Lu Y, Mann D, Li H, Dai H. Hydrogenation and Hydrocarbonation and etching of single-walled carbon nanotubes. Journal of American Chemical Society. 2006;**128**:6026-6027. DOI: 10.1021/ja061324b

[44] Lee H, Nguyen MC, Ihm J. Titanium-functional group complexes for high-capacity hydrogen storage materials. Solid State Communication. 2008;**146**:431-434. DOI: 10.1016/j.ssc.2008.03.018

Edited by Mohammed Muzibur Rahman and Abdullah Mohamed Asiri

The book *Carbon Nanotubes - Recent Progress* contains a number of recent researches on synthesis, growth, characterization, development, and potential applications on carbon materials especially CNTs in nanoscale. It is a promising novel research from top to bottom that has received a lot of interest in the last few decades. It covers the advanced topics on the physical, chemical, and potential applications of CNTs. Here, the interesting reports on cutting-edge science and technology related to synthesis, morphology, control, hybridization, and prospective applications of CNTs are concluded. This potentially unique work offers various approaches on the R&D implementation of carbon-related materials and their hybrids. Basically, we know that nanotechnology offers the regulating of substances at the nanoscale and nanodimension substances in few nanometers, in which exclusive phenomenon facilitates us to control the novel practical applications with carbon materials or CNTs. Here, in this book, an overview of current CNTs' fundamental and substantial applications and enactment of the research worldwide is presented. The techniques of CNT preparation, types of carbon material utilization, and possible applications related with CNTs or carbon-hybrid material researches were investigated. It is an important booklet for research organizations, governmental research centers, academic libraries, and R&D affianced in recent research and development of carbon nanotubes.

Published in London, UK

IntechOpen

ISBN 978-1-83881-343-7